Dispersively improved vector-meson-dominance approaches to precision observables

Dissertation
zur
Erlangung des Doktorgrades (Dr. rer. nat.)
der
Mathematisch-Naturwissenschaftlichen Fakultät
der
Rheinischen Friedrich-Wilhelms-Universität Bonn

vorgelegt von
Marvin Zanke
aus
Bonn

Bonn, April 2024

Angefertigt mit Genehmigung der Mathematisch-Naturwissenschaftlichen Fakultät
der Rheinischen Friedrich-Wilhelms-Universität Bonn

Gutachter/Betreuer:	PD Dr. Bastian Kubis
Gutachter:	Prof. Dr. Christoph Hanhart
Tag der Promotion:	10.07.2024
Erscheinungsjahr:	2024

To my parents,
Rüdiger and Gudrun

I saw my life branching out before me like the green fig tree in the story.
From the tip of every branch, like a fat purple fig,
a wonderful future beckoned and winked.
One fig was a husband and a happy home and children,
and another fig was a famous poet
and another fig was a brilliant professor,
and another fig was Ee Gee, the amazing editor,
and another fig was Europe and Africa and South America,
and another fig was Constantin and Socrates and Attila
and a pack of other lovers with queer names and offbeat professions,
and another fig was an Olympic lady crew champion,
and beyond and above these figs were many more figs I couldn't quite make out.
I saw myself sitting in the crotch of this fig tree, starving to death,
just because I couldn't make up my mind which of the figs I would choose.
I wanted each and every one of them, but choosing one meant losing all the rest,
and, as I sat there, unable to decide, the figs began to wrinkle and go black,
and, one by one, they plopped to the ground at my feet.

A quote from the book *The Bell Jar* by Sylvia Plath

Abstract

To this day, describing the interaction of hadrons poses a challenge. Although quantum chromodynamics is well established by now, its non-perturbative nature at low energies renders it impossible to perform perturbative calculations in this energy regime, as, *e.g.*, feasible in the realm of quantum electrodynamics. Conjectured to be related to this behavior is the observation of confinement, stating that quarks and gluons cannot exist as free particles under ordinary conditions but invariably form hadronic bound states, which thus represent the pertinent degrees of freedom at low and intermediate energies.

Together with the weak force, quantum chromo- and electrodynamics provide the framework that describes the non-gravitational interactions of the fundamental building blocks of nature we know of today, as compiled in the standard model of particle physics. Crucially, the standard model is known to be incomplete, reasons for this being, *e.g.*, its incompatibility with gravity, dark matter, and the apparent matter–antimatter asymmetry in the universe. However, the proper extension of the standard model remains to be identified, and to this end, it is necessary to scrutinize this model with the utmost diligence.

In this thesis, we discuss various probes of the standard model at the precision frontier. One such test is the anomalous magnetic moment of the muon, $(g-2)_\mu$, which is the subject of discussion in Part I and its Addendum. Therein, we analyze the transition form factors of axial-vector mesons, which are essential input quantities for an improved evaluation of the axial-vector contributions to hadronic light-by-light scattering. For our analysis, we use the framework of vector-meson dominance, include short-distance constraints from the light-cone expansion, and constrain the free parameters from experiment. Our final result consists of novel parameterizations for the transition form factors of the f_1, f_1', and a_1, which are eligible for a revised estimate of the axial-vector contributions to $(g-2)_\mu$.

Another test of the standard model at the precision frontier is provided by rare semileptonic $\eta^{(\prime)}$ decays, which are investigated in Part II. Due to the strong suppression of these decays within the standard model, they are excellent candidates for searches for physics beyond this theory. For the analysis of the semileptonic $\eta^{(\prime)}$ decays, we consider vector-meson-dominance parameterizations and determine the free parameters from phenomenological input. Using the constructed framework, we calculate branching ratios and differential distributions, which can be confronted with experimental measurements.

In Part III, we study $B \to \gamma^*$ form factors, which entail valuable information on the leading-twist B-meson light-cone distribution amplitude. Our study is based on a set of dispersion relations that link these form factors to their $B \to V$ analogs. This is accompanied by a parameterization that employs a series expansion in a conformal variable and a vector-meson-dominance ansatz, with the free parameters fixed from input on $B \to V$. The phenomenological analysis is performed in terms of integrated as well as differential branching ratios and forward–backward asymmetries for the four-lepton decay, which can probe our understanding of the standard model when compared with experiment.

List of publications

- The contents of Part I of this thesis have been published in a slightly modified version in

  M. Zanke, M. Hoferichter, and B. Kubis, *On the transition form factors of the axial-vector resonance $f_1(1285)$ and its decay into e^+e^-*, JHEP **07**, 106 (2021) [arXiv:2103.09829 [hep-ph]],

  which is partly based on

  M. Zanke, *On the Transition Form Factors of the Axial-Vector Resonance f_1 and its Decay into e^+e^-*, Master's thesis, University of Bonn (2020).

- The formalism presented in Part I was refined in

  M. Hoferichter, B. Kubis, and M. Zanke, *Axial-vector transition form factors and $e^+e^- \to f_1\pi^+\pi^-$*, JHEP **08**, 209 (2023) [arXiv:2307.14413 [hep-ph]],

  which served as a basis for the Addendum to Part I.

- The publication

  H. Schäfer, M. Zanke, Y. Korte, and B. Kubis, *The semileptonic decays $\eta^{(\prime)} \to \pi^0\ell^+\ell^-$ and $\eta' \to \eta\ell^+\ell^-$ in the standard model* Phys. Rev. D **108**, 074025 (2023) [arXiv:2307.10357 [hep-ph]]

  provided the basis for Part II and was supplemented by additional material for this work.

- The main results of Part III have been published in

  S. Kürten, M. Zanke, B. Kubis, and D. van Dyk, *Dispersion relations for $B^- \to \ell^-\bar{\nu}_\ell\ell'^-\ell'^+$ form factors*, Phys. Rev. D **107**, 053006 (2023) [arXiv:2210.09832 [hep-ph]],

  which was complemented by further details and plots as well as an analysis of the identical-lepton mode for this dissertation.

Contents

Prolegomena

According to current knowledge, the universe originated from an incredibly microscopic, extremely hot cluster of space, matter, and energy of yet unknown genesis during what is commonly referred to as the big bang, nearly 14 billion years ago. The initially unified forces acting in this newborn entity are expected to have split into the four fundamental forces of nature we know of today, that is gravity, the strong, the weak, and the electromagnetic force, only a small fraction of a second after the universe came into existence. After the expansion and cooling of the universe had advanced for roughly nine billion years—with many more intriguing events such as the emergence of hadrons from quarks, the formation of nuclei from nucleons, and the production of atoms from nuclei and electrons having occurred throughout that time—the star of humankind's planetary system, the sun, was born in the galaxy that we inhabit, the milky way. From the matter that orbited the sun, many planets and among these the one us human beings populate formed and cooled down in the following several hundred million years—earth was spawned [1, 2].

Life on earth made its debut in the form of self-replicating underwater organisms of primarily single-celled bacteria and slowly developed into more complex lifeforms in the following era—a fauna and flora rich in diversity emerged. From early on, planet earth was plagued by disastrous events, including collisions with comets and asteroids; changes in earth's climate, in particular recurring ice ages and periods of global warming, required the living organisms to adapt to unprecedented conditions. Although such disasters repeatedly led to mass extinctions amongst the otherwise blooming life, they did, perhaps, play a key role in paving the way for the genus we represent, *homo*. It is widely agreed upon by scientists that the modern human whose genes we are composed of to a large extent today, the species *homo sapiens*, evolved and populated earth as early as 150 000–200 000 years ago. There is, however, no prevailing consensus about when our direct ancestors first wandered earth, with some estimates presently dating back around 300 000 years [2–7].

One crucial reason for the dominance of *homo sapiens* over its fellow inhabitants is believed to be its language capabilities. Not only did our ancestors forge the most sophisticated tools and deadliest weapons of their time, but they were capable of communicating with increasing complexity. There is no doubt that other types of extant apes, our closest relatives in the animal kingdom, are capable of vocally alerting their tribe members to approaching enemies, and they might even acquire primitive problem-solving and reasoning skills that require more cognitive ability than, *e.g.*, fetching a stick does, but they most certainly cannot grasp or talk about abstract concepts such as religion or political institutions, let alone calculus. Ultimately, *homo sapiens* itself brought death and mass extinction to nowadays long-forgotten genera of animals, becoming the deadliest species in the annals of biology and the nemesis of many precedent rulers of planet earth [3, 8, 9].

With the above timescales in mind, it seems almost ironic that it was not until the publication of NEWTON's *Philosophiae Naturalis Principia Mathematica* in 1687—less than 400 years ago—that physics started to develop into the natural science it has become today. NEWTON's work obviated the once prevalent idea of absolute space and laid the foundations for classical mechanics by formulating universal laws of motion and gravitation, thus also providing a well-founded framework for the fundamental description of planetary motion. To this day, these laws can account for a vast amount of the physical phenomena of our everyday lives, where the involved velocities are not "too high", the involved masses not "too large", and the involved length scales not "too small" [10].

The next major revolution in the realm of physics was initiated in 1865—almost 200 years later—when MAXWELL completed his work on the unification of electric and magnetic fields into an integral theory of electromagnetism, thereby also providing a proper theory for the propagation of light. According to MAXWELL's theory, electromagnetic fields propagate through space and time as waves of fixed speed, which, at that time, inevitably gave rise to the nowadays discarded notion of an ether, a supposedly ubiquitous substance that acts as a carrier of light. Although MICHELSON and MORLEY were able to experimentally debunk the ether already in 1887, it was only after EINSTEIN published his special theory of relativity in 1905 that the ether was condemned to oblivion. In addition to giving up absolute space, as had been established through NEWTON's work, the special theory of relativity also abandoned the idea of absolute time; instead, it postulated that light travels at the same constant speed for every observer, irrespective of the observer's velocity relative to the light source, with space and time being intimately related manifestations of a concept called space-time. Special relativity becomes essential when describing physical phenomena where the involved velocities are not negligible compared to the speed of light. The theory's postulates have far-reaching consequences for the daily business of modern-day physicists, including the equivalence of mass and energy, $E = mc^2$, and the fact that nothing can travel faster than the speed of light, preventing any kind of information from being transferred faster than that. Despite its great success, special relativity is thus irreconcilable with NEWTON's theory of gravity, which, on the contrary, predicts an instantaneous propagation of gravitational effects. This inconsistency was only resolved with the publication of EINSTEIN's general theory of relativity in 1915, which gives us our modern understanding of gravity and, once more, revolutionized the way we think about space and time. According to the general theory of relativity, space-time is curved by the mass and energy present in it—as opposed to the flat space-time of special relativity—and, conversely, the curvature of space-time dictates the trajectories of the matter contained in it. General relativity is most relevant when dealing with strong gravitational fields, *i.e.*, in the proximity of massive bodies and high energy densities, or when describing phenomena that NEWTON's law of gravitation cannot consistently account for, *e.g.*, the deflection and energy loss of light in a gravitational field [2, 10–12].

Around the same time, in 1900, PLANCK found that the radiation spectrum of a black body can be explained by assuming the energy in electromagnetic waves to be quantized, with each quantum having an energy that is directly proportional to the frequency it is emitted at.[1] This discovery and a host of further developments ultimately led HEISENBERG, SCHRÖDINGER, and others to the formulation of quantum mechanics in the 1920s.

[1] This interpretation of PLANCK's observation was only conceived in 1905 when EINSTEIN postulated what we now call photons as the quanta of the electromagnetic field to explain the photoelectric effect.

Crucially, quantum mechanics dispenses with the notion of classical particles and—in the formalism devised by Schrödinger in 1926—instead adopts the concept of wave functions that describe probability distributions, *e.g.*, of an electron's location in space. An important implication is Heisenberg's uncertainty principle, which states that pairs of conjugate variables, such as the position and momentum of an electron, cannot both be known, say measured, with arbitrary precision at the same time. In essence, quantum mechanics continues to provide our modern account of physical phenomena that proceed on small length scales; however, it was realized promptly that a single-particle theory of relativistic quantum mechanics, as obtained by the naive incorporation of special relativity into the framework of quantum mechanics, results in severe difficulties. While a proper quantum-mechanical treatment of the electromagnetic field required the application of the quantization rationale to classical fields either way, it was rather soon understood that a wholly consistent unification of special relativity and quantum mechanics imposes a field-quantization procedure also for particles that were once considered classical.[2] In such a formalism, not only is all matter described in a single framework, but the resulting quantum theory of fields, or, in short, quantum field theory, corresponds to an intrinsically many-body theory that allows for observable processes such as the creation of particle–antiparticle pairs from the vacuum as well as their annihilation. Here, a particular milestone was Dirac's derivation of a relativistic wave equation for the electron in 1928, which forced physicists to postulate the existence of the positron, the electron's antiparticle. Although it is widely accepted today that a crucial next step would be the unification of general relativity and quantum mechanics, these two understandings of nature presently seem to be hardly compatible with one another. Besides a certain elegance of a coherent quantum theory of gravity, some phenomena such as the big bang or black holes are believed to be fully comprehensible only in a theory that integrates general relativity into the quantum realm. In fact, the space-time singularities that general relativity predicts at these points might even disappear in such a theory, just like quantum mechanics resolved the problem of electrons crashing into the atomic nucleus, as a classical picture suggests. So far, the attempts to construct a theory of quantum gravity have been inconclusive, but potential candidates include string theory and loop quantum gravity [2, 10–14].[3]

By the end of the 1940s, the field-quantized formulation of electrodynamics—quantum electrodynamics—had been refined by, among others, Feynman and Schwinger. The success of this theory in explaining various experimental observations played an important role in establishing quantum field theory as a paradigm to construct theories for the weak and the strong interactions. A unification of the weak and electromagnetic forces into a theory of electroweak interactions was accomplished in 1967, based on work published by Glashow, Salam, and Weinberg throughout the 1960s and utilizing the Higgs mechanism as proposed in 1964. Furthermore, the quark hypothesis devised by Gell-Mann and Zweig in 1964 culminated in the development of quantum chromodynamics as a means to describe the strong force, which was completed in the early 1970s [2, 10–12].

[2]Photons as the quanta of the electromagnetic field are a quantum-mechanical concept to begin with; the description of the native electromagnetic field is based on Maxwell's theory. This is opposite to other matter such as the electron, which was initially thought of as a classical particle that behaves according to Newton's laws. While an electron's wave function in quantum mechanics admits a probabilistic interpretation, this is still different from the quantization of a classical field as is essential for the photon.

[3]String theory actually emerged as a byproduct of an attempt to find a theory for the strong force in the 1960s and only regained interest in the 1980s, partly due to its by then identified relation to gravity.

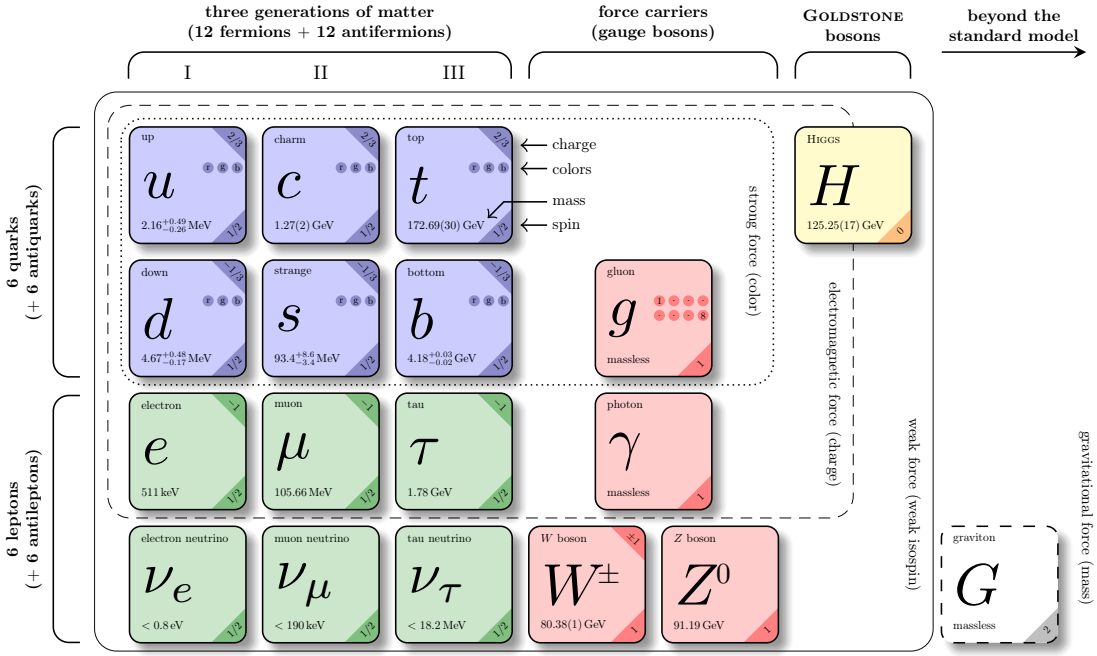

Figure 1: The particle content of the standard model, with the numerical values of the masses taken from Ref. [15]. A few remarks are in order: (i) antifermions have an electric charge that is opposite to that of the corresponding fermion; (ii) while quarks carry one of the color charges red, green, or blue, antiquarks carry one of the respective anticolors; (iii) gluons carry color plus anticolor, with the physical composition being specified by non-trivial linear combinations, in particular leading to the fact that there are eight instead of the naively expected nine gluons; (iv) the W boson is charged and as such can interact with the photon; (v) as explained in the preceding discussion, no consistent quantum theory of gravity is known, so that the graviton is, in principle, a hypothetical tensor boson that lies beyond the standard model. Further extensions of the standard model, *e.g.*, supersymmetry or additional Higgs bosons, are not considered for this illustration.

Together, the strong, weak, and electromagnetic forces constitute the ensemble of interactions that are accounted for within the so-called standard model of particle physics. More specifically, the standard model is a gauge theory that is based on the symmetry group

$$G_{\mathrm{SM}} = \mathrm{SU}(3)_{\mathrm{c}} \times \mathrm{SU}(2)_{\mathrm{L}} \times \mathrm{U}(1)_Y, \tag{1}$$

with the particle or rather field content as given in Fig. 1. Here, $\mathrm{SU}(3)_{\mathrm{c}}$ is the color group of the strong interactions, which corresponds to a Yang–Mills theory that implicates eight massless, color-carrying gauge bosons—the gluons—as the mediators of the strong force.[4] Since this part of the symmetry group acts on particles that carry (notional) color charges, it is also referred to as quantum chromodynamics. The product $\mathrm{SU}(2)_{\mathrm{L}} \times \mathrm{U}(1)_Y$ relates to the electroweak sector, with $\mathrm{SU}(2)_{\mathrm{L}}$ involving three massless (unphysical) gauge bosons denoted by (W_1, W_2, W_3) and $\mathrm{U}(1)_Y$ implicating one additional such gauge boson called B.

[4]By a Yang–Mills theory, we refer to a gauge theory that is based on the non-abelian group $\mathrm{SU}(N)$, resulting in the emergence of $N^2 - 1$ massless gauge bosons.

While the former group acts on left-chiral fermions that live in doublets and carry weak isospin, the latter group pertains to those particles that hold a weak hypercharge Y. Up to this point, the electroweak symmetry has been assumed unbroken, which presumably reflected nature shortly after the big bang, just before the temperature of the universe dropped below $\Lambda_{\mathrm{EW}} \sim 100\,\mathrm{GeV}$ ($T_{\mathrm{EW}} \sim 10^{15}\,K$), the scale of electroweak symmetry breaking.[5] Below this scale, however, the vacuum, *i.e.*, the ground state of the theory, acquires a definite expectation value and thus ceases to respect the symmetry. In this way, a symmetry on the level of LAGRANGE densities gets broken, or rather hidden, in a process referred to as spontaneous symmetry breaking due to the system (spontaneously) falling into a singled-out ground state.[6] For the standard model, this mechanism is implemented in terms of an $\mathrm{SU}(2)_{\mathrm{L}}$ HIGGS doublet, which has four degrees of freedom and upon attaining a vacuum expectation value breaks the symmetry group according to

$$G_{\mathrm{SM}} \to G_{\mathrm{SM}}^{\mathrm{B}} = \mathrm{SU}(3)_{\mathrm{c}} \times \mathrm{U}(1)_{\mathrm{EM}}, \tag{2}$$

where $\mathrm{U}(1)_{\mathrm{EM}}$ is the group associated with electromagnetic interactions, as described by quantum electrodynamics. Within the broken symmetry, the photon and the massive gauge bosons (W^+, W^-, Z^0) of the weak sector correspond to specific linear combinations of the (unphysical) gauge bosons (W_1, W_2, W_3) and B; here, the masses of the weak gauge bosons derive from three of the four degrees of freedom of the HIGGS doublet, with the remaining degree of freedom accounting for the physical HIGGS field. The fermion masses in the standard model are generated on the basis of the HIGGS doublet as well, albeit through a different process, namely via so-called YUKAWA couplings. To the present day, the HIGGS mechanism is the only known method to consistently generate masses for gauge bosons and fermions in the standard model without violating gauge invariance [11, 16–20].

At low and intermediate energies, the electroweak sector is perturbative, that is it is feasible to calculate electromagnetic and weak processes proceeding at such energies, order by order, using a perturbative expansion. The underlying expansion parameter is given by the coupling constant that determines the strength of interactions mediated via the respective force; this coupling varies with the energy scale, and, accordingly, the property of being perturbative is a consequence of the coupling constant's numerical value being sufficiently small at the implied energies, which renders a perturbative series meaningful in the first place.[7] Going to (very) high energies, the coupling of electroweak interactions formally becomes strong, and the perturbative expansion eventually breaks down as higher-order terms gain in relevance until, at some point, they even exceed those of low order.

[5] In so-called grand unified theories, the strong and electroweak interactions are merged into a single force; it is speculated that such a symmetry might have been realized in the very early universe when the temperature was above the grand-unification scale $\Lambda_{\mathrm{GUT}} \sim 10^{16}\,\mathrm{GeV}$ ($T_{\mathrm{GUT}} \sim 10^{29}\,K$). Even before this, when the temperature of the universe was beyond the PLANCK scale $\Lambda_{\mathrm{Pl}} \sim 10^{19}$ ($T_{\mathrm{Pl}} \sim 10^{32}\,K$), gravity is conjectured to have been part of this synergy as well, forming a theory of everything.

[6] With the symmetry initially being manifest, it is impossible to distinguish between the members of a weak-isospin doublet, similar to how quantum chromodynamics does not allow to differentiate between the members of a quark color triplet. In this sense, it is the vacuum that perceives a difference between the members of a weak-isospin doublet below Λ_{EW}, thus leading to the spontaneous breaking of the symmetry.

[7] In fact, these perturbative expansions are known to have limitations also for low and intermediate energies. Although quantum electrodynamics, for example, yields meaningful results in all practical calculations, the series is expected to diverge when going beyond a certain order in the expansion. When thinking in terms of FEYNMAN diagrams, this is due to the fact that the growth in the number of diagrams for higher orders outweighs the suppression from the corresponding power of the coupling constant.

The theory of the strong interactions, on the other hand, behaves exactly opposite to this: quarks and gluons interact weakly at high energies, thereby allowing for the use of perturbative methods in the ultraviolet regime, but the coupling strength grows large for low and intermediate energies, rendering a perturbative expansion ill-defined in this region.[8] Having a coupling constant that diminishes with increasing energy, quantum chromodynamics is said to be asymptotically free, meaning that the interactions between quarks and gluons become asymptotically weaker and that both building blocks resemble free, *i.e.*, non-interacting, particles at high energies. Crucially, however, the theory shows another peculiar feature, namely color confinement, stating that quarks and gluons do not actually materialize as tangible particles under ordinary conditions but only manifest themselves in color-neutral hadronic bound states, which thus represent the pertinent degrees of freedom.[9] The spectrum of hadrons consists of so-called mesons, which are quark–antiquark bound states and thus bosons, and baryons, which are bound states of three (anti-)quarks and thus fermions, as well as further exotic structures such as tetra- or pentaquarks, that is bound states of four or five quarks. While the strong force also mediates interactions among hadrons, it shows rather distinct characteristics within this scope, in particular a comparatively short effective range due to the color-neutral nature of hadrons [16, 18–21].

To treat the non-perturbative domain of quantum chromodynamics, various approaches have been developed over the years. Among these methods are effective field theories, dispersion relations, and quantum chromodynamics on the lattice, as will be briefly discussed in turn below. The first of these techniques follows the rationale to alter the degrees of freedom, *i.e.*, instead of expressing strong interactions at low and intermediate energies using occult quarks and gluons, effective field theories provide a formulation in terms of hadrons—similar to how it is non-essential to know anything about atoms to describe the motion of a ball. By constructing Lagrange densities that implement the relevant symmetries and establishing an ordering scheme that allows one to organize all possible contributions with regard to their relative importance, effective field theories yield a perturbative framework to calculate processes involving hadrons. The paradigm of such a theory is chiral perturbation theory, which is based on the approximate chiral symmetry of quantum chromodynamics for light quarks. Dispersion relations, in contrast, are based on a non-perturbative ansatz and thus represent a very different approach. Here, the main ingredients are the fundamental principles of analyticity (relating to causality), unitarity (corresponding to probability conservation), and crossing symmetry, which can be translated into a model-independent tool to reconstruct physical amplitudes from their discontinuities (containing information on intermediate states and their interactions). Finally, solving quantum chromodynamics on the lattice provides a numerical, likewise non-perturbative, approach in which space-time is discretized on a finite grid of points with non-zero spacing. To recover the continuum limit of quantum chromodynamics, it is necessary to consider (the limit of) an infinitely large grid and take the lattice spacing to zero [22–25].

[8] This behavior of quantum chromodynamics invariably holds true as long as there are no more than 16 quark flavors in nature, which all observations to date seem to confirm.

[9] The phenomenon of confinement is commonly visualized by means of an untearable rubber band that is attached to the quarks; separating the quarks from each other by exerting a force increases the potential energy of the system, to the point where it becomes energetically favorable to create, *e.g.*, a quark–antiquark pair from the vacuum to form two hadrons with each having one (shorter) rubber band. As opposed to asymptotic freedom, confinement currently still lacks an analytic proof and is therefore merely a hypothesis, albeit a heuristically well-founded one.

The great success of the standard model in explaining a large variety of phenomena quickly led to its general acceptance in the scientific community. However, the standard model in its current form is known to be incomplete. Besides the discussed incompatibility with gravity, the theory also fails to account for several cosmological phenomena such as dark matter and the apparent matter–antimatter asymmetry in the universe. More specifically, measurements suggest that the mass of the visible matter in the universe adds up to a mere $\sim 5\%$ of the total mass–energy content of the universe. Another $\sim 27\%$ can be attributed to some hypothetical substance that seems to be hidden from our sight because it does not interact with light—the so-called dark matter—and the remaining $\sim 68\%$ are ascribable to an enigmatic drive referred to as dark energy. While dark matter is needed to interpret a number of astronomical observations related to gravitational effects within the general theory of relativity, dark energy is conceived as the origin of the force that induces the accelerated expansion of the universe. These two entities share the property of being oblivious to photons but, other than that, manifest very differently: dark matter pulls galaxies together, whereas dark energy counters gravity and pushes them apart.[10] The asymmetry between matter and antimatter, on the other hand, relates to the peculiarity that there appears to be an enormous abundance of matter against antimatter in the universe—in fact, everything around us almost exclusively consists of matter.[11] In addition to these phenomena, the standard model is presently also ineligible to address oscillations between different flavors of neutrinos; such transitions are experimentally observed, though, and require non-vanishing neutrino masses, whereas neutrinos are assumed to be massless within the standard model. There are further open questions that, to some degree, have a philosophical character and to which the standard model does not provide an answer either. These are questions that can be classified as problems of naturalness, in particular the hierarchy and the fine-tuning problem; a discussion of these is, however, beyond the scope of these prolegomena [1, 11, 26–28].

Today, there exist a plethora of extensions of the standard model that attempt to resolve, at least partially, issues like those described above. Still, identifying the proper extension to account for these so-called physics beyond the standard model proves to be a formidable task. Aside from cosmological studies of, *e.g.*, dark matter or the matter–antimatter asymmetry, the search for new physics can be divided into two main categories: the energy frontier and the precision frontier. Of these, the energy frontier is mostly concerned with the discovery of (very) heavy particles in collisions performed at unprecedented energies, as, *e.g.*, predicted by grand unified theories or possible within the framework of supersymmetry. The precision frontier, on the contrary, involves scrutinizing imprints of physics beyond the standard model on observables that either have a minor background from the standard model or can be calculated to a very high precision within the theory. In this thesis, we discuss three such precision observables: the anomalous magnetic moment of the muon, which is the subject of discussion in Part I and its Addendum; rare semileptonic $\eta^{(\prime)}$ decays, which are investigated in Part II; and $B \to \gamma^*$ form factors, which are studied in Part III. The Synthesis of the thesis summarizes the main results of these parts and gives a condensed outlook; some fundamental material is collected in the Foundations part.

[10] An illustrative analogy for the expansion of the universe is a lightly inflated balloon with two dots on its surface; similar to how the balloon expands upon further inflation, space-time can be pictured to expand, and similar to how the distance between the dots increases upon inflation—albeit the dots themselves are stationary—stellar objects can be visualized to move apart.

[11] Only a fraction of this imbalance can be explained within the standard model.

References

[1] D. H. Lyth, *The History of the Universe*, Springer, 2015.

[2] N. D. Tyson, *Astrophysics for People in a Hurry: Essays on the Universe and Our Place Within It*, W. W. Norton & Company, 2017.

[3] Y. N. Harari, *Sapiens: A brief History of Humankind*, McClelland & Stewart, 2014.

[4] E. Delson, I. Tattersall, J. van Couvering, and A. S. Brooks, *Encyclopedia of Human Evolution and Prehistory*, Routledge, 2000.

[5] E. Callaway, Nature (2017), *Oldest Homo sapiens fossil claim rewrites our species' history.*

[6] J.-J. Hublin, A. Ben-Ncer, S. E. Bailey, *et al.*, Nature **546**, 289 (2017), *New fossils from Jebel Irhoud, Morocco and the pan-African origin of Homo sapiens.*

[7] D. Richter, R. Grün, R. Joannes-Boyau, *et al.*, Nature **546**, 293 (2017), *The age of the hominin fossils from Jebel Irhoud, Morocco, and the origins of the Middle Stone Age.*

[8] J. Call, Cognition **105**, 1 (2007), *Apes know that hidden objects can affect the orientation of other objects.*

[9] S. J. Ebel, Animal Cognition **22**, 791 (2019), *Innovative problem solving in great apes: the role of visual feedback in the floating peanut task.*

[10] S. Hawking, *A brief History of Time: From the Big Bang to Black Holes*, Transworld Publishers, 2011.

[11] K. Simonyi, *A Cultural History of Physics*, CRC Press, Taylor & Francis Group, 2012.

[12] C. A. Pickover, *The Physics Book: From the Big Bang to Quantum Resurrection, 250 Milestones in the History of Physics*, Sterling, 2011.

[13] F. Schwabl, *Advanced Quantum Mechanics*, Springer, 2008.

[14] S. Carroll, *Something Deeply Hidden: Quantum Worlds and the Emergence of Spacetime*, Oneworld Publications, 2019.

[15] R. L. Workman *et al.* [Particle Data Group], PTEP **2022**, 083C01 (2022).

[16] T.-P. Cheng and L.-F. Li, *Gauge theory of elementary particle physics*, Oxford University Press, 1995.

[17] A. J. Beekman, L. Rademaker, and J. van Wezel, SciPost Phys. Lect. Notes **11**, 1 (2019) [arXiv:1909.01820 [hep-th]].

[18] S. Weinberg, *The Quantum Theory of Fields: Volume I*, Cambridge University Press, 2005.

[19] S. Weinberg, *The Quantum Theory of Fields: Volume II*, Cambridge University Press, 2005.

[20] S. Weinberg, *The Quantum Theory of Fields: Volume III*, Cambridge University Press, 2005.

[21] F. J. Dyson, Phys. Rev. **85**, 631 (1952).

[22] U.-G. Meißner and A. Rusetsky, *Effective Field Theories*, Cambridge University Press, 2022.

[23] S. Scherer and M. R. Schindler, *A Primer for Chiral Perturbation Theory*, Springer, 2012.

[24] J. A. Oller, *A Brief Introduction to Dispersion Relations, With Modern Applications*, Springer, 2019.

[25] C. Gattringer and C. B. Lang, *Quantum Chromodynamics on the Lattice*, Springer, 2010.

[26] C. Giunti and C. W. Kim, *Fundamentals of Neutrino Physics and Astrophysics*, Oxford University Press, 2007.

[27] A. Hanslmeier, *Introduction to Astronomy and Astrophysics*, Springer, 2023.

[28] Z.-z. Xing and S. Zhou, *Neutrinos in Particle Physics, Astronomy and Cosmology*, Springer, 2011.

Foundations

In this part of the thesis, we establish the definitions and conventions that will be used throughout this work. Furthermore, we collect and derive several formulae and identities that are employed in the main part, and we outline certain topics that are essential for this dissertation. For easy reference, the contents presented here are collectively listed in the Foundations index, right after the Glossary, at the end of this work.

Definitions and conventions

Minkowski space

The Minkowski space is one of the most prominent concepts of modern particle physics. It unifies time and three-dimensional space into a four-dimensional vector space $\mathrm{M} = \mathbb{R}^{1,3}$ referred to as space-time and thus allows for an elegant incorporation of Einstein's theory of relativity into the formulation of, *e.g.*, quantum field theory. We equip this vector space with a scalar product using the metric tensor

$$g = \mathrm{diag}(1, -1, -1, -1) \tag{3}$$

of signature $(+,-,-,-)$, as opposed to $\bar{g} = \mathrm{diag}(-1, 1, 1, 1)$ with signature $(-,+,+,+)$, which, on the contrary, is more common in mathematics and other fields of physics [1, 2]. For two vectors $a, b \in \mathrm{M}$, this induces

$$\begin{aligned} a \cdot b &= a^\mu b_\mu = a_\mu b^\mu = a_\mu g^{\mu\nu} b_\nu = a^\mu g_{\mu\nu} b^\nu \\ &= a_0 b_0 - \sum_{i=1}^{3} a_i b_i = a^0 b^0 - \sum_{i=1}^{3} a^i b^i. \end{aligned} \tag{4}$$

Here, we implicitly introduced the Einstein summation convention, implying a summation over all values of Greek indices appearing once as an upper and once as a lower index in a single term. Likewise, two lower or two upper Latin indices in a single term commonly involve a summation, but we will generally make such sums explicit to avoid ambiguity. It is customary in many applications to omit the multiplication sign in the scalar product, *i.e.*, to write $ab \equiv a \cdot b$. Most notably, this abuse of notation facilitates the differentiation between the Minkowski scalar product and the Euclidean scalar product

$$\boldsymbol{c} \cdot \boldsymbol{d} = \sum_{i=1}^{3} c_i d_i = \sum_{i=1}^{3} c^i d^i, \tag{5}$$

with $\boldsymbol{c}, \boldsymbol{d} \in \mathbb{R}^3$, which can further be distinguished by the boldface font that we use to depict three-dimensional vectors.

Levi-Civita symbol

We define the four-dimensional Levi-Civita symbol as

$$\epsilon^{\mu_0\mu_1\mu_2\mu_3} = \epsilon^{\pi(0)\pi(1)\pi(2)\pi(3)} = \epsilon(\pi)\epsilon^{0123}, \tag{6}$$

where $\pi \in \mathrm{Sym}(\{0,1,2,3\})$ is the permutation that fulfills $\pi(i) = \mu_i$ and $\epsilon(\pi)$ is its signature. Throughout this thesis, we adopt the convention $\epsilon^{0123} = +1$ (or, equivalently, $\epsilon_{0123} = -1$). Disregarding any mathematical details on the notion of tensors [3], we will refer to the Levi-Civita symbol as the Levi-Civita tensor in this work.

Natural units

Throughout this thesis, we work in natural units, *i.e.*, we set the speed of light c and the reduced Planck constant $\hbar$ to unity.

Fermionic field operators

In quantum field theory, particles are represented as the quanta of field operators. Fermions, *i.e.*, particles of half-integer spin, in particular, are described by fermionic field operators $\Psi(x)$, which are multi-component objects $\Psi_i(t,\boldsymbol{x}) = [\Psi(x)]_i$ that obey the equal-time anticommutation relations [4]

$$\{\Psi_i(\boldsymbol{x}), \Psi_j(\boldsymbol{y})\} = 0, \qquad \{\Psi_i^\dagger(\boldsymbol{x}), \Psi_j^\dagger(\boldsymbol{y})\} = 0, \qquad \{\Psi_i(\boldsymbol{x}), \Psi_j^\dagger(\boldsymbol{y})\} = \delta^{(3)}(\boldsymbol{x}-\boldsymbol{y})\delta_{ij}. \tag{7}$$

Here, the components i, j of two fermionic fields that describe distinct fermion species act as if they were two independent components of a single type of fermion.

For spin-1/2 fermions, the free fields can be expanded according to [5]

$$\Psi(x) = \int \frac{\mathrm{d}^3p}{(2\pi)^3} \frac{1}{\sqrt{2E_{\boldsymbol{p}}}} \sum_s \left[a_{\boldsymbol{p}}^s u^s(p) \mathrm{e}^{-\mathrm{i}px} + b_{\boldsymbol{p}}^{s\,\dagger} v^s(p) \mathrm{e}^{\mathrm{i}px}\right], \tag{8}$$

where the sum extends over the two spin projections s; $a_{\boldsymbol{p}}^{s\,(\dagger)}$ and $b_{\boldsymbol{p}}^{s\,(\dagger)}$ are annihilation (creation) operators for fermions and antifermions of spin projection s, three-momentum $\boldsymbol{p}$, and energy $E_{\boldsymbol{p}} = (\boldsymbol{p}^2 + m^2)^{1/2}$, respectively, with m being the mass of the fermion species; $u^s(p)$ and $v^s(p)$ are the corresponding four-component Dirac spinors. Similar expressions apply for bosons, *i.e.*, particles of integer spin, with the anticommutators replaced by commutators, which, however, will not be needed for this thesis.

Gamma matrices

The gamma matrices $\{\gamma^\mu\}_{\mu=0,1,2,3}$ are generators of the Dirac algebra; they satisfy the defining anticommutation relation [4]

$$\{\gamma^\mu, \gamma^\nu\} = 2g^{\mu\nu}. \tag{9}$$

In the course of this thesis, we will use the Feynman slash notation $\not{A} = A_\mu\gamma^\mu$ and denote the Dirac adjoint by $\bar{B} = B^\dagger\gamma^0$. We further define a fifth gamma matrix via

$$\gamma^5 = \mathrm{i}\gamma^0\gamma^1\gamma^2\gamma^3 = -\frac{\mathrm{i}}{4!}\epsilon_{\mu\nu\rho\sigma}\gamma^\mu\gamma^\nu\gamma^\rho\gamma^\sigma, \tag{10}$$

where the sign in the last equality is due to the chosen convention of the Levi-Civita tensor.

Chirality projection operators

Using the fifth gamma matrix, we introduce the projection operators $P_{L/R} = (1 \mp \gamma_5)/2$, which project onto the left- and right-chiral components of a DIRAC spinor, respectively [5]. The properties $P_L + P_R = \mathbb{1}$, $P_{L/R}^2 = P_{L/R}$, and $P_{L/R}P_{R/L} = 0$ are readily verified.

Time ordering

Time ordering will be denoted by an operation T acting on a product of either bosonic or fermionic field operators $\{\mathcal{O}_i^{\boldsymbol{\mu_i}}(x_i)\}_{i=1,\dots,N}$, $\boldsymbol{\mu_i} = (\mu_i^1, \dots, \mu_i^{M_i})$, according to [6]

$$\mathrm{T}\{\mathcal{O}_1^{\boldsymbol{\mu_1}}(x_1)\dots\mathcal{O}_N^{\boldsymbol{\mu_N}}(x_N)\} = \begin{cases} \mathcal{O}_{\sigma(1)}^{\boldsymbol{\mu_{\sigma(1)}}}(x_{\sigma(1)})\dots\mathcal{O}_{\sigma(N)}^{\boldsymbol{\mu_{\sigma(N)}}}(x_{\sigma(N)}), & \text{if bosonic,} \\ \epsilon(\sigma)\mathcal{O}_{\sigma(1)}^{\boldsymbol{\mu_{\sigma(1)}}}(x_{\sigma(1)})\dots\mathcal{O}_{\sigma(N)}^{\boldsymbol{\mu_{\sigma(N)}}}(x_{\sigma(N)}), & \text{if fermionic.} \end{cases} \tag{11}$$

Here, with all x_i^0 different, $\sigma \in S_N$ is the permutation that orders the expression such that $x_{\sigma(1)}^0 > \dots > x_{\sigma(N)}^0$ and $\epsilon(\sigma)$ is its signature. The potential sign for fermionic field operators arises from their anticommutative property. We will only encounter the special cases $N = 2$, $M_i \leq 1$ in this thesis, for which time ordering reduces to [5]

$$\mathrm{T}\{\mathcal{O}_1^{(\mu)}(x)\mathcal{O}_2^{(\nu)}(y)\} = \theta(x^0 - y^0)\mathcal{O}_1^{(\mu)}(x)\mathcal{O}_2^{(\nu)}(y) \pm \theta(y^0 - x^0)\mathcal{O}_2^{(\nu)}(y)\mathcal{O}_1^{(\mu)}(x), \tag{12}$$

where $\theta(x^0) = \mathbb{1}_{x^0>0}$ is the HEAVISIDE step function; the upper sign holds for bosonic and the lower sign for fermionic field operators. In this dissertation, we will further only consider bosonic field operators in time-ordered products, so that, in principle, we do not have to bother about this relative sign.

KÄLLÉN function

The KÄLLÉN function

$$\lambda(a, b, c) = a^2 + b^2 + c^2 - 2ab - 2ac - 2bc \tag{13}$$

frequently appears as a kinematic function in the description of scattering and decay processes in particle physics. It is readily verified to be symmetric in all of its arguments.

Fine-structure constant

The dimensionless fine-structure constant $\alpha = e^2/(4\pi)$ is commonly used in place of the electric charge e. Its numerical value can be approximated as $\alpha \approx 1/137.036$ [7].

Particle abbreviations

For convenience, we introduce the following abbreviations in the notation of vector mesons:

$$\begin{aligned} \rho &\equiv \rho(770), & \omega &\equiv \omega(782), & \phi &\equiv \phi(1020), \\ \rho' &\equiv \rho(1450), & \omega' &\equiv \omega(1420), & \phi' &\equiv \phi(1680), \\ \rho'' &\equiv \rho(1700), & \omega'' &\equiv \omega(1650), & \phi'' &\equiv \phi(2170), \end{aligned} \tag{14}$$

$K^* \equiv K^*(892)$. Furthermore, we write

$$a_1 \equiv a_1(1260), \qquad f_1 \equiv f_1(1285), \qquad f_1' \equiv f_1(1420) \tag{15}$$

for the relevant axial-vector mesons and $\eta' \equiv \eta'(958)$ as well as $a_2 \equiv a_2(1320)$.

Formulae and identities

Lorentz transformations

Lorentz transformations are those transformations Λ that leave the Minkowski scalar product invariant, *i.e.*, $(\Lambda a)\cdot(\Lambda b) = a\cdot b$ for $a, b \in \mathrm{M}$. In practice, we will use the elements referred to as boosts and rotations [5] to transform between different reference frames in a way consistent with relativity; parity and time reversal are irrelevant for our purposes.

Consider a particle with momentum $p = (E, \boldsymbol{p})^\intercal$, *i.e.*, energy E and three-momentum $\boldsymbol{p}$, in a fixed frame of reference; its velocity $\boldsymbol{\beta}$ is given by [7]

$$\boldsymbol{\beta} = \frac{\boldsymbol{p}}{E}. \tag{16}$$

We denote the momentum of the particle in a frame that moves with velocity $\boldsymbol{\beta}_\mathrm{f}$ relative to the fixed frame by $p^* = (E^*, \boldsymbol{p}^*)^\intercal$. The three-momenta can be split into parts that are parallel and parts that are perpendicular with respect to the velocity of the moving frame as per $\boldsymbol{p}^{(*)} = \boldsymbol{p}_\parallel^{(*)} + \boldsymbol{p}_\perp^{(*)}$. Defining $p_\parallel^{(*)} = |\boldsymbol{p}_\parallel^{(*)}|$ and $\beta_\mathrm{f} = |\boldsymbol{\beta}_\mathrm{f}|$, we then have

$$\boldsymbol{p}_\parallel^{(*)} = p_\parallel^{(*)}\frac{\boldsymbol{\beta}_\mathrm{f}}{\beta_\mathrm{f}} = \frac{\boldsymbol{\beta}_\mathrm{f}\cdot\boldsymbol{p}^{(*)}}{\beta_\mathrm{f}}\frac{\boldsymbol{\beta}_\mathrm{f}}{\beta_\mathrm{f}}. \tag{17}$$

The momenta p and p^* are related by a Lorentz transformation according to [7]

$$\begin{pmatrix} E^* \\ p_\parallel^* \\ p_\perp^* \end{pmatrix} = \begin{pmatrix} \gamma_\mathrm{f} & -\gamma_\mathrm{f}\beta_\mathrm{f} & 0 \\ -\gamma_\mathrm{f}\beta_\mathrm{f} & \gamma_\mathrm{f} & 0 \\ 0 & 0 & 1 \end{pmatrix} \begin{pmatrix} E \\ p_\parallel \\ p_\perp \end{pmatrix}, \tag{18}$$

where $\gamma_\mathrm{f} = (1-\beta_\mathrm{f}^2)^{-1/2}$ is the so-called Lorentz factor and $p_\perp^{(*)} = |\boldsymbol{p}_\perp^{(*)}|$ are the magnitudes of the perpendicular components of the three-momenta $\boldsymbol{p}^{(*)}$. Note that, in fact, we have $\boldsymbol{p}_\perp^* = \boldsymbol{p}_\perp$ also for the vectors and not only for their magnitudes $p_\perp^*$ and $p_\perp$. Hence, the full momentum p^* after the Lorentz transformation is given by

$$\begin{aligned} \begin{pmatrix} E^* \\ \boldsymbol{p}^* \end{pmatrix} = \begin{pmatrix} E^* \\ \boldsymbol{p}_\parallel^* + \boldsymbol{p}_\perp^* \end{pmatrix} &= \begin{pmatrix} \gamma_\mathrm{f}E - \gamma_\mathrm{f}\beta_\mathrm{f}p_\parallel \\ \left[\gamma_\mathrm{f}p_\parallel - \gamma_\mathrm{f}\beta_\mathrm{f}E\right]\frac{\boldsymbol{\beta}_\mathrm{f}}{\beta_\mathrm{f}} + \boldsymbol{p}_\perp \end{pmatrix} = \begin{pmatrix} \gamma_\mathrm{f}E - \gamma_\mathrm{f}\left(\boldsymbol{\beta}_\mathrm{f}\cdot\boldsymbol{p}\right) \\ \gamma_\mathrm{f}\boldsymbol{p}_\parallel - \gamma_\mathrm{f}E\boldsymbol{\beta}_\mathrm{f} + \boldsymbol{p}_\perp \end{pmatrix} \\ &= \begin{pmatrix} \gamma_\mathrm{f}E - \gamma_\mathrm{f}\left(\boldsymbol{\beta}_\mathrm{f}\cdot\boldsymbol{p}\right) \\ \gamma_\mathrm{f}\frac{\boldsymbol{\beta}_\mathrm{f}\cdot\boldsymbol{p}}{\beta_\mathrm{f}}\frac{\boldsymbol{\beta}_\mathrm{f}}{\beta_\mathrm{f}} - \gamma_\mathrm{f}E\boldsymbol{\beta}_\mathrm{f} + \boldsymbol{p}_\perp \end{pmatrix}. \end{aligned} \tag{19}$$

Given the particle's momentum in the frame moving with velocity $\boldsymbol{\beta}_\mathrm{f}$ instead, its momentum in the initially fixed frame can be obtained with the inverse transformation

$$\begin{pmatrix} E \\ p_\parallel \\ p_\perp \end{pmatrix} = \begin{pmatrix} \gamma_\mathrm{f} & \gamma_\mathrm{f}\beta_\mathrm{f} & 0 \\ \gamma_\mathrm{f}\beta_\mathrm{f} & \gamma_\mathrm{f} & 0 \\ 0 & 0 & 1 \end{pmatrix} \begin{pmatrix} E^* \\ p_\parallel^* \\ p_\perp^* \end{pmatrix}, \tag{20}$$

which is equivalent to the transformation in Eq. (18) with $\boldsymbol{\beta}_\mathrm{f} \to -\boldsymbol{\beta}_\mathrm{f}$. The full momentum p then turns out to be

$$\begin{pmatrix} E \\ \boldsymbol{p} \end{pmatrix} = \begin{pmatrix} \gamma_\mathrm{f}E^* + \gamma_\mathrm{f}\left(\boldsymbol{\beta}_\mathrm{f}\cdot\boldsymbol{p}^*\right) \\ \gamma_\mathrm{f}\frac{\boldsymbol{\beta}_\mathrm{f}\cdot\boldsymbol{p}^*}{\beta_\mathrm{f}}\frac{\boldsymbol{\beta}_\mathrm{f}}{\beta_\mathrm{f}} + \gamma_\mathrm{f}E^*\boldsymbol{\beta}_\mathrm{f} + \boldsymbol{p}_\perp^* \end{pmatrix}. \tag{21}$$

It is straightforward to verify that the above group of transformations indeed leaves the scalar product $p_1\cdot p_2$ of two momenta $p_1, p_2 \in \mathrm{M}$ invariant.

DIRAC equation

The motion of free spin-1/2 particles is governed by the DIRAC equation [4]

$$(\mathrm{i}\partial\!\!\!/ - m)\Psi(x) = 0, \tag{22}$$

where $\Psi(x)$ is a fermionic field whose quanta have mass m. For the corresponding DIRAC spinors $u^s(p)$ and $v^s(p)$, this implies

$$(p\!\!\!/ - m)u^s(p) = 0, \qquad (p\!\!\!/ + m)v^s(p) = 0 \tag{23}$$

in momentum space. The DIRAC equation for the adjoint fermionic field $\bar{\Psi}(x)$ reads

$$\bar{\Psi}(x)(\mathrm{i}\overleftarrow{\partial\!\!\!/} + m) = 0, \tag{24}$$

as readily obtained from Eq. (22), and the spinor analogs become

$$\bar{u}^s(p)(p\!\!\!/ - m) = 0, \qquad \bar{v}^s(p)(p\!\!\!/ + m) = 0. \tag{25}$$

Translation of field operators

Consider a pair of field operators $\mathcal{O}^{(\mu)}_{i=1,2}(x)$ that are allowed to have vector structure in LORENTZ space. Their transformation property under translations is given by [4]

$$\mathcal{O}^{(\mu)}_i(x+a) = \mathrm{e}^{\mathrm{i}a\hat{P}}\mathcal{O}^{(\mu)}_i(x)\mathrm{e}^{-\mathrm{i}a\hat{P}}, \tag{26}$$

with $\hat{P}_\alpha = \mathrm{i}\partial_\alpha$ being the four-momentum operator from the POINCARÉ algebra that generates infinitesimal translations. For the time-ordered product of the two field operators, we then deduce

$$\begin{aligned}
\langle k,\beta|\mathrm{T}\{\mathcal{O}^{(\mu)}_1(x)\mathcal{O}^{(\nu)}_2(y)\}|p,\alpha\rangle &= \mathrm{e}^{-\mathrm{i}yp}\theta(x^0-y^0)\,\langle k,\beta|\mathcal{O}^{(\mu)}_1(x)\mathrm{e}^{\mathrm{i}y\hat{P}}\mathcal{O}^{(\nu)}_2(0)|p,\alpha\rangle \\
&\quad \pm \mathrm{e}^{\mathrm{i}yk}\theta(y^0-x^0)\,\langle k,\beta|\mathcal{O}^{(\nu)}_2(0)\mathrm{e}^{-\mathrm{i}y\hat{P}}\mathcal{O}^{(\mu)}_1(x)|p,\alpha\rangle \\
&= \mathrm{e}^{-\mathrm{i}y(p-k)}\theta(x^0-y^0)\,\langle k,\beta|\mathcal{O}^{(\mu)}_1(x-y)\mathcal{O}^{(\nu)}_2(0)|p,\alpha\rangle \\
&\quad \pm \mathrm{e}^{\mathrm{i}y(k-p)}\theta(y^0-x^0)\,\langle k,\beta|\mathcal{O}^{(\nu)}_2(0)\mathcal{O}^{(\mu)}_1(x-y)|p,\alpha\rangle \\
&= \mathrm{e}^{\mathrm{i}y(k-p)}\,\langle k,\beta|\mathrm{T}\{\mathcal{O}^{(\mu)}_1(x-y)\mathcal{O}^{(\nu)}_2(0)\}|p,\alpha\rangle
\end{aligned} \tag{27}$$

and, in complete analogy,

$$\langle k,\beta|\mathrm{T}\{\mathcal{O}^{(\mu)}_1(x)\mathcal{O}^{(\nu)}_2(y)\}|p,\alpha\rangle = \mathrm{e}^{\mathrm{i}x(k-p)}\,\langle k,\beta|\mathrm{T}\{\mathcal{O}^{(\mu)}_1(0)\mathcal{O}^{(\nu)}_2(y-x)\}|p,\alpha\rangle\,. \tag{28}$$

Two special cases that are particularly relevant for this thesis follow for $|k,\beta\rangle = |0\rangle$ being the vacuum and $y = x$, *i.e.*, a set of local field operators, namely

$$\begin{aligned}
\langle 0|\mathrm{T}\{\mathcal{O}^{(\mu)}_1(x)\mathcal{O}^{(\nu)}_2(y)\}|p,\alpha\rangle &= \mathrm{e}^{-\mathrm{i}yp}\,\langle 0|\mathrm{T}\{\mathcal{O}^{(\mu)}_1(x-y)\mathcal{O}^{(\nu)}_2(0)\}|p,\alpha\rangle \\
&= \mathrm{e}^{-\mathrm{i}xp}\,\langle 0|\mathrm{T}\{\mathcal{O}^{(\mu)}_1(0)\mathcal{O}^{(\nu)}_2(y-x)\}|p,\alpha\rangle
\end{aligned} \tag{29}$$

and

$$\langle k,\beta|\mathrm{T}\{\mathcal{O}^{(\mu)}_1(x)\mathcal{O}^{(\nu)}_2(x)\}|p,\alpha\rangle = \mathrm{e}^{\mathrm{i}x(k-p)}\,\langle k,\beta|\mathrm{T}\{\mathcal{O}^{(\mu)}_1(0)\mathcal{O}^{(\nu)}_2(0)\}|p,\alpha\rangle\,. \tag{30}$$

Equal-time commutators

In the following, we investigate equal-time commutators of the type

$$\mathfrak{C} = [\psi_a^\dagger(\bar{x})\mathcal{O}_1^{(\mu)}\psi_b(\bar{x}), \psi_c^\dagger(\bar{y})\mathcal{O}_2^{(\nu)}\psi_d(\bar{y})], \tag{31}$$

where $\bar{x} = (x^0 = 0, \boldsymbol{x})^\intercal$, $\bar{y} = (y^0 = 0, \boldsymbol{y})^\intercal$, and $f \in \{a, b, c, d\}$ labels the flavor of the corresponding fermionic field $\psi_f(\bar{x})$. Here, the operators $\mathcal{O}_{i=1,2}^{(\mu)}$ are assumed to have a structure in Dirac space and, potentially, Lorentz space, *e.g.*, composed of gamma matrices and numerical factors such as charges.

It is instructive to first consider a similar commutator for a single flavor of fermions and operators without Lorentz structure, namely

$$\begin{aligned}\mathfrak{c} &= [\psi^\dagger(\bar{x})\widetilde{\mathcal{O}}_1\psi(\bar{x}), \psi^\dagger(\bar{y})\widetilde{\mathcal{O}}_2\psi(\bar{y})] \\ &= (\widetilde{\mathcal{O}}_1)_{ij}(\widetilde{\mathcal{O}}_2)_{mn}[\psi_i^\dagger(\bar{x})\psi_j(\bar{x}), \psi_m^\dagger(\bar{y})\psi_n(\bar{y})],\end{aligned} \tag{32}$$

where $s \in \{i, j, m, n\}$ labels the respective spinor component in Dirac space, as induced by the four-component fermionic fields, and we used that the components of the operators $\widetilde{\mathcal{O}}_i$ correspond to commuting numbers. Here and in the following, a summation over repeated Latin indices is implicit. We then apply the identity

$$[AB, CD] = A\{B, C\}D - AC\{B, D\} + \{A, C\}DB - C\{A, D\}B \tag{33}$$

to obtain

$$\begin{aligned}\mathfrak{c} = (\widetilde{\mathcal{O}}_1)_{ij}(\widetilde{\mathcal{O}}_2)_{mn}\big(&\psi_i^\dagger(\bar{x})\{\psi_j(\bar{x}), \psi_m^\dagger(\bar{y})\}\psi_n(\bar{y}) - \psi_i^\dagger(\bar{x})\psi_m^\dagger(\bar{y})\{\psi_j(\bar{x}), \psi_n(\bar{y})\} \\ &+ \{\psi_i^\dagger(\bar{x}), \psi_m^\dagger(\bar{y})\}\psi_n(\bar{y})\psi_j(\bar{x}) - \psi_m^\dagger(\bar{y})\{\psi_i^\dagger(\bar{x}), \psi_n(\bar{y})\}\psi_j(\bar{x})\big).\end{aligned} \tag{34}$$

Inserting the canonical equal-time anticommutation relations for fermionic fields, Eq. (7), we find

$$\begin{aligned}\mathfrak{c} &= (\widetilde{\mathcal{O}}_1)_{ij}(\widetilde{\mathcal{O}}_2)_{mn}\big(\delta^{(3)}(\boldsymbol{x} - \boldsymbol{y})\delta_{jm}\psi_i^\dagger(\bar{x})\psi_n(\bar{y}) - \delta^{(3)}(\boldsymbol{x} - \boldsymbol{y})\delta_{in}\psi_m^\dagger(\bar{y})\psi_j(\bar{x})\big) \\ &= \delta^{(3)}(\boldsymbol{x} - \boldsymbol{y})\big(\psi^\dagger(\bar{x})\widetilde{\mathcal{O}}_1\widetilde{\mathcal{O}}_2\psi(\bar{y}) - \psi^\dagger(\bar{y})\widetilde{\mathcal{O}}_2\widetilde{\mathcal{O}}_1\psi(\bar{x})\big).\end{aligned} \tag{35}$$

Let us now consider Eq. (31), for which analogous arguments—in particular the commuting property of the components of the operators $\mathcal{O}_i^{(\mu)}$—lead to

$$\begin{aligned}\mathfrak{C} &= (\mathcal{O}_1^{(\mu)})_{ij}(\mathcal{O}_2^{(\nu)})_{mn}[\psi_{a,i}^\dagger(\bar{x})\psi_{b,j}(\bar{x}), \psi_{c,m}^\dagger(\bar{y})\psi_{d,n}(\bar{y})] \\ &= (\mathcal{O}_1^{(\mu)})_{ij}(\mathcal{O}_2^{(\nu)})_{mn}\big(\psi_{a,i}^\dagger(\bar{x})\{\psi_{b,j}(\bar{x}), \psi_{c,m}^\dagger(\bar{y})\}\psi_{d,n}(\bar{y}) - \psi_{a,i}^\dagger(\bar{x})\psi_{c,m}^\dagger(\bar{y})\{\psi_{b,j}(\bar{x}), \psi_{d,n}(\bar{y})\} \\ &\qquad + \{\psi_{a,i}^\dagger(\bar{x}), \psi_{c,m}^\dagger(\bar{y})\}\psi_{d,n}(\bar{y})\psi_{b,j}(\bar{x}) - \psi_{c,m}^\dagger(\bar{y})\{\psi_{a,i}^\dagger(\bar{x}), \psi_{d,n}(\bar{y})\}\psi_{b,j}(\bar{x})\big) \\ &= (\mathcal{O}_1^{(\mu)})_{ij}(\mathcal{O}_2^{(\nu)})_{mn}\big(\delta^{(3)}(\boldsymbol{x} - \boldsymbol{y})\delta_{jm}\delta_{bc}\psi_{a,i}^\dagger(\bar{x})\psi_{d,n}(\bar{y}) - \delta^{(3)}(\boldsymbol{x} - \boldsymbol{y})\delta_{in}\delta_{ad}\psi_{c,m}^\dagger(\bar{y})\psi_{b,j}(\bar{x})\big) \\ &= \delta^{(3)}(\boldsymbol{x} - \boldsymbol{y})\big(\delta_{bc}\psi_a^\dagger(\bar{x})\mathcal{O}_1^{(\mu)}\mathcal{O}_2^{(\nu)}\psi_d(\bar{y}) - \delta_{ad}\psi_c^\dagger(\bar{y})\mathcal{O}_2^{(\nu)}\mathcal{O}_1^{(\mu)}\psi_b(\bar{x})\big).\end{aligned} \tag{36}$$

Here, we used that the anticommutation relations for fields of different flavors act as if these were different spinor components of a single flavor. The rationale behind this behavior is that each spin component of a single fermionic field, just like the field components of different flavors, actually represents an independent degree of freedom.

CHISHOLM identity

Due to the four-dimensional nature of space-time, the identity [8]

$$\mathrm{i}\epsilon^{\mu\nu\rho\sigma}\gamma_\sigma\gamma_5 = \gamma^\mu\gamma^\nu\gamma^\rho - g^{\mu\nu}\gamma^\rho + g^{\mu\rho}\gamma^\nu - g^{\nu\rho}\gamma^\mu \tag{37}$$

holds, which we refer to as the CHISHOLM identity in the course of this thesis. It is straightforward to show its validity via a proof by cases, for which we introduce the abuse of notation[12]

$$(-1)^\mu = \begin{cases} 1, & \mu = 0, \\ -1, & \mu = 1, 2, 3. \end{cases} \tag{38}$$

We first consider the case with at least two indices from the tuple (μ, ν, ρ) being equal, so that, due to the antisymmetry of the LEVI-CIVITA tensor, Eq. (37) reduces to

$$\gamma^\mu\gamma^\nu\gamma^\rho = g^{\mu\nu}\gamma^\rho - g^{\mu\rho}\gamma^\nu + g^{\nu\rho}\gamma^\mu. \tag{39}$$

Using the defining property of the DIRAC algebra, Eq. (9), and $(\gamma^0)^2 = 1 = -(\gamma^k)^2$ [4] for $k = 1, 2, 3$, we then find

$$\gamma^\mu\gamma^\nu\gamma^\rho = \begin{cases} (-1)^\mu\gamma^\mu, & \mu = \nu = \rho, \\ (-1)^\mu\gamma^\rho, & \mu = \nu \neq \rho, \\ -(-1)^\mu\gamma^\nu, & \mu = \rho \neq \nu, \\ (-1)^\nu\gamma^\mu, & \nu = \rho \neq \mu, \end{cases} \tag{40}$$

and the right-hand side of Eq. (39) agrees with this expression because the metric tensor fulfills $g^{\mu\nu} = (-1)^\mu$ for $\mu = \nu$ and zero otherwise.

For the second case, we assume all indices from the tuple (μ, ν, ρ) to take distinct values. In this case, $g^{\mu\nu} = 0$ for all metric tensors of Eq. (37), so that the CHISHOLM identity becomes

$$-\epsilon^{\mu\nu\rho\sigma}\gamma_\sigma\gamma^0\gamma^1\gamma^2\gamma^3 = \gamma^\mu\gamma^\nu\gamma^\rho, \tag{41}$$

where we inserted the definition of γ_5, Eq. (10). Here, the implicit sum over the index σ collapses to a single term because σ necessarily needs to be different from μ, ν, and ρ. We note that the left-hand side of the above equation is antisymmetric under the exchange of any of the two indices $\mu \leftrightarrow \nu$, $\mu \leftrightarrow \rho$, or $\nu \leftrightarrow \rho$; naturally, the same applies to the right-hand side due to the DIRAC algebra. Hence, we can, without loss of generality, restrict ourselves to the permutations $(\mu, \nu, \rho) = (0, 1, 2), (0, 1, 3), (0, 2, 3), (1, 2, 3)$. Using that $\gamma_\mu = (-1)^\mu\gamma^\mu$ numerically, the left-hand side of Eq. (41) yields

$$-\epsilon^{\mu\nu\rho\sigma}\gamma_\sigma\gamma^0\gamma^1\gamma^2\gamma^3 = \begin{cases} \epsilon^{0123}\gamma^0\gamma^1\gamma^2, & (\mu, \nu, \rho) = (0, 1, 2), \\ -\epsilon^{0132}\gamma^0\gamma^1\gamma^3, & (\mu, \nu, \rho) = (0, 1, 3), \\ \epsilon^{0231}\gamma^0\gamma^2\gamma^3, & (\mu, \nu, \rho) = (0, 2, 3), \\ -\epsilon^{1230}\gamma^1\gamma^2\gamma^3, & (\mu, \nu, \rho) = (1, 2, 3), \end{cases} \tag{42}$$

which trivially equals the right-hand side.

[12] This notation is to be understood numerically, *i.e.*, it makes sense only for a given value of the index, but it does not induce any kind of LORENTZ covariance.

N-body phase space

For the description of scattering and decay processes, we need the differential n-body phase space [7]

$$\mathrm{d}\Phi_n(P;p_1,\ldots,p_n) = (2\pi)^4\delta^{(4)}\Big(P-\sum_{l=1}^{n}p_l\Big)\prod_{i=1}^{n}\frac{\mathrm{d}^3p_i}{(2\pi)^3 2p_i^0}. \tag{43}$$

Here, P is the total momentum of the incoming state and $\{p_i\}_{i=1,\ldots,n}$ are the momenta of the outgoing particles, with $p_i^0 = (\boldsymbol{p}_i^2 + m_i^2)^{1/2}$ their energies and m_i the corresponding masses. For decay processes, P is a single momentum, while for scattering processes, P is a sum of the momenta of the incoming particles; in practice, we will only encounter scattering reactions with two incoming particles, so that here, $P = P_1 + P_2$ for our purposes. The integration of Eq. (43) is performed over the whole domain of the integration variables $\boldsymbol{p}_i$. Given that the integration volumes $\mathrm{d}^3p_i/[(2\pi)^3 2p_i^0]$ are LORENTZ-invariant quantities [5], the integrations can be carried out in distinct, conveniently chosen reference frames.

The phase space takes a remarkably simple form for $n = 2$, namely [5]

$$\mathrm{d}\Phi_2(P;p_1,p_2) = \theta\big(E_{\mathrm{CMS}} - (m_1+m_2)\big)\frac{|\boldsymbol{p}_{\mathrm{CMS}}^{\mathrm{out}}|}{16\pi^2 E_{\mathrm{CMS}}}\,\mathrm{d}\Omega_{\mathrm{CMS}}. \tag{44}$$

Here, all quantities are given in the center-of-mass system, as indicated by the subscript "CMS". The differential solid angle is denoted by $\mathrm{d}\Omega_{\mathrm{CMS}}$, which needs to be integrated over the two-sphere $S^2 = \{\boldsymbol{r}\in\mathbb{R}^3\colon |\boldsymbol{r}| = 1\}$; E_{CMS} is the total energy of the incoming state, and $|\boldsymbol{p}_{\mathrm{CMS}}^{\mathrm{out}}|$ depicts the magnitude of the three-momentum of either outgoing particle.

In the following, we derive the recursion relation [7]

$$\mathrm{d}\Phi_n(P;p_1,\ldots,p_n) = \mathrm{d}\Phi_j(q;p_1,\ldots,p_j)\,\mathrm{d}\Phi_{n-j+1}(P;q,p_{j+1},\ldots,p_n)\,\frac{\mathrm{d}q^2}{2\pi}, \tag{45}$$

where $j < n$ and $q = \sum_{m=1}^{j} p_m$. This formula allows one to split the n-body phase space into a product of two smaller phase spaces, which is particularly useful for the description of processes with subsequent decays of other decay products. Since the integration measures are intertwined, the order of the differentials becomes crucial in the integral form of the relation,

$$\begin{aligned}\int\mathrm{d}\Phi_n(P;p_1,\ldots,p_n) = \int\frac{\mathrm{d}q^2}{2\pi}\int\frac{\mathrm{d}^3q}{(2\pi)^3 2q^0}\int\prod_{i=j+1}^{n}\frac{\mathrm{d}^3p_i}{(2\pi)^3 2p_i^0}\,(2\pi)^4\delta^{(4)}\Big(P-q-\sum_{l=j+1}^{n}p_l\Big)\\ \times\int\prod_{k=1}^{j}\frac{\mathrm{d}^3p_k}{(2\pi)^3 2p_k^0}\,(2\pi)^4\delta^{(4)}\Big(q-\sum_{m=1}^{j}p_m\Big).\end{aligned} \tag{46}$$

The LORENTZ invariance of the integration measures implies that one can choose different frames to perform the various integrations separately. Note that we omitted brackets around the products of phase-space measures in Eq. (46) for notational convenience; it is important to keep in mind, however, that these products implicitly refer to the integral measures only here and in the following.

To prove the recursion relation, we observe the following representations of unity:

$$1 = \int \frac{\mathrm{d}^4 q}{(2\pi)^4}\,(2\pi)^4\delta^{(4)}\Big(q - \sum_{m=1}^{j} p_m\Big) = \int \frac{\mathrm{d}^4 q}{(2\pi)^4}\,(2\pi)^4\delta^{(4)}\Big(q - \sum_{m=1}^{j} p_m\Big)\theta(q^0),$$
$$1 = \int \frac{\mathrm{d}s}{2\pi}\,(2\pi)\delta(s - q^2). \tag{47}$$

Here, $\theta(q^0)$ in the first representation eliminates unphysical negative-energy solutions; it can be inserted without changing the result due to the assumption of positive energies, $\sum_{m=1}^{j} p_m^0 \geq 0$. We can obtain a third representation of unity by combining the two representations, leading to

$$\begin{aligned} 1 &= \int \frac{\mathrm{d}s}{2\pi} \int \frac{\mathrm{d}^4 q}{(2\pi)^4}\,(2\pi)\delta(s - q^2)(2\pi)^4\delta^{(4)}\Big(q - \sum_{m=1}^{j} p_m\Big)\theta(q^0) \\ &= \int \frac{\mathrm{d}s}{2\pi} \int \frac{\mathrm{d}^3 q}{(2\pi)^3 2q^0}\,(2\pi)^4\delta^{(4)}\Big(q - \sum_{m=1}^{j} p_m\Big)\Big|_{q^0=(\boldsymbol{q}^2+s)^{1/2}}. \end{aligned} \tag{48}$$

In the second line, we applied the formula [9]

$$\delta\big(f(x)\big) = \sum_{\substack{x_0\,:\,\text{zeroes}\\ \text{of } f}} \frac{\delta(x - x_0)}{|f'(x_0)|}, \tag{49}$$

which holds for functions $f(x)$ that possess a finite set of simple zeroes and implies

$$\delta(s - q^2) = \delta\big((q^0)^2 - \boldsymbol{q}^2 - s\big) = \frac{\delta\Big(q^0 - \sqrt{\boldsymbol{q}^2 + s}\Big) - \delta\Big(q^0 + \sqrt{\boldsymbol{q}^2 + s}\Big)}{2\sqrt{\boldsymbol{q}^2 + s}}. \tag{50}$$

Next, we rewrite the differential n-body phase space, Eq. (43), as

$$\mathrm{d}\Phi_n(P; p_1, \ldots, p_n) = (2\pi)^4\delta^{(4)}\Big(P - \sum_{l=1}^{n} p_l\Big) \prod_{k=1}^{j} \frac{\mathrm{d}^3 p_k}{(2\pi)^3 2p_k^0} \prod_{i=j+1}^{n} \frac{\mathrm{d}^3 p_i}{(2\pi)^3 2p_i^0}. \tag{51}$$

By multiplying this equation with the representation of unity given in Eq. (48) and performing the remaining integrations over the phase-space variables p_i, we obtain

$$\begin{aligned} \int \mathrm{d}\Phi_n(P; p_1, \ldots, p_n) = \int \frac{\mathrm{d}s}{2\pi} \int \frac{\mathrm{d}^3 q}{(2\pi)^3 2q^0} \int \prod_{i=j+1}^{n} \frac{\mathrm{d}^3 p_i}{(2\pi)^3 2p_i^0}\,(2\pi)^4\delta^{(4)}\Big(P - \sum_{l=1}^{n} p_l\Big) \\ \times \int \prod_{k=1}^{j} \frac{\mathrm{d}^3 p_k}{(2\pi)^3 2p_k^0}\,(2\pi)^4\delta^{(4)}\Big(q - \sum_{m=1}^{j} p_m\Big)\Big|_{q^0=(\boldsymbol{q}^2+s)^{1/2}} \end{aligned} \tag{52}$$

This formula is readily verified to be equivalent to Eq. (46). To this end, we note that both delta distributions have to be fulfilled simultaneously, so that $\delta^{(4)}(P - \sum_{l=1}^{n} p_l) = \delta^{(4)}(P - q - \sum_{l=j+1}^{n} p_l)$ in the first line; furthermore, $q^0 = (\boldsymbol{q}^2 + s)^{1/2}$ implies $s = q^2$.

Decay rate

For an unstable particle with momentum P and mass M decaying into n particles with momenta $\{p_i\}_{i=1,\dots,n}$ and masses m_i, the differential decay rate is given by [7]

$$\mathrm{d}\Gamma(P \to p_1, \dots, p_n) = \frac{1}{2M} |\mathcal{M}(P \to p_1, \dots, p_n)|^2 \, \mathrm{d}\Phi_n(P; p_1, \dots, p_n), \tag{53}$$

where $\mathcal{M}(P \to p_1, \dots, p_n)$ is the invariant amplitude describing the process. In many cases, one is interested in unpolarized decay widths; in this case, the absolute square of the amplitude further needs to be averaged over the polarizations as well as the spins of the initial particles, if applicable, and summed over those of the final state. This procedure is commonly referred to as spin-averaging or spin-summing, which we also follow in this thesis. We reserve for ourselves to not make this procedure explicit in all formulae and, where not otherwise stated, assume squared amplitudes to also involve spin-averaging and spin-summing. With indistinguishable particles in the final state, an additional symmetry factor needs to be taken into account upon integrating Eq. (53); more specifically, one gets a factor $1/m!$ per m identical particles. The rationale behind this factor is that one is counting the possible momentum configurations $(\boldsymbol{p}_{i_1}, \dots, \boldsymbol{p}_{i_m}) = (\boldsymbol{p}_{i_{\sigma(1)}}, \dots, \boldsymbol{p}_{i_{\sigma(m)}})$, $\sigma \in S_m$ and $\{i_1, \dots, i_m\} \subseteq \{1, \dots, n\}$, multiple times in the naive phase-space integration. Dividing the calculated decay width by the total width Γ of the decaying particle, one obtains the so-called branching ratio $B(P \to p_1, \dots, p_n)$.

Using Eq. (44), the differential decay rate for two outgoing particles, $n = 2$, becomes

$$\mathrm{d}\Gamma(P \to p_1, p_2) = \theta\big(M - (m_1 + m_2)\big) \frac{|\boldsymbol{p}^{\mathrm{out}}_{\mathrm{CMS}}|}{32\pi^2 M^2} |\mathcal{M}(P \to p_1, p_2)|^2 \, \mathrm{d}\Omega_{\mathrm{CMS}}. \tag{54}$$

Here, the magnitude of the three-momentum is given by $|\boldsymbol{p}^{\mathrm{out}}_{\mathrm{CMS}}| = \lambda(M^2, m_1^2, m_2^2)^{1/2}/(2M)$ and we used $E_{\mathrm{CMS}} = M$. Consequently, the integration is trivial to carry out if the amplitude does not induce any angular dependence, leading to

$$\Gamma(P \to p_1, p_2) = S \frac{|\boldsymbol{p}^{\mathrm{out}}_{\mathrm{CMS}}|}{8\pi M^2} |\mathcal{M}(P \to p_1, p_2)|^2 \, \theta\big(M - (m_1 + m_2)\big). \tag{55}$$

For indistinguishable final-state particles, we have $S = 1/2$ because $(\boldsymbol{p}_1, \boldsymbol{p}_2) = (\boldsymbol{p}_2, \boldsymbol{p}_1)$ is counted twice in the integration, whereas $S = 1$ otherwise.

Cross section

Together with decay rates, cross sections are among the most important observables in particle physics. Consider two particles with momenta P_1, P_2 and masses M_1, M_2 that scatter into n particles with momenta $\{p_i\}_{i=1,\dots,n}$. Once $\mathcal{M}(P_1, P_2 \to p_1, \dots, p_n)$ is known, the differential cross section is determined according to [7]

$$\mathrm{d}\sigma(P_1, P_2 \to p_1, \dots, p_n) = \frac{1}{4F} |\mathcal{M}(P_1, P_2 \to p_1, \dots, p_n)|^2 \, \mathrm{d}\Phi_n(P_1 + P_2; p_1, \dots, p_n). \tag{56}$$

Here, the kinematic factor $F = [(P_1 \cdot P_2)^2 - M_1^2 M_2^2]^{1/2}$ becomes $F = |\boldsymbol{p}^{\mathrm{in}}_{\mathrm{CMS}}|\sqrt{s}$ in the center-of-mass system, where $|\boldsymbol{p}^{\mathrm{in}}_{\mathrm{CMS}}| = \lambda(s, M_1^2, M_2^2)^{1/2}/(2s^{1/2})$ is the magnitude of the three-momentum of either incoming particle and $s = (P_1 + P_2)^2$. If the final state contains indistinguishable particles, symmetry factors similar to those considered for the decay width need to be accounted for upon performing the phase-space integration.

Three-body phase space for decays

In the following, we deduce several convenient forms for the phase space of three-body decays. The description of two-particle scattering reactions with three particles in the final state is more intricate and, in essence, equals that of decays with four particles in the final state; due to one more particle being involved, two additional angles need to be taken into account here. Although such phase spaces will also be used throughout this thesis, we restrict ourselves to the phase space for three-body decays as an example here.

We start by using the recursion relation stated in Eq. (45) to write

$$\mathrm{d}\Phi_3(P;p_1,p_2,p_3) = \mathrm{d}\Phi_2(q;p_1,p_2)\,\mathrm{d}\Phi_2(P;q,p_3)\,\frac{\mathrm{d}q^2}{2\pi}, \tag{57}$$

where $q = p_1 + p_2$ is the momentum of the subsystem that consists of the particles with momenta p_1 and p_2. In order to insert the explicit form of the two-body phase space given in Eq. (44), it is convenient to first analyze the kinematics of the process in the corresponding center-of-mass systems. For $\mathrm{d}\Phi_2(q;p_1,p_2)$, we consider the center-of-mass frame of the particles with momenta p_1 and p_2. In this frame, we denote the explicit four-momenta by $p_1^* = (E_1^*, \boldsymbol{p}_1^*)^\intercal$ and $p_2^* = (E_2^*, -\boldsymbol{p}_1^*)^\intercal$, where the magnitude of the three-momentum and the corresponding energies are found to be

$$|\boldsymbol{p}_1^*| = \frac{\sqrt{\lambda(q^2,m_1^2,m_2^2)}}{2\sqrt{q^2}}, \qquad E_1^* = \frac{q^2+m_1^2-m_2^2}{2\sqrt{q^2}}, \qquad E_2^* = \frac{q^2-m_1^2+m_2^2}{2\sqrt{q^2}}, \tag{58}$$

with $E_{\mathrm{CMS}}^* = E_1^* + E_2^* = \sqrt{q^2}$. To evaluate $\mathrm{d}\Phi_2(P;q,p_3)$, we look at the rest frame of the decaying particle; this frame coincides with the center-of-mass system of the subsystem described by q and the particle with momentum p_3. Here, we write $q = (E_q, \boldsymbol{q})^\intercal$ and $p_3 = (E_3, -\boldsymbol{q})^\intercal$, where

$$|\boldsymbol{q}| = \frac{\sqrt{\lambda(M^2,q^2,m_3^2)}}{2M}, \qquad E_q = \frac{M^2+q^2-m_3^2}{2M}, \qquad E_3 = \frac{M^2-q^2+m_3^2}{2M}, \tag{59}$$

with $E_{\mathrm{CMS}} = E_q + E_3 = M$.

Using Eq. (44), together with the above kinematics, Eq. (57) becomes

$$\mathrm{d}\Phi_3(P;p_1,p_2,p_3) = \theta\big(\sqrt{q^2}-(m_1+m_2)\big)\theta\big(M-(\sqrt{q^2}+m_3)\big)\frac{|\boldsymbol{p}_1^*||\boldsymbol{q}|}{512\pi^5 M\sqrt{q^2}}\,\mathrm{d}q^2\,\mathrm{d}\Omega_1^*\,\mathrm{d}\Omega_q. \tag{60}$$

The solid angles $\mathrm{d}\Omega_1^* = (\cos\theta_1^*, \phi_1^*)$ and $\mathrm{d}\Omega_q = (\cos\theta_q, \phi_q)$ are given with respect to the particle with momentum p_1 and the subsystem with momentum q in the coordinate systems associated with the center-of-mass frames investigated above, see Fig. 2.[13] When interested in spin-averaged observables, it is possible to perform all but one angular integrations of Eq. (60) by rotating the coordinate systems appropriately. For this purpose, we align the three-vector $\boldsymbol{q}$ along the z-axis and place $\boldsymbol{p}_1^*$ in the xz-plane, which we choose to match the x^*z^*-plane, *i.e.*, $\boldsymbol{q} = |\boldsymbol{q}|(0,0,1)^\intercal$ and $\boldsymbol{p}_1^* = |\boldsymbol{p}_1^*|(\sin\theta,0,\cos\theta)^\intercal$, with $\theta = \theta_1^* = \sphericalangle(\boldsymbol{p}_1^*,\boldsymbol{q})$ the only non-trivial angle of the process, see Fig. 2. Performing the integrations over the trivial angles in Eq. (60), we then find

$$\mathrm{d}\Phi_3(P;p_1,p_2,p_3) = \theta\big(\sqrt{q^2}-(m_1+m_2)\big)\theta\big(M-(\sqrt{q^2}+m_3)\big)\frac{|\boldsymbol{p}_1^*||\boldsymbol{q}|}{64\pi^3 M\sqrt{q^2}}\,\mathrm{d}q^2\,\mathrm{d}\cos\theta. \tag{61}$$

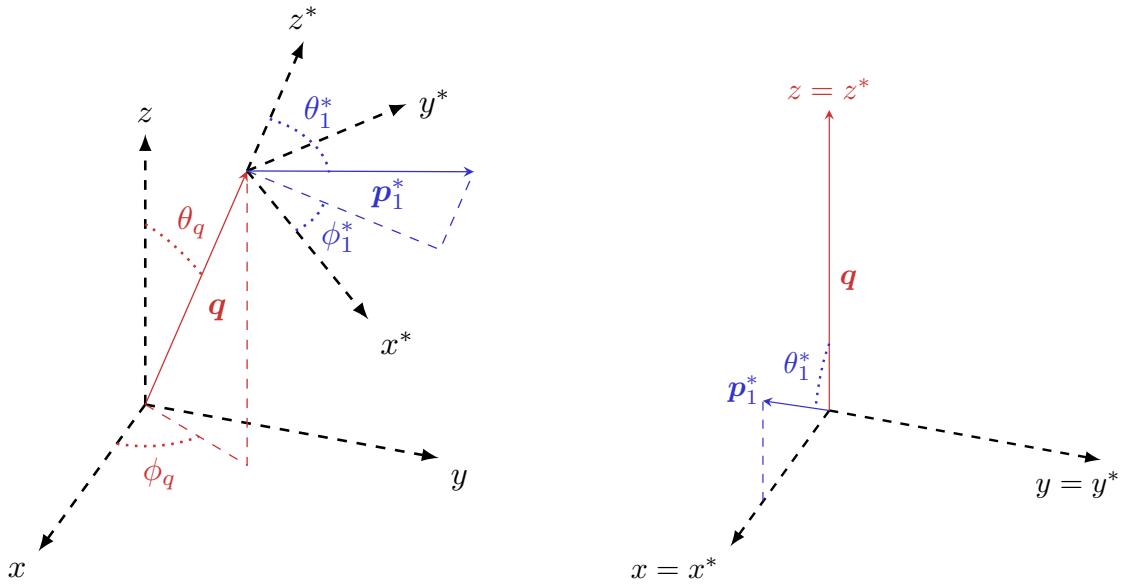

Figure 2: The coordinate systems associated with the center-of-mass frames discussed in the text before (*left*) and after (*right*) performing the rotations that render three angles trivial in the phase-space integration. Note that we chose the z^* axis to be aligned with the direction of $\boldsymbol{q}$ already in the initial illustration for pure convenience. Moreover, the origins of the coordinate systems are put on top of each other in the final representation.

It is further possible to replace the angular integration by an integration over k^2, where $k = p_2 + p_3$. To this end, we use Eq. (21) and perform a LORENTZ transformation from the center-of-mass system of the particles with momenta p_1 and p_2, described by the explicit four-vectors p_1^* and p_2^* in this frame, to the rest frame of the decaying particle, where $p_1 = (E_1, \boldsymbol{p}_1)^\intercal$ and $p_2 = (E_2, \boldsymbol{p}_2)^\intercal$. This leads to

$$p_1 = \begin{pmatrix} \gamma_q(E_1^* + \beta_q |\boldsymbol{p}_1^*| \cos\theta) \\ |\boldsymbol{p}_1^*| \sin\theta \\ 0 \\ \gamma_q(\beta_q E_1^* + |\boldsymbol{p}_1^*| \cos\theta) \end{pmatrix}, \qquad p_2 = \begin{pmatrix} \gamma_q(E_2^* - \beta_q |\boldsymbol{p}_1^*| \cos\theta) \\ -|\boldsymbol{p}_1^*| \sin\theta \\ 0 \\ \gamma_q(\beta_q E_2^* - |\boldsymbol{p}_1^*| \cos\theta) \end{pmatrix}, \tag{62}$$

where $\beta_q = |\boldsymbol{q}|/E_q$ and $\gamma_q = (1 - \beta_q^2)^{-1/2}$. With p_2 and p_3 given in a unique reference frame, we can then calculate $k^2 = (E_2 + E_3)^2 - (\boldsymbol{p}_2 - \boldsymbol{q})^2$ to obtain

$$\left| \frac{\mathrm{d}k^2}{\mathrm{d}\cos\theta} \right| = \frac{2M|\boldsymbol{p}_1^*||\boldsymbol{q}|}{\sqrt{q^2}}, \tag{63}$$

and, hence,

$$\mathrm{d}\Phi_3(P; p_1, p_2, p_3) = \theta\big(\sqrt{q^2} - (m_1 + m_2)\big)\theta\big(M - (\sqrt{q^2} + m_3)\big) \frac{1}{128\pi^3 M^2} \, \mathrm{d}q^2 \, \mathrm{d}k^2. \tag{64}$$

[13] By noting that $\mathrm{d}q^2/\mathrm{d}\sqrt{q^2} = 2\sqrt{q^2}$, we can also replace the differential $\mathrm{d}q^2$ by $2\sqrt{q}\,\mathrm{d}\sqrt{q^2}$.

The integration over k^2 is to be performed over a fairly complicated region. This is most conveniently seen by repeating the above calculation with $q^* = (E_q^*, \boldsymbol{q}^*)^\intercal$ and $p_3^* = (E_3^*, \boldsymbol{p}_3^*)^\intercal$, *i.e.*, by using Eq. (19) to transform the momenta q and p_3 from the rest frame of the decaying particle to the center-of-mass system of the particles with momenta p_1 and p_2 instead. In this case, we find $q^* = (E_q^*, 0, 0, 0)^\intercal$ and $p_3^* = (E_3^*, 0, 0, -|\boldsymbol{p}_3^*|)^\intercal$, with

$$|\boldsymbol{p}_3^*| = \frac{\sqrt{\lambda(M^2, q^2, m_3^2)}}{2\sqrt{q^2}}, \qquad E_q^* = \sqrt{q^2}, \qquad E_3^* = \frac{M^2 - q^2 - m_3^2}{2\sqrt{q^2}}. \tag{65}$$

Then, we have

$$k^2 = (E_2^* + E_3^*)^2 - (|\boldsymbol{p}_1^*|^2 + |\boldsymbol{p}_3^*|^2 + 2|\boldsymbol{p}_1^*||\boldsymbol{p}_3^*|\cos\theta), \tag{66}$$

which reproduces Eq. (60) due to $|\boldsymbol{p}_3^*| = |\boldsymbol{q}|M/\sqrt{q^2}$. For the integration domain of k^2, we now note that $\theta \in [0, \pi]$, that is $\cos\theta \in [-1, 1]$, so that the minimum and maximum are obtained if the three-vectors are (anti-)parallel [7],

$$k^2_{\text{min/max}} = (E_2^* + E_3^*)^2 - \left(\sqrt{(E_2^*)^2 - m_2^2} \pm \sqrt{(E_3^*)^2 - m_3^2}\,\right)^2. \tag{67}$$

In order to simplify calculations with the integration domain, we can perform yet another variable transformation to $\nu = k^2 - l^2$, where $l = p_1 + p_3$. To this end, we define the LORENTZ invariant $\Sigma = q^2 + k^2 + l^2$, which fulfills $\Sigma = M^2 + m_1^2 + m_2^2 + m_3^2$ because of momentum conservation, $P = p_1 + p_2 + p_3$. With Σ, we can write

$$k^2 = \frac{\Sigma - q^2 + \nu}{2}, \qquad l^2 = \frac{\Sigma - q^2 - \nu}{2}, \qquad \nu = 2k^2 + q^2 - \Sigma, \tag{68}$$

so that the Jacobian of the transformation $(q^2, k^2) \to (q^2, \nu)$ is given by

$$J_\nu = \begin{pmatrix} \frac{\mathrm{d}q^2}{\mathrm{d}q^2} & \frac{\mathrm{d}q^2}{\mathrm{d}\nu} \\ \frac{\mathrm{d}k^2}{\mathrm{d}q^2} & \frac{\mathrm{d}k^2}{\mathrm{d}\nu} \end{pmatrix} = \begin{pmatrix} 1 & 0 \\ -\frac{1}{2} & \frac{1}{2} \end{pmatrix}, \tag{69}$$

where $|\det J_\nu| = 1/2$.[14] Hence, Eq. (64) becomes

$$\mathrm{d}\Phi_3(P; p_1, p_2, p_3) = \theta\big(\sqrt{q^2} - (m_1 + m_2)\big)\theta\big(M - (\sqrt{q^2} + m_3)\big)\frac{1}{256\pi^3 M^2}\,\mathrm{d}q^2\,\mathrm{d}\nu. \tag{70}$$

For the domain of integration, we can use the explicit four-momenta to calculate

$$\nu = \frac{(M^2 - m_3^2)(m_2^2 - m_1^2) - \cos\theta\sqrt{\lambda(M^2, q^2, m_3^2)}\sqrt{\lambda(q^2, m_1^2, m_2^2)}}{q^2}, \tag{71}$$

with $\cos\theta \in [-1, 1]$, or insert Eq. (67) into $\nu = 2k^2 + q^2 - \Sigma$, both leading to the boundaries

$$\nu_{\text{min/max}} = \frac{(M^2 - m_3^2)(m_2^2 - m_1^2) \mp \sqrt{\lambda(M^2, q^2, m_3^2)}\sqrt{\lambda(q^2, m_1^2, m_2^2)}}{q^2}. \tag{72}$$

Here, the integration region vanishes ($\nu_{\text{min}} = \nu_{\text{max}}$) at the boundaries of the phase space in $q^2 \in [(m_1 + m_2)^2, (M - m_3)^2]$.

[14] In our case, the same result is obtained by differentiating k^2 with respect to ν, yielding $\mathrm{d}k^2 = \mathrm{d}\nu/2$.

Unitarity and dispersion relations

The principle of maximal analyticity [10] states that physical amplitudes are functions in the complex plane that are analytic in all continuous variables except for a countable set of poles and branch points associated with physical states. In particular, the connection between singularities and physical intermediate states can be made explicit by means of the unitarity relation. Due to probability conservation, the S-matrix—which describes the transition between initial and final states—fulfills $S^\dagger S = \mathbb{1}$ [4]. Writing $S = \mathbb{1} + \mathrm{i}T$, we separate the interaction part T of the S-matrix from the trivial component that is accounted for by unity; the amplitude $\mathcal{M}(i \to f)$ is then defined via

$$\langle f|T|i\rangle = (2\pi)^4 \delta^{(4)}(p_i - p_f)\mathcal{M}(i \to f), \tag{73}$$

where p_i and p_f denote the total momenta of the initial state $|i\rangle$ and final state $|f\rangle$, respectively. Consequently, unitarity of the S-matrix implies

$$T - T^\dagger = \mathrm{i}T^\dagger T, \tag{74}$$

and, hence,

$$\mathcal{M}(i \to f) - \mathcal{M}(f \to i)^* = \mathrm{i}\sum_n \int \mathrm{d}\Phi_n(p_i; p_n)\, \mathcal{M}(i \to n)\mathcal{M}(f \to n)^*, \tag{75}$$

where we inserted a complete set of (discrete and continuous) n-body intermediate states [5] with momentum p_n, $\sum\!\!\!\!\!\!\int_n |n\rangle\langle n| = \mathbb{1}$,[15] and omitted a common factor of $\delta^{(4)}(p_i - p_f)$ for overall momentum conservation on both sides of the equation.

For practical purposes, we restrict ourselves to two-particle initial and final states in the following, $|i\rangle = |i_1, i_2\rangle$, $|f\rangle = |f_1, f_2\rangle$, with the corresponding momenta denoted by p_1 through p_4. In this case, Lorentz covariance dictates the amplitude to be a function of the Mandelstam variables $s = (p_1 + p_2)^2$, $t = (p_1 - p_3)^2$, and $u = (p_1 - p_4)^2$ only, $\mathcal{M}(i \to f) = \mathcal{M}(s, t, u)$, where $s + t + u = \sum_{j=1}^4 m_j^2$, and m_j is the mass of the particle described by p_j. The case of forward scattering, $|i\rangle = |f\rangle$ with $p_i = p_f$, leads to the so-called optical theorem [5]

$$\mathrm{Im}\,\mathcal{M}(i \to i) = 2|\boldsymbol{p}^{\mathrm{in}}_{\mathrm{CMS}}|\sqrt{s}\sum_n \sigma(i \to n), \tag{76}$$

see Eq. (56). To go beyond the scattering in forward direction, we note that [11]

$$\begin{aligned}\mathcal{M}(i \to f) &= \lim_{\epsilon \to 0^+} \mathcal{M}(s + \mathrm{i}\epsilon, t, u),\\ \mathcal{M}(f \to i)^* &= \lim_{\epsilon \to 0^+} \mathcal{M}(s - \mathrm{i}\epsilon, t, u),\end{aligned} \tag{77}$$

so that Eq. (75) translates to

$$\begin{aligned}\mathrm{disc}_s \mathcal{M}(s, t, u) &= \lim_{\epsilon \to 0^+} \big[\mathcal{M}(s + \mathrm{i}\epsilon, t, u) - \mathcal{M}(s - \mathrm{i}\epsilon, t, u)\big]\\ &= \mathrm{i}\sum_n \int \mathrm{d}\Phi_n(p_i; p_n)\, \mathcal{M}(i \to n)\mathcal{M}(f \to n)^*.\end{aligned} \tag{78}$$

[15] Note the abuse of notation in generically labeling an n-body intermediate state by $|n\rangle$ for, in particular, there can be more than one n-body intermediate state, *e.g.*, $|\tilde{n}\rangle$.

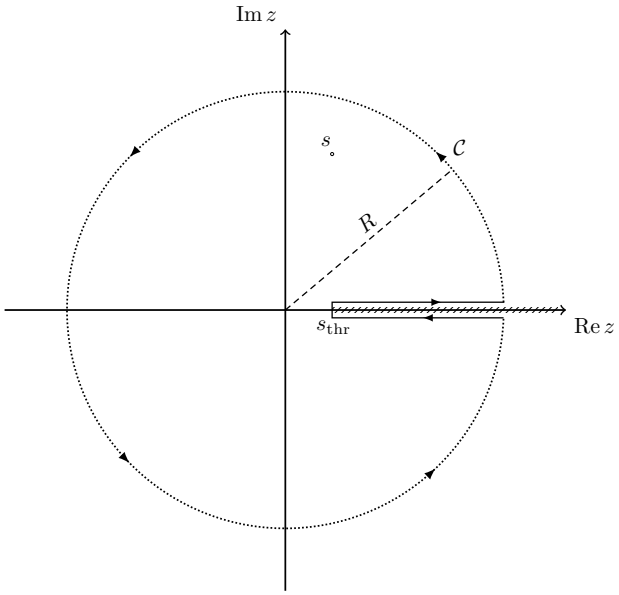

Figure 3: The closed contour $\mathcal{C}$ that encircles s and avoids the branch cut starting at s_{thr}, leading to the dispersion relation given in Eq. (80) upon $R \to \infty$.

Assuming that Schwarz' reflection principle [9] holds further implies $\mathcal{M}(s - \mathrm{i}\epsilon, t, u) = \mathcal{M}(s + \mathrm{i}\epsilon, t, u)^*$,[16] leading to $\mathrm{disc}_s \mathcal{M}(s,t,u) = 2\mathrm{i} \lim_{\epsilon \to 0^+} \mathrm{Im}\, \mathcal{M}(s + \mathrm{i}\epsilon, t, u)$ and thus a purely imaginary discontinuity, in analogy to Eq. (76). Taken together, the amplitude acquires a contribution to its imaginary part—or, more generally, a discontinuity—with each intermediate state that can go on shell; neglecting effects from crossed-channel singularities and denoting the threshold of the lowest-lying intermediate state by s_{thr}, the discontinuity consequently vanishes for $s < s_{\mathrm{thr}}$.

Dispersion relations provide a tool to reconstruct physical amplitudes from their discontinuities. The foundation of dispersion relations is given by Cauchy's integral formula [9], stating that

$$f(s) = \frac{1}{2\pi\mathrm{i}} \oint_{\mathcal{C}} \mathrm{d}z \, \frac{f(z)}{z - s} \tag{79}$$

for a complex function $f(z)$ that is analytic within the region bounded by and on the closed contour $\mathcal{C}$ encircling the (arbitrary) point s. Supposing that $f(s)$ has a single branch cut that starts at s_{thr} and choosing the contour as depicted in Fig. 3,[17] one then finds

$$f(s) = \frac{1}{2\pi\mathrm{i}} \int_{s_{\mathrm{thr}}}^{\infty} \mathrm{d}x \, \frac{\mathrm{disc} f(x)}{x - s} \tag{80}$$

if the function falls of sufficiently fast for $|s| \to \infty$, $f(s) = \mathcal{O}(s^d)$, $d < 0$. As will be discussed next, a weaker asymptotic decrease of $f(s)$ requires the introduction of so-called subtractions: for one thing, the contribution from the arc depicted in Fig. 3 does not vanish and for another thing, the integral given in Eq. (80) does not converge in this case.

[16] Here, the usual (but restrictive) argument from the physical perspective is that $\mathcal{M}(f \to i) = \mathcal{M}(i \to f)$ due to symmetry, which, together with Eq. (77), yields the desired property; see also Ref. [11].

[17] For simplicity, we disregard further right-hand cuts ($s \geq 0$) as well as left-hand cuts ($s < 0$) here. The latter, especially, may emerge from crossed-channel singularities in, *e.g.*, t or u; see also Eq. (78).

Subtracted dispersion relations

The dispersion relation given in Eq. (80) is valid provided that the integrand falls off sufficiently fast, $f(s) = \mathcal{O}(s^d)$, $d < 0$. For $f(s) \sim s^a$, $a \in [n-1, n)$, $n \in \mathbb{N}_{>0}$, asymptotically, in particular, it is possible to establish the convergent, n-times subtracted dispersion relation

$$f(s) = P_{n-1}(s) + \frac{\prod_{i=1}^{n}(s - s_i)}{2\pi\mathrm{i}} \int_{s_\mathrm{thr}}^{\infty} \mathrm{d}x \, \frac{\mathrm{disc} f(x)}{(x-s)\prod_{j=1}^{n}(x - s_j)}. \tag{81}$$

Here, $\{s_i\}_{i=1,\ldots,n}$ is a set of subtraction points that fulfill $s_i < s_\mathrm{thr}$; $P_{n-1}(s)$ is a polynomial of degree $n-1$ in s, which induces n undetermined subtraction constants. The dispersion relation is thus rendered convergent at the cost of introducing a set of free parameters.

We prove Eq. (81) by induction, starting with the initial case $n = 1$. To this end, assume $f(s) \sim s^b$ asymptotically with some $b \in [0, 1)$ and consider the function

$$\widetilde{f}(s) = \frac{f(s) - f(s_1)}{s - s_1}. \tag{82}$$

Since $\widetilde{f}(s) \sim s^{\tilde{b}}$, $\tilde{b} \in [-1, 0)$, for $s \to \infty$, with $\widetilde{f}(s_1)$ finite due to L'HÔSPITAL's rule [9], we can use Eq. (80) to write $\widetilde{f}(s)$ in terms of an unsubtracted dispersion relation as per

$$\widetilde{f}(s) = \frac{1}{2\pi\mathrm{i}} \int_{s_\mathrm{thr}}^{\infty} \mathrm{d}x \, \frac{\mathrm{disc}\widetilde{f}(x)}{x - s} = \frac{1}{2\pi\mathrm{i}} \int_{s_\mathrm{thr}}^{\infty} \mathrm{d}x \, \frac{\mathrm{disc} f(x)}{(x-s)(x-s_1)}. \tag{83}$$

Here, we used that $(x \pm \mathrm{i}\epsilon - s_i)^{-1} = (x - s_i)^{-1} + \mathcal{O}(\epsilon)$ and thus

$$\mathrm{disc}_x\left[\frac{f(x) - f(s_i)}{x - s_i}\right] = \frac{f(x + \mathrm{i}\epsilon) - f(s_i)}{x + \mathrm{i}\epsilon - s_i} - \frac{f(x - \mathrm{i}\epsilon) - f(s_i)}{x - \mathrm{i}\epsilon - s_i} = \frac{\mathrm{disc} f(x)}{x - s_i}. \tag{84}$$

Hence, we find

$$f(s) = f(s_1) + \frac{s - s_1}{2\pi\mathrm{i}} \int_{s_\mathrm{thr}}^{\infty} \mathrm{d}x \, \frac{\mathrm{disc} f(x)}{(x-s)(x-s_1)}, \tag{85}$$

where $P_0(s) = f(s_1)$ is a polynomial of degree zero in s, in accordance with Eq. (81).

For the induction step $n \to n+1$, take $f(s) \sim s^c$ for $c \in [n, n+1)$ and define

$$\widetilde{f}(s) = \frac{f(s) - f(s_{n+1})}{s - s_{n+1}}. \tag{86}$$

Since $\widetilde{f}(s) \sim s^a$ with $a \in [n-1, n)$, we can use our induction statement for n to write

$$\widetilde{f}(s) = P_{n-1}(s) + \frac{\prod_{i=1}^{n}(s - s_i)}{2\pi\mathrm{i}} \int_{s_\mathrm{thr}}^{\infty} \mathrm{d}x \, \frac{\mathrm{disc}\widetilde{f}(x)}{(x-s)\prod_{j=1}^{n}(x - s_j)}. \tag{87}$$

Using Eq. (84), *i.e.*, $\mathrm{disc}\widetilde{f}(x) = \mathrm{disc} f(x)/(x - s_{n+1})$, and rearranging the resulting equation, we obtain

$$f(s) = f(s_{n+1}) + (s - s_{n+1})P_{n-1}(s) + \frac{\prod_{i=1}^{n+1}(s - s_i)}{2\pi\mathrm{i}} \int_{s_\mathrm{thr}}^{\infty} \mathrm{d}x \, \frac{\mathrm{disc} f(x)}{(x-s)\prod_{j=1}^{n+1}(x - s_j)}, \tag{88}$$

with $P_n(s) = f(s_{n+1}) + (s - s_{n+1})P_{n-1}(s)$ a polynomial of degree n in s, as claimed.

An alternative representation of n-times subtracted dispersion relations is found by performing an n-fold differentiation of Eq. (81) with respect to s, leading to

$$\frac{\mathrm{d}^n f(s)}{\mathrm{d}s^n} = \frac{n!}{2\pi\mathrm{i}} \int_{s_\mathrm{thr}}^\infty \mathrm{d}x \, \frac{\mathrm{disc} f(x)}{(x-s)^{n+1}}, \tag{89}$$

which is equivalent to

$$\frac{\mathrm{d}^n}{\mathrm{d}s^n} \left[\frac{\prod_{i=1}^n (s-s_i)}{2\pi\mathrm{i}} \int_{s_\mathrm{thr}}^\infty \mathrm{d}x \, \frac{\mathrm{disc} f(x)}{(x-s)\prod_{j=1}^n (x-s_j)} \right] = \frac{n!}{2\pi\mathrm{i}} \int_{s_\mathrm{thr}}^\infty \mathrm{d}x \, \frac{\mathrm{disc} f(x)}{(x-s)^{n+1}} \tag{90}$$

because $P_{n-1}(s)$ is a polynomial of degree $n-1$, vanishing upon n-fold differentiation.

To prove Eq. (89), we again proceed by induction. With

$$f(s) = P_0(s) + \frac{s-s_1}{2\pi\mathrm{i}} \int_{s_\mathrm{thr}}^\infty \mathrm{d}x \, \frac{\mathrm{disc} f(x)}{(x-s)(x-s_1)}, \tag{91}$$

the initial case $n=1$ follows as

$$\frac{\mathrm{d}f(s)}{\mathrm{d}s} = \frac{1}{2\pi\mathrm{i}} \int_{s_\mathrm{thr}}^\infty \mathrm{d}x \, \frac{\mathrm{disc} f(x)(x-s) + \mathrm{disc} f(x)(s-s_1)}{(x-s)^2(x-s_1)} = \frac{1}{2\pi\mathrm{i}} \int_{s_\mathrm{thr}}^\infty \mathrm{d}x \, \frac{\mathrm{disc} f(x)}{(x-s)^2}. \tag{92}$$

For the induction step $n \to n+1$, we start from Eq. (81) for $n+1$,

$$f(s) = P_n(s) + \frac{\prod_{i=1}^{n+1} (s-s_i)}{2\pi\mathrm{i}} \int_{s_\mathrm{thr}}^\infty \mathrm{d}x \, \frac{\mathrm{disc} f(x)}{(x-s)\prod_{j=1}^{n+1} (x-s_j)}, \tag{93}$$

so that, using $\prod_{i=1}^{n+1}(s-s_i) = (s-s_{n+1}+x-x)\prod_{i=1}^n (s-s_i)$,

$$\begin{aligned} \frac{\mathrm{d}^{n+1} f(s)}{\mathrm{d}s^{n+1}} = \frac{\mathrm{d}^{n+1}}{\mathrm{d}s^{n+1}} \Bigg[& \frac{\prod_{i=1}^n (s-s_i)}{2\pi\mathrm{i}} \int_{s_\mathrm{thr}}^\infty \mathrm{d}x \, \frac{\mathrm{disc} f(x)}{(x-s)\prod_{j=1}^n (x-s_j)} \\ & - \frac{\prod_{i=1}^n (s-s_i)}{2\pi\mathrm{i}} \int_{s_\mathrm{thr}}^\infty \mathrm{d}x \, \frac{\mathrm{disc} f(x)}{\prod_{j=1}^{n+1} (x-s_j)} \Bigg]. \end{aligned} \tag{94}$$

Here, the second term is a product of a polynomial of degree n in s and an integral that is independent of s; hence,

$$\begin{aligned} \frac{\mathrm{d}^{n+1} f(s)}{\mathrm{d}s^{n+1}} &= \frac{\mathrm{d}}{\mathrm{d}s} \frac{\mathrm{d}^n}{\mathrm{d}s^n} \left[\frac{\prod_{i=1}^n (s-s_i)}{2\pi\mathrm{i}} \int_{s_\mathrm{thr}}^\infty \mathrm{d}x \, \frac{\mathrm{disc} f(x)}{(x-s)\prod_{j=1}^n (x-s_j)} \right] \\ &= \frac{\mathrm{d}}{\mathrm{d}s} \frac{n!}{2\pi\mathrm{i}} \int_{s_\mathrm{thr}}^\infty \mathrm{d}x \, \frac{\mathrm{disc} f(x)}{(x-s)^{n+1}} \end{aligned} \tag{95}$$

upon inserting the induction statement in the form Eq. (90). Finally, performing the derivative leads to

$$\frac{\mathrm{d}^{n+1} f(s)}{\mathrm{d}s^{n+1}} = \frac{(n+1)!}{2\pi\mathrm{i}} \int_{s_\mathrm{thr}}^\infty \mathrm{d}x \, \frac{\mathrm{disc} f(x)}{(x-s)^{n+2}}, \tag{96}$$

as claimed in Eq. (89). Note that one can in principle start from an unsubtracted dispersion relation for $f(s)$ to arrive at Eq. (89) in a straightforward manner. However, since the corresponding integral does not necessarily converge, swapping the order of differentiation and integration is a potentially invalid operation.

Cauchy principal value and Sokhotski–Plemelj theorem

The Cauchy-principal-value prescription allows to assign meaningful values to certain types of otherwise ill-defined integrals. To illustrate the concept, we consider the example [9]

$$\begin{aligned}\int_{-a}^{b} \mathrm{d}x\, \frac{1}{x} &= \lim_{\delta_1\to 0^+} \int_{-a}^{-\delta_1} \mathrm{d}x\, \frac{1}{x} + \lim_{\delta_2\to 0^+} \int_{\delta_2}^{b} \mathrm{d}x\, \frac{1}{x} = \lim_{\delta_1\to 0^+} \int_{a}^{\delta_1} \mathrm{d}x\, \frac{1}{x} + \lim_{\delta_2\to 0^+} \int_{\delta_2}^{b} \mathrm{d}x\, \frac{1}{x} \\ &= \lim_{\delta_1\to 0^+} \log\delta_1 - \log a + \log b - \lim_{\delta_2\to 0^+} \log\delta_2, \end{aligned} \tag{97}$$

with $a, b > 0$, which is not well-defined due to the logarithmic divergence at $x = 0$ and the independence of the limits in approaching zero, *e.g.*, $\delta_2 = 2\delta_1$. For such an integral over a function $f(x)$ with an isolated singularity at x_0, $x_l < x_0 < x_u$, the Cauchy principal value is defined as [9]

$$⨍_{x_l}^{x_u} \mathrm{d}x\, f(x) = \lim_{\delta\to 0^+} \left[\int_{x_l}^{x_0-\delta} \mathrm{d}x\, f(x) + \int_{x_0+\delta}^{x_u} \mathrm{d}x\, f(x) \right]. \tag{98}$$

By imposing the use of a single infinitesimal parameter δ for the limit, the Cauchy principal value of the integral investigated in Eq. (97) thus evaluates to a finite and definite result,

$$⨍_{-a}^{b} \mathrm{d}x\, \frac{1}{x} = \lim_{\delta\to 0^+} \left[\int_{-a}^{-\delta} \mathrm{d}x\, \frac{1}{x} + \int_{\delta}^{b} \mathrm{d}x\, \frac{1}{x} \right] = \log b - \log a. \tag{99}$$

For our purposes, in particular, the Cauchy principal value becomes relevant when calculating integrals of the form [12]

$$\mathfrak{I}_\pm(x_0) = \lim_{\epsilon\to 0^+} \int_{x_l}^{x_u} \mathrm{d}x\, \frac{f(x)}{x - x_0 \pm \mathrm{i}\epsilon}, \tag{100}$$

with $x_l < x_0 < x_u$, as before, and $f(x)$ continuous on the integration interval and non-singular in a neighborhood of it; through the infinitesimal shift of x_0 into the complex plane, the integration along the real line avoids the pole of the integrand for $\epsilon = 0$ at $x = x_0$. We can rewrite Eq. (100) according to

$$\mathfrak{I}_\pm(x_0) = ⨍_{x_l}^{x_u} \mathrm{d}x\, \frac{f(x)}{x - x_0} + \lim_{\delta\to 0^+} \int_{\mathcal{C}_\delta^\pm} \mathrm{d}x\, \frac{f(x)}{x - x_0}, \tag{101}$$

where $\mathcal{C}_\delta^\pm$ is the arc specified by the contour $x_\delta^\pm = x_0 - \delta \mathrm{e}^{\mp \mathrm{i}t}$, $t \in [0, \pi]$. The integral over the arc evaluates to

$$\lim_{\delta\to 0^+} \int_{\mathcal{C}_\delta^\pm} \mathrm{d}x\, \frac{f(x)}{x - x_0} = \mp\mathrm{i} \lim_{\delta\to 0^+} \int_0^\pi \mathrm{d}t\, f(x_0 - \delta \mathrm{e}^{\mp \mathrm{i}t}) = \mp\mathrm{i}\pi f(x_0) \tag{102}$$

by expanding $f(x_0 - \delta \mathrm{e}^{\mp \mathrm{i}t}) = f(x_0) - \delta \mathrm{e}^{\mp \mathrm{i}t} f'(x_0) + \mathcal{O}(\delta^2)$ under the integral. Hence, we obtain the Sokhotski–Plemelj formula,[18]

$$\mathfrak{I}_\pm(x_0) = ⨍_{x_l}^{x_u} \mathrm{d}x\, \frac{f(x)}{x - x_0} \mp \mathrm{i}\pi f(x_0). \tag{103}$$

If x_0 was not contained in the integration interval, the imaginary part would vanish.

[18] For a more general version of the Sokhotski–Plemelj theorem, see, *e.g.*, Ref. [13].

Advanced topics

Symmetries and quantum numbers

Symmetries are among the most important concepts of modern physics. They enable us to group the vast amount of particles we know of today into certain categories and determine whether a given scattering or decay process is forbidden, suppressed, or allowed. Here, a crucial role is played by the discrete symmetries parity, charge conjugation, and time reversal, the product of which is conserved in all cases relevant to us according to the venerable CPT theorem [14, 15]. Electromagnetic interactions do, in fact, conserve all three of these symmetries separately. Phenomenologically, the same holds true for the strong interactions, even though the θ-term of quantum chromodynamics in principle implicates violations of parity and time reversal while conserving charge conjugation. The weak sector, on the other hand, generally induces parity, charge-conjugation, and time-reversal violations; when disregarding the complex phase of the Cabibbo–Kobayashi–Maskawa matrix, though, the weak interactions still conserve the combination of parity and charge conjugation, *i.e.*, time reversal as per the CPT theorem.[19] Presently, no conventional mechanism to generate an interaction that conserves only parity—and thus violates charge conjugation and time reversal—is known within the realm of the standard model [16, 17].

Beyond the (potential) conservation of the quantum numbers associated with the discrete symmetries discussed above, charge, (angular—including spin) momentum, and energy are paradigms of universally conserved quantities. For a system of particles, the allowed values of total angular momentum are obtained following the rules of angular-momentum addition. Furthermore, the total parity is given by the product of the intrinsic parities of the individual particles and, for the example of a two-particle system, an additional contribution $P = (-1)^L$ from a relative orbital angular momentum L between these. Since the intrinsic parity of antifermions is opposite to that of fermions—contrary to (anti-)bosons with equal parities—fermion–antifermion systems have a parity of $P = (-1)^{L+1}$. Regarding charge conjugation, we note that a definite charge parity can only be assigned to electrically neutral particles that are their own antiparticles, neutral particle–antiparticle systems, and systems composed of such eigenstates. In the second case, in particular, the charge parity reads $C = (-1)^{L+S}$ for scalar bosons and fermions, where S is the total spin of the system and L is the relative orbital angular momentum between its constituents. For systems of particles or compounds thereof with a definite behavior under charge conjugation, the total charge parity is given by the product of the corresponding charge parities.

To classify particles, one commonly uses the notation $J^{P(C)}$, denoting the total angular momentum, parity, and charge-conjugation parity of the state, respectively. Another (approximately conserved) quantum number of paramount importance to us is isospin, which is associated with an approximate symmetry of the strong interactions and coupled in analogy to spin. By combining charge conjugation with isospin, we can assign a so-called G-parity to a broader spectrum of particles than possible with charge parity. Together with isospin and G-parity, the classifying notation for particles as described above can then be extended to $I^G(J^{PC})$. There are further (additive) quantum numbers like the baryon and lepton number or the flavor quantum numbers strangeness, charm, bottomness, and topness; a discussion of these is, however, beyond the scope of this summary.

[19] Describing a parity-conserving process with an odd number of particles behaving unnatural under parity, *e.g.*, pseudoscalar and axial-vector mesons, requires the amplitude to involve a Levi-Civita tensor.

Form factors and vector-meson dominance

In the context of this thesis, form factors refer to functions that parameterize the (non-perturbative) electromagnetic interactions of hadronic matter. One of the most basic examples in this regard is the pion vector form factor $F_\pi^{\mathrm{V}}(q^2)$, which is defined via

$$\langle \pi^+(p')\pi^-(p)|J^\mu_{\mathrm{EM}}(0)|0\rangle = (p'-p)^\mu F_\pi^{\mathrm{V}}(q^2), \tag{104}$$

with $q = p' + p$ and

$$J^\mu_{\mathrm{EM}}(x) = \bar{q}(x)\mathcal{Q}\gamma^\mu q(x), \quad q(x) = (u(x), d(x), s(x))^\intercal, \quad \mathcal{Q} = \frac{1}{3}\mathrm{diag}(2,-1,-1). \tag{105}$$

This form factor entails information on the respective $\pi\pi\gamma$ coupling, that is either the creation (annihilation) of a pair of charged pions from (into) a photon or—through crossing symmetry—the scattering of a charged pion in an electromagnetic field. If the scattering induces the conversion of a hadron into another particle, the functions are commonly called transition form factors;[20] a simple example is the electromagnetic transition of a vector into a pseudoscalar meson or crossed processes thereof, *i.e.*, the coupling $VP\gamma$ in general. In particular, this definition includes the conversion of a hadron into an additional photon, *e.g.*, the vertex $A\gamma\gamma$, which describes the coupling of an axial-vector meson to two photons.

The interaction of hadrons with photons ($J^{PC} = 1^{--}$) can be modeled using the framework of vector-meson dominance [18–25]; see Refs. [26–28] for pedagogical and more recent reviews. At the foundation of vector-meson dominance is the assumption that the electromagnetic interactions of hadrons are mediated by neutral ρ-, ω-, and ϕ-like vector mesons ($J^{PC} = 1^{--}$). Without requiring insights into the underlying theory of quantum chromodynamics, this hypothesis leads to a remarkably accurate description of the low- and intermediate-energy region in a vast amount of applications. More specifically, some form factor $\mathcal{F}(q_1^2, \ldots, q_N^2)$, with photons of momenta $\{q_i\}_{i=1,\ldots,N}$ coupling to hadronic matter via the vector mesons $\{V_{i,j}\}_{j=1,\ldots,M}$ specified above, can then effectively be parameterized as a sum of propagator poles and *a priori* undetermined (dimensionless) coupling constants $\{C_j\}_{j=1,\ldots,M}$ according to

$$\mathcal{F}(q_1^2, \ldots, q_N^2) = (-1)^N \sum_{j=1}^{M} C_j \prod_{i=1}^{N} \frac{M_{V_{i,j}}^2}{q_i^2 - M_{V_{i,j}}^2 + \mathrm{i}\epsilon}. \tag{106}$$

In principle, the sum extends over all combinations of vector mesons that are allowed by symmetry, and the factor $(-1)^N$ ensures the normalization $\mathcal{F}(0,\ldots,0) = \sum_{j=1}^{M} C_j$; in practice, it usually suffices to take into account the few lowest-lying vector mesons to obtain an adequate representation. In writing Eq. (106), we assumed the narrow-width approximation for the vector mesons, *i.e.*, that their widths are negligible compared to their masses. To provide a realistic description of broad resonances, especially, we will incorporate the (in general energy-dependent) widths of the vector mesons by means of Breit–Wigner propagators, which implies $M_{V_{i,j}}^2 \to M_{V_{i,j}}^2 - \mathrm{i}\sqrt{q_i^2}\,\Gamma_{V_{i,j}}(q_i^2)$ in the denominators. We will also consider dispersively improved variants of the propagators—so-called spectral representations—which improve the analyticity properties of the form factors. Further extrinsic information on the form factors, such as their high-energy behavior, can be implemented, *e.g.*, by an appropriate choice of the coupling constants C_j.

[20] We will not be strict about this naming scheme throughout the dissertation and, in some cases, refer to what are actually transition form factors merely as form factors.

Energy-dependent widths and spectral representation

The width of a particle is a result of its instability and the decay into other particles in an interacting theory. For an unstable resonance R with mass M_R, the energy-dependent width can be parameterized in terms of its partial widths $\Gamma_{R\to X_i}$ into the available decay channels X_i as per[21]

$$\Gamma_R(q^2) = \sum_{X_i} \frac{\gamma_{R\to X_i}(q^2)}{\gamma_{R\to X_i}(M_R^2)} \Gamma_{R\to X_i}. \tag{107}$$

Here, $\Gamma_R(M_R^2) = \Gamma_R$ corresponds to the total width of the resonance, and the functions $\gamma_{R\to X_i}(q^2)$ can be constructed by considering the formulae of the decay widths $\Gamma(R \to X_i)$ for variable mass, $M_R \to \sqrt{q^2}$. The proper threshold behavior is implicit in the above, *i.e.*, $\gamma_{R\to X_i}(q^2) = 0$ for $q^2 \leq s_{\text{thr}}^i$, with s_{thr}^i being the threshold for the decay $R \to X_i$. If $\Gamma_R/M_R \ll 1$, the precise parameterization of the energy-dependent width in the Breit–Wigner propagator

$$P_R^{\text{BW}}(q^2) = \frac{1}{q^2 - M_R^2 + \mathrm{i}\sqrt{q^2}\,\Gamma_R(q^2)} \tag{108}$$

plays a minor role. Consequently, using a constant width, $\sqrt{q^2}\,\Gamma_R(q^2) \approx M_R\Gamma_R$ in the propagator, is expected to yield a reasonable approximation; in general, this does, however, induce unphysical imaginary parts below the threshold and spoil the analytic structure.

While the above energy-dependent widths have the proper threshold behavior, they typically feature an unphysical steep rise for large q^2, which can be particularly problematic once inserted into loop processes. In the following, we will establish a spectral representation of the Breit–Wigner propagators to improve their analyticity properties. To this end, we postulate an unsubtracted dispersion relation, see Eq. (80), for a dispersively improved propagator $P_R^{\text{disp}}(q^2)$ according to

$$P_R^{\text{disp}}(q^2) = \frac{1}{2\pi\mathrm{i}} \int_{s_{\text{thr}}}^{\infty} \mathrm{d}x\, \frac{\text{disc}\,[P_R^{\text{disc}}(x)]}{x - q^2} = \frac{1}{\pi} \int_{s_{\text{thr}}}^{\infty} \mathrm{d}x\, \frac{\text{Im}\,[P_R^{\text{disc}}(x)]}{x - q^2}, \tag{109}$$

where $s_{\text{thr}} = \min\{s_{\text{thr}}^i\}$ is the lowest threshold immanent in Eq. (107), marking the onset of the (first) branch cut; the evaluation of the imaginary part along the branch cut implicitly involves $x \to x + \mathrm{i}\epsilon$ ($\epsilon \to 0^+$). By identifying the spectral function with the imaginary part of the Breit–Wigner propagator, $\text{Im}\,[P_R^{\text{disc}}(x)] = \text{Im}\,[P_R^{\text{BW}}(x)]$, we find

$$P_R^{\text{disp}}(q^2) = -\frac{1}{\pi} \int_{s_{\text{thr}}}^{\infty} \mathrm{d}x\, \frac{\text{Im}\,[P_R^{\text{BW}}(x)]}{q^2 - x}, \tag{110}$$

with

$$\text{Im}\,[P_R^{\text{BW}}(x)] = \frac{-\sqrt{x}\,\Gamma_R(x)}{(x - M_R^2)^2 + x\Gamma_R(x)^2}. \tag{111}$$

Using the Sokhotski–Plemelj theorem, Eq. (103), we can compute this expression infinitesimally close to the branch cut, especially, by means of

$$\lim_{\epsilon\to 0^+} P_R^{\text{disp}}(q^2 \pm \mathrm{i}\epsilon) = -\frac{1}{\pi} \fint_{s_{\text{thr}}}^{\infty} \mathrm{d}x\, \frac{\text{Im}\,[P_R^{\text{BW}}(x)]}{q^2 - x} \pm \mathrm{i}\,\text{Im}\,[P_R^{\text{BW}}(q^2)], \tag{112}$$

where $\theta(q^2 - s_{\text{thr}})$ for the imaginary part is implied by the factor $\Gamma_R(x)$ in $\text{Im}\,[P_R^{\text{BW}}(q^2)]$.

[21] For all practical purposes, we will only take into account the dominant decay channels. In this case, the partial widths have to be rescaled such that $\Gamma_R(M_R^2) = \Gamma_R$ holds true.

Bardeen–Tung–Tarrach procedure

In the following, we outline a procedure that allows one to decompose amplitudes for processes involving photons into Lorentz structures and form factors free of kinematic singularities and zeroes, as developed by Bardeen, Tung, and Tarrach [29, 30]. While dynamic singularities, *i.e.*, poles and cuts of genuinely physical nature, are inherent to the amplitude and dictate the analytic structure of the form factors, those of kinematic origin correspond to redundant singularities in the external momenta. Kinematic zeroes, in contrast, refer to sets of constraints in the form of linear dependencies. Crucially, the singularity-free property of the form factors is a requirement to set up dispersion relations, with the zero-free property rendering any *ad hoc* subtractions unnecessary [29].

To illustrate the convenience of the method established by Bardeen, Tung, and Tarrach, let us consider a generic tensor matrix element $\mathcal{M}^{\mu_1\cdots\mu_N}(q_1,\ldots,q_N,p_1,\ldots,p_M)$, with $Q=\{q_i\}_{i=1,\ldots,N}$ being photon momenta and $P=\{p_j\}_{j=1,\ldots,M}$ the momenta of the remaining external particles;[22] for ease of notation, we omitted further Lorentz indices from, *e.g.*, massive spin-1 particles, as may be present among the particles described by p_j. The full amplitude is obtained upon contracting the tensor matrix element with the polarization vectors of the photons and, potentially, multiplying by any additional fermionic spinors. We now expand the tensor matrix element in terms of a basis of Lorentz structures $\{L_k^{\mu_1\cdots\mu_N}\}_{k=1,\ldots,L}$ and associated form factors $\{\mathcal{F}_k\}_{k=1,\ldots,L}$ according to

$$\mathcal{M}^{\mu_1\cdots\mu_N}(Q,P)=\sum_{k=1}^{L}L_k^{\mu_1\cdots\mu_N}(Q,P)\,\mathcal{F}_k(\{Q,P\}^2), \tag{113}$$

where $\{Q,P\}^2$ indicates all independent scalar invariants that can be built with the two sets of momenta. With the holistic amplitude having only dynamic singularities [29], kinematic singularities in the structures imply that the form factors must develop kinematic zeroes at the same points to mutually cancel and *vice versa*; similarly, linear dependencies, *i.e.*, kinematic zeroes, in the structures are linked to kinematic singularities in the form factors. Had we considered an amplitude for a process without massless gauge bosons, the construction of a basis free of kinematic singularities and zeroes would be rather straightforward: singularities in the structures could be avoided by choosing polynomials in the four-momenta to construct the tensor basis,[23] and apparent zeroes from, *e.g.*, the discrete symmetries parity, charge conjugation, and time reversal could readily be eliminated; see Refs. [29–31] and references therein. In what follows, we assume Eq. (113) to consist of such a polynomial tensor basis with the trivial kinematic zeroes removed.

On account of the Ward identity, which is a special case of the Ward–Takahashi identity in quantum electrodynamics and intimately related to gauge invariance, the photons, for all q_i, enforce [4, 5]

$$q_{i\mu_i}\mathcal{M}^{\mu_1\cdots\mu_N}(q_1,\ldots,q_N,p_1,\ldots,p_M)=0 \tag{114}$$

in physical kinematic configuration, *i.e.*, with non-photon external asymptotic-state particles assumed on shell. Hence, Eq. (113) must additionally obey equations of the form

$$0=\sum_{k=1}^{L}\left[q_{i\mu_i}L_k^{\mu_1\cdots\mu_N}(Q,P)\right]\mathcal{F}_k(\{Q,P\}^2), \tag{115}$$

[22] Momentum conservation does, in fact, reduce the number of linearly independent momenta by one.
[23] Note that the structures possibly hold gamma matrices and might thus also reside in Dirac space.

which induce a linear dependence, *i.e.*, kinematic zeroes, among the form factors and thus lead to non-trivial complications in the procedure described above. In principle, the resulting equations can be solved manually to obtain a subset of independent form factors; however, besides posing an in general tedious task, such an approach does not guarantee the absence of further kinematic zeroes in the remaining form factors [29].

Instead, we follow Refs. [29, 30] and define a set of gauge projectors $\{\mathcal{I}_i^{\nu_i\mu_i}\}_{i=1,\dots,N}$,

$$\mathcal{I}_i^{\nu_i\mu_i} = g^{\nu_i\mu_i} - \frac{k_i^{\nu_i} q_i^{\mu_i}}{k_i \cdot q_i}, \tag{116}$$

where k_i is any momentum from Q or P that is distinct from q_i.[24] Let us start by investigating the properties of these gauge projectors. First of all, we observe that

$$q_{i\nu_i}\, \mathcal{I}_i^{\nu_i\mu_i} = 0, \tag{117}$$

so that contracting the gauge projectors with any tensor, *e.g.*, $T^{\mu_1\cdots\mu_N}$, gives a gauge-invariant quantity, $q_{i\nu_i}\mathcal{I}_i^{\nu_i}{}_{\mu_i} T^{\mu_1\cdots\mu_N} = 0$. Furthermore, given a gauge-invariant tensor, *e.g.*, $G^{\mu_1\cdots\mu_N}$ with $q_{i\mu_i} G^{\mu_1\cdots\mu_N} = 0$, we have

$$\mathcal{I}_i^{\nu_i}{}_{\mu_i}\, G^{\mu_1\cdots\mu_i\cdots\mu_N} = G^{\mu_1\cdots\nu_i\cdots\mu_N}. \tag{118}$$

In other words, applying the gauge projectors to already gauge-invariant quantities has no effect beyond some trivial relabeling. Another property reads

$$\mathcal{I}_i^{\nu_i}{}_{\mu_i}\, k_i^{\mu_i} = 0, \tag{119}$$

i.e., terms proportional to $k_i^{\mu_i}$ vanish upon contraction with the gauge projectors.

Applying the full set of projectors to the matrix element given in Eq. (113) leads to

$$\begin{aligned}\widetilde{\mathcal{M}}^{\nu_1\cdots\nu_N}(Q,P) &= \sum_{k=1}^{L}\Big[\Big(\prod_{i=1}^{N}\mathcal{I}_i^{\nu_i}{}_{\mu_i}\Big) L_k^{\mu_1\cdots\mu_N}(Q,P)\Big]\mathcal{F}_k(\{Q,P\}^2) \\ &= \sum_{m\in J}\widetilde{L}_m^{\nu_1\cdots\nu_N}(Q,P)\,\mathcal{F}_m(\{Q,P\}^2),\end{aligned} \tag{120}$$

where $J \subseteq \{1,\dots,L\}$. Due to the properties of the gauge projectors shown above, the structures $\{\widetilde{L}_m^{\nu_1\cdots\nu_N}\}_{m\in J}$ and thus $\widetilde{\mathcal{M}}^{\nu_1\cdots\nu_N}(Q,P)$ satisfy gauge invariance by construction. At the same time, the number of (non-zero) structures is potentially reduced, eliminating linear dependencies induced by Eq. (115) at least partly, with the form factors $\{\mathcal{F}_m\}_{m\in J}$ remaining free of kinematic singularities as a subset of the initial form factors. However, due to kinematic singularities in the structures $\widetilde{L}_m^{\nu_1\cdots\nu_N}$ that arise from the poles $P(k_i,q_i) = k_i\cdot q_i$ of the projectors, additional kinematic zeroes can be present among the form factors [29]. To remove the singularities in the structures, we proceed as follows [30]:

- eliminate as many highest-order poles $\prod_i P(k_i,q_i)$ as possible by constructing linear combinations of the structures with non-singular coefficients;
- if no more highest-order poles can be removed in this way, reduce the order of these poles by one by multiplying the corresponding structures with some $P(k_i,q_i)$;

[24] The results obtained with different choices for k_i will be physically equivalent [29].

- repeat this procedure with the now highest-order poles and continue until no poles are left in the structures.

We thus obtain a basis of structures $\{\widehat{L}_n^{\nu_1\cdots\nu_N}\}_{n\in I}$ and associated form factors $\{\widehat{\mathcal{F}}_n\}_{n\in I}$, with $I \subseteq J$, that are free from kinematic singularities and zeroes originating from gauge invariance.[25] With all other kinematic singularities and zeroes eliminated already in Eq. (113), the final form of the matrix element is given by

$$\widehat{\mathcal{M}}^{\nu_1\cdots\nu_N}(Q,P) = \sum_{n\in I} \widehat{L}_n^{\nu_1\cdots\nu_N}(Q,P)\,\widehat{\mathcal{F}}_n(\{Q,P\}^2). \tag{121}$$

In order to compare different tensor bases with each other, we consider two such bases $\{L_i^{\mu_1\cdots\mu_N}\}_{i=1,\ldots,H}$ and $\{S_j^{\mu_1\cdots\mu_N}\}_{j=1,\ldots,H}$, with any dependence of the structures on the momenta being suppressed for notational convenience.[26] Either of these bases can be expressed in terms of the respective other by means of

$$L_i^{\mu_1\cdots\mu_N} = \sum_{j=1}^{H} \beta_{ij} S_j^{\mu_1\cdots\mu_N} \qquad \Leftrightarrow \qquad L^{\mu_1\cdots\mu_N} = \beta S^{\mu_1\cdots\mu_N}, \tag{122}$$

where β_{ij} are the corresponding coefficients, $|\{\beta_{ij}\}_{i,j=1,\ldots,H}| = H^2$. Contracting both sides of this equation with the structures $\{S_k^{\mu_1\cdots\mu_N}\}_{k=1,\ldots,H}$ results in the system of equations

$$L_i^{\mu_1\cdots\mu_N} S_{k\mu_1\cdots\mu_N} = \sum_{j=1}^{H} \beta_{ij} S_j^{\mu_1\cdots\mu_N} S_{k\mu_1\cdots\mu_N}, \tag{123}$$

which gives H independent equations for each $i = 1, \ldots, H$ that can be solved for β_{ij}.

Let us further denote the form factors associated with the two bases by $\{\mathcal{F}_i\}_{i=1,\ldots,H}$ and $\{\mathcal{G}_j\}_{j=1,\ldots,H}$, respectively, again suppressing any dependence on the scalar invariants. For the tensor matrix elements, we then write

$$\mathcal{M}_L^{\mu_1\cdots\mu_N} = \sum_{i=1}^{H} L_i^{\mu_1\cdots\mu_N}\mathcal{F}_i, \qquad \mathcal{M}_S^{\mu_1\cdots\mu_N} = \sum_{j=1}^{H} S_j^{\mu_1\cdots\mu_N}\mathcal{G}_j. \tag{124}$$

With the two bases describing the same process, we have $\mathcal{M}_L^{\mu_1\cdots\mu_N} = \mathcal{M}_S^{\mu_1\cdots\mu_N}$ and thus

$$\sum_{i=1}^{H} L_i^{\mu_1\cdots\mu_N}\mathcal{F}_i = \sum_{i,j=1}^{H} \beta_{ij} S_j^{\mu_1\cdots\mu_N}\mathcal{F}_i = \sum_{j=1}^{H} S_j^{\mu_1\cdots\mu_N}\mathcal{G}_j. \tag{125}$$

Consequently, the form factors are related according to

$$\mathcal{G}_j = \sum_{i=1}^{H} \beta_{ij}\mathcal{F}_i = \sum_{i=1}^{H} \beta_{ji}^{\intercal}\mathcal{F}_i \qquad \Leftrightarrow \qquad \mathcal{G} = \beta^{\intercal}\mathcal{F}. \tag{126}$$

[25] Here, we assume the existence of such a basis, which is not necessarily given; see, *e.g.*, Refs. [30, 32].

[26] Although, in principle, similar relations as derived here can be obtained if the two sets of structures have different dimensions H_L and H_S, such a comparison would lack definiteness because at most one of the sets can constitute a basis. In this case, β would not correspond to a square matrix and the relations between the bases could, in particular, not be inverted.

Anomalous magnetic moment of the muon

The spin $\boldsymbol{s}$ of the muon induces an intrinsic magnetic moment [33, 34]

$$\boldsymbol{\mu} = -g_\mu \frac{e}{2m_\mu} \boldsymbol{s}, \tag{127}$$

which leads to an interaction $\propto \boldsymbol{\mu} \cdot \boldsymbol{B}$ with a magnetic field $\boldsymbol{B}$ (or, in general, with an electromagnetic field, *i.e.*, a photon). For the gyromagnetic ratio, the DIRAC equation predicts $g_\mu = 2$; the corresponding tree-level process is illustrated in the top-left diagram of Fig. 4. This value is subject to higher-order corrections, motivating the definition of the anomalous magnetic moment of the muon as the relative deviation from $g_\mu = 2$,

$$a_\mu = \frac{g_\mu - 2}{2}. \tag{128}$$

Within the standard model, the corrections are conveniently divided into contributions from quantum electrodynamics, the electroweak sector, and those of hadronic nature according to $a_\mu^{\mathrm{SM}} = a_\mu^{\mathrm{QED}} + a_\mu^{\mathrm{EW}} + a_\mu^{\mathrm{had}}$. Regarding the first of these, SCHWINGER pioneered the calculation of the leading-order result [35, 36]

$$a_\mu^{\mathrm{QED,\,LO}} = \frac{\alpha}{2\pi} \approx 116\,140\,972 \times 10^{-11}, \tag{129}$$

which, by far, gives the largest contribution to a_μ^{SM};[27] see the top-right diagram of Fig. 4. Beyond this one-loop result, corrections from quantum electrodynamics have presently been calculated up to five-loop order, yielding [37, 38]

$$a_\mu^{\mathrm{QED},\,\mathcal{O}(\alpha^5)} = 116\,584\,718.931(104) \times 10^{-11}, \tag{130}$$

as also compiled in Ref. [39]. This figure accounts for all but $1 - a_\mu^{\mathrm{QED}}/a_\mu^{\mathrm{exp}} = 63$ parts per million of the current experimental world average's central value [40–45],

$$a_\mu^{\mathrm{exp}} = 116\,592\,059(22) \times 10^{-11}. \tag{131}$$

Electroweak corrections comprise at least one of the electroweak gauge bosons W, Z or the HIGGS boson H; two of the dominant one-loop diagrams are obtained by replacing the photon in the top-right diagram of Fig. 4 by a Z or H boson. The final result quoted in Ref. [39], including two-loop contributions, reads [46, 47]

$$a_\mu^{\mathrm{EW}} = 153.6(1.0) \times 10^{-11}. \tag{132}$$

While the uncertainties on a_μ^{QED} and a_μ^{EW} are under sufficient control, the non-perturbative nature of the strong interactions impedes a reliable determination of the hadronic contributions. Here, the coupling of hadrons to muons necessarily proceeds via photons, W, Z, or HIGGS bosons since quantum chromodynamics does not allow for a direct coupling to leptons. The hadronic corrections then decompose further into those attributable to either hadronic vacuum polarization or hadronic light-by-light scattering as per $a_\mu^{\mathrm{had}} = a_\mu^{\mathrm{HVP}} + a_\mu^{\mathrm{HLbL}}$; the leading-order insertions of hadronic vacuum polarization and hadronic light-by-light scattering as related to the magnetic moment of the muon are depicted in the bottom-left and bottom-right diagrams of Fig. 4. Given the high precision of the experimental value, Eq. (131), and the expected improvements beyond this result, higher-order insertions have to be taken into account as well, which include the following [48–50]:

[27] Note that SCHWINGER's result was misprinted in the original publication, Ref. [35]; see also Ref. [36].

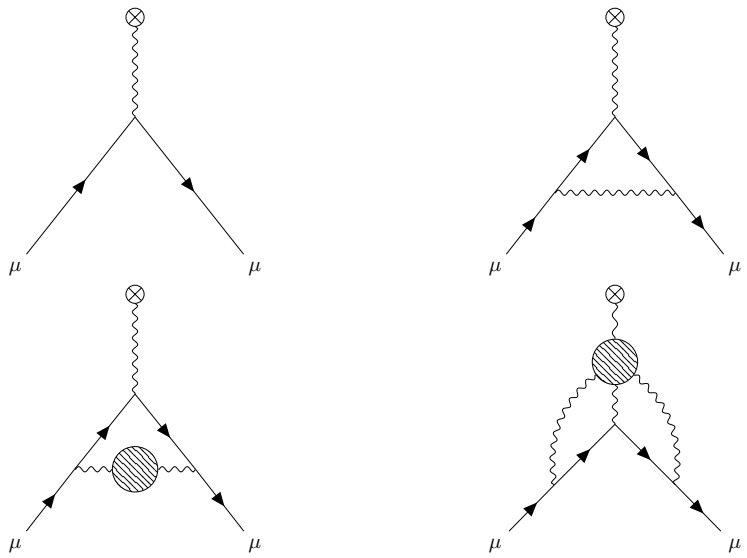

Figure 4: Diagrammatic illustration of the magnetic moment of the muon at tree level (*top left*), its leading-order correction in quantum electrodynamics (*top right*), and the leading-order insertions of hadronic vacuum polarization (*bottom left*) and hadronic light-by-light scattering (*bottom right*). The shaded blobs represent hadronic intermediate states.

- an additional photon exchange between the muon legs or a second hadronic/leptonic vacuum polarization bubble on the photon line in the bottom-left diagram of Fig. 4;
- a leptonic vacuum polarization bubble on one of the photon lines connected to the muon legs in the bottom-right diagram of Fig. 4;

see also the compilation in Ref. [39]. Furthermore, the interpretation in terms of hadronic intermediate states as the relevant degrees of freedom has to be reconciled with quark-loop contributions and matched to short-distance constraints, a discussion of which is, however, beyond the scope of this compendium; for extensive reviews, see Refs. [33, 34, 39]. After all, there are two modern approaches to calculate a_μ^{had}: either using a data-driven dispersive method or by solving quantum chromodynamics numerically on the lattice; see Ref. [39] and references therein. The former strategy requires data on $e^+e^- \to \text{hadrons}$ to compute a_μ^{HVP} and, *inter alia*, information on the axial-vector transition form factors $A \to \gamma^*\gamma^*$, $A = f_1, f_1', a_1$, to determine a_μ^{HLbL}. According to the theory consensus of Ref. [39], the total standard-model prediction, including results from both approaches, is then given by [37, 38, 46–63]

$$a_\mu^{\text{SM}} = 116\,591\,810(43) \times 10^{-11}, \tag{133}$$

which differs from Eq. (131) by 5.2σ and potentially hints at physics beyond the standard model. Rather recently, the CMD-3 measurement of $e^+e^- \to \pi^+\pi^-$ [64, 65] raised a puzzle in the data-driven evaluation of hadronic vacuum polarization, which Ref. [39] quotes as $a_\mu^{\text{HVP}} = 6845(40) \times 10^{-11}$ [48, 49, 51–55]; this puzzle and further tensions with determinations from the lattice community are briefly addressed in Part I of this thesis. Therein, we also discuss the contribution from hadronic light-by-light scattering obtained with the phenomenological approach in more detail. When including results from both approaches, on the contrary, Ref. [39] quotes $a_\mu^{\text{HLbL}} = 92(19) \times 10^{-11}$ [34, 50, 56–63, 66–70].

Tensor loop integrals and Passarino–Veltman decomposition

The Passarino–Veltman decomposition [71, 72] is based on the fact that any one-loop integral can be reduced to a finite sum of predefined master integrals. To illustrate the reduction procedure, we consider the one-loop topology of Feynman diagrams depicted in Fig. 5. Such an N-point one-loop diagram leads to the generic expression [73]

$$D_N = \int \frac{\mathrm{d}^4k}{(2\pi)^4} \frac{F(k,p_1,\dots,p_N)}{[k^2-m_1^2]\,[(q_1+k)^2-m_2^2]\,[(q_2+k)^2-m_3^2]\dots[(q_{N-1}+k)^2-m_N^2]}, \quad (134)$$

where $q_i = \sum_{j=1}^{i} p_j$, with $q_N = 0$ due to momentum conservation; for notational convenience, we suppress the $(+\mathrm{i}\epsilon)$-prescription in the propagators here and in the following and, *ad libitum*, omit the arguments of, *e.g.*, D_N that remain after performing the loop integration.[28] The function $F(k,p_1,\dots,p_N)$ can consist of scalar invariants formed with polarization vectors, spinors, gamma matrices, and polynomials in the loop momentum k and the external momenta $\{p_i\}_{i=1,\dots,N}$.[29] We can separate the dependence on the loop momentum in $F(k,p_1,\dots,p_N)$ from the rest, *e.g.*, by writing $k\cdot p_i = k_\mu p_i^\mu$. Hence, Eq. (134) can be written as a sum of integrals of the form

$$I_N^{\boldsymbol{\mu}} = \int \frac{\mathrm{d}^4k}{(2\pi)^4} \frac{f^{\boldsymbol{\mu}}(k)}{[k^2-m_1^2]\,[(q_1+k)^2-m_2^2]\,[(q_2+k)^2-m_3^2]\dots[(q_{N-1}+k)^2-m_N^2]}, \quad (135)$$

multiplied by and contracted with the corresponding polarization vectors, spinors, gamma matrices, and polynomials in the external momenta as well as scalar invariants thereof. In general, the $I_N^{\boldsymbol{\mu}}$ are tensor loop integrals and the $f^{\boldsymbol{\mu}}(k)$ tensor fields, $\boldsymbol{\mu} = (\mu_1,\dots,\mu_r)$. If $f^{\boldsymbol{\mu}}(k) \sim 1$ does not depend on k, the integral is referred to as a scalar loop integral. With $f^{\boldsymbol{\mu}}(k) \sim f(k^2)$ being a scalar function of k^2 only, we can use $k^2 = k^2 - m_i^2 + m_i^2$ and shift the loop momentum as per $k \to k - p_i$ to decompose the expression into a sum of scalar and purely tensor loop integrals, where the latter have no dependence on k^2 in the numerator left, *i.e.*, $f^{\boldsymbol{\mu}}(k) \sim k^{\mu_1}\dots k^{\mu_r}$. Similarly, the most general case, with $f^{\boldsymbol{\mu}}(k)$ containing both factors of k^2 and tensor structures k^{μ_j}, can be reduced to a sum consisting of scalar and purely tensor loop integrals only. Consequently, we will, without loss of generality, assume $f^{\boldsymbol{\mu}}(k) \sim \{1, k^{\mu_1}\dots k^{\mu_r}\}$ in the following.

From a dimensional analysis, one finds that $I_N^{\boldsymbol{\mu}}$ holds ultraviolet divergences, *i.e.*, divergences that are due to the integration region of large momenta, if the rank r of loop momenta in $f^{\boldsymbol{\mu}}(k)$ is such that $r \geq 2N-4$; here, equality yields a logarithmic divergence. Since $r = 0$ for scalar loop integrals, only one- and two-point scalar loop integrals can be ultraviolet divergent. Renormalizable quantum field theories, such as the standard model [74], obey $r \leq N$ [73], so that ultraviolet divergences are restricted to a very narrow set of integrals in these theories, see Table 1. A discussion of other types of divergences, *e.g.*, infrared divergences, which originate from integration regions of small momenta and are related to the presence of massless particles, is beyond the scope of this compendium. Divergent loop integrals are most conveniently regularized in the framework of dimensional regularization [75], in which Eq. (135) becomes an integral in $D = 4-2\epsilon$ dimensions,

$$I_N^{\boldsymbol{\mu}} = \mu^{4-D} \int \frac{\mathrm{d}^Dk}{(2\pi)^D} \frac{f^{\boldsymbol{\mu}}(k)}{[k^2-m_1^2]\,[(q_1+k)^2-m_2^2]\,[(q_2+k)^2-m_3^2]\dots[(q_{N-1}+k)^2-m_N^2]}. \quad (136)$$

[28] To include (energy-dependent) widths, one can use the spectral representation given in Eq. (110).

[29] Closed fermion loops yield an additional factor of (-1).

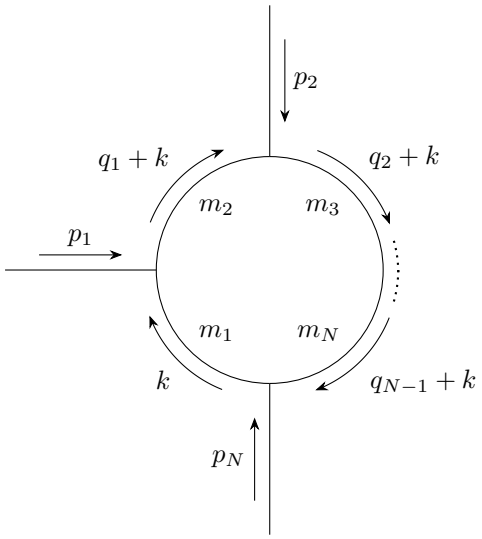

Figure 5: A topological subset of one-loop FEYNMAN diagrams, leading to a generic expression of the form given in Eq. (134), as discussed in the main text.

Here, μ is a dimensionful parameter that is introduced to retain the mass dimension of $I_N^{\boldsymbol{\mu}}$, and the generalization of the four-vectors and the MINKOWSKI scalar product to D spacetime dimensions is implicitly understood.[30] In what follows, we will write all integrals in their dimensionally regularized form, irrespective of their convergence; if the integral converges in $D = 4$, the implied limit $\epsilon \to 0^+$ can, in principle, be taken at any stage.

The condition $r \leq N$ in renormalizable theories motivates the definition of the following scalar and tensor loop integrals [71–73]: the tadpole diagram

$$A_0(m_1) = \mu^{4-D} \int \frac{\mathrm{d}^D k}{\mathrm{i}\pi^2} \frac{1}{k^2 - m_1^2}, \tag{137}$$

the bubble diagrams

$$\begin{aligned} B_0(p_1, m_1, m_2) &= \mu^{4-D} \int \frac{\mathrm{d}^D k}{\mathrm{i}\pi^2} \frac{1}{[k^2 - m_1^2][(q_1 + k)^2 - m_2^2]}, \\ B^{\mu;\mu\nu}(p_1, m_1, m_2) &= \mu^{4-D} \int \frac{\mathrm{d}^D k}{\mathrm{i}\pi^2} \frac{k^\mu; k^\mu k^\nu}{[k^2 - m_1^2][(q_1 + k)^2 - m_2^2]}, \end{aligned} \tag{138}$$

the triangle diagrams

$$\begin{aligned} C_0(p_1, p_2, m_1, m_2, m_3) &= \mu^{4-D} \int \frac{\mathrm{d}^D k}{\mathrm{i}\pi^2} \frac{1}{[k^2 - m_1^2][(q_1 + k)^2 - m_2^2][(q_2 + k)^2 - m_3^2]}, \\ C^{\mu;\mu\nu;\mu\nu\alpha}(p_1, p_2, m_1, m_2, m_3) &= \mu^{4-D} \int \frac{\mathrm{d}^D k}{\mathrm{i}\pi^2} \frac{k^\mu; k^\mu k^\nu; k^\mu k^\nu k^\alpha}{[k^2 - m_1^2][(q_1 + k)^2 - m_2^2][(q_2 + k)^2 - m_3^2]}, \end{aligned} \tag{139}$$

[30] Note that the external quantities that we separated from the tensor integral, as, *e.g.*, the gamma matrices, have to be analytically continued to D dimensions as well. For the fifth gamma matrix, γ_5, in particular, this is problematic on its own [75].

	$N=1$	$N=2$	$N=3$	$N=4$	$N=5$	$N=6$	$N=7$
$r=0$	∞	∞					
$r=1$	0	∞					
$r=2$	$[\infty]$	∞	∞				
$r=3$	[0]	$[\infty]$	∞				
$r=4$	$[\infty]$	$[\infty]$	$[\infty]$	∞			
$r=5$	[0]	$[\infty]$	$[\infty]$	$[\infty]$			
$r=6$	$[\infty]$	$[\infty]$	$[\infty]$	$[\infty]$	$[\infty]$		
$r=7$	[0]	$[\infty]$	$[\infty]$	$[\infty]$	$[\infty]$	[ ]	

Table 1: The ultraviolet behavior for loop integrals of the form given in Eq. (135). Here, infinities and empty cells indicate diverging and converging integrals, respectively; zeroes symbolize integrals that show up as divergent from simple power counting but vanish upon explicit calculation. Square brackets flag integrals that do not exist in renormalizable quantum field theories such as the standard model.

and the box diagrams

$$\begin{aligned}
&D_0(p_1,p_2,p_3,m_1,m_2,m_3,m_4)\\
&=\mu^{4-D}\int\frac{\mathrm{d}^Dk}{\mathrm{i}\pi^2}\frac{1}{[k^2-m_1^2][(q_1+k)^2-m_2^2][(q_2+k)^2-m_3^2][(q_3+k)^2-m_4^2]},\\
&D^{\mu;\mu\nu;\mu\nu\alpha;\mu\nu\alpha\beta}(p_1,p_2,p_3,m_1,m_2,m_3,m_4)\\
&=\mu^{4-D}\int\frac{\mathrm{d}^Dk}{\mathrm{i}\pi^2}\frac{k^\mu;k^\mu k^\nu;k^\mu k^\nu k^\alpha;k^\mu k^\nu k^\alpha k^\beta}{[k^2-m_1^2][(q_1+k)^2-m_2^2][(q_2+k)^2-m_3^2][(q_3+k)^2-m_4^2]},
\end{aligned}\tag{140}$$

and an extension of this scheme to higher (N,r) is straightforward; writing the integration measures with a factor $1/(\mathrm{i}\pi^2)$ is purely conventional. Note that a tadpole integral with $r=1$, $A^\mu(m_1)$, vanishes for symmetry reasons, as readily verified via the transformation $k\to-k$; see also Table 1 for $N=1$ and odd r. This is in line with the observation that Lorentz covariance would dictate such an integral to be proportional to a structure with a free Lorentz index, of which there is none among the arguments of a tadpole diagram. Since the scalar integrals have no structure in Lorentz space, they can only depend on scalar invariants formed with the specified arguments, which we refrained from making explicit in their arguments to ensure a consistent notation with the tensor integrals. Following the procedure developed by Passarino and Veltman [71], the tensor integrals can—based on Lorentz covariance—be reduced to a linear combination of scalar loop integrals. Crucially, the intrinsically four-dimensional nature of space-time further allows to reduce scalar loop integrals with $N>4$ to a sum of scalar loop integrals with $N=4$; see Refs. [73, 76] and references therein. Consequently, any one-loop integral can be written in terms of the four master integrals $A_0(m_1)$, $B_0(p_1,m_1,m_2)$, $C_0(p_1,p_2,m_1,m_2,m_3)$, and $D_0(p_1,p_2,p_3,m_1,m_2,m_3,m_4)$, whose analytic expressions can be fairly complicated, being composed of functions including (di-)logarithms and terms singular in $D-4$ [72, 76].

In order to outline the *modus operandi* of the Passarino–Veltman decomposition, we observe that Lorentz covariance dictates an expansion of the tensor loop integrals according to

$$\begin{aligned} B^{\mu}(p_1, m_1, m_2) &= p_1^{\mu} B_1, \\ B^{\mu\nu}(p_1, m_1, m_2) &= g^{\mu\nu} B_{00} + p_1^{\mu} p_1^{\nu} B_{11} \end{aligned} \tag{141}$$

for the bubble integrals,

$$\begin{aligned} C^{\mu}(p_1, p_2, m_1, m_2, m_3) &= p_1^{\mu} C_1 + p_2^{\mu} C_2, \\ C^{\mu\nu}(p_1, p_2, m_1, m_2, m_3) &= g^{\mu\nu} C_{00} + \sum_{i,j=1}^{2} p_i^{\mu} p_j^{\nu} C_{ij}, \\ C^{\mu\nu\alpha}(p_1, p_2, m_1, m_2, m_3) &= \sum_{i=1}^{2} (g^{\mu\nu} p_i^{\alpha} + g^{\mu\alpha} p_i^{\nu} + g^{\nu\alpha} p_i^{\mu}) C_{00i} + \sum_{i,j,k=1}^{2} p_i^{\mu} p_j^{\nu} p_k^{\alpha} C_{ijk} \end{aligned} \tag{142}$$

for the triangle integrals, and

$$\begin{aligned} D^{\mu}(p_1, p_2, p_3, m_1, m_2, m_3, m_4) &= p_1^{\mu} D_1 + p_2^{\mu} D_2 + p_3^{\mu} D_3, \\ D^{\mu\nu}(p_1, p_2, p_3, m_1, m_2, m_3, m_4) &= g^{\mu\nu} D_{00} + \sum_{i,j=1}^{3} p_i^{\mu} p_j^{\nu} D_{ij}, \\ D^{\mu\nu\alpha}(p_1, p_2, p_3, m_1, m_2, m_3, m_4) &= \sum_{i=1}^{3} (g^{\mu\nu} p_i^{\alpha} + g^{\mu\alpha} p_i^{\nu} + g^{\nu\alpha} p_i^{\mu}) D_{00i} + \sum_{i,j,k=1}^{3} p_i^{\mu} p_j^{\nu} p_k^{\alpha} D_{ijk}, \\ D^{\mu\nu\alpha\beta}(p_1, p_2, p_3, m_1, m_2, m_3, m_4) &= (g^{\mu\nu} g^{\alpha\beta} + g^{\mu\alpha} g^{\nu\beta} + g^{\mu\beta} g^{\nu\alpha}) D_{0000} \\ &\quad + \sum_{i,j=1}^{3} (g^{\mu\nu} p_i^{\alpha} p_j^{\beta} + g^{\mu\alpha} p_i^{\nu} p_j^{\beta} + g^{\mu\beta} p_i^{\nu} p_j^{\alpha} + g^{\nu\alpha} p_i^{\mu} p_j^{\beta} + g^{\nu\beta} p_i^{\mu} p_j^{\alpha} + g^{\alpha\beta} p_i^{\mu} p_j^{\nu}) D_{00ij} \\ &\quad + \sum_{i,j,k,l=1}^{3} p_i^{\mu} p_j^{\nu} p_k^{\alpha} p_l^{\beta} D_{ijkl} \end{aligned} \tag{143}$$

for the box integrals. Here, the coefficient functions $\{B_1, B_{00}, B_{11}, \ldots\}$ carry indices in a suggestive way, indicating the momenta they are associated with; their dependence on the available Lorentz invariants is suppressed for notational convenience. Due to the symmetry of the tensor integrals under permutations of the indices, see Eq. (138)–Eq. (140), the coefficient functions fulfill certain relations; some of these, *e.g.*, a unique C_{00i}, have already been incorporated in Eq. (141)–Eq. (143), while others, such as $C_{12} = C_{21}$, are straightforward to deduce. Similarly, symmetry forbids the parity-odd Levi-Civita tensor to be part of the above expansions. By contracting Eq. (141)–Eq. (143) with the respectively available Lorentz structures, one obtains a system of equations that can be solved to yield expressions for the coefficient functions in dependence of scalar loop integrals only. We demonstrate this procedure exemplarily for the two-point loop integrals here; the three- and four-point integrals require significantly more algebraic effort, which is most conveniently performed using Gram matrices [71, 73, 76].

In the two-point case, the available quantities to contract Eq. (141) with are p_1^μ, $g^{\mu\nu}$, and $p_1^\mu p_1^\nu$, leading to

$$\begin{aligned}
p_{1\mu} B^\mu(p_1, m_1, m_2) &= \mu^{4-D} \int \frac{\mathrm{d}^D k}{\mathrm{i}\pi^2} \frac{p_1 \cdot k}{[k^2 - m_1^2][(p_1+k)^2 - m_2^2]} = p_1^2 B_1, \\
g_{\mu\nu} B^{\mu\nu}(p_1, m_1, m_2) &= \mu^{4-D} \int \frac{\mathrm{d}^D k}{\mathrm{i}\pi^2} \frac{k^2}{[k^2 - m_1^2][(p_1+k)^2 - m_2^2]} = D B_{00} + p_1^2 B_{11}, \\
p_{1\mu} p_{1\nu} B^{\mu\nu}(p_1, m_1, m_2) &= \mu^{4-D} \int \frac{\mathrm{d}^D k}{\mathrm{i}\pi^2} \frac{(p_1 \cdot k)^2}{[k^2 - m_1^2][(p_1+k)^2 - m_2^2]} = p_1^2 B_{00} + (p_1^2)^2 B_{11},
\end{aligned} \tag{144}$$

where we inserted $q_1 = p_1$. Rewriting

$$p_1 \cdot k = \frac{[(p_1+k)^2 - m_2^2] - (k^2 - m_1^2) + (m_2^2 - m_1^2 - p_1^2)}{2} \tag{145}$$

and shifting $k \to k - p_1$ in one of the resulting integrals, the first integral equation gives[31]

$$B_1 = \frac{A_0(m_1) - A_0(m_2) + (m_2^2 - m_1^2 - p_1^2) B_0(p_1, m_1, m_2)}{2p_1^2}. \tag{146}$$

For the second equation, we proceed in analogy, using $k^2 = k^2 - m_1^2 + m_1^2$, to find

$$D B_{00} + p_1^2 B_{11} = A_0(m_2) + m_1^2 B_0(p_1, m_1, m_2). \tag{147}$$

The third equation requires some more algebra but otherwise similar techniques, resulting in

$$\begin{aligned}
p_1^2 B_{00} + (p_1^2)^2 B_{11} &= \mu^{4-D} \frac{p_{1\mu}}{2} \Bigg[\int \frac{\mathrm{d}^D k}{\mathrm{i}\pi^2} \frac{k^\mu}{k^2 - m_1^2} - \int \frac{\mathrm{d}^D k}{\mathrm{i}\pi^2} \frac{k^\mu}{(p_1+k)^2 - m_2^2} \\
&\qquad + (m_2^2 - m_1^2 - p_1^2) \int \frac{\mathrm{d}^D k}{\mathrm{i}\pi^2} \frac{k^\mu}{[k^2 - m_1^2][(p_1+k)^2 - m_2^2]} \Bigg] \\
&= \frac{p_1^2 A_0(m_2) + (m_2^2 - m_1^2 - p_1^2) p_1^2 B_1}{2},
\end{aligned} \tag{148}$$

where we additionally used that a one-point tensor loop integral vanishes. We can solve the two equations containing B_{00} and B_{11} to obtain

$$\begin{aligned}
B_{00} &= \frac{A_0(m_2) + 2m_1^2 B_0(p_1, m_1, m_2) - (m_2^2 - m_1^2 - p_1^2) B_1}{2(D-1)}, \\
B_{11} &= \frac{A_0(m_2) + (m_2^2 - m_1^2 - p_1^2) B_1 - 2B_{00}}{2p_1^2},
\end{aligned} \tag{149}$$

with B_1 as specified in Eq. (146). In principle, we can thus write B_1, B_{00}, and B_{11} solely in terms of the scalar loop integrals A_0 and B_0, each with fairly complicated expressions, however. Similar relations apply for the higher tensor integrals, where the coefficient functions $\{C_1, C_2, C_{00}, \ldots\}$ can be written in terms of scalar loop integrals with smaller or equal N.

[31] Note that the case $p_1^2 = 0$ is a known limitation of the Passarino–Veltman procedure and needs to be treated separately. Similar problems can appear in other loop integrals and particle kinematics, which, in matrix notation, correspond to vanishing Gram determinants [73, 76].

Scalar loop integrals

In the following, we derive an analytic expression for the scalar loop integral $A_0(m_1)$ and outline the calculation of $B_0(p_1, m_1, m_2)$ [72]. To this end,[32] we will use the formula [12]

$$\int \mathrm{d}^D k \, \frac{1}{[k^2 - \Delta + \mathrm{i}\epsilon]^n} = (-1)^n \mathrm{i}\pi^{D/2} \Delta^{D/2-n} \frac{\Gamma(n - D/2)}{\Gamma(n)}, \tag{150}$$

with the gamma function $\Gamma(z)$ being expandable around its poles at $z \in \{0, -1, -2, \ldots\}$ according to [12]

$$\begin{aligned} \Gamma(\epsilon) &= \frac{1}{\epsilon} - \gamma_\mathrm{E} + \mathcal{O}(\epsilon), \\ \Gamma(-n + \epsilon) &= \frac{(-1)^n}{n!} \left[\frac{1}{\epsilon} - \gamma_\mathrm{E} + \sum_{j=1}^{n} \frac{1}{j} + \mathcal{O}(\epsilon) \right], \quad \text{for } n \in \mathbb{N}_{>0}. \end{aligned} \tag{151}$$

Here, $\epsilon \to 0^+$ is infinitesimal and $\gamma_\mathrm{E} \approx 0.5772$ is the Euler–Mascheroni constant. The tadpole integral, for $D = 4 - 2\epsilon$, then becomes

$$A_0(m_1) = -m_1^2 \left(\frac{\mu^2}{\pi m_1^2} \right)^\epsilon \Gamma(-1 + \epsilon) = m_1^2 \left[\frac{1}{\epsilon} - \gamma_\mathrm{E} + 1 + \log\left(\frac{\mu^2}{\pi m_1^2} \right) + \mathcal{O}(\epsilon) \right], \tag{152}$$

where we used $x^\epsilon = \mathrm{e}^{\epsilon \log x} = 1 + \epsilon \log x + \mathcal{O}(\epsilon^2)$. Crucially, the simplification of logarithms, *e.g.*, using $\log(a/b) = \log a - \log b$, needs to be done with due diligence here, depending on the actual values of their possibly complex arguments.

For the calculation of $B_0(p_1, m_1, m_2)$, we rewrite the bubble integral by introducing a Feynman parameter [5], leading to

$$\begin{aligned} B_0(p_1, m_1, m_2) &= \frac{\mu^{4-D}}{\mathrm{i}\pi^2} \int \mathrm{d}^D k \int_0^1 \mathrm{d}\alpha \, \frac{1}{\big[\alpha[(p_1 + k)^2 - m_2^2 + \mathrm{i}\epsilon] + (1 - \alpha)[k^2 - m_1^2 + \mathrm{i}\epsilon]\big]^2} \\ &= \frac{\mu^{4-D}}{\mathrm{i}\pi^2} \int \mathrm{d}^D k \int_0^1 \mathrm{d}\alpha \, \frac{1}{[k^2 - \Delta_B + \mathrm{i}\epsilon]^2}, \end{aligned} \tag{153}$$

where we defined $\Delta_B \equiv \Delta_B(\alpha) = p_1^2 \alpha(\alpha - 1) - m_1^2(\alpha - 1) + \alpha m_2^2$ and shifted the loop momentum $k \to k - \alpha p_1$. Hence, we can use Eq. (150) to find

$$B_0(p_1, m_1, m_2) = \int_0^1 \mathrm{d}\alpha \left(\frac{\mu^2}{\pi \Delta_B} \right)^\epsilon \Gamma(\epsilon) = \frac{1}{\epsilon} - \gamma_\mathrm{E} + \int_0^1 \mathrm{d}\alpha \, \log\left(\frac{\mu^2}{\pi \Delta_B} \right) + \mathcal{O}(\epsilon), \tag{154}$$

and performing the remaining integration, one obtains [77]

$$\begin{aligned} B_0(p_1, m_1, m_2) = \frac{1}{\epsilon} - \gamma_\mathrm{E} + 2 + \log\left(\frac{\mu^2}{\pi m_2^2} \right) + \frac{m_2^2 - m_1^2 - p_1^2}{2p_1^2} \log\left(\frac{m_1^2}{m_2^2} \right) \\ + \frac{\sqrt{\lambda(p_1^2, m_1^2, m_2^2)}}{p_1^2} \log\left(\frac{\sqrt{\lambda(p_1^2, m_1^2, m_2^2)} + m_1^2 + m_2^2 - p_1^2}{2 m_1 m_2} \right) + \mathcal{O}(\epsilon). \end{aligned} \tag{155}$$

Closed expressions for the three- and four-point scalar loop integral are more intricate and, among other things, additionally involve dilogarithms [72, 76]; a further discussion of analytic expressions for these integrals is, however, beyond the scope of this summary.

[32] Alternatively to the strategy pursued here, the finite parts of the scalar loop integrals could also be calculated by determining the discontinuity of the respective diagram and evaluating a dispersion relation.

Conformal mappings and z expansion

Complex functions $f(z)$ that preserve the magnitude and orientation of angles at which curves intersect are called conformal mappings [13]. It can be shown that this property follows for holomorphic—that is analytic—functions that fulfill $f'(z) \neq 0$; as being a holomorphic bijection implies $f'(z) \neq 0$, biholomorphic mappings, especially, are conformal [78]. A vast collection of examples of conformal mappings can, *e.g.*, be found in Ref. [79]. By Riemann's mapping theorem [13, 78], we further know that every simply connected and open proper subdomain of the complex plane is conformally equivalent to the open unit disk $D = \{z \in \mathbb{C} \colon |z| < 1\}$, *i.e.*, there exists a conformal mapping from that subdomain to D.[33] Hence, conformal mappings provide a tool to bring physical problems into a canonical form and allow for the application of certain techniques related to functional optimization [80]. In particular, this applies to the analyticity domain of scattering amplitudes and form factors, which can thus be mapped onto the unit disk D.

In the following, we will study a specific conformal mapping in more detail. Consider the function[34]

$$z(t) = z(t, t_0) = \frac{\sqrt{t_\mathrm{R} - t} - \sqrt{t_\mathrm{R} - t_0}}{\sqrt{t_\mathrm{R} - t} + \sqrt{t_\mathrm{R} - t_0}}, \tag{156}$$

which, as we will demonstrate, maps the complex plane cut along the real axis for $t \geq t_\mathrm{R}$, $\mathbb{C}^- = \mathbb{C}\backslash[t_\mathrm{R}, \infty)$, conformally onto the open unit disk, $z(t) \colon \mathbb{C}^- \to D$, see Fig. 6. Here, t_0 is a free parameter from the analyticity domain that gets mapped to the origin, $z(t_0) = 0$; for definiteness, we choose this parameter to be real, $t_0 < t_\mathrm{R}$ [80]. The square-root branch cut of Eq. (156) requires the introduction of two Riemann sheets to provide a continuous function. If not otherwise stated, we will restrict ourselves to the first (physical) sheet in what follows, $\arg[t_\mathrm{R} - t] \in (-\pi, \pi)$, where the evaluation on the cut is defined by the infinitesimal limit from above, $t \to t^+ = t + \mathrm{i}\epsilon$ ($\epsilon \to 0^+$) for $t \geq t_\mathrm{R}$, corresponding to $\arg[t_\mathrm{R} - t] = -\pi$; taking the limit $t \to t^- = t - \mathrm{i}\epsilon$, on the other hand, results in $\arg[t_\mathrm{R} - t] = \pi$. The analytic continuation to the second Riemann sheet will be outlined at the end of our discussion.

We start by showing that Eq. (156) maps the cut complex plane $\mathbb{C}^-$ into D, *i.e.*,

1. $|z(t)| < 1$ for $t \in \mathbb{C}^-$.

Indeed, for $t \in \mathbb{C}^-$, we have $t_\mathrm{R} - t = r\mathrm{e}^{\mathrm{i}\varphi}$ with $\varphi \in (-\pi, \pi)$ and $0 < r = |t_\mathrm{R} - t| < \infty$, so that

$$\begin{aligned} |z(t)| &= \left| \frac{\sqrt{r}\cos(\varphi/2) - \sqrt{t_\mathrm{R} - t_0} + \mathrm{i}\sqrt{r}\sin(\varphi/2)}{\sqrt{r}\cos(\varphi/2) + \sqrt{t_\mathrm{R} - t_0} + \mathrm{i}\sqrt{r}\sin(\varphi/2)} \right| \\ &= \left(\frac{r + t_\mathrm{R} - t_0 - 2\sqrt{r}\sqrt{t_\mathrm{R} - t_0}\cos(\varphi/2)}{r + t_\mathrm{R} - t_0 + 2\sqrt{r}\sqrt{t_\mathrm{R} - t_0}\cos(\varphi/2)} \right)^{1/2} < 1. \end{aligned} \tag{157}$$

In particular, the analytic segments of the real axis map onto the reals according to

2. $z(-\infty < t \leq t_0) \in [0, 1)$;
3. $z(t_0 \leq t < t_\mathrm{R}) \in (-1, 0]$.

[33] The Osgood–Carathéodory theorem asserts the existence of a continuous extension of the mapping to the boundary if the subdomain is bounded by a simple closed contour [13].

[34] In the literature, this mapping is sometimes written with an additional prefactor of (-1); see, *e.g.*, Ref. [80]. The generalization of the results presented here to this convention is straightforward.

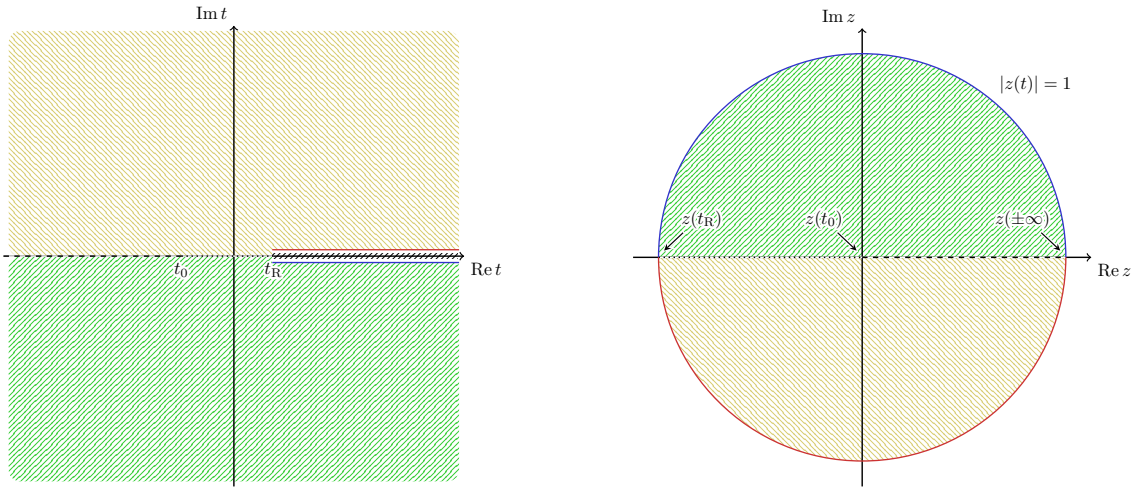

Figure 6: Illustration of the cut complex plane $\mathbb{C}^-$ (*left*) that is mapped onto the open unit disk D (*right*) by $z(t)$, Eq. (156). The upper (lower) rim of the branch cut is mapped onto the lower (upper) unit semicircle; see text for more information.

For the former of these, we note that $z(t_{\leq t_0}) \geq 0$ for $t_{\leq t_0} \in (-\infty, t_0]$ and thus also

$$z(t_{\leq t_0}) = |z(t_{\leq t_0})| < \frac{\sqrt{t_\mathrm{R} - t_{\leq t_0}} + \sqrt{t_\mathrm{R} - t_0}}{\sqrt{t_\mathrm{R} - t_{\leq t_0}} + \sqrt{t_\mathrm{R} - t_0}} = 1 \tag{158}$$

by the triangle inequality $|a+b| \leq |a|+|b|$, with equality holding if and only if a and b are both non-negative or non-positive. Concerning the latter interval, $t_{\geq t_0} \in [t_0, t_\mathrm{R})$ results in $z(t_{\geq t_0}) \leq 0$ and $z(t_{\geq t_0}) = -|z(t_{\geq t_0})| > -1$ by a similar argument to the above.

Evaluating Eq. (156) infinitesimally close to the branch cut, we observe that

4. the upper (lower) rim of the cut, $t^+ = t + \mathrm{i}\epsilon$ ($t^- = t - \mathrm{i}\epsilon$), $t \geq t_\mathrm{R}$, is mapped onto the unit semicircle $\xi = \mathrm{e}^{\mathrm{i}\theta}$ with $\theta \leq 0$ ($\theta \geq 0$).

To deduce this, we first establish $|z(t^\pm)| = 1$ for $t \geq t_\mathrm{R}$, as can be obtained from the second equality of Eq. (157), with $t = t^+$ ($t = t^-$) corresponding to $\varphi = -\pi$ ($\varphi = \pi$) and $r = t - t_\mathrm{R} \geq 0$. Furthermore,

$$z(t) = \frac{r - t_\mathrm{R} + t_0 + 2\mathrm{i}\sqrt{r}\sqrt{t_\mathrm{R} - t_0}\sin(\varphi/2)}{r + t_\mathrm{R} - t_0 + 2\sqrt{r}\sqrt{t_\mathrm{R} - t_0}\cos(\varphi/2)} \tag{159}$$

gives

$$z(t^\pm) = \frac{r - t_\mathrm{R} + t_0 \mp 2\mathrm{i}\sqrt{r}\sqrt{t_\mathrm{R} - t_0}}{r + t_\mathrm{R} - t_0}, \tag{160}$$

and since $|z(t^\pm)| = 1$, we may write $z(t^\pm) = \mathrm{e}^{\mathrm{i}\theta(t^\pm)}$. For some general $z = R\mathrm{e}^{\mathrm{i}\theta}$, the argument can be determined via

$$\theta = \mathrm{sgn}[\mathrm{Im}\, z] \arccos\left(\frac{\mathrm{Re}\, z}{R}\right), \tag{161}$$

which, in our case, leads to

$$\theta(t^\pm) = \mp \arccos\left(1 - 2\frac{t_\mathrm{R} - t_0}{r + t_\mathrm{R} - t_0}\right) \in [0, \mp\pi]. \tag{162}$$

Moreover, we find the special values

5. $z(t_\mathrm{R}) = -1$;

6. $\lim_{t\to\pm\infty} z(t) = 1$.

Both $z(t_\mathrm{R}) = -1$ and $\lim_{t\to-\infty} z(t) = 1$ are, in fact, direct consequences of Eq. (156), whereas $\lim_{t\to\infty} z(t) = \lim_{t\to\infty} z(t^\pm) = 1$ follows from $\theta(t^\pm) = 0$ for $r \to \infty$, see Eq. (162).

Next, we want to prove that

7. $z(t)\colon \mathbb{C}^- \to D$ is biholomorphic, with the inverse mapping

$$t(z) = \frac{t_0(1+z)^2 - 4t_\mathrm{R}z}{(1-z)^2}. \tag{163}$$

In order to show injectivity, we take $t_1, t_2 \in \mathbb{C}^-$ and calculate

$$\begin{aligned} z(t_1) = z(t_2) \Leftrightarrow \big(\sqrt{t_\mathrm{R}-t_1} - \sqrt{t_\mathrm{R}-t_0}\big)\big(\sqrt{t_\mathrm{R}-t_2} + \sqrt{t_\mathrm{R}-t_0}\big) \\ = \big(\sqrt{t_\mathrm{R}-t_2} - \sqrt{t_\mathrm{R}-t_0}\big)\big(\sqrt{t_\mathrm{R}-t_1} + \sqrt{t_\mathrm{R}-t_0}\big) \Leftrightarrow t_1 = t_2, \end{aligned} \tag{164}$$

where we used that the denominator of Eq. (156) does not vanish anywhere ($|z(t)| \leq 1$). For surjectivity, we need to find a $t_x \in \mathbb{C}^- \;\forall\, z_x \in D$ such that $z(t_x) = z_x$. This $t_x = t(z_x)$ is readily found with Eq. (163), which thus gives the inverse mapping, as claimed:[35]

$$z(t(z_x)) = \frac{\sqrt{(1+z_x)^2/(1-z_x)^2} - 1}{\sqrt{(1+z_x)^2/(1-z_x)^2} + 1} = \frac{(1+z_x)/(1-z_x) - 1}{(1+z_x)/(1-z_x) + 1} = z_x. \tag{165}$$

Here, squaring $1 + z_x = \rho\mathrm{e}^{\mathrm{i}\alpha}$, $\alpha \in (-\pi/2, \pi/2)$, and subsequently taking the square root is a trivial operation to carry out since we remain on the principal branch, that is $\arg[(1+z_x)^2] \in (-\pi, \pi)$. For $w = 1 - z_x$, however, squaring leads to $w^2 = \widetilde{w}^2$, with $\widetilde{w} = z_x - 1$, and we have to choose the proper value of $\sqrt{w^2} = \sqrt{\widetilde{w}^2}$ by hand. To this end, we note that upon squaring $\widetilde{w} = \rho\mathrm{e}^{\mathrm{i}\alpha}$, $\pi/2 < |\alpha| \leq \pi$, the value of the argument exceeds the domain of the principal branch, thus necessitating the addition of an appropriate multiple of 2π to remain on the first Riemann sheet. For $w = \rho\mathrm{e}^{\mathrm{i}\alpha}$, on the contrary, we have $\alpha \in (-\pi/2, \pi/2)$, as for $1 + z_x$, and thus remain on the principal branch, $\arg w^2 \in (-\pi, \pi)$. The proper choice for the square root is then found to be given by $\sqrt{w^2} = \sqrt{\widetilde{w}^2} = w$; see Fig. 7 for a graphical illustration. What remains to be proven is that $z(t)\colon \mathbb{C}^- \to D$ is holomorphic, which we will do by writing it as the composition of three (trivially) holomorphic functions with matching (co-)domains. Consider [13, 79]

$$\begin{aligned} &f(t) = t_\mathrm{R} - t, \quad \text{holomorphic on } \mathbb{C}, \quad g(z) = \sqrt{z}, \quad \text{holomorphic on } \mathbb{C}\setminus(-\infty, 0], \\ &h(z) = \frac{z - \sqrt{t_\mathrm{R}-t_0}}{z + \sqrt{t_\mathrm{R}-t_0}}, \quad \text{holomorphic on } \mathbb{C}\setminus\{-\sqrt{t_\mathrm{R}-t_0}\}, \end{aligned} \tag{166}$$

in terms of which $z(t) = h(g(f(t)))$. We start by observing that $f(t)$ is holomorphic on $\mathbb{C}^-$ because it is holomorphic on $\mathbb{C}$, and the domain is mapped according to $f(\mathbb{C}^-) = \widetilde{\mathbb{C}}^-$, with $\widetilde{\mathbb{C}}^- = \mathbb{C}\setminus(-\infty, 0]$. The function $g(z)$ is holomorphic on the resulting region $\widetilde{\mathbb{C}}^-$ and we have $g(\widetilde{\mathbb{C}}^-) = \mathfrak{H}$, $\mathfrak{H} = \{z \in \mathbb{C}\colon \mathrm{Re}\, z > 0\}$. Furthermore, $h(z)$ is holomorphic on $\mathfrak{H}$ as its only non-analytic point is $-\sqrt{t_\mathrm{R}-t_0} \notin \mathfrak{H}$; here, we already know that $h(\mathfrak{H}) = D$.

[35] The value provided by Eq. (163) for $z_x \in D$ necessarily also fulfills $t(z_x) \in \mathbb{C}^-$ because otherwise, $z_x = z(t(z_x)) \in D$ for some $t(z_x) \in [t_\mathrm{R}, \infty)$, which contradicts what we have shown before.

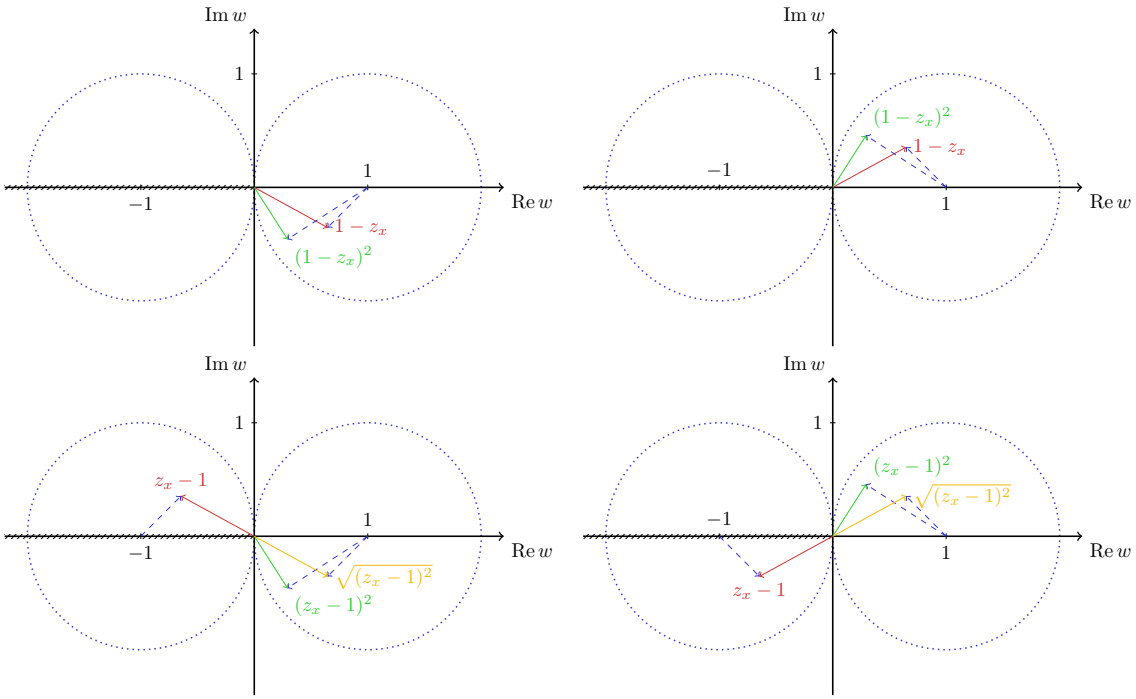

Figure 7: Illustration of $\sqrt{w^2} = \sqrt{\widetilde{w}^2} = w$ for $w = 1 - z_x$ (*top left* and *top right*) and $\widetilde{w} = z_x - 1$ (*bottom left* and *bottom right*) by choosing the appropriate branch of the square-root function for two exemplary values of $z_x \in D$; see text for details.

As we have argued in the beginning, the square-root branch cut of Eq. (156) leads to the emergence of a second (unphysical) RIEMANN sheet, with our discussion having been restricted to the first (physical) sheet up to this point. To show that

8. the analytic continuation to the second RIEMANN sheet is given by $z_{\mathrm{II}}(t) = 1/z(t)$,

we impose $z_{\mathrm{II}}(t^-) = z(t^+)$ upon crossing the cut on the negative real axis at $\varphi = -\pi$ and use SCHWARZ' reflection principle [9], $z(t^*) = z(t)^*$.[36] Accordingly, we obtain

$$z_{\mathrm{II}}(t^-) = z(t^+) = z(t^-)^* = \frac{1}{z(t^-)}, \tag{167}$$

where we used that $1 = |z(t^-)|^2 = z(t^-)z(t^-)^*$ in the last step, and the continuation away from the cut, $z_{\mathrm{II}}(t) = 1/z(t)$, follows by uniqueness. Since $|z(t)| \leq 1$ on the first RIEMANN sheet, points on the second sheet are mapped to the exterior of the unit disk, $|z_{\mathrm{II}}(t)| \geq 1$.

The mapping given in Eq. (156) can be modified to additionally account for a left-hand cut along $t \leq t_{\mathrm{L}}$ [80],

$$z(t) = \frac{\sqrt{t_{\mathrm{R}} - t} - C\sqrt{t - t_{\mathrm{L}}}}{\sqrt{t_{\mathrm{R}} - t} + C\sqrt{t - t_{\mathrm{L}}}}, \qquad C = \frac{\sqrt{t_{\mathrm{R}} - t_0}}{\sqrt{t_0 - t_{\mathrm{L}}}}. \tag{168}$$

A further discussion of this extension is, however, beyond the scope of this compendium.

[36] The conditions needed for SCHWARZ' reflection principle to hold are readily checked to be met. However, it is also straightforward to verify explicitly that $z(t)$ fulfills, especially, $z(t^+) = z(t^-)^*$, see Eq. (160).

The usage of conformal mappings in solving physical problems has a long history, including but not being restricted to applications in high-energy physics [81–84]. One such application is the determination of dispersive bounds for hadronic form factors, as will be discussed in the following, based on an example from Ref. [80]. To this end, we consider the vacuum–vacuum two-point correlation function

$$\Pi^{\mathrm{V}}_{\mu\nu}(q) = \mathrm{i}\int \mathrm{d}^4x\, \mathrm{e}^{\mathrm{i}qx}\, \langle 0|\mathrm{T}\{J^{\mathrm{V}}_\mu(x) J^{\mathrm{V}\dagger}_\nu(0)\}|0\rangle\,, \tag{169}$$

where $J^{\mathrm{V}}_\mu(x) = \bar{q}_2(x)\gamma_\mu q_1(x)$ is a vector quark-transition current, and the corresponding correlator for, *e.g.*, the axial-vector current $J^{\mathrm{A}}_\mu(x) = \bar{q}_2(x)\gamma_\mu\gamma_5 q_1(x)$ can be treated in complete analogy. By means of Lorentz covariance, we may expand this tensor in terms of two polarization functions according to[37]

$$\Pi^{\mathrm{V}}_{\mu\nu}(q) = \left(\frac{q_\mu q_\nu}{q^2} - g_{\mu\nu}\right)\Pi^{\mathrm{V}}_{\mathrm{T}}(q^2) + \frac{q_\mu q_\nu}{q^2}\Pi^{\mathrm{V}}_{\mathrm{L}}(q^2), \tag{170}$$

with $\Pi^{\mathrm{V}}_{\mathrm{T}}(q^2)$ and $\Pi^{\mathrm{V}}_{\mathrm{L}}(q^2)$ denoting the transversal (spin-1) and longitudinal (spin-0) components, respectively. To project $\Pi^{\mathrm{V}}_{\mu\nu}(q)$ onto these scalar functions, we can use

$$\mathcal{P}^{\mu\nu}_{\mathrm{T}}(q) = \frac{1}{3}\left(\frac{q^\mu q^\nu}{q^2} - g^{\mu\nu}\right), \qquad \mathcal{P}^{\mu\nu}_{\mathrm{L}}(q) = \frac{q^\mu q^\nu}{q^2}, \qquad \mathcal{P}^{\mu\nu}_{\mathrm{L}}(q) - 3\mathcal{P}^{\mu\nu}_{\mathrm{T}}(q) = g^{\mu\nu}, \tag{171}$$

i.e., $\Pi^{\mathrm{V}}_{\mathrm{T,L}}(q^2) = \mathcal{P}^{\mu\nu}_{\mathrm{T,L}}(q)\Pi^{\mathrm{V}}_{\mu\nu}(q)$, as readily verified. Crucially, $\Pi^{\mathrm{V}}_{\mathrm{T}}(q^2)$ and $\Pi^{\mathrm{V}}_{\mathrm{L}}(q^2)$ fulfill dispersion relations of the form given in Eq. (89), with the number of subtractions determined from the asymptotic behavior predicted by perturbative quantum chromodynamics in the deep Euclidean region [85], which, in our case, leads to [80]

$$\begin{aligned}
\chi^{\mathrm{V}}_{\mathrm{T}}(q^2) &= \frac{1}{2}\frac{\mathrm{d}^2\Pi^{\mathrm{V}}_{\mathrm{T}}(q^2)}{\mathrm{d}(q^2)^2} = \frac{1}{2\pi\mathrm{i}}\int_0^\infty \mathrm{d}t\, \frac{\mathrm{disc}_t\Pi^{\mathrm{V}}_{\mathrm{T}}(t)}{(t-q^2)^3}, \\
\chi^{\mathrm{V}}_{\mathrm{L}}(q^2) &= \frac{\mathrm{d}\Pi^{\mathrm{V}}_{\mathrm{L}}(q^2)}{\mathrm{d}q^2} = \frac{1}{2\pi\mathrm{i}}\int_0^\infty \mathrm{d}t\, \frac{\mathrm{disc}_t\Pi^{\mathrm{V}}_{\mathrm{L}}(t)}{(t-q^2)^2}.
\end{aligned} \tag{172}$$

Perturbative quantum chromodynamics can further be used to compute $\chi^{\mathrm{V}}_{\mathrm{T,L}}(q^2)$ in the region of (space-like) q^2 where non-perturbative effects are absent. The hypothesis of quark-hadron duality then states that the resulting spectral functions can be analytically continued to match the description in terms of hadrons [80]. Consequently, we can equally use unitarity to write [86, 87]

$$\mathrm{disc}_{q^2}\Pi^{\mathrm{V}}_{\mathrm{T,L}}(q^2) = \mathcal{P}^{\mu\nu}_{\mathrm{T,L}}(q)\Big[\mathrm{i}\sum_n \int \mathrm{d}\Phi_n(q;p_1,\ldots,p_n)\, \langle 0|J^{\mathrm{V}}_\mu(0)|n\rangle\, \langle n|J^{\mathrm{V}\dagger}_\nu(0)|0\rangle\Big], \tag{173}$$

with the sum, in principle, extending over all hadronic n-body intermediate states that couple the given vector current to the vacuum. In practice, however, one usually takes into account the lowest terms only, which allows us to obtain lower bounds on the spectral functions in Eq. (172) as the higher states, in particular, yield positive contributions [80].

[37] For a conserved current, $\partial^\mu J^{\mathrm{V}}_\mu(x) = 0$, we would have $0 = q^\mu\Pi^{\mathrm{V}}_{\mu\nu}(q) = q_\nu\Pi^{\mathrm{V}}_{\mathrm{L}}(q^2)$, so that the longitudinal polarization function needed to vanish, $\Pi^{\mathrm{V}}_{\mathrm{L}}(q^2) = 0$.

For illustrative purposes, we will restrict ourselves to the lightest pair of pseudoscalar mesons in what follows, with one of them containing a quark q_1 and the other a quark $\bar{q}_2$, in line with the content specified by $J_\mu^{\mathrm{V}}(x)$. The corresponding matrix element required to calculate the contribution to the unitarity sum is related to [80]

$$\langle P'(p')|J_\mu^{\mathrm{V}}(0)|P(p)\rangle = \Big(p_\mu + p'_\mu - \frac{m^2-m'^2}{q^2}q_\mu\Big) f_{P\to P'}^{+}(q^2) + \frac{m^2-m'^2}{q^2}q_\mu\, f_{P\to P'}^{0}(q^2) \quad (174)$$

via crossing symmetry, where m and m' are the meson masses and $q = p - p'$. Using the kinematics of the crossed process, $p' \to -p'$, $q = p + p'$, and inserting the two-body phase space, Eq. (44), we thus obtain

$$\mathrm{disc}_{q^2}\Pi_{\mathrm{T,L}}^{\mathrm{V}}(q^2) \geq \theta\big(\sqrt{q^2} - (m+m')\big)\frac{\mathrm{i}\sqrt{\lambda(q^2,m^2,m'^2)}}{8\pi q^2}\mathcal{A}_{\mathrm{T,L}}(q^2), \quad (175)$$

with[38]

$$\begin{aligned}\mathcal{A}_\lambda(q^2) &= \mathcal{P}_\lambda^{\mu\nu}(q)\,\langle 0|J_\mu^{\mathrm{V}}(0)|P(p)\bar{P}'(p')\rangle\,\langle 0|J_\nu^{\mathrm{V}}(0)|P(p)\bar{P}'(p')\rangle^* \\ &= \begin{cases} \dfrac{\lambda(q^2,m^2,m'^2)}{3q^2}|f_{P\to P'}^{+}(q^2)|^2, & \lambda = \mathrm{T}, \\ \dfrac{(m^2-m'^2)^2}{q^2}|f_{P\to P'}^{0}(q^2)|^2, & \lambda = \mathrm{L}. \end{cases}\end{aligned} \quad (176)$$

Hence, Eq. (172) becomes

$$\begin{aligned}\chi_{\mathrm{T}}^{\mathrm{V}}(q^2) &\geq \frac{1}{2\pi\mathrm{i}}\int_{t_+}^{\infty}\mathrm{d}t\,\frac{w_{\mathrm{T}}(t)|f_{P\to P'}^{+}(t)|^2}{(t-q^2)^3}, \quad w_{\mathrm{T}}(t) = \frac{\mathrm{i}(t-t_+)^{3/2}(t-t_-)^{3/2}}{24\pi t^2}, \\ \chi_{\mathrm{L}}^{\mathrm{V}}(q^2) &\geq \frac{1}{2\pi\mathrm{i}}\int_{t_+}^{\infty}\mathrm{d}t\,\frac{w_{\mathrm{L}}(t)|f_{P\to P'}^{0}(t)|^2}{(t-q^2)^2}, \quad w_{\mathrm{L}}(t) = \frac{\mathrm{i}\,t_+t_-(t-t_+)^{1/2}(t-t_-)^{1/2}}{8\pi t^2},\end{aligned} \quad (177)$$

where we defined $t_\pm = (m \pm m')^2$ for the (pseudo-)threshold.[39] By including more states in the unitarity sum, *i.e.*, other two-particle and higher intermediate states but also the disregarded one-particle intermediate states, these bounds can gradually be refined.

For the parameterization of the form factors, we will postulate a series expansion in the conformal variable $z(t)$, Eq. (156), which shows an improved rate of convergence as compared to an expansion in, *e.g.*, t [88, 89]; this effect can be enhanced by optimizing the choice of the parameter t_0 [80], in such a way that, generally, only the first few terms of the expansion are needed to obtain a reasonable approximation. More specifically, the z expansion for some form factor $F(t)$ that is analytic within the complex plane cut for $t \geq t_+$ reads

$$F(t) = \sum_{n=0}^{\infty} a_n z(t)^n, \quad (178)$$

[38] We omit a discussion about potential isospin degeneracy factors arising from different charge channels.

[39] The common notation $t_\pm = (m \pm m')^2$ for the (pseudo-)threshold—instead of $t_{\mathrm{R}} = (m+m')^2$—is not to be confused with $t^\pm = t \pm \mathrm{i}\epsilon$ ($\epsilon \to 0^+$), as introduced for the preceding discussion of Eq. (156).

where $a_n \in \mathbb{R}$ if $F(t)$ obeys SCHWARZ' reflection principle and $\dim[a_n] = \dim[F(t)]$. The monomials $z(t)^n = \xi^n = \mathrm{e}^{\mathrm{i}n\theta}$ are orthonormal on the unit circle $\partial D = \{z \in \mathbb{C}\colon |z| = 1\}$ with respect to the scalar product

$$\langle f, g\rangle = \frac{1}{2\pi\mathrm{i}} \int_{\partial D} \frac{\mathrm{d}z}{z}\, f(z)^* g(z), \tag{179}$$

that is

$$\langle \xi^n, \xi^m\rangle = \frac{1}{2\pi} \int_{-\pi}^{\pi} \mathrm{d}\theta\, \mathrm{e}^{\mathrm{i}(m-n)\theta} = \delta_{nm}. \tag{180}$$

To find the Jacobian for the variable transformation $t \to z(t)$ in the integrals of Eq. (177), we note that Eq. (163) yields

$$t(z) = t_+ - \frac{(t_+ - t_0)[1 - R^2(4 - R^2) + 2R^2\cos(2\theta)] + 4\mathrm{i}R(1 - R^2)(t_+ - t_0)\sin\theta}{(1 + R^2 - 2R\cos\theta)^2} \tag{181}$$

for some general $z = R\mathrm{e}^{\mathrm{i}\theta}$. From the upper and lower unit semicircles, *i.e.*, $z^\pm = \mathrm{e}^{\mathrm{i}\theta^\pm}$ with $\theta^\pm \in [0, \pm\pi]$, we thus recover $t^\mp = t(\theta^\pm)$ infinitesimally below and above the cut,

$$t(\theta^\pm) = t_0 + 2\frac{t_+ - t_0}{1 - \cos\theta^\pm} \mp \mathrm{i}\epsilon. \tag{182}$$

Here, the inverse function

$$\theta(t^\pm) = \mp \arccos\left(1 - 2\frac{t_+ - t_0}{t - t_0}\right) \tag{183}$$

is in accordance with Eq. (162) upon inserting $t_+ - t = r\mathrm{e}^{\mathrm{i}\varphi}$ and taking $\varphi = \mp\pi$, and we identify $\theta^\pm = \theta(t^\mp)$. Consequently, we have

$$\begin{aligned}
\frac{1}{2\pi\mathrm{i}} \int_{\partial D} \frac{\mathrm{d}z}{z} |F(t(z))|^2 &= \frac{1}{2\pi}\left(\int_{-\pi}^{0} \mathrm{d}\theta^-\, |F(t(\theta^-))|^2 + \int_0^{\pi} \mathrm{d}\theta^+\, |F(t(\theta^+))|^2\right) \\
&= \frac{1}{2\pi}\left(\int_{t_+}^{\infty} \mathrm{d}t\, \frac{\mathrm{d}\theta(t^+)}{\mathrm{d}t}\, |F(t^+)|^2 + \int_{\infty}^{t_+} \mathrm{d}t\, \frac{\mathrm{d}\theta(t^-)}{\mathrm{d}t}\, |F(t^-)|^2\right) \\
&= \frac{1}{\pi}\int_{t_+}^{\infty} \mathrm{d}t \left|\frac{\mathrm{d}\theta(t^\pm)}{\mathrm{d}t}\right| |F(t^\pm)|^2,
\end{aligned} \tag{184}$$

where

$$\frac{\mathrm{d}\theta(t^\pm)}{\mathrm{d}t} = \pm\frac{\sqrt{t_+ - t_0}}{(t - t_0)\sqrt{t - t_+}} \tag{185}$$

and we assumed SCHWARZ' reflection principle for $F(t)$ in the last step. Since $|z(t^\pm)| = 1$ on the cut, we can further replace the Jacobian by

$$\left|\frac{\mathrm{d}z(t^\pm)}{\mathrm{d}t}\right| = \left|\frac{\mathrm{d}z(t^\pm)}{\mathrm{d}\theta^\mp}\frac{\mathrm{d}\theta(t^\pm)}{\mathrm{d}t}\right| = \left|\frac{\mathrm{d}\theta(t^\pm)}{\mathrm{d}t}\right|, \tag{186}$$

with the identification $z^\pm = z(t^\mp)$. Moreover, we can use the scalar product defined in Eq. (179) to project onto the coefficients of the expansion in Eq. (178). Due to the

orthonormality of the monomials $z(t)^n = \xi^n = \mathrm{e}^{\mathrm{i}n\theta}$ on the unit circle, we deduce

$$\begin{aligned} a_m = \langle \xi^m, F(t)\rangle &= \frac{1}{2\pi}\Big(\int_{-\pi}^{0} \mathrm{d}\theta^- \, F(t(\theta^-))\mathrm{e}^{-\mathrm{i}m\theta^-} + \int_{0}^{\pi} \mathrm{d}\theta^+ \, F(t(\theta^+))\mathrm{e}^{-\mathrm{i}m\theta^+}\Big) \\ &= \frac{1}{\pi}\Big(\int_{0}^{\pi} \mathrm{d}\theta^+ \, \mathrm{Re}\,[F(t(\theta^+))]\cos(m\theta^+) + \int_{0}^{\pi} \mathrm{d}\theta^+ \, \mathrm{Im}\,[F(t(\theta^+))]\sin(m\theta^+)\Big) \\ &= \frac{1}{\pi}\Big(\int_{-\pi}^{0} \mathrm{d}\theta^- \, \mathrm{Re}\,[F(t(\theta^-))]\cos(m\theta^-) + \int_{-\pi}^{0} \mathrm{d}\theta^- \, \mathrm{Im}\,[F(t(\theta^-))]\sin(m\theta^-)\Big), \end{aligned} \tag{187}$$

where we used that

$$\begin{aligned} \int_{-\pi}^{0} \mathrm{d}\theta^- \, F(t(\theta^-))\mathrm{e}^{-\mathrm{i}m\theta^-} &= \int_{t_+}^{\infty} \mathrm{d}t \, \frac{\mathrm{d}\theta(t^+)}{\mathrm{d}t} \, F(t^+)\mathrm{e}^{-\mathrm{i}m\theta(t^+)} = \int_{\infty}^{t_+} \mathrm{d}t \, \frac{\mathrm{d}\theta(t^-)}{\mathrm{d}t} \, F(t^-)^*\mathrm{e}^{\mathrm{i}m\theta(t^-)} \\ &= \int_{0}^{\pi} \mathrm{d}\theta^+ \, F(t(\theta^+))^*\mathrm{e}^{\mathrm{i}m\theta^+}, \\ \int_{0}^{\pi} \mathrm{d}\theta^+ \, F(t(\theta^+))\mathrm{e}^{-\mathrm{i}m\theta^+} &= \int_{\infty}^{t_+} \mathrm{d}t \, \frac{\mathrm{d}\theta(t^-)}{\mathrm{d}t} \, F(t^-)\mathrm{e}^{-\mathrm{i}m\theta(t^-)} = \int_{t_+}^{\infty} \mathrm{d}t \, \frac{\mathrm{d}\theta(t^+)}{\mathrm{d}t} \, F(t^+)^*\mathrm{e}^{\mathrm{i}m\theta(t^+)} \\ &= \int_{-\pi}^{0} \mathrm{d}\theta^- \, F(t(\theta^-))^*\mathrm{e}^{\mathrm{i}m\theta^-}. \end{aligned} \tag{188}$$

Hence, we find

$$a_0 = \frac{1}{\pi}\int_{0}^{\pi} \mathrm{d}\theta^+ \, \mathrm{Re}\,[F(t(\theta^+))] = \frac{1}{\pi}\int_{-\pi}^{0} \mathrm{d}\theta^- \, \mathrm{Re}\,[F(t(\theta^-))], \tag{189}$$

and since $F(t)$ was assumed to be analytic, *i.e.*, $a_{m<0} = 0$ [90], we obtain

$$\begin{aligned} \int_{0}^{\pi} \mathrm{d}\theta^+ \, \mathrm{Re}\,[F(t(\theta^+))]\cos(m\theta^+) &= \int_{0}^{\pi} \mathrm{d}\theta^+ \, \mathrm{Im}\,[F(t(\theta^+))]\sin(m\theta^+), \\ \int_{-\pi}^{0} \mathrm{d}\theta^- \, \mathrm{Re}\,[F(t(\theta^-))]\cos(m\theta^-) &= \int_{-\pi}^{0} \mathrm{d}\theta^- \, \mathrm{Im}\,[F(t(\theta^-))]\sin(m\theta^-), \end{aligned} \tag{190}$$

which leads to ($m > 0$)

$$\begin{aligned} a_m &= \frac{2}{\pi}\int_{0}^{\pi} \mathrm{d}\theta^+ \, \mathrm{Re}\,[F(t(\theta^+))]\cos(m\theta^+) = \frac{2}{\pi}\int_{0}^{\pi} \mathrm{d}\theta^+ \, \mathrm{Im}\,[F(t(\theta^+))]\sin(m\theta^+), \\ &= \frac{2}{\pi}\int_{-\pi}^{0} \mathrm{d}\theta^- \, \mathrm{Re}\,[F(t(\theta^-))]\cos(m\theta^-) = \frac{2}{\pi}\int_{-\pi}^{0} \mathrm{d}\theta^- \, \mathrm{Im}\,[F(t(\theta^-))]\sin(m\theta^-). \end{aligned} \tag{191}$$

Transforming to the variable t, the above formulae become ($m > 0$)

$$a_0 = \frac{1}{\pi}\int_{t_+}^{\infty} \mathrm{d}t \left|\frac{\mathrm{d}\theta(t^\pm)}{\mathrm{d}t}\right| \mathrm{Re}\,F(t^\pm), \tag{192}$$

$$a_m = \frac{2}{\pi}\int_{t_+}^{\infty} \mathrm{d}t \left|\frac{\mathrm{d}\theta(t^\pm)}{\mathrm{d}t}\right| \mathrm{Re}\,F(t^\pm)\cos(m\theta(t^\pm)) = \frac{2}{\pi}\int_{t_+}^{\infty} \mathrm{d}t \left|\frac{\mathrm{d}\theta(t^\pm)}{\mathrm{d}t}\right| \mathrm{Im}\,F(t^\pm)\sin(m\theta(t^\pm)).$$

Coming back to Eq. (177), we use Eq. (184) and rewrite these inequalities as

$$\begin{aligned}
1 &\geq \frac{1}{\pi}\int_{t_+}^{\infty}\mathrm{d}t\,\frac{\sqrt{t_+-t_0}}{(t-t_0)\sqrt{t-t_+}}|\phi_{\mathrm{T}}(t,q^2)f^+_{P\to P'}(t)|^2 = \frac{1}{2\pi\mathrm{i}}\int_{\partial D}\frac{\mathrm{d}z}{z}|\phi_{\mathrm{T}}(t(z),q^2)f^+_{P\to P'}(t(z))|^2,\\
1 &\geq \frac{1}{\pi}\int_{t_+}^{\infty}\mathrm{d}t\,\frac{\sqrt{t_+-t_0}}{(t-t_0)\sqrt{t-t_+}}|\phi_{\mathrm{L}}(t,q^2)f^0_{P\to P'}(t)|^2 = \frac{1}{2\pi\mathrm{i}}\int_{\partial D}\frac{\mathrm{d}z}{z}|\phi_{\mathrm{L}}(t(z),q^2)f^0_{P\to P'}(t(z))|^2,
\end{aligned} \tag{193}$$

where we defined

$$\begin{aligned}
|\phi_{\mathrm{T}}(t,q^2)|^2 &= \frac{(t-t_+)^2(t-t_-)^{3/2}(t-t_0)}{48\pi\chi^{\mathrm{V}}_{\mathrm{T}}(q^2)(t_+-t_0)^{1/2}t^2(t-q^2)^3},\\
|\phi_{\mathrm{L}}(t,q^2)|^2 &= \frac{t_+t_-(t-t_+)(t-t_-)^{1/2}(t-t_0)}{16\pi\chi^{\mathrm{V}}_{\mathrm{L}}(q^2)(t_+-t_0)^{1/2}t^2(t-q^2)^2}.
\end{aligned} \tag{194}$$

Performing series expansions for $F^{+,0}(t) = \phi_{\mathrm{T,L}}(t,q^2)f^{+,0}_{P\to P'}(t)$ as given in Eq. (178) requires analyticity within the open unit disk D. Here, $\phi_{\mathrm{T,L}}(t,q^2)$ are so-called outer functions, which can, in principle, be continued to functions analytic within D from their modulus on the boundary through an integral representation [80]. A mathematically rigorous treatment of this is, however, beyond the scope of this summary and also involves a discussion of Hardy spaces; see, *e.g.*, Refs. [91–95] for extensive reviews. For our purposes, it suffices to observe that the functions $\phi_{\mathrm{T,L}}(t,q^2) = \sqrt{|\phi_{\mathrm{T,L}}(t,q^2)|^2}$ can effectively be rendered analytic within D by replacing poles and branch points as per[40]

$$\left(\frac{1}{t-X}\right)^k \to \left(\frac{-z(t,X)}{t-X}\right)^k. \tag{195}$$

Crucially, we have $z(X,X)=0$, and $|z(t,X)|=1$, $t\geq t_+$, leaves the modulus on the unit circle unchanged, see Eq. (156) and the discussion thereof; various applications of this method can, *e.g.*, be found in Refs. [96–101]. For our example, this procedure results in

$$\begin{aligned}
\phi_{\mathrm{T}}(t,q^2) &= \frac{t-t_+}{[48\pi\chi^{\mathrm{V}}_{\mathrm{T}}(q^2)]^{1/2}(t_+-t_0)^{1/4}}\left(\frac{z(t,0)}{-t}\right)\left(\frac{t_--t}{z(t,t_-)}\right)^{3/4}\left(\frac{t_0-t}{z(t,t_0)}\right)^{1/2}\left(\frac{z(t,q^2)}{q^2-t}\right)^{3/2},\\
\phi_{\mathrm{L}}(t,q^2) &= \frac{t_+t_-}{[16\pi\chi^{\mathrm{V}}_{\mathrm{L}}(q^2)]^{1/2}(t_+-t_0)^{1/4}}\left(\frac{z(t,0)}{-t}\right)\left(\frac{t_+-t}{z(t,t_+)}\right)^{1/2}\left(\frac{t_--t}{z(t,t_-)}\right)^{1/4}\left(\frac{t_0-t}{z(t,t_0)}\right)^{1/2}\\
&\quad\times\left(\frac{z(t,q^2)}{q^2-t}\right),
\end{aligned} \tag{196}$$

with the trivial simplification $z(t,t_+)=1$. Another complication arises if the form factors $f^{+,0}_{P\to P'}(t)$ possess subthreshold singularities—that is poles on the real axis below the onset of the branch cut—since the form factors will be non-analytic at these points.[41] Let t_p be the position of such a subthreshold pole and $z_p = z(t_p,t_0)$, where $|z_p|<1$ as $t_p<t_+$. To render the corresponding form factor analytic within the open unit disk D without changing its modulus on the boundary, we can multiply it by the Blaschke factor [80]

$$B(z,z_p) = \frac{z-z_p}{1-z_p^*z}, \tag{197}$$

[40] We use $-z(t,X)$ instead of $z(t,X)$ because $z(t,X)\geq 0$ for $-\infty<t\leq X$ and $z(t,X)\leq 0$ for $X\leq t<t_+$.
[41] Above-threshold poles are, *e.g.*, discussed in Refs. [102, 103].

which is a representative from a class of functions called inner functions [91–93]; as for outer functions, a general discussion of these is beyond the scope of this compendium. Trivially, we have $B(z_p, z_p) = 0$ and z_p is the only zero of the function.[42] Furthermore, the Blaschke factor indeed has the following properties:

1. $B(z, z_p)$ is analytic for $|z| < 1$;
2. $|B(z, z_p)\,| < 1$ for $|z| < 1$;
3. $|B(z, z_p)| = 1$ for $|z| = 1$.

These statements are direct consequences of the identity

$$B(z, z_p) = B(z(t, t_0), z(t_p, t_0)) = \frac{z(t, t_0) - z(t_p, t_0)}{1 - z(t_p, t_0)^* z(t, t_0)} = z(t, t_p) \tag{198}$$

and the properties we have shown for Eq. (156); in fact, $B(z, z_p)\colon D \to D$ thus maps the open unit disk D conformally onto itself. Since the modulus of the Blaschke factor on the unit circle is unity, the form factors $\widetilde{F}^{+,0}(t) = B\big(z(t), z(t_p^{+,0})\big)\phi_{\mathrm{T,L}}(t, q^2) f^{+,0}_{P\to P'}(t)$ fulfill the same boundary conditions as specified in Eq. (193), namely

$$\begin{aligned} 1 &\geq \frac{1}{2\pi \mathrm{i}} \int_{\partial D} \frac{\mathrm{d}z}{z} |B(z, z_p^+)\phi_{\mathrm{T}}(t(z), q^2) f^+_{P\to P'}(t(z))|^2, \\ 1 &\geq \frac{1}{2\pi \mathrm{i}} \int_{\partial D} \frac{\mathrm{d}z}{z} |B(z, z_p^0)\phi_{\mathrm{L}}(t(z), q^2) f^0_{P\to P'}(t(z))|^2. \end{aligned} \tag{199}$$

For simplicity, we here assume $t_p^{+,0}$ to be the only subthreshold poles of the form factors, where $z_p^{+,0} = z(t_p^{+,0})$; the extension to several subthreshold poles is trivial and requires the multiplication with additional Blaschke factors. Expanding $\widetilde{F}^{+,0}(t)$ in a series in powers of the conformal variable $z(t)$,

$$\widetilde{F}^{+,0}(t) = \sum_{n=0}^{\infty} a_n^{+,0} z(t)^n, \tag{200}$$

and using Eq. (180) for $z(t)$ on the unit circle, we obtain the so-called dispersive (or unitarity) bounds

$$1 \geq \sum_{n=0}^{\infty} (a_n^{+,0})^2. \tag{201}$$

Depending on the context, the Blaschke factor $B(z, z_p)$ is sometimes replaced by the inverse of a simple pole $R(t) = (1 - t/t_p)^{-1}$, in which case the series expansion is referred to as a simplified series expansion [100, 104]; see also the application in Part III of this thesis.

[42] Note that the only pole of the function, $1/z_p^*$, is not contained in D, as $|1/z_p^*| > 1$ due to $|z_p| < 1$.

References

[1] G. L. Naber, *The Geometry of Minkowski Spacetime*, Springer, 2012.

[2] R. M. Wald, *General Relativity*, University of Chicago Press, 1984.

[3] S. M. Carroll, *Spacetime and Geometry*, Addison Wesley, 2003.

[4] C. Itzykson and J.-B. Zuber, *Quantum Field Theory*, McGraw-Hill, 1980.

[5] M. D. Schwartz, *Quantum Field Theory and the Standard Model*, Cambridge University Press, 2014.

[6] P. A. Martin and F. Rothen, *Many-Body Problems and Quantum Field Theory*, Springer, 2004.

[7] R. L. Workman *et al.* [Particle Data Group], PTEP **2022**, 083C01 (2022).

[8] P. B. Pal, *Representation-independent manipulations with Dirac spinors* (2007) [arXiv:physics/0703214].

[9] G. B. Arfken, H. J. Weber, and F. E. Harris, *Mathematical Methods for Physicists*, Academic Press, 2012.

[10] S. Mizera, Phys. Rept. **1047**, 1 (2024) [arXiv:2306.05395 [hep-th]].

[11] D. I. Olive, Nuovo Cimento **26**, 73 (1962).

[12] M. E. Peskin and D. V. Schroeder, *An Introduction to Quantum Field Theory*, Westview Press, 2015.

[13] M. J. Ablowitz and A. S. Fokas, *Complex Variables: Introduction and Applications*, Cambridge University Press, 2003.

[14] G. Lüders, Kong. Dan. Vid. Sel. Mat. Fys. Med. **28N5**, 1 (1954).

[15] W. Pauli, *Niels Bohr and the Development of Physics*, McGraw-Hill, 1955.

[16] H. Akdag, B. Kubis, and A. Wirzba, JHEP **06**, 154 (2023) [arXiv:2212.07794 [hep-ph]].

[17] M. H. Akdag, PhD thesis, University of Bonn (2023).

[18] J. J. Sakurai, Annals Phys. **11**, 1 (1960).

[19] J. J. Sakurai and D. Schildknecht, Phys. Lett. B **40**, 121 (1972).

[20] J. J. Sakurai and D. Schildknecht, Phys. Lett. B **41**, 489 (1972).

[21] J. J. Sakurai and D. Schildknecht, Phys. Lett. B **42**, 216 (1972).

[22] B. Gorczyca and D. Schildknecht, Phys. Lett. B **47**, 71 (1973).

[23] V. N. Gribov, Zh. Eksp. Teor. Fiz. **57**, 1306 (1969).

[24] K. Fujikawa, Phys. Rev. D **4**, 2794 (1971).

[25] A. Bramon, E. Etim, and M. Greco, Phys. Lett. B **41**, 609 (1972).

[26] A. Donnachie and G. Shaw, *Electromagnetic Interactions of Hadrons: Volume 2*, Springer, 1978.

[27] D. Schildknecht, Acta Phys. Polon. B **37**, 595 (2006) [arXiv:hep-ph/0511090].

[28] S.-s. Fang, B. Kubis, and A. Kupść, Prog. Part. Nucl. Phys. **120**, 103884 (2021) [arXiv:2102.05922 [hep-ph]].

[29] W. A. Bardeen and W. K. Tung, Phys. Rev. **173**, 1423 (1968), [Erratum: Phys.Rev.D 4, 3229–3229 (1971)].

[30] R. Tarrach, Nuovo Cim. A **28**, 409 (1975).

[31] A. C. Hearn, Nuovo Cimento **21**, 333 (1961).

[32] G. Colangelo, M. Hoferichter, M. Procura, and P. Stoffer, JHEP **09**, 074 (2015) [arXiv:1506.01386 [hep-ph]].

[33] F. Jegerlehner and A. Nyffeler, Phys. Rept. **477**, 1 (2009) [arXiv:0902.3360 [hep-ph]].

[34] F. Jegerlehner, *The Anomalous Magnetic Moment of the Muon*, Springer, 2017.

[35] J. S. Schwinger, Phys. Rev. **73**, 416 (1948).

[36] J. S. Schwinger, Phys. Rev. **76**, 790 (1949).

[37] T. Aoyama, M. Hayakawa, T. Kinoshita, and M. Nio, Phys. Rev. Lett. **109**, 111808 (2012) [arXiv:1205.5370 [hep-ph]].

[38] T. Aoyama, T. Kinoshita, and M. Nio, Atoms **7**, 28 (2019).

[39] T. Aoyama *et al.*, Phys. Rept. **887**, 1 (2020) [arXiv:2006.04822 [hep-ph]].

[40] G. W. Bennett *et al.* [Muon $g-2$], Phys. Rev. D **73**, 072003 (2006) [arXiv:hep-ex/0602035].

[41] B. Abi *et al.* [Muon $g-2$], Phys. Rev. Lett. **126**, 141801 (2021) [arXiv:2104.03281 [hep-ex]].

[42] T. Albahri *et al.* [Muon $g-2$], Phys. Rev. D **103**, 072002 (2021) [arXiv:2104.03247 [hep-ex]].

[43] T. Albahri *et al.* [Muon $g-2$], Phys. Rev. A **103**, 042208 (2021) [arXiv:2104.03201 [hep-ex]].

[44] T. Albahri *et al.* [Muon $g-2$], Phys. Rev. Accel. Beams **24**, 044002 (2021) [arXiv:2104.03240 [physics.acc-ph]].

[45] D. P. Aguillard *et al.* [Muon g-2], Phys. Rev. Lett. **131**, 161802 (2023) [arXiv:2308.06230 [hep-ex]].

[46] A. Czarnecki, W. J. Marciano, and A. Vainshtein, Phys. Rev. D **67**, 073006 (2003) [arXiv:hep-ph/0212229], [Erratum: Phys.Rev.D 73, 119901 (2006)].

[47] C. Gnendiger, D. Stöckinger, and H. Stöckinger-Kim, Phys. Rev. D **88**, 053005 (2013) [arXiv:1306.5546 [hep-ph]].

[48] A. Keshavarzi, D. Nomura, and T. Teubner, Phys. Rev. D **101**, 014029 (2020) [arXiv:1911.00367 [hep-ph]].

[49] A. Kurz, T. Liu, P. Marquard, and M. Steinhauser, Phys. Lett. B **734**, 144 (2014) [arXiv:1403.6400 [hep-ph]].

[50] G. Colangelo, M. Hoferichter, A. Nyffeler, M. Passera, and P. Stoffer, Phys. Lett. B **735**, 90 (2014) [arXiv:1403.7512 [hep-ph]].

[51] M. Davier, A. Hoecker, B. Malaescu, and Z. Zhang, Eur. Phys. J. C **77**, 827 (2017) [arXiv:1706.09436 [hep-ph]].

[52] A. Keshavarzi, D. Nomura, and T. Teubner, Phys. Rev. D **97**, 114025 (2018) [arXiv:1802.02995 [hep-ph]].

[53] G. Colangelo, M. Hoferichter, and P. Stoffer, JHEP **02**, 006 (2019) [arXiv:1810.00007 [hep-ph]].

[54] M. Hoferichter, B.-L. Hoid, and B. Kubis, JHEP **08**, 137 (2019) [arXiv:1907.01556 [hep-ph]].

[55] M. Davier, A. Hoecker, B. Malaescu, and Z. Zhang, Eur. Phys. J. C **80**, 241 (2020) [arXiv:1908.00921 [hep-ph]], [Erratum: Eur.Phys.J.C 80, 410 (2020)].

[56] K. Melnikov and A. Vainshtein, Phys. Rev. D **70**, 113006 (2004) [arXiv:hep-ph/0312226].

[57] P. Masjuan and P. Sánchez-Puertas, Phys. Rev. D **95**, 054026 (2017) [arXiv:1701.05829 [hep-ph]].

[58] G. Colangelo, M. Hoferichter, M. Procura, and P. Stoffer, JHEP **04**, 161 (2017) [arXiv:1702.07347 [hep-ph]].

[59] M. Hoferichter, B.-L. Hoid, B. Kubis, S. Leupold, and S. P. Schneider, JHEP **10**, 141 (2018) [arXiv:1808.04823 [hep-ph]].

[60] A. Gérardin, H. B. Meyer, and A. Nyffeler, Phys. Rev. D **100**, 034520 (2019) [arXiv:1903.09471 [hep-lat]].

[61] J. Bijnens, N. Hermansson-Truedsson, and A. Rodríguez-Sánchez, Phys. Lett. B **798**, 134994 (2019) [arXiv:1908.03331 [hep-ph]].

[62] G. Colangelo, F. Hagelstein, M. Hoferichter, L. Laub, and P. Stoffer, JHEP **03**, 101 (2020) [arXiv:1910.13432 [hep-ph]].

[63] T. Blum, N. Christ, M. Hayakawa, T. Izubuchi, L. Jin, C. Jung, and C. Lehner, Phys. Rev. Lett. **124**, 132002 (2020) [arXiv:1911.08123 [hep-lat]].

[64] F. V. Ignatov *et al.* [CMD-3] [arXiv:2302.08834 [hep-ex]].

[65] F. V. Ignatov *et al.* [CMD-3] [arXiv:2309.12910 [hep-ex]].

[66] V. Pauk and M. Vanderhaeghen, Eur. Phys. J. C **74**, 3008 (2014) [arXiv:1401.0832 [hep-ph]].

[67] I. Danilkin and M. Vanderhaeghen, Phys. Rev. D **95**, 014019 (2017) [arXiv:1611.04646 [hep-ph]].

[68] M. Knecht, S. Narison, A. Rabemananjara, and D. Rabetiarivony, Phys. Lett. B **787**, 111 (2018) [arXiv:1808.03848 [hep-ph]].

[69] G. Eichmann, C. S. Fischer, and R. Williams, Phys. Rev. D **101**, 054015 (2020) [arXiv:1910.06795 [hep-ph]].

[70] P. Roig and P. Sánchez-Puertas, Phys. Rev. D **101**, 074019 (2020) [arXiv:1910.02881 [hep-ph]].

[71] G. Passarino and M. J. G. Veltman, Nucl. Phys. B **160**, 151 (1979).

[72] G. 't Hooft and M. J. G. Veltman, Nucl. Phys. B **153**, 365 (1979).

[73] R. K. Ellis, Z. Kunszt, K. Melnikov, and G. Zanderighi, Phys. Rept. **518**, 141 (2012) [arXiv:1105.4319 [hep-ph]].

[74] G. 't Hooft, Nucl. Phys. B **35**, 167 (1971).

[75] G. 't Hooft and M. J. G. Veltman, Nucl. Phys. B **44**, 189 (1972).

[76] S. Weinzierl, Fields Inst. Commun. **50**, 345 (2007) [arXiv:hep-ph/0604068].

[77] H. H. Patel, Comput. Phys. Commun. **197**, 276 (2015) [arXiv:1503.01469 [hep-ph]].

[78] W. Fischer and I. Lieb, *A Course in Complex Analysis: From Basic Results to Advanced Topics*, Vieweg & Teubner, 2011.

[79] B. P. Palka, *An Introduction to Complex Function Theory*, Springer, 1991.

[80] I. Caprini, *Functional Analysis and Optimization Methods in Hadron Physics*, Springer, 2019.

[81] N. N. Meiman, Zh. Eksp. Teor. Fiz. **44**, 1228 (1963), [Sov. Phys. JETP **17**, 830 (1963)].

[82] S. Okubo, Phys. Rev. D **3**, 2807 (1971).

[83] S. Okubo, Phys. Rev. D **4**, 725 (1971).

[84] S. Okubo and I.-F. Shih, Phys. Rev. D **4**, 2020 (1971).

[85] C. Bourrely, B. Machet, and E. de Rafael, Nucl. Phys. B **189**, 157 (1981).

[86] P. Colangelo and A. Khodjamirian, *QCD sum rules, a modern perspective* in *At The Frontier of Particle Physics*, pp. 1495–1576 (2000) [arXiv:hep-ph/0010175].

[87] A. Khodjamirian, *Hadron Form Factors: From Basic Phenomenology to QCD Sum Rules*, CRC Press, Taylor & Francis Group, 2020.

[88] S. Ciulli and J. Fischer, Nucl. Phys. **24**, 465 (1961).

[89] I. Caprini and J. Fischer, Phys. Rev. D **60**, 054014 (1999) [arXiv:hep-ph/9811367].

[90] R. J. Hill and G. Paz, Phys. Rev. D **82**, 113005 (2010) [arXiv:1008.4619 [hep-ph]].

[91] P. Koosis, *Introduction to H_p Spaces*, Cambridge University Press, 1980.

[92] P. L. Duren, *Theory of H_p Spaces*, Dover Publications, 2000.

[93] J. B. Garnett, *Bounded Analytic Functions*, Springer, 2006.

[94] B. Simon, *Orthogonal Polynomials on the Unit Circle: Part 1*, Colloquium Publications, 2005.

[95] B. Simon, *Orthogonal Polynomials on the Unit Circle: Part 2*, Colloquium Publications, 2005.

[96] C. G. Boyd and M. J. Savage, Phys. Rev. D **56**, 303 (1997) [arXiv:hep-ph/9702300].

[97] W. W. Buck and R. F. Lebed, Phys. Rev. D **58**, 056001 (1998) [arXiv:hep-ph/9802369].

[98] R. J. Hill, eConf **C060409**, 027 (2006) [arXiv:hep-ph/0606023].

[99] R. J. Hill, Phys. Rev. D **74**, 096006 (2006) [arXiv:hep-ph/0607108].

[100] A. Bharucha, T. Feldmann, and M. Wick, JHEP **09**, 090 (2010) [arXiv:1004.3249 [hep-ph]].

[101] T. Blake, S. Meinel, M. Rahimi, and D. van Dyk, Phys. Rev. D **108**, 094509 (2023) [arXiv:2205.06041 [hep-ph]].

[102] B. Grinstein and R. F. Lebed, Phys. Rev. D **92**, 116001 (2015) [arXiv:1509.04847 [hep-ph]].

[103] I. Caprini, B. Grinstein, and R. F. Lebed, Phys. Rev. D **96**, 036015 (2017) [arXiv:1705.02368 [hep-ph]].

[104] C. Bourrely, I. Caprini, and L. Lellouch, Phys. Rev. D **79**, 013008 (2009) [arXiv:0807.2722 [hep-ph]], [Erratum: Phys.Rev.D 82, 099902 (2010)].

Part I

On the transition form factors of the axial-vector resonance $f_1(1285)$ and its decay into e^+e^-

based on a project

in collaboration with
Martin Hoferichter and Bastian Kubis

published in
JHEP **07**, 106 (2021) [arXiv:2103.09829 [hep-ph]]

Prologue

The anomalous magnetic moment of the muon a_μ is one of today's most precisely measured quantities and as such demands similarly precise calculations on the theoretical side, with a longstanding tension between the experiment and the standard-model prediction potentially hinting at physics beyond the standard model. For the data-driven calculations, robust input for the transition form factors of axial-vector mesons—*i.e.*, the scalar functions that parameterize their non-perturbative coupling to two electromagnetic currents—is crucial for estimating the hadronic light-by-light contribution to a_μ, in particular, for intermediate photon virtualities and the transition to short-distance constraints.[*] At present, the axial-vector contribution included in the standard-model prediction for a_μ [9–33, 66–68] is responsible for a large fraction of the final phenomenological uncertainty, $a_\mu^{\mathrm{HLbL}} = 92(19) \times 10^{-11}$ [9, 22–31, 59–64], especially, when taking into account the interplay with short-distance constraints. In view of the (expected) experimental improvements beyond the world average including run-1 data from Fermilab [34–38]—with the latter providing a precision comparable to that of the Brookhaven measurement—the uncertainty in the hadronic light-by-light contribution should be reduced by another factor of 2 to ensure that it does not play a role in the interpretation of the experiment [54, 56].

The author of this thesis investigated the transition form factors of axial-vector mesons already throughout his master's thesis [115]. Therein, many foundations have been outlined in great detail, including an evaluation of some of the data available at that time in a preliminary vector-meson-dominance framework, which eventually formed the basis for the analysis presented in this part of the dissertation. Since the formalism has been thoroughly refined and a comprehensible account would otherwise be cumbersome, some important contents and formulae of the author's master's thesis are recapitulated in this work; chapters that contain such peculiarities are provided with a footnote that summarizes any potential parallels. However, it shall be emphasized that no parts of the author's master's thesis have been replicated for this work, and possible duplications are condensed in such a way that the overlap is minimized.

The data-driven analysis of the axial-vector transition form factors performed in this thesis is based on the decomposition of the corresponding amplitude into the three Lorentz structures and form factors obtained in Ref. [93], which follows from a procedure by Bardeen, Tung, and Tarrach [94, 95] and ensures the absence of kinematic singularities, thus allowing for a dispersive treatment. This decomposition is briefly reviewed by the author of this dissertation, along with a discussion of the short-distance constraints on the form factors that follow from the light-cone expansion, as derived in Ref. [93]. In

[*] If U(3) symmetry is assumed, it suffices to determine the transition form factors for the f_1 to be able to estimate the effect of the entire triplet including the f_1' and a_1.

the next step, the form factors are decomposed into their isospin components, which are subsequently linked to each other by the author under the assumption of U(3) symmetry and using the mixing angle of the $J^{PC} = 1^{++}$ axial-vector nonet determined by the L3 collaboration [7, 8].

Following these general considerations, the isovector components of the transition form factors are parameterized using two distinct vector-meson-dominance ansätze, including the implementation of energy-dependent widths and dispersively improved variants, which have been constructed in joint efforts by the author of this dissertation, Martin Hoferichter, and Bastian Kubis; here, an implicit change of basis for the transition form factors that proves convenient for the vector-meson-dominance framework has been worked out by the author of this thesis and its consequences on the asymptotic constraints are analyzed accordingly. For the isoscalar components of the form factors, a simplified vector-meson-dominance parameterization is utilized by the author, as agreed upon with Martin Hoferichter and Bastian Kubis in extensive discussions. In order to arrive at a description of the transition form factors that is valid in the whole energy range, the vector-meson-dominance parameterizations are then complemented by asymptotic contributions, obtained by rewriting the expressions resulting from the light-cone expansion into double-spectral representations, which the author of this thesis deduced in analogy to Refs. [26, 27, 135].

Due to the Landau–Yang theorem [1, 2], see also Ref. [115], any experiment sensitive to the axial-vector transition form factors needs to involve at least one virtual photon, which complicates their measurement. Phenomenologically, the situation is best for the f_1 resonance, for which available data on $e^+e^- \to e^+e^- f_1$ [5–7], $f_1 \to 4\pi$ [99], $f_1 \to \rho\gamma$ [99, 100], $f_1 \to \phi\gamma$ [99, 101], and $f_1 \to e^+e^-$ [102] is studied in this part of the thesis. To extract information from these processes, the corresponding observables are calculated within the scope of the established vector-meson-dominance framework by the author of this dissertation. For the one-loop process $f_1 \to e^+e^-$, the calculation is performed by means of a Passarino–Veltman reduction by the author, carried out and evaluated in an automated way using *FeynCalc* [139–141], *FeynHelpers* [142–144], and *LoopTools* [145]. This is supplemented by an alternative strategy pursued by Martin Hoferichter, who performed the calculation in a direct way via the introduction of Feynman parameters, resulting in analytic expressions that lead to numerical values in agreement with those from the automated method, as has also been cross-checked by the author of this thesis.[‡] Using the compiled constraints, a global χ^2 fit is carried out; for this combined phenomenological analysis, the fit for the branching ratio of $f_1 \to \rho\gamma$ from the Particle Data Group [99] is further assessed to be flawed, so that, instead, a revised fit is used by the author.

In the appendices of this part of the thesis, the asymptotic contributions in their double-spectral form are generalized to partly include mass effects from the light-cone expansion, as derived by the author of this thesis with the assistance of Martin Hoferichter. Furthermore, the phenomenological Lagrangians and couplings needed for the main part of the analysis are discussed in the appendices, where the author benefitted from keen insights of Martin Hoferichter and Bastian Kubis. The appendices also contain a comparison—worked out by the author of this dissertation—of the proposed form-factor

[‡]The calculation using Feynman parameters provides an independent cross-check of the evaluation with *LoopTools* [145], which acts as a black box, in particular regarding the proper analytic continuation in the arguments of the loop functions.

parameterizations with previous ansätze from the literature. Finally, the appendices include a calculation of the branching ratio for $f_1 \to 4\pi$ via the $a_1\pi$ intermediate state, which was performed by the author of this thesis to explain the discrepancy observed between the calculation of $f_1 \to 4\pi$ proceeding via the $\rho\rho$ intermediate state and the experimental value.[§]

[§]Note also that all plots in this part of the thesis have been created by the author of the dissertation.

Chapter 1

Introduction

The interaction of an axial-vector resonance A with two electromagnetic (EM) currents, as parameterized in terms of their transition form factors (TFFs), is subject to the venerable Landau–Yang theorem [1, 2], which states that a spin-1 particle cannot decay into two on-shell photons. Accordingly, the decay $A \to \gamma\gamma$ is forbidden, and the simplest process from which information on the general $A \to \gamma^*\gamma^*$ matrix element can be extracted is the singly-virtual process. Such measurements are available from the (space-like) reaction $e^+e^- \to e^+e^-A$ for $A = f_1$ and $A = f_1'$ [3–8], providing results for the so-called equivalent two-photon decay width $\widetilde{\Gamma}_{\gamma\gamma}$—from which the mixing angle between the two f_1 states can be deduced—as well as some constraints on the momentum dependence of the process. Assuming U(3) symmetry then allows some inference also for $A = a_1$, but other direct phenomenological input is scarce.

Recently, renewed interest in the EM properties of axial-vector resonances has been triggered by hadronic corrections to the anomalous magnetic moment of the muon, with the standard-model (SM) prediction [9–33] according to the theory consensus of Ref. [9],

$$a_\mu^{\text{SM}} = 116\,591\,810(43) \times 10^{-11}, \tag{1.1}$$

differing from experiment including run-1 data from Fermilab [34–38],

$$a_\mu^{\text{exp}} = 116\,592\,061(41) \times 10^{-11}, \tag{1.2}$$

by 4.2σ.[1] While the uncertainty is at present dominated by hadronic vacuum polarization (HVP), with an emerging tension between the determination from e^+e^- data [9, 14–20] and quantum chromodynamics (QCD) on the lattice [9, 40–49], see Refs. [50–53], the precision (expected) from the Fermilab [54] and J-PARC [55] experiments demands that also the second-most-uncertain contribution, hadronic light-by-light (HLbL) scattering, be further improved [56].[2] The uncertainty of the current phenomenological estimate, $a_\mu^{\text{HLbL}} = 92(19) \times 10^{-11}$ [9, 22–31, 59–64], is dominated by the intermediate- and high-energy regions of the loop integral. In fact, while at low energies the few dominant hadronic

[1] The tension increases to 5.2σ when comparing to the experimental world average including, in addition, the recent analysis of run-2 and run-3 data from Fermilab [39], $a_\mu^{\text{exp}} = 116\,592\,059(22) \times 10^{-11}$.

[2] Using the latest $e^+e^- \to \pi^+\pi^-$ data from CMD-3 [57, 58] to determine the HVP contribution, the tension in a_μ reduces drastically. The origin of the disagreement with the other e^+e^- measurements is subject to ongoing research and requires further investigation before a conclusive judgement can be made.

channels can be taken into account explicitly in a dispersive approach [65–71]—in terms of pseudoscalar TFFs and partial-wave amplitudes for $\gamma^*\gamma^* \to \pi\pi$ [72–77]—multi-hadron channels become relevant between (1–2) GeV, which ultimately need to be matched to short-distance constraints for the HLbL amplitude [22, 29–31, 78–83]. At these intermediate energies, though, the potentially most sizable contribution originates from hadronic channels that include axial-vector resonances, especially in view of the role they may play in the transition to the asymptotic constraints [22, 61, 64, 84–87]. So far, however, the available estimates of axial-vector contributions are model dependent, both because evaluated with a Lagrangian model for the HLbL tensor itself and because of uncertainties in the interaction with the EM currents, *i.e.*, their TFFs. Further efforts to improve the uncertainty of the HLbL contribution in lattice QCD are ongoing as well [88–92].

As a first step to improving this situation, a systematic analysis of the axial-vector TFFs has been presented recently in Ref. [93], including the decomposition into Lorentz structures that guarantee the absence of kinematic singularities in the TFFs, following the recipe of Bardeen, Tung, and Tarrach (BTT) [94, 95], and the derivation of short-distance constraints in analogy to the light-cone expansion (LCE) of Brodsky and Lepage (BL) [96–98]. Here, we provide a comprehensive analysis of the TFFs of the f_1, for which the most phenomenological input is available. In addition to $e^+e^- \to e^+e^- f_1$ [5–7], there is data available for $f_1 \to 4\pi$ [99], $f_1 \to \rho\gamma$ [99, 100], $f_1 \to \phi\gamma$ [99, 101], and, more recently, $f_1 \to e^+e^-$ [102], all of which probe different aspects of the TFFs, as we will study in detail in this part of the thesis.

Given that there are three independent TFFs, in contrast to just one in the case of pseudoscalar mesons, a full dispersive reconstruction, as done in Refs. [26, 27, 103–107] for the π^0 or in progress for η, η' [108–112], appears not feasible given the available data. Accordingly, we will study the simplest vector-meson-dominance (VMD) ansatz to elucidate which parameters can presently be determined from experiment. In contrast to previous work [113, 114], our parameterization ensures the absence of kinematic singularities, includes short-distance constraints, and accounts for the spectral functions of the isovector resonances. In particular, we critically examine which of the processes listed above do allow for an unambiguous extraction of TFF properties. We focus on the $f_1 \to e^+e^-$ decay, evidence for which has been observed only recently by the SND collaboration [102], with future improvements possible in the context of the ongoing program to measure $e^+e^- \to$ hadrons cross sections. Further, since this process involves a loop integration that depends on all three TFFs, it should provide some sensitivity also to the doubly-virtual TFFs, which are particularly difficult to measure otherwise.

The outline of this part of the thesis is as follows: in Ch. 2, we review the BTT decomposition of the $A \to \gamma^*\gamma^*$ matrix element and the asymptotic constraints. In Ch. 3, we then construct a minimal VMD ansatz as well as an extended version and study their asymptotic behavior. The tree-level processes $e^+e^- \to e^+e^- f_1$, $f_1 \to 4\pi$, and $f_1 \to V\gamma$ ($V = \rho, \phi, \omega$) used to constrain the parameters are discussed in Ch. 4, followed by the $f_1 \to e^+e^-$ decay in Ch. 5. The full phenomenological analysis is provided in Ch. 6, before we summarize our findings in Ch. 7. Further details are provided in the appendices.

Chapter 2

Lorentz decomposition and Brodsky–Lepage limit†

The matrix element for the decay of an axial-vector meson into two virtual photons, $A(P,\lambda_A) \to \gamma^*(q_1,\lambda_1)\gamma^*(q_2,\lambda_2)$, is given by [93]

$$\langle\gamma^*(q_1,\lambda_1)\gamma^*(q_2,\lambda_2)|A(P,\lambda_A)\rangle = \mathrm{i}(2\pi)^4\delta^{(4)}(q_1+q_2-P)\,\mathcal{M}\big(\{A,\lambda_A\}\to\{\gamma^*,\lambda_1\}\{\gamma^*,\lambda_2\}\big) \tag{2.1}$$

in terms of the helicity amplitudes

$$\mathcal{M}\big(\{A,\lambda_A\}\to\{\gamma^*,\lambda_1\}\{\gamma^*,\lambda_2\}\big) = e^2\epsilon_\mu^{\lambda_1\,*}(q_1)\epsilon_\nu^{\lambda_2\,*}(q_2)\epsilon_\alpha^{\lambda_A}(P)\mathcal{M}^{\mu\nu\alpha}(q_1,q_2), \tag{2.2}$$

where we introduced the tensor matrix element $\mathcal{M}^{\mu\nu\alpha}(q_1,q_2)$ by means of

$$\begin{aligned}\mathcal{M}^{\mu\nu}(\{P,\lambda_A\}\to q_1,q_2) &= \epsilon_\alpha^{\lambda_A}(P)\mathcal{M}^{\mu\nu\alpha}(q_1,q_2)\\ &= \mathrm{i}\int \mathrm{d}^4x\,\mathrm{e}^{\mathrm{i}q_1\cdot x}\,\langle 0|\mathrm{T}\{J^\mu_{\mathrm{EM}}(x)J^\nu_{\mathrm{EM}}(0)\}|A(P,\lambda_A)\rangle.\end{aligned} \tag{2.3}$$

In deriving these relations, the axial-vector meson is treated as an asymptotic state in the narrow-width approximation; furthermore, the EM quark current is given by

$$J^\mu_{\mathrm{EM}}(x) = \bar q(x)\mathcal{Q}\gamma^\mu q(x), \qquad q(x) = (u(x),d(x),s(x))^\intercal, \qquad \mathcal{Q} = \frac{1}{3}\mathrm{diag}(2,-1,-1). \tag{2.4}$$

2.1 Lorentz structures

Following the BTT approach [94, 95], the tensor matrix element $\mathcal{M}^{\mu\nu\alpha}(q_1,q_2)$ can be decomposed into three independent Lorentz structures and scalar functions $\mathcal{F}_i(q_1^2,q_2^2)$ that are free of kinematic singularities, with the result [93]

$$\mathcal{M}^{\mu\nu\alpha}(q_1,q_2) = \frac{\mathrm{i}}{m_A^2}\sum_{i=1}^{3} T_i^{\mu\nu\alpha}(q_1,q_2)\mathcal{F}_i(q_1^2,q_2^2), \tag{2.5}$$

†The decomposition of the amplitude into structures and form factors, including their symmetry properties, and the formula for the equivalent two-photon decay width briefly summarized in this chapter have already been detailed in the master's thesis of the author [115].

where m_A is the mass of the respective axial-vector meson and

$$\begin{aligned} T_1^{\mu\nu\alpha}(q_1,q_2) &= \epsilon^{\mu\nu\beta\gamma} q_{1\beta} q_{2\gamma} (q_1^\alpha - q_2^\alpha), \\ T_2^{\mu\nu\alpha}(q_1,q_2) &= \epsilon^{\alpha\nu\beta\gamma} q_{1\beta} q_{2\gamma} q_1^\mu + \epsilon^{\alpha\mu\nu\beta} q_{2\beta} q_1^2, \\ T_3^{\mu\nu\alpha}(q_1,q_2) &= \epsilon^{\alpha\mu\beta\gamma} q_{1\beta} q_{2\gamma} q_2^\nu + \epsilon^{\alpha\mu\nu\beta} q_{1\beta} q_2^2. \end{aligned} \tag{2.6}$$

Under photon crossing ($\mu \leftrightarrow \nu$ and $q_1 \leftrightarrow q_2$), the structures transform according to $T_1^{\nu\mu\alpha}(q_2,q_1) = -T_1^{\mu\nu\alpha}(q_1,q_2)$ and $T_2^{\nu\mu\alpha}(q_2,q_1) = -T_3^{\mu\nu\alpha}(q_1,q_2)$, so that for the form factors we find $\mathcal{F}_1(q_2^2,q_1^2) = -\mathcal{F}_1(q_1^2,q_2^2)$ and $\mathcal{F}_2(q_2^2,q_1^2) = -\mathcal{F}_3(q_1^2,q_2^2)$ on account of Bose symmetry, $\mathcal{M}^{\mu\nu\alpha}(q_1,q_2) = \mathcal{M}^{\nu\mu\alpha}(q_2,q_1)$. The prefactor i/m_A^2 in Eq. (2.5) has been chosen to obtain dimensionless TFFs $\mathcal{F}_i(q_1^2,q_2^2)$ with real-valued normalization.

The Landau–Yang theorem [1, 2] forbids the decay into two on-shell photons, *i.e.*, at least one photon has to be virtual. In particular, the decay width[3]

$$\Gamma(A \to \gamma\gamma) = \frac{1}{32\pi m_A} |\mathcal{M}(A \to \gamma\gamma)|^2 \tag{2.7}$$

vanishes [93], where $|\mathcal{M}(A \to \gamma\gamma)|^2$ is the squared spin-average of the helicity amplitudes, Eq. (2.2), for on-shell photons. Instead, the so-called equivalent two-photon decay width is defined as [5][4]

$$\widetilde{\Gamma}_{\gamma\gamma} = \lim_{q_1^2 \to 0} \frac{1}{2} \frac{m_A^2}{q_1^2} \Gamma(A \to \gamma_\mathrm{L}^* \gamma_\mathrm{T}), \tag{2.8}$$

where the spin-averaged (longitudinal–transversal) width is given by

$$\Gamma(A \to \gamma_\mathrm{L}^* \gamma_\mathrm{T}) = \frac{1}{3} \sum_{\substack{\lambda_A = 0,\pm \\ \lambda_2 = \pm}} \int \mathrm{d}\Gamma^{0\lambda_2|\lambda_A}_{A \to \gamma^*\gamma^*} \Big|_{q_2^2 = 0}, \tag{2.9}$$

and the differential decay width for fixed polarization reads

$$\mathrm{d}\Gamma^{\lambda_1\lambda_2|\lambda_A}_{A \to \gamma^*\gamma^*} = \frac{1}{32\pi^2 m_A^2} \frac{\sqrt{\lambda(m_A^2, q_1^2, q_2^2)}}{2m_A} |\mathcal{M}(\{A,\lambda_A\} \to \{\gamma^*,\lambda_1\}\{\gamma^*,\lambda_2\})|^2 \mathrm{d}\Omega, \tag{2.10}$$

with the center-of-mass solid angle Ω. In terms of the $\mathcal{F}_i(q_1^2,q_2^2)$, one has [93]

$$\widetilde{\Gamma}_{\gamma\gamma} = \frac{\pi\alpha^2}{12} m_A |\mathcal{F}_2(0,0)|^2 = \frac{\pi\alpha^2}{12} m_A |\mathcal{F}_3(0,0)|^2. \tag{2.11}$$

2.2 Asymptotic constraints

In analogy to the asymptotic limits of the pseudoscalar TFF derived in Refs. [96–98], one can use a LCE to obtain the asymptotic behavior of the axial-vector TFFs. Using the

[3] This expression includes a factor 1/2 due to the indistinguishability of the two on-shell photons.

[4] The equivalent two-photon decay width is sometimes defined without the factor of 1/2, see Ref. [116].

distribution amplitudes from Refs. [117, 118], the asymptotic behavior is given by [93]

$$\begin{aligned}
\mathcal{F}_1(q_1^2,q_2^2) &= \mathcal{O}(1/q_i^6),\\
\mathcal{F}_2(q_1^2,q_2^2) &= F_A^{\text{eff}} m_A^3 \int_0^1 \mathrm{d}u\, \frac{u\phi(u)}{(uq_1^2+(1-u)q_2^2-u(1-u)m_A^2)^2} + \mathcal{O}(1/q_i^6),\\
\mathcal{F}_3(q_1^2,q_2^2) &= -F_A^{\text{eff}} m_A^3 \int_0^1 \mathrm{d}u\, \frac{(1-u)\phi(u)}{(uq_1^2+(1-u)q_2^2-u(1-u)m_A^2)^2} + \mathcal{O}(1/q_i^6),
\end{aligned} \tag{2.12}$$

where we generically denoted powers of asymptotic momenta by $q_i = q_1, q_2$, and the wave function $\phi(u) = 6u(1-u)$ is the asymptotic form that already contributes to the pseudoscalar case. In writing Eq. (2.12), we furthermore introduced an effective decay constant

$$F_A^{\text{eff}} = 4\sum_a C_a F_A^a, \tag{2.13}$$

where the decay constants F_A^a are defined via

$$\langle 0|\bar{q}(0)\gamma_\mu\gamma_5 \frac{\lambda^a}{2} q(0)|A(P,\lambda_A)\rangle = F_A^a m_A \epsilon_\mu. \tag{2.14}$$

The Gell-Mann matrices λ_a and the conveniently normalized unit matrix $\lambda_0 = \sqrt{2/3}\,\mathbb{1}$ determine the flavor decomposition, with the flavor weights C_a in the effective decay constant given by $C_a = 1/2\,\mathrm{Tr}[\mathcal{Q}^2\lambda^a]$, *i.e.*, $C_0 = 2/(3\sqrt{6})$, $C_3 = 1/6$, and $C_8 = 1/(6\sqrt{3})$.

We retained the leading mass effects in the denominators of Eq. (2.12) but stress that this does not suffice for a consistent treatment of such corrections; we will thus mostly set $m_A = 0$ in the denominators when implementing the short-distance constraints and address the treatment of the leading mass effects in App. A. Rewriting the results in terms of the average photon virtuality Q^2 and the asymmetry parameter w,

$$Q^2 = \frac{q_1^2+q_2^2}{2} \in [0,\infty), \qquad\qquad w = \frac{q_1^2-q_2^2}{q_1^2+q_2^2} \in [-1,1], \tag{2.15}$$

one finds the scaling [93]

$$\begin{aligned}
\mathcal{F}_1(q_1^2,q_2^2) &= \mathcal{O}(1/Q^6),\\
\mathcal{F}_i(q_1^2,q_2^2) &= \frac{F_A^{\text{eff}} m_A^3}{Q^4} f_i(w) + \mathcal{O}(1/Q^6), \qquad i=2,3,
\end{aligned} \tag{2.16}$$

with

$$f_{2/3}(w) = \frac{3}{4w^3}\left(3 \mp 2w + \frac{(3\pm w)(1\mp w)}{2w}\log\frac{1-w}{1+w}\right). \tag{2.17}$$

The asymmetry functions $f_{2/3}(w)$ are shown in Fig. 2.1, where we also illustrate the values of the function $f_2(w)$ for the limiting cases $w=-1$ ($q_1^2=0$), $w=0$ ($q_1^2=q_2^2$), and $w=1$ ($q_2^2=0$); since $f_2(-w) = -f_3(w)$, the analogous limits for $f_3(w)$ follow accordingly.

More specifically, the symmetric doubly-virtual and singly-virtual asymptotic $\mathcal{O}(1/q^4)$ limits of the TFFs—the latter often being referred to as the BL limit—become

$$\begin{aligned}
\mathcal{F}_2(q^2,q^2) &= \frac{F_A^{\text{eff}} m_A^3}{2q^4} + \mathcal{O}(1/q^6), \qquad & \mathcal{F}_2(q^2,0) &= \frac{3F_A^{\text{eff}} m_A^3}{q^4} + \mathcal{O}(1/q^6),\\
\mathcal{F}_3(q^2,q^2) &= -\frac{F_A^{\text{eff}} m_A^3}{2q^4} + \mathcal{O}(1/q^6), \qquad & \mathcal{F}_3(0,q^2) &= -\frac{3F_A^{\text{eff}} m_A^3}{q^4} + \mathcal{O}(1/q^6),
\end{aligned} \tag{2.18}$$

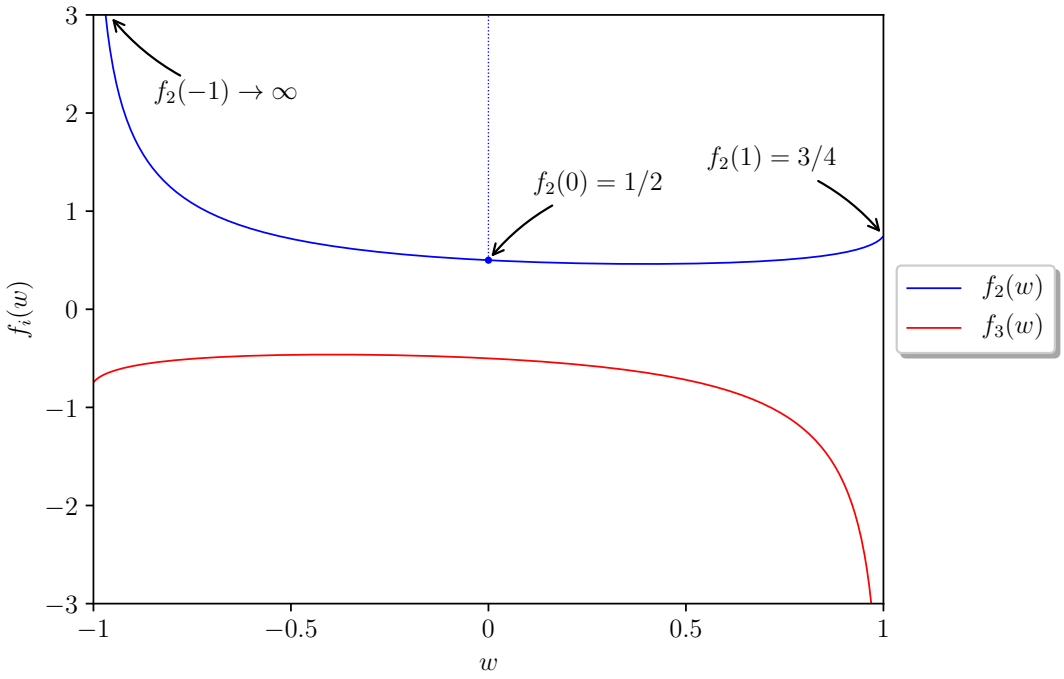

Figure 2.1: Asymmetry functions $f_2(w)$ and $f_3(w)$, Eq. (2.17), with values for the limiting cases $w = -1, 0, 1$ of $f_2(w)$, corresponding to $q_1^2 = 0$, $q_1^2 = q_2^2$, and $q_2^2 = 0$, respectively. The analogous limits for $f_3(w)$ follow from $f_2(-w) = -f_3(w)$.

while the expressions for $\mathcal{F}_2(0, q^2)$ and $\mathcal{F}_3(q^2, 0)$ diverge. Given that the derivation of Eq. (2.12) can only be justified from the operator product expansion (OPE) for $|w| < 1/2$ [119, 120], the singly-virtual limits need to be treated with care.[5] However, physical helicity amplitudes only depend on the well-defined limits in Eq. (2.18), in such a way that the problematic limits $\mathcal{F}_2(0, q^2)$ and $\mathcal{F}_3(q^2, 0)$ do not contribute to observables. We will return to this point in the context of the $f_1 \to e^+e^-$ loop integral.

[5] In soft-collinear effective theory (SCET), the BL factorization can be derived with the kernel corresponding to the perturbatively calculable SCET Wilson coefficient and the wave function to the non-perturbative matrix element of a SCET operator [121–123]. The asymptotic result as given in Eq. (2.12) follows in the limit of conformal symmetry of QCD [124].

Chapter 3

Vector-meson dominance[†]

Given the scarcity of data for axial-vector resonances, we will perform our phenomenological analysis in the context of a VMD description, which has proven to provide successful approximations for a plethora of low-energy hadron–photon processes [125–130]. Most notably, the underlying assumption that the interaction is dominated by the exchange of vector mesons predicts the charge radius of the pion at the level of 10%. Even though the ensuing model dependence is hard to estimate *a priori*, this approach allows us to analyze all experimental constraints simultaneously in a common framework, which could be refined as soon as improved data becomes available.

To construct VMD representations of the TFFs as defined in Ch. 2, it is convenient to recast them in terms of their symmetric (s) and antisymmetric (a) combinations

$$\begin{aligned}
\mathcal{F}_{\mathrm{a}_1}(q_1^2,q_2^2) &= \mathcal{F}_1(q_1^2,q_2^2),\\
\mathcal{F}_{\mathrm{a}_2}(q_1^2,q_2^2) &= \mathcal{F}_2(q_1^2,q_2^2)+\mathcal{F}_3(q_1^2,q_2^2),\\
\mathcal{F}_{\mathrm{s}}(q_1^2,q_2^2) &= \mathcal{F}_2(q_1^2,q_2^2)-\mathcal{F}_3(q_1^2,q_2^2),
\end{aligned} \tag{3.1}$$

with the indicated symmetry properties under the exchange of momenta, $q_1^2 \leftrightarrow q_2^2$. Consequently, the basis of structures transforms according to

$$\begin{aligned}
T_{\mathrm{a}_1}^{\mu\nu\alpha}(q_1,q_2) &= T_1^{\mu\nu\alpha}(q_1,q_2)\\
&= \epsilon^{\mu\nu\beta\gamma} q_{1\beta} q_{2\gamma} (q_1^\alpha - q_2^\alpha),\\
T_{\mathrm{a}_2}^{\mu\nu\alpha}(q_1,q_2) &= \frac{1}{2}\left[T_2^{\mu\nu\alpha}(q_1,q_2)+T_3^{\mu\nu\alpha}(q_1,q_2)\right]\\
&= \frac{1}{2} q_{1\beta} q_{2\gamma} \Big(\epsilon^{\alpha\nu\beta\gamma} q_1^\mu + \epsilon^{\alpha\mu\beta\gamma} q_2^\nu\Big) + \frac{1}{2}\epsilon^{\alpha\mu\nu\beta}(q_{2\beta} q_1^2 + q_{1\beta} q_2^2),\\
T_{\mathrm{s}}^{\mu\nu\alpha}(q_1,q_2) &= \frac{1}{2}\left[T_2^{\mu\nu\alpha}(q_1,q_2)-T_3^{\mu\nu\alpha}(q_1,q_2)\right]\\
&= \frac{1}{2} q_{1\beta} q_{2\gamma} \Big(\epsilon^{\alpha\nu\beta\gamma} q_1^\mu - \epsilon^{\alpha\mu\beta\gamma} q_2^\nu\Big) + \frac{1}{2}\epsilon^{\alpha\mu\nu\beta}(q_{2\beta} q_1^2 - q_{1\beta} q_2^2),
\end{aligned} \tag{3.2}$$

[†]The (anti-)symmetrization of the form factors carried out in this chapter has already been performed in the master's thesis of the author [115], along with a preliminary estimate for the ratio of isoscalar to isovector contributions. Moreover, a predecessor model of the (dispersively improved) minimal VMD representation for the isovector contributions presented here has already been discussed therein, using, however, more elementary parameterizations for the energy-dependent widths and spectral representations.

where these functions fulfill the same symmetry properties under photon crossing. Given this alternative basis, the equivalent two-photon decay width, Eq. (2.11), becomes

$$\widetilde{\Gamma}_{\gamma\gamma} = \frac{\pi\alpha^2}{48} m_A |\mathcal{F}_{\mathrm{s}}(0,0)|^2, \tag{3.3}$$

and the tensor matrix element of Eq. (2.5) takes the form

$$\mathcal{M}^{\mu\nu\alpha}(q_1,q_2) = \frac{\mathrm{i}}{m_A^2} \sum_{i=\mathrm{a}_1,\mathrm{a}_2,\mathrm{s}} T_i^{\mu\nu\alpha}(q_1,q_2)\mathcal{F}_i(q_1^2,q_2^2). \tag{3.4}$$

3.1 Quantum numbers and mixing effects

Since by far the best phenomenological information is available for the f_1, we will focus on this resonance in this part of the thesis but remark that information on the f_1' and the a_1 can be derived when assuming U(3) flavor symmetry. As a first step towards constructing our VMD ansatz for the TFFs,[6] we review the relevant quantum numbers and mixing patterns. From the G-parity of the f_1, $G = +$, it is immediately clear that both photons have to be either in their isoscalar or isovector state when neglecting isospin-breaking effects. Hence, the VMD coupling can only proceed via $\rho\rho$-like or via some combination of an ω- and ϕ-like vector meson, each of which will in turn be discussed in Sec. 3.2 and Sec. 3.3, respectively. As we will show in the following, it is the isovector channel that dominates, with isoscalar corrections typically at the level of 5%.

To this end, we have to take into account mixing effects between the (physical) mesons of the corresponding $J^{PC} = 1^{++}$ axial-vector nonet, *i.e.*, the mixing pattern [99]

$$\begin{pmatrix} f_1 \\ f_1' \end{pmatrix} = \begin{pmatrix} \cos\theta_A & \sin\theta_A \\ -\sin\theta_A & \cos\theta_A \end{pmatrix} \begin{pmatrix} f^0 \\ f^8 \end{pmatrix}, \tag{3.5}$$

where f^0 and f^8 denote the isoscalar singlet and octet states of the $J^{PC} = 1^{++}$ nonet and θ_A is the corresponding mixing angle. Pure octet/singlet mixing is reproduced for $\theta_A = \pi/2$, whereas ideal mixing is obtained for $\theta_A = \arctan(1/\sqrt{2})$.

Including only the two resonances f_1 and f_1', the U(3) parameterization of the $J^{PC} = 1^{++}$ axial vectors reads

$$\Phi_\mu^A = \begin{pmatrix} \sqrt{\frac{2}{3}} f^0 + \frac{1}{\sqrt{3}} f^8 & 0 & 0 \\ 0 & \sqrt{\frac{2}{3}} f^0 + \frac{1}{\sqrt{3}} f^8 & 0 \\ 0 & 0 & \sqrt{\frac{2}{3}} f^0 - \frac{2}{\sqrt{3}} f^8 \end{pmatrix}_\mu, \tag{3.6}$$

and when splitting the charge matrix into isovector and isoscalar components according to $\mathcal{Q} = \mathcal{Q}_3 + \mathcal{Q}_8$,

$$\mathcal{Q}_3 = \frac{1}{2}\mathrm{diag}(1,-1,0), \qquad \mathcal{Q}_8 = \frac{1}{6}\mathrm{diag}(1,1,-2), \tag{3.7}$$

[6] Related models for the f_1 have previously been constructed in the literature [113, 114]; see App. C for a more detailed comparison.

one finds

$$\begin{aligned}\mathrm{Tr}[\Phi_\mu^A \mathcal{Q}_3 \mathcal{Q}_3] &= \frac{f_{1\mu}(\sqrt{2}\cos\theta_A + \sin\theta_A) + f'_{1\mu}(\cos\theta_A - \sqrt{2}\sin\theta_A)}{2\sqrt{3}},\\ \mathrm{Tr}[\Phi_\mu^A \mathcal{Q}_8 \mathcal{Q}_8] &= \frac{f_{1\mu}(\sqrt{2}\cos\theta_A - \sin\theta_A) - f'_{1\mu}(\cos\theta_A + \sqrt{2}\sin\theta_A)}{6\sqrt{3}}.\end{aligned} \tag{3.8}$$

Using the mixing angle $\theta_A = 62(5)^\circ$, as determined by the L3 collaboration [7, 8], see Sec. 4.1, one thus finds that the ratio $R_{\mathrm{S/V}}$ of isoscalar to isovector contributions for the $f_1\gamma\gamma$ coupling is given by

$$R_{\mathrm{S/V}} = \frac{\sqrt{2} - \tan\theta_A}{3(\sqrt{2} + \tan\theta_A)} = -4.7(3.4)\%. \tag{3.9}$$

3.2 Isovector contributions

For the isovector contributions to the TFFs in Eq. (3.1), we include the ρ and the ρ' since this is the minimal particle content that produces a non-vanishing contribution for the antisymmetric TFFs. We propose the minimal parameterizations

$$\begin{aligned}\mathcal{F}^{I=1}_{\mathrm{a}_{1/2}}(q_1^2, q_2^2) &= \frac{C_{\mathrm{a}_{1/2}} M_\rho^2 M_{\rho'}^2}{(q_1^2 - M_\rho^2 + \mathrm{i}\sqrt{q_1^2}\,\Gamma_\rho(q_1^2))(q_2^2 - M_{\rho'}^2 + \mathrm{i}\sqrt{q_2^2}\,\Gamma_{\rho'}(q_2^2))} - (q_1 \leftrightarrow q_2),\\ \mathcal{F}^{I=1}_{\mathrm{s}}(q_1^2, q_2^2) &= \frac{C_{\mathrm{s}} M_\rho^4}{(q_1^2 - M_\rho^2 + \mathrm{i}\sqrt{q_1^2}\,\Gamma_\rho(q_1^2))(q_2^2 - M_\rho^2 + \mathrm{i}\sqrt{q_2^2}\,\Gamma_\rho(q_2^2))},\end{aligned} \tag{3.10}$$

where $\Gamma_\rho(q^2)$ and $\Gamma_{\rho'}(q^2)$ are yet to be specified energy-dependent widths.[7] Moreover, $\rho\rho'$ and $\rho'\rho'$ terms will be added to $\mathcal{F}_{\mathrm{s}}(q_1^2, q_2^2)$ below, to help incorporate the asymptotic constraints from Sec. 2.2. We adopt the dispersion-theoretical point of view to model the singularities of the TFFs based on vector-meson poles and refrain from constructing these using effective Lagrangians in order to facilitate the implementation of high-energy constraints.

Concerning the energy-dependent width $\Gamma_\rho(q^2)$, the decay $\rho \to \pi\pi$ is described by

$$\Gamma_\rho(q^2) = \theta\big(q^2 - 4M_\pi^2\big)\frac{\gamma_{\rho\to\pi\pi}(q^2)}{\gamma_{\rho\to\pi\pi}(M_\rho^2)}\Gamma_\rho, \qquad \gamma_{\rho\to\pi\pi}(q^2) = \frac{(q^2 - 4M_\pi^2)^{3/2}}{q^2}, \tag{3.11}$$

where $\gamma_{\rho\to\pi\pi}(q^2)$ is constructed to be in accordance with the behavior of the decay width for variable $M_\rho^2 = q^2$, see Eq. (B.9), and Γ_ρ is the total width of the ρ meson. For the energy-dependent width $\Gamma_{\rho'}(q^2)$, on the other hand, we will consider two different parameterizations: first, we assume the decay channel $\rho' \to 4\pi$ to be dominant and thus adopt the near-threshold behavior of the four-pion phase space [131, 132]. Secondly, we construct a spectral shape from the decay channels $\rho' \to \omega\pi$ ($\omega \to 3\pi$) and $\rho' \to \pi\pi$,

[7] In writing the propagator poles of our VMD model with energy-dependent widths, we stick to the convention of Ref. [106].

neglecting, however, another significant contribution from $\rho' \to a_1\pi$ ($a_1 \to 3\pi$) [99]. These parameterizations read

$$\Gamma_{\rho'}^{(4\pi)}(q^2) = \theta\big(q^2 - 16M_\pi^2\big)\frac{\gamma_{\rho'\to 4\pi}(q^2)}{\gamma_{\rho'\to 4\pi}(M_{\rho'}^2)}\Gamma_{\rho'}, \qquad \gamma_{\rho'\to 4\pi}(q^2) = \frac{(q^2-16M_\pi^2)^{9/2}}{(q^2)^2}, \tag{3.12}$$

where $\gamma_{\rho'\to 4\pi}(q^2)$ is taken from Refs. [131, 132] and $\Gamma_{\rho'}$ is the total decay width of the ρ' meson, and

$$\begin{aligned}\Gamma_{\rho'}^{(\omega\pi,\pi\pi)}(q^2) &= \theta\big(q^2 - (M_\omega + M_\pi)^2\big)\frac{\gamma_{\rho'\to\omega\pi}(q^2)}{\gamma_{\rho'\to\omega\pi}(M_{\rho'}^2)}\Gamma_{\rho'\to\omega\pi} \\ &\quad + \theta\big(q^2 - 4M_\pi^2\big)\frac{\gamma_{\rho'\to\pi\pi}(q^2)}{\gamma_{\rho'\to\pi\pi}(M_{\rho'}^2)}\Gamma_{\rho'\to\pi\pi},\end{aligned} \tag{3.13}$$

where

$$\gamma_{\rho'\to\omega\pi}(q^2) = \frac{\lambda(q^2,M_\omega^2,M_\pi^2)^{3/2}}{(q^2)^{3/2}}, \qquad \gamma_{\rho'\to\pi\pi}(q^2) = \frac{(q^2-4M_\pi^2)^{3/2}}{q^2}. \tag{3.14}$$

Estimates for the branching fractions required to evaluate these expressions are provided in App. B. Finally, the standard form of the $\rho \to \pi\pi$ spectral function in Eq. (3.11) proves disadvantageous for the evaluation of the superconvergence relations in Sec. 3.4 due to its high-energy behavior. We thus follow Refs. [133, 134] and introduce barrier factors according to

$$\begin{aligned}\Gamma_\rho^{(1)}(q^2) &= \Gamma_\rho(q^2)\frac{M_\rho^2 - 4M_\pi^2 + 4p_R^2}{q^2 - 4M_\pi^2 + 4p_R^2}, \qquad p_R = 202.4\,\text{MeV}, \\ \Gamma_\rho^{(2)}(q^2) &= \Gamma_\rho^{(1)}(q^2)\frac{\sqrt{q^2}}{M_\rho},\end{aligned} \tag{3.15}$$

where concurrent adjustments to the $\rho' \to \pi\pi$ channel of $\Gamma_{\rho'}^{(\omega\pi,\pi\pi)}(q^2)$, Eq. (3.13), are implied. In the end, the numerical impact of the choice of the ρ spectral function is subdominant, and our results will be shown for $\Gamma_\rho^{(2)}(q^2)$ (both for the ρ and the 2π component of $\Gamma_{\rho'}^{(\omega\pi,\pi\pi)}(q^2)$), which is identified as the best phenomenological description for the ρ meson in Ref. [133].

For the one-loop process $f_1 \to e^+e^-$ discussed in Ch. 5, we will use dispersively improved variants of the isovector form factors to ensure the correct analyticity properties when inserting the TFFs into the loop integral. The corresponding spectral representations are constructed from the energy-dependent widths, *i.e.*,

$$\begin{aligned}\widehat{\mathcal{F}}_{\mathrm{a}_{1/2}}^{I=1}(q_1^2,q_2^2) &= \frac{C_{\mathrm{a}_{1/2}}M_\rho^2 M_{\rho'}^2}{N_\mathrm{a}}\Big[P_\rho^{\mathrm{disp}}(q_1^2)P_{\rho'}^{\mathrm{disp}}(q_2^2) - P_{\rho'}^{\mathrm{disp}}(q_1^2)P_\rho^{\mathrm{disp}}(q_2^2)\Big], \\ \widehat{\mathcal{F}}_{\mathrm{s}}^{I=1}(q_1^2,q_2^2) &= \frac{C_\mathrm{s}M_\rho^4}{N_\mathrm{s}}P_\rho^{\mathrm{disp}}(q_1^2)P_\rho^{\mathrm{disp}}(q_2^2),\end{aligned} \tag{3.16}$$

where the dispersive ρ and ρ' propagators are given by

$$\begin{aligned}P_\rho^{\mathrm{disp}}(q^2) &= -\frac{1}{\pi}\int_{4M_\pi^2}^\infty \mathrm{d}x\,\frac{\mathrm{Im}\left[P_\rho^{\mathrm{BW}}(x)\right]}{q^2 - x + \mathrm{i}\epsilon}, \\ P_{\rho'}^{\mathrm{disp}}(q^2) &= -\frac{1}{\pi}\int_{s_\mathrm{thr}}^\infty \mathrm{d}y\,\frac{\mathrm{Im}\left[P_{\rho'}^{\mathrm{BW}}(y)\right]}{q^2 - y + \mathrm{i}\epsilon}.\end{aligned} \tag{3.17}$$

$\Gamma_{\rho'}(q^2)$	N_a	N_s	$\widetilde{N}_\mathrm{s}$
$\Gamma_{\rho'}^{(4\pi)}(q^2)$	$0.577^{-0.037}_{+0.045}$	0.805	$0.805(1-\epsilon_1-\epsilon_2)+0.577^{-0.037}_{+0.045}\epsilon_1+0.414^{-0.051}_{+0.067}\epsilon_2$
$\Gamma_{\rho'}^{(\omega\pi,\pi\pi)}(q^2)$	$0.642^{-0.039}_{+0.046}$	0.805	$0.805(1-\epsilon_1-\epsilon_2)+0.642^{-0.039}_{+0.046}\epsilon_1+0.512^{-0.060}_{+0.076}\epsilon_2$

Table 3.1: Numerical values of the normalization constants given in Eq. (3.19) and Eq. (3.22). The uncertainties refer to the variation $\Gamma_{\rho'} = (400 \pm 60)\,\mathrm{MeV}$, see App. E.

The Breit–Wigner (BW) spectral functions are

$$\begin{aligned}\mathrm{Im}\left[P_\rho^\mathrm{BW}(x)\right] &= \frac{-\sqrt{x}\,\Gamma_\rho(x)}{(x-M_\rho^2)^2+x\Gamma_\rho(x)^2},\\ \mathrm{Im}\left[P_{\rho'}^\mathrm{BW}(y)\right] &= \frac{-\sqrt{y}\,\Gamma_{\rho'}(y)}{(y-M_{\rho'}^2)^2+y\Gamma_{\rho'}(y)^2},\end{aligned} \tag{3.18}$$

and the threshold $s_\mathrm{thr} = 16M_\pi^2, 4M_\pi^2$ depends on the choice of $\Gamma_{\rho'}(q^2)$, Eq. (3.12) or Eq. (3.13). The normalization constants N_a and N_s are introduced in order to retain the normalizations $C_{\mathrm{a}_{1/2}}$ and C_s of the form factors from Eq. (3.10),

$$\begin{aligned}N_\mathrm{a} &= M_\rho^2 M_{\rho'}^2 P_\rho^\mathrm{disp}(0) P_{\rho'}^\mathrm{disp}(0),\\ N_\mathrm{s} &= M_\rho^4 P_\rho^\mathrm{disp}(0) P_\rho^\mathrm{disp}(0),\end{aligned} \tag{3.19}$$

i.e., to ensure that the constants $C_{\mathrm{a}_{1/2}}$ and C_s carry the same meaning in the original and the dispersively improved VMD parameterizations, see Table 3.1. With these conventions, we will drop the distinction between $\mathcal{F}_i(q_1^2,q_2^2)$ and $\widehat{\mathcal{F}}_i(q_1^2,q_2^2)$ in the following, the understanding being that $f_1 \to e^+e^-$ is evaluated with the dispersively improved variants.

Given that excited ρ mesons need to be introduced for the antisymmetric TFFs, it is natural to consider an extended VMD parameterization of the symmetric form factor that includes $\rho\rho'$ and $\rho'\rho'$ terms,

$$\begin{aligned}\widetilde{\mathcal{F}}_\mathrm{s}^{I=1}(q_1^2,q_2^2) = C_\mathrm{s}\Bigg[&\frac{(1-\epsilon_1-\epsilon_2)M_\rho^4}{(q_1^2-M_\rho^2+\mathrm{i}\sqrt{q_1^2}\,\Gamma_\rho(q_1^2))(q_2^2-M_\rho^2+\mathrm{i}\sqrt{q_2^2}\,\Gamma_\rho(q_2^2))}\\ &+\frac{(\epsilon_1/2)M_\rho^2 M_{\rho'}^2}{(q_1^2-M_\rho^2+\mathrm{i}\sqrt{q_1^2}\,\Gamma_\rho(q_1^2))(q_2^2-M_{\rho'}^2+\mathrm{i}\sqrt{q_2^2}\,\Gamma_{\rho'}(q_2^2))}\\ &+\frac{(\epsilon_1/2)M_{\rho'}^2 M_\rho^2}{(q_1^2-M_{\rho'}^2+\mathrm{i}\sqrt{q_1^2}\,\Gamma_{\rho'}(q_1^2))(q_2^2-M_\rho^2+\mathrm{i}\sqrt{q_2^2}\,\Gamma_\rho(q_2^2))}\\ &+\frac{\epsilon_2 M_{\rho'}^4}{(q_1^2-M_{\rho'}^2+\mathrm{i}\sqrt{q_1^2}\,\Gamma_{\rho'}(q_1^2))(q_2^2-M_{\rho'}^2+\mathrm{i}\sqrt{q_2^2}\,\Gamma_{\rho'}(q_2^2))}\Bigg],\end{aligned} \tag{3.20}$$

which is normalized in such a way that $\widetilde{\mathcal{F}}_\mathrm{s}^{I=1}(0,0) = C_\mathrm{s} = \mathcal{F}_\mathrm{s}^{I=1}(0,0)$. Here, ϵ_1 and ϵ_2 could be treated as additional free parameters, but we will instead use this freedom to match to the asymptotic constraints in Sec. 3.4. Similarly to Eq. (3.16), the spectral

representation for $\widetilde{\mathcal{F}}_{\mathrm{s}}^{I=1}(q_1^2, q_2^2)$ is given by

$$\widetilde{\mathcal{F}}_{\mathrm{s}}^{I=1}(q_1^2, q_2^2) = \frac{C_{\mathrm{s}}}{\widetilde{N}_{\mathrm{s}}}\Big[(1-\epsilon_1-\epsilon_2)M_\rho^4 P_\rho^{\mathrm{disp}}(q_1^2)P_\rho^{\mathrm{disp}}(q_2^2) + \frac{\epsilon_1 M_\rho^2 M_{\rho'}^2}{2}P_\rho^{\mathrm{disp}}(q_1^2)P_{\rho'}^{\mathrm{disp}}(q_2^2) + \frac{\epsilon_1 M_{\rho'}^2 M_\rho^2}{2}P_{\rho'}^{\mathrm{disp}}(q_1^2)P_\rho^{\mathrm{disp}}(q_2^2) + \epsilon_2 M_{\rho'}^4 P_{\rho'}^{\mathrm{disp}}(q_1^2)P_{\rho'}^{\mathrm{disp}}(q_2^2)\Big], \quad (3.21)$$

with normalization

$$\widetilde{N}_{\mathrm{s}} = (1-\epsilon_1-\epsilon_2)M_\rho^4 P_\rho^{\mathrm{disp}}(0)P_\rho^{\mathrm{disp}}(0) + \epsilon_1 M_\rho^2 M_{\rho'}^2 P_\rho^{\mathrm{disp}}(0)P_{\rho'}^{\mathrm{disp}}(0) + \epsilon_2 M_{\rho'}^4 P_{\rho'}^{\mathrm{disp}}(0)P_{\rho'}^{\mathrm{disp}}(0), \quad (3.22)$$

see Table 3.1.

3.3 Isoscalar contributions

In the following, we estimate the isoscalar contributions to the TFFs of Eq. (3.1) under the assumption of U(3) flavor symmetry, where we will include the resonances ω and ϕ as well as their excited equivalents ω' and ϕ' into our parameterization. Mixing effects between the (physical) mesons of the corresponding $J^{PC} = 1^{--}$ vector-meson nonets are taken into account via the pattern [99]

$$\begin{pmatrix}\omega^{(\prime)}\\ \phi^{(\prime)}\end{pmatrix} = \begin{pmatrix}\cos\theta_{V^{(\prime)}} & \sin\theta_{V^{(\prime)}}\\ -\sin\theta_{V^{(\prime)}} & \cos\theta_{V^{(\prime)}}\end{pmatrix}\begin{pmatrix}\omega^{0(\prime)}\\ \omega^{8(\prime)}\end{pmatrix}, \quad (3.23)$$

where $\omega^{0(\prime)}$ and $\omega^{8(\prime)}$ denote the isoscalar singlet and octet states of the respective vector-meson nonet with mixing angle $\theta_{V^{(\prime)}}$. For our considerations, we assume both nonets to be ideally mixed, *i.e.*, $\theta_V = \arctan(1/\sqrt{2}) = \theta_{V'}$. Finally, we need the U(3) parameterization of the $J^{PC} = 1^{--}$ vector mesons, which reads

$$\Phi_\mu^{V^{(\prime)}} = \begin{pmatrix}\rho^{0(\prime)} + \omega^{(\prime)} & 0 & 0\\ 0 & -\rho^{0(\prime)} + \omega^{(\prime)} & 0\\ 0 & 0 & -\sqrt{2}\phi^{(\prime)}\end{pmatrix}_\mu \quad (3.24)$$

when including only the aforementioned resonances.

Since the U(3) couplings $f_1\omega\phi$, $f_1\omega'\phi$, and $f_1\omega\phi'$ vanish for ideally mixed vector mesons, we propose the minimal parameterizations

$$\mathcal{F}_{\mathrm{a}_{1/2}}^{I=0}(q_1^2, q_2^2) = \frac{C_{\mathrm{a}_{1/2}}^{\omega\omega'} M_\omega^2 M_{\omega'}^2}{(q_1^2 - M_\omega^2)(q_2^2 - M_{\omega'}^2)} + \frac{C_{\mathrm{a}_{1/2}}^{\phi\phi'} M_\phi^2 M_{\phi'}^2}{(q_1^2 - M_\phi^2)(q_2^2 - M_{\phi'}^2)} - (q_1 \leftrightarrow q_2),$$
$$\mathcal{F}_{\mathrm{s}}^{I=0}(q_1^2, q_2^2) = \frac{C_{\mathrm{s}}^{\omega\omega} M_\omega^4}{(q_1^2 - M_\omega^2)(q_2^2 - M_\omega^2)} + \frac{C_{\mathrm{s}}^{\phi\phi} M_\phi^4}{(q_1^2 - M_\phi^2)(q_2^2 - M_\phi^2)}. \quad (3.25)$$

The resonances ω and ϕ should be well described by a narrow-resonance approximation—with $M_V^2 \to M_V^2 - \mathrm{i}\epsilon$ for time-like applications—while for a realistic description of the

excited-state isoscalar resonances, their widths would need to be taken into account. Due to the expected smallness of the isoscalar contributions, see Eq. (3.9), we refrain from giving an extended VMD parameterization analogous to Eq. (3.20).

With the U(3) parameterization of the axial-vector mesons, Φ_μ^A, and the charge matrix $\mathcal{Q}$ from Sec. 3.1, the ratios of isoscalar to isovector couplings are found to be[8]

$$\frac{C_{\mathrm{a}_{1/2}}^{\omega\omega'}}{C_{\mathrm{a}_{1/2}}} = \frac{C_{\mathrm{s}}^{\omega\omega}}{C_{\mathrm{s}}} = \frac{\mathrm{Tr}[\Phi_\mu^A \Phi_\nu^V \Phi_\kappa^{V^{(\prime)}}]\big|_{f_{1\mu}\omega_\nu\omega_\kappa^{(\prime)}} \mathrm{Tr}[\Phi_\alpha^V \mathcal{Q}]|_{\omega_\alpha} \mathrm{Tr}[\Phi_\beta^{V^{(\prime)}} \mathcal{Q}]\big|_{\omega_\beta^{(\prime)}}}{\mathrm{Tr}[\Phi_\mu^A \Phi_\nu^V \Phi_\kappa^{V^{(\prime)}}]\big|_{f_{1\mu}\rho_\nu\rho_\kappa^{(\prime)}} \mathrm{Tr}[\Phi_\alpha^V \mathcal{Q}]|_{\rho_\alpha} \mathrm{Tr}[\Phi_\beta^{V^{(\prime)}} \mathcal{Q}]\big|_{\rho_\beta^{(\prime)}}} = \frac{1}{9}, \tag{3.26}$$

$$\frac{C_{\mathrm{a}_{1/2}}^{\phi\phi'}}{C_{\mathrm{a}_{1/2}}} = \frac{C_{\mathrm{s}}^{\phi\phi}}{C_{\mathrm{s}}} = \frac{\mathrm{Tr}[\Phi_\mu^A \Phi_\nu^V \Phi_\kappa^{V^{(\prime)}}]\big|_{f_{1\mu}\phi_\nu\phi_\kappa^{(\prime)}} \mathrm{Tr}[\Phi_\alpha^V \mathcal{Q}]|_{\phi_\alpha} \mathrm{Tr}[\Phi_\beta^{V^{(\prime)}} \mathcal{Q}]\big|_{\phi_\beta^{(\prime)}}}{\mathrm{Tr}[\Phi_\mu^A \Phi_\nu^V \Phi_\kappa^{V^{(\prime)}}]\big|_{f_{1\mu}\rho_\nu\rho_\kappa^{(\prime)}} \mathrm{Tr}[\Phi_\alpha^V \mathcal{Q}]|_{\rho_\alpha} \mathrm{Tr}[\Phi_\beta^{V^{(\prime)}} \mathcal{Q}]\big|_{\rho_\beta^{(\prime)}}} = \frac{2(\sqrt{2} - 2\tan\theta_A)}{9(\sqrt{2} + \tan\theta_A)},$$

which, using the mixing angle $\theta_A = 62(5)^\circ$ as determined by the L3 collaboration [7, 8], see Sec. 4.1, implies

$$R^\omega = \frac{C_{\mathrm{a}_{1/2}}^{\omega\omega'}}{C_{\mathrm{a}_{1/2}}} = \frac{C_{\mathrm{s}}^{\omega\omega}}{C_{\mathrm{s}}} = \frac{1}{9}, \qquad R^\phi = \frac{C_{\mathrm{a}_{1/2}}^{\phi\phi'}}{C_{\mathrm{a}_{1/2}}} = \frac{C_{\mathrm{s}}^{\phi\phi}}{C_{\mathrm{s}}} = -0.158(34). \tag{3.27}$$

The additional suppression in Eq. (3.9) then results from a cancellation between ω and ϕ contributions

$$R_{\mathrm{S/V}} = R^\omega + R^\phi = 11.1\% - 15.8(3.4)\% = -4.7(3.4)\%. \tag{3.28}$$

In practice, we will restrict the analysis of isoscalar contributions to the symmetric TFF. For one thing, $\mathcal{F}_{\mathrm{s}}(q_1^2, q_2^2)$ gives the dominant contribution to the observables, so that the most important isoscalar correction is expected from there. In addition, we would need to include the excited ω' and ϕ' states for the antisymmetric TFFs, incurring significant uncertainties from their spectral functions and, especially for the $f_1 \to e^+e^-$ application, the asymptotic matching due to their large masses. Alternatively, isoscalar antisymmetric TFFs could be produced via deviations from ideal ϕ–ω mixing, but, again, the uncertainties would be difficult to control. For these reasons, we conclude that the isoscalar contributions to the antisymmetric TFFs should be irrelevant at present, with future refinements possible once better data becomes available.

3.4 Asymptotics

The VMD representations for the TFFs should comply with the asymptotic constraints reviewed in Sec. 2.2, mainly to ensure that the $f_1 \to e^+e^-$ loop integral does not receive unphysical contributions in the high-energy region; we will focus on the isovector amplitudes, given the strong suppression of the isoscalar contributions. Translated to the basis

[8] The notation is to be understood in such a way that, for each term, the prefactor of the fields indicated as a subscript is taken, with the U(3) parameterizations from Eq. (3.6), Eq. (3.7), and Eq. (3.24). In the ratios, only the traces are relevant as the common Lagrangian parameters cancel.

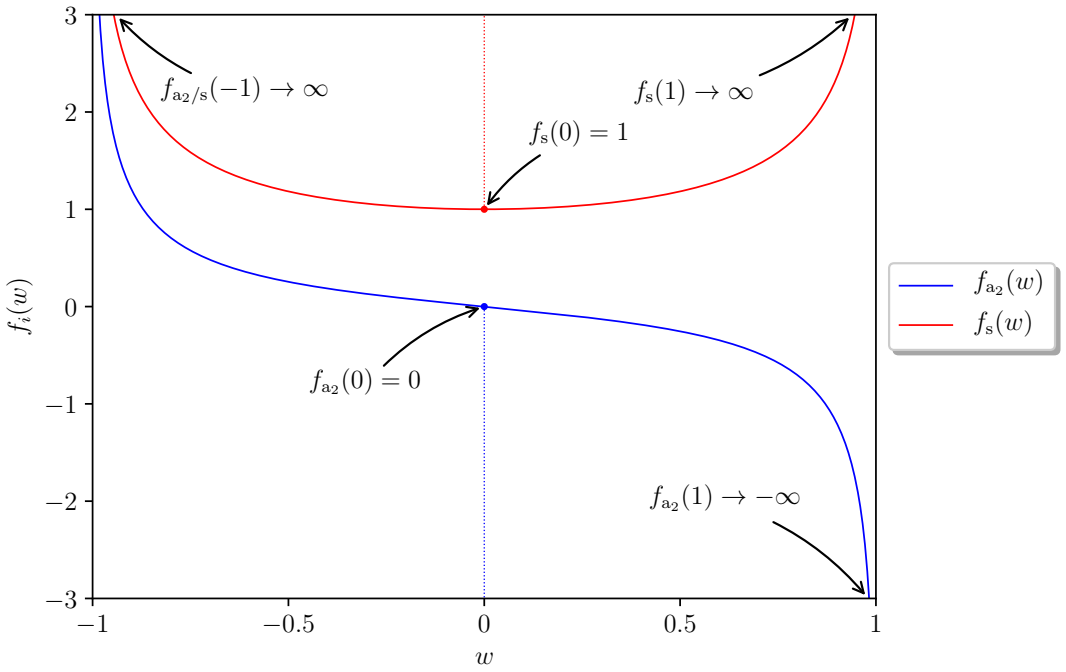

Figure 3.1: Asymmetry functions $f_{a_2}(w)$ and $f_s(w)$, Eq. (3.29), with values for the limiting cases $w = -1, 0, 1$, corresponding to $q_1^2 = 0$, $q_1^2 = q_2^2$, and $q_2^2 = 0$, respectively.

of (anti-)symmetric TFFs, we have

$$\begin{aligned}
&\mathcal{F}_{a_1}(q_1^2, q_2^2) = \mathcal{O}(1/Q^6), \\
&\mathcal{F}_{a_2}(q_1^2, q_2^2) = \frac{F_{f_1}^{\text{eff}} m_{f_1}^3}{Q^4} f_{a_2}(w) + \mathcal{O}(1/Q^6), \quad f_{a_2}(w) = \frac{3}{4w^3}\left(6 + \frac{3-w^2}{w}\log\frac{1-w}{1+w}\right), \\
&\mathcal{F}_{s}(q_1^2, q_2^2) = \frac{F_{f_1}^{\text{eff}} m_{f_1}^3}{Q^4} f_{s}(w) + \mathcal{O}(1/Q^6), \quad f_{s}(w) = -\frac{3}{2w^3}\left(2w + \log\frac{1-w}{1+w}\right),
\end{aligned} \tag{3.29}$$

see Fig. 3.1. The symmetrical doubly-virtual $\mathcal{O}(1/q^4)$ limits become ($\lambda \approx 1$)

$$\begin{aligned}
\mathcal{F}_{a_2}(q^2, \lambda q^2) &= -\frac{6F_{f_1}^{\text{eff}} m_{f_1}^3}{q^4} k(\lambda) + \mathcal{O}(1/q^6), \qquad \mathcal{F}_{s}(q^2, q^2) = \frac{F_{f_1}^{\text{eff}} m_{f_1}^3}{q^4} + \mathcal{O}(1/q^6), \\
k(\lambda) &= \frac{3\lambda^2 - (\lambda^2 + 4\lambda + 1)\log\lambda - 3}{(\lambda-1)^4} = \mathcal{O}(\lambda - 1),
\end{aligned} \tag{3.30}$$

but, upon symmetrization, all singly-virtual limits of $\mathcal{F}_{a_2/s}(q_1^2, q_2^2)$ diverge. For this reason, the asymptotic limits for $\mathcal{F}_{a_2/s}(q_1^2, q_2^2)$ cannot be considered in isolation but need to be implemented in such a way as to reproduce the physical behavior of $\mathcal{F}_{2/3}(q_1^2, q_2^2)$.

We first consider the asymptotic behavior of the minimal VMD parameterization,

	$\mathcal{F}_{\mathrm{a}_1}(q_1^2,q_2^2)$		$\mathcal{F}_{\mathrm{a}_2}(q_1^2,q_2^2)$	$\mathcal{F}_{\mathrm{s}}(q_1^2,q_2^2)$	$\mathcal{F}_2(q_1^2,q_2^2)$
	$q_{1/2}^2 \approx q^2$	$q_2^2 = 0$	$q_{1/2}^2 \approx q^2$	$q_{1/2}^2 = q^2$	$q_2^2 = 0$
LCE	$1/q^6$	$1/q_1^6$	$1/q^4$	$1/q^4$	$1/q_1^4$
VMD (isovector)	$1/q^6$	$1/q_1^2$	$1/q^6$	$1/q^4$	$1/q_1^2$
$\widetilde{\text{VMD}}$ (isovector)	$1/q^6$	$1/q_1^2$	$1/q^6$	$1/q^6$	$1/q_1^4$

Table 3.2: Comparison of the asymptotic behavior of the TFFs as predicted by the LCE, Eq. (3.29) and Eq. (3.30), with the implementation in the VMD representations, Eq. (3.10) and Eq. (3.20). The doubly-virtual limits of $\widetilde{\text{VMD}}$ are tailored to decrease as $1/q^6$, so that the behavior of the LCE is reproduced by adding Eq. (3.47). Note that from the LCE, both $\mathcal{F}_2(0,q^2)$ and $\mathcal{F}_3(q^2,0)$ and thus also all singly-virtual limits of $\mathcal{F}_{\mathrm{a}_2/\mathrm{s}}(q_1^2,q_2^2)$ diverge, whereas $\mathcal{F}_3(0,q^2) = -\mathcal{F}_2(q^2,0)$ for the well-defined singly-virtual limits.

Eq. (3.10),

$$\begin{aligned} \mathcal{F}^{I=1}_{\mathrm{a}_{1/2}}(q^2,\lambda q^2) &\propto \frac{\lambda-1}{\lambda^2}\frac{1}{q^6}, & \mathcal{F}^{I=1}_{\mathrm{a}_{1/2}}(q^2,0) &\propto \frac{1}{q^2}, \\ \mathcal{F}^{I=1}_{\mathrm{s}}(q^2,q^2) &\propto \frac{1}{q^4}, & \mathcal{F}^{I=1}_{\mathrm{s}}(q^2,0) &\propto \frac{1}{q^2}. \end{aligned} \tag{3.31}$$

In this case, the scaling is correct in the doubly-virtual direction of $\mathcal{F}^{I=1}_{\mathrm{a}_1/\mathrm{s}}(q_1^2,q_2^2)$, while $\mathcal{F}^{I=1}_{\mathrm{a}_2}(q_1^2,q_2^2)$ drops too fast and the well-defined singly-virtual limits too slowly, see Table 3.2. Phenomenologically, the symmetric TFF gives the dominant contribution to $f_1 \to e^+e^-$, see Ch. 5, so that the coefficient also deserves some attention here. Comparing the asymptotic limit of Eq. (3.10) with Eq. (3.30), the VMD ansatz for $\mathcal{F}_{\mathrm{s}}(q_1^2,q_2^2)$ implies the estimate

$$F_{f_1}^{\text{eff}}\Big|_{\text{VMD}} = \frac{C_{\mathrm{s}} M_\rho^4}{m_{f_1}^3} = 159(19)\,\text{MeV} \tag{3.32}$$

for the effective decay constant defined in Eq. (2.13), where we already used the L3 result for C_{s} including the isoscalar contribution; see Eq. (4.7) below. Within uncertainties, this value agrees with the result from light-cone sum rules (LCSRs) [93, 118],

$$F_{f_1}^{\text{eff}}\Big|_{\text{LCSRs}} = 146(7)_{\text{LCSRs}}(12)_{\theta_A}\,\text{MeV}, \tag{3.33}$$

so that even the minimal VMD ansatz should display a reasonable asymptotic behavior.

To go beyond this minimal implementation, we now turn to the extended VMD ansatz for $\mathcal{F}_{\mathrm{s}}(q_1^2,q_2^2)$. We follow the strategy from Refs. [26, 27] and add an explicit asymptotic term that incorporates the correct doubly-virtual behavior, obtained by rewriting Eq. (2.12) in terms of a dispersion relation; see also Ref. [135]. Accordingly, we need to ensure that the isovector VMD contribution to $\mathcal{F}_{\mathrm{s}}(q^2,q^2)$ behaves $\propto 1/q^6$, resulting in

$$\epsilon_2 = \frac{(1-\epsilon_1)M_\rho^4 + \epsilon_1 M_\rho^2 M_{\rho'}^2}{M_\rho^4 - M_{\rho'}^4}. \tag{3.34}$$

This leaves the freedom to choose ϵ_1, which we use to implement the physical singly-virtual scaling of $\mathcal{F}_2^{I=1}(q^2,0) = [\mathcal{F}_{\mathrm{a}_2}^{I=1}(q^2,0) + \widetilde{\mathcal{F}}_{\mathrm{s}}^{I=1}(q^2,0)]/2 \propto 1/q^4$, leading to

$$\epsilon_1 = -2\frac{C_{\mathrm{a}_2}(M_\rho^4 - M_{\rho'}^4) + C_{\mathrm{s}} M_\rho^2 M_{\rho'}^2}{C_{\mathrm{s}}(M_\rho^2 - M_{\rho'}^2)^2}. \tag{3.35}$$

Further, the coefficient of $1/q^4$ in the resulting $\mathcal{F}_2^{I=1}(q^2,0)$ only depends on C_{s}, and matching to Eq. (2.18) implies

$$F_{f_1}^{\mathrm{eff}}\Big|_{\widetilde{\mathrm{VMD}}} = \frac{C_{\mathrm{s}} M_\rho^2 M_{\rho'}^2}{6 m_{f_1}^3} = 95(12)\,\mathrm{MeV}, \tag{3.36}$$

reasonably close to the LCSR estimate of Eq. (3.33). In general, the choice for ϵ_1 in Eq. (3.35) enforces the expected singly-virtual behavior at the expense of a large coefficient, *e.g.*, $\epsilon_1 = -1.08$ for $C_{\mathrm{a}_2} = 0$, so that a better low-energy phenomenology might be achieved when considering ϵ_1 a free parameter instead. We will continue to use Eq. (3.35) as a benchmark scenario in comparison to the minimal VMD ansatz, keeping this caveat regarding ϵ_1 in mind.

In choosing the above $\epsilon_{1/2}$, we did not take the spectral representations of Eq. (3.16) and Eq. (3.21) into account, which would lead to a set of superconvergence relations that need to be fulfilled, but instead made an approximate choice in terms of Eq. (3.20) and Eq. (3.10). More specifically, these superconvergence relations read

$$\begin{aligned}
\mathcal{O}(1/q^6) &= \frac{C_{\mathrm{s}}}{\widetilde{N}_{\mathrm{s}} q^4}\Big[(1-\epsilon_1-\epsilon_2) M_\rho^4 P_\rho^0 P_\rho^0 + \epsilon_1 M_\rho^2 M_{\rho'}^2 P_\rho^0 P_{\rho'}^0 + \epsilon_2 M_{\rho'}^4 P_{\rho'}^0 P_{\rho'}^0\Big], \\
\mathcal{O}(1/q^4) &= -\frac{C_{\mathrm{a}_2} M_\rho^2 M_{\rho'}^2}{2 N_{\mathrm{a}} q^2}\Big[P_\rho^0 \bar{P}_{\rho'}^0 - P_{\rho'}^0 \bar{P}_\rho^0\Big] \\
&\quad - \frac{C_{\mathrm{s}}}{2 N_{\mathrm{s}} q^2}\Big[(1-\epsilon_1-\epsilon_2) M_\rho^4 P_\rho^0 \bar{P}_\rho^0 + \frac{\epsilon_1 M_\rho^2 M_{\rho'}^2}{2}\Big(P_\rho^0 \bar{P}_{\rho'}^0 + P_{\rho'}^0 \bar{P}_\rho^0\Big) + \epsilon_2 M_{\rho'}^4 P_{\rho'}^0 \bar{P}_{\rho'}^0\Big],
\end{aligned} \tag{3.37}$$

where we defined

$$\begin{aligned}
P_\rho^0 &= -\frac{1}{\pi}\int_{4M_\pi^2}^\infty \mathrm{d}x\, \mathrm{Im}\left[P_\rho^{\mathrm{BW}}(x)\right], & \bar{P}_\rho^0 &= -\frac{1}{\pi}\int_{4M_\pi^2}^\infty \mathrm{d}x\, \frac{\mathrm{Im}\left[P_\rho^{\mathrm{BW}}(x)\right]}{x}, \\
P_{\rho'}^0 &= -\frac{1}{\pi}\int_{s_{\mathrm{thr}}}^\infty \mathrm{d}y\, \mathrm{Im}\left[P_{\rho'}^{\mathrm{BW}}(y)\right], & \bar{P}_{\rho'}^0 &= -\frac{1}{\pi}\int_{s_{\mathrm{thr}}}^\infty \mathrm{d}y\, \frac{\mathrm{Im}\left[P_{\rho'}^{\mathrm{BW}}(y)\right]}{y}.
\end{aligned} \tag{3.38}$$

Solving this for ϵ_2 and ϵ_1, we find (note that $\bar{P}_\rho^0$ and $\bar{P}_{\rho'}^0$ drop out)

$$\begin{aligned}
\epsilon_2 &= \frac{(1-\epsilon_1)\big(M_\rho^2 P_\rho^0\big)^2 + \epsilon_1 M_\rho^2 P_\rho^0 M_{\rho'}^2 P_{\rho'}^0}{\big(M_\rho^2 P_\rho^0\big)^2 - \big(M_{\rho'}^2 P_{\rho'}^0\big)^2}, \\
\epsilon_1 &= -2\frac{\frac{C_{\mathrm{a}_2}}{N_{\mathrm{a}}}\big[\big(M_\rho^2 P_\rho^0\big)^2 - \big(M_{\rho'}^2 P_{\rho'}^0\big)^2\big] + \frac{C_{\mathrm{s}}}{N_{\mathrm{s}}} M_\rho^2 P_\rho^0 M_{\rho'}^2 P_{\rho'}^0}{\frac{C_{\mathrm{s}}}{N_{\mathrm{s}}}(M_\rho^2 P_\rho^0 - M_{\rho'}^2 P_{\rho'}^0)^2},
\end{aligned} \tag{3.39}$$

in accordance with Eq. (3.34) and Eq. (3.35) upon the replacements

$$\begin{aligned}
M_\rho^2 &\to M_\rho^2 P_\rho^0, & M_{\rho'}^2 &\to M_{\rho'}^2 P_{\rho'}^0, \\
C_{\mathrm{a}_2} &\to \frac{C_{\mathrm{a}_2}}{N_{\mathrm{a}}}, & C_{\mathrm{s}} &\to \frac{C_{\mathrm{s}}}{N_{\mathrm{s}}}.
\end{aligned} \tag{3.40}$$

$\Gamma_{\rho^{(\prime)}}(q^2)$	$\Gamma_{\rho}^{(2)}(q^2)$	$\Gamma_{\rho'}^{(4\pi)}(q^2)$	$\Gamma_{\rho'}^{(\omega\pi,\pi\pi)}(q^2)$
$P^0_{\rho^{(\prime)}}$	1.023	$0.718^{-0.057}_{+0.070}$	$0.918^{-0.073}_{+0.087}$

Table 3.3: Numerical values of P^0_ρ and $P^0_{\rho'}$, Eq. (3.38), as obtained with the parameterizations $\Gamma_\rho^{(2)}(q^2)$, $\Gamma_{\rho'}^{(4\pi)}(q^2)$, and $\Gamma_{\rho'}^{(\omega\pi,\pi\pi)}(q^2)$, Eq. (3.15), Eq. (3.12), and Eq. (3.13), and needed for Eq. (3.39). The uncertainties refer to the variation $\Gamma_{\rho'} = (400 \pm 60)\,\text{MeV}$, see App. E.

Numerical values for P^0_ρ and $P^0_{\rho'}$ are collected in Table 3.3. These results show that most correction factors are close to unity, in which case the only potentially significant correction arises from the different normalizations N_a and N_s for ϵ_1, see Table 3.1. However, our central results will employ $\Gamma_{\rho'}^{(\omega\pi,\pi\pi)}(q^2)$, and given the abovementioned caveats in the choice of ϵ_1, we conclude that the naive VMD expressions Eq. (3.34) and Eq. (3.35) are sufficient at the current level of accuracy.

The doubly-virtual behavior is implemented as follows [26, 27]: first of all, we rewrite the asymptotic form factors $\mathcal{F}_2(q_1^2, q_2^2)$ and $\mathcal{F}_3(q_1^2, q_2^2)$ from Eq. (2.12) into a double-spectral representation, which allows us to isolate the different energy regions, in particular those that give rise to the correct asymptotic limits. Setting $m_A = 0$ in the respective integrands of Eq. (2.12), we observe that

$$\begin{aligned}
\mathcal{F}_2(q_1^2, q_2^2) &= -F_A^\text{eff} m_A^3 \frac{\partial}{\partial q_1^2} \int_0^1 \mathrm{d}u\, \frac{\phi(u)}{u q_1^2 + (1-u) q_2^2} + \mathcal{O}(1/q_i^6), \\
\mathcal{F}_3(q_1^2, q_2^2) &= F_A^\text{eff} m_A^3 \frac{\partial}{\partial q_2^2} \int_0^1 \mathrm{d}u\, \frac{\phi(u)}{u q_1^2 + (1-u) q_2^2} + \mathcal{O}(1/q_i^6)
\end{aligned} \tag{3.41}$$

take exactly the same form as for the pseudoscalar case, except for the partial derivatives with respect to q_i^2. Accordingly, the same arguments as in Refs. [26, 27, 135] apply, and the integral over the wave function can formally be expressed by a double-spectral representation,

$$I(q_1^2, q_2^2) = \int_0^1 \mathrm{d}u\, \frac{\phi(u)}{u q_1^2 + (1-u) q_2^2} = \frac{1}{\pi^2} \int_0^\infty \mathrm{d}x \int_0^\infty \mathrm{d}y\, \frac{\rho^\text{asym}(x,y)}{(x - q_1^2)(y - q_2^2)}. \tag{3.42}$$

To identify the double-spectral density $\rho^\text{asym}(x,y)$, we transform $u \to -q_2^2/(x - q_2^2)$ for space-like q_2^2, leading to

$$I(q_1^2, q_2^2) = \frac{1}{\pi} \int_0^\infty \mathrm{d}x\, \frac{\operatorname{Im} I(x, q_2^2)}{x - q_1^2}, \qquad \operatorname{Im} I(x, q_2^2) = -\frac{\pi}{x - q_2^2}\, \phi\!\left(\frac{x}{x - q_2^2}\right). \tag{3.43}$$

We then write $\operatorname{Im} I(x, q_2^2)$ in terms of another dispersion relation to obtain

$$\rho^\text{asym}(x,y) = \frac{1}{2\mathrm{i}} \operatorname{disc}_y\big[\operatorname{Im} I(x,y)\big] = \frac{3\pi x y}{2\mathrm{i}} \frac{\partial^2}{\partial x^2} \operatorname{disc}_y\left[\frac{1}{x-y}\right], \tag{3.44}$$

where we inserted $\phi(u) = 6u(1-u)$. Using the Sokhotski–Plemelj theorem, we have

$$\operatorname{disc}_y\left[\frac{1}{x-y}\right] = \left[\frac{1}{x - y - \mathrm{i}\epsilon} - \frac{1}{x - y + \mathrm{i}\epsilon}\right] = 2\mathrm{i}\pi\delta(x-y), \tag{3.45}$$

and, hence,

$$\rho^{\text{asym}}(x,y) = 3\pi^2 xy\delta''(x-y). \tag{3.46}$$

The asymptotic form arises from the high-energy part of these integrals, so that, to avoid overlap with the VMD contribution at low energies, we impose a lower cutoff s_m, which, in the language of LCSRs, could be identified with the continuum threshold. Evaluating the partial derivatives and dropping surface terms in the evaluation of the δ distribution [26, 27], we find (note that the chain rules gives $\delta''(x-y) = -\partial_x\partial_y\delta(x-y)$)

$$\begin{aligned}
\mathcal{F}_2^{\text{asym}}(q_1^2,q_2^2) &= -F_A^{\text{eff}} m_A^3 \frac{\partial}{\partial q_1^2}\left[\frac{1}{\pi^2}\int_{s_\text{m}}^\infty \mathrm{d}x \int_{s_\text{m}}^\infty \mathrm{d}y\, \frac{\rho^{\text{asym}}(x,y)}{(x-q_1^2)(y-q_2^2)}\right] + \mathcal{O}(1/q_i^6) \\
&= 3F_A^{\text{eff}} m_A^3 \frac{\partial}{\partial q_1^2}\int_{s_\text{m}}^\infty \mathrm{d}x\, \frac{q_1^2 q_2^2}{(x-q_1^2)^2(x-q_2^2)^2} + \mathcal{O}(1/q_i^6) \\
&= 3F_A^{\text{eff}} m_A^3 \int_{s_\text{m}}^\infty \mathrm{d}x\, \frac{q_2^2(x+q_1^2)}{(x-q_1^2)^3(x-q_2^2)^2} + \mathcal{O}(1/q_i^6), \\
\mathcal{F}_3^{\text{asym}}(q_1^2,q_2^2) &= -3F_A^{\text{eff}} m_A^3 \int_{s_\text{m}}^\infty \mathrm{d}y\, \frac{q_1^2(y+q_2^2)}{(y-q_1^2)^2(y-q_2^2)^3} + \mathcal{O}(1/q_i^6).
\end{aligned} \tag{3.47}$$

By construction, the asymptotic contributions in this form saturate the doubly-virtual limits of Eq. (3.30), while not affecting the singly-virtual contributions $\mathcal{F}_2(q^2,0)$, $\mathcal{F}_3(0,q^2)$ already taken into account via the extended VMD representation. The opposite (unphysical) cases $\mathcal{F}_2(0,q^2)$, $\mathcal{F}_3(q^2,0)$, which do not contribute to helicity amplitudes, yield

$$\mathcal{F}_2(0,q^2) = \frac{3F_A^{\text{eff}} m_A^3}{s_\text{m} q^2} + \mathcal{O}(1/q^4), \qquad \mathcal{F}_3(q^2,0) = -\frac{3F_A^{\text{eff}} m_A^3}{s_\text{m} q^2} + \mathcal{O}(1/q^4) \tag{3.48}$$

in the double-spectral form and are equally suppressed in the $f_1 \to e^+e^-$ loop integral, see Ch. 5. Given that $m_A > 1\,\text{GeV}$, it is also worthwhile to consider the potential impact of mass corrections to the asymptotic constraints; a formulation in terms of a generalized double-spectral density is given in App. A.

In conclusion, the extended VMD ansatz together with the asymptotic contribution of Eq. (3.47) complies with the short-distance constraints of Eq. (2.12), apart from the singly-virtual behavior of $\mathcal{F}_{\text{a}_1}(q_1^2,q_2^2)$ and small violations due to the isoscalar contributions of the form factors, see Eq. (3.9). As we will demonstrate below that $\mathcal{F}_{\text{a}_1}(q_1^2,q_2^2)$ gives the smallest contribution to the $f_1 \to e^+e^-$ loop integral, see Eq. (5.5), the resulting VMD representation should provide a decent approximation to its high-energy part. In particular, the sensitivity to the high-energy assumptions can be monitored by comparing the two VMD variants constructed in this chapter.

Chapter 4

Tree-level processes[†]

The VMD parameterizations constructed in the previous chapter involve the free parameters C_{a_1}, C_{a_2}, and C_{s} (and, for the extended variant, the onset of the asymptotic contributions s_{m}). In the following, we collect the available data that can, in principle, be used to determine these parameters, starting with the processes in which the TFFs appear at tree level:

1. $e^+e^- \to e^+e^- f_1$, which mainly determines the equivalent two-photon decay width $\widetilde{\Gamma}^{f_1}_{\gamma\gamma}$, see Sec. 4.1;

2. $f_1 \to 4\pi$, sensitive to the TFFs via $f_1 \to \rho\rho \to 4\pi$, see Sec. 4.2;

3. $f_1 \to \rho\gamma$, whose branching fraction and helicity components encode information on the TFFs, see Sec. 4.3.

In a more rigorous, dispersive reconstruction of the TFFs, the (partially) hadronic final states would serve as input to a determination of their discontinuities. The strategy to investigate the impact of these reactions on a determination of the various TFFs has already been followed in Refs. [113, 114], albeit with rather different form factor parameterizations. Moreover, we investigate the following tree-level decays:

4. $f_1 \to \phi\gamma$ and $f_1 \to \omega\gamma$, where the measured branching fraction of the former allows for a consistency check of our U(3) assumption for the isoscalar TFFs, and the latter predicts a branching ratio that can be confronted with potential future measurements, see Sec. 4.4.

4.1 $e^+e^- \to e^+e^- f_1$

In contrast to (pseudo-)scalar or tensor resonances, axial-vector resonances are only visible in e^+e^- collisions, see Fig. 4.1, provided that at least one of the photons is off shell—an

[†]The L3 data for $e^+e^- \to e^+e^- f_1$ analyzed in this chapter has already been studied to some extent in the author's master's thesis [115], in particular regarding the matching of a monopole ansatz to the L3 dipole parameterization. Furthermore, formulae for the branching ratios of $f_1 \to 4\pi$ and $f_1 \to \rho\gamma$ as well as the ratio of the ρ-meson's helicity amplitudes for the latter process were derived therein; however, this was done only for the simplest variant possible, *i.e.*, in the minimal VMD parameterization and without potential contributions from excited vector mesons.

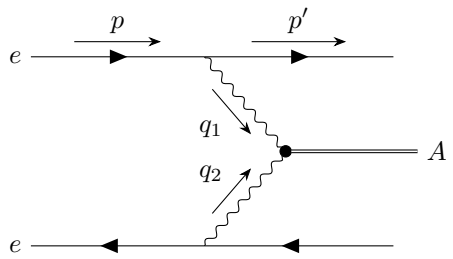

Figure 4.1: Feynman diagram for two-photon hadron formation in electron–positron scattering.

immediate consequence of the Landau–Yang theorem [1, 2]. The required challenging measurements have been performed for the f_1 and f_1', by the MARK II [3, 4], the TPC/Two-Gamma [5, 6], and, more recently, by the L3 [7, 8] collaborations. With both measurements required to constrain the mixing angle θ_A from the data, we will restrict our analysis to the L3 data, given that it is more accurate than the results from the preceding experiments. The L3 analyses are based on the model of Ref. [136], which assumes $\mathcal{F}_1(q_1^2, q_2^2) = 0$ for the first form factor from Eq. (2.5) and uses a dipole ansatz for $\mathcal{F}_2(q^2, 0) = -\mathcal{F}_3(0, q^2)$, with

$$\mathcal{F}_\mathrm{D}(q^2, 0) = \frac{\mathcal{F}_\mathrm{D}(0,0)}{(1 - q^2/\Lambda_\mathrm{D}^2)^2}. \tag{4.1}$$

Under the assumption $B(f_1' \to K\bar{K}\pi) = 1$—which appears justified in light of the smallness of the other available channels [99]—the measured parameters are

$$\begin{aligned} \widetilde{\Gamma}_{\gamma\gamma}^{f_1} &= 3.5(6)(5)\,\mathrm{keV}, & \Lambda_{f_1} &= 1.04(6)(5)\,\mathrm{GeV}, \\ \widetilde{\Gamma}_{\gamma\gamma}^{f_1'} &= 3.2(6)(7)\,\mathrm{keV}, & \Lambda_{f_1'} &= 0.926(72)(32)\,\mathrm{GeV}, \end{aligned} \tag{4.2}$$

where the quoted uncertainties are statistical and systematic, respectively. Employing the two-photon decay widths of the f_1 and f_1', the mixing angle of the $J^{PC} = 1^{++}$ axial-vector nonet as defined in Eq. (3.5) can be extracted as follows: one calculates the coupling of the axial-vector mesons f_1 and f_1' to two photons in analogy to Eq. (3.8), yielding

$$\mathrm{Tr}[\Phi_\mu^A \mathcal{Q}\mathcal{Q}] = \frac{f_{1\mu}(2\sqrt{2}\cos\theta_A + \sin\theta_A) + f_{1\mu}'(\cos\theta_A - 2\sqrt{2}\sin\theta_A)}{3\sqrt{3}}, \tag{4.3}$$

so that using the formula for the equivalent two-photon decay width $\widetilde{\Gamma}_{\gamma\gamma}$, Eq. (2.11), one finds

$$\frac{\widetilde{\Gamma}_{\gamma\gamma}^{f_1}}{\widetilde{\Gamma}_{\gamma\gamma}^{f_1'}} = \frac{m_{f_1}}{m_{f_1'}} \left| \frac{2\sqrt{2} + \tan\theta_A}{1 - 2\sqrt{2}\tan\theta_A} \right|^2 = \frac{m_{f_1}}{m_{f_1'}} \cot^2(\theta_A - \theta_0), \tag{4.4}$$

where $\theta_0 = \arcsin(1/3)$. Solving for θ_A and inserting the above values for $\widetilde{\Gamma}_{\gamma\gamma}^{f_1}$ and $\widetilde{\Gamma}_{\gamma\gamma}^{f_1'}$, one finds the result of Refs. [7, 8],

$$\theta_A = 62(5)^\circ, \tag{4.5}$$

where the statistical and systematic uncertainties have been added in quadrature.

Next, the measurement of $\widetilde{\Gamma}^{f_1}_{\gamma\gamma}$ determines the normalization of the symmetric TFF, $|C_\mathrm{s}| = |\mathcal{F}_\mathrm{s}^{I=1}(0,0)|$ when neglecting the isoscalar contributions, according to Eq. (3.3),

$$|C_\mathrm{s}| = 0.89(10). \tag{4.6}$$

Taking into account the isoscalar contributions and, in particular, the ratios R^ω and R^ϕ of isoscalar to isovector couplings, Eq. (3.27), the normalization of the symmetric TFF becomes $|\mathcal{F}_\mathrm{s}^{I=1}(0,0) + \mathcal{F}_\mathrm{s}^{I=0}(0,0)| = (1 + R^\omega + R^\phi)|C_\mathrm{s}| = 0.953(34)|C_\mathrm{s}|$, resulting in

$$|C_\mathrm{s}| = 0.93(11), \tag{4.7}$$

which is slightly larger than Eq. (4.6), as expected from the negative ratio found in the estimate of Eq. (3.9). In the following, we will use Eq. (4.7) for the normalization of the symmetric TFF.

In addition, Eq. (4.2) determines the slope of $\mathcal{F}_2(q^2,0)$, based on the assumption of a dipole form. The asymptotic behavior matches onto Eq. (2.18) with [93]

$$F^\mathrm{eff}_{f_1}\Big|_\mathrm{L3} = \frac{C_\mathrm{s}\Lambda^4_{f_1}}{6m^3_{f_1}} = 86(28)\,\mathrm{MeV}, \tag{4.8}$$

below both the LCSR estimate, Eq. (3.33), and the effective decay constant implied by VMD, Eq. (3.32), though close to the scale derived from the singly-virtual behavior of the extended VMD representation, Eq. (3.36).[9] The uncertainty in Eq. (4.8) is mainly driven by the dipole parameter Λ_D. In fact, most of the data points measured by the L3 collaboration lie well below the obtained dipole scale, in such a way that the data should be similarly well described by a monopole ansatz,

$$\mathcal{F}_\mathrm{M}(q^2,0) = \frac{\mathcal{F}_\mathrm{M}(0,0)}{1 - q^2/\Lambda^2_\mathrm{M}}, \tag{4.9}$$

when adjusting the slopes of the parameterizations to coincide at $q^2 = 0$. The corresponding monopole scale becomes

$$\Lambda_\mathrm{M} = \frac{\Lambda_\mathrm{D}}{\sqrt{2}} = 0.74(6)\,\mathrm{GeV} \approx M_\rho, \tag{4.10}$$

thus providing strong motivation for the VMD representation constructed in Ch. 3.

To constrain the singly-virtual VMD limits further, we need to match the L3 parameterization onto the full description of the $e^+e^- \to e^+e^- f_1$ cross section, which depends on the combination [93]

$$\left|\left(1 - \frac{q^2}{m^2_{f_1}}\right)\mathcal{F}_1(q^2,0) - \frac{q^2}{m^2_{f_1}}\mathcal{F}_2(q^2,0)\right|^2 - \frac{2q^2}{m^2_{f_1}}\left|\mathcal{F}_2(q^2,0)\right|^2 = \frac{-q^2}{m^2_{f_1}}\left(2 - \frac{q^2}{m^2_{f_1}}\right)|\mathcal{F}_\mathrm{D}(q^2,0)|^2. \tag{4.11}$$

[9] Matching the effective decay constant in the doubly-virtual direction to the quark model of Ref. [136] instead, one would obtain $F^\mathrm{eff}_{f_1}\big|_\mathrm{L3} = C_\mathrm{s}\Lambda^4_{f_1}/(4m^3_{f_1}) = 129(42)\,\mathrm{MeV}$, closer to Eq. (3.32) and Eq. (3.33). This reflects the factor 3/2 by which the relative coefficients of the singly- and doubly-virtual limits differ between the quark model and the BL prediction [93].

The normalization agrees by construction, while matching the slopes at $q^2 = 0$ leads to

$$\frac{2}{\Lambda_{\mathrm{D}}^2} = \frac{1}{N_{\omega\phi}}\left[\frac{1}{M_\rho^2} + \frac{R^\omega}{M_\omega^2} + \frac{R^\phi}{M_\phi^2} + \frac{M_{\rho'}^2 - M_\rho^2}{M_\rho^2 M_{\rho'}^2}\frac{C_{\mathrm{a}_1} + C_{\mathrm{a}_2}}{C_{\mathrm{s}}} - \frac{m_{f_1}^2 (M_{\rho'}^2 - M_\rho^2)^2}{M_\rho^4 M_{\rho'}^4 N_{\omega\phi}}\left(\frac{C_{\mathrm{a}_1}}{C_{\mathrm{s}}}\right)^2\right] \tag{4.12}$$

for the minimal VMD representation and

$$\frac{2}{\Lambda_{\mathrm{D}}^2} = \frac{1}{N_{\omega\phi}}\left[\frac{1}{M_\rho^2} + \frac{1}{M_{\rho'}^2} + \frac{R^\omega}{M_\omega^2} + \frac{R^\phi}{M_\phi^2} + \frac{M_{\rho'}^2 - M_\rho^2}{M_\rho^2 M_{\rho'}^2}\frac{C_{\mathrm{a}_1}}{C_{\mathrm{s}}} - \frac{m_{f_1}^2 (M_{\rho'}^2 - M_\rho^2)^2}{M_\rho^4 M_{\rho'}^4 N_{\omega\phi}}\left(\frac{C_{\mathrm{a}_1}}{C_{\mathrm{s}}}\right)^2\right] \tag{4.13}$$

for the extended one. The factor $N_{\omega\phi} = 1 + R^\omega + R^\phi$ arises from accounting for the isoscalar terms in the normalization, see Eq. (4.7).

4.2 $f_1 \to 4\pi$

In addition to $e^+e^- \to e^+e^- f_1$, the normalization of the symmetric TFF would be accessible in the process $f_1 \to \rho\rho \to 4\pi$ if the ρ intermediate states largely saturated the decay within regions of the phase space reasonably close to their mass shell. In fact, up to corrections due to the two-pion channel $\rho' \to \pi^+\pi^-$, such an identification appears natural within the VMD approach. In constructing an amplitude $\mathcal{M}(f_1 \to \pi^+\pi^-\pi^+\pi^-)$, which can be obtained by means of $\mathcal{M}(f_1 \to \rho^{0*}\rho^{0*})$ and the $\rho\pi\pi$ coupling dictated by Eq. (B.8), only the symmetric form factor $\mathcal{F}_{\mathrm{s}}^{I=1}(q_1^2, q_2^2)$ and the symmetric LORENTZ structure $T_{\mathrm{s}}^{\mu\nu\alpha}(q_1, q_2)$ are relevant under the above assumptions and when restricting to the minimal VMD parameterization. More specifically, we use the amplitude $\mathcal{M}(f_1 \to \gamma^*\gamma^*)$ in the decomposition of Eq. (3.4) and remove the external photons by dropping the relevant ρ-meson propagator poles and the factors of e, at the same time dividing by the $\rho\gamma$ coupling $\widetilde{g}_{\rho\gamma}$, Eq. (B.7), for each cut photon. In doing so, we arrive at

$$\begin{aligned}\mathcal{M}(f_1 \to \rho^{0*}\rho^{0*}) = \frac{C_{f\rho\rho}}{2}&\epsilon_\mu^*(q_1)\epsilon_\nu^*(q_2)\epsilon_\alpha(P)\\ &\times\Big[q_{1\beta}q_{2\gamma}\Big(\epsilon^{\alpha\nu\beta\gamma}q_1^\mu - \epsilon^{\alpha\mu\beta\gamma}q_2^\nu\Big) + \epsilon^{\alpha\mu\nu\beta}(q_{2\beta}q_1^2 - q_{1\beta}q_2^2)\Big],\end{aligned} \tag{4.14}$$

where we defined $C_{f\rho\rho} = C_{\mathrm{s}} M_\rho^4/(m_{f_1}^2 \widetilde{g}_{\rho\gamma}^2)$. Observing that there exist two diagrams for $f_1 \to \pi^+\pi^-\pi^+\pi^-$ due to the indistinguishability of the two π^+ and π^-—see Fig. 4.2—we use the $\rho\pi\pi$ coupling as prescribed by Eq. (B.8) to deduce

$$\begin{aligned}\mathcal{M}(f_1 \to \pi^+\pi^-\pi^+\pi^-) = &\frac{2C_{f\rho\rho}g_{\rho\pi\pi}^2}{\big(q_1^2 - M_\rho^2 + \mathrm{i}\sqrt{q_1^2}\,\Gamma_\rho(q_1^2)\big)\big(q_2^2 - M_\rho^2 + \mathrm{i}\sqrt{q_2^2}\,\Gamma_\rho(q_2^2)\big)}\epsilon_\alpha(P)\epsilon^{\alpha\mu\nu\beta}\\ &\times\Big[\big(M_\pi^2 + (p_1\cdot p_2)\big)k_{1\beta}k_{2\nu}(p_2 - p_1)_\mu - \big(M_\pi^2 + (k_1\cdot k_2)\big)p_{1\beta}p_{2\mu}(k_2 - k_1)_\nu\Big]\\ &+ (p_1 \leftrightarrow k_1).\end{aligned} \tag{4.15}$$

Here, the momenta are defined as in Fig. 4.2 and the pions are on shell, $p_{1/2}^2 = M_\pi^2 = k_{1/2}^2$.

Given this amplitude, one can calculate the decay width and thus branching ratio via the four-body phase-space integration of

$$\mathrm{d}\Gamma(f_1 \to \pi^+\pi^-\pi^+\pi^-) = \frac{1}{2m_{f_1}}\big|\mathcal{M}(f_1 \to \pi^+\pi^-\pi^+\pi^-)\big|^2 \mathrm{d}\Phi_4(P; p_1, p_2, k_1, k_2). \tag{4.16}$$

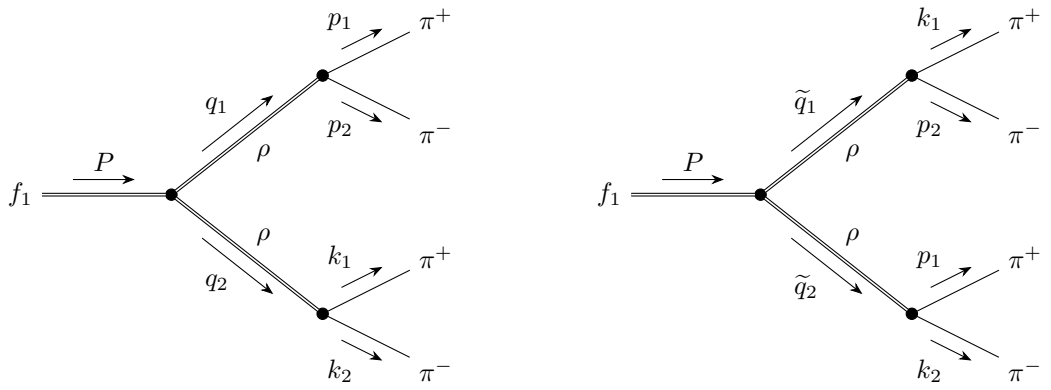

Figure 4.2: FEYNMAN diagrams for $f_1 \to \pi^+\pi^-\pi^+\pi^-$ via two ρ mesons. Since the two π^+ and π^- are each mutually indistinguishable, there exist two contributions (*left* and *right*).

We use the differential four-body phase space $\mathrm{d}\Phi_4(P; p_1, p_2, k_1, k_2)$ in the form [99]

$$\mathrm{d}\Phi_4(P; p_1, p_2, k_1, k_2) = \mathrm{d}\Phi_2(q_1; p_1, p_2)\, \mathrm{d}\Phi_2(q_2; k_1, k_2)\, \mathrm{d}\Phi_2(P; q_1, q_2)\, \frac{\mathrm{d}q_1^2}{2\pi}\, \frac{\mathrm{d}q_2^2}{2\pi}, \tag{4.17}$$

where $\mathrm{d}\Phi_2(P; q_1, q_2)$, $\mathrm{d}\Phi_2(q_1; p_1, p_2)$, and $\mathrm{d}\Phi_2(q_2; k_1, k_2)$ are the respective two-body phase spaces of the subsystems $\{\rho(q_1), \rho(q_2)\}$, $\{\pi^+(p_1), \pi^-(p_2)\}$, and $\{\pi^+(k_1), \pi^-(k_2)\}$. Since the integration volumes of the phase spaces are LORENTZ invariant, each two-body phase space can be evaluated in the corresponding center-of-mass frame, and we have to perform an explicit LORENTZ transformation from the center-of-mass frames of $\{\pi^+(p_1), \pi^-(p_2)\}$ and $\{\pi^+(k_1), \pi^-(k_2)\}$ into the one of $\{\rho(q_1), \rho(q_2)\}$ in order to evaluate scalar products of the kind $(p_i \cdot k_j)$, $i, j \in \{1, 2\}$, appearing in $|\mathcal{M}(f_1 \to \pi^+\pi^-\pi^+\pi^-)|^2$; see, *e.g.*, Ref. [137] for more details.[10] We perform the phase-space integration numerically with the *Cuhre* algorithm from the *Cuba* library [138], where the energy-dependent width $\Gamma_\rho(q^2)$ is as specified in Eq. (3.15), and obtain [115]

$$\Gamma(f_1 \to \pi^+\pi^-\pi^+\pi^-) = |C_\mathrm{s}|^2 |g_{\rho\gamma}|^4 |g_{\rho\pi\pi}|^4 \times 0.63 \times 10^{-10}\,\mathrm{GeV}. \tag{4.18}$$

Combining the above result with the values $|g_{\rho\gamma}| = 4.96$ and $|g_{\rho\pi\pi}| = 5.98$, Eq. (B.3) and Eq. (B.11), we find the branching ratio to be given by

$$B(f_1 \to \pi^+\pi^-\pi^+\pi^-) = |C_\mathrm{s}|^2 \times 0.215(10)\%. \tag{4.19}$$

The comparison with the experimental ratio $B(f_1 \to \pi^+\pi^-\pi^+\pi^-) = 10.9(6)\%$ [99] yields

$$|C_\mathrm{s}| = 7.1(3), \tag{4.20}$$

in serious disagreement with Eq. (4.7).

Including ρ' contributions within the minimal VMD representation, there are four additional diagrams as compared to Fig. 4.2, that is two for the intermediate state (ρ, ρ')

[10] While two diagrams contribute, as shown in Fig. 4.2, the decay rate involves an additional symmetry factor of $S = 1/(2!)^2$ because of the two pairs of indistinguishable particles in the final state.

$\Gamma_{\rm s}^{(1)}$	$\Gamma_{\rm s}^{(2)}$	$\Gamma_{\rm s}^{(3)}$	$\Gamma_{\rm s}^{(4)}$	$\Gamma_{\rm s}^{(5)}$	$\Gamma_{\rm s}^{(6)}$
0.63	0.01	0.00	0.16	0.01	0.00
$\Gamma_{\rm a_1}$	$\Gamma_{\rm a_2}$	$\Gamma_{\rm a_1,a_2}$			
0.02	0.18	-0.06			
$\Gamma_{\rm a_1,s}^{(1)}$	$\Gamma_{\rm a_2,s}^{(1)}$	$\Gamma_{\rm a_1,s}^{(2)}$	$\Gamma_{\rm a_2,s}^{(2)}$	$\Gamma_{\rm a_1,s}^{(3)}$	$\Gamma_{\rm a_2,s}^{(3)}$
-0.12	0.54	-0.01	0.05	0.00	0.00

Table 4.1: Decay rates (in units of $10^{-10}\,\text{GeV}$) needed for the evaluation of Eq. (4.21) and Eq. (4.23). The ρ and ρ' spectral functions are evaluated with Eq. (3.15) and Eq. (3.13), respectively. The latter variant is chosen for consistency with the estimate of the $\rho' \to \pi\pi$ coupling via Eq. (4.22), see App. B.

and two for (ρ', ρ). The corresponding master formula then takes the form

$$\begin{aligned}\Gamma(f_1 \to \pi^+\pi^-\pi^+\pi^-) = |g_{\rho\gamma}|^4 |g_{\rho\pi\pi}|^4 \Big[& C_{\rm a_1}^2 \kappa^2 \Gamma_{\rm a_1} + C_{\rm a_2}^2 \kappa^2 \Gamma_{\rm a_2} + C_{\rm s}^2 \Gamma_{\rm s}^{(1)} + C_{\rm a_1} C_{\rm a_2} \kappa^2 \Gamma_{\rm a_1,a_2} \\ & + C_{\rm a_1} C_{\rm s} \kappa \Gamma_{\rm a_1,s}^{(1)} + C_{\rm a_2} C_{\rm s} \kappa \Gamma_{\rm a_2,s}^{(1)} \Big], \end{aligned} \tag{4.21}$$

where

$$\kappa = \frac{M_{\rho'}^2}{M_\rho^2} \frac{\widetilde{g}_{\rho\gamma}}{\widetilde{g}_{\rho'\gamma}} \frac{g_{\rho'\pi\pi}}{g_{\rho\pi\pi}} = \frac{g_{\rho'\gamma} g_{\rho'\pi\pi}}{g_{\rho\gamma} g_{\rho\pi\pi}} \approx -0.7, \tag{4.22}$$

see Eq. (B.23); the numerical values of the defined decay rates are collected in Table 4.1. For the extended VMD representation, yet two additional diagrams with the intermediate state (ρ', ρ') have to be taken into account, resulting in the master formula

$$\begin{aligned}\Gamma(f_1 \to \pi^+\pi^-\pi^+\pi^-) = {} & |g_{\rho\gamma}|^4 |g_{\rho\pi\pi}|^4 \\ & \times \Big[C_{\rm a_1}^2 \kappa^2 \Gamma_{\rm a_1} + C_{\rm a_2}^2 \kappa^2 \Gamma_{\rm a_2} + C_{\rm s}^2 \Big[(1-\epsilon_1-\epsilon_2)^2 \Gamma_{\rm s}^{(1)} + \epsilon_1^2 \kappa^2 \Gamma_{\rm s}^{(2)} + \epsilon_2^2 \kappa^4 \Gamma_{\rm s}^{(3)} \\ & + (1-\epsilon_1-\epsilon_2)\epsilon_1 \kappa \Gamma_{\rm s}^{(4)} + (1-\epsilon_1-\epsilon_2)\epsilon_2 \kappa^2 \Gamma_{\rm s}^{(5)} + \epsilon_1 \epsilon_2 \kappa^3 \Gamma_{\rm s}^{(6)} \Big] \\ & + C_{\rm a_1} C_{\rm a_2} \kappa^2 \Gamma_{\rm a_1,a_2} + C_{\rm a_1} C_{\rm s} \Big[(1-\epsilon_1-\epsilon_2)\kappa \Gamma_{\rm a_1,s}^{(1)} + \epsilon_1 \kappa^2 \Gamma_{\rm a_1,s}^{(2)} + \epsilon_2 \kappa^3 \Gamma_{\rm a_1,s}^{(3)} \Big] \\ & + C_{\rm a_2} C_{\rm s} \Big[(1-\epsilon_1-\epsilon_2)\kappa \Gamma_{\rm a_2,s}^{(1)} + \epsilon_1 \kappa^2 \Gamma_{\rm a_2,s}^{(2)} + \epsilon_2 \kappa^3 \Gamma_{\rm a_2,s}^{(3)} \Big] \Big]; \end{aligned} \tag{4.23}$$

see Table 4.1 for the numerical values of the decay rates. The numerical pattern shows that even though the coupling κ itself is $\mathcal{O}(1)$, ρ' contributions are significantly suppressed, both due to the propagators in Eq. (4.15) and because the ρ' can never be on shell in the available phase space. For the solutions of the global phenomenological analysis in Ch. 6, we find that the interference effects tend to even slightly reduce the branching ratio in the minimal VMD case, while the large values of $(1-\epsilon_1-\epsilon_2)$ in the extended VMD fits can increase $B(f_1 \to \pi^+\pi^-\pi^+\pi^-)$ to the level of 1%, still far below the experimental value.

The reason for this incompatibility can be understood as follows: the available phase space prohibits the two ρ mesons from being simultaneously on shell, and the corresponding

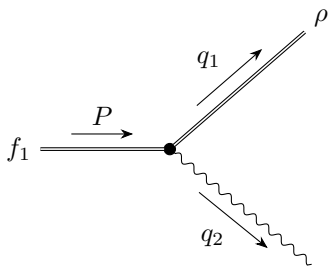

Figure 4.3: FEYNMAN diagram for $f_1 \to \rho\gamma$ consistent with $\mathcal{M}(f_1 \to \gamma^*\gamma^*)$.

loss of resonance enhancement for two intermediate ρ mesons implies that other decay mechanisms become more important. A candidate for such a mechanism is given by the decay $f_1 \to a_1\pi \to \rho\pi\pi \to 4\pi$; see App. D for an estimate of this decay channel. From this analysis, we indeed infer that the intermediate state $a_1\pi$ likely saturates the decay width to a large extent, so that we have to conclude that the decay $f_1 \to 4\pi$ does not allow one to extract further information on the f_1 TFFs. We will thus disregard this input entirely and adopt Eq. (4.7) for the symmetric normalization. With the couplings C_{a_1}, C_{a_2}, and C_{s} all assumed real, we will further fix the global sign by demanding that C_{s} be positive,

$$C_{\mathrm{s}} = 0.93(11). \tag{4.24}$$

4.3 $f_1 \to \rho\gamma$

The construction of the amplitude for $f_1 \to \rho\gamma$ proceeds along the same lines as for $f_1 \to 4\pi$, via $\mathcal{M}(f_1 \to \gamma^*\gamma^*)$, either by using the minimal or the extended VMD parameterization. By definition, this decay channel only probes the isovector contribution, up to negligible isospin-breaking effects.

For the amplitude $\mathcal{M}(f_1 \to \rho\gamma)$, we then proceed as stated above, starting with the minimal VMD ansatz, and consider the ρ meson and photon on shell, $q_1^2 = M_\rho^2$, $q_2^2 = 0$, and $\epsilon^*(q_1)\cdot q_1 = 0 = \epsilon^*(q_2)\cdot q_2$, which also implies $\Gamma_\rho(q_2^2 = 0) = 0 = \Gamma_{\rho'}(q_2^2 = 0)$ according to Eq. (3.11)–Eq. (3.15). The corresponding diagram is depicted in Fig. 4.3, and we find

$$\begin{aligned}\mathcal{M}(f_1 \to \rho\gamma) &= C_{f\rho\gamma}\epsilon_\mu^*(q_1)\epsilon_\nu^*(q_2)\epsilon_\alpha(P)\\ &\quad\times\left[C_{\mathrm{a}_1}\epsilon^{\mu\nu\beta\gamma}q_{1\beta}q_{2\gamma}(q_1^\alpha - q_2^\alpha) + \frac{M_\rho^2}{2}C_{\mathrm{a}_2}\epsilon^{\alpha\mu\nu\beta}q_{2\beta} + \frac{M_\rho^2}{2}C_{\mathrm{s}}\epsilon^{\alpha\mu\nu\beta}q_{2\beta}\right],\end{aligned} \tag{4.25}$$

where we introduced $C_{f\rho\gamma} = eM_\rho^2/(\widetilde{g}_{\rho\gamma}m_{f_1}^2)$. The branching ratio of the decay is given by

$$B(f_1 \to \rho\gamma) = \frac{B_1 C_{\mathrm{a}_1}^2 + B_2\big(C_{\mathrm{a}_2}^2 + C_{\mathrm{s}}^2 + 2C_{\mathrm{a}_2}C_{\mathrm{s}}\big) - B_3\big(C_{\mathrm{a}_1}C_{\mathrm{a}_2} + C_{\mathrm{a}_1}C_{\mathrm{s}}\big)}{\Gamma_f}, \tag{4.26}$$

where—as throughout this part of the thesis—the coupling constants are assumed to be

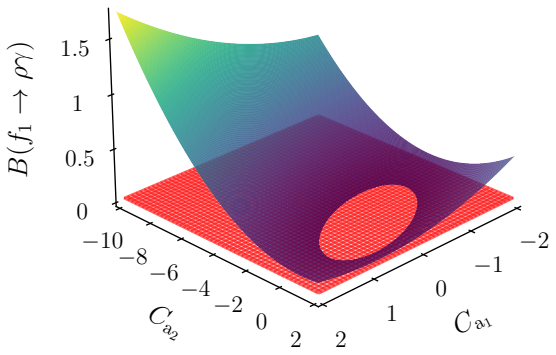

Figure 4.4: Surface plot of $B(f_1 \to \rho\gamma)$ (*blue-yellow textured*), Eq. (4.26), using the central value of $C_\mathrm{s} = 0.93(11)$, Eq. (4.24), together with the central value of $B(f_1 \to \rho\gamma) = 4.2(1.0)\%$ (*red*), see Ch. 6.

purely real and we defined the coefficients

$$B_1 = \frac{\alpha|g_{\rho\gamma}|^2\left(m_{f_1}^2 - M_\rho^2\right)^5}{24m_{f_1}^9}, \qquad B_2 = \frac{\alpha|g_{\rho\gamma}|^2 M_\rho^2\left(m_{f_1}^2 - M_\rho^2\right)^3\left(m_{f_1}^2 + M_\rho^2\right)}{96m_{f_1}^9},$$
$$B_3 = \frac{\alpha|g_{\rho\gamma}|^2 M_\rho^2\left(m_{f_1}^2 - M_\rho^2\right)^4}{24m_{f_1}^9}. \tag{4.27}$$

As depicted in Fig. 4.4, the solution of Eq. (4.26) in terms of the unknown couplings C_{a_1} and C_{a_2} represents an ellipse, where we used the central values of $C_\mathrm{s} = 0.93(11)$ and $B(f_1 \to \rho\gamma) = 4.2(1.0)\%$, see Ch. 6, to illustrate the cut surfaces. Although it is straightforward to actually solve Eq. (4.26) for such an equation, we refrain from doing so here as there exists no unique solution without further input.

The equivalent amplitude in the extended VMD representation reads

$$\widetilde{\mathcal{M}}(f_1 \to \rho\gamma) = C_{f\rho\gamma}\epsilon_\mu^*(q_1)\epsilon_\nu^*(q_2)\epsilon_\alpha(P) \tag{4.28}$$
$$\times \left[C_{\mathrm{a}_1}\epsilon^{\mu\nu\beta\gamma}q_{1\beta}q_{2\gamma}(q_1^\alpha - q_2^\alpha) + \frac{M_\rho^2}{2}C_{\mathrm{a}_2}\epsilon^{\alpha\mu\nu\beta}q_{2\beta} + \frac{M_\rho^2}{2}C_\mathrm{s}\left(1 - \frac{\epsilon_1}{2} - \epsilon_2\right)\epsilon^{\alpha\mu\nu\beta}q_{2\beta}\right],$$

the only difference compared to the minimal VMD parameterization being that $C_\mathrm{s} \to \widetilde{C}_\mathrm{s} = (1 - \epsilon_1/2 - \epsilon_2)C_\mathrm{s}$. Hence, the branching ratio given in Eq. (4.26) becomes

$$\widetilde{B}(f_1 \to \rho\gamma) = \frac{B_1 C_{\mathrm{a}_1}^2 + B_2\left(C_{\mathrm{a}_2}^2 + \widetilde{C}_\mathrm{s}^2 + 2C_{\mathrm{a}_2}\widetilde{C}_\mathrm{s}\right) - B_3\left(C_{\mathrm{a}_1}C_{\mathrm{a}_2} + C_{\mathrm{a}_1}\widetilde{C}_\mathrm{s}\right)}{\Gamma_f}, \tag{4.29}$$

which, when inserting ϵ_1 and ϵ_2 from Sec. 3.4, simplifies to

$$\widetilde{B}(f_1 \to \rho\gamma) = \frac{B_1 C_{\mathrm{a}_1}^2 + \widetilde{B}_2 C_\mathrm{s}^2 - \widetilde{B}_3 C_{\mathrm{a}_1}C_\mathrm{s}}{\Gamma_f}, \tag{4.30}$$

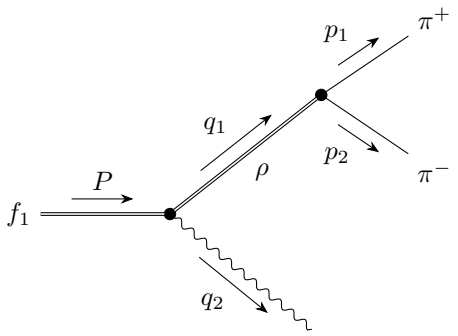

Figure 4.5: FEYNMAN diagram for $f_1 \to \rho\gamma \to \pi^+\pi^-\gamma$ consistent with $\mathcal{M}(f_1 \to \gamma^*\gamma^*)$.

where we defined the coefficients

$$\widetilde{B}_2 = \frac{M_{\rho'}^4}{(M_{\rho'}^2 - M_\rho^2)^2} B_2, \qquad \widetilde{B}_3 = \frac{M_{\rho'}^2}{M_{\rho'}^2 - M_\rho^2} B_3. \tag{4.31}$$

In this variant, the dependence on C_{a_2} thus drops out of the branching fraction, which is a subtle consequence of the correlation between C_{a_2} and C_{s} imposed via the singly-virtual high-energy behavior, see Eq. (3.35).

Another measured quantity of interest with regard to $f_1 \to \rho\gamma$ is the ratio of the ρ-meson's helicity amplitudes in its rest frame, which is accessible through the subsequent decay $\rho \to \pi^+\pi^-$. In a similar manner to how we obtained the $f_1 \to \rho\gamma$ amplitudes in Eq. (4.25) and Eq. (4.28), we can construct an amplitude for $f_1 \to \rho\gamma \to \pi^+\pi^-\gamma$, where we indeed consider the subsequent decay of an on-shell ρ meson and furthermore use the $\rho\pi\pi$ coupling given by Eq. (B.8); the process is depicted in Fig. 4.5.

Imposing $q_1^2 = M_\rho^2$, thus also $\Gamma_\rho(q_1^2 = M_\rho^2) = \Gamma_\rho$ according to Eq. (3.15), $q_2^2 = 0 = \epsilon^*(q_2) \cdot q_2$, and $p_1^2 = M_\pi^2 = p_2^2$, we find

$$\begin{aligned}\mathcal{M}(f_1 \to \rho\gamma \to \pi^+\pi^-\gamma) = \frac{C_{f\rho\gamma} g_{\rho\pi\pi}}{M_\rho \Gamma_\rho} \epsilon_\nu^*(q_2) \epsilon_\alpha(P)(p_2 - p_1)_\mu \\ \times \Big[C_{\mathrm{a}_1} \epsilon^{\mu\nu\beta\gamma} q_{1\beta} q_{2\gamma} (q_1^\alpha - q_2^\alpha) + \frac{M_\rho^2}{2} C_{\mathrm{a}_2} \epsilon^{\alpha\mu\nu\beta} q_{2\beta} + \frac{M_\rho^2}{2} C_{\mathrm{s}} \epsilon^{\alpha\mu\nu\beta} q_{2\beta} \Big]\end{aligned} \tag{4.32}$$

with the minimal VMD parameterization, where the constant $C_{f\rho\gamma} = eM_\rho^2/(\widetilde{g}_{\rho\gamma} m_{f_1}^2)$ is defined as in Eq. (4.25). The equivalent expression $\widetilde{\mathcal{M}}(f_1 \to \rho\gamma \to \pi^+\pi^-\gamma)$ in the extended VMD variant is obtained for $C_{\mathrm{s}} \to \widetilde{C}_{\mathrm{s}} = (1 - \epsilon_1/2 - \epsilon_2) C_{\mathrm{s}}$. Transforming into the rest frame of the ρ meson, one finds the spin-averaged amplitude squared to be of the form

$$\big|\mathcal{M}(f_1 \to \rho\gamma \to \pi^+\pi^-\gamma)\big|^2 = \mathrm{M_{TT}} \sin^2\theta_{\pi^+\gamma} + \mathrm{M_{LL}} \cos^2\theta_{\pi^+\gamma}, \tag{4.33}$$

where $\theta_{\pi^+\gamma}$ is the angle between the final-state π^+ and photon, and

$$r_{\rho\gamma} = \frac{\mathrm{M_{LL}}}{\mathrm{M_{TT}}} = \frac{2 m_{f_1}^2 M_\rho^2}{\big[M_\rho^2 - 2\big(m_{f_1}^2 - M_\rho^2\big) C_{\mathrm{a}_1} / \big(C_{\mathrm{a}_2} + C_{\mathrm{s}}\big)\big]^2} \tag{4.34}$$

is the corresponding ratio of the longitudinal and transversal ρ-meson helicity amplitudes. In the extended VMD case, one again needs to replace $C_{\mathrm{s}} \to \widetilde{C}_{\mathrm{s}} = (1 - \epsilon_1/2 - \epsilon_2) C_{\mathrm{s}}$, which

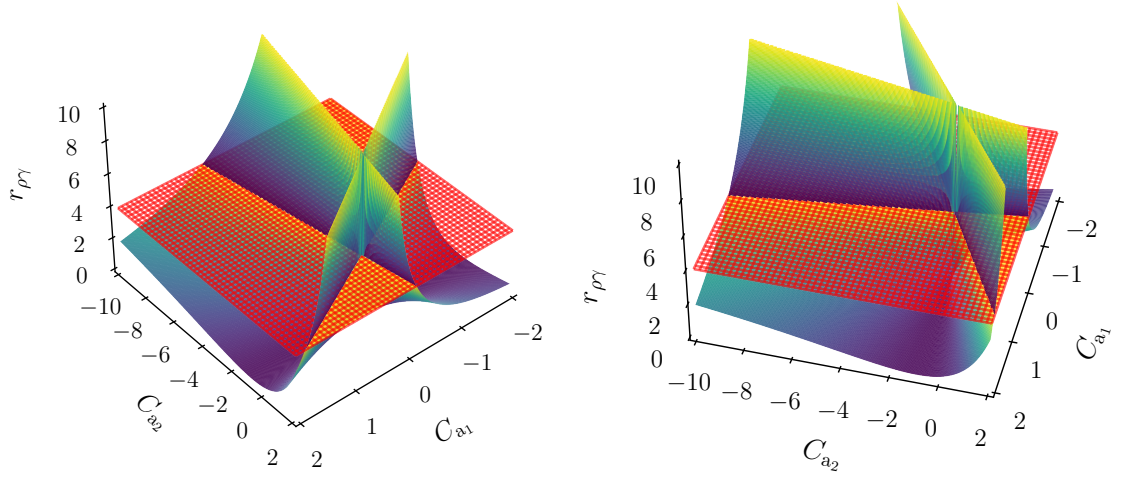

Figure 4.6: Surface plots of $r_{\rho\gamma}$ (*blue-yellow textured*), Eq. (4.34), using the central value of $C_\mathrm{s} = 0.93(11)$, Eq. (4.24), together with the central value of the measurement $r_{\rho\gamma} = 3.9(1.3)$ [100] (*red*) from two different perspectives (*left* and *right*).

then further simplifies to

$$\widetilde{r}_{\rho\gamma} = \frac{\widetilde{\mathrm{M}}_\mathrm{LL}}{\widetilde{\mathrm{M}}_\mathrm{TT}} = \frac{2m_{f_1}^2 M_\rho^2 M_{\rho'}^4}{\left[M_\rho^2 M_{\rho'}^2 - 2\left(m_{f_1}^2 - M_\rho^2\right)\left(M_{\rho'}^2 - M_\rho^2\right)C_{\mathrm{a}_1}/C_\mathrm{s}\right]^2} \tag{4.35}$$

when inserting ϵ_1 and ϵ_2 from Sec. 3.4. The coupling C_{a_2} therefore does not contribute to either $f_1 \to \rho\gamma$ observable in the extended VMD ansatz.

The solution of Eq. (4.34) in terms of the unknown couplings C_{a_1} and C_{a_2} is given by four unconnected straight lines, as apparent from Fig. 4.6, where we used the central values of $C_\mathrm{s} = 0.93(11)$, Eq. (4.24), and the measurement $r_{\rho\gamma} = 3.9(0.9)(1.0) = 3.9(1.3)$ [100] for illustration. Similar to the discussion regarding $B(f_1 \to \rho\gamma)$, we refrain from giving the explicit form of the solution here and postpone the phenomenological analysis to Ch. 6.

4.4 $f_1 \to \phi\gamma$ and $f_1 \to \omega\gamma$

The branching ratio of $f_1 \to \phi\gamma$ has been measured experimentally, $B(f_1 \to \phi\gamma) = 0.74(26) \times 10^{-3}$ [99, 101], and thus allows for another consistency check of our VMD representations, in particular the U(3) assumptions for the isoscalar TFFs. Similarly, we can predict the branching fraction for $f_1 \to \omega\gamma$ once all the parameters are determined, which could be confronted with potential future measurements.

In complete analogy to Sec. 4.3, we construct amplitudes for $f_1 \to V\gamma$, $V = \phi, \omega$, *i.e.*,

$$\begin{aligned}\mathcal{M}(f_1 \to V\gamma) = {} & C_{fV\gamma}\epsilon_\mu^*(q_1)\epsilon_\nu^*(q_2)\epsilon_\alpha(P) \\ & \times \left[C_{\mathrm{a}_1}^{VV'}\epsilon^{\mu\nu\beta\gamma}q_{1\beta}q_{2\gamma}(q_1^\alpha - q_2^\alpha) + \frac{M_V^2}{2}C_{\mathrm{a}_2}^{VV'}\epsilon^{\alpha\mu\nu\beta}q_{2\beta} + \frac{M_V^2}{2}C_\mathrm{s}^{VV}\epsilon^{\alpha\mu\nu\beta}q_{2\beta}\right],\end{aligned} \tag{4.36}$$

where we defined $C_{fV\gamma} = eM_V^2/(\widetilde{g}_{V\gamma} m_{f_1}^2)$. In terms of the ratio $R^V = R^\phi, R^\omega$ of isoscalar to isovector couplings, Eq. (3.27), the branching ratio of the decay is given by

$$B(f_1 \to V\gamma) = (R^V)^2 \frac{B_1^V C_{\mathrm{a}_1}^2 + B_2^V \left(C_{\mathrm{a}_2}^2 + C_{\mathrm{s}}^2 + 2C_{\mathrm{a}_2}C_{\mathrm{s}}\right) - B_3^V \left(C_{\mathrm{a}_1}C_{\mathrm{a}_2} + C_{\mathrm{a}_1}C_{\mathrm{s}}\right)}{\Gamma_f}, \quad (4.37)$$

cf. Eq. (4.26), where we defined the coefficients

$$B_1^V = \frac{\alpha |g_{V\gamma}|^2 \left(m_{f_1}^2 - M_V^2\right)^5}{24 m_{f_1}^9}, \qquad B_2^V = \frac{\alpha |g_{V\gamma}|^2 M_V^2 \left(m_{f_1}^2 - M_V^2\right)^3 \left(m_{f_1}^2 + M_V^2\right)}{96 m_{f_1}^9},$$
$$B_3^V = \frac{\alpha |g_{V\gamma}|^2 M_V^2 \left(m_{f_1}^2 - M_V^2\right)^4}{24 m_{f_1}^9}. \quad (4.38)$$

The generalization to the extended VMD representation would be straightforward once applied to the isoscalar sector.

Chapter 5

$f_1 \to e^+e^-$[†]

As the discussion in Ch. 4 shows, the constraints from $e^+e^- \to e^+e^- f_1$, $f_1 \to 4\pi$, and $f_1 \to \rho\gamma$ do, in general, not suffice to reliably determine all three free VMD parameters, with the branching fraction of $f_1 \to 4\pi$ not providing any additional input at all due to significant contamination from decay channels not related to the TFFs. In this way, the evidence for the decay $f_1 \to e^+e^-$ reported by the SND collaboration [102] is extremely interesting because future improved measurements of the decay have the potential to overconstrain the system of C_{a_1}, C_{a_2}, and C_{s}, as we will demonstrate in Ch. 6. In this chapter, we provide the required formalism to extract information on the f_1 TFFs from its decay into e^+e^-; *cf.* also Ref. [113].

The Feynman diagram for the one-loop process is depicted in Fig. 5.1, and the general form of the amplitude is

$$\mathcal{M}(f_1 \to e^+e^-) = e^4 \epsilon_\mu(P) \bar{u}^s(p_1) \gamma^\mu \gamma^5 A_1\big(m_{f_1}^2, m_e^2 = 0, m_e^2 = 0\big) v^r(p_2), \tag{5.1}$$

which implies

$$\big|\mathcal{M}(f_1 \to e^+e^-)\big|^2 = \frac{4e^8 m_{f_1}^2}{3} |A_1|^2 \tag{5.2}$$

for the spin-averaged amplitude squared and a decay width of

$$\Gamma(f_1 \to e^+e^-) = \frac{64\pi^3\alpha^4 m_{f_1}}{3} |A_1|^2. \tag{5.3}$$

Here and in the following, the arguments of the reduced amplitude A_1 will be suppressed and we will work in the limit $m_e = 0$. To extract A_1 from the full amplitude, we first consider the amplitude $\mathcal{M}(f_1 \to \gamma^*\gamma^*)$ and recast it into the more convenient form

$$\begin{aligned}\mathcal{M}(f_1 \to \gamma^*\gamma^*) = \frac{\mathrm{i}e^2}{m_{f_1}^2} \epsilon^{\mu\nu\beta\gamma} \Big[& \mathcal{F}_{\mathrm{a}_1}(q_1^2, q_2^2) \epsilon_\mu^*(q_1) \epsilon_\nu^*(q_2) \epsilon_\alpha(P) q_{1\beta} q_{2\gamma} (q_1^\alpha - q_2^\alpha) \\ & - \frac{1}{2}\big[\mathcal{F}_{\mathrm{a}_2}(q_1^2, q_2^2) + \mathcal{F}_{\mathrm{s}}(q_1^2, q_2^2)\big] \epsilon_\nu^*(q_2) \epsilon_\mu(P) q_{2\beta} \big[q_{1\gamma} \epsilon_\alpha^*(q_1) q_1^\alpha - \epsilon_\gamma^*(q_1) q_1^2\big] \\ & + \frac{1}{2}\big[\mathcal{F}_{\mathrm{a}_2}(q_1^2, q_2^2) - \mathcal{F}_{\mathrm{s}}(q_1^2, q_2^2)\big] \epsilon_\nu^*(q_1) \epsilon_\mu(P) q_{1\beta} \big[q_{2\gamma} \epsilon_\alpha^*(q_2) q_2^\alpha - \epsilon_\gamma^*(q_2) q_2^2\big] \Big].\end{aligned} \tag{5.4}$$

[†]The generic forms of the amplitude and decay width for $f_1 \to e^+e^-$ stated in this chapter have already been derived in the master's thesis of the author [115]; the explicit expressions and calculations have, however, been thoroughly refined for this thesis, among other things regarding novel contributions not considered in Ref. [115] and an analytic cross-check for the numerical evaluation of the loop integral.

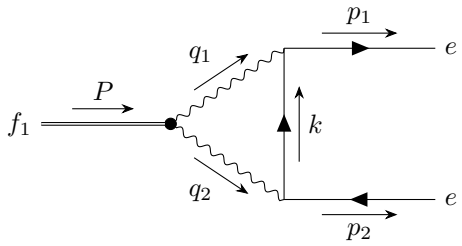

Figure 5.1: FEYNMAN diagram for the decay of the axial-vector meson f_1 into an electron–positron pair.

Inserting this amplitude into the quantum-electrodynamics (QED) loop, the full amplitude can be written as

$$\begin{aligned}\mathcal{M}(f_1 \to e^+e^-) = {}& \frac{4\mathrm{i}e^4}{m_{f_1}^2}\epsilon_\alpha(P)P_\mu\bar{u}^s(p_1)\gamma_\beta\gamma^5 v^r(p_2)\int\frac{\mathrm{d}^4k}{(2\pi)^4}\frac{k^\mu k^\beta k^\alpha}{k^2q_1^2q_2^2}\mathcal{F}_{\mathrm{a}_1}(q_1^2,q_2^2) \\ &+ \frac{\mathrm{i}e^4}{m_{f_1}^2}\epsilon_\beta(P)\bar{u}^s(p_1)\gamma_\mu\gamma^5 v^r(p_2) \\ &\quad\times\int\frac{\mathrm{d}^4k}{(2\pi)^4}\frac{k^\mu k^\beta}{k^2q_1^2q_2^2}\big[(q_2^2-q_1^2)\mathcal{F}_{\mathrm{a}_2}(q_1^2,q_2^2)-(q_2^2+q_1^2)\mathcal{F}_{\mathrm{s}}(q_1^2,q_2^2)\big] \\ &+ \frac{\mathrm{i}e^4}{2m_{f_1}^2}\epsilon_\mu(P)\bar{u}^s(p_1)\gamma^\mu\gamma^5 v^r(p_2) \\ &\quad\times\int\frac{\mathrm{d}^4k}{(2\pi)^4}\frac{\big[2q_1^2q_2^2+k^2(q_1^2+q_2^2)\big]\mathcal{F}_{\mathrm{s}}(q_1^2,q_2^2)+k^2\big(q_1^2-q_2^2\big)\mathcal{F}_{\mathrm{a}_2}(q_1^2,q_2^2)}{k^2q_1^2q_2^2},\end{aligned} \tag{5.5}$$

where we have used the on-shell condition for the fermions, neglected their masses, and written the loop integration in the most symmetric way.[11] In particular, rewriting the TFF combinations as

$$\begin{aligned}(q_2^2-q_1^2)\mathcal{F}_{\mathrm{a}_2}(q_1^2,q_2^2)-(q_2^2+q_1^2)\mathcal{F}_{\mathrm{s}}(q_1^2,q_2^2) &= -2q_1^2\mathcal{F}_2(q_1^2,q_2^2)+2q_2^2\mathcal{F}_3(q_1^2,q_2^2), \\ \big[2q_1^2q_2^2+k^2(q_1^2+q_2^2)\big]\mathcal{F}_{\mathrm{s}}(q_1^2,q_2^2)+k^2\big(q_1^2-q_2^2\big)\mathcal{F}_{\mathrm{a}_2}(q_1^2,q_2^2) &= 2(k^2+q_2^2)q_1^2\mathcal{F}_2(q_1^2,q_2^2) \\ &\quad -2(k^2+q_1^2)q_2^2\mathcal{F}_3(q_1^2,q_2^2)\end{aligned} \tag{5.6}$$

shows that the ill-defined BL limits—see Eq. (2.18) and the subsequent comment—always appear suppressed by the respective on-shell virtuality, as expected from the form of the physical helicity amplitudes. We conclude that these integration regions will therefore be of minor importance. Moreover, all remaining integrals are ultraviolet and infrared convergent by inspection of the parameterization of the form factors in Eq. (3.10) and Eq. (3.20). However, inserting the (isovector) VMD expressions directly into the loop integral would produce unphysical imaginary parts, which can be avoided by using the spectral representations of Eq. (3.16) and Eq. (3.21) instead, ensuring the correct analytic properties.

[11] By the most symmetric way, we refer to a symmetrization over two forms of the initial term [115] $I_{\mathrm{s}} = \int \mathrm{d}^4k\, q_1^{-2}q_2^{-2}[2(p_1\cdot p_2)+2k^2]\mathcal{F}_{\mathrm{s}}(q_1^2,q_2^2)$, namely $I_{\mathrm{s}} = \int \mathrm{d}^4k\, q_1^{-2}q_2^{-2}(m_{f_1}^2+2k^2)\mathcal{F}_{\mathrm{s}}(q_1^2,q_2^2)$ and $I_{\mathrm{s}} = \int \mathrm{d}^4k\, q_1^{-2}q_2^{-2}(m_{f_1}^2+2(p_1-p_2-k)^2)\mathcal{F}_{\mathrm{s}}(q_1^2,q_2^2)$, which are related via a momentum shift $k' = p_1-p_2-k$ in the loop integral and the symmetry property of $\mathcal{F}_{\mathrm{s}}(q_1^2,q_2^2)$.

We performed the remaining Passarino–Veltman (PV) reduction in two ways:

(i) in an automated way using *FeynCalc* [139–141], *FeynHelpers* [142] (which merges *FeynCalc* with *FIRE* [143] and *Package-X* [144]), and *LoopTools* [145];

(ii) directly by introducing Feynman parameters in Eq. (5.5).

Decomposing the amplitude as

$$\begin{aligned}\mathcal{M}(f_1 \to e^+e^-) &= e^4\epsilon_\mu(P)\bar{u}^s(p_1)\gamma^\mu\gamma^5 A_1 v^r(p_2), \\ A_1 &= \big(D_1^{I=1}+D_1^{I=0}\big)C_{\mathrm{a}_1} + \big(D_2^{I=1}+D_2^{I=0}\big)C_{\mathrm{a}_2} + \big(D_3^{I=1}+D_3^{I=0}\big)C_{\mathrm{s}} + D_{\mathrm{asym}},\end{aligned} \tag{5.7}$$

the latter approach, in the minimal VMD ansatz, leads to the representation

$$\begin{aligned}D_{1/2}^{I=1} &= \frac{M_\rho^2 M_{\rho'}^2}{16\pi^4 N_{\mathrm{a}} m_{f_1}^4}\int_{4M_\pi^2}^\infty \mathrm{d}x \int_{s_{\mathrm{thr}}}^\infty \mathrm{d}y \int_0^1 \mathrm{d}z\, \mathrm{Im}\big[P_\rho^{\mathrm{BW}}(x)\big]\,\mathrm{Im}\big[P_{\rho'}^{\mathrm{BW}}(y)\big] f_{1/2}(x,y,z,m_{f_1}), \\ D_3^{I=1} &= \frac{M_\rho^4}{16\pi^4 N_{\mathrm{s}} m_{f_1}^4}\int_{4M_\pi^2}^\infty \mathrm{d}x \int_{4M_\pi^2}^\infty \mathrm{d}y \int_0^1 \mathrm{d}z\, \mathrm{Im}\big[P_\rho^{\mathrm{BW}}(x)\big]\,\mathrm{Im}\big[P_\rho^{\mathrm{BW}}(y)\big] f_3(x,y,z,m_{f_1}),\end{aligned} \tag{5.8}$$

where

$$\begin{aligned}f_1 &= \frac{\bar{x}-\bar{y}}{\bar{x}\bar{y}}\left[\frac{\bar{x}z\log\frac{\Delta(\bar{x},\bar{y},z)}{-\bar{x}z}}{\Delta(\bar{y},z)} - (1-z)\log\Delta(\bar{x},\bar{y},z)\right] \\ &\quad + \frac{z}{\bar{x}\bar{y}}\Big[\bar{x}\log(-\bar{x}z) - \bar{y}\log(-\bar{y}z)\Big] + \frac{(1-z)(1-3z)\log\frac{\Delta(\bar{y},z)}{\Delta(\bar{x},z)}}{2\bar{x}\bar{y}} - (x\leftrightarrow y), \\ f_2 &= \frac{\bar{x}-\bar{y}}{2\bar{x}\bar{y}}\left[\frac{\bar{x}z\log\frac{\Delta(\bar{x},\bar{y},z)}{-\bar{x}z}}{\Delta(\bar{y},z)} + z\log\Delta(\bar{x},\bar{y},z) + \frac{1}{4}\right] - \frac{3z-2}{2\bar{x}\bar{y}}\Big[\bar{x}\log\Delta(\bar{x},z) - \bar{y}\log\Delta(\bar{y},z)\Big] \\ &\quad - \frac{z}{\bar{x}\bar{y}}\Big[\bar{x}\log(-\bar{x}z) - \bar{y}\log(-\bar{y}z)\Big] - \frac{(1-z)(1-3z)\log\frac{\Delta(\bar{y},z)}{\Delta(\bar{x},z)}}{2\bar{x}\bar{y}} - (x\leftrightarrow y), \\ f_3 &= -\frac{2z-1}{2\bar{x}\bar{y}\Delta(\bar{y},z)^3} \\ &\quad \times\left[2z^3\bar{x}^2\log\frac{\Delta(\bar{x},\bar{y},z)}{-\bar{x}z} + (1-z)\bar{y}\Delta(\bar{y},z)\Big[2\bar{x}z + \Delta(\bar{y},z)\Big(1-3z+2(\bar{x}+\bar{y})\Big)\Big]\right] \\ &\quad + \frac{z(4z-2+\bar{x}(22z-5))}{4\bar{x}\bar{y}\Delta(\bar{y},z)^2}\Big[\bar{x}z\log\frac{\Delta(\bar{x},\bar{y},z)}{-\bar{x}z} + (1-z)\Delta(\bar{y},z)\Big] - \frac{z^2(5+9\bar{x})}{2\bar{y}}\frac{\log\frac{\Delta(\bar{x},\bar{y},z)}{-\bar{x}z}}{\Delta(\bar{y},z)} \\ &\quad + \frac{(1-z)\Big[5(8z^2-7z+1)+18(2\bar{x}z+\bar{y}(1-z))\Big]\log\Delta(\bar{x},\bar{y},z)}{4\bar{x}\bar{y}} + \frac{\bar{x}^2-1}{4\bar{y}}\log\frac{1-\bar{x}}{-\bar{x}} \\ &\quad + \frac{\bar{y}^2-1}{4\bar{x}}\log\frac{1-\bar{y}}{-\bar{y}} - \frac{3}{2\bar{y}}\log(-\bar{x}) - \frac{3}{2\bar{x}}\log(-\bar{y}) + \frac{7+19(\bar{x}+\bar{y})+6(\bar{x}^2+\bar{y}^2)}{24\bar{x}\bar{y}},\end{aligned} \tag{5.9}$$

with

$$\Delta(x,y,z) = z(1-z) - zx - (1-z)y, \quad \Delta(x,z) = z - x, \quad \bar{x} = \frac{x}{m_{f_1}^2}, \quad \bar{y} = \frac{y}{m_{f_1}^2}, \tag{5.10}$$

and the correct analytic continuation is specified by $x \to x - \mathrm{i}\epsilon$, $y \to y - \mathrm{i}\epsilon$ in the logarithms. Similar expressions apply for the isoscalar parts and the extended VMD parameterization, the latter including the asymptotic contribution

$$\begin{aligned}
D_{\text{asym}} &= \frac{3F_{f_1}^{\text{eff}}}{8\pi^2 m_{f_1}^3} \int_{s_\text{m}}^\infty \mathrm{d}x \int_0^1 \mathrm{d}z\, f_{\text{asym}}(x,z,m_{f_1}), \\
f_{\text{asym}} &= \frac{z^4(1-z)^2}{2\bar{x}(\bar{x}-z)^4(z(1-z)-\bar{x})^2}\Big[(2-z)z^2\big(8-23z+27z^2-14z^3\big) \\
&\qquad - \bar{x}z\big(32-100z+131z^2-76z^3+14z^4\big) + \bar{x}^2\big(16-46z+51z^2-18z^3\big)\Big] \\
&\quad + \frac{z(1-z)}{2\bar{x}(\bar{x}-z)^3}\Big[z^2\big(17-37z+37z^2-14z^3\big) + \bar{x}\big(2+11z-17z^2+10z^3\big) - 3\bar{x}^2(2z+1)\Big] \\
&\quad - \frac{z^2(z(z+2)+2\bar{x}(5-2z)-9\bar{x}^2)}{2(\bar{x}-z)^4}\log\frac{z(1-z)-\bar{x}}{-\bar{x}z}.
\end{aligned} \tag{5.11}$$

In all cases, the numerical integration is performed with the *Cuhre* algorithm from the *Cuba* library [138].

For the numerical analysis, we further write the coefficients in Eq. (5.7) according to

$$\begin{aligned}
D_i &= D_i^{I=1} + D_i^{I=0}, \quad i=1,2,3, & D_{\text{asym}} &= \frac{F_{f_1}^{\text{eff}} m_{f_1}^3}{M_\rho^4}\bar{D}_{\text{asym}}, \\
D_i^{I=1} &= \frac{D_i^{\rho\rho'}}{N_\text{a}}, \quad D_i^{I=0} = 0, \quad i=1,2, & D_3^{I=0} &= R^\omega D_3^{\omega\omega} + R^\phi D_3^{\phi\phi}, \\
D_3^{I=1}\big|_{\widetilde{\text{VMD}}} &= \frac{D_3^{\rho\rho}(1-\epsilon_1-\epsilon_2) + D_3^{\rho\rho'}\epsilon_1 + D_3^{\rho'\rho'}\epsilon_2}{\widetilde{N}_\text{s}}, & D_3^{I=1}\big|_{\text{VMD}} &= \frac{D_3^{\rho\rho}}{N_\text{s}},
\end{aligned} \tag{5.12}$$

where the prefactor for D_{asym} is motivated from Eq. (3.32) to ensure that the resulting dimensionless coefficients can be compared in a meaningful way. Our numerical results are shown in Table 5.1, including the uncertainties from the variation in $\Gamma_{\rho'}$. Even after taking the change in the normalizations into account, see Table 3.1, these results show that the uncertainties due to the spectral shape and the width itself can lead to comparable effects.

To be able to better compare the various contributions, we also show the coefficients including their normalizations, see Table 5.2, where we used the value of Eq. (3.33) for the asymptotic contribution. These numbers show that the symmetric contribution still produces the largest coefficient, but not by much. Accordingly, the $f_1 \to e^+e^-$ decay proves sensitive to the antisymmetric TFFs, about which not much is known at present. For the extended VMD ansatz, this observation implies an important caveat regarding the numbers shown in the table, which have been produced under the assumption that $C_{\text{a}_2} = 0$. In this case, one observes distinct differences between the two VMD versions, which can be traced back to the different weight given to the $\rho\rho'$ contribution. Finally, the real part of the isoscalar coefficient comes out larger than expected from Eq. (3.9); this is due to the fact that the loop integral is effectively regularized by the vector-meson mass, and the masses of ω and ϕ differ by a sufficient amount that the cancellation in Eq. (3.28) between the two contributions becomes less effective. The imaginary part of the loop integral is finite also in the infinite-mass limit, so that its size complies better with the expected isoscalar suppression.

	$\Gamma_{\rho'}^{(4\pi)}(q^2)$	$\Gamma_{\rho'}^{(\omega\pi,\pi\pi)}(q^2)$
$D_1^{\rho\rho'} \times 10^3$	$(-0.126)^{+0.026}_{-0.031} + (-1.501)^{+0.099}_{-0.121}\,\mathrm{i}$	$(-0.173)^{+0.030}_{-0.034} + (-1.659)^{+0.107}_{-0.126}\,\mathrm{i}$
$D_2^{\rho\rho'} \times 10^3$	$(-0.978)^{+0.030}_{-0.038} + 1.593^{-0.119}_{+0.144}\,\mathrm{i}$	$(-1.032)^{+0.030}_{-0.036} + 1.755^{-0.129}_{+0.150}\,\mathrm{i}$
$D_3^{\rho\rho} \times 10^3$	$3.189 + 2.338\,\mathrm{i}$	
$D_3^{\rho\rho'} \times 10^3$	$4.66^{-0.30}_{+0.37} + 0.88^{-0.05}_{+0.06}\mathrm{i}$	$5.26^{-0.33}_{+0.39} + 0.99^{-0.05}_{+0.06}\,\mathrm{i}$
$D_3^{\rho'\rho'} \times 10^3$	$6.78^{-0.90}_{+1.19} + 0.06^{+0.00}_{-0.00}\,\mathrm{i}$	$8.85^{-1.14}_{+1.45} + 0.09^{+0.01}_{-0.01}\,\mathrm{i}$
$D_3^{\omega\omega} \times 10^3$	$3.835 + 3.193\,\mathrm{i}$	
$D_3^{\phi\phi} \times 10^3$	$8.736 + 3.775\,\mathrm{i}$	
$\bar{D}_{\mathrm{asym}} \times 10^3$	0.146 0.038 0.019 0.011	

Table 5.1: Numerical results for the constants defined in Eq. (5.12) for the two ρ' spectral functions $\Gamma_{\rho'}(q^2) = \Gamma_{\rho'}^{(4\pi)}(q^2)$, Eq. (3.12), and $\Gamma_{\rho'}(q^2) = \Gamma_{\rho'}^{(\omega\pi,\pi\pi)}(q^2)$, Eq. (3.13). The uncertainties refer to the variation $\Gamma_{\rho'} = (400 \pm 60)\,\mathrm{MeV}$, see App. E, which gives the dominant parametric effect. The constant $\bar{D}_{\mathrm{asym}}$ is given for the reference points $\sqrt{s_{\mathrm{m}}} = 1.0\,\mathrm{GeV}, 1.3\,\mathrm{GeV}, 1.5\,\mathrm{GeV}, 1.7\,\mathrm{GeV}$.

Since the coupling constants are real, we use the decay width from Eq. (5.3) to obtain a branching ratio of

$$B(f_1 \to e^+e^-) = \frac{E_1 C_{\mathrm{a}_1}^2 + E_2 C_{\mathrm{a}_2}^2 + E_3 C_{\mathrm{s}}^2 + E_{1,2} C_{\mathrm{a}_1} C_{\mathrm{a}_2} + E_{1,3} C_{\mathrm{a}_1} C_{\mathrm{s}} + E_{2,3} C_{\mathrm{a}_2} C_{\mathrm{s}}}{\Gamma_f} + \frac{E_{1,\mathrm{asym}} C_{\mathrm{a}_1} + E_{2,\mathrm{asym}} C_{\mathrm{a}_2} + E_{3,\mathrm{asym}} C_{\mathrm{s}} + E_{\mathrm{asym}}}{\Gamma_f}, \tag{5.13}$$

where we defined

$$\begin{aligned} E_i &= \frac{64\pi^3\alpha^4 m_{f_1}}{3}|D_i|^2, \quad i = 1,2,3, \\ E_{i,j} &= \frac{128\pi^3\alpha^4 m_{f_1}}{3}\mathrm{Re}\,[D_i D_j^*], \quad (i,j) = (1,2),(1,3),(2,3), \\ E_{i,\mathrm{asym}} &= \frac{128\pi^3\alpha^4 m_{f_1}}{3}\mathrm{Re}\,[D_i D_{\mathrm{asym}}], \quad i = 1,2,3, \qquad E_{\mathrm{asym}} = \frac{64\pi^3\alpha^4 m_{f_1}}{3}|D_{\mathrm{asym}}|^2, \end{aligned} \tag{5.14}$$

and the terms involving D_{asym} are only included in the extended VMD representation.

Similarly to Eq. (4.26), the solution of Eq. (5.13) in terms of the unknown couplings C_{a_1} and C_{a_2} represents an ellipse in the minimal VMD case, which, however, changes for the extended VMD representation, see Fig. 5.2. Here, we used the central value of $C_{\mathrm{s}} = 0.93(11)$, Eq. (4.24), to remove one unknown and set $\sqrt{s_{\mathrm{m}}} = 1.3\,\mathrm{GeV}$ for the asymptotic contribution [26, 27]. In fact, the results in Table 5.1 and Table 5.2 show that D_{asym} remains small for a wide range of matching scales s_{m}, so that the details of the matching play a minor role in view of the present experimental uncertainties. For definiteness, we will continue to use $\sqrt{s_{\mathrm{m}}} = 1.3\,\mathrm{GeV}$ in the following, with the understanding that the matching can be refined once improved data becomes available, along the lines described in App. A.

	$\Gamma^{(4\pi)}_{\rho'}(q^2)$	$\Gamma^{(\omega\pi,\pi\pi)}_{\rho'}(q^2)$
$D_1^{I=1} \times 10^3$	$(-0.218)^{+0.033}_{-0.034} + (-2.601)^{+0.007}_{-0.007}\,\mathrm{i}$	$(-0.269)^{+0.032}_{-0.032} + (-2.583)^{+0.011}_{-0.010}\,\mathrm{i}$
$D_2^{I=1} \times 10^3$	$(-1.695)^{-0.060}_{+0.062} + 2.760^{-0.033}_{+0.031}\,\mathrm{i}$	$(-1.606)^{-0.053}_{+0.054} + 2.732^{-0.038}_{+0.036}\,\mathrm{i}$
$D_3^{I=1}\big\vert_{\mathrm{VMD}} \times 10^3$	$3.961 + 2.904\,\mathrm{i}$	
$D_3^{I=1}\big\vert_{\widetilde{\mathrm{VMD}}} \times 10^3$	$2.163^{+0.121}_{-0.148} + 3.592^{-0.061}_{+0.077}\,\mathrm{i}$	$1.930^{+0.128}_{-0.147} + 3.685^{-0.070}_{+0.085}\,\mathrm{i}$
$D_3^{I=0} \times 10^3$	$-0.95(30) - 0.24(13)\,\mathrm{i}$	
$D_{\mathrm{asym}} \times 10^3$	$0.125(12)$ $0.032(3)$	$0.017(2)$ $0.009(1)$

Table 5.2: Coefficients from Eq. (5.12), based on Table 5.1 and the normalizations from Table 3.1. For the extended VMD version, the result in general depends on $\epsilon_{1/2}$; here, we show the special case for $C_{\mathrm{a}_2} = 0$. For $D_3^{I=0}$ and D_{asym}, the error is propagated from Eq. (3.27) and Eq. (3.33), respectively.

In order to solve for all couplings, we need to consider a combined analysis of all constraints, see Ch. 6. However, given that the biggest contribution tends to come from the symmetric term, see Table 5.1, it is instructive to study the case $C_{\mathrm{a}_1} = 0 = C_{\mathrm{a}_2}$ and consider the $f_1 \to e^+e^-$ decay as an independent determination of C_{s}. For the minimal VMD ansatz, we find

$$C_{\mathrm{s}} = 1.7^{+0.6}_{-0.5}, \tag{5.15}$$

where the isoscalar contribution implies an increase by about 0.3(1). The extended variant gives[12]

$$C_{\mathrm{s}} = 1.9^{+0.8}_{-0.6}, \tag{5.16}$$

where the uncertainties from the dependence on the ρ' spectral function, its width, and the asymptotic contribution, $\Delta C_{\mathrm{s}} \lesssim 0.03$, are negligible compared to both the experimental error and the uncertainty from the isoscalar contribution. Both values are larger than the L3 result given in Eq. (4.24), indicating that a significant contribution from the antisymmetric TFFs should indeed be expected, which in view of the results from Table 5.2 is well possible with plausible values of $C_{\mathrm{a}_{1/2}}$. Finally, the difference between Eq. (5.15) and Eq. (5.16) gives a first estimate of the sensitivity to the chosen VMD ansatz.

[12] Due to the interference with the asymptotic contribution, there are, in principle, two solutions, which, however, are very close in magnitude.

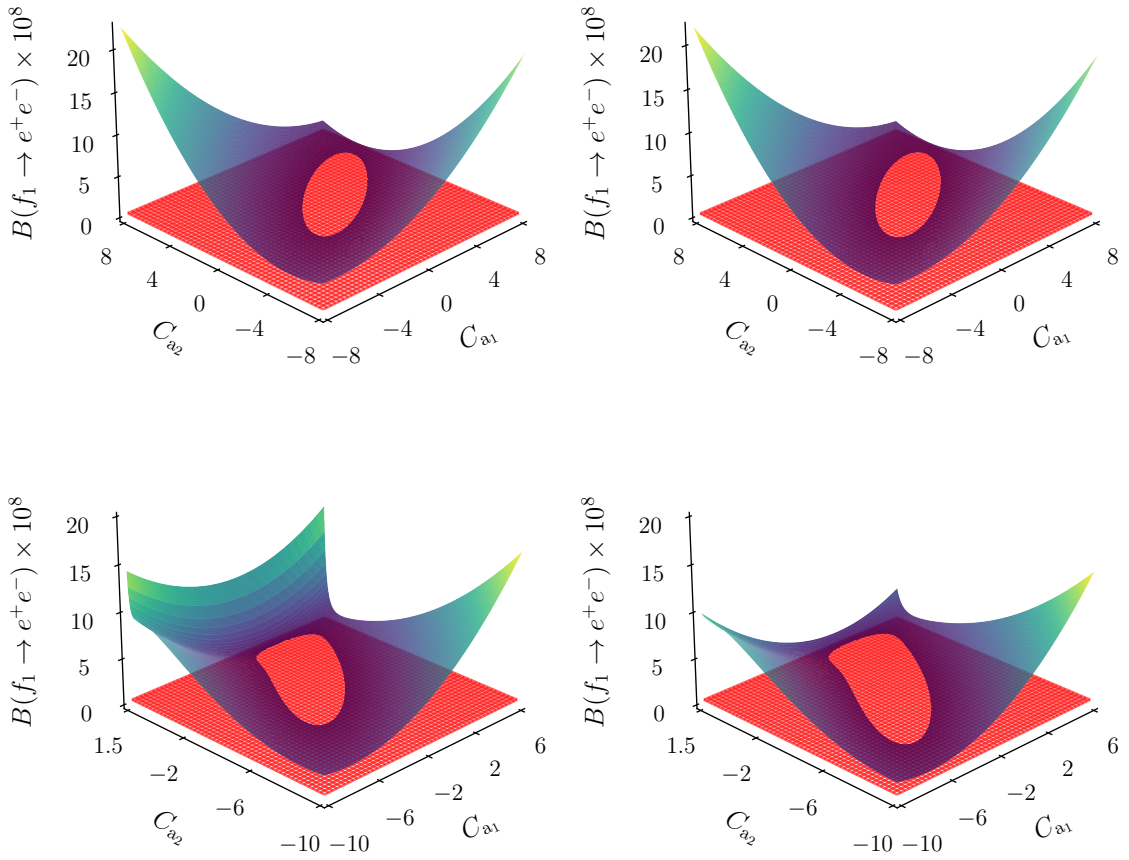

Figure 5.2: Surface plots of $B(f_1 \to e^+e^-)$ (*blue-yellow textured*), Eq. (5.13), as obtained with the minimal (*top*) and extended (*bottom*) VMD parameterization (reference point $\sqrt{s_\mathrm{m}} = 1.3\,\mathrm{GeV}$ for the latter) and using the central value of $C_\mathrm{s} = 0.93(11)$, Eq. (4.24), $\Gamma_{\rho'}(q^2) = \Gamma_{\rho'}^{(4\pi)}(q^2)$ (*left*), Eq. (3.12), and $\Gamma_{\rho'}(q^2) = \Gamma_{\rho'}^{(\omega\pi,\pi\pi)}(q^2)$ (*right*), Eq. (3.13), together with the central value of the measurement $B(f_1 \to e^+e^-) = 5.1^{+3.7}_{-2.7} \times 10^{-9}$ [102] (*red*).

Chapter 6

Combined phenomenological analysis

In this chapter, we perform a global analysis of the experimental constraints from $e^+e^- \to e^+e^- f_1$, $f_1 \to \rho\gamma$, and $f_1 \to e^+e^-$. We will also consider $f_1 \to \phi\gamma$ due to its relation via U(3) symmetry but not include $f_1 \to 4\pi$ for the reasons stated in Sec. 4.2 and App. D. Most of the input quantities follow in a straightforward way from the experimental references and the compilation in Ref. [99], see Table 6.1, except for the branching fraction of the $\rho\gamma$ channel, for which the fit by the Particle Data Group (PDG) and the direct measurement by VES [100] disagree by 2.5σ.

The PDG fit proceeds in terms of the five branching fractions for $f_1 \to 4\pi$, $a_0(980)\pi$ (excluding $a_0(980) \to K\bar{K}$), $\eta\pi\pi$ (excluding $a_0(980)\pi$), $K\bar{K}\pi$, and $\rho\gamma$, including data on

1. $\Gamma(f_1 \to K\bar{K}\pi)/\Gamma(f_1 \to 4\pi)$ [146–148],
2. $\Gamma(f_1 \to 4\pi)/\Gamma(f_1 \to \eta\pi\pi)$ [149, 150],
3. $\Gamma(f_1 \to \rho\gamma)/\Gamma(f_1 \to 4\pi)$ [151],
4. $\Gamma(f_1 \to a_0(980)\pi\,[\text{excluding } K\bar{K}\pi])/\Gamma(f_1 \to \eta\pi\pi)$ [149, 152, 153],
5. $\Gamma(f_1 \to K\bar{K}\pi)/\Gamma(f_1 \to \eta\pi\pi)$ [149, 152–156],
6. $\Gamma(f_1 \to \eta\pi\pi)/\Gamma(f_1 \to \rho\gamma)$ [153, 154, 157],

however, with the notable exception of the constraint from Ref. [100].[13] This fit has a reduced $\chi^2/\text{dof} = 24.0/14 = 1.71$, reflecting the significant tensions in the data base. These tensions become aggravated when including Ref. [100] in the fit, leading to a slightly smaller $\rho\gamma$ branching fraction of 5.3%, with $\chi^2/\text{dof} = 33.5/15 = 2.23$. The origin of the tensions can be traced back to the input for $\Gamma(f_1 \to \eta\pi\pi)/\Gamma(f_1 \to \rho\gamma)$, which is measured as 21.3(4.4) [153], 10(1)(2) [154], and 7.5(1.0) [157],[14] with some additional sensitivity to the $\rho\gamma$ channel from $\Gamma(f_1 \to \rho\gamma)/\Gamma(f_1 \to 4\pi)$ [151].

[13] Reference [100] only quotes the final $\rho\gamma$ branching fraction but not $\Gamma(f_1 \to \eta\pi\pi)/\Gamma(f_1 \to \rho\gamma)$, as measured in the experiment; however, the $\eta\pi\pi$ branching fraction from Ref. [158] is very close to the one from Ref. [99], rendering the systematic error from the conversion negligible.

[14] The latter value is given as 5.0(7) in Ref. [157] for $\eta\pi^+\pi^-$ and has thus been increased by the isospin factor 3/2 in the PDG listing. There is also a limit $B(f_1 \to \rho\gamma) < 5\%$ at 95% confidence level from Ref. [159], in tension with Refs. [154, 157].

Reference	$B(f_1 \to \rho\gamma)$	$r_{\rho\gamma}$	$B(f_1 \to \phi\gamma)$	$B(f_1 \to e^+e^-)$
VES [100]	2.8(9)%	3.9(1.3)		
PDG [99]	6.1(1.0)%			
Our fit	4.2(1.0)%			
Serpukhov [99, 101]			$0.74(26) \times 10^{-3}$	
SND [102]				$(5.1^{+3.7}_{-2.7}) \times 10^{-9}$

Table 6.1: Summary of the experimental measurements used in our global analysis. In addition, we use the L3 data for $e^+e^- \to e^+e^- f_1$, see Sec. 4.1.

The main reason why the fit prefers the $\rho\gamma$ branching fraction from Refs. [154, 157] is that the χ^2 minimization is set up in terms of $\Gamma(f_1 \to \eta\pi\pi)/\Gamma(f_1 \to \rho\gamma)$ rather than the inverse quantity, as would be canonical given that $\Gamma(f_1 \to \rho\gamma)$ is the smallest of the fit components and could thus be treated perturbatively. Using $\Gamma(f_1 \to \rho\gamma)/\Gamma(f_1 \to \eta\pi\pi)$ in the minimization instead gives a similar $\chi^2/\text{dof} = 24.9/14 = 1.78$ but reduces the $\rho\gamma$ branching fraction to 4.9(9)% (including the scale factor from Ref. [99]), close to the naive average of Refs. [151, 153, 154, 157] when taking the respective normalization channel from the fit. Including, in addition, the measurement from Ref. [100], we find $\chi^2/\text{dof} = 28.6/15 = 1.91$ and

$$\begin{aligned}
B(f_1 \to 4\pi) &= 33.4(1.8)\% && [32.7(1.9)\%],\\
B(f_1 \to a_0(980)\pi\,[\text{excluding}\, a_0(980) \to K\bar{K}]) &= 38.6(4.2)\% && [38.0(4.0)\%],\\
B(f_1 \to \eta\pi\pi\,[\text{excluding}\, a_0(980)\pi]) &= 14.6(4.1)\% && [14.0(4.0)\%],\\
B(f_1 \to K\bar{K}\pi) &= 9.2(4)\% && [9.0(4)\%],\\
B(f_1 \to \rho\gamma) &= 4.3(8)\% && [6.1(1.0)\%],
\end{aligned} \tag{6.1}$$

where the results of the PDG fit are indicated in brackets (for better comparison, the same channel-specific scale factors have been applied as in Ref. [99]). Finally, the limit from Ref. [159] tends to further reduce the average a little, which, together with a slightly increased scale factor when including Refs. [100, 159], leads us to quote

$$B(f_1 \to \rho\gamma) = 4.2(1.0)\% \tag{6.2}$$

as our final average for the subsequent analysis, see Table 6.1. While our main argument in favor of this procedure is the avoidance of a fit bias towards the larger $\rho\gamma$ branching fractions, one may also compare with theoretical expectations. The models considered in Refs. [153, 160–163] do, in general, prefer smaller $\rho\gamma$ branching fractions, but the spread among the models is too large to make that comparison conclusive.

The results of the global analysis are shown in Table 6.2 and Table 6.3, restricted to the parameterization $\Gamma_{\rho'}^{(\omega\pi,\pi\pi)}(y)$ due to the dominant experimental uncertainties. The latter are propagated as given in Table 6.1, except for $B(f_1 \to \phi\gamma)$, for which we use $B(f_1 \to \phi\gamma)/(R^\phi)^2 = 3.0(1.6)\%$ in the minimization, including the uncertainty on R^ϕ from Eq. (3.27). As a side result, Table 6.2 and Table 6.3 also contain predictions for the branching fraction of the yet unmeasured decay $f_1 \to \omega\gamma$. The outcome in the four

$f_1 \to \phi\gamma$	No		Yes	
	Solution 1	Solution 2	Solution 1	Solution 2
χ^2/dof	$2.72/2 = 1.36$	$6.60/2 = 3.30$	$8.67/3 = 2.89$	$8.28/3 = 2.76$
p-value	0.26	0.04	0.03	0.04
C_{s}	0.97(13)	1.01(18)	0.95(18)	0.99(17)
C_{a_1}	−0.23(13)	0.91(21)	−0.09(14)	0.80(17)
C_{a_2}	0.51(21)	0.53(39)	0.17(25)	0.34(30)
ρ_{sa_1}	0.43	0.41	0.21	0.31
ρ_{sa_2}	−0.42	−0.13	−0.50	−0.37
$\rho_{\mathrm{a}_1\mathrm{a}_2}$	−0.44	0.77	−0.29	0.66
$B(f_1 \to e^+e^-) \times 10^9$	2.7(6)	0.7(3)	1.8(6)	0.7(3)
$B(f_1 \to \phi\gamma) \times 10^3$	2.5(1.3)	1.5(1.1)	1.3(8)	1.1(7)
$B(f_1 \to \omega\gamma) \times 10^3$	5.6(1.7)	4.4(2.2)	2.7(1.3)	3.3(1.4)

Table 6.2: Best-fit results for the three VMD couplings C_{s}, C_{a_1}, and C_{a_2} in the minimal VMD representation. Each fit includes the constraints from the normalization and slope of the TFF measured by L3 in $e^+e^- \to e^+e^- f_1$ as well as from $B(f_1 \to \rho\gamma)$, $r_{\rho\gamma}$, and $B(f_1 \to e^+e^-)$. In addition, we show the variants including $B(f_1 \to \phi\gamma)$ as a sixth constraint, assuming U(3) symmetry. The uncertainties include the scale factor $S = \sqrt{\chi^2/\mathrm{dof}}$. We also show the correlations ρ_{ij} among the three couplings and the value of $B(f_1 \to e^+e^-)$ preferred by each fit. Since the experimental uncertainties dominate by far in the case of $B(f_1 \to e^+e^-)$, we only show the results for $\Gamma_{\rho'}^{(\omega\pi,\pi\pi)}(y)$ and $\sqrt{s_{\mathrm{m}}} = 1.3\,\mathrm{GeV}$ and do not include the theory uncertainties discussed in detail in Ch. 5. The uncertainties quoted for $B(f_1 \to V\gamma)$ refer to the fit errors and R^V but do not include any U(3) uncertainties.

cases considered—minimal and extended VMD representations, each with and without the constraint from $B(f_1 \to \phi\gamma)$—is illustrated in Fig. 6.1 and Fig. 6.2. In all cases, the parameter C_{s} is by far best constrained; its value hardly changes compared to the L3 reference point given in Eq. (4.24), with a slight preference for a small upward shift. The main distinctions concern the couplings C_{a_1} and C_{a_2}, with qualitative differences between the two VMD scenarios. In each case, we find two sets of solutions, corresponding to a small negative value of C_{a_1} (Solution 1) or a sizable positive one (Solution 2), respectively, both of which are shown in the tables and figures. In most cases, Solution 1 is strongly preferred, the exception being the minimal VMD fit including $B(f_1 \to \phi\gamma)$, in which Solution 2 displays a slightly better fit quality.

In the minimal VMD representation, all constraints are sensitive to C_{a_2}, but especially once including $B(f_1 \to \phi\gamma)$, a significant tension among the different bands emerges. In Solution 2, the region preferred by all constraints but $B(f_1 \to e^+e^-)$, which thus dominate the fit, would imply a much smaller value of $B(f_1 \to e^+e^-)$ than reported by SND [102], while Solution 1 is better in line with the SND result. An improved measurement of $B(f_1 \to e^+e^-)$ could therefore differentiate between these scenarios. In addition, we

$f_1 \to \phi\gamma$	No		Yes	
	Solution 1	Solution 2	Solution 1	Solution 2
χ^2/dof	$2.25/2 = 1.12$	$4.40/2 = 2.20$	$4.01/3 = 1.34$	$7.53/3 = 2.51$
p-value	0.33	0.11	0.26	0.06
C_{s}	1.00(10)	1.02(14)	1.00(11)	1.02(15)
C_{a_1}	−0.18(12)	0.85(14)	−0.19(12)	0.85(15)
C_{a_2}	1.03(36)	1.17(32)	−0.20(29)	0.13(47)
ρ_{sa_1}	0.10	0.86	0.10	0.86
ρ_{sa_2}	0.00	0.21	−0.34	−0.32
$\rho_{\mathrm{a}_1\mathrm{a}_2}$	0.08	0.19	0.18	−0.27
ϵ_1	2.59(1.33)	3.00(1.15)	−1.79(1.01)	−0.64(1.65)
$B(f_1 \to e^+e^-) \times 10^9$	5.1(3.3)	5.1(4.7)	1.5(4)	0.3(4)
$B(f_1 \to \phi\gamma) \times 10^3$	4.4(2.4)	3.4(2.0)	0.8(6)	0.8(7)
$B(f_1 \to \omega\gamma) \times 10^3$	9.1(3.1)	6.8(2.2)	1.9(1.0)	3.3(1.1)

Table 6.3: The same as Table 6.2 but for the extended VMD case, including the resulting parameter ϵ_1.

compare the resulting relevant form factor combination to the L3 dipole fit—see Sec. 4.1—in Fig. 6.3. While some tension is expected due to the singly-virtual asymptotic behavior of $\mathcal{F}_{\mathrm{a}_1}(q_1^2, q_2^2)$, see Table 3.2, the resulting curves for Solution 2 start to depart from the L3 band already around $\sqrt{Q^2} = 0.5\,\mathrm{GeV}$, which further disfavors this set of solutions.

In the extended VMD representation, the dependence on C_{a_2} disappears in all observables apart from $B(f_1 \to e^+e^-)$ and, where applicable, $B(f_1 \to \phi\gamma)$. Accordingly, in the fit without the latter, the value of C_{a_2} is solely determined by $B(f_1 \to e^+e^-)$, and the best-fit value of this branching fraction thus coincides with the input. There is good consistency among the other constraints, as reflected by a reduced χ^2 around unity; in this case, an improved measurement of $B(f_1 \to e^+e^-)$ could thus be interpreted as a determination of C_{a_2}. Once $B(f_1 \to \phi\gamma)$ is included, one obtains an additional constraint on C_{a_2}, which, however, needs to be treated with care. First, the uncertainties on R^ϕ have been included in the fit, but in addition, there are U(3) uncertainties that are difficult to quantify. Moreover, the isoscalar contributions have been treated in their minimal variant throughout, but if excited ω' and ϕ' states were included, the dependence on C_{a_2} would again change, even disappear in a scenario similar to the extended VMD representation constructed for the isovector contributions. Since the fit including $B(f_1 \to \phi\gamma)$ favors a value of $B(f_1 \to e^+e^-)$ smaller than SND (for Solution 1 similar in size to the ones for Solution 1 in the minimal VMD case), an improved measurement of $B(f_1 \to e^+e^-)$ would also allow one to differentiate between these scenarios. In addition to the worse χ^2, Solution 2 is again disfavored by the comparison to L3, see Fig. 6.3.

In contrast, for Solution 1 of both the minimal and the extended VMD fit, departures from the L3 dipole only arise around $\sqrt{Q^2} = 1\,\mathrm{GeV}$, which implies agreement with all data

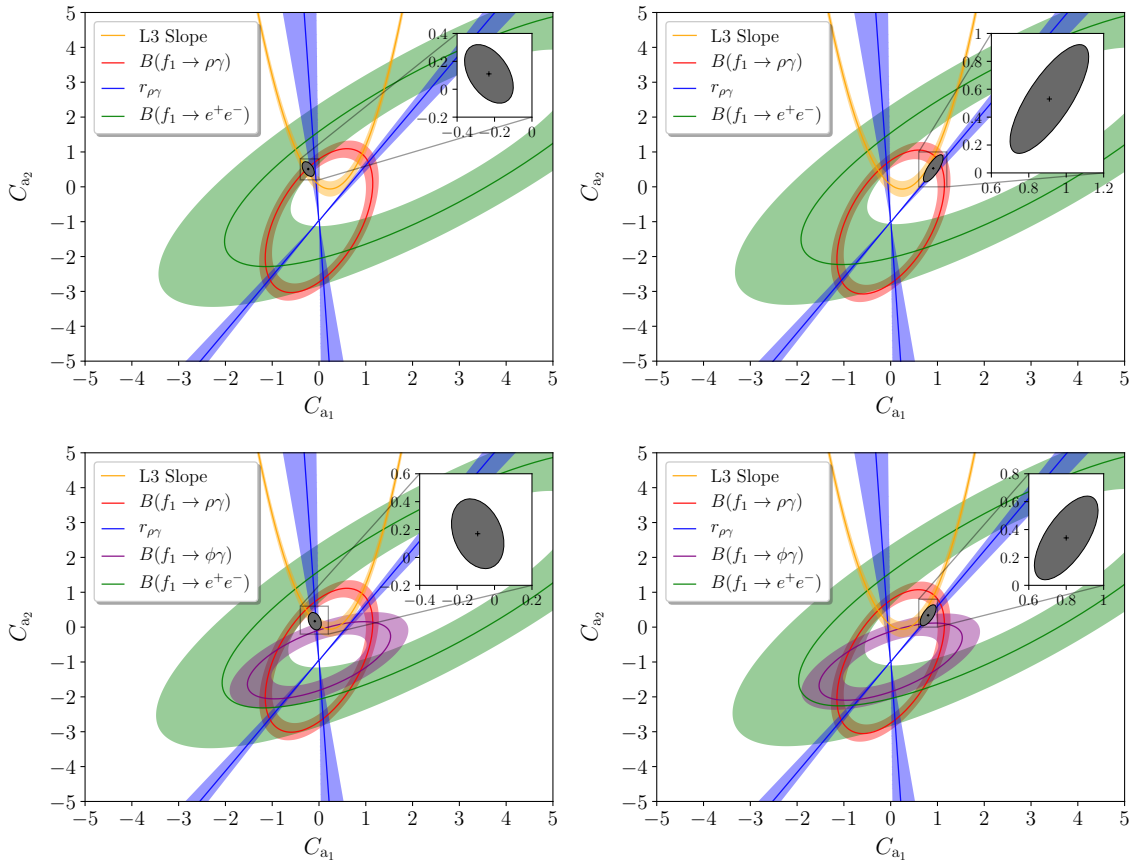

Figure 6.1: Contours in the C_{a_1}–C_{a_2} plane for the best-fit value of C_s in the minimal VMD representation: for Solution 1 (*left*) and Solution 2 (*right*), without (*upper*) and including (*lower*) the constraint from $B(f_1 \to \phi\gamma)$. The best-fit region is indicated by the $\Delta\chi^2 = 1$ ellipse (inflated by the scale factor).

points of Ref. [7] but the last one (centered around $\sqrt{Q^2} = 1.8\,\text{GeV}$, where the curves still agree within uncertainties). In fact, a large part of the pull is a result of the slightly increased value of C_s from the global fit, while the impact of the asymptotic behavior of $\mathcal{F}_{a_1}(-Q^2, 0)$ remains small. Finally, we observe that most extended VMD fits require a substantial ρ' contribution, as reflected by the large values of ϵ_1 shown in Table 6.3. In fact, for the fit without $B(f_1 \to \phi\gamma)$, it even exceeds the coefficient of the ρ contribution, which could be considered an indication that smaller values of $B(f_1 \to e^+e^-)$ are preferred. We also implemented a variant of the extended VMD fit in which ϵ_1 was allowed to float freely, but this did not improve the fit quality, with results for ϵ_1 consistent with the ones imposed via Eq. (3.35).

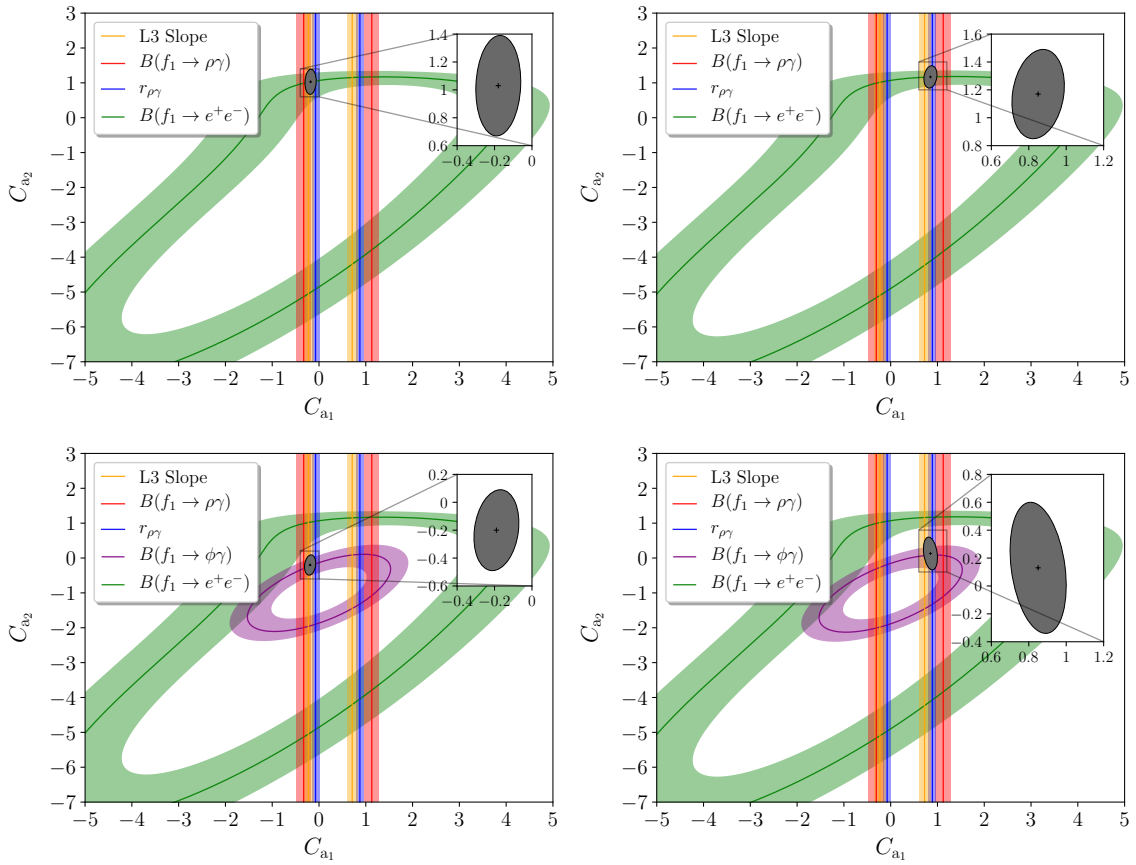

Figure 6.2: Contours in the C_{a_1}–C_{a_2} plane for the best-fit value of C_s in the extended VMD representation: for Solution 1 (*left*) and Solution 2 (*right*), without (*upper*) and including (*lower*) the constraint from $B(f_1 \to \phi\gamma)$. The best-fit region is indicated by the $\Delta\chi^2 = 1$ ellipse (inflated by the scale factor). We do not consider equivalent solutions with very large negative C_{a_2}, as arise without the $B(f_1 \to \phi\gamma)$ constraint. Further local minima when including $B(f_1 \to \phi\gamma)$ mirror the indicated Solutions 1 and 2 on the lower branch of the ellipse but display a worse χ^2/dof and are thus discarded.

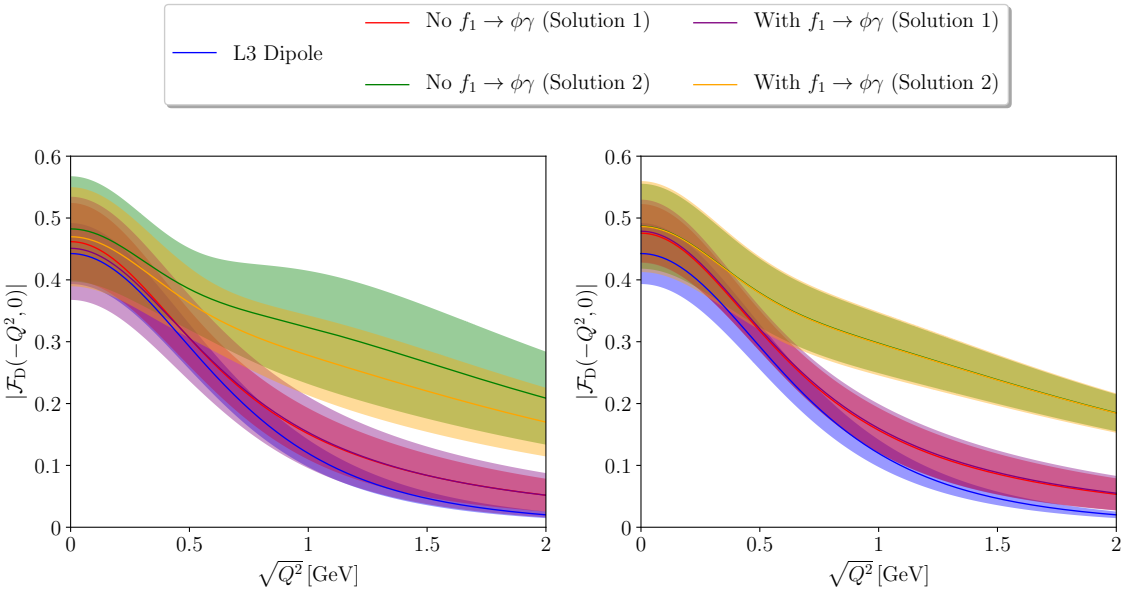

Figure 6.3: Comparison of the fit solutions for the effective form factor probed in $e^+e^- \to e^+e^- f_1$ with the L3 measurement [7], according to Eq. (4.11), for the minimal VMD representation (*left*) and the extended one (*right*). The L3 dipole band includes the uncertainties on $|\mathcal{F}_{\rm D}(0,0)|$ and $\Lambda_{\rm D}$, as given by Eq. (4.2), added in quadrature; our bands propagate the uncertainties from Table 6.2 and Table 6.3, respectively.

Chapter 7

Summary and outlook

In this part of the thesis, we performed a comprehensive analysis of the TFFs of the axial-vector resonance f_1, motivated by its contribution to HLbL scattering in the anomalous magnetic moment of the muon. Our study is based on the available constraints from $e^+e^- \to e^+e^- f_1$, $f_1 \to 4\pi$, $f_1 \to \rho\gamma$, $f_1 \to \phi\gamma$, and $f_1 \to e^+e^-$, all of which are sensitive to different aspects of the $f_1 \to \gamma^*\gamma^*$ transition. Since the amount of data is limited, a completely model-independent determination of all three TFFs is not feasible at present, leading us to consider parameterizations motivated by VMD. To assess the sensitivity to the chosen parameterization, we constructed two variants: a minimal one that produces non-vanishing results for all TFFs and an extension that improves the asymptotic behavior by matching to short-distance constraints. In each case, this leaves three coupling constants as free parameters, C_s, C_{a_1}, and C_{a_2}, for the symmetric and the two antisymmetric TFFs, in terms of which the analysis is set up.

As a first step, we derived master formulae for all processes in terms of these couplings and performed cross-checks when analyzing each process in terms of the dominant coupling C_s. This reveals that the decay $f_1 \to 4\pi$ does not provide further information on the TFFs, as the mechanism $f_1 \to a_1\pi \to \rho\pi\pi \to 4\pi$ likely dominates with respect to $f_1 \to \rho\rho \to 4\pi$ and only the latter can be related to the f_1 TFFs. The process is thus discarded in the subsequent analysis. For the remaining observables, we performed detailed uncertainty estimates, including the subleading isoscalar contributions, the properties of the ρ' meson and its spectral function, and the matching to short-distance constraints. In all cases, we conclude that the dominant uncertainties are currently of experimental origin.

Combining all constraints in a global fit, we found that the symmetric coupling C_s is by far best determined, with substantial differences in C_{a_1} and C_{a_2} among the different scenarios; see Table 6.2, Table 6.3, Fig. 6.1, and Fig. 6.2 for our central results. Out of two sets of solutions—Solution 1 with a small negative value of C_{a_1} and Solution 2 with a sizable positive one—the former is in general preferred by the fit, with Solution 2 further disfavored by the comparison to space-like $e^+e^- \to e^+e^- f_1$ data, see Fig. 6.3. In the case of the minimal VMD representation, we observed some tension between $B(f_1 \to e^+e^-)$ and the remaining constraints especially when including $B(f_1 \to \phi\gamma)$ in the fit, leading to a preference for a branching fraction below the value recently reported by the SND collaboration. In the extended parameterization, the dependence on C_{a_2} disappears from all observables but $B(f_1 \to e^+e^-)$ and, where applicable, $B(f_1 \to \phi\gamma)$, but limited information about the isoscalar sector together with necessary U(3) assumptions render

the latter constraint less reliable. While the $f_1 \to \phi\gamma$ branching fraction seems to prefer a smaller value of $B(f_1 \to e^+e^-)$ (similar to the minimal VMD fit), we conclude that the parameter that controls its size, C_{a_2}, is largely unconstrained at the moment and would thus profit most from an improved measurement of $B(f_1 \to e^+e^-)$.

In general, new measurements of $B(f_1 \to e^+e^-)$—as possible in the context of $e^+e^- \to$ hadrons energy scans at SND and CMD-3—would be highly beneficial to further constrain the f_1 TFFs, given that the resulting constraints are complementary to other observables, in particular, providing sensitivity to doubly-virtual kinematics and the antisymmetric TFFs. Apart from a more reliable determination of C_{a_2}, one could also validate and, if necessary, refine the underlying VMD assumptions. Furthermore, improved measurements of $e^+e^- \to e^+e^- f_1$ would be valuable to further constrain the singly-virtual TFFs—in particular the asymptotic behavior of $\mathcal{F}_{\mathrm{a}_1}(q^2, 0)$—ideally adding new data points above 1 GeV and using the full momentum dependence given in Eq. (4.11) to avoid the corresponding limitation in the interpretation of the L3 data. Such analyses are possible at BESIII [164] and Belle II [165]. To go beyond VMD parameterizations, the energy dependence in the (dispersively improved) BW propagators would need to be constrained by data, which would require differential information on f_1 decays. At the moment, our analysis gives a first summary of the combined information on the f_1 TFFs that can be extracted from the available data in terms of simple parameterizations.

Appendix A

Asymptotic behavior including mass effects

In this appendix, we generalize the considerations of Refs. [26, 27] regarding a double-spectral representation of the BL scaling to include mass effects that arise from the kinematic variables in the denominator. Starting from

$$\begin{aligned}\mathcal{F}_2(q_1^2,q_2^2) &= -F_A^{\text{eff}} m_A^3 \frac{\partial}{\partial q_1^2}\int_0^1 \mathrm{d}u\,\frac{\phi(u)}{uq_1^2+(1-u)q_2^2-u(1-u)m_A^2}+\mathcal{O}(1/q_i^6),\\ \mathcal{F}_3(q_1^2,q_2^2) &= F_A^{\text{eff}} m_A^3 \frac{\partial}{\partial q_2^2}\int_0^1 \mathrm{d}u\,\frac{\phi(u)}{uq_1^2+(1-u)q_2^2-u(1-u)m_A^2}+\mathcal{O}(1/q_i^6),\end{aligned} \tag{A.1}$$

see Eq. (2.12), we see that the asymptotic behavior of the axial-vector TFFs can still be deduced from the simpler pseudoscalar case, which leads us to study the generic integral

$$\tilde{I}(q_1^2,q_2^2,m^2) = \int_0^1 \mathrm{d}u\,\frac{\phi(u)}{uq_1^2+(1-u)q_2^2-u(1-u)m^2}, \tag{A.2}$$

which, in the case $q_1^2 = -Q^2 = q_2^2$, evaluates to

$$\begin{aligned}\tilde{I}(-Q^2,-Q^2,m^2) &= -\frac{6}{Q^2\xi}\left[1-\frac{2}{\sqrt{\xi(4+\xi)}}\log\frac{\sqrt{4+\xi}+\sqrt{\xi}}{\sqrt{4+\xi}-\sqrt{\xi}}\right]\\ &= -\frac{1}{Q^2}\left(1-\frac{\xi}{5}+\frac{3}{70}\xi^2-\frac{\xi^3}{105}+\mathcal{O}\big(\xi^4\big)\right), \qquad \xi=\frac{m^2}{Q^2}.\end{aligned} \tag{A.3}$$

Given the large masses of the axial-vector mesons, $m = m_A$, such corrections in ξ may become relevant and Eq. (A.2) defines a convenient test case to study their impact.

As a first step, we observe that Eq. (A.2) can still be formulated as a single dispersion relation [135] via the transformation $x = -\big(q_2^2 - m^2 u\big)(1-u)/u$,

$$\begin{aligned}\tilde{I}(q_1^2,q_2^2,m^2) &= \frac{1}{\pi}\int_0^\infty \mathrm{d}x\,\frac{\operatorname{Im}\tilde{I}(x,q_2^2,m^2)}{x-q_1^2},\\ \operatorname{Im}\tilde{I}(x,y,m^2) &= \frac{3\pi}{m^4}\left(\frac{(x-y)^2-m^2(x+y)}{\sqrt{\lambda(x,y,m^2)}}-x+y\right),\end{aligned} \tag{A.4}$$

where $y = q_2^2$ has been assumed space-like. Analytic continuation in q_2^2 then allows one to rewrite the imaginary part in Eq. (A.4) in terms of another dispersion relation, leading to

$$\begin{aligned}\tilde{I}(q_1^2, q_2^2, m^2) &= \frac{1}{\pi^2}\int_0^\infty \mathrm{d}x \int_0^\infty \mathrm{d}y\, \frac{\tilde{\rho}(x,y,m^2)}{(x-q_1^2)(y-q_2^2)} \\ &= -\frac{6}{m^2}\left[1 + \frac{q_1^2}{m^2}\log\left(1-\frac{m^2}{q_1^2}\right) + \frac{q_2^2}{m^2}\log\left(1-\frac{m^2}{q_2^2}\right)\right] \\ &\quad + \frac{q_1^2 q_2^2}{\pi^2}\int_0^\infty \mathrm{d}x \int_0^\infty \mathrm{d}y\, \frac{\tilde{\rho}(x,y,m^2)}{x(x-q_1^2)y(y-q_2^2)},\end{aligned} \tag{A.5}$$

with the double-spectral function

$$\tilde{\rho}(x,y,m^2) = \frac{1}{2\mathrm{i}}\mathrm{disc}_y\big[\mathrm{Im}\,\tilde{I}(x,y,m^2)\big] = \frac{3\pi}{m^4}\frac{(x-y)^2 - m^2(x+y)}{\sqrt{-\lambda(x,y,m^2)}}\theta\big(-\lambda(x,y,m^2)\big). \tag{A.6}$$

Here, the unsubtracted and subtracted dispersion relations of Eq. (A.5) are related via

$$\frac{1}{x-q_1^2} = \frac{1}{x} + \frac{q_1^2}{x(x-q_1^2)}, \qquad\qquad \frac{1}{y-q_2^2} = \frac{1}{y} + \frac{q_2^2}{y(y-q_2^2)}. \tag{A.7}$$

Restricting the integration in x, y should then allow one to isolate the asymptotic contributions while keeping the leading mass corrections. In the subtracted version, the singly-virtual limits become explicit since, with one $q_i^2 = 0$,

$$-\frac{6}{m^2}\left[1 + \frac{q_i^2}{m^2}\log\left(1-\frac{m^2}{q_i^2}\right)\right] = \int_0^1 \mathrm{d}u\, \frac{\phi(u)}{uq_i^2 - u(1-u)m^2}. \tag{A.8}$$

Further, to make the connection with the massless limit of Eq. (3.47), which amounts to

$$\tilde{I}(q_1^2, q_2^2, m^2) \overset{m\to 0}{\to} I(q_1^2, q_2^2) \to -3q_1^2 q_2^2 \int_{s_\mathrm{m}}^\infty \frac{\mathrm{d}x}{(x-q_1^2)^2(x-q_2^2)^2}, \tag{A.9}$$

see Eq. (3.42), we first note that this variant had been constructed in such a way that the singly-virtual contributions are removed, suggesting a matching in the limit $q_1^2 = -Q^2 = q_2^2$, in which

$$-3q_1^2 q_2^2 \int_{s_\mathrm{m}}^\infty \frac{\mathrm{d}x}{(x-q_1^2)^2(x-q_2^2)^2} = -\frac{1}{Q^2}\left[1 - 3\frac{s_\mathrm{m}}{Q^2} + 6\left(\frac{s_\mathrm{m}}{Q^2}\right)^2 - 10\left(\frac{s_\mathrm{m}}{Q^2}\right)^3 + \mathcal{O}\left(\left(\frac{s_\mathrm{m}}{Q^2}\right)^4\right)\right]. \tag{A.10}$$

To evaluate Eq. (A.5) in the same limit, we symmetrize the integration to $v = x + y$, $w = x - y$ and introduce a step function $\theta(v - v_\mathrm{m})$. In these variables, the w integration extends between $w_\pm = \pm\sqrt{2m^2 v - m^4}$, which shows that in the massless limit, the double-spectral density indeed collapses to a δ distribution, see Eq. (3.46). For $q_1^2 = -Q^2 = q_2^2$, the w integration can be performed analytically, leading to

$$\begin{aligned}\tilde{I}(-Q^2, -Q^2, m^2) &= \frac{6}{m^4}\int_{v_\mathrm{m}}^\infty \mathrm{d}v \left(\frac{(v+2Q^2)^2 - m^2 v}{(v+2Q^2)\sqrt{(v+2Q^2)^2 - 2m^2 v + m^4}} - 1\right) \\ &= -12Q^2 \int_{v_\mathrm{m}}^\infty \mathrm{d}v\, \frac{v+Q^2}{(v+2Q^2)^4} + \mathcal{O}\big(m^2\big) \\ &= -\frac{1}{Q^2}\left[1 - 3\frac{v_\mathrm{m}}{4Q^2} + 6\left(\frac{v_\mathrm{m}}{4Q^2}\right)^2 - 8\left(\frac{v_\mathrm{m}}{4Q^2}\right)^3 + \mathcal{O}\left(\left(\frac{v_\mathrm{m}}{Q^2}\right)^5\right)\right] + \mathcal{O}\big(m^2\big).\end{aligned} \tag{A.11}$$

The first three terms in the expansion thus match upon the identification $v_\mathrm{m} = 4s_\mathrm{m}$.

Appendix B

Phenomenological Lagrangians[†]

In this appendix, we define the Lagrangians used for the $\rho\gamma$, $\rho\pi\pi$, and $\rho\omega\pi$ couplings and discuss the information that can be extracted for their ρ' analogs. In particular, we derive estimates for the branching ratios $B(\rho' \to \pi\pi)$ and $B(\rho' \to \omega\pi)$, which are necessary inputs for the construction of the energy-dependent width $\Gamma_{\rho'}^{(\omega\pi,\pi\pi)}(q^2)$ in Eq. (3.13).

For the coupling of photons to the vector mesons $\{\rho, \omega, \phi, \rho', \ldots\}$, we use the effective interaction Lagrangian [129]

$$\mathcal{L}_{V\gamma} = -\frac{e}{2} F^{\mu\nu} \left(\frac{\rho_{\mu\nu}}{g_{\rho\gamma}} + \frac{\omega_{\mu\nu}}{g_{\omega\gamma}} + \frac{\phi_{\mu\nu}}{g_{\phi\gamma}} + \frac{\rho'_{\mu\nu}}{g_{\rho'\gamma}} + \ldots \right), \tag{B.1}$$

where $F^{\mu\nu} = \partial^\mu A^\nu - \partial^\nu A^\mu$ is the EM field strength tensor with the photon field A^μ, $\{\rho_{\mu\nu}^{(\prime)}, \rho_\mu^{(\prime)}\}$, $\{\omega_{\mu\nu}, \omega_\mu\}$, and $\{\phi_{\mu\nu}, \phi_\mu\}$ are the respective vector-meson equivalents, and the ellipsis refers to excited isoscalar vector mesons that we omit from the following discussion for simplicity. The couplings of the three ground-state vector mesons are linked via SU(3) symmetry according to $g_{\rho\gamma} : g_{\omega\gamma} : g_{\phi\gamma} = 1 : 3 : 3/\sqrt{2}$ [129], with the sign of $g_{\phi\gamma}$ adjusted according to Eq. (3.24). In the following, we neglect complex phases associated with actual pole residues (which are known to be tiny [166]) and work with the phase convention $\operatorname{sgn} g_{\rho\gamma} = +1$. From the Lagrangian, the partial decay width of the vector mesons into e^+e^- follows as

$$\Gamma(V \to e^+e^-) = \frac{4\pi\alpha^2}{3|g_{V\gamma}|^2} \left(1 + \frac{2m_e^2}{M_V^2}\right) \sqrt{M_V^2 - 4m_e^2}. \tag{B.2}$$

For the ρ meson, one can solve for the coupling and insert the (experimental) value $\Gamma(\rho \to e^+e^-) = 7.04\,\text{keV}$ [99] to find

$$g_{\rho\gamma} = 4.96. \tag{B.3}$$

This value agrees well with the residue $|g_{\rho\gamma}| = 4.9(1)$ extracted from the pion vector form factor [166] and is also close to the expectation from SU(3) symmetry, $g_{\rho\gamma}^{\text{SU(3)}} = g_{\omega\gamma}/3 = 5.6$, where $g_{\omega\gamma}$ can similarly be extracted from $\Gamma(\omega \to e^+e^-) = B(\omega \to e^+e^-)\Gamma_\omega = 0.625\,\text{keV}$ [99],

$$g_{\omega\gamma} = 16.7. \tag{B.4}$$

[†]The momentum-independent coupling of photons to vector mesons as well as the coupling of vector mesons to pions obtained in this appendix have already been derived in a less sophisticated manner and only for the non-excited vector mesons in the master's thesis of the author [115].

Furthermore, one can use $\Gamma(\phi \to e^+e^-) = 1.27\,\text{keV}$ to solve for the coupling of the ϕ meson, yielding

$$g_{\phi\gamma} = 13.38. \tag{B.5}$$

For the VMD application considered in this part of the thesis, we also need a formulation in which the coupling of photons to vector mesons is momentum independent, with the respective vector meson considered on shell. Such a coupling can formally be defined via the Lagrangian

$$\widetilde{\mathcal{L}}_{V\gamma} = eA^\mu\big(\widetilde{g}_{\rho\gamma}\rho_\mu + \widetilde{g}_{\omega\gamma}\omega_\mu + \widetilde{g}_{\phi\gamma}\phi_\mu + \widetilde{g}_{\rho'\gamma}\rho'_\mu + \dots\big), \tag{B.6}$$

where matching the amplitudes resulting from Eq. (B.1) and Eq. (B.6) for on-shell mesons determines

$$\widetilde{g}_{V\gamma} = \frac{M_V^2}{g_{V\gamma}}. \tag{B.7}$$

In particular, we carry over the sign convention for the coupling constants $\widetilde{g}_{V\gamma}$ from $g_{V\gamma}$ above.

In order to describe the coupling of (uncharged) isovector vector mesons to two pions, we employ the effective interaction Lagrangian [129]

$$\mathcal{L}_{\rho^{(\prime)}\pi\pi} = \big(g_{\rho\pi\pi}\rho_\mu + g_{\rho'\pi\pi}\rho'_\mu\big)\big(\pi^+\partial^\mu\pi^- - \pi^-\partial^\mu\pi^+\big), \tag{B.8}$$

where $\pi^\pm$ denote the pion fields of definite charge and the coupling to two neutral pions is forbidden by Bose symmetry. For $\rho^{(\prime)} \to \pi^+\pi^-$, we thus find the decay width

$$\Gamma\big(\rho^{(\prime)} \to \pi^+\pi^-\big) = \frac{M_{\rho^{(\prime)}}|g_{\rho^{(\prime)}\pi\pi}|^2}{48\pi}\left(1 - \frac{4M_\pi^2}{M_{\rho^{(\prime)}}^2}\right)^{3/2}. \tag{B.9}$$

A VMD ansatz for the pion vector form factor,[15]

$$F_\pi^{\mathrm{V}}(q^2) \approx \frac{g_{\rho\pi\pi}}{g_{\rho\gamma}}\frac{M_\rho^2}{M_\rho^2 - q^2 - \mathrm{i}\sqrt{q^2}\Gamma_\rho(q^2)} + \frac{g_{\rho'\pi\pi}}{g_{\rho'\gamma}}\frac{M_{\rho'}^2}{M_{\rho'}^2 - q^2 - \mathrm{i}\sqrt{q^2}\Gamma_{\rho'}(q^2)}, \tag{B.10}$$

dictates $g_{\rho\pi\pi}$ to have the same sign as $g_{\rho\gamma}$, so that under the assumption $\Gamma(\rho \to \pi^+\pi^-) = \Gamma_\rho$ [99], we obtain

$$g_{\rho\pi\pi} = 5.98, \tag{B.11}$$

again close to the actual residue $|g_{\rho\pi\pi}| = 6.01^{+0.04}_{-0.07}$ [167].

Finally, starting from the anomalous interaction Lagrangian $\mathcal{L}_{V\Phi}^{(3)}$ given in Ref. [129], we write down the Lagrangian that describes the coupling of the neutral isovector vector mesons to $\omega\pi^0$,

$$\mathcal{L}_{\rho^{(\prime)}\omega\pi} = \frac{\epsilon^{\mu\nu\alpha\beta}}{2}(\partial_\beta\pi^0)\Big[g_{\rho\omega\pi}\big[(\partial_\mu\ \rho_\nu)\omega_\alpha + (\partial_\mu\omega_\nu)\rho_\alpha\big] + g_{\rho'\omega\pi}\big[(\partial_\mu\ \rho'_\nu)\omega_\alpha + (\partial_\mu\omega_\nu)\rho'_\alpha\big]\Big]. \tag{B.12}$$

[15] Strictly speaking, this form is based on Eq. (B.6) rather than Eq. (B.1), but the difference essentially amounts to a constant that does not affect the relative signs.

The corresponding $\rho' \to \omega\pi$ decay width is given by

$$\Gamma(\rho' \to \omega\pi) = \frac{|g_{\rho'\omega\pi}|^2}{96\pi M_{\rho'}^3} \lambda\big(M_{\rho'}^2, M_\omega^2, M_\pi^2\big)^{3/2}. \tag{B.13}$$

In the following, we estimate the couplings $|g_{\rho'\gamma}|$, $|g_{\rho'\pi\pi}|$, and $|g_{\rho'\omega\pi}|$ as well as the relevant signs between these. One purpose is the construction of the energy-dependent width $\Gamma_{\rho'}^{(\omega\pi,\pi\pi)}(q^2)$ in Eq. (3.13), which—besides the shape of the decay widths $\Gamma(\rho' \to \pi\pi)$ and $\Gamma(\rho' \to \omega\pi)$—requires the branching ratios $B(\rho' \to \pi\pi)$ and $B(\rho' \to \omega\pi)$ as input. In addition, this allows us to assess the relative importance of ρ' contributions in $f_1 \to \gamma^*\gamma^*$ as compared to those in $f_1 \to 4\pi$.

Analyses of the pion vector form factor using improved variants of Eq. (B.10) suggest a ρ' contribution relative to the dominant ρ therein of an approximate strength [104, 168, 169]

$$\frac{g_{\rho'\pi\pi}/g_{\rho'\gamma}}{g_{\rho\pi\pi}/g_{\rho\gamma}} \approx -\frac{1}{10}. \tag{B.14}$$

On the other hand, the $\omega \to \pi\gamma^*$ TFF [104, 170] can be approximated in a VMD framework according to

$$f_{\omega\pi}(q^2) \approx \frac{g_{\rho\omega\pi}}{g_{\rho\gamma}} \frac{M_\rho^2}{M_\rho^2 - q^2 - \mathrm{i}\sqrt{q^2}\Gamma_\rho(q^2)} + \frac{g_{\rho'\omega\pi}}{g_{\rho'\gamma}} \frac{M_{\rho'}^2}{M_{\rho'}^2 - q^2 - \mathrm{i}\sqrt{q^2}\Gamma_{\rho'}(q^2)}. \tag{B.15}$$

The asymptotic behavior $f_{\omega\pi}(q^2) = \mathcal{O}(q^{-4})$ [96, 97, 171, 172] implies the superconvergence sum-rule constraint

$$\frac{g_{\rho'\omega\pi}/g_{\rho'\gamma}}{g_{\rho\omega\pi}/g_{\rho\gamma}} = -\frac{M_\rho^2}{M_{\rho'}^2} \approx -\frac{1}{4} \tag{B.16}$$

on the couplings of Eq. (B.15), which is consistent with the experimental analysis of Ref. [170]. From the experimental width $\Gamma(\omega \to \pi\gamma) = 0.71\,\mathrm{MeV}$ [99] and the corresponding formula [104]

$$\Gamma(\omega \to \pi\gamma) = \frac{\alpha(M_\omega^2 - M_\pi^2)^3}{24 M_\omega^3} |f_{\omega\pi}(0)|^2, \tag{B.17}$$

we furthermore obtain the normalization $|f_{\omega\pi}(0)| = 2.3\,\mathrm{GeV}^{-1}$ and thus

$$g_{\rho\omega\pi} \approx 15.4\,\mathrm{GeV}^{-1} \tag{B.18}$$

when combined with Eq. (B.16), choosing a positive sign convention for $f_{\omega\pi}(0)$. Moreover, from Eq. (B.14) and Eq. (B.16), one deduces the ratio

$$\frac{g_{\rho'\omega\pi}}{g_{\rho'\pi\pi}} \approx 6.4\,\mathrm{GeV}^{-1}, \tag{B.19}$$

so that under the assumption $\Gamma_{\rho'} \approx \Gamma(\rho' \to \pi\pi) + \Gamma(\rho' \to \omega\pi)$—neglecting another significant contribution from $\rho' \to a_1\pi$ $(a_1 \to 3\pi)$[16] —one can use Eq. (B.9) and Eq. (B.13) to obtain

$$|g_{\rho'\pi\pi}| \approx 1.60, \qquad |g_{\rho'\omega\pi}| \approx 10.3\,\mathrm{GeV}^{-1}. \tag{B.20}$$

[16]References [173, 174] show that $e^+e^- \to a_1\pi$, the second-largest subchannel of $e^+e^- \to 4\pi$ beyond $e^+e^- \to \omega\pi$, is already important at the ρ' mass. Adding the $a_1\pi$ channel will decrease the $g_{\rho'\pi\pi}$ and $g_{\rho'\omega\pi}$ couplings in parallel, with the ratio of branching fractions $B(\rho' \to \pi\pi)/B(\rho' \to \omega\pi)$ kept fixed, but they will not add up to 100% anymore.

The branching ratios then become

$$B(\rho' \to \pi\pi) \approx 6\%, \qquad B(\rho' \to \omega\pi) \approx 94\%, \tag{B.21}$$

and, for completeness, the $\rho'\gamma$ coupling is estimated as

$$|g_{\rho'\gamma}| \approx 13.3. \tag{B.22}$$

The estimate Eq. (B.21) agrees with the expectation that the ρ' should be largely inelastic, and the resulting spectral function in Eq. (3.13) thus essentially defines an estimate of the 4π channel dominated by $\omega\pi$. We stress that these considerations should only be considered rough estimates, the main point being to define another plausible variant that allows us to assess the sensitivity of our results to the assumptions made for the ρ' spectral function. Finally, for our analysis of $f_1 \to 4\pi$ including effects of the ρ', we require the ratio of coupling constants

$$\frac{g_{\rho'\pi\pi}\, g_{\rho'\gamma}}{g_{\rho\pi\pi}\, g_{\rho\gamma}} \approx -0.7. \tag{B.23}$$

Appendix C

Comparison to the literature[†]

In this appendix, we briefly compare the basis of LORENTZ structures and TFFs as well as the parameterization of the latter for the f_1 used in this part of the thesis to the previous analysis of Refs. [113, 114]. Since the TFFs are not (anti-)symmetrized in Ref. [113], we use the basis introduced in Ch. 2 for our comparison, that is, in particular, the structures from Eq. (2.6). When using Eq. (2.2) to translate the amplitude $\mathcal{M}(f_1 \to \gamma^*\gamma^*)$ from Ref. [113] to the tensor matrix element given in Eq. (2.5), we find the structures to be related by

$$\begin{aligned} T^{\mu\nu\alpha}_{1\,[113]}(q_1,q_2) &= -T^{\mu\nu\alpha}_{1}(q_1,q_2), \\ T^{\mu\nu\alpha}_{2\,[113]}(q_1,q_2) &= -T^{\mu\nu\alpha}_{3}(q_1,q_2), \\ T^{\mu\nu\alpha}_{3\,[113]}(q_1,q_2) &= T^{\mu\nu\alpha}_{2}(q_1,q_2) \end{aligned} \tag{C.1}$$

and the TFFs to be linked via

$$\begin{aligned} \mathcal{F}_1^{[113]}(q_1^2,q_2^2) &= -4\pi\mathcal{F}_1(q_1^2,q_2^2), \\ \mathcal{F}_2^{[113]}(q_1^2,q_2^2) &= -4\pi\mathcal{F}_3(q_1^2,q_2^2), \\ \mathcal{F}_3^{[113]}(q_1^2,q_2^2) &= 4\pi\mathcal{F}_2(q_1^2,q_2^2). \end{aligned} \tag{C.2}$$

While the structures are thus identical to ours except for two global signs and a permutation, the additional factor of 4π in the TFFs appears due to the fact that the fine-structure constant α is used in the definition of their matrix element instead of the factor e^2. The symmetry properties of the TFFs in their basis are given by $\mathcal{F}_1^{[113]}(q_2^2,q_1^2) = -\mathcal{F}_1^{[113]}(q_1^2,q_2^2)$ and $\mathcal{F}_2^{[113]}(q_2^2,q_1^2) = \mathcal{F}_3^{[113]}(q_1^2,q_2^2)$, where an (anti-)symmetrization similar to Eq. (3.1) would be straightforward. Moreover, the two-photon decay width, Eq. (2.11), becomes

$$\widetilde{\Gamma}^{[113]}_{\gamma\gamma} = \frac{\alpha^2}{192\pi} m_A |\mathcal{F}_2^{[113]}(0,0)|^2 = \frac{\alpha^2}{192\pi} m_A |\mathcal{F}_3^{[113]}(0,0)|^2. \tag{C.3}$$

The strategy that is used in Ref. [113] to determine the explicit parameterization of the TFFs in line with a VMD model is, in fact, quite different from our approach—above all,

[†]The mapping to the basis of structures and form factors of Ref. [113] performed in this appendix has already been detailed in the master's thesis of the author [115], however, with no further discussion, *e.g.*, about the actual VMD nature of the reference's parameterization of the form factors.

their model does not correspond to a strict VMD ansatz. Instead of proposing a VMD-like parameterization for the form factors $\mathcal{F}_i^{[113]}(q_1^2, q_2^2)$ as we did in Eq. (3.10), three form factors $h_i(q_1^2, q_2^2)$ are introduced, based on which an amplitude $\mathcal{M}(f_1 \to \rho^{0*}\rho^{0*})$ is constructed by replacing $\mathcal{F}_i^{[113]}(q_1^2, q_2^2) \to h_i(q_1^2, q_2^2)$ in $\mathcal{M}(f_1 \to \gamma^*\gamma^*)$; analogously, two complex coupling constants g_1 and g_2 are introduced to construct an amplitude $\mathcal{M}(f_1 \to \rho\gamma)$. We object that such complex couplings are allowed since the resulting imaginary parts need to reflect the actual analytic structure of the amplitude. Moreover, the explicit form of the $h_i(q_1^2, q_2^2)$, accounting for an off-shell dependence of the ρ mesons, introduces unphysical kinematic singularities.

By employing a $\rho\gamma$ coupling similar to the one we introduced by means of Eq. (B.1), the form factors $\mathcal{F}_i^{[113]}(q_1^2, q_2^2)$ and $h_i(q_1^2, q_2^2)$ are then related to each other in Ref. [113], where the latter can further be linked to the coupling constants g_1 and g_2. Using the $\rho\gamma$ coupling in the convention of this thesis, the form factors are found to be

$$\begin{aligned}
\mathcal{F}_1^{[113]}(q_1^2, q_2^2) &= \frac{e g_1 (M_\rho^2 - \mathrm{i} M_\rho \Gamma_\rho)(q_2^2 - q_1^2)}{g_{\rho\gamma}(q_1^2 - M_\rho^2 + \mathrm{i} M_\rho \Gamma_\rho)(q_2^2 - M_\rho^2 + \mathrm{i} M_\rho \Gamma_\rho)}, \\
\mathcal{F}_{2/3}^{[113]}(q_1^2, q_2^2) &= -\frac{e g_2 M_\rho^2 (M_\rho^2 - \mathrm{i} M_\rho \Gamma_\rho)}{g_{\rho\gamma}(q_1^2 - M_\rho^2 + \mathrm{i} M_\rho \Gamma_\rho)(q_2^2 - M_\rho^2 + \mathrm{i} M_\rho \Gamma_\rho)},
\end{aligned} \tag{C.4}$$

the width Γ_ρ being the (energy-independent) total width of the ρ meson, as opposed to our energy-dependent parameterization of Eq. (3.11) and Eq. (3.15). Moreover, the magnitude of the couplings g_1 and g_2 is determined in Ref. [113] by making use of experimental data on $f_1 \to \rho\gamma$, see Ch. 3; the relative phase between these coupling constants remains undetermined, despite using, in addition, input from $f_1 \to 4\pi$.

By rewriting Eq. (C.4) as

$$\mathcal{F}_1^{[113]}(q_1^2, q_2^2) = \frac{e g_1 (M_\rho^2 - \mathrm{i} M_\rho \Gamma_\rho)}{g_{\rho\gamma}(q_1^2 - M_\rho^2 + \mathrm{i} M_\rho \Gamma_\rho)} - \frac{e g_1 (M_\rho^2 - \mathrm{i} M_\rho \Gamma_\rho)}{g_{\rho\gamma}(q_2^2 - M_\rho^2 + \mathrm{i} M_\rho \Gamma_\rho)}, \tag{C.5}$$

one observes that $\mathcal{F}_1^{[113]}(q_1^2, q_2^2)$ does not correspond to a VMD ansatz in the strict sense but rather arises from two diagrams, each being composed of one direct photon coupling and one VMD-like ρ coupling. As we argued in Ch. 3, an actual VMD representation of the antisymmetric TFFs requires the introduction of a second multiplet. Further, Eq. (C.4) shows that the second and third TFFs are parameterized symmetrically, *i.e.*, the antisymmetric part is neglected. In either case, we contend that the $f_1 \to 4\pi$ decay does not allow one to extract information on the f_1 TFFs, for the reasons described in Sec. 4.2 and App. D.

Finally, we would like so stress that, in addition to using complex couplings, constant widths are problematic when inserted into the $f_1 \to e^+e^-$ loop integral, leading to imaginary parts below the respective thresholds and thus distorting the analytic structure. Given, in addition, the appearance of kinematic singularities and a different high-energy behavior, it is difficult to compare our phenomenological results to the ones of Refs. [113, 114].

Appendix D

$f_1 \to a_1\pi \to \rho\pi\pi \to 4\pi$

In order to investigate whether the intermediate state $a_1(\to \rho\pi)\pi$ can account for the discrepancy in the branching ratio of $f_1 \to 4\pi$ found in Sec. 4.2, we use the effective interaction Lagrangians

$$\begin{aligned}\mathcal{L}_{f_1a_1\pi} &= \frac{g_{f_1a_1\pi}}{2}\epsilon^{\mu\nu\alpha\beta}(\partial_\beta\pi^\mp)\big[(\partial_\mu\, a_{1\,\nu}^\pm)f_{1\alpha} + (\partial_\mu f_{1\nu})a_{1\,\alpha}^\pm\big],\\ \mathcal{L}_{a_1\rho\pi} &= g_{a_1\rho\pi}\big(a_{1\,\mu}^-\rho^\mu\pi^+ - a_{1\,\mu}^+\rho^\mu\pi^-\big),\end{aligned} \tag{D.1}$$

where $\mathcal{L}_{f_1a_1\pi}$ is constructed in analogy to Eq. (B.12) and $\mathcal{L}_{a_1\rho\pi}$ represents the simplest Lagrangian possible, the relative sign originating from isospin symmetry.[17] Before constructing an amplitude for $f_1 \to a_1\pi \to \rho\pi\pi \to 4\pi$, we will in the following estimate the couplings $g_{f_1a_1\pi}$ and (the magnitude of) $g_{a_1\rho\pi}$.

For the estimate of $g_{f_1a_1\pi}$, we start from the observation that the Wess–Zumino–Witten anomaly [99, 175, 176]

$$F_{\pi^0\gamma^*\gamma^*}(0,0) = \frac{1}{4\pi^2F_\pi} = 0.2745(3)\,\text{GeV}^{-1} \tag{D.2}$$

is largely saturated by the VMD ansatz

$$\begin{aligned}F_{\pi^0\gamma^*\gamma^*}(0,0) &\approx \frac{g_{\rho\omega\pi}}{g_{\rho\gamma}g_{\omega\gamma}}\left[\frac{M_\rho^2M_\omega^2}{(M_\rho^2 - q_1^2 - \mathrm{i}\sqrt{q_1^2}\Gamma_\rho(q_1^2))(M_\omega^2 - q_2^2)} + (q_1 \leftrightarrow q_2)\right]\Bigg|_{q_1^2=0=q_2^2}\\ &= \frac{2g_{\rho\omega\pi}}{g_{\rho\gamma}g_{\omega\gamma}} = \frac{2g_{\rho\omega\pi}F_\rho F_\omega}{M_\rho M_\omega} \approx 0.37\,\text{GeV}^{-1},\end{aligned} \tag{D.3}$$

where we used Eq. (B.3), Eq. (B.4), and Eq. (B.18). The decay constants of the ρ and ω meson,

$$\langle 0|J^\mu_{\text{EM}}(0)|V(p,\lambda_V)\rangle = F_V M_V \epsilon_\mu(p), \quad V = \rho,\omega, \tag{D.4}$$

are related to our previous notation by $g_{V\gamma} = M_V/F_V$. The rough agreement between Eq. (D.2) and Eq. (D.3) suggests that an estimate of the axial-vector analogs can be obtained in a similar manner, leading to the axial-vector-meson-dominance ansatz

$$F_{\pi^0\gamma^*\gamma^*}(0,0) \approx \frac{2g_{f_1a_1\pi}F_{a_1}F_{f_1}}{m_{a_1}m_{f_1}}, \tag{D.5}$$

[17] To see this, consider $\mathcal{L}_{a_1\rho\pi} \propto \text{Tr}[\boldsymbol{\rho}\,[\boldsymbol{a_1},\boldsymbol{\pi}]]$, where, *e.g.*, $\boldsymbol{\rho} = \rho^i\tau^i$, with ρ^i the isospin fields and τ^i the Pauli matrices. Then, $\mathcal{L}_{a_1\rho\pi} \propto \epsilon_{ijk}\rho^i a_1^j\pi^k$, and transforming from the isospin basis to charge states, *e.g.*, $\rho^\pm = (\rho^1 \pm \mathrm{i}\rho^2)/\sqrt{2}$, $\rho^0 = \rho^3$, gives $\mathcal{L}_{a_1\rho\pi} \propto a_1^-\rho^0\pi^+ - a_1^+\rho^0\pi^- + a_1^+\rho^-\pi^0 - a_1^-\rho^+\pi^0 + a_1^0\rho^+\pi^- - a_1^0\rho^-\pi^+$.

with the corresponding decay constants defined by

$$\langle 0|\bar{q}(0)\gamma_\mu\gamma_5\mathcal{Q}q(0)|A(p,\lambda_A)\rangle = F_A m_A \epsilon_\mu(p), \quad A = a_1, f_1. \tag{D.6}$$

Comparing the two parameterizations results in

$$\frac{g_{f_1 a_1 \pi}}{g_{\rho\omega\pi}} \approx \frac{F_\rho F_\omega}{M_\rho M_\omega}\frac{m_{a_1} m_{f_1}}{F_{a_1} F_{f_1}} \approx 1.3, \tag{D.7}$$

where we used $F_{a_1} = 168(7)\,\text{MeV}$, $F_{f_1} = 87(7)\,\text{MeV}$ [93, 118].

An estimate of $|g_{a_1\rho\pi}|$ is obtained by calculating the decay width of $a_1 \to \rho\pi$ and matching to the experimental width under the assumption $\Gamma(a_1 \to \rho\pi) = \Gamma_{a_1}$, taking into account that $\Gamma(a_1 \to \rho\pi) = \Gamma(a_1^\pm \to \rho^\pm\pi^0) + \Gamma(a_1^\pm \to \rho^0\pi^\pm) = 2\Gamma(a_1^\pm \to \rho^0\pi^\pm)$ for the charged channel due to the two possible final states for a decaying a_1^+ or a_1^-. We find[18]

$$\Gamma(a_1 \to \rho\pi) = \frac{|g_{a_1\rho\pi}|^2}{8\pi}\frac{|\mathbf{p}_\rho|}{m_{a_1}^2}\left(1 + \frac{|\mathbf{p}_\rho|^2}{3M_\rho^2}\right) \to \frac{|g_{a_1\rho\pi}|^2}{8\pi}\frac{|\mathbf{p}_\rho|}{m_{a_1}^2}, \tag{D.8}$$

where $|\mathbf{p}_\rho| = \sqrt{\lambda(m_{a_1}^2, M_\rho^2, M_\pi^2)}/(2m_{a_1})$ is the magnitude of the three-momentum in the center-of-mass frame, yielding

$$|g_{a_1\rho\pi}| = (3.7\ldots5.7)\,\text{GeV}, \tag{D.9}$$

where the given variation is due to the width of the a_1.

The amplitude for $f_1 \to a_1\pi \to \rho\pi\pi \to 4\pi$ can be constructed with Eq. (D.1) and Eq. (B.8), where eight diagrams have to be taken into account, see Fig. D.1, leading to

$$\begin{aligned}\mathcal{M}_{a_1\pi}(f_1 \to \pi^+\pi^-\pi^+\pi^-) = {}& \frac{g_{f_1 a_1\pi} g_{a_1\rho\pi} g_{\rho\pi\pi}}{\big(p_{a_1}^2 - m_{a_1}^2 + \mathrm{i}\sqrt{p_{a_1}^2}\Gamma_{a_1}(p_{a_1}^2)\big)\big(p_\rho^2 - M_\rho^2 + \mathrm{i}\sqrt{p_\rho^2}\Gamma_\rho(p_\rho^2)\big)} \\ & \times \epsilon^\mu(P)\epsilon_{\mu\nu\alpha\beta}\Big[2k_-^\nu p_-^\alpha p_+^\beta + k_-^\nu k_+^\alpha (p_+ - p_-)^\beta\Big] + (p_- \leftrightarrow k_-) + (p_+ \leftrightarrow k_+) \\ & + (p_+ \leftrightarrow k_+, p_- \leftrightarrow k_-) - (k_+ \leftrightarrow k_-) - (k_+ \leftrightarrow k_-, p_- \leftrightarrow k_-) \\ & - (k_+ \leftrightarrow k_-, p_+ \leftrightarrow k_+) - (k_+ \leftrightarrow k_-, p_+ \leftrightarrow k_+, p_- \leftrightarrow k_-),\end{aligned} \tag{D.10}$$

with the momenta defined as in Fig. D.1 and the pions on shell, $p_\pm^2 = M_\pi^2 = k_\pm^2$. For the energy-dependent width of the a_1 meson, we choose an ansatz based on Eq. (D.8),

$$\Gamma_{a_1}(q^2) = \theta\big(q^2 - (M_\rho + M_\pi)^2\big)\frac{\gamma_{a_1\to\rho\pi}(q^2)}{\gamma_{a_1\to\rho\pi}(m_{a_1}^2)}\Gamma_{a_1}, \qquad \gamma_{a_1\to\rho\pi}(q^2) = \frac{\sqrt{\lambda(q^2, M_\rho^2, M_\pi^2)}}{(q^2)^{3/2}}, \tag{D.11}$$

and the energy-dependent width $\Gamma_\rho(q^2)$ is as specified in Eq. (3.15). The decay width and thus branching ratio can then be calculated via the four-body phase-space integration of

$$\mathrm{d}\Gamma_{a_1\pi}(f_1 \to \pi^+\pi^-\pi^+\pi^-) = \frac{1}{2m_{f_1}}\big|\mathcal{M}_{a_1\pi}(f_1 \to \pi^+\pi^-\pi^+\pi^-)\big|^2 \mathrm{d}\Phi_4(P; p_+, p_-, k_+, k_-). \tag{D.12}$$

[18] Note that, in addition to the expected S-wave phase space, the Lagrangian $\mathcal{L}_{a_1\rho\pi}$ also produces a numerically small D-wave contribution proportional to $|\mathbf{p}_\rho|^3$, which—strictly speaking—would only vanish when performing a partial-wave projection. Given the uncertainties inherent in the $f_1 \to a_1\pi \to \rho\pi\pi \to 4\pi$ estimate presented here, especially in view of the width and spectral shape of the a_1, a more refined treatment is not warranted and we simply remove these terms in Eq. (D.8).

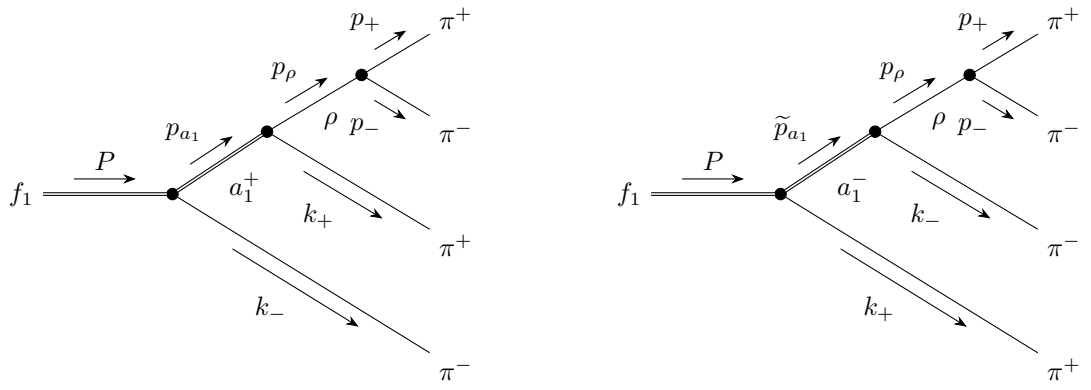

Figure D.1: FEYNMAN diagrams for $f_1 \to \pi^+\pi^-\pi^+\pi^-$ via $a_1\pi$. Since the two π^+ and π^- are each mutually indistinguishable, there exist eight diagrams in total, that is four diagrams with a_1^+ (*left*) and four diagrams with a_1^- (*right*), which are obtained by permuting the momenta appropriately.

Although we could proceed in complete analogy to Sec. 4.2, see in particular Eq. (4.16) and Eq. (4.17), it is instructive to write the differential four-body phase space differently from Eq. (4.17), namely in the form [99]

$$\mathrm{d}\Phi_4(P;p_+,p_-,k_+,k_-) = \mathrm{d}\Phi_2(p_\rho;p_+,p_-)\,\mathrm{d}\Phi_2(p_{a_1};p_\rho,k_+)\,\mathrm{d}\Phi_2(P;p_{a_1},k_-)\,\frac{\mathrm{d}p_{a_1}^2}{2\pi}\,\frac{\mathrm{d}p_\rho^2}{2\pi}, \tag{D.13}$$

where $\mathrm{d}\Phi_2(P;p_{a_1},k_-)$, $\mathrm{d}\Phi_2(p_{a_1};p_\rho,k_+)$, and $\mathrm{d}\Phi_2(p_\rho;p_+,p_-)$ are the respective two-body phase spaces of the subsystems $\{a_1(p_{a_1}),\pi^-(k_-)\}$, $\{\rho(p_\rho),\pi^+(k_+)\}$, and $\{\pi^+(p_+),\pi^-(p_-)\}$. As argued in Sec. 4.2, each two-body phase space can be evaluated in the corresponding center-of-mass frame, and we have to perform an explicit LORENTZ transformation from the center-of-mass frames of $\{a_1(p_{a_1}),\pi^-(k_-)\}$ and $\{\pi^+(p_+),\pi^-(p_-)\}$ into the one of $\{\rho(p_\rho),\pi^+(k_+)\}$ in order to evaluate all the scalar products appearing in $|\mathcal{M}_{a_1\pi}(f_1 \to \pi^+\pi^-\pi^+\pi^-)|^2$.[19] We perform the phase-space integration numerically with the *Cuhre* algorithm from the *Cuba* library [138], obtaining

$$\Gamma_{a_1\pi}(f_1 \to \pi^+\pi^-\pi^+\pi^-) = |g_{f_1a_1\pi}|^2|g_{a_1\rho\pi}|^2|g_{\rho\pi\pi}|^2 \times (3.27\ldots2.46)\times 10^{-9}\,\mathrm{GeV}. \tag{D.14}$$

Combining the above result with $|g_{f_1a_1\pi}| \approx 1.3 \times 15.4\,\mathrm{GeV}^{-1}$, $|g_{a_1\rho\pi}| = (3.7\ldots5.7)\,\mathrm{GeV}$, and $|g_{\rho\pi\pi}| = 5.98$, Eq. (D.7), Eq. (B.18), Eq. (D.9), and Eq. (B.11), we find the branching ratio to be given by

$$B_{a_1\pi}(f_1 \to \pi^+\pi^-\pi^+\pi^-) \approx (2.8\ldots5.0)\%, \tag{D.15}$$

in fair agreement with the experimental value $B(f_1 \to \pi^+\pi^-\pi^+\pi^-) = 10.9(6)\%$ [99]. We also considered the variant of this estimate obtained when further approximating the decay $f_1 \to a_1\pi \to \rho\pi\pi \to 4\pi$ by $f_1 \to a_1\pi \to \rho\pi\pi$, assuming that the ρ decays into two charged pions only:

$$\Gamma_{a_1\pi}(f_1 \to \rho\pi\pi) = |g_{f_1a_1\pi}|^2|g_{a_1\rho\pi}|^2 \times (2.40\ldots2.06)\times 10^{-7}\,\mathrm{GeV} \tag{D.16}$$

[19] As in Sec. 4.2, the decay rate involves an additional symmetry factor of $S = 1/(2!)^2$ due to the two pairs of indistinguishable particles in the final state.

and

$$B_{a_1\pi}(f_1 \to \rho\pi\pi) \approx (5.8 \ldots 11.8)\%, \tag{D.17}$$

leading to a result closer to the experimental branching fraction, which indicates that ρ dominance in this decay mode is again subject to sizable corrections. In both estimates, given that the VMD saturation of the anomaly, Eq. (D.3), actually overpredicts the expected value, Eq. (D.2), a somewhat smaller value of $|g_{f_1 a_1 \pi}|$ may be favored.

We stress that the estimates presented here are merely supposed to give an indication for why the VMD description of $f_1 \to 4\pi$ in Sec. 4.2 is in serious disagreement with the experimental branching ratio, *i.e.*, we do not claim to have a reliable prediction for $B_{a_1\pi}(f_1 \to \pi^+\pi^-\pi^+\pi^-)$, as, in particular, the uncertainty in assuming an axial-vector saturation of the anomaly is difficult to quantify. Still, the arguments leading to Eq. (D.15) and Eq. (D.17) should make plausible that the intermediate state $a_1\pi$ can indeed cover the experimental branching ratio to a large degree, thus rendering the $f_1 \to 4\pi$ decay unsuitable for extracting information on the f_1 TFFs.

Appendix E

Constants and parameters

In this appendix, we collect the particle masses and decay widths used throughout this part of the thesis, see Table E.1. Isospin-breaking effects can safely be neglected, in particular, the pion mass is identified with the mass of the charged pion. Some comments are in order, however, regarding the treatment of broad resonances, most notably the ρ' and, to a lesser extent, the ρ. Especially for the former, the quoted masses and widths are strongly reaction dependent, as referring to BW parameters rather than the model-independent pole parameters. We thus need to make sure that we use determinations that apply to the channels we consider here. Since the main application concerns the description of multi-pion decay channels in the VMD propagators, both for the ρ and the ρ', it appears most natural to consider reactions that provide access to both resonances, which points towards the decay $\tau \to \pi\pi\nu_\tau$ from Ref. [168] and the scattering process $e^+e^- \to \pi\pi$ from Ref. [177]. In particular, this allows us to see if there are relevant systematic differences between the charged and neutral channel. For the ρ, the mass parameter agrees well between all channels, but while there is also good agreement between Refs. [168, 177] for the width, the compilation from Ref. [99] quotes a significantly lower value for the neutral channel. Accordingly, we will use its ρ parameters from the charged channel in our analysis. Regarding the ρ', the mass from Ref. [99] lies halfway between Refs. [168, 177], with a width that agrees well with both channels within uncertainties. We will therefore take over the recommended parameters for the ρ'.

Quantity	Variable	Value	Reference
Mass pion	M_π	139.57 MeV	
Mass $a_1(1260)$	m_{a_1}	1230(40) MeV	
Mass $f_1(1285)$	m_{f_1}	1281.9(5) MeV	
Mass $f_1(1420)$	$m_{f_1'}$	1426.3(9) MeV	
Mass $\omega(782)$	M_ω	782.65(12) MeV	
Mass $\phi(1020)$	M_ϕ	1019.461(16) MeV	
Mass $\rho(770)$ (charged)	M_ρ	775.11(34) MeV	[99]
Mass $\rho(1450)$	$M_{\rho'}$	1465(25) MeV	
Total width $a_1(1260)$	Γ_{a_1}	(250 . . . 600) MeV	
Total width $f_1(1285)$	Γ_{f_1}	22.7(1.1) MeV	
Total width $f_1(1420)$	$\Gamma_{f_1'}$	54.5(2.6) MeV	
Total width $\rho(770)$ (charged)	Γ_ρ	149.1(8) MeV	
Total width $\rho(1450)$	$\Gamma_{\rho'}$	400(60) MeV	
Mass $\rho(770)$ (charged)	M_ρ	774.9(6) MeV	
Mass $\rho(1450)$ (charged)	$M_{\rho'}$	1428(30) MeV	[168]
Total width $\rho(770)$ (charged)	Γ_ρ	148.6(1.8) MeV	
Total width $\rho(1450)$ (charged)	$\Gamma_{\rho'}$	413(58) MeV	
Mass $\rho(770)$ (neutral)	M_ρ	775.02(35) MeV	
Mass $\rho(1450)$ (neutral)	$M_{\rho'}$	1493(15) MeV	[177]
Total width $\rho(770)$ (neutral)	Γ_ρ	149.59(67) MeV	
Total width $\rho(1450)$ (neutral)	$\Gamma_{\rho'}$	427(31) MeV	

Table E.1: Selected masses and decay widths from Ref. [99], in comparison to the ρ and ρ' parameters from Refs. [168, 177].

References

[1] L. D. Landau, Dokl. Akad. Nauk SSSR **60**, 207 (1948).

[2] C.-N. Yang, Phys. Rev. **77**, 242 (1950).

[3] G. Gidal *et al.* [MARK II], Phys. Rev. Lett. **59**, 2012 (1987).

[4] G. Gidal *et al.* [MARK II], Phys. Rev. Lett. **59**, 2016 (1987).

[5] H. Aihara *et al.* [TPC/Two Gamma], Phys. Rev. D **38**, 1 (1988).

[6] H. Aihara *et al.* [TPC/Two Gamma], Phys. Lett. B **209**, 107 (1988).

[7] P. Achard *et al.* [L3], Phys. Lett. B **526**, 269 (2002) [arXiv:hep-ex/0110073].

[8] P. Achard *et al.* [L3], JHEP **03**, 018 (2007).

[9] T. Aoyama *et al.*, Phys. Rept. **887**, 1 (2020) [arXiv:2006.04822 [hep-ph]].

[10] T. Aoyama, M. Hayakawa, T. Kinoshita, and M. Nio, Phys. Rev. Lett. **109**, 111808 (2012) [arXiv:1205.5370 [hep-ph]].

[11] T. Aoyama, T. Kinoshita, and M. Nio, Atoms **7**, 28 (2019).

[12] A. Czarnecki, W. J. Marciano, and A. Vainshtein, Phys. Rev. D **67**, 073006 (2003) [arXiv:hep-ph/0212229], [Erratum: Phys.Rev.D 73, 119901 (2006)].

[13] C. Gnendiger, D. Stöckinger, and H. Stöckinger-Kim, Phys. Rev. D **88**, 053005 (2013) [arXiv:1306.5546 [hep-ph]].

[14] M. Davier, A. Hoecker, B. Malaescu, and Z. Zhang, Eur. Phys. J. C **77**, 827 (2017) [arXiv:1706.09436 [hep-ph]].

[15] A. Keshavarzi, D. Nomura, and T. Teubner, Phys. Rev. D **97**, 114025 (2018) [arXiv:1802.02995 [hep-ph]].

[16] G. Colangelo, M. Hoferichter, and P. Stoffer, JHEP **02**, 006 (2019) [arXiv:1810.00007 [hep-ph]].

[17] M. Hoferichter, B.-L. Hoid, and B. Kubis, JHEP **08**, 137 (2019) [arXiv:1907.01556 [hep-ph]].

[18] M. Davier, A. Hoecker, B. Malaescu, and Z. Zhang, Eur. Phys. J. C **80**, 241 (2020) [arXiv:1908.00921 [hep-ph]], [Erratum: Eur.Phys.J.C 80, 410 (2020)].

[19] A. Keshavarzi, D. Nomura, and T. Teubner, Phys. Rev. D **101**, 014029 (2020) [arXiv:1911.00367 [hep-ph]].

[20] B.-L. Hoid, M. Hoferichter, and B. Kubis, Eur. Phys. J. C **80**, 988 (2020) [arXiv:2007.12696 [hep-ph]].

[21] A. Kurz, T. Liu, P. Marquard, and M. Steinhauser, Phys. Lett. B **734**, 144 (2014) [arXiv:1403.6400 [hep-ph]].

[22] K. Melnikov and A. Vainshtein, Phys. Rev. D **70**, 113006 (2004) [arXiv:hep-ph/0312226].

[23] P. Masjuan and P. Sánchez-Puertas, Phys. Rev. D **95**, 054026 (2017) [arXiv:1701.05829 [hep-ph]].

[24] G. Colangelo, M. Hoferichter, M. Procura, and P. Stoffer, Phys. Rev. Lett. **118**, 232001 (2017) [arXiv:1701.06554 [hep-ph]].

[25] G. Colangelo, M. Hoferichter, M. Procura, and P. Stoffer, JHEP **04**, 161 (2017) [arXiv:1702.07347 [hep-ph]].

[26] M. Hoferichter, B.-L. Hoid, B. Kubis, S. Leupold, and S. P. Schneider, Phys. Rev. Lett. **121**, 112002 (2018) [arXiv:1805.01471 [hep-ph]].

[27] M. Hoferichter, B.-L. Hoid, B. Kubis, S. Leupold, and S. P. Schneider, JHEP **10**, 141 (2018) [arXiv:1808.04823 [hep-ph]].

[28] A. Gérardin, H. B. Meyer, and A. Nyffeler, Phys. Rev. D **100**, 034520 (2019) [arXiv:1903.09471 [hep-lat]].

[29] J. Bijnens, N. Hermansson-Truedsson, and A. Rodríguez-Sánchez, Phys. Lett. B **798**, 134994 (2019) [arXiv:1908.03331 [hep-ph]].

[30] G. Colangelo, F. Hagelstein, M. Hoferichter, L. Laub, and P. Stoffer, Phys. Rev. D **101**, 051501 (2020) [arXiv:1910.11881 [hep-ph]].

[31] G. Colangelo, F. Hagelstein, M. Hoferichter, L. Laub, and P. Stoffer, JHEP **03**, 101 (2020) [arXiv:1910.13432 [hep-ph]].

[32] T. Blum, N. Christ, M. Hayakawa, T. Izubuchi, L. Jin, C. Jung, and C. Lehner, Phys. Rev. Lett. **124**, 132002 (2020) [arXiv:1911.08123 [hep-lat]].

[33] G. Colangelo, M. Hoferichter, A. Nyffeler, M. Passera, and P. Stoffer, Phys. Lett. B **735**, 90 (2014) [arXiv:1403.7512 [hep-ph]].

[34] G. W. Bennett *et al.* [Muon $g-2$], Phys. Rev. D **73**, 072003 (2006) [arXiv:hep-ex/0602035].

[35] B. Abi *et al.* [Muon $g-2$], Phys. Rev. Lett. **126**, 141801 (2021) [arXiv:2104.03281 [hep-ex]].

[36] T. Albahri *et al.* [Muon $g-2$], Phys. Rev. D **103**, 072002 (2021) [arXiv:2104.03247 [hep-ex]].

[37] T. Albahri *et al.* [Muon $g-2$], Phys. Rev. A **103**, 042208 (2021) [arXiv:2104.03201 [hep-ex]].

[38] T. Albahri *et al.* [Muon $g-2$], Phys. Rev. Accel. Beams **24**, 044002 (2021) [arXiv:2104.03240 [physics.acc-ph]].

[39] D. P. Aguillard *et al.* [Muon $g-2$], Phys. Rev. Lett. **131**, 161802 (2023) [arXiv:2308.06230 [hep-ex]].

[40] B. Chakraborty *et al.* [Fermilab Lattice, LATTICE-HPQCD, MILC], Phys. Rev. Lett. **120**, 152001 (2018) [arXiv:1710.11212 [hep-lat]].

[41] S. Borsanyi *et al.* [Budapest-Marseille-Wuppertal], Phys. Rev. Lett. **121**, 022002 (2018) [arXiv:1711.04980 [hep-lat]].

[42] T. Blum, P. A. Boyle, V. Gülpers, T. Izubuchi, L. Jin, C. Jung, A. Jüttner, C. Lehner, A. Portelli, and J. T. Tsang [RBC, UKQCD], Phys. Rev. Lett. **121**, 022003 (2018) [arXiv:1801.07224 [hep-lat]].

[43] D. Giusti, V. Lubicz, G. Martinelli, F. Sanfilippo, and S. Simula, Phys. Rev. D **99**, 114502 (2019) [arXiv:1901.10462 [hep-lat]].

[44] E. Shintani and Y. Kuramashi [PACS], Phys. Rev. D **100**, 034517 (2019) [arXiv:1902.00885 [hep-lat]].

[45] C. T. H. Davies *et al.* [Fermilab Lattice, LATTICE-HPQCD, MILC], Phys. Rev. D **101**, 034512 (2020) [arXiv:1902.04223 [hep-lat]].

[46] A. Gérardin, M. Cè, G. von Hippel, B. Hörz, H. B. Meyer, D. Mohler, K. Ottnad, J. Wilhelm, and H. Wittig, Phys. Rev. D **100**, 014510 (2019) [arXiv:1904.03120 [hep-lat]].

[47] C. Aubin, T. Blum, C. Tu, M. Golterman, C. Jung, and S. Peris, Phys. Rev. D **101**, 014503 (2020) [arXiv:1905.09307 [hep-lat]].

[48] D. Giusti and S. Simula, PoS **LATTICE2019**, 104 (2019) [arXiv:1910.03874 [hep-lat]].

[49] S. Borsanyi *et al.*, Nature **593**, 51 (2021) [arXiv:2002.12347 [hep-lat]].

[50] A. Crivellin, M. Hoferichter, C. A. Manzari, and M. Montull, Phys. Rev. Lett. **125**, 091801 (2020) [arXiv:2003.04886 [hep-ph]].

[51] A. Keshavarzi, W. J. Marciano, M. Passera, and A. Sirlin, Phys. Rev. D **102**, 033002 (2020) [arXiv:2006.12666 [hep-ph]].

[52] B. Malaescu and M. Schott, Eur. Phys. J. C **81**, 46 (2021) [arXiv:2008.08107 [hep-ph]].

[53] G. Colangelo, M. Hoferichter, and P. Stoffer, Phys. Lett. B **814**, 136073 (2021) [arXiv:2010.07943 [hep-ph]].

[54] J. Grange *et al.* [Muon $g-2$] [arXiv:1501.06858 [physics.ins-det]].

[55] M. Abe *et al.*, PTEP **2019**, 053C02 (2019) [arXiv:1901.03047 [physics.ins-det]].

[56] G. Colangelo *et al.* [arXiv:2203.15810 [hep-ph]].

[57] F. V. Ignatov *et al.* [CMD-3] [arXiv:2302.08834 [hep-ex]].

[58] F. V. Ignatov *et al.* [CMD-3] [arXiv:2309.12910 [hep-ex]].

[59] V. Pauk and M. Vanderhaeghen, Eur. Phys. J. C **74**, 3008 (2014) [arXiv:1401.0832 [hep-ph]].

[60] I. Danilkin and M. Vanderhaeghen, Phys. Rev. D **95**, 014019 (2017) [arXiv:1611.04646 [hep-ph]].

[61] F. Jegerlehner, *The Anomalous Magnetic Moment of the Muon*, Springer, 2017.

[62] M. Knecht, S. Narison, A. Rabemananjara, and D. Rabetiarivony, Phys. Lett. B **787**, 111 (2018) [arXiv:1808.03848 [hep-ph]].

[63] G. Eichmann, C. S. Fischer, and R. Williams, Phys. Rev. D **101**, 054015 (2020) [arXiv:1910.06795 [hep-ph]].

[64] P. Roig and P. Sánchez-Puertas, Phys. Rev. D **101**, 074019 (2020) [arXiv:1910.02881 [hep-ph]].

[65] M. Hoferichter, G. Colangelo, M. Procura, and P. Stoffer, Int. J. Mod. Phys. Conf. Ser. **35**, 1460400 (2014) [arXiv:1309.6877 [hep-ph]].

[66] G. Colangelo, M. Hoferichter, M. Procura, and P. Stoffer, JHEP **09**, 091 (2014) [arXiv:1402.7081 [hep-ph]].

[67] G. Colangelo, M. Hoferichter, B. Kubis, M. Procura, and P. Stoffer, Phys. Lett. B **738**, 6 (2014) [arXiv:1408.2517 [hep-ph]].

[68] G. Colangelo, M. Hoferichter, M. Procura, and P. Stoffer, JHEP **09**, 074 (2015) [arXiv:1506.01386 [hep-ph]].

[69] I. Danilkin, M. Hoferichter, and P. Stoffer, Phys. Lett. B **820**, 136502 (2021) [arXiv:2105.01666 [hep-ph]].

[70] S. Holz, C. Hanhart, M. Hoferichter, and B. Kubis, Eur. Phys. J. C **82**, 434 (2022) [arXiv:2202.05846 [hep-ph]], [Addendum: Eur. Phys. J. C **82**, 1159 (2022)].

[71] J. Lüdtke, M. Procura, and P. Stoffer, JHEP **04**, 125 (2023) [arXiv:2302.12264 [hep-ph]].

[72] R. García-Martín and B. Moussallam, Eur. Phys. J. C **70**, 155 (2010) [arXiv:1006.5373 [hep-ph]].

[73] M. Hoferichter, D. R. Phillips, and C. Schat, Eur. Phys. J. C **71**, 1743 (2011) [arXiv:1106.4147 [hep-ph]].

[74] B. Moussallam, Eur. Phys. J. C **73**, 2539 (2013) [arXiv:1305.3143 [hep-ph]].

[75] I. Danilkin and M. Vanderhaeghen, Phys. Lett. B **789**, 366 (2019) [arXiv:1810.03669 [hep-ph]].

[76] M. Hoferichter and P. Stoffer, JHEP **07**, 073 (2019) [arXiv:1905.13198 [hep-ph]].

[77] I. Danilkin, O. Deineka, and M. Vanderhaeghen, Phys. Rev. D **101**, 054008 (2020) [arXiv:1909.04158 [hep-ph]].

[78] M. Knecht, JHEP **08**, 056 (2020) [arXiv:2005.09929 [hep-ph]].

[79] J. Lüdtke and M. Procura, Eur. Phys. J. C **80**, 1108 (2020) [arXiv:2006.00007 [hep-ph]].

[80] J. Bijnens, N. Hermansson-Truedsson, L. Laub, and A. Rodríguez-Sánchez, JHEP **10**, 203 (2020) [arXiv:2008.13487 [hep-ph]].

[81] J. Bijnens, N. Hermansson-Truedsson, L. Laub, and A. Rodríguez-Sánchez, JHEP **04**, 240 (2021) [arXiv:2101.09169 [hep-ph]].

[82] G. Colangelo, F. Hagelstein, M. Hoferichter, L. Laub, and P. Stoffer, Eur. Phys. J. C **81**, 702 (2021) [arXiv:2106.13222 [hep-ph]].

[83] J. Bijnens, N. Hermansson-Truedsson, and A. Rodríguez-Sánchez, JHEP **02**, 167 (2023) [arXiv:2211.17183 [hep-ph]].

[84] J. Leutgeb and A. Rebhan, Phys. Rev. D **101**, 114015 (2020) [arXiv:1912.01596 [hep-ph]].

[85] L. Cappiello, O. Catà, G. D'Ambrosio, D. Greynat, and A. Iyer, Phys. Rev. D **102**, 016009 (2020) [arXiv:1912.02779 [hep-ph]].

[86] P. Masjuan, P. Roig, and P. Sánchez-Puertas, J. Phys. G **49**, 015002 (2022) [arXiv:2005.11761 [hep-ph]].

[87] J. Leutgeb, J. Mager, and A. Rebhan, Phys. Rev. D **107**, 054021 (2023) [arXiv:2211.16562 [hep-ph]].

[88] E.-H. Chao, R. J. Hudspith, A. Gérardin, J. R. Green, H. B. Meyer, and K. Ottnad, Eur. Phys. J. C **81**, 651 (2021) [arXiv:2104.02632 [hep-lat]].

[89] E.-H. Chao, R. J. Hudspith, A. Gérardin, J. R. Green, and H. B. Meyer, Eur. Phys. J. C **82**, 664 (2022) [arXiv:2204.08844 [hep-lat]].

[90] T. Blum, N. Christ, M. Hayakawa, T. Izubuchi, L. Jin, C. Jung, C. Lehner, and C. Tu [RBC, UKQCD] [arXiv:2304.04423 [hep-lat]].

[91] C. Alexandrou *et al.* [ETM], Phys. Rev. D **108**, 054509 (2023) [arXiv:2212.06704 [hep-lat]].

[92] A. Gérardin *et al.* [BMWc] [arXiv:2305.04570 [hep-lat]].

[93] M. Hoferichter and P. Stoffer, JHEP **05**, 159 (2020) [arXiv:2004.06127 [hep-ph]].

[94] W. A. Bardeen and W. K. Tung, Phys. Rev. **173**, 1423 (1968), [Erratum: Phys.Rev.D 4, 3229–3229 (1971)].

[95] R. Tarrach, Nuovo Cim. A **28**, 409 (1975).

[96] G. P. Lepage and S. J. Brodsky, Phys. Lett. B **87**, 359 (1979).

[97] G. P. Lepage and S. J. Brodsky, Phys. Rev. D **22**, 2157 (1980).

[98] S. J. Brodsky and G. P. Lepage, Phys. Rev. D **24**, 1808 (1981).

[99] P. A. Zyla *et al.* [Particle Data Group], PTEP **2020**, 083C01 (2020).

[100] D. V. Amelin *et al.*, Z. Phys. C **66**, 71 (1995).

[101] S. I. Bityukov *et al.*, Phys. Lett. B **203**, 327 (1988).

[102] M. N. Achasov *et al.* [SND], Phys. Lett. B **800**, 135074 (2020) [arXiv:1906.03838 [hep-ex]].

[103] F. Niecknig, B. Kubis, and S. P. Schneider, Eur. Phys. J. C **72**, 2014 (2012) [arXiv:1203.2501 [hep-ph]].

[104] S. P. Schneider, B. Kubis, and F. Niecknig, Phys. Rev. D **86**, 054013 (2012) [arXiv:1206.3098 [hep-ph]].

[105] M. Hoferichter, B. Kubis, and D. Sakkas, Phys. Rev. D **86**, 116009 (2012) [arXiv:1210.6793 [hep-ph]].

[106] M. Hoferichter, B. Kubis, S. Leupold, F. Niecknig, and S. P. Schneider, Eur. Phys. J. C **74**, 3180 (2014) [arXiv:1410.4691 [hep-ph]].

[107] M. Hoferichter, B.-L. Hoid, B. Kubis, and J. Lüdtke, Phys. Rev. Lett. **128**, 172004 (2022) [arXiv:2105.04563 [hep-ph]].

[108] F. Stollenwerk, C. Hanhart, A. Kupść, U.-G. Meißner, and A. Wirzba, Phys. Lett. B **707**, 184 (2012) [arXiv:1108.2419 [nucl-th]].

[109] C. Hanhart, A. Kupść, U.-G. Meißner, F. Stollenwerk, and A. Wirzba, Eur. Phys. J. C **73**, 2668 (2013) [arXiv:1307.5654 [hep-ph]], [Erratum: Eur.Phys.J.C 75, 242 (2015)].

[110] B. Kubis and J. Plenter, Eur. Phys. J. C **75**, 283 (2015) [arXiv:1504.02588 [hep-ph]].

[111] S. Holz, J. Plenter, C.-W. Xiao, T. Dato, C. Hanhart, B. Kubis, U.-G. Meißner, and A. Wirzba, Eur. Phys. J. C **81**, 1002 (2021) [arXiv:1509.02194 [hep-ph]].

[112] L. Gan, B. Kubis, E. Passemar, and S. Tulin, Phys. Rept. **945**, 1 (2022) [arXiv:2007.00664 [hep-ph]].

[113] A. S. Rudenko, Phys. Rev. D **96**, 076004 (2017) [arXiv:1707.00545 [hep-ph]].

[114] A. I. Milstein and A. S. Rudenko, Phys. Lett. B **800**, 135117 (2020) [arXiv:1909.07938 [hep-ph]].

[115] M. Zanke, Master's thesis, University of Bonn (2020).

[116] J. Olsson, Nucl. Phys. B Proc. Suppl. **3**, 613 (1988).

[117] K.-C. Yang, JHEP **10**, 108 (2005) [arXiv:hep-ph/0509337].

[118] K.-C. Yang, Nucl. Phys. B **776**, 187 (2007) [arXiv:0705.0692 [hep-ph]].

[119] A. S. Gorsky, Yad. Fiz. **46**, 938 (1987).

[120] A. V. Manohar, Phys. Lett. B **244**, 101 (1990).

[121] C. W. Bauer, S. Fleming, D. Pirjol, I. Z. Rothstein, and I. W. Stewart, Phys. Rev. D **66**, 014017 (2002) [arXiv:hep-ph/0202088].

[122] I. Z. Rothstein, Phys. Rev. D **70**, 054024 (2004) [arXiv:hep-ph/0301240].

[123] Y. Grossman, M. König, and M. Neubert, JHEP **04**, 101 (2015) [arXiv:1501.06569 [hep-ph]].

[124] V. M. Braun, G. P. Korchemsky, and D. Müller, Prog. Part. Nucl. Phys. **51**, 311 (2003) [arXiv:hep-ph/0306057].

[125] J. J. Sakurai, Annals Phys. **11**, 1 (1960).

[126] J. J. Sakurai, *Currents and Mesons*, University of Chicago Press, 1969.

[127] L. G. Landsberg, Phys. Rept. **128**, 301 (1985).

[128] U.-G. Meißner, Phys. Rept. **161**, 213 (1988).

[129] F. Klingl, N. Kaiser, and W. Weise, Z. Phys. A **356**, 193 (1996) [arXiv:hep-ph/9607431].

[130] S.-s. Fang, B. Kubis, and A. Kupść, Prog. Part. Nucl. Phys. **120**, 103884 (2021) [arXiv:2102.05922 [hep-ph]].

[131] H. Leutwyler, *Electromagnetic form-factor of the pion* in *Continuous Advances in QCD 2002/Arkadyfest (honoring the 60th birthday of Prof. Arkady Vainshtein)*, pp. 23–40 (2002) [arXiv:hep-ph/0212324].

[132] C. Hanhart, Phys. Lett. B **715**, 170 (2012) [arXiv:1203.6839 [hep-ph]].

[133] C. Adolph *et al.* [COMPASS], Phys. Rev. D **95**, 032004 (2017) [arXiv:1509.00992 [hep-ex]].

[134] F. Von Hippel and C. Quigg, Phys. Rev. D **5**, 624 (1972).

[135] A. Khodjamirian, Eur. Phys. J. C **6**, 477 (1999) [arXiv:hep-ph/9712451].

[136] G. A. Schuler, F. A. Berends, and R. van Gulik, Nucl. Phys. B **523**, 423 (1998) [arXiv:hep-ph/9710462].

[137] F.-K. Guo, B. Kubis, and A. Wirzba, Phys. Rev. D **85**, 014014 (2012) [arXiv:1111.5949 [hep-ph]].

[138] T. Hahn, Comput. Phys. Commun. **168**, 78 (2005) [arXiv:hep-ph/0404043].

[139] R. Mertig, M. Bohm, and A. Denner, Comput. Phys. Commun. **64**, 345 (1991).

[140] V. Shtabovenko, R. Mertig, and F. Orellana, Comput. Phys. Commun. **207**, 432 (2016) [arXiv:1601.01167 [hep-ph]].

[141] V. Shtabovenko, R. Mertig, and F. Orellana, Comput. Phys. Commun. **256**, 107478 (2020) [arXiv:2001.04407 [hep-ph]].

[142] V. Shtabovenko, Comput. Phys. Commun. **218**, 48 (2017) [arXiv:1611.06793 [physics.comp-ph]].

[143] A. V. Smirnov, Comput. Phys. Commun. **189**, 182 (2015) [arXiv:1408.2372 [hep-ph]].

[144] H. H. Patel, Comput. Phys. Commun. **197**, 276 (2015) [arXiv:1503.01469 [hep-ph]].

[145] T. Hahn and M. Pérez-Victoria, Comput. Phys. Commun. **118**, 153 (1999) [arXiv:hep-ph/9807565].

[146] T. A. Armstrong *et al.* [WA76], Z. Phys. C **43**, 55 (1989).

[147] T. A. Armstrong *et al.* [WA76], Phys. Lett. B **228**, 536 (1989).

[148] D. Barberis *et al.* [WA102], Phys. Lett. B **413**, 225 (1997) [arXiv:hep-ex/9707022].

[149] A. Gurtu *et al.* [Amsterdam-CERN-Nijmegen-Oxford], Nucl. Phys. B **151**, 181 (1979).

[150] T. Bolton *et al.*, Phys. Lett. B **278**, 495 (1992).

[151] D. Coffman *et al.* [MARK-III], Phys. Rev. D **41**, 1410 (1990).

[152] M. J. Corden *et al.*, Nucl. Phys. B **144**, 253 (1978).

[153] R. Dickson *et al.* [CLAS], Phys. Rev. C **93**, 065202 (2016) [arXiv:1604.07425 [nucl-ex]].

[154] D. Barberis *et al.* [WA102], Phys. Lett. B **440**, 225 (1998) [arXiv:hep-ex/9810003].

[155] J. H. Campbell, S. Lichtman, F. J. Loeffler, D. H. Miller, R. J. Miller, W. J. Miller, and R. B. Willmann, Phys. Rev. Lett. **22**, 1204 (1969).

[156] C. Defoix, A. Do Nascimento, J. S. O' Neall, J. Siaud, R. Bizzarri, L. Dobrzynski, S. N. Ganguli, L. Montanet, S. Reucroft, and T. Yamagata, Nucl. Phys. B **44**, 125 (1972).

[157] T. A. Armstrong *et al.* [WA76], Z. Phys. C **54**, 371 (1992).

[158] K. Hikasa *et al.* [Particle Data Group], Phys. Rev. D **45**, S1 (1992), [Erratum: Phys.Rev.D 46, 5210 (1992)].

[159] S. I. Bityukov *et al.*, Sov. J. Nucl. Phys. **54**, 318 (1991).

[160] J. Babcock and J. L. Rosner, Phys. Rev. D **14**, 1286 (1976).

[161] S. Ishida, K. Yamada, and M. Oda, Phys. Rev. D **40**, 1497 (1989).

[162] M. F. M. Lutz and S. Leupold, Nucl. Phys. A **813**, 96 (2008) [arXiv:0801.3821 [nucl-th]].

[163] A. A. Osipov and M. K. Volkov, Phys. Rev. D **97**, 074020 (2018) [arXiv:1801.08192 [hep-ph]].

[164] M. Ablikim *et al.* [BESIII], Chin. Phys. C **44**, 040001 (2020) [arXiv:1912.05983 [hep-ex]].

[165] W. Altmannshofer *et al.* [Belle-II], PTEP **2019**, 123C01 (2019) [arXiv:1808.10567 [hep-ex]], [Erratum: PTEP 2020, 029201 (2020)].

[166] M. Hoferichter, B. Kubis, and M. Zanke, Phys. Rev. D **96**, 114016 (2017) [arXiv:1710.00824 [hep-ph]].

[167] R. García-Martín, R. Kamiński, J. R. Peláez, and J. Ruiz de Elvira, Phys. Rev. Lett. **107**, 072001 (2011) [arXiv:1107.1635 [hep-ph]].

[168] M. Fujikawa *et al.* [Belle], Phys. Rev. D **78**, 072006 (2008) [arXiv:0805.3773 [hep-ex]].

[169] P. Roig, Nucl. Phys. B Proc. Suppl. **225-227**, 161 (2012) [arXiv:1112.0962 [hep-ph]].

[170] M. N. Achasov *et al.*, Phys. Rev. D **94**, 112001 (2016) [arXiv:1610.00235 [hep-ex]].

[171] G. R. Farrar and D. R. Jackson, Phys. Rev. Lett. **35**, 1416 (1975).

[172] A. I. Vainshtein and V. I. Zakharov, Phys. Lett. B **72**, 368 (1978).

[173] E. A. Kozyrev *et al.*, EPJ Web Conf. **212**, 03008 (2019).

[174] R. R. Akhmetshin *et al.* [CMD-2], Phys. Lett. B **466**, 392 (1999) [arXiv:hep-ex/9904024].

[175] J. Wess and B. Zumino, Phys. Lett. B **37**, 95 (1971).

[176] E. Witten, Nucl. Phys. B **223**, 422 (1983).

[177] J. P. Lees *et al.* [BaBar], Phys. Rev. D **86**, 032013 (2012) [arXiv:1205.2228 [hep-ex]].

Addendum to Part I

Axial-vector transition form factors and $e^+e^- \to f_1\pi^+\pi^-$

based on a project

in collaboration with
Martin Hoferichter and Bastian Kubis

published in
JHEP **08**, 209 (2023) [arXiv:2307.14413 [hep-ph]]

Prologue

With the publication of Ref. [32], the author of this thesis calculated the cross section of the process $e^+e^- \to f_1\pi^+\pi^-$ within the framework established in Part I. This cross section had been measured by the BaBar collaboration in the year 2007 [11], where the f_1 was observed in the decay $f_1 \to \eta\pi^+\pi^-$, and, rather recently, in 2022 [12], with an f_1 signal reported in the channel $f_1 \to K_S^0 K^\pm\pi^\mp$. Although the analysis presented in Ref. [32] suggests that the cross section for $e^+e^- \to f_1\pi^+\pi^-$ displays prominent resonance features from excited ρ resonances not included in the parameterization proposed in Part I, such as the $\rho(2150)$, the underlying formalism ought to largely respect the data when the latter is interpreted as an upper limit, in particular in the asymptotic regime. Contrary to this constraint, however, the cross section that the author of this dissertation calculated exceeded the data by at least an order of magnitude. By a thorough investigation and from insightful discussions with Martin Hoferichter and Bastian Kubis, the author was able to identify the major reason for this mismatch to be related to the asymptotic behavior of the transition form factors in the singly-fixed direction, *i.e.*, in kinematic configurations with one virtuality kept fixed at a finite but non-zero value.[¶] The idea to use the $e^+e^- \to f_1\pi^+\pi^-$ data as an upper bound on the non-resonant background then evolved further into the revised analysis presented in this addendum. Crucially, besides implying stringent limits on the high-energy behavior of the transition form factors, the inclusion of the $e^+e^- \to f_1\pi^+\pi^-$ data within an improved vector-meson-dominance framework allows for an unambiguous determination of the couplings corresponding to the two antisymmetric TFFs.

The fundamental ideas for the refined parameterizations considered in this addendum were developed in joint efforts by the author of this dissertation, Martin Hoferichter, and Bastian Kubis during a one-week visit of Martin Hoferichter to the University of Bonn. More specifically, this concerns the assessment of the minimal particle content necessary to construct transition form factors in a vector-meson-dominance framework that individually obey the asymptotic constraints predicted by the light-cone expansion [8], in particular with regard to the steep decrease in the singly-fixed direction required by the $e^+e^- \to f_1\pi^+\pi^-$ data [11, 12]. Ultimately, and with the aim to treat the isovector and isoscalar components of the transition form factors equally, this required the inclusion of yet another multiplet of isovector and isoscalar vector mesons.

After an extensive discussion of the revised parameterizations and an analysis of

[¶]Limits of this type have not been analyzed in Part I at all, where, instead, only the singly- and doubly-virtual limits of the transition form factors were considered. Besides the issue in the singly-fixed direction, there is also some potential finetuning involved in this parameterization, given that two of the form factors are intertwined according to Eq. (3.35). Note furthermore that the isovector and isoscalar transition form factors were not treated equally in Part I, since no extended vector-meson-dominance parameterization was constructed for the isoscalar component therein.

their asymptotic properties, formulae for the observables related to $e^+e^- \to e^+e^- f_1$ [4], $f_1 \to V\gamma$ [1–3], $V = \rho, \omega, \phi$, and $f_1 \to e^+e^-$ [5] are derived by the author of this thesis, which is done in close analogy to Part I. While the $f_1 \to e^+e^-$ calculation is performed via a PASSARINO–VELTMAN reduction by the author, carried out and evaluated in an automated way using *FeynCalc* [42–44] and *Collier* [45–48], Martin HOFERICHTER contributed an independent cross-check of those results by using the analytic expressions—obtained in a direct way by introducing FEYNMAN parameters—provided in Part I.[‖] Furthermore, the calculation of the $e^+e^- \to f_1\pi^+\pi^-$ cross section within the refined vector-meson-dominance framework is outlined in great detail by the author of this dissertation. With the compiled constraints, a combined phenomenological analysis is performed in terms of a χ^2 fit; here, the author benefitted, in particular, from discussions with Martin HOFERICHTER and Bastian KUBIS on how to include the $e^+e^- \to f_1\pi^+\pi^-$ data in the fit in a meaningful way. Finally, under the assumption of U(3) symmetry, parameterizations for the transition form factors of the f_1' and a_1 are proposed by the author, where the assistance of Martin HOFERICHTER proved valuable in constructing, especially, the form factors of the a_1, given its different isospin structure and the resulting intricacy.[×]

[‖] The native Fortran library *Collier* is used in C++ through the interface published in Ref. [49], to the development of which the author of this dissertation made significant contributions.

[×] Note also that all plots in this addendum have been created by the author of this dissertation.

Chapter 8

Introduction

With the compilation of the constraints on the f_1 TFFs that follow from the radiative decays $f_1 \to \rho\gamma$ [1, 2] and $f_1 \to \phi\gamma$ [1, 3] as well as $e^+e^- \to e^+e^- f_1$ [4] and $f_1 \to e^+e^-$ [5] in Part I, we improved on previous work [6, 7] by employing parameterizations that ensure the absence of kinematic singularities [8–10], include short-distance constraints [8], and incorporate the spectral functions of the isovector resonances. However, our conclusion was that the exploited data is not sufficient to identify a unique solution for all three TFFs; especially the normalizations of the two antisymmetric TFFs and the momentum dependence of all three TFFs were only poorly determined. In the future, these limitations could be overcome by better data for $e^+e^- \to e^+e^- f_1$ and $f_1 \to e^+e^-$, the latter process, in particular, being a very interesting observable, yet not at the current level of precision [5]; in this addendum, we instead propose to study existing data for $e^+e^- \to f_1\pi^+\pi^-$ [11, 12].[20] This process is also sensitive to all three TFFs, for one photon virtuality centered at the ρ mass and the other one determined by the center-of-mass energy of the e^+e^- pair. Phenomenologically, the reaction displays prominent resonance features from excited ρ resonances [32], primarily the $\rho(2150)$, but, when interpreted as a limit on the non-resonant contribution, entails powerful constraints on the TFFs of the f_1, both on the asymptotic behavior and the respective normalizations.

The outline of this addendum is as follows: in Ch. 9, we define improved VMD parameterizations that implement the asymptotic behavior observed in $e^+e^- \to f_1\pi^+\pi^-$. We then summarize the relevant observables in the new VMD framework and present the formalism in which we will analyze $e^+e^- \to f_1\pi^+\pi^-$ in Ch. 10. The phenomenological analysis, including a review of the data base, a global fit, and a summary of the resulting TFF parameterizations, will be presented in Ch. 11, before concluding in Ch. 12. Finally, in App. F, we collect the constants and parameters used throughout this addendum.

[20] The measurement of the $e^+e^- \to 2(\pi^+\pi^-)\eta$ [11] and $e^+e^- \to K_S K^\pm\pi^\mp\pi^+\pi^-$ [12] cross sections, in which the f_1 peak can be identified, is partly motivated by HVP. The impact of such high-multiplicity channels on the HVP contribution to a_μ, though, is much smaller than the current tensions observed between data-driven evaluations [13–24] and lattice QCD [25–29], *e.g.*, $a_\mu^{\text{HVP}}[2(\pi^+\pi^-)\eta] = 0.8(1)\times 10^{-11}$ [18], which is at the same level as potential uncertainties from $\mathcal{O}(\alpha^4)$ hadronic corrections [30]. The CMD-3 measurement of $e^+e^- \to 3(\pi^+\pi^-)\pi^0$ [31] includes results for $e^+e^- \to 2(\pi^+\pi^-)\eta$ but no additional information on $e^+e^- \to f_1\pi^+\pi^-$.

Chapter 9

Vector-meson dominance

The minimal particle content necessary for a VMD construction of TFFs that individually obey the asymptotic constraints [8] discussed in Sec. 3.4 requires the inclusion of three multiplets. More specifically, we will use ρ, ρ', and ρ'' for the isovector contributions and ω, ω', ω'' as well as ϕ, ϕ', ϕ'' for the isoscalar contributions. The introduction of a third multiplet, as required to obtain the correct asymptotic behavior for the antisymmetric TFFs, goes beyond the parameterizations of Ch. 3, ultimately, because the data on $e^+e^- \to f_1\pi^+\pi^-$ demands such a steep decrease, including in kinematic configurations in which one virtuality is kept fixed at a finite but non-zero value.

9.1 Isovector contributions

In the space-like region, $q_i^2 < 0$, we propose to extend the isovector parameterizations from Sec. 3.2 as follows:

$$\begin{aligned}
\mathcal{F}^{I=1}_{\mathrm{a}_{1/2}}(q_1^2,q_2^2) &= C_{\mathrm{a}_{1/2}}\Bigg[\frac{(1-\epsilon^{(1)}_{\mathrm{a}_{1/2}}-\epsilon^{(2)}_{\mathrm{a}_{1/2}})M_\rho^2 M_{\rho'}^2}{(q_1^2-M_\rho^2)(q_2^2-M_{\rho'}^2)}+\frac{\epsilon^{(1)}_{\mathrm{a}_{1/2}}M_\rho^2 M_{\rho''}^2}{(q_1^2-M_\rho^2)(q_2^2-M_{\rho''}^2)}\\
&\qquad+\frac{\epsilon^{(2)}_{\mathrm{a}_{1/2}}M_{\rho'}^2 M_{\rho''}^2}{(q_1^2-M_{\rho'}^2)(q_2^2-M_{\rho''}^2)}\Bigg]-(q_1\leftrightarrow q_2),\\
\mathcal{F}^{I=1}_{\mathrm{s}}(q_1^2,q_2^2) &= C_{\mathrm{s}}\Bigg[\frac{(1-\epsilon^{(1)}_{\mathrm{s}}-\epsilon^{(2)}_{\mathrm{s}})M_\rho^4}{(q_1^2-M_\rho^2)(q_2^2-M_\rho^2)}+\frac{(\epsilon^{(1)}_{\mathrm{s}}/2)M_\rho^2 M_{\rho'}^2}{(q_1^2-M_\rho^2)(q_2^2-M_{\rho'}^2)}\\
&\qquad+\frac{(\epsilon^{(1)}_{\mathrm{s}}/2)M_{\rho'}^2 M_\rho^2}{(q_1^2-M_{\rho'}^2)(q_2^2-M_\rho^2)}+\frac{\epsilon^{(2)}_{\mathrm{s}}M_{\rho'}^4}{(q_1^2-M_{\rho'}^2)(q_2^2-M_{\rho'}^2)}\Bigg],
\end{aligned}\tag{9.1}$$

first given in this form to emphasize that, upon a partial-fraction decomposition, each term corresponds to adding vector-meson propagators with fixed coefficients. To implement the correct singly-virtual asymptotic behavior, we choose

$$\begin{aligned}
\epsilon^{(1)}_{\mathrm{a}_{1/2}} &= -\frac{M_{\rho'}^2}{M_{\rho''}^2-M_{\rho'}^2+M_\rho^2}, & \epsilon^{(2)}_{\mathrm{a}_{1/2}} &= \frac{M_\rho^2}{M_{\rho''}^2-M_{\rho'}^2+M_\rho^2},\\
\epsilon^{(1)}_{\mathrm{s}} &= -\frac{2M_\rho^2 M_{\rho'}^2}{(M_{\rho'}^2-M_\rho^2)^2}, & \epsilon^{(2)}_{\mathrm{s}} &= \frac{M_\rho^4}{(M_{\rho'}^2-M_\rho^2)^2},
\end{aligned}\tag{9.2}$$

leading to

$$\mathcal{F}^{I=1}_{\mathrm{a}_{1/2}}(q_1^2,q_2^2) = \frac{C_{\mathrm{a}_{1/2}}\zeta_\rho M_\rho^4 M_{\rho'}^4 M_{\rho''}^4 (q_1^2-q_2^2)}{(q_1^2-M_\rho^2)(q_2^2-M_\rho^2)(q_1^2-M_{\rho'}^2)(q_2^2-M_{\rho'}^2)(q_1^2-M_{\rho''}^2)(q_2^2-M_{\rho''}^2)},$$
$$\mathcal{F}^{I=1}_{\mathrm{s}}(q_1^2,q_2^2) = \frac{C_{\mathrm{s}} M_\rho^4 M_{\rho'}^4}{(q_1^2-M_\rho^2)(q_2^2-M_\rho^2)(q_1^2-M_{\rho'}^2)(q_2^2-M_{\rho'}^2)}, \tag{9.3}$$

with

$$\zeta_V = \frac{(M_{V''}^2-M_{V'}^2)(M_{V''}^2-M_V^2)(M_{V'}^2-M_V^2)}{M_{V''}^2 M_{V'}^2 M_V^2 (M_{V''}^2-M_{V'}^2+M_V^2)}. \tag{9.4}$$

The resulting asymptotic behavior of the TFFs becomes

$$\mathcal{F}^{I=1}_{\mathrm{a}_{1/2}}(q_1^2,q_2^2) \propto \frac{1}{q_2^4}, \qquad \mathcal{F}^{I=1}_{\mathrm{a}_{1/2}}(q^2,\lambda q^2) \propto \frac{1-\lambda}{\lambda^3}\frac{1}{q^{10}},$$
$$\mathcal{F}^{I=1}_{\mathrm{s}}(q_1^2,q_2^2) \propto \frac{1}{q_2^4}, \qquad \mathcal{F}^{I=1}_{\mathrm{s}}(q^2,\lambda q^2) \propto \frac{1}{q^8}, \tag{9.5}$$

with q_1^2 fixed to a finite value distinct from q_2^2 (*left*) and in the doubly-virtual direction (*right*). Crucially, the singly-virtual asymptotics now match the LCE result from Sec. 3.4 for arbitrary fixed q_1^2, which, for $q_1^2 = M_\rho^2$, is mandatory for a realistic description of the $e^+e^- \to f_1\pi^+\pi^-$ data (the opposite case with fixed q_2^2 follows from symmetry).[21] For time-like applications, the replacements $M^2 \to M^2 - \mathrm{i}M\Gamma$ apply in the denominators of Eq. (9.3), *i.e.*, after imposing the asymptotic behavior of the TFFs; due to the large widths of the ρ-like mesons, a narrow-width approximation, $M^2 \to M^2 - \mathrm{i}\epsilon$ in the denominators, in general becomes insufficient here. A consequence of the faster decrease in the singly-virtual directions concerns an even faster decrease in the doubly-virtual case, much below the LCE expectation. Accordingly, in the final representation for the TFFs, we add the asymptotic contribution [8, 33–35]

$$\mathcal{F}^{\mathrm{asym}}_{\mathrm{a}_2}(q_1^2,q_2^2) = 3F^{\mathrm{eff}}_{f_1} m_{f_1}^3 (q_1^2-q_2^2) \int_{s_\mathrm{m}}^\infty \mathrm{d}x\, \frac{q_1^2q_2^2 - x^2 + x(q_1^2+q_2^2)}{(x-q_1^2)^3(x-q_2^2)^3},$$
$$\mathcal{F}^{\mathrm{asym}}_{\mathrm{s}}(q_1^2,q_2^2) = 3F^{\mathrm{eff}}_{f_1} m_{f_1}^3 \int_{s_\mathrm{m}}^\infty \mathrm{d}x\, \frac{(q_1^2+q_2^2)(x^2-q_1^2q_2^2) - x(q_1^2-q_2^2)^2}{(x-q_1^2)^3(x-q_2^2)^3}, \tag{9.6}$$

as derived in Sec. 3.4, where s_m is a parameter that determines the scale of the transition. The implementation of these asymptotic contributions, or their variant including mass effects, see App. A, becomes relevant for the axial-vector contributions in the HLbL loop integral. Here, we focus on the determination of the low-energy couplings in the VMD component of the parameterization, as can be obtained from, *inter alia*, $e^+e^- \to f_1\pi^+\pi^-$.

[21] For $\mathcal{F}^{I=1}_{\mathrm{a}_1}(q_1^2,q_2^2)$, the LCE predicts an even faster decrease in the singly-virtual direction, but we do not consider yet another multiplet for the following reasons: (i) information from the LCE on this TFF is limited, *i.e.*, no non-vanishing contribution survives at $\mathcal{O}(1/Q^4)$, in such a way that, in contrast to the other TFFs, we cannot add an LCE term to repair the behavior in the doubly-virtual direction and thus need to choose a compromise; (ii) the fit to $e^+e^- \to f_1\pi^+\pi^-$ produces a small coupling C_{a_1}, in line with the LCE suppression; (iii) another multiplet would have a mass already in the energy range in which the data is to be described, so that no meaningful suppression could be generated even when introducing another state.

9.2 Isoscalar contributions

In complete analogy to the above, the isoscalar parts of the form factors are parameterized according to[22]

$$\mathcal{F}^{I=0}_{\mathrm{a}_{1/2}}(q_1^2,q_2^2) = \sum_{V=\omega,\phi} \frac{C^V_{\mathrm{a}_{1/2}}\zeta_V M_V^4 M_{V'}^4 M_{V''}^4 (q_1^2-q_2^2)}{(q_1^2-M_V^2)(q_2^2-M_V^2)(q_1^2-M_{V'}^2)(q_2^2-M_{V'}^2)(q_1^2-M_{V''}^2)(q_2^2-M_{V''}^2)},$$
$$\mathcal{F}^{I=0}_{\mathrm{s}}(q_1^2,q_2^2) = \sum_{V=\omega,\phi} \frac{C^V_{\mathrm{s}} M_V^4 M_{V'}^4}{(q_1^2-M_V^2)(q_2^2-M_V^2)(q_1^2-M_{V'}^2)(q_2^2-M_{V'}^2)}, \tag{9.7}$$

with the same asymptotic properties as in Eq. (9.5). Again, time-like applications imply the replacements $M^2 \to M^2 - \mathrm{i}M\Gamma$ in the denominators since the large widths of the excited isoscalar resonances do not allow for a narrow-width approximation. Finally, under the assumption of U(3) symmetry, the isoscalar coupling constants can be related to the isovector analogs, leading to the same approximations as in Sec. 3.3,

$$R^\omega = \frac{C^\omega_{\mathrm{a}_{1/2}}}{C_{\mathrm{a}_{1/2}}} = \frac{C^\omega_{\mathrm{s}}}{C_{\mathrm{s}}} = \frac{1}{9},$$
$$R^\phi = \frac{C^\phi_{\mathrm{a}_{1/2}}}{C_{\mathrm{a}_{1/2}}} = \frac{C^\phi_{\mathrm{s}}}{C_{\mathrm{s}}} = \frac{2\sqrt{2}}{9}\cot(\theta_A+\theta_1) = -0.158(34), \tag{9.8}$$

with $\theta_1 = \arctan\sqrt{2} = (\pi+2\theta_0)/4$, $\theta_0 = \arcsin(1/3)$, and $\theta_A = 62(5)^\circ$ [4, 36].

[22] We assume ideal mixing for the vector mesons, which prevents crossed terms involving ω and ϕ states.

Chapter 10

Observables

10.1 $e^+e^- \to e^+e^- f_1$

Within the modified VMD framework, the determination of the normalization of the symmetric TFF via the equivalent two-photon decay width, Eq. (3.3), naturally remains unchanged. Taking into account the isoscalar contributions, $|\mathcal{F}_{\rm s}^{I=1}(0,0) + \mathcal{F}_{\rm s}^{I=0}(0,0)| = (1 + R^\omega + R^\phi)|C_{\rm s}| = 0.953(34)|C_{\rm s}|$, we thus carry over Eq. (4.7),

$$C_{\rm s} = 0.93(11), \tag{10.1}$$

adopting the sign convention established in Part I.

The singly-virtual VMD limits can be further constrained according to Eq. (4.11), where matching the slopes at $q^2 = 0$ with the parameterizations from this addendum leads to

$$\begin{aligned}\frac{2}{\Lambda_{\rm D}^2} = \frac{1}{N_{\omega\phi}}\Bigg[&\frac{1}{M_\rho^2} + \frac{1}{M_{\rho'}^2} + R^\omega\left(\frac{1}{M_\omega^2} + \frac{1}{M_{\omega'}^2}\right) + R^\phi\left(\frac{1}{M_\phi^2} + \frac{1}{M_{\phi'}^2}\right) \\ &+ (\zeta_\rho + \zeta_\omega R^\omega + \zeta_\phi R^\phi)\frac{C_{\rm a_1} + C_{\rm a_2}}{C_{\rm s}} - \frac{m_{f_1}^2(\zeta_\rho + \zeta_\omega R^\omega + \zeta_\phi R^\phi)^2}{N_{\omega\phi}}\left(\frac{C_{\rm a_1}}{C_{\rm s}}\right)^2\Bigg].\end{aligned} \tag{10.2}$$

Here, the factor $N_{\omega\phi} = 1 + R^\omega + R^\phi$ accounts for the isoscalar terms in the normalization and $\Lambda_{\rm D} = 1.04(6)(5)\,\text{GeV}$ [4] is as specified in Eq. (4.2).

10.2 $f_1 \to \rho\gamma$ and $f_1 \to \phi\gamma$

From the procedure outlined in Ch. 4, it is straightforward to obtain the branching ratio of $f_1 \to V\gamma$, $V = \rho, \omega, \phi$, for the improved VMD parameterizations in the form

$$B(f_1 \to V\gamma) = (R^V)^2\frac{B_1^V\left(\widetilde{C}_{\rm a_1}^V\right)^2 + B_2^V\left(\widetilde{C}_{\rm a_2}^V + \widetilde{C}_{\rm s}^V\right)^2 - B_3^V\widetilde{C}_{\rm a_1}^V\left(\widetilde{C}_{\rm a_2}^V + \widetilde{C}_{\rm s}^V\right)}{\Gamma_f}, \tag{10.3}$$

where the coefficients B_i^V are as defined in Eq. (4.38) and the couplings

$$\widetilde{C}_{\rm a_{1/2}}^V = J_{\rm a}^V C_{\rm a_{1/2}}, \qquad\qquad \widetilde{C}_{\rm s}^V = J_{\rm s}^V C_{\rm s} \tag{10.4}$$

are rescaled by

$$J_{\rm a}^V = \frac{M_{V''}^2 - M_{V'}^2}{M_{V''}^2 - M_{V'}^2 + M_V^2}, \qquad J_{\rm s}^V = \frac{M_{V'}^2}{M_{V'}^2 - M_V^2}. \tag{10.5}$$

The normalizations R^V, $V = \omega, \phi$, are given by Eq. (9.8) and $R^\rho = 1$.

Similarly, for $V = \rho$, the ratio of helicity amplitudes for $f_1 \to \rho\gamma \to \pi^+\pi^-\gamma$ results from a straightforward modification of the result presented in Sec. 4.3,

$$r_{\rho\gamma} = \frac{\mathrm{M_{LL}}}{\mathrm{M_{TT}}} = \frac{2m_{f_1}^2 M_\rho^2}{\left[M_\rho^2 - 2\big(m_{f_1}^2 - M_\rho^2\big)\widetilde{C}_{\rm a_1}/\big(\widetilde{C}_{\rm a_2} + \widetilde{C}_{\rm s}\big)\right]^2}, \tag{10.6}$$

where $\mathrm{M_{LL}}$ and $\mathrm{M_{TT}}$ are as defined in Eq. (4.33).

10.3 $f_1 \to e^+e^-$

We follow Ch. 5 and write the decay rate for $f_1 \to e^+e^-$ as

$$\Gamma(f_1 \to e^+e^-) = \frac{64\pi^3\alpha^4 m_{f_1}}{3}|A_1|^2, \tag{10.7}$$

where the scalar amplitude A_1 is implicitly defined by Eq. (5.1) and, according to Eq. (5.7), further decomposes into terms proportional to the three VMD couplings (with isoscalar and isovector coefficients D_i^I) and an asymptotic contribution $D_{\rm asym}$,

$$A_1 = \big(D_1^{I=1} + D_1^{I=0}\big)C_{\rm a_1} + \big(D_2^{I=1} + D_2^{I=0}\big)C_{\rm a_2} + \big(D_3^{I=1} + D_3^{I=0}\big)C_{\rm s} + D_{\rm asym}. \tag{10.8}$$

For the case of products of narrow-resonance propagators as in Eq. (9.1), with squared masses x and y, the integral representation

$$D_i = \frac{xy}{16\pi^2 m_{f_1}^4}\int_0^1 \mathrm{d}z\, f_i(x, y, z, m_{f_1}) \tag{10.9}$$

applies, with the analytic expressions for the functions $f_i(x, y, z, m_{f_1})$ given in Ch. 5. In that chapter, we also provided evaluations of the asymptotic contribution $D_{\rm asym}$ and studied in detail the sensitivity of the integrals to the spectral functions assumed for ρ and ρ' resonances when going beyond a narrow-resonance picture, to avoid unphysical imaginary parts in the loop integrals [37–39]. In the decay region of the f_1, by far the most important correction arises from the width of the ρ; here, we provide a simple evaluation of $B(f_1 \to e^+e^-)$ for the representations constructed in Ch. 9 that captures this main effect, to ensure that our final solutions do not conflict with the SND measurement [5]. To this end, we replace

$$\begin{aligned}
\mathcal{F}_{\rm a_{1/2}}^{I=1}(q_1^2, q_2^2) \to{}& \frac{C_{\rm a_{1/2}}}{N_{\rm a_{1/2}}}\frac{M_{\rho'}^2 M_{\rho''}^2 (M_{\rho''}^2 - M_{\rho'}^2)(q_1^2 - q_2^2)}{(q_1^2 - M_{\rho'}^2)(q_2^2 - M_{\rho'}^2)(q_1^2 - M_{\rho''}^2)(q_2^2 - M_{\rho''}^2)} \\
&\times \frac{1}{\pi}\int_{4M_\pi^2}^\infty \mathrm{d}x\, \frac{x(M_{\rho''}^2 - x)(M_{\rho'}^2 - x)\rho(x)}{(M_{\rho''}^2 - M_{\rho'}^2 + x)(q_1^2 - x)(q_2^2 - x)}, \\
\mathcal{F}_{\rm s}^{I=1}(q_1^2, q_2^2) \to{}& \frac{C_{\rm s}}{N_{\rm s}^2}\frac{M_{\rho'}^4}{(q_1^2 - M_{\rho'}^2)(q_2^2 - M_{\rho'}^2)}\frac{1}{\pi^2}\int_{4M_\pi^2}^\infty \mathrm{d}x \int_{4M_\pi^2}^\infty \mathrm{d}y\, \frac{xy\rho(x)\rho(y)}{(q_1^2 - x)(q_2^2 - y)}
\end{aligned} \tag{10.10}$$

	Narrow-resonance limit		Spectral function for ρ	
$D_1^{I=1} \times 10^3$	$0.23 - 1.68\mathrm{i}$		$0.15 - 1.42\mathrm{i}$	
$D_2^{I=1} \times 10^3$	$-1.70 + 1.81\mathrm{i}$		$-1.36 + 1.64\mathrm{i}$	
$D_3^{I=1} \times 10^3$	$1.25 + 4.38\mathrm{i}$		$3.00 + 4.10\mathrm{i}$	
$D_1^{\omega} \times 10^3$	$0.30 - 1.65\mathrm{i}$			
$D_2^{\omega} \times 10^3$	$-1.89 + 1.81\mathrm{i}$			
$D_3^{\omega} \times 10^3$	$1.06 + 4.61\mathrm{i}$			
$D_1^{\phi} \times 10^3$	$-0.98 - 1.09\mathrm{i}$			
$D_2^{\phi} \times 10^3$	$0.19 + 2.42\mathrm{i}$			
$D_3^{\phi} \times 10^3$	$6.02 + 5.97\mathrm{i}$			
$D_{\text{asym}} \times 10^3$	0.125(12)	0.032(3)	0.017(2)	0.009(1)

Table 10.1: Numerical values for the coefficients D_i^I in Eq. (10.8) (obtained using the *Cuba* library [51]). The total isoscalar one follows as $D_i^{I=0} = R^{\omega} D_i^{\omega} + R^{\phi} D_i^{\phi}$, and D_{asym} is given for the matching points $\sqrt{s_{\text{m}}} = 1.0\,\text{GeV}, 1.3\,\text{GeV}, 1.5\,\text{GeV}, 1.7\,\text{GeV}$. The left column gives the reference point for which the widths of all vector mesons are neglected and the right column the more realistic case that includes the spectral function of the ρ (used as input for Table 11.2).

in Eq. (9.3), where the normalizations $N_{\text{a}_{1/2}}$, N_{s} of the spectral function $\rho(x)$ (taken from Eq. (3.15) [40, 41]) are determined by demanding that the meaning of the couplings $C_{\text{a}_{1/2}}$, C_{s} remain unaltered compared to the zero-width limit; numerical results for the coefficients D_i are collected in Table 10.1.[23] Once improved data on $B(f_1 \to e^+e^-)$ becomes available, more refined analyses can be performed along the lines of Part I and Ref. [50].

10.4 $e^+e^- \to f_1\rho$

The scattering process $e^+e^- \to f_1\pi^+\pi^-$ probes the f_1 TFFs in the time-like region via $e^+e^- \to \gamma^* \to f_1\rho \to f_1\pi^+\pi^-$, see Fig. 10.1. For our analysis, we thus define amputated $f_1 \to \rho\gamma^*$ form factors, which are related to $\gamma^* \to f_1\rho$ via crossing symmetry, according to

$$\begin{aligned}
\bar{\mathcal{F}}^{I=1}_{\text{a}_{1/2}}(q_2^2) &= C_{\text{a}_{1/2}}\left[\frac{(1-\epsilon^{(1)}_{\text{a}_{1/2}}-\epsilon^{(2)}_{\text{a}_{1/2}})M_\rho^2 M_{\rho'}^2}{q_2^2 - M_{\rho'}^2} + \frac{\epsilon^{(1)}_{\text{a}_{1/2}} M_\rho^2 M_{\rho''}^2}{q_2^2 - M_{\rho''}^2}\right] = -\frac{C_{\text{a}_{1/2}}\bar{\zeta}_{\text{a}}}{(q_2^2 - M_{\rho'}^2)(q_2^2 - M_{\rho''}^2)} \\
&\to -\frac{C_{\text{a}_{1/2}}\bar{\zeta}_{\text{a}}}{(q_2^2 - M_{\rho'}^2 + \mathrm{i}M_{\rho'}\Gamma_{\rho'})(q_2^2 - M_{\rho''}^2 + \mathrm{i}M_{\rho''}\Gamma_{\rho''})}, \\
\bar{\mathcal{F}}^{I=1}_{\text{s}}(q_2^2) &= C_{\text{s}}\left[\frac{(1-\epsilon^{(1)}_{\text{s}}-\epsilon^{(2)}_{\text{s}})M_\rho^4}{q_2^2 - M_\rho^2} + \frac{(\epsilon^{(1)}_{\text{s}}/2) M_\rho^2 M_{\rho'}^2}{q_2^2 - M_{\rho'}^2}\right] = -\frac{C_{\text{s}}\bar{\zeta}_{\text{s}}}{(q_2^2 - M_\rho^2)(q_2^2 - M_{\rho'}^2)} \\
&\to -\frac{C_{\text{s}}\bar{\zeta}_{\text{s}}}{(q_2^2 - M_\rho^2 + \mathrm{i}M_\rho\Gamma_\rho)(q_2^2 - M_{\rho'}^2 + \mathrm{i}M_{\rho'}\Gamma_{\rho'})},
\end{aligned} \tag{10.11}$$

[23] Besides the analytic evaluation using the functions $f_i(x, y, z, m_{f_1})$, we performed cross-checks by means of a PV decomposition, obtained with *FeynCalc* [42–44], and the subsequent calculation of the loop integrals with *Collier* [45–49].

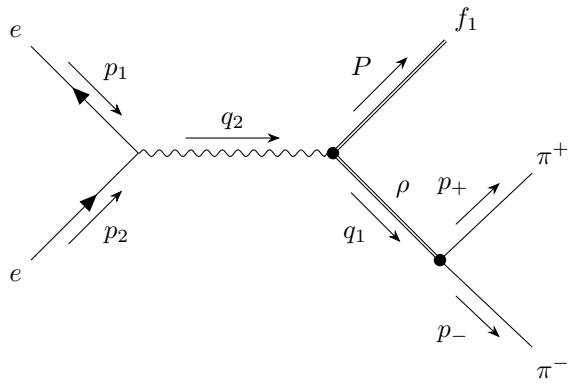

Figure 10.1: FEYNMAN diagram for $e^+e^- \to f_1\rho \to f_1\pi^+\pi^-$ consistent with $\mathcal{M}(\gamma^* \to f_1\rho^{0^*})$.

where

$$\bar{\zeta}_\mathrm{a} = \frac{M_\rho^2 M_{\rho'}^2 M_{\rho''}^2 (M_{\rho''}^2 - M_{\rho'}^2)}{M_{\rho''}^2 - M_{\rho'}^2 + M_\rho^2}, \qquad \bar{\zeta}_\mathrm{s} = \frac{M_\rho^4 M_{\rho'}^4}{M_{\rho'}^2 - M_\rho^2}, \tag{10.12}$$

and a width has been inserted into the denominators for the time-like application.

As a first approximation, we consider the case in which the process $e^+e^- \to f_1\pi^+\pi^-$ is described by $e^+e^- \to f_1\rho$, see Fig. 10.2, whose amplitude can be constructed from Eq. (3.4) and Eq. (9.1) by amputating the ρ propagator,

$$\begin{aligned}\mathcal{M}(\gamma^* \to f_1\rho^{0^*}) = {}& \frac{e}{\widetilde{g}_{\rho\gamma} m_{f_1}^2} \epsilon_\mu^*(q_1)\epsilon_\nu(q_2)\epsilon_\alpha^*(P) \\ & \times \Big[T_{\mathrm{a}_1}^{\mu\nu\alpha}(-q_1,q_2)\bar{\mathcal{F}}_{\mathrm{a}_1}(q_2^2) + T_{\mathrm{a}_2}^{\mu\nu\alpha}(-q_1,q_2)\bar{\mathcal{F}}_{\mathrm{a}_2}(q_2^2) + T_{\mathrm{s}}^{\mu\nu\alpha}(-q_1,q_2)\bar{\mathcal{F}}_{\mathrm{s}}(q_2^2)\Big],\end{aligned} \tag{10.13}$$

and the prefactor follows in analogy to the derivation of $f_1 \to V\gamma$ in Ch. 4, with $\widetilde{g}_{\rho\gamma}$ as defined in Eq. (B.7). In order to determine the amplitude for $e^+e^- \to \gamma^* \to f_1\rho$, we calculate the diagram shown in Fig. 10.2, leading to

$$\begin{aligned}\mathcal{M}(e^+e^- \to f_1\rho) = {}& \frac{e^2}{\widetilde{g}_{\rho\gamma} m_{f_1}^2} \epsilon_\mu^*(q_1)\epsilon_\alpha^*(P) \frac{\bar{v}^s(p_1)\gamma_\nu u^r(p_2)}{q_2^2} \\ & \times \Big[T_{\mathrm{a}_1}^{\mu\nu\alpha}(-q_1,q_2)\bar{\mathcal{F}}_{\mathrm{a}_1}(q_2^2) + T_{\mathrm{a}_2}^{\mu\nu\alpha}(-q_1,q_2)\bar{\mathcal{F}}_{\mathrm{a}_2}(q_2^2) + T_{\mathrm{s}}^{\mu\nu\alpha}(-q_1,q_2)\bar{\mathcal{F}}_{\mathrm{s}}(q_2^2)\Big]\Big|_{q_1^2=M_\rho^2},\end{aligned} \tag{10.14}$$

where we dropped an unobservable overall phase.

Spin-averaging the squared amplitude and performing the angular integration, we find

$$\begin{aligned}\sigma(e^+e^- \to f_1\rho)(s) = {}& \frac{e^4 |g_{\rho\gamma}|^2 |\boldsymbol{p}_\rho| (s+2m_e^2)}{384\pi m_{f_1}^6 M_\rho^4 s^3 |\boldsymbol{p}_e|} \\ & \times \Big[T_{\mathrm{a}_1,\mathrm{a}_1}(q_1^2,s)\big|\bar{\mathcal{F}}_{\mathrm{a}_1}(s)\big|^2 + T_{\mathrm{a}_2,\mathrm{a}_2}(q_1^2,s)\big|\bar{\mathcal{F}}_{\mathrm{a}_2}(s)\big|^2 + T_{\mathrm{s,s}}(q_1^2,s)\big|\bar{\mathcal{F}}_{\mathrm{s}}(s)\big|^2 \\ & \quad + 2T_{\mathrm{a}_1,\mathrm{a}_2}(q_1^2,s)\mathrm{Re}\left[\bar{\mathcal{F}}_{\mathrm{a}_1}(s)\bar{\mathcal{F}}_{\mathrm{a}_2}^*(s)\right] + 2T_{\mathrm{a}_1,\mathrm{s}}(q_1^2,s)\mathrm{Re}\left[\bar{\mathcal{F}}_{\mathrm{a}_1}(s)\bar{\mathcal{F}}_{\mathrm{s}}^*(s)\right] \\ & \quad + 2T_{\mathrm{a}_2,\mathrm{s}}(q_1^2,s)\mathrm{Re}\left[\bar{\mathcal{F}}_{\mathrm{a}_2}(s)\bar{\mathcal{F}}_{\mathrm{s}}^*(s)\right]\Big]\Big|_{q_1^2=M_\rho^2}\end{aligned} \tag{10.15}$$

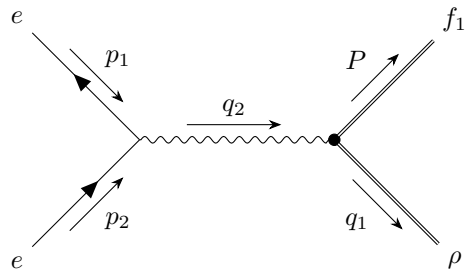

Figure 10.2: FEYNMAN diagram for $e^+e^- \to f_1\rho$ consistent with $\mathcal{M}(\gamma^* \to f_1\rho^{0^*})$.

for the total cross section, with $s = q_2^2$, initial- and final-state momenta

$$|\boldsymbol{p}_e| = \frac{\sqrt{s-4m_e^2}}{2}, \qquad |\boldsymbol{p}_\rho| = \frac{\sqrt{\lambda(s,q_1^2,m_{f_1}^2)}}{2\sqrt{s}}, \tag{10.16}$$

and the kinematic functions

$$\begin{aligned}
T_{\mathrm{a}_1,\mathrm{a}_1}(q_1^2,s) &= 4\lambda(s,q_1^2,m_{f_1}^2)^2, \\
T_{\mathrm{a}_2,\mathrm{a}_2}(q_1^2,s) &= m_{f_1}^6(s+q_1^2) - m_{f_1}^4(s^2+q_1^4-6sq_1^2) - m_{f_1}^2(s-q_1^2)^2(s+q_1^2) + (s-q_1^2)^4, \\
T_{\mathrm{s},\mathrm{s}}(q_1^2,s) &= m_{f_1}^2(s+q_1^2)\big(m_{f_1}^4 - s^2 - q_1^4 + 18sq_1^2\big) - m_{f_1}^4(s^2+q_1^4+14sq_1^2) + (s^2-q_1^4)^2, \\
T_{\mathrm{a}_1,\mathrm{a}_2}(q_1^2,s) &= 2\lambda(s,q_1^2,m_{f_1}^2)\big[(s-q_1^2)^2 - m_{f_1}^2(s+q_1^2)\big], \\
T_{\mathrm{a}_1,\mathrm{s}}(q_1^2,s) &= -2\lambda(s,q_1^2,m_{f_1}^2)(s-q_1^2)(s+q_1^2-m_{f_1}^2), \\
T_{\mathrm{a}_2,\mathrm{s}}(q_1^2,s) &= -(s-q_1^2)\Big[m_{f_1}^6 - m_{f_1}^4(s+q_1^2) - m_{f_1}^2(s^2+q_1^4-6sq_1^2) + (s-q_1^2)^2(s+q_1^2)\Big].
\end{aligned} \tag{10.17}$$

In a compact way, the cross section can be expressed in terms of the amputated helicity amplitudes [8]

$$\begin{aligned}
\bar{H}_{++;0}(q_1^2,s) &= \frac{\lambda(s,q_1^2,m_{f_1}^2)}{2m_{f_1}^3}\bar{\mathcal{F}}_1(s) - \frac{q_1^2(m_{f_1}^2-q_1^2+s)}{2m_{f_1}^3}\bar{\mathcal{F}}_2(s) - \frac{s(m_{f_1}^2+q_1^2-s)}{2m_{f_1}^3}\bar{\mathcal{F}}_3(s), \\
\bar{H}_{+0;+}(q_1^2,s) &= \frac{q_1^2 s}{\xi_2 m_{f_1}^2}\bar{\mathcal{F}}_2(s) + \frac{s(m_{f_1}^2-q_1^2-s)}{2\xi_2 m_{f_1}^2}\bar{\mathcal{F}}_3(s), \\
\bar{H}_{0+;-}(q_1^2,s) &= -\frac{q_1^2(m_{f_1}^2-q_1^2-s)}{2\xi_1 m_{f_1}^2}\bar{\mathcal{F}}_2(s) - \frac{q_1^2 s}{\xi_1 m_{f_1}^2}\bar{\mathcal{F}}_3(s),
\end{aligned} \tag{10.18}$$

with polarization-vector normalizations $\xi_1^2 = q_1^2$, $\xi_2^2 = s$, leading to

$$\sigma(e^+e^- \to f_1\rho)(s) = \frac{e^4|g_{\rho\gamma}|^2|\boldsymbol{p}_\rho|(s+2m_e^2)}{24\pi M_\rho^4 s^3|\boldsymbol{p}_e|}\sum_\lambda \big|\bar{H}_\lambda(M_\rho^2,s)\big|^2, \tag{10.19}$$

and the sum extends over the three amplitudes in Eq. (10.18).

10.5 $e^+e^- \to f_1\pi^+\pi^-$

To obtain a reasonable threshold behavior, it is mandatory to go beyond the approximation of a narrow ρ and instead consider the full amplitude $e^+e^- \to f_1\pi^+\pi^-$. To this end, we

use

$$\mathcal{M}(\rho \to \pi^+\pi^-) = g_{\rho\pi\pi}\epsilon_\mu(p_\rho)(p_- - p_+)^\mu, \tag{10.20}$$

see also Eq. (B.8), to calculate the diagram shown in Fig. 10.1, leading to

$$\begin{aligned}\mathcal{M}(e^+e^- \to f_1\pi^+\pi^-) = \frac{e^2 g_{\rho\pi\pi}}{\widetilde{g}_{\rho\gamma} m_{f_1}^2}\epsilon_\alpha^*(P)\frac{(p_- - p_+)_\mu}{q_1^2 - M_\rho^2 + \mathrm{i}M_\rho\Gamma_\rho}\frac{\bar{v}^s(p_1)\gamma_\nu u^r(p_2)}{q_2^2} \\ \times\Big[T_{\mathrm{a}_1}^{\mu\nu\alpha}(-q_1,q_2)\bar{\mathcal{F}}_{\mathrm{a}_1}(q_2^2) + T_{\mathrm{a}_2}^{\mu\nu\alpha}(-q_1,q_2)\bar{\mathcal{F}}_{\mathrm{a}_2}(q_2^2) + T_{\mathrm{s}}^{\mu\nu\alpha}(-q_1,q_2)\bar{\mathcal{F}}_{\mathrm{s}}(q_2^2)\Big],\end{aligned} \tag{10.21}$$

where we again dropped an unobservable phase. From the spin-averaged squared matrix element and after carrying out the angular integrations, we obtain the differential cross section

$$\begin{aligned}\frac{\mathrm{d}\sigma(e^+e^- \to f_1\pi^+\pi^-)}{\mathrm{d}q_1^2}(s) = \frac{e^4|g_{\rho\pi\pi}|^2|g_{\rho\gamma}|^2|\boldsymbol{p}_\rho|(s+2m_e^2)(q_1^2-4M_\pi^2)^{3/2}}{18432\pi^3 m_{f_1}^6 M_\rho^4 s^3\sqrt{q_1^2}|\boldsymbol{p}_e|\big[(q_1^2-M_\rho^2)^2+M_\rho^2\Gamma_\rho^2\big]} \\ \times\Big[T_{\mathrm{a}_1,\mathrm{a}_1}(q_1^2,s)\big|\bar{\mathcal{F}}_{\mathrm{a}_1}(s)\big|^2 + T_{\mathrm{a}_2,\mathrm{a}_2}(q_1^2,s)\big|\bar{\mathcal{F}}_{\mathrm{a}_2}(s)\big|^2 + T_{\mathrm{s},\mathrm{s}}(q_1^2,s)\big|\bar{\mathcal{F}}_{\mathrm{s}}(s)\big|^2 \\ + 2T_{\mathrm{a}_1,\mathrm{a}_2}(q_1^2,s)\mathrm{Re}\big[\bar{\mathcal{F}}_{\mathrm{a}_1}(s)\bar{\mathcal{F}}_{\mathrm{a}_2}^*(s)\big] + 2T_{\mathrm{a}_1,\mathrm{s}}(q_1^2,s)\mathrm{Re}\big[\bar{\mathcal{F}}_{\mathrm{a}_1}(s)\bar{\mathcal{F}}_{\mathrm{s}}^*(s)\big] \\ + 2T_{\mathrm{a}_2,\mathrm{s}}(q_1^2,s)\mathrm{Re}\big[\bar{\mathcal{F}}_{\mathrm{a}_2}(s)\bar{\mathcal{F}}_{\mathrm{s}}^*(s)\big]\Big],\end{aligned} \tag{10.22}$$

with the kinematic functions $T_{i,j}(q_1^2,s)$ as in Eq. (10.17); in terms of the amputated helicity amplitudes, we obtain

$$\frac{\mathrm{d}\sigma(e^+e^- \to f_1\pi^+\pi^-)}{\mathrm{d}q_1^2}(s) = \frac{e^4|g_{\rho\pi\pi}|^2|g_{\rho\gamma}|^2|\boldsymbol{p}_\rho|(s+2m_e^2)(q_1^2-4M_\pi^2)^{3/2}}{1152\pi^3 M_\rho^4 s^3\sqrt{q_1^2}|\boldsymbol{p}_e|\big[(q_1^2-M_\rho^2)^2+M_\rho^2\Gamma_\rho^2\big]}\sum_\lambda\big|\bar{H}_\lambda(q_1^2,s)\big|^2. \tag{10.23}$$

In general, the remaining integration over q_1^2 needs to be performed numerically, but it is instructive to consider the limit of a narrow resonance [52],

$$\frac{1}{(q_1^2-M_\rho^2)^2+M_\rho^2\Gamma_\rho^2} \to \frac{\pi}{M_\rho\Gamma_\rho}\delta\big(q_1^2-M_\rho^2\big). \tag{10.24}$$

In this approximation, together with Eq. (B.9),

$$\Gamma_\rho = \frac{|g_{\rho\pi\pi}|^2(M_\rho^2-4M_\pi^2)^{3/2}}{48\pi M_\rho^2}, \tag{10.25}$$

the q_1^2 integration of Eq. (10.23) indeed reproduces Eq. (10.19). For the phenomenological analysis of the $e^+e^- \to f_1\pi^+\pi^-$ data, we will use the full expression given in Eq. (10.22).

Chapter 11

Phenomenological analysis

11.1 Data input for $e^+e^- \to e^+e^- f_1$ and $f_1 \to V\gamma$

The experimental data we will use for the space-like reaction $e^+e^- \to e^+e^- f_1$ and the radiative decays $f_1 \to V\gamma$ is summarized in Table 11.1. For the former, this concerns normalization and slope from the L3 experiment [4], with isoscalar corrections evaluated using the mixing angle that follows from a combined analysis with the analogous quantities for the f_1' [36], see Sec. 4.1 and Sec. 10.1. For $B(f_1 \to \rho\gamma)$, we use the results of the global fit from Ch. 6, including data on $\Gamma(f_1 \to K\bar{K}\pi)/\Gamma(f_1 \to 4\pi)$ [53–55], $\Gamma(f_1 \to 4\pi)/\Gamma(f_1 \to \eta\pi\pi)$ [56, 57], $\Gamma(f_1 \to \rho\gamma)/\Gamma(f_1 \to 4\pi)$ [58], $\Gamma(f_1 \to a_0(980)\pi\,[\text{excluding } K\bar{K}\pi])/\Gamma(f_1 \to \eta\pi\pi)$ [56, 59, 60], $\Gamma(f_1 \to K\bar{K}\pi)/\Gamma(f_1 \to \eta\pi\pi)$ [56, 59–63], and $\Gamma(f_1 \to \rho\gamma)/\Gamma(f_1 \to \eta\pi\pi)$ [2, 60, 61, 64]. For $B(f_1 \to \phi\gamma)$, there is a single measurement from Ref. [3], and, similar to Part I, we will consider fit variants with and without this additional input, given both the tenuous data situation and the required U(3) assumptions.[24] Finally, two event candidates for $f_1 \to e^+e^-$ have been observed in Ref. [5], which, when interpreted as a signal, translates to $B(f_1 \to e^+e^-) = 5.1^{+3.7}_{-2.7} \times 10^{-9}$, while being quoted as $B(f_1 \to e^+e^-) < 9.4 \times 10^{-9}$ (90% C.L.) in Ref. [1]. In Part I, we performed a detailed analysis of the constraints that can be obtained from the dilepton decay, but in view of its unclear status and large uncertainties, we do not include this channel in our global fit here and instead focus on $e^+e^- \to f_1\pi^+\pi^-$. Further input parameters are collected in App. F.

11.2 Data input for $e^+e^- \to f_1\pi^+\pi^-$

The process $e^+e^- \to f_1\pi^+\pi^-$ has been measured in two different decay channels, $f_1 \to \eta\pi\pi$ [11] and $f_1 \to K\bar{K}\pi$ [12]. The data for the cross section from both reconstruction methods is well compatible, indicating that systematic errors are smaller than the statistical uncertainties of the measurements. In the following, we will therefore assume that the data is indeed dominated by statistics.

Next, around $\sqrt{s} \simeq 2\,\text{GeV}$, the cross section displays resonance structures [32], most prominently the $\rho(2150)$ and, potentially, further excited ρ states. This implies that we cannot expect our theoretical description based on Eq. (10.22) to provide an adequate

[24] The limit $B(f_1 \to \phi\gamma) < 0.45 \times 10^{-3}$ [1, 61] (95% C.L.) supports a rather small branching fraction to $\phi\gamma$, indicating a value at the lower end of the range from Ref. [3]. Both measurements are also consistent with $B(f_1 \to \phi\gamma) < 0.9 \times 10^{-3}$ [2] (95% C.L.).

Quantity	Value	Reference
$\widetilde{\Gamma}^{f_1}_{\gamma\gamma}$ [keV]	3.5(6)(5)	[4]
Λ_{f_1} [GeV]	1.04(6)(5)	[4]
$B(f_1 \to \rho\gamma)$	4.2(1.0)%	Ch. 6
$r_{\rho\gamma}$	3.9(1.3)	[2]
$B(f_1 \to \phi\gamma)$	$0.74(26) \times 10^{-3}$	[1, 3]

Table 11.1: Data for $e^+e^- \to e^+e^- f_1$ and $f_1 \to V\gamma$ used in our analysis.

fit to the data, because ρ excitations beyond the ρ'' are not included. However, the data still provides a valuable upper bound for the background contributions that our TFF parameterizations do describe; in fact, this constraint proves extremely stringent, immediately ruling out, by at least an order of magnitude, parameterizations that do not implement the doubly-virtual asymptotic behavior of Eq. (9.5). Even more, writing the cross section in terms of the couplings $C_{\mathrm{a}_{1/2}}$, C_s, one observes that moderate cancellations among the different terms are required to obey the upper limit implied by the $e^+e^- \to f_1\pi^+\pi^-$ data. With C_s reasonably well determined from the L3 equivalent two-photon decay width, this thus implies a valuable constraint on the antisymmetric TFFs.

To quantify this constraint, we proceed as follows: we first define the χ^2 function

$$\chi^2_{\mathrm{BaBar}}(C_\mathrm{s}, C_{\mathrm{a}_1}, C_{\mathrm{a}_2}) = \sum_{i=1}^{n_{\mathrm{BaBar}}} \frac{(\sigma(s_i, C_\mathrm{s}, C_{\mathrm{a}_1}, C_{\mathrm{a}_2}) - \sigma_i^{\mathrm{exp}})^2}{(\Delta\sigma_i^{\mathrm{exp}})^2} \theta\big[\sigma(s_i, C_\mathrm{s}, C_{\mathrm{a}_1}, C_{\mathrm{a}_2}) - \sigma_i^{\mathrm{exp}}\big], \tag{11.1}$$

where $n_{\mathrm{BaBar}} = 52$ is the combined number of data points from Refs. [11, 12], σ_i^{exp} and $\Delta\sigma_i^{\mathrm{exp}}$ are central value and error at center-of-mass energy $\sqrt{s_i}$, respectively, and the Heaviside function demands that contributions to χ^2_{BaBar} only arise when the theoretical model exceeds the central value of the data, thus not penalizing a potential excess of the latter due to excited ρ resonances. Interpreting this χ^2 function in the usual statistical sense, however, puts an undue emphasis on the $e^+e^- \to f_1\pi^+\pi^-$ data, especially in view of the uncertainties from the contamination of resonant contributions. For this reason, we instead study contours in the C_{a_1}–C_{a_2} plane for which $\chi^2_{\mathrm{BaBar}}/\mathrm{dof} = 1$ at a given value of C_s, which should provide a reasonable measure of the consistency of the encompassed values of $C_{\mathrm{a}_{1/2}}$ with the experimental constraints. We repeat this procedure for the relevant range of C_s and formulate the resulting constraint on $C_{\mathrm{a}_{1/2}}$ in terms of an ellipse whose parameters are interpolated as a function of C_s. The final constraint is then written as

$$\chi^2_{\mathrm{BaBar,\,eff}}(C_\mathrm{s}, C_{\mathrm{a}_1}, C_{\mathrm{a}_2}) = \Delta\boldsymbol{y}_\mathrm{a}^\intercal C_\mathrm{a}^{-1} \Delta\boldsymbol{y}_\mathrm{a}, \tag{11.2}$$

where

$$\Delta\boldsymbol{y}_\mathrm{a} = \begin{pmatrix} C_{\mathrm{a}_1} - C_{\mathrm{a}_1}^{(0)} \\ C_{\mathrm{a}_2} - C_{\mathrm{a}_2}^{(0)} \end{pmatrix}, \tag{11.3}$$

with the central values $C_{\mathrm{a}_{1/2}}^{(0)}$ and the covariance matrix C_a—which are determined via the $\chi^2_{\mathrm{BaBar}}/\mathrm{dof} = 1$ contour ellipse—implicitly depending on C_s; this effective χ^2 function is

	$f_1 \to \phi\gamma$	
	No	Yes
χ^2/dof	$5.6/3 = 1.86$	$18.1/4 = 4.52$
p-value	0.13	1.2×10^{-3}
C_s	0.95(13)	0.76(16)
C_{a_1}	−0.16(18)	−0.07(18)
C_{a_2}	0.47(25)	0.09(32)
ρ_{sa_1}	0.34	0.31
ρ_{sa_2}	−0.11	−0.34
$\rho_{\mathrm{a}_1\mathrm{a}_2}$	−0.52	−0.35
$B(f_1 \to \phi\gamma) \times 10^3$	3.4(1.7)	1.6(1.0)
$B(f_1 \to \omega\gamma) \times 10^3$	5.5(1.6)	2.5(1.1)
$B(f_1 \to e^+e^-) \times 10^9$	2.2(6)	1.2(5)
$B(f_1' \to \phi\gamma) \times 10^3$	11.0(3.0)	5.2(2.2)
$B(f_1' \to \rho\gamma) \times 10^3$	4.8(2.6)	2.2(1.4)

Table 11.2: Best-fit results for the three VMD couplings C_s, C_{a_1}, and C_{a_2}. The fit includes the constraints from the normalization and slope measured by L3 in $e^+e^- \to e^+e^- f_1$, from $B(f_1 \to \rho\gamma)$, $r_{\rho\gamma}$, and $\sigma(e^+e^- \to f_1\pi^+\pi^-)$ as well as, in the right column, from $B(f_1 \to \phi\gamma)$. All uncertainties are inflated by the scale factor $S = \sqrt{\chi^2/\mathrm{dof}}$. The table also shows the correlations ρ_{ij} among the three couplings and the values of $B(f_1 \to V\gamma)$, $V = \omega, \phi$, and $B(f_1 \to e^+e^-)$ implied by the fit result (the latter for $\sqrt{s_\mathrm{m}} = 1.3\,\mathrm{GeV}$). The uncertainties for $B(f_1 \to V\gamma)$ include the fit errors and ΔR^ϕ but no additional estimate of U(3) uncertainties. The predictions for $B(f_1' \to \phi\gamma)$ and $B(f_1' \to \rho\gamma)$ use the U(3) relations from Eq. (11.5).

then used as input in the global fit, counted as two data points in the number of degrees of freedom. Our procedure is further motivated by the fact that the constraints imposed by the cross-section measurements at different energies will be highly correlated: if the upper limit is fulfilled at some point s_i for a set of couplings C_{a_1}, C_{a_2}, C_s, the smoothness of the cross section makes it likely that the same holds true at neighboring points.

11.3 Global fit

The results of the global fit are summarized in Table 11.2, Fig. 11.1, and Fig. 11.2, for variants with and without the U(3) constraint from $B(f_1 \to \phi\gamma)$. Without this input, we observe reasonable consistency among the various constraints, with a final value for C_s close to the L3 value in Eq. (10.1). The coupling C_{a_1} comes out consistent with zero, while a non-zero value of C_{a_2} is obtained at 2σ significance. Crucially, owing to the inclusion of

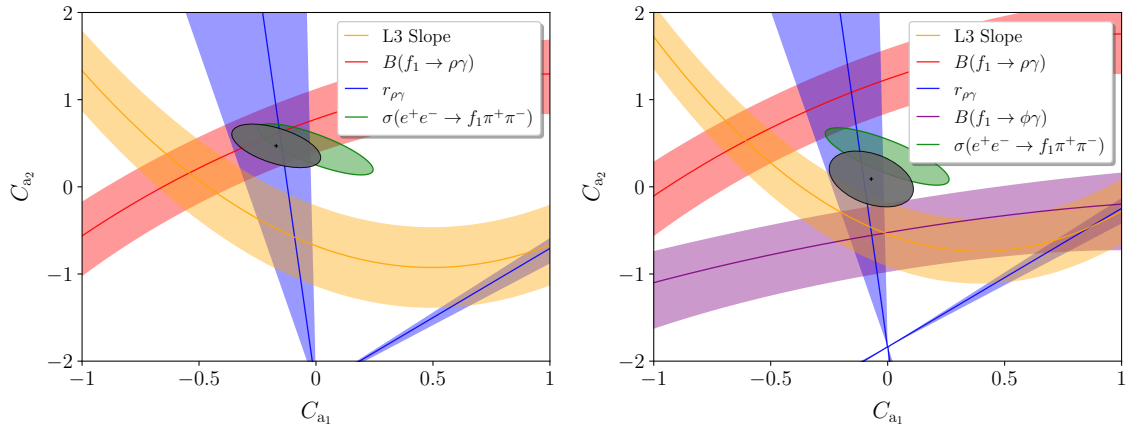

Figure 11.1: *Left*: constraints in the C_{a_1}–C_{a_2} plane for the respective best-fit value of C_s (see Table 11.2) from L3 normalization and slope, $B(f_1 \to \rho\gamma)$, $r_{\rho\gamma}$, and $\sigma(e^+e^- \to f_1\pi^+\pi^-)$. The gray ellipse represents the result of the global fit. *Right*: the same figure for the global fit including, in addition, $B(f_1 \to \phi\gamma)$.

the BaBar data on $e^+e^- \to f_1\pi^+\pi^-$ [11, 12], we are now able to provide an unambiguous solution for all three TFFs, including the two antisymmetric ones encoded in $C_{a_{1/2}}$. The best-fit point lies within the ellipse from $\sigma(e^+e^- \to f_1\pi^+\pi^-)$, and, accordingly, the central line in Fig. 11.2 respects the bound for almost all data points, leaving a deficit that could be well explained by a $\rho(2150)$-resonance signal. Moreover, the resulting prediction for $B(f_1 \to e^+e^-)$ is consistent with SND [5], suggesting a potential signal at the lower end of their range. In contrast, the prediction for $B(f_1 \to \phi\gamma)$ comes out slightly too large in comparison to Ref. [3], in tension at the level of 1.5σ.

The same tension is visible in the global fit including $B(f_1 \to \phi\gamma)$, as the χ^2/dof deteriorates appreciably. Including the resulting scale factor $S = 2.1$ in the error estimates, all three couplings are consistent with the global fit without $B(f_1 \to \phi\gamma)$, but C_s decreases compared to L3 and the central value of C_{a_2} moves much closer to zero. Within the sizable uncertainties, the cross section for $e^+e^- \to f_1\pi^+\pi^-$ is still consistent with the experiment, but the central line exceeds the data above the $\rho(2150)$, in accordance with the best-fit point in Fig. 11.1 lying slightly outside the $\sigma(e^+e^- \to f_1\pi^+\pi^-)$ ellipse. The resulting prediction for $B(f_1 \to e^+e^-)$ is still consistent with SND, and $B(f_1 \to \phi\gamma)$ now agrees by construction. Table 11.2 also includes the predictions for $B(f_1 \to \omega\gamma)$, $B(f_1' \to \phi\gamma)$, and $B(f_1' \to \rho\gamma)$, the latter two being related to the already determined couplings via the U(3) arguments in Sec. 11.4.

11.4 Final representations

To summarize, we propose that the low-energy contributions to the TFFs of the f_1 be described by the parameterizations

$$\mathcal{F}^{f_1,I=1}_{a_{1/2}}(q_1^2, q_2^2) = \frac{R^\rho C_{a_{1/2}} \zeta_\rho M_\rho^4 M_{\rho'}^4 M_{\rho''}^4 (q_1^2 - q_2^2)}{(q_1^2 - M_\rho^2)(q_2^2 - M_\rho^2)(q_1^2 - M_{\rho'}^2)(q_2^2 - M_{\rho'}^2)(q_1^2 - M_{\rho''}^2)(q_2^2 - M_{\rho''}^2)},$$

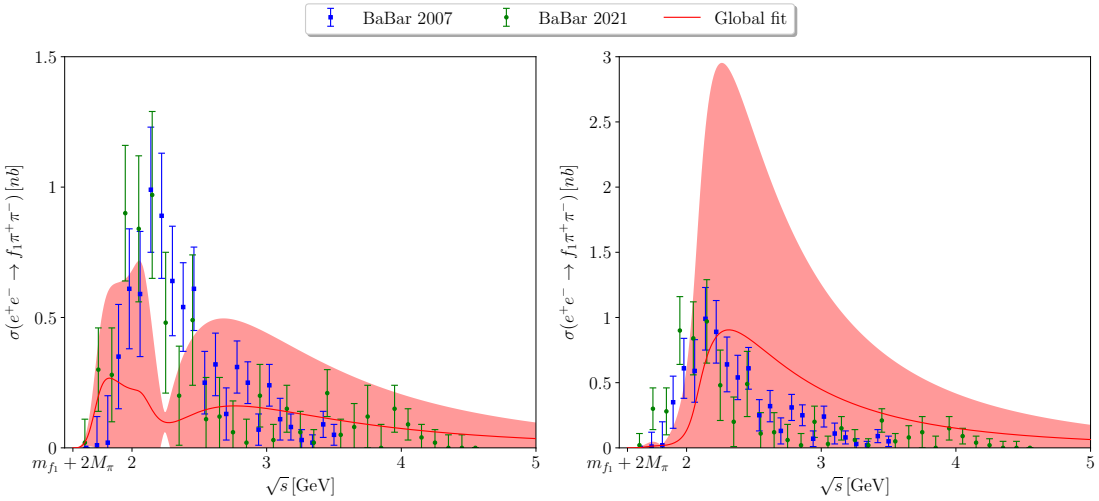

Figure 11.2: Comparison of our global fit results to the BaBar data [11, 12] for $\sigma(e^+e^- \to f_1\pi^+\pi^-)$, without (*left*) and including (*right*) the constraint from $B(f_1 \to \phi\gamma)$. The red line denotes the central result, and the band reflects the uncertainties propagated from C_s, C_{a_1}, and C_{a_2}.

$$\begin{aligned}
\mathcal{F}_\mathrm{s}^{f_1,I=1}(q_1^2,q_2^2) &= \frac{R^\rho C_\mathrm{s} M_\rho^4 M_{\rho'}^4}{(q_1^2-M_\rho^2)(q_2^2-M_\rho^2)(q_1^2-M_{\rho'}^2)(q_2^2-M_{\rho'}^2)},\\
\mathcal{F}_{\mathrm{a}_{1/2}}^{f_1,I=0}(q_1^2,q_2^2) &= \sum_{V=\omega,\phi} \frac{R^V C_{\mathrm{a}_{1/2}} \zeta_V M_V^4 M_{V'}^4 M_{V''}^4 (q_1^2-q_2^2)}{(q_1^2-M_V^2)(q_2^2-M_V^2)(q_1^2-M_{V'}^2)(q_2^2-M_{V'}^2)(q_1^2-M_{V''}^2)(q_2^2-M_{V''}^2)},\\
\mathcal{F}_\mathrm{s}^{f_1,I=0}(q_1^2,q_2^2) &= \sum_{V=\omega,\phi} \frac{R^V C_\mathrm{s} M_V^4 M_{V'}^4}{(q_1^2-M_V^2)(q_2^2-M_V^2)(q_1^2-M_{V'}^2)(q_2^2-M_{V'}^2)},
\end{aligned} \tag{11.4}$$

see Eq. (9.3), Eq. (9.4), Eq. (9.7), and Eq. (9.8), with the couplings C_s, C_{a_1}, and C_{a_2} as determined in Table 11.2 (and $R^\rho = 1$). These low-energy contributions are then to be supplemented by the asymptotic contributions from the LCE, see Sec. 3.4, to arrive at a complete description.

In order to estimate the impact of f_1' and a_1, we also quote the corresponding expressions that follow from U(3) symmetry. For the f_1', the analogous results are obtained by replacing

$$\begin{aligned}
R^\rho &\to R^\rho_{f_1'} = \cot(\theta_A+\theta_1) = -0.50(11),\\
R^\omega &\to R^\omega_{f_1'} = \frac{1}{9}\cot(\theta_A+\theta_1) = -0.06(1),\\
R^\phi &\to R^\phi_{f_1'} = -\frac{2\sqrt{2}}{9} = -0.31,
\end{aligned} \tag{11.5}$$

where the errors only refer to the uncertainties propagated in θ_A, *cf.* Eq. (9.8). The coefficients in Eq. (11.5) show that isoscalar contributions will become much more important for the f_1' than for the f_1, especially the ϕ. This observation is reflected by some evidence for a signal in the decay to the $\phi\gamma$ final state, $B(f_1' \to \phi\gamma) = 3(2) \times 10^{-3}$ [61], which,

within uncertainties, agrees with the predictions from Table 11.2 for the fit including $B(f_1 \to \phi\gamma)$, while the fit without $B(f_1 \to \phi\gamma)$ predicts a larger branching fraction. The same reference also gives a limit $B(f_1' \to \rho\gamma) < 0.02$ (95% C.L.), in agreement with both fits from Table 11.2.

The TFFs of the a_1 display a different isospin structure, with one isoscalar and one isovector photon each. Moreover, for ideal mixing, there is no contribution from the ϕ and its excitations, so that only contributions of the type ρ–ω survive. Accordingly, the overall scaling compared to the couplings in the f_1 TFFs is measured relative to the sum of all isovector and isoscalar contributions, leading to

$$R_{a_1} = \frac{1 + R^\omega + R^\phi}{\sqrt{3}\cos(\theta_A - \theta_0)} = \frac{2}{3\sin(\theta_A + \theta_1)} = 0.75(3). \tag{11.6}$$

Choosing a symmetric decomposition of ζ_V onto the ρ and ω contributions, we obtain

$$\begin{aligned}
\mathcal{F}^{a_1}_{\mathrm{a}_{1/2}}(q_1^2, q_2^2) &= \frac{R_{a_1} C_{\mathrm{a}_{1/2}} \sqrt{\zeta_\rho \zeta_\omega} M_\rho^2 M_{\rho'}^2 M_{\rho''}^2 M_\omega^2 M_{\omega'}^2 M_{\omega''}^2 (q_1^2 - q_2^2)}{2(q_1^2 - M_\rho^2)(q_2^2 - M_\omega^2)(q_1^2 - M_{\rho'}^2)(q_2^2 - M_{\omega'}^2)(q_1^2 - M_{\rho''}^2)(q_2^2 - M_{\omega''}^2)} \\
&\quad + (\rho \leftrightarrow \omega), \\
\mathcal{F}^{a_1}_{\mathrm{s}}(q_1^2, q_2^2) &= \frac{R_{a_1} C_{\mathrm{s}} M_\rho^2 M_{\rho'}^2 M_\omega^2 M_{\omega'}^2}{2(q_1^2 - M_\rho^2)(q_2^2 - M_\omega^2)(q_1^2 - M_{\rho'}^2)(q_2^2 - M_{\omega'}^2)} + (\rho \leftrightarrow \omega).
\end{aligned} \tag{11.7}$$

Chapter 12

Conclusions

The TFFs of axial-vector mesons are key input quantities for a data-driven evaluation of HLbL scattering in the anomalous magnetic moment of the muon, yet they are notoriously poorly determined from experiment. Here, we performed a global analysis of all experimental constraints available for the f_1 and outlined how the f_1' and a_1 contributions can be estimated from U(3) symmetry. A crucial role is played by data for the cross section of $e^+e^- \to f_1\pi^+\pi^-$, which provides valuable input on the asymptotic behavior and allowed us to find an unambiguous solution also for the antisymmetric TFFs.

The process $e^+e^- \to f_1\pi^+\pi^-$ probes all three TFFs at one photon virtuality determined by the center-of-mass energy and the other one by the $\pi^+\pi^-$ invariant mass, which, in turn, is dominated by the ρ. Accordingly, the data extending from threshold up to about 4.5 GeV is sensitive to the asymptotic behavior for one virtuality fixed at the ρ mass. The corresponding constraint demonstrates that the asymptotic behavior predicted by the LCE needs to set in early, for otherwise, the cross section exceeds the data by an order of magnitude. We implemented this conclusion using a VMD ansatz, leading to the parameterizations summarized in Sec. 11.4. To account for contributions from even higher excited ρ resonances, such as the $\rho(2150)$, we formulated the quantitative analysis as an upper limit, which still entails valuable constraints especially on the otherwise poorly determined couplings characterizing the antisymmetric TFFs. The global fit, see Sec. 11.3, shows good consistency with the data for $e^+e^- \to e^+e^-f_1$ and $f_1 \to \rho\gamma$, predicting a branching fraction for $f_1 \to e^+e^-$ at the lower end of the signal strength reported by SND. Some tension is observed with $f_1 \to \phi\gamma$, which might point towards limitations of U(3) symmetry and/or the data base.

The final parameterizations describe the TFFs at low and intermediate virtualities, to be supplemented by an additional term from the LCE [8], see also Part I, that ensures the correct asymptotic behavior also in the doubly-virtual direction. Using this combined input, work is ongoing to evaluate the axial-vector contributions both in the HLbL basis of Ref. [65] and in the formalism of Ref. [66]. In combination with the short-distance constraints from Refs. [67–69], the results presented here will thus be instrumental to arrive at a complete data-driven evaluation of HLbL scattering and to reduce the uncertainties to the level required by the final precision expected from the Fermilab experiment.

Appendix F

Constants and parameters

In Table F.1, we collect the masses and decay widths used in this part of the thesis, in large part taken from Ref. [1]. For most quantities, possible effects from isospin breaking can be safely neglected, but some ambiguity arises for the mass and width of the ρ. For the $e^+e^- \to f_1\pi^+\pi^-$ process as the focus of this part, it would be natural to identify the ρ parameters with the ρ^0, whose width is quoted at an appreciably lower value than for the charged channel. However, we follow the arguments from App. E, observing that determinations sensitive also to the excited ρ states both in the neutral [70] and charged mode [71] tend to support the charged-channel values from Ref. [1] and, therefore, use the latter ones throughout. In particular, via Eq. (10.25), this determines $|g_{\rho\pi\pi}| = 5.98$, in good agreement with dispersive determinations [72, 73]; see also App. B. Similarly, the photon couplings are calculated from Eq. (B.2) with the branching fractions from Ref. [1], leading to

$$|g_{\rho\gamma}| = 4.96, \qquad |g_{\omega\gamma}| = 16.51, \qquad |g_{\phi\gamma}| = 13.40, \tag{F.1}$$

slightly deviating from the values given in App. B due to updated input quantities. Finally, we quote the values for masses and decay widths of the axial-vector resonances from Ref. [1]. For the a_1, the (reaction-dependent) BW parameters can also be compared to attempts to extract the pole position from $\tau \to 3\pi\nu_\tau$ data, $\sqrt{s_{a_1}} = m_{a_1} - \mathrm{i}\Gamma_{a_1}/2 = \left[1209(4)(^{+12}_{-9}) - \mathrm{i}288(6)(^{+45}_{-10})\right]\,\mathrm{MeV}$ [74]. In addition, Ref. [1] quotes the average $\Gamma_{a_1} = 420(35)\,\mathrm{MeV}$ [75, 76], in line with the center of the estimated range quoted in Table F.1. Based on the same two references, one would conclude the mass average $m_{a_1} = 1250(20)\,\mathrm{MeV}$.

Quantity	Variable	Value	Reference
Mass pion	M_π	139.57 MeV	
Mass $f_1(1285)$	m_{f_1}	1281.9(5) MeV	
Mass $f_1(1420)$	$m_{f_1'}$	1426.3(9) MeV	
Mass $a_1(1260)$	m_{a_1}	1230(40) MeV	
Mass $\omega(782)$	M_ω	782.66(13) MeV	
Mass $\omega(1420)$	$M_{\omega'}$	1410(60) MeV	
Mass $\omega(1650)$	$M_{\omega''}$	1670(30) MeV	
Mass $\phi(1020)$	M_ϕ	1019.461(16) MeV	
Mass $\phi(1680)$	$M_{\phi'}$	1680(20) MeV	
Mass $\phi(2170)$	$M_{\phi''}$	2163(7) MeV	[1]
Mass $\rho(770)$ (charged)	M_ρ	775.11(34) MeV	
Mass $\rho(1450)$	$M_{\rho'}$	1465(25) MeV	
Mass $\rho(1700)$	$M_{\rho''}$	1720(20) MeV	
Total width $f_1(1285)$	Γ_{f_1}	22.7(1.1) MeV	
Total width $f_1(1420)$	$\Gamma_{f_1'}$	54.5(2.6) MeV	
Total width $a_1(1260)$	Γ_{a_1}	(250 . . . 600) MeV	
Total width $\rho(770)$ (charged)	Γ_ρ	149.1(8) MeV	
Total width $\rho(1450)$	$\Gamma_{\rho'}$	400(60) MeV	
Total width $\rho(1700)$	$\Gamma_{\rho''}$	250(100) MeV	
Mass $\rho(770)$ (charged)	M_ρ	774.9(6) MeV	
Mass $\rho(1450)$ (charged)	$M_{\rho'}$	1428(30) MeV	
Mass $\rho(1700)$ (charged)	$M_{\rho''}$	1694(98) MeV	[70]
Total width $\rho(770)$ (charged)	Γ_ρ	148.6(1.8) MeV	
Total width $\rho(1450)$ (charged)	$\Gamma_{\rho'}$	413(58) MeV	
Total width $\rho(1700)$ (charged)	$\Gamma_{\rho''}$	135(62) MeV	
Mass $\rho(770)$ (neutral)	M_ρ	775.02(35) MeV	
Mass $\rho(1450)$ (neutral)	$M_{\rho'}$	1493(15) MeV	
Mass $\rho(1700)$ (neutral)	$M_{\rho''}$	1861(17) MeV	[71]
Total width $\rho(770)$ (neutral)	Γ_ρ	149.59(67) MeV	
Total width $\rho(1450)$ (neutral)	$\Gamma_{\rho'}$	427(31) MeV	
Total width $\rho(1700)$ (neutral)	$\Gamma_{\rho''}$	316(26) MeV	

Table F.1: Masses and decay widths from Ref. [1] as used in this part of the thesis (first panel), in comparison to the ρ, ρ', and ρ'' parameters from Refs. [70, 71].

References

[1] R. L. Workman *et al.* [Particle Data Group], PTEP **2022**, 083C01 (2022).

[2] D. V. Amelin *et al.* [VES], Z. Phys. C **66**, 71 (1995).

[3] S. I. Bityukov *et al.*, Phys. Lett. B **203**, 327 (1988).

[4] P. Achard *et al.* [L3], Phys. Lett. B **526**, 269 (2002) [arXiv:hep-ex/0110073].

[5] M. N. Achasov *et al.* [SND], Phys. Lett. B **800**, 135074 (2020) [arXiv:1906.03838 [hep-ex]].

[6] A. S. Rudenko, Phys. Rev. D **96**, 076004 (2017) [arXiv:1707.00545 [hep-ph]].

[7] A. I. Milstein and A. S. Rudenko, Phys. Lett. B **800**, 135117 (2020) [arXiv:1909.07938 [hep-ph]].

[8] M. Hoferichter and P. Stoffer, JHEP **05**, 159 (2020) [arXiv:2004.06127 [hep-ph]].

[9] W. A. Bardeen and W. K. Tung, Phys. Rev. **173**, 1423 (1968), [Erratum: Phys. Rev. D **4**, 3229 (1971)].

[10] R. Tarrach, Nuovo Cim. A **28**, 409 (1975).

[11] B. Aubert *et al.* [BaBar], Phys. Rev. D **76**, 092005 (2007) [arXiv:0708.2461 [hep-ex]], [Erratum: Phys. Rev. D **77**, 119902 (2008)].

[12] J. P. Lees *et al.* [BaBar], Phys. Rev. D **107**, 072001 (2023) [arXiv:2207.10340 [hep-ex]].

[13] M. Davier, A. Hoecker, B. Malaescu, and Z. Zhang, Eur. Phys. J. C **77**, 827 (2017) [arXiv:1706.09436 [hep-ph]].

[14] A. Keshavarzi, D. Nomura, and T. Teubner, Phys. Rev. D **97**, 114025 (2018) [arXiv:1802.02995 [hep-ph]].

[15] G. Colangelo, M. Hoferichter, and P. Stoffer, JHEP **02**, 006 (2019) [arXiv:1810.00007 [hep-ph]].

[16] M. Hoferichter, B.-L. Hoid, and B. Kubis, JHEP **08**, 137 (2019) [arXiv:1907.01556 [hep-ph]].

[17] M. Davier, A. Hoecker, B. Malaescu, and Z. Zhang, Eur. Phys. J. C **80**, 241 (2020) [arXiv:1908.00921 [hep-ph]], [Erratum: Eur. Phys. J. C **80**, 410 (2020)].

[18] A. Keshavarzi, D. Nomura, and T. Teubner, Phys. Rev. D **101**, 014029 (2020) [arXiv:1911.00367 [hep-ph]].

[19] B.-L. Hoid, M. Hoferichter, and B. Kubis, Eur. Phys. J. C **80**, 988 (2020) [arXiv:2007.12696 [hep-ph]].

[20] D. Stamen, D. Hariharan, M. Hoferichter, B. Kubis, and P. Stoffer, Eur. Phys. J. C **82**, 432 (2022) [arXiv:2202.11106 [hep-ph]].

[21] G. Colangelo, A. X. El-Khadra, M. Hoferichter, A. Keshavarzi, C. Lehner, P. Stoffer, and T. Teubner, Phys. Lett. B **833**, 137313 (2022) [arXiv:2205.12963 [hep-ph]].

[22] G. Colangelo, M. Hoferichter, B. Kubis, and P. Stoffer, JHEP **10**, 032 (2022) [arXiv:2208.08993 [hep-ph]].

[23] M. Hoferichter, G. Colangelo, B.-L. Hoid, B. Kubis, J. Ruiz de Elvira, D. Schuh, D. Stamen, and P. Stoffer, Phys. Rev. Lett. **131**, 161905 (2023) [arXiv:2307.02532 [hep-ph]].

[24] M. Hoferichter, B.-L. Hoid, B. Kubis, and D. Schuh, JHEP **08**, 208 (2023) [arXiv:2307.02546 [hep-ph]].

[25] S. Borsanyi *et al.* [BMWc], Nature **593**, 51 (2021) [arXiv:2002.12347 [hep-lat]].

[26] M. Cè *et al.*, Phys. Rev. D **106**, 114502 (2022) [arXiv:2206.06582 [hep-lat]].

[27] C. Alexandrou *et al.* [ETM], Phys. Rev. D **107**, 074506 (2023) [arXiv:2206.15084 [hep-lat]].

[28] A. Bazavov *et al.* [Fermilab Lattice, HPQCD, MILC], Phys. Rev. D **107**, 114514 (2023) [arXiv:2301.08274 [hep-lat]].

[29] T. Blum *et al.* [RBC, UKQCD], Phys. Rev. D **108**, 054507 (2023) [arXiv:2301.08696 [hep-lat]].

[30] M. Hoferichter and T. Teubner, Phys. Rev. Lett. **128**, 112002 (2022) [arXiv:2112.06929 [hep-ph]].

[31] R. R. Akhmetshin *et al.* [CMD-3], Phys. Lett. B **792**, 419 (2019) [arXiv:1902.06449 [hep-ex]].

[32] X. Liu, Q.-S. Zhou, and L.-M. Wang, Phys. Rev. D **106**, 094012 (2022) [arXiv:2209.11525 [hep-ph]].

[33] A. Khodjamirian, Eur. Phys. J. C **6**, 477 (1999) [arXiv:hep-ph/9712451].

[34] M. Hoferichter, B.-L. Hoid, B. Kubis, S. Leupold, and S. P. Schneider, Phys. Rev. Lett. **121**, 112002 (2018) [arXiv:1805.01471 [hep-ph]].

[35] M. Hoferichter, B.-L. Hoid, B. Kubis, S. Leupold, and S. P. Schneider, JHEP **10**, 141 (2018) [arXiv:1808.04823 [hep-ph]].

[36] P. Achard *et al.* [L3], JHEP **03**, 018 (2007).

[37] E. L. Lomon and S. Pacetti, Phys. Rev. D **85**, 113004 (2012) [arXiv:1201.6126 [hep-ph]], [Erratum: Phys. Rev. D **86**, 039901 (2012)].

[38] B. Moussallam, Eur. Phys. J. C **73**, 2539 (2013) [arXiv:1305.3143 [hep-ph]].

[39] A. Crivellin and M. Hoferichter, Phys. Rev. D **108**, 013005 (2023) [arXiv:2211.12516 [hep-ph]].

[40] C. Adolph *et al.* [COMPASS], Phys. Rev. D **95**, 032004 (2017) [arXiv:1509.00992 [hep-ex]].

[41] F. von Hippel and C. Quigg, Phys. Rev. D **5**, 624 (1972).

[42] R. Mertig, M. Bohm, and A. Denner, Comput. Phys. Commun. **64**, 345 (1991).

[43] V. Shtabovenko, R. Mertig, and F. Orellana, Comput. Phys. Commun. **207**, 432 (2016) [arXiv:1601.01167 [hep-ph]].

[44] V. Shtabovenko, R. Mertig, and F. Orellana, Comput. Phys. Commun. **256**, 107478 (2020) [arXiv:2001.04407 [hep-ph]].

[45] A. Denner and S. Dittmaier, Nucl. Phys. B **658**, 175 (2003) [arXiv:hep-ph/0212259].

[46] A. Denner and S. Dittmaier, Nucl. Phys. B **734**, 62 (2006) [arXiv:hep-ph/0509141].

[47] A. Denner and S. Dittmaier, Nucl. Phys. B **844**, 199 (2011) [arXiv:1005.2076 [hep-ph]].

[48] A. Denner, S. Dittmaier, and L. Hofer, Comput. Phys. Commun. **212**, 220 (2017) [arXiv:1604.06792 [hep-ph]].

[49] H. Schäfer, M. Zanke, Y. Korte, and B. Kubis, Phys. Rev. D **108**, 074025 (2023) [arXiv:2307.10357 [hep-ph]].

[50] M. Hoferichter, B.-L. Hoid, B. Kubis, and J. Lüdtke, Phys. Rev. Lett. **128**, 172004 (2022) [arXiv:2105.04563 [hep-ph]].

[51] T. Hahn, Comput. Phys. Commun. **168**, 78 (2005) [arXiv:hep-ph/0404043].

[52] M. Hoferichter, B. Kubis, and D. Sakkas, Phys. Rev. D **86**, 116009 (2012) [arXiv:1210.6793 [hep-ph]].

[53] T. A. Armstrong *et al.* [WA76], Z. Phys. C **43**, 55 (1989).

[54] T. A. Armstrong *et al.* [WA76], Phys. Lett. B **228**, 536 (1989).

[55] D. Barberis *et al.* [WA102], Phys. Lett. B **413**, 225 (1997) [arXiv:hep-ex/9707022].

[56] A. Gurtu *et al.* [Amsterdam-CERN-Nijmegen-Oxford], Nucl. Phys. B **151**, 181 (1979).

[57] T. Bolton *et al.* [MARK III], Phys. Lett. B **278**, 495 (1992).

[58] D. Coffman *et al.* [MARK III], Phys. Rev. D **41**, 1410 (1990).

[59] M. J. Corden *et al.*, Nucl. Phys. B **144**, 253 (1978).

[60] R. Dickson *et al.* [CLAS], Phys. Rev. C **93**, 065202 (2016) [arXiv:1604.07425 [nucl-ex]].

[61] D. Barberis *et al.* [WA102], Phys. Lett. B **440**, 225 (1998) [arXiv:hep-ex/9810003].

[62] J. H. Campbell, S. Lichtman, F. J. Loeffler, D. H. Miller, R. J. Miller, W. J. Miller, and R. B. Willmann, Phys. Rev. Lett. **22**, 1204 (1969).

[63] C. Defoix, A. Do Nascimento, J. S. O' Neall, J. Siaud, R. Bizzarri, L. Dobrzynski, S. N. Ganguli, L. Montanet, S. Reucroft, and T. Yamagata, Nucl. Phys. B **44**, 125 (1972).

[64] T. A. Armstrong *et al.* [WA76], Z. Phys. C **54**, 371 (1992).

[65] G. Colangelo, F. Hagelstein, M. Hoferichter, L. Laub, and P. Stoffer, Eur. Phys. J. C **81**, 702 (2021) [arXiv:2106.13222 [hep-ph]].

[66] J. Lüdtke, M. Procura, and P. Stoffer, JHEP **04**, 125 (2023) [arXiv:2302.12264 [hep-ph]].

[67] J. Bijnens, N. Hermansson-Truedsson, L. Laub, and A. Rodríguez-Sánchez, JHEP **10**, 203 (2020) [arXiv:2008.13487 [hep-ph]].

[68] J. Bijnens, N. Hermansson-Truedsson, L. Laub, and A. Rodríguez-Sánchez, JHEP **04**, 240 (2021) [arXiv:2101.09169 [hep-ph]].

[69] J. Bijnens, N. Hermansson-Truedsson, and A. Rodríguez-Sánchez, JHEP **02**, 167 (2023) [arXiv:2211.17183 [hep-ph]].

[70] M. Fujikawa *et al.* [Belle], Phys. Rev. D **78**, 072006 (2008) [arXiv:0805.3773 [hep-ex]].

[71] J. P. Lees *et al.* [BaBar], Phys. Rev. D **86**, 032013 (2012) [arXiv:1205.2228 [hep-ex]].

[72] R. García-Martín, R. Kamiński, J. R. Peláez, and J. Ruiz de Elvira, Phys. Rev. Lett. **107**, 072001 (2011) [arXiv:1107.1635 [hep-ph]].

[73] M. Hoferichter, B. Kubis, and M. Zanke, Phys. Rev. D **96**, 114016 (2017) [arXiv:1710.00824 [hep-ph]].

[74] M. Mikhasenko, A. Pilloni, M. Albaladejo, C. Fernández-Ramírez, A. Jackura, V. Mathieu, J. Nys, A. Rodas, B. Ketzer, and A. P. Szczepaniak [JPAC], Phys. Rev. D **98**, 096021 (2018) [arXiv:1810.00016 [hep-ph]].

[75] P. d'Argent, N. Skidmore, J. Benton, J. Dalseno, E. Gersabeck, S. Harnew, P. Naik, C. Prouve, and J. Rademacker, JHEP **05**, 143 (2017) [arXiv:1703.08505 [hep-ex]].

[76] M. Aghasyan *et al.* [COMPASS], Phys. Rev. D **98**, 092003 (2018) [arXiv:1802.05913 [hep-ex]].

Part II

The semileptonic decays $\eta^{(\prime)} \to \pi^0 \ell^+ \ell^-$ and $\eta' \to \eta \ell^+ \ell^-$ in the standard model

based on a project

in collaboration with
Hannah Schäfer, Yannis Korte, and Bastian Kubis

published in
Phys. Rev. D **108**, 074025 (2023) [arXiv:2307.10357 [hep-ph]]

Prologue

Due to their strongly suppressed decay rates within the standard model, the semileptonic decays $\eta^{(\prime)} \to \pi^0\ell^+\ell^-$ and $\eta' \to \eta\ell^+\ell^-$, $\ell = e, \mu$, are considered rare processes. The reason for this strong suppression is an implicit consequence of the conservation of charge-conjugation symmetry within strong and electromagnetic interactions—the primary forces mediating these decays. More specifically, the positive intrinsic charge parity of the pseudoscalar mesons requires the underlying decay mechanism to involve an even number of photons—each possessing an odd intrinsic charge parity—so that the processes are driven in terms of a one-loop diagram with two photons at lowest order. Contributions from physics beyond the standard model [1–6], on the other hand, can be mediated through charge-conjugation-violating mechanisms, *i.e.*, via a one-photon exchange, and thus proceed at tree-level, potentially countering the suppression that would otherwise be characteristic for such a contribution in comparison to the standard-model prediction. For this reason, the aforementioned semileptonic $\eta^{(\prime)}$ decays are excellent candidates for searches for physics beyond the standard model, with any signal conclusively deviating from the standard-model value giving a distinctive indication of new physics. In order to unambiguously interpret experimental measurements [16–18, 46–48] in this regard, the theoretical calculations need to be performed with high precision and specify a reasonable, conservative uncertainty estimate, in particular in light of the improved results expected from the REDTOP collaboration [49, 50], which plans to search for rare decays with an unprecedented number of $\eta^{(\prime)}$ events.

The author of this thesis started to work on the project presented in this part of the dissertation in the year 2021. At that time, Hannah Schäfer was investigating semileptonic $\eta^{(\prime)}$ decays as part of her master's thesis [91], providing an estimate within the framework of plain vector-meson dominance that improved on previous analyses [30] by taking into account the dependence on the photon virtualities in the parameterizations. Indeed, this additional momentum dependence has significant effects on the final results, as will be demonstrated in this part of the thesis. Given the initially underestimated complexity of the problem, the early advisory role of the author soon came to be a full-time involvement in the project, which took another one and a half years to be finalized; ultimately, this culminated in the development of a C++ interface [75] for the native Fortran library *Collier* [77–80], which—somewhat obscurely—solved many of the difficulties that formerly had to be overcome with *Collier*'s competitor *LoopTools* [81], as will be explained in the course of this dissertation.*

The analysis of the semileptonic $\eta^{(\prime)}$ decays performed in this thesis is based on the

*Moreover, in the process of work on this project, the author of this thesis found an error in the calculations of Ref. [30], which eventually led to the publication of an Erratum to that article.

assumption that the underlying two-photon processes $\eta^{(\prime)} \to \pi^0\gamma^*\gamma^*$ and $\eta' \to \eta\gamma^*\gamma^*$ are dominated by the exchange of vector mesons [12–14, 29]. Accordingly, the calculation of the full semileptonic amplitudes requires knowledge of the corresponding vector-to-pseudoscalar transition form factors [31, 32], the normalizations of which are determined from phenomenological input [15] in this thesis, as carried out independently by the author of this dissertation and Hannah Schäfer.

Having spelled out the amplitudes for the semileptonic decays, the momentum dependence of the form factors is modeled using vector-meson dominance—including constraints from isospin and U(3) flavor symmetry—for which various parameterizations are discussed by the author. More specifically, this includes a monopole as well as a dipole ansatz, with the latter tailored such that the expected high-energy behavior [41–45] is ensured; furthermore, for each of these, a variant that assumes constant widths for the vector mesons as well as a modification thereof that incorporates the energy dependence of the significant widths [69–71] is examined, implemented in terms of dispersively improved Breit–Wigner propagators. For reference, an ansatz corresponding to a point-like interaction is considered, which drops any dependence on the photon virtualities in the vector-to-pseudoscalar transition form factors [30]. The foundations for all these parameterizations have been worked out by the author of this dissertation in collaboration with Hannah Schäfer and Bastian Kubis, following which Hannah Schäfer focused on the explicit construction of the monopole form factors for both constant and energy-dependent widths, benefitting from the assistance and cross-checks of this thesis' author; the thesis' author, on the other hand, concentrated on the construction of the dipole variants, which were subsequently cross-checked by Hannah Schäfer. Next, contributions beyond the vector-meson-dominance model are analyzed by studying S-wave rescattering effects for the decay $\eta \to \pi^0\ell^+\ell^-$, which is based on a dispersive framework established by, among others, Yannis Korte [28, 82–86, 92]. Although the author of this thesis contributed to several discussions on this part, the actual implementation of the scalar rescattering effects was developed by Hannah Schäfer, Yannis Korte, and Bastian Kubis.

The following phenomenological analysis is performed in terms of integrated branching ratios as well as singly- and doubly-differential decay widths, obtained by performing a Passarino–Veltman decomposition of the amplitude with *FeynCalc* [72–74] and the subsequent numerical evaluation with *Collier*; here, the differential distributions are restricted to the variants assuming constant widths for the vector mesons. Crucially, the numerical evaluation of certain loop functions with *LoopTools* resulted in severe numerical instabilities for the variant with energy-dependent widths, as is discussed in detail by the author of this dissertation. Through insightful discussions with Bastian Kubis, the author was able to ascribe these problems to very specific regions of the phase space and was the first to suggest the use of the library *Collier*. Ultimately, this led to the development of a C++ interface for the native Fortran library *Collier*, with an instrumental role played by the author of this thesis, benefitting, in particular, from the assistance of Andreas Nogga. The numerical computations for the phenomenological analysis were split as follows: while the benchmark scenario of a point-like interaction has been calculated independently by the author of this dissertation and Hannah Schäfer, the author mainly focused on calculating the observables with the monopole form factors for both constant and energy-dependent widths; of these, the integrated branching ratios were cross-checked by Hannah Schäfer. Hannah Schäfer, on the other hand, concentrated

on calculating the integrated branching ratios with the dipole parameterizations, which were subsequently cross-checked by the author of this thesis.[‡] The numerical evaluation of the scalar rescattering effects was entirely performed by Hannah Schäfer and Yannis Korte. Furthermore, to normalize the integrated branching ratios of the semileptonic decays to their corresponding two-photon analogs, the branching ratios for $\eta^{(\prime)} \to \pi^0\gamma\gamma$ and $\eta' \to \eta\gamma\gamma$, along with the complementary differential distributions, are calculated by the author of this thesis, which have also been reproduced by Hannah Schäfer.

In the appendices of this part of the thesis, arguments needed for the construction of the vector-meson-dominance form factors and the determination of the relative signs between these are outlined, which were obtained independently by the author of this thesis and Hannah Schäfer, resorting to keen insights of Bastian Kubis.[§]

[‡]The differential distributions for the dipole variant given in this part of the thesis were calculated by the author of the dissertation and are not included in the published article.

[§]Note also that all plots except for Fig. 5.1 and Fig. 5.2 in this part of the thesis have been created by the author of the dissertation.

Chapter 1

Introduction

Within the SM of particle physics, both the strong and EM interactions conserve the symmetries parity ("P"), charge conjugation ("C"), and time reversal ("T") separately. For this reason, the decays $\eta^{(\prime)} \to \pi^0\ell^+\ell^-$ and $\eta' \to \eta\ell^+\ell^-$ can—mediated via the strong and EM force—only proceed via a C-even two-photon mechanism due to $\mathrm{C}(\eta^{(\prime)}) = +1 = \mathrm{C}(\pi^0)$, that is they appear as one-loop processes at lowest order.[1] As a result, the SM contribution to those decays is strongly suppressed, rendering them well-suited candidates for searches for physics beyond the SM (BSM). In fact, BSM contributions to the discussed decays, either mediated via a C-odd one-photon exchange [1–4] or due to other BSM mechanisms such as new light scalars [5] and unconventional sources of CP violation [6], are themselves subject to ongoing analyses.

Historically, calculations of $\eta \to \pi^0\ell^+\ell^-$ were based on different models for the $\eta \to \pi^0\gamma^*\gamma^*$ vertex as the conversion $\gamma^*\gamma^* \to \ell^+\ell^-$ depends solely on QED and is thus straightforward. This is not unlike the rare dilepton decays of the lightest flavor-neutral pseudoscalars, $P \to \ell^+\ell^-$, $P = \pi^0$, η, η', similarly loop-induced and completely calculable once the corresponding $P \to \gamma^*\gamma^*$ TFFs are known; see Refs. [7–9] for recent work and references therein. For these decays, a reasonable behavior of the TFFs for large photon virtualities is not only a requirement for a precision calculation but a necessity to regularize the otherwise ultraviolet-divergent loop integral. This was equally recognized in early theoretical work on $\eta \to \pi^0\ell^+\ell^-$ in the late 1960s, which was based on the simplest possible, point-like effective operator for $\eta \to \pi^0\gamma\gamma$ [10, 11]: the loop was rendered finite either with an *ad hoc* form factor [10] or reconstructed dispersively from the unambiguously calculable imaginary part with a finite energy cutoff [11]. As the effective operator only contained S-wave interactions in both cases—leading to helicity suppression of the resulting dilepton mechanism—these calculations only determined a subdominant contribution, underestimating, in particular, the $\eta \to \pi^0 e^+e^-$ rate by orders of magnitude.

On the other hand, a first VMD model calculation [12], which based the $\eta \to \pi^0\gamma\gamma$ amplitude on ρ and ω exchange, required no such further regularization: the additional vector-meson propagators, singularities in the crossed channels providing so-called left-hand cuts, dampen the high-energy behavior sufficiently such that the loop integral is convergent, see Fig. 1.1. Here, the coupling constants for the $V \to P\gamma$ transition, $V = \rho, \omega$, $P = \eta, \pi^0$—largely unknown at the time—had to be estimated in a quark model; in this way, realistic rates $B(\eta \to \pi^0 e^+e^-)/B(\eta \to \pi^0\gamma\gamma) \approx 10^{-5}$ were obtained. In the

[1] Contributions from the weak interactions are also required to vanish at tree level.

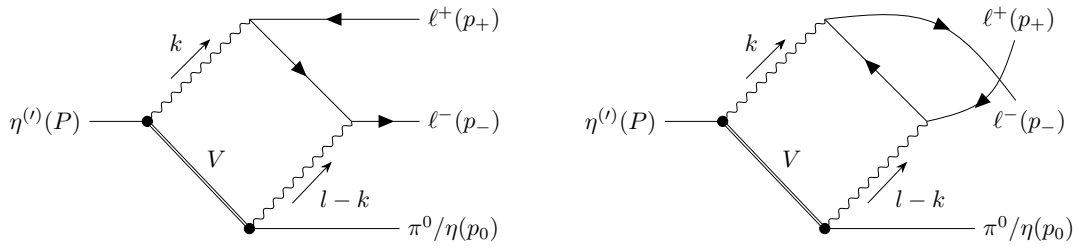

Figure 1.1: The t- (*left*) and u-channel (*right*) diagrams that contribute to $\eta^{(\prime)} \to [\pi^0/\eta]\ell^+\ell^-$ under the assumption that the underlying two-photon amplitudes are dominated by the exchange of the vector mesons $V = \rho, \omega, \phi$.

1990s, the two decays $\eta \to \pi^0 e^+ e^-$ and $\eta \to \pi^0 \mu^+ \mu^-$ were reconsidered by calculating unitarity bounds [13, 14]. These are based on the observation that the amplitude $\eta \to \pi^0\gamma\gamma$ (with real photons) model-independently determines the imaginary part of the dilepton amplitude, thus providing a lower limit on the corresponding rates. The diphoton decays were calculated in VMD, supplemented with scalar $a_0(980)$ exchange [13], or based on a constituent-quark-box model [14]; the numerical results of these older calculations are collected in Table 1.1.

Today, we understand the mechanism for $\eta \to \pi^0\gamma\gamma$ (and the related η' decays) much better, while precision calculations are still a challenge. Chiral perturbation theory [19] allows us to understand this reaction in terms of a systematic expansion at low momenta, where the dominant contribution originates from a set of next-to-next-to-leading-order counterterms [20, 21], whose size can phenomenologically be estimated in terms of vector-meson exchanges. The resulting predictions agree with the data [22–24] rather well [25], and rescattering corrections in the scalar channel [26, 27] are moderate in size [28]. Similarly, vector-meson exchanges dominate the decays $\eta' \to \pi^0\gamma\gamma$ and $\eta' \to \eta\gamma\gamma$ [29], with only minor S-wave corrections to the $\gamma\gamma$ spectra.

The most recent theoretical work on the decays $\eta^{(\prime)} \to \pi^0\ell^+\ell^-$ and $\eta' \to \eta\ell^+\ell^-$ [30] employs this modern knowledge to a large extent. Using the current phenomenological information on vector–pseudoscalar–photon couplings, it once more models the two-photon amplitudes with a VMD ansatz, superseding Ref. [12] by retaining all lepton-mass effects and Ref. [13] by calculating the real parts of the amplitudes explicitly. Perhaps surprisingly, what has still not been implemented is the dependence on the photon virtualities, *i.e.*, the vector-to-pseudoscalar TFFs [31, 32]. These have garnered significant interest in the last few years, both phenomenologically [33–36] and, in particular for the $\rho \to \pi$ TFF, on the lattice [37–40]. Furthermore, the behavior of these form factors for asymptotically large momentum transfers is known [41–45]. This is the major novelty of the analysis presented in this part of the thesis and the main advance compared to Ref. [30]: by providing a realistic model for $\eta^{(\prime)} \to \pi^0\gamma^*\gamma^*$ and $\eta' \to \eta\gamma^*\gamma^*$, including the dependence on the photon virtualities, we are able to give a more reliable prediction for the rates of the corresponding dilepton decays in the SM. Furthermore, by lifting the (somewhat artificial) dependence of the loop regularization on the left-hand cuts, we can, for the first time, also test the effect of S-wave rescattering contributions. Varying the form-factor models allows us to assess the remaining theoretical uncertainties of our predictions.

Experimentally, the decay $\eta \to \pi^0 e^+ e^-$ has been searched for since the 1960s [46–48],

	Branching ratio	Ancillary information	Reference
$\eta \to \pi^0 e^+ e^-$	9.9×10^{-9}	VMD model	[12]
$\eta \to \pi^0 e^+ e^-$	$8.4^{+4.6}_{-3.8} \times 10^{-10}$	Unitarity bounds, VMD model	[13]
$\eta \to \pi^0 e^+ e^-$	$9.2(1.5) \times 10^{-10}$	Quark-box model, $m_q = 330\,\text{MeV}$	[14]
$\eta \to \pi^0 \mu^+ \mu^-$	$3.8^{+2.3}_{-1.5} \times 10^{-10}$	Unitarity bounds, VMD model	[13]
	$6.9^{+4.6}_{-3.8} \times 10^{-10}$	As above, supplemented by a_0	
$\eta \to \pi^0 \mu^+ \mu^-$	$3.3(5) \times 10^{-9}$	Quark-box model, $m_q = 330\,\text{MeV}$	[14]
$\eta \to \pi^0 e^+ e^-$	$< 7.5 \times 10^{-6}$	3×10^7 η events	WASA-at-COSY [16]
$\eta \to \pi^0 \mu^+ \mu^-$	$< 5 \times 10^{-6}$	2×10^7 η events	Dzhelyadin *et al.* [17]
$\eta' \to \pi^0 e^+ e^-$	$< 1.4 \times 10^{-3}$	1.3×10^6 η' events	CLEO [18]
$\eta' \to \pi^0 \mu^+ \mu^-$	$< 6 \times 10^{-5}$	10^7 η' events	Dzhelyadin *et al.* [17]
$\eta' \to \eta e^+ e^-$	$< 2.4 \times 10^{-3}$	1.3×10^6 η' events	CLEO [18]
$\eta' \to \eta \mu^+ \mu^-$	$< 1.5 \times 10^{-5}$	10^7 η' events	Dzhelyadin *et al.* [17]

Table 1.1: Historical theoretical results on the branching ratio for $\eta \to \pi^0 \ell^+ \ell^-$ and experimental upper limits for the different decay channels $\eta^{(\prime)} \to [\pi^0/\eta] \ell^+ \ell^-$, the latter at 90% confidence level. For reasons of consistency with the experimental upper limits, we converted the theoretical results from decay widths to branching ratios by using an up-to-date central value [15] for the η width; see Table D.1 for the numerical values used in this part of the thesis.

motivated by the search for possible C violation in the strong and EM interactions. To date, only upper limits have been established for all decays studied in this part of the thesis, the most rigorous ones being collected in Table 1.1.[2] The most stringent upper limits, those for $\eta \to \pi^0 e^+ e^-$ from WASA-at-COSY [16] and for $\eta \to \pi^0 \mu^+ \mu^-$ from Lepton-G [17], are still more than three orders of magnitude above the theoretical SM branching ratios; for the η' decays, this margin is even larger. There is, even so, the prospect of improved experimental results by the REDTOP collaboration [49, 50], which plans to search for rare decays with an unprecedented number of η and η' events.

This part of the thesis is structured as follows: in Ch. 2, we construct the amplitudes for $\eta^{(\prime)} \to \pi^0 \ell^+ \ell^-$ and $\eta' \to \eta \ell^+ \ell^-$ as well as the corresponding two-photon analogs, with the latter serving as normalization channels. For the semileptonic decays, a set of form factors that incorporate the non-perturbative physics of the process is introduced and their normalizations are determined from phenomenological input. These form factors are then parameterized in Ch. 3 by means of two distinct VMD models, including the construction of dispersively improved variants. In Ch. 4, we discuss the calculation of observables—branching ratios as well as differential distributions—via a PV decomposition, and scalar rescattering contributions are analyzed in Ch. 5. Our numerical results are discussed

[2] Note that those upper limits were obtained assuming a flat Dalitz-plot distribution, which our results indicate to be an insufficient assumption; see the discussion in Sec. 6.1.

in Ch. 6, and we summarize our findings in Ch. 7. Further details are provided in the appendices.

Chapter 2

Amplitudes

The construction of the C-even decay amplitudes for

$$\begin{aligned}\eta^{(\prime)}(P) &\to \pi^0(p_0)\ell^+(p_+)\ell^-(p_-),\\ \eta'(P) &\to \eta(p_0)\ell^+(p_+)\ell^-(p_-),\end{aligned} \tag{2.1}$$

where $\ell = e, \mu$, is based on the assumption that the underlying $\eta^{(\prime)} \to \pi^0\gamma^*\gamma^*$ and $\eta' \to \eta\gamma^*\gamma^*$ amplitudes are dominated by the exchange of the vector mesons $V = \rho, \omega, \phi$, see Fig. 1.1. For our analysis, we define the MANDELSTAM variables

$$s = (p_+ + p_-)^2, \qquad t = (p_- + p_0)^2, \qquad u = (p_+ + p_0)^2, \tag{2.2}$$

which describe the invariant mass squares of the lepton pair and the lepton–pseudoscalar subsystems, respectively; they fulfill the relation $\Sigma = s + t + u = M^2_{\eta^{(\prime)}} + M^2_{\pi^0/\eta} + 2m^2_\ell$. The relevant vector-to-pseudoscalar TFFs $\mathcal{F}_{VP}(q^2)$ are defined as per

$$\langle P(p)|J^{\mathrm{EM}}_\mu(0)|V(p_V)\rangle = e\epsilon_{\mu\nu\alpha\beta}\epsilon^\nu(p_V)p^\alpha q^\beta \mathcal{F}_{VP}(q^2), \tag{2.3}$$

where $J^{\mathrm{EM}}_\mu(x) = e(2\bar{u}(x)\gamma_\mu u(x) - \bar{d}(x)\gamma_\mu d(x) - \bar{s}(x)\gamma_\mu s(x))/3$ denotes the EM current and $q = p_V - p$. The normalizations $|\mathcal{F}_{VP}(0)|$ at the real-photon point can be derived from phenomenological input in a straightforward manner,

$$\begin{aligned}\Gamma(V \to P\gamma) &= \frac{\alpha(M_V^2 - M_P^2)^3}{24M_V^3}|\mathcal{F}_{VP}(0)|^2,\\ \Gamma(P \to V\gamma) &= \frac{\alpha(M_P^2 - M_V^2)^3}{8M_P^3}|\mathcal{F}_{VP}(0)|^2,\end{aligned} \tag{2.4}$$

leading to Table 2.1 with input from Ref. [15].

Using Eq. (2.3) and summing over the t- and u-channel diagrams shown in Fig. 1.1 as well as $V = \rho, \omega, \phi$, we find the amplitude $\mathcal{M} \equiv \mathcal{M}(\eta^{(\prime)} \to [\pi^0/\eta]\ell^+\ell^-)$ to be given by

$$\begin{aligned}\mathcal{M} = \frac{\mathrm{i}\alpha^2}{\pi^2}\sum_V \int \mathrm{d}^4k\, g^{\beta_1\beta_2}\epsilon_{\mu_1\nu_1\alpha_1\beta_1}\epsilon_{\mu_2\nu_2\alpha_2\beta_2}P^{\alpha_1}k^{\mu_1}\big(P^{\alpha_2}k^{\mu_2} - P^{\alpha_2}l^{\mu_2} + k^{\alpha_2}l^{\mu_2}\big)\\ \times P_V^{\mathrm{BW}}\big((P-k)^2\big)P_\gamma(k^2)P_\gamma\big((l-k)^2\big)\mathcal{F}_{V\eta^{(\prime)}}(k^2)\mathcal{F}_{V[\pi^0/\eta]}\big((l-k)^2\big)\\ \times \bar{u}_s\left[\gamma^{\nu_2}\frac{\not{k} - \not{p}_+ + m_\ell}{(k-p_+)^2 - m_\ell^2}\gamma^{\nu_1} + \gamma^{\nu_1}\frac{\not{p}_- - \not{k} + m_\ell}{(p_- - k)^2 - m_\ell^2}\gamma^{\nu_2}\right]v_r,\end{aligned} \tag{2.5}$$

	$\Gamma/\,\mathrm{keV}$ [15]	$\lvert\mathcal{F}_{VP}(0)\rvert/\,\mathrm{GeV}^{-1}$
$\rho \to \pi^0\gamma$	69(12)	0.73(6)
$\omega \to \pi^0\gamma$	725(26)	2.33(4)
$\phi \to \pi^0\gamma$	5.61(21)	0.1355(26)
$\rho \to \eta\gamma$	44.2(3.1)	1.58(6)
$\omega \to \eta\gamma$	3.91(35)	0.449(20)
$\phi \to \eta\gamma$	55.3(1.1)	0.691(7)
$\eta' \to \rho\gamma$	55.5(1.9)	1.299(23)
$\eta' \to \omega\gamma$	4.74(20)	0.401(9)
$\phi \to \eta'\gamma$	0.264(9)	0.712(12)

Table 2.1: The normalizations $|\mathcal{F}_{VP}(0)|$ at the real-photon point obtained from Eq. (2.4) and phenomenological input determined from Ref. [15]; see also Table D.1.

with $\bar{u}_s \equiv \bar{u}_s(p_-)$ and $v_r \equiv v_r(p_+)$. Here, we defined $l = p_+ + p_-$ and the BW propagators

$$P_V^{\mathrm{BW}}(q^2) = \frac{1}{q^2 - M_V^2 + \mathrm{i}M_V\Gamma_V}, \qquad P_\gamma(q^2) = \frac{1}{q^2 + \mathrm{i}\epsilon}, \tag{2.6}$$

where M_V is the mass of the respective vector meson and Γ_V its width. Due to their narrowness, a constant-width approximation is well justified for the ω and ϕ, whereas the broad ρ meson necessitates an energy-dependent width to avoid sizable (unphysical) imaginary parts below threshold. We will implement such a parameterization for the ρ in Sec. 3.3 using a dispersively improved BW propagator. Our final results will be quoted for both a variant "CW" with constant widths for all vector mesons and a variant "VW" that instead employs an energy-dependent width for the ρ.

For the eventual computations, it will turn out useful to apply the Dirac equation and make the replacements

$$\begin{aligned}\bar{u}_s\gamma^{\tilde{\nu}}(\not{k} - \not{p}_+ + m_\ell)\gamma^\nu v_r &= \bar{u}_s(\gamma^{\tilde{\nu}}\not{k}\gamma^\nu - 2p_+^\nu\gamma^{\tilde{\nu}})v_r,\\ \bar{u}_s\gamma^\nu(\not{p}_- - \not{k} + m_\ell)\gamma^{\tilde{\nu}} v_r &= \bar{u}_s(2p_-^\nu\gamma^{\tilde{\nu}} - \gamma^\nu\not{k}\gamma^{\tilde{\nu}})v_r\end{aligned} \tag{2.7}$$

in Eq. (2.5).

The branching ratios of the semileptonic decays are commonly normalized to the two-photon analogs

$$\begin{aligned}\eta^{(\prime)}(P) &\to \pi^0(p_0)\gamma(q_1)\gamma(q_2),\\ \eta'(P) &\to \eta(p_0)\gamma(q_1)\gamma(q_2);\end{aligned} \tag{2.8}$$

see also Fig. 2.1. For these decays, we define the Mandelstam variables[3]

$$s = (q_1+q_2)^2, \qquad t_\gamma = (q_2+p_0)^2, \qquad u_\gamma = (q_1+p_0)^2, \tag{2.9}$$

[3]Note that the Mandelstam variable $s = (P-p_0)^2$ is identical in the semileptonic and the diphoton case.

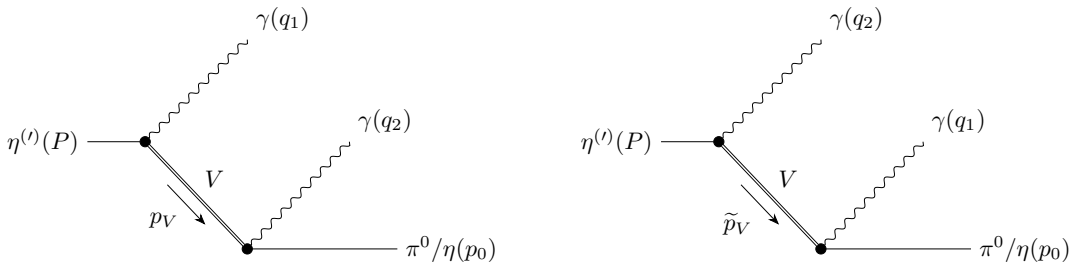

Figure 2.1: The two diagrams contributing to the two-photon decays $\eta^{(\prime)} \to [\pi^0/\eta]\gamma\gamma$, which are related via $q_1 \leftrightarrow q_2$ (*left* and *right*).

which fulfill $\Sigma_\gamma = s + t_\gamma + u_\gamma = M^2_{\eta^{(\prime)}} + M^2_{\pi^0/\eta}$, and denote the corresponding helicity amplitudes by $H_{\lambda\lambda'} \equiv H_{\lambda\lambda'}(s, t_\gamma)$,

$$\langle\gamma(q_1,\lambda)\gamma(q_2,\lambda')|S|\eta^{(\prime)}(P)[\pi^0/\eta](p_0)\rangle = \mathrm{i}(2\pi)^4\delta^{(4)}(P + p_0 - q_1 - q_2)\,4\pi\alpha\, e^{\mathrm{i}(\lambda-\lambda')\varphi}H_{\lambda\lambda'}. \tag{2.10}$$

Here, $\lambda^{(\prime)}$ are the helicities of the photons and we factored out the dependence of the electric charge $e^2 = 4\pi\alpha$ and the azimuthal angle φ. Using Eq. (2.3) and the normalization of the form factors, $|C_{VP\gamma}| = |\mathcal{F}_{VP}(0)|$, as will be introduced in Ch. 3, we obtain the VMD helicity amplitudes

$$H_{\lambda\lambda'} = \epsilon_\lambda^{\alpha_1\,*}(q_1)\epsilon_{\lambda'}^{\alpha_2\,*}(q_2)\sum_V C_{V\eta^{(\prime)}\gamma}C_{V[\pi^0/\eta]\gamma}\big[P_V^{\mathrm{BW}}(t_\gamma)H^t_{\alpha_1\alpha_2} + P_V^{\mathrm{BW}}(u_\gamma)H^u_{\alpha_1\alpha_2}\big], \tag{2.11}$$

where $\epsilon^*_\lambda(q_i)$ denote the polarization vectors of the outgoing photons and

$$\begin{aligned} H^t_{\alpha_1\alpha_2} &= g^{\mu_1\mu_2}\epsilon_{\mu_1\nu_1\alpha_1\beta_1}\epsilon_{\mu_2\nu_2\alpha_2\beta_2}p_V^{\nu_1}q_1^{\beta_1}p_0^{\nu_2}q_2^{\beta_2}, \\ H^u_{\alpha_1\alpha_2} &= g^{\mu_1\mu_2}\epsilon_{\mu_1\nu_1\alpha_1\beta_1}\epsilon_{\mu_2\nu_2\alpha_2\beta_2}p_0^{\nu_1}q_1^{\beta_1}\widetilde{p}_V^{\nu_2}q_2^{\beta_2}, \end{aligned} \tag{2.12}$$

with $p_V = q_2 + p_0$ and $\widetilde{p}_V = q_1 + p_0$ being the momenta of the intermediate vector mesons. In principle, the contractions can be carried out, leading to the cumbersome expressions

$$\begin{aligned} H^t_{\alpha_1\alpha_2} &= \frac{1}{2}\bigg[\frac{g^{\alpha_1\alpha_2}}{2}\Big(M^2_{\pi^0/\eta}(M^2_{\pi^0/\eta} - \Sigma_\gamma) + t_\gamma(u_\gamma - s)\Big) + (M^2_{\pi^0/\eta} - t_\gamma)p_0^{\alpha_1}q_1^{\alpha_2} + sp_0^{\alpha_1}p_0^{\alpha_2} \\ &\quad + sp_0^{\alpha_1}q_2^{\alpha_2} + (M^2_{\pi^0/\eta} - u_\gamma)q_2^{\alpha_1}p_0^{\alpha_2} + (M^2_{\pi^0/\eta} + t_\gamma)q_2^{\alpha_1}q_1^{\alpha_2} + (M^2_{\pi^0/\eta} - u_\gamma)q_2^{\alpha_1}q_2^{\alpha_2}\bigg], \\ H^u_{\alpha_1\alpha_2} &= H^t_{\alpha_2\alpha_1}\big|_{q_1\leftrightarrow q_2\,(t_\gamma\leftrightarrow u_\gamma)}. \end{aligned} \tag{2.13}$$

However, when discussing observables related to the two-photon decays in Ch. 4, the form given in Eq. (2.12) proves more convenient for the actual calculations.[4]

[4]Similarly, the contractions in Eq. (2.5) could be carried out. In this case, the resulting expression is even more cumbersome and the to-be-performed loop integration renders such an operation rather pointless.

Chapter 3

Form factors

In order to parameterize the form factors $\mathcal{F}_{VP}(q^2)$, we use the framework of VMD. As a consequence, the photon couplings at the $VP\gamma^*$ vertices of the diagrams in Fig. 1.1 are mediated via two intermediate vector mesons V_1 and V_2, see Fig. 3.1. We will construct two distinct such models: a monopole parameterization "MP" with $V_i = \rho, \omega, \phi$ and a dipole ansatz "DP" with $V_i = \rho^{(\prime)}, \omega^{(\prime)}, \phi^{(\prime)}$ that ensures the expected high-energy behavior of the form factors [41–45]. For reference, we also include a model calculation "PL" with constant form factors, *i.e.*, a point-like interaction, which closely resembles the parameterization of Ref. [30].

The conservation of isospin—and thus G-parity combined with C—imposes fundamental constraints on V_1 and V_2 in dependence of the initial and final states as well as the t- or u-channel vector meson V. However, some of the couplings, namely $\eta^{(\prime)}\omega\phi^{(\prime)}$, $\eta^{(\prime)}\phi\omega^{(\prime)}$, $\pi^0\rho\phi^{(\prime)}$, and $\pi^0\phi\rho^{(\prime)}$, are, although isospin-allowed, vanishing under the assumption of U(3) flavor symmetry and ideally mixed vector-meson multiplets, see App. A. Since the contribution of $V = \phi$ would otherwise vanish entirely for $\eta^{(\prime)} \to \pi^0\ell^+\ell^-$, we nonetheless include the Okubo–Zweig–Iizuka-suppressed (OZI-suppressed) [51–53] couplings $\pi^0\phi\rho^{(\prime)}$ in our calculations; the remaining vector mesons V_i are collected in Table 3.1.

3.1 Monopole model

The MP model only takes the lowest-lying vector mesons ρ, ω, and ϕ into account, so that the form factors are parameterized according to

$$\mathcal{F}_{VP}(q^2) = C_{VP\gamma} M_{V_i}^2 P_{V_i}^{\mathrm{BW}}(q^2), \tag{3.1}$$

with the assignments of $V_i \in \{\rho, \omega, \phi\}$ specified in Table 3.1. Here, we assume $|C_{VP\gamma}| = |\mathcal{F}_{VP}(0)|$ at the real-photon point, see Table 2.1, which determines the coupling constants $C_{VP\gamma}$ up to an overall phase. This assumption omits corrections due to the constant, non-zero widths in the BW propagators, which are negligible for $V = \omega, \phi$ but potentially significant for $V = \rho$.[5] Since the energy-dependent width of the ρ meson will be chosen to have the proper threshold behavior, these complications only exist for the variant CW but not VW. In the following, all coupling constants are assumed to be real; to fix the relative

[5] Note that $P_V^{\mathrm{BW}}(0) \simeq -1/M_V^2$, so that $\mathcal{F}_{VP}(0) = -C_{VP\gamma}$, which, however, corresponds to an unobservable overall phase.

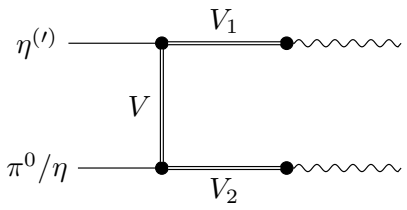

Figure 3.1: The modeling of the two-photon decay mechanism in the VMD framework via two vector mesons V_1 and V_2. Constraints on (V_1, V_2) in dependence of the initial and final state as well as V are given in Table 3.1.

signs between them, we resort to U(3) flavor symmetry and analyses of $e^+e^- \to 3\pi$ and $e^+e^- \to \pi\gamma$ [54–56], see App. A. Without loss of generality, we adopt a positive sign for the coupling $C_{\rho\eta\gamma}$ and establish the consistent sign convention compiled in Table 3.2.

3.2 Dipole model

By including the next-higher multiplet of vector mesons, ρ', ω', and ϕ', and tuning a free parameter ϵ_V accordingly, the expected asymptotic behavior $\mathcal{F}_{VP}(q^2) \propto q^{-4}$ of the vector-to-pseudoscalar TFFs [41–45] can be obtained.[6] For the DP model, we thus make the ansatz

$$\widetilde{\mathcal{F}}_{VP}(q^2) = C_{VP\gamma}\big[(1-\epsilon_{V_i})M_{V_i}^2 P_{V_i}^{\mathrm{BW}}(q^2) + \epsilon_{V_i} M_{V_i'}^2 P_{V_i'}^{\mathrm{BW}}(q^2)\big], \tag{3.2}$$

where we assume the excited vector states to couple according to the exact same symmetry restrictions as the ground-state multiplet, *cf.* Table 3.1; $P_{V'}^{\mathrm{BW}}(q^2)$ is defined as in Eq. (2.6), with $M_{V'}$ and $\Gamma_{V'}$ the mass and width of the respective excited vector meson. Due to the large widths of the excited vector mesons, a constant-width approximation leads to a rather poor description of these mesons, however. We will therefore, analogously to the ρ and based on energy-dependent widths, construct dispersively improved BW propagators for ρ', ω', and ϕ' in Sec. 3.3, leading to replacements of the kind $P_{V'}^{\mathrm{BW}}(q^2) \to P_{V'}^{\mathrm{disp}}(q^2)$. Similarly to the MP, our final results for the DP will be quoted for both the variant CW with constant widths for all vector mesons and the variant VW, *i.e.*, using constant widths for the ω and ϕ but energy-dependent ones for $\rho^{(\prime)}$, ω', and ϕ'. The form factors in Eq. (3.2) are assumed to be normalized such that $\widetilde{F}_{VP}(0) = -C_{VP\gamma}$, which, as for the MP, holds up to potential corrections due to the constant widths in the propagators. In order to obtain the desired high-energy behavior, the free parameter needs to be chosen as $\epsilon_V = M_V^2/(M_V^2 - M_{V'}^2)$.

3.3 Spectral representation

While the variant CW yields a simple approximate description, the large widths of the mesons $\rho^{(\prime)}$, ω', and ϕ' actually require an energy-dependent parameterization to avoid

[6] Data on both $e^+e^- \to \omega\pi^0$ [57] and $e^+e^- \to \rho^0\eta$ [58–60] suggests that the required cancellation indeed largely occurs between the contributions of the two lowest vector states, *i.e.*, ρ and ρ' in those cases.

	$V\pi^0\gamma$			$V\eta^{(\prime)}\gamma$		
V	ρ	ω	ϕ	ρ	ω	ϕ
V_i	$\omega^{(\prime)}$	$\rho^{(\prime)}$	$\rho^{(\prime)}$	$\rho^{(\prime)}$	$\omega^{(\prime)}$	$\phi^{(\prime)}$

Table 3.1: The constraints on the vector mesons V_i of Fig. 3.1 in dependence of V derived from isospin conservation and U(3) flavor symmetry with ideally mixed vector-meson multiplets. We include the OZI-suppressed couplings $\phi\pi^0\rho^{(\prime)}$; see text and App. A for more information.

significant (unphysical) imaginary parts below threshold.[7] In this section, we construct these energy-dependent widths; to ensure the correct analytic properties when inserting the form factors into the amplitude, Eq. (2.5), we will furthermore introduce dispersively improved variants [68] of the form factors that contain a $\rho^{(\prime)}$-, ω'-, or ϕ'-meson propagator, which lay the foundation for the variant VW in both the MP and DP model.

For the ρ meson, we will use the energy-dependent width [69]

$$\begin{aligned}\Gamma_\rho(q^2) &= \theta(q^2-4M_{\pi^\pm}^2)\frac{\gamma_{\rho\to\pi^+\pi^-}(q^2)}{\gamma_{\rho\to\pi^+\pi^-}(M_\rho^2)}f(q^2)\Gamma_\rho,\\ \gamma_{\rho\to\pi^+\pi^-}(q^2) &= \frac{(q^2-4M_{\pi^\pm}^2)^{3/2}}{q^2},\end{aligned} \tag{3.3}$$

where the so-called barrier factor [70, 71]

$$f(q^2) = \frac{\sqrt{q^2}}{M_\rho}\frac{M_\rho^2-4M_{\pi^\pm}^2+4p_R^2}{q^2-4M_{\pi^\pm}^2+4p_R^2}, \qquad p_R = 202.4\,\text{MeV}, \tag{3.4}$$

has been introduced to ensure convergence of the superconvergence relations evaluated in Eq. (3.14) below. We calculate the dispersive ρ propagator via

$$\begin{aligned}P_V^{\text{disp}}(q^2) &= -\frac{1}{\pi}\int_{s_\text{thr}}^\infty \mathrm{d}x\,\frac{\text{Im}\,[P_V^\text{BW}(x)]}{q^2-x+\mathrm{i}\epsilon},\\ \text{Im}\,[P_V^\text{BW}(x)] &= \frac{-\sqrt{x}\,\Gamma_V(x)}{(x-M_V^2)^2+x\Gamma_V(x)^2},\end{aligned} \tag{3.5}$$

where $s_\text{thr} = 4M_{\pi^\pm}^2$ is the threshold for $\rho\to\pi^+\pi^-$. The spectral representations of the form factors $\mathcal{F}_{VP}(q^2)$ for $VP\in\{\rho\eta^{(\prime)},\omega\pi^0,\phi\pi^0\}$ are thus given by

$$\widehat{\mathcal{F}}_{VP}(q^2) = \frac{C_{VP\gamma}}{N_\rho}M_\rho^2 P_\rho^\text{disp}(q^2), \tag{3.6}$$

where the normalization constant

$$N_\rho = -M_\rho^2 P_\rho^\text{disp}(0) \approx 0.898 \tag{3.7}$$

[7] In principle, such unphysical imaginary parts could be avoided for the ρ exchange by reconstructing the latter in terms of dispersion relations for $\gamma^{(*)}\pi\to\pi\pi$ [40, 61, 62] and $\eta^{(\prime)}\to\pi\pi\gamma^{(*)}$ [60, 63–65]; *cf.* also Refs. [66, 67]. We refrain from further refining the amplitude in such a way here.

$C_{\rho\pi^0\gamma}$	$C_{\omega\pi^0\gamma}$	$C_{\phi\pi^0\gamma}$
$+$	$+$	$-$
$C_{\rho\eta\gamma}$	$C_{\omega\eta\gamma}$	$C_{\phi\eta\gamma}$
$+$	$+$	$-$
$C_{\rho\eta'\gamma}$	$C_{\omega\eta'\gamma}$	$C_{\phi\eta'\gamma}$
$+$	$+$	$+$

Table 3.2: The signs $\mathrm{sgn}[C_{VP\gamma}]$ of the coupling constants defined in Eq. (3.1). Here, we fixed the global sign of $C_{\rho\eta\gamma}$ to be positive; see App. A for details.

is introduced to retain $\widehat{\mathcal{F}}_{VP}(0) = -C_{VP\gamma}$, *i.e.*, to ensure that the coupling constants have the same meaning in the original and the dispersively improved VMD parameterization. For reasons of consistency, we also replace the ρ propagator in the left-hand cuts, $P_\rho^{\mathrm{BW}}(q^2)$ in Eq. (2.5), by a dispersively improved variant,

$$P_\rho^{\mathrm{BW}}(q^2) \to \frac{1}{N_\rho^{\mathrm{LHC}}} P_\rho^{\mathrm{disp}}(q^2), \tag{3.8}$$

where the normalization constant

$$N_\rho^{\mathrm{LHC}} = \mathrm{i} M_\rho \Gamma_\rho P_\rho^{\mathrm{disp}}(M_\rho^2) \approx 1 \tag{3.9}$$

is introduced in order to retain $P_\rho^{\mathrm{BW}}(M_\rho^2) = 1/(\mathrm{i} M_\rho \Gamma_\rho)$, in line with the VMD assumption.[8] To evaluate $P_\rho^{\mathrm{disp}}(M_\rho^2)$, we use the Sokhotski–Plemelj theorem, leading to

$$P_\rho^{\mathrm{disp}}(M_\rho^2) = \frac{1}{\pi} \int_{s_{\mathrm{thr}}}^\infty \mathrm{d}x \, \frac{\mathrm{Im}\,[P_\rho^{\mathrm{BW}}(x)]}{x - M_\rho^2} + \mathrm{i}\,\mathrm{Im}\,[P_\rho^{\mathrm{BW}}(M_\rho^2)]. \tag{3.10}$$

With the above conventions, we will drop the distinction between $\mathcal{F}_{VP}(q^2)$ and $\widehat{\mathcal{F}}_{VP}(q^2)$ in the following, and it will always be clear from context which representation is used.

For the dipole variant, the widths of the excited vector mesons ρ', ω', ϕ' are modeled using the dominant quasi-two-particle thresholds. We condense the decays $\rho' \to \omega\pi$, $\omega' \to \rho\pi$, and $\phi' \to K^* \bar{K}$ in the notation $V' \to VP$, such that

$$\begin{aligned} \Gamma_{V'}(q^2) &= \theta\big(q^2 - (M_V + M_P)^2\big) \frac{\gamma_{V'\to VP}(q^2)}{\gamma_{V'\to VP}(M_{V'}^2)} \Gamma_{V'}, \\ \gamma_{V'\to VP}(q^2) &= \frac{\lambda(q^2, M_V^2, M_P^2)^{3/2}}{(q^2)^{3/2}}. \end{aligned} \tag{3.11}$$

Here, we disregard any distinction between the various charge channels and use the neutral masses for the numerical evaluation. The dispersive ρ', ω', and ϕ' propagators and spectral functions are defined similarly to Eq. (3.5), with the threshold $s_{\mathrm{thr}} = (M_V + M_P)^2$. In analogy to Eq. (3.2), the dipole form factors read

$$\widetilde{\mathcal{F}}_{VP}(q^2) = \frac{C_{VP\gamma}}{\widetilde{N}_{V_i}} \big[(1 - \epsilon_{V_i}) M_{V_i}^2 P_{V_i}(q^2) + \epsilon_{V_i} M_{V_i'}^2 P_{V_i'}(q^2)\big], \tag{3.12}$$

[8] We ignore the fact that the ρ pole in the complex plane does not exactly agree with the BW parameters.

ϵ_ρ	$(-0.47)^{-0.07}_{+0.06}$	$\widetilde{N}_\rho$	$0.99^{+0.04}_{-0.03}$
ϵ_ω	$(-0.43)^{-0.25}_{+0.16}$	$\widetilde{N}_\omega$	$1.10^{+0.17}_{-0.10}$
ϵ_ϕ	$(-0.42)^{-0.08}_{+0.06}$	$\widetilde{N}_\phi$	$1.03^{+0.05}_{-0.04}$

Table 3.3: The values of the parameter ϵ_V derived from the superconvergence relations, Eq. (3.15), and the normalization constants of Eq. (3.13). Here, tiny imaginary parts in the normalization constants have been neglected. The uncertainties refer to the variations of $\Gamma_{\rho'}$, $\Gamma_{\omega'}$, and $\Gamma_{\phi'}$, see Table D.1, and are omitted in the subsequent analysis.

with $P_{V_i'}(q^2) \in \{P^{\mathrm{BW}}_{V_i'}(q^2), P^{\mathrm{disp}}_{V_i'}(q^2)\}$, where the simplifying assumption of constant widths for ω and ϕ propagators is always implicitly understood. Here, we introduced the normalization constants

$$\widetilde{N}_V = -\big[(1-\epsilon_V)M_V^2 P_V(0) + \epsilon_V M_{V'}^2 P_{V'}(0)\big], \tag{3.13}$$

which ensure $\widetilde{\mathcal{F}}_{VP}(0) = -C_{VP\gamma}$. The parameters ϵ_V have to be tuned differently in the dispersively improved variant, namely via the superconvergence relations

$$\begin{aligned} 0 &= (1-\epsilon_V)M_V^2 P_V^0 + \epsilon_V M_{V'}^2 P_{V'}^0, \\ P_V^0 &= \begin{cases} 1, & V = \omega, \phi, \\ -\dfrac{1}{\pi}\displaystyle\int_{s_{\mathrm{thr}}}^{\infty} \mathrm{d}x\, \mathrm{Im}\,[P_V^{\mathrm{BW}}(x)], & V = \rho^{(\prime)}, \omega', \phi', \end{cases} \end{aligned} \tag{3.14}$$

such that terms of $\mathcal{O}(1/q^2)$ in the form factors cancel. We collect the numerical results for

$$\epsilon_V = \frac{M_V^2 P_V^0}{M_V^2 P_V^0 - M_{V'}^2 P_{V'}^0} \tag{3.15}$$

and $\widetilde{N}_V$ in Table 3.3, where we include the uncertainties due to the large errors on $\Gamma_{V'}$; in what follows, their effect is, however, assumed to be insignificant and thus discarded.

Chapter 4

Observables

The phenomenological analysis in this part of the thesis will be performed in terms of doubly- and singly-differential decay widths as well as integrated branching ratios. We define $\nu = t - u$, in terms of which the twofold differential decay width $\mathrm{d}\Gamma \equiv \mathrm{d}\Gamma(\eta^{(\prime)} \to [\pi^0/\eta]\ell^+\ell^-)$ is given by [15]

$$\mathrm{d}\Gamma = \frac{1}{512\pi^3 M_{\eta^{(\prime)}}^3} |\overline{\mathcal{M}}|^2 \mathrm{d}s\, \mathrm{d}\nu. \tag{4.1}$$

Here, $|\overline{\mathcal{M}}|^2$ is the spin-summed square of the amplitude, Eq. (2.5), and the integration region is bounded by the available phase space

$$s \in [4m_\ell^2, (M_{\eta^{(\prime)}} - M_{\pi^0/\eta})^2], \qquad \nu \in [-\nu_{\max}, \nu_{\max}], \qquad \nu_{\max} = \sigma(s)\sqrt{\lambda(s)}, \tag{4.2}$$

with

$$\sigma(s) = \sqrt{1 - \frac{4m_\ell^2}{s}}, \qquad\qquad \lambda(s) \equiv \lambda(M_{\eta^{(\prime)}}^2, s, M_{\pi^0/\eta}^2). \tag{4.3}$$

The singly-differential decay width $\mathrm{d}\Gamma/\mathrm{d}s$ follows from an integration of Eq. (4.1) over ν, and the branching ratio

$$B(\eta^{(\prime)} \to [\pi^0/\eta]\ell^+\ell^-) = \frac{\Gamma}{\Gamma_{\eta^{(\prime)}}} \tag{4.4}$$

is obtained after performing the full three-body phase-space integration, *i.e.*, by additionally integrating over s.

In order to calculate $|\overline{\mathcal{M}}|^2$, we perform a PV decomposition of Eq. (2.5) with *FeynCalc* [72–74] after inserting explicit expressions for the form factors. For both the MP and DP model and in both variants CW and VW, this results in an expression of the generic form

$$\mathcal{M} = 16\pi^2\alpha^2\big[\mathcal{M}_{\mathrm{QED}}^{uv}\mathcal{M}_{\mathrm{H}}^{uv} + \mathcal{M}_{\mathrm{QED}}^{u0v}\mathcal{M}_{\mathrm{H}}^{u0v}\big], \qquad \mathcal{M}_{\mathrm{H}}^{u(0)v} = \sum_V C_V \mathcal{M}_V^{u(0)v},$$
$$\mathcal{M}_{\mathrm{QED}}^{uv} = m_\ell \bar{u}_s v_r, \qquad \mathcal{M}_{\mathrm{QED}}^{u0v} = \bar{u}_s \not{p}_0 v_r, \qquad C_V = C_{V\eta^{(\prime)}\gamma} C_{V[\pi^0/\eta]\gamma}, \tag{4.5}$$

	$C_\rho/\,\mathrm{GeV}^{-2}$	$C_\omega/\,\mathrm{GeV}^{-2}$	$C_\phi/\,\mathrm{GeV}^{-2}$
$\eta \to \pi^0\ell^+\ell^-$	1.16(11)	1.05(5)	0.0936(20)
$\eta' \to \pi^0\ell^+\ell^-$	0.95(8)	0.937(26)	−0.0965(25)
$\eta' \to \eta\ell^+\ell^-$	2.05(8)	0.180(9)	−0.492(10)

Table 4.1: Numerical values of the coupling constants defined in Eq. (4.5) for the different processes.

where the quantities $\mathcal{M}_V^{u(0)v}$ account for the different vector-meson contributions in the result of the PV decomposition, *cf.* the sum in Eq. (2.5); they amount to cumbersome expressions containing PV functions.[9] The numerical values of the process-specific coupling constants C_V are provided in Table 4.1. Upon squaring and spin-summing, the above amplitude leads to

$$\begin{aligned}|\overline{\mathcal{M}}|^2 = 256\pi^4\alpha^4\big[&C_\rho^2\,|\overline{\mathcal{M}}_{\rho,\rho}|^2 + C_\omega^2\,|\overline{\mathcal{M}}_{\omega,\omega}|^2 + C_\phi^2\,|\overline{\mathcal{M}}_{\phi,\phi}|^2 \\ &+ C_\rho C_\omega\,|\overline{\mathcal{M}}_{\rho,\omega}|^2 + C_\rho C_\phi\,|\overline{\mathcal{M}}_{\rho,\phi}|^2 + C_\omega C_\phi\,|\overline{\mathcal{M}}_{\omega,\phi}|^2\big],\end{aligned} \tag{4.6}$$

where we defined

$$\begin{aligned}|\overline{\mathcal{M}}_{V,V}|^2 &= |\overline{\mathcal{M}}^{uv}_{\mathrm{QED}}|^2|\mathcal{M}_V^{uv}|^2 + |\overline{\mathcal{M}}^{u0v}_{\mathrm{QED}}|^2|\mathcal{M}_V^{u0v}|^2 + 2\,\overline{\mathcal{M}}^{uv,u0v}_{\mathrm{QED}}\mathrm{Re}\left[\mathcal{M}_V^{uv}\mathcal{M}_V^{u0v*}\right], \\ |\overline{\mathcal{M}}_{V_1,V_2}|^2 &= 2\,|\overline{\mathcal{M}}^{uv}_{\mathrm{QED}}|^2\mathrm{Re}\left[\mathcal{M}_{V_1}^{uv}\mathcal{M}_{V_2}^{uv*}\right] + 2\,|\overline{\mathcal{M}}^{u0v}_{\mathrm{QED}}|^2\mathrm{Re}\left[\mathcal{M}_{V_1}^{u0v}\mathcal{M}_{V_2}^{u0v*}\right] \\ &\quad + 2\,\overline{\mathcal{M}}^{uv,u0v}_{\mathrm{QED}}\mathrm{Re}\left[\mathcal{M}_{V_1}^{uv}\mathcal{M}_{V_2}^{u0v*} + \mathcal{M}_{V_1}^{u0v}\mathcal{M}_{V_2}^{uv*}\right]\end{aligned} \tag{4.7}$$

for $V_1 \neq V_2$, with

$$\begin{aligned}|\overline{\mathcal{M}}^{uv}_{\mathrm{QED}}|^2 &= 2m_\ell^2(s-4m_\ell^2), & |\overline{\mathcal{M}}^{u0v}_{\mathrm{QED}}|^2 &= \frac{\lambda(s)-\nu^2}{2}, \\ \overline{\mathcal{M}}^{uv,u0v}_{\mathrm{QED}} &= -2m_\ell^2\nu.\end{aligned} \tag{4.8}$$

Similarly to the semileptonic decays, the branching ratio of the two-photon analogs is defined by

$$B(\eta^{(\prime)} \to [\pi^0/\eta]\gamma\gamma) = \frac{\Gamma_\gamma}{\Gamma_{\eta^{(\prime)}}}, \tag{4.9}$$

where $\Gamma_\gamma \equiv \Gamma(\eta^{(\prime)} \to [\pi^0/\eta]\gamma\gamma)$ and

$$\mathrm{d}\Gamma_\gamma = \frac{\alpha^2}{32\pi M^3_{\eta^{(\prime)}}}|\bar{H}|^2\mathrm{d}s\,\mathrm{d}\nu_\gamma, \tag{4.10}$$

with the phase space being bounded by

$$s \in [0, (M_{\eta^{(\prime)}} - M_{\pi^0/\eta})^2], \qquad \nu_\gamma \in [-\nu_\gamma^{\max}, \nu_\gamma^{\max}], \qquad \nu_\gamma^{\max} = \sqrt{\lambda(s)}. \tag{4.11}$$

[9] These expressions are attached as text files to the published article [75].

Due to the indistinguishability of the two photons in the final state, an additional factor of 1/2 has to be taken into account upon integration. From Eq. (2.11), one finds the polarization-summed amplitude squared

$$\begin{aligned}|\bar{H}|^2 = \frac{1}{8}\Bigg[\sum_V C_V^2 \Big(\big|P_V(t_\gamma)\big|^2 |H^{t,t}|^2 + \big|P_V(u_\gamma)\big|^2 |H^{u,u}|^2 + 2\mathrm{Re}\left[P_V(t_\gamma) P_V^*(u_\gamma)\right] |H^{t,u}|^2 \Big) \\ + \sum_{(V_1,V_2)} 2 C_{V_1} C_{V_2} \Big(\mathrm{Re}\left[P_{V_1}(t_\gamma) P_{V_2}^*(t_\gamma)\right] |H^{t,t}|^2 + \mathrm{Re}\left[P_{V_1}(u_\gamma) P_{V_2}^*(u_\gamma)\right] |H^{u,u}|^2 \\ + \mathrm{Re}\left[P_{V_1}(t_\gamma) P_{V_2}^*(u_\gamma) + P_{V_1}(u_\gamma) P_{V_2}^*(t_\gamma)\right] |H^{t,u}|^2 \Big) \Bigg], \end{aligned} \tag{4.12}$$

where the second sum extends over $(V_1, V_2) = (\rho,\omega), (\rho,\phi), (\omega,\phi)$ and we introduced

$$\begin{aligned} |H^{t,t}|^2 &= g^{\alpha_1\tilde{\alpha}_1} g^{\alpha_2\tilde{\alpha}_2} H^t_{\alpha_1\alpha_2} H^t_{\tilde{\alpha}_1\tilde{\alpha}_2}, \\ |H^{u,u}|^2 &= g^{\alpha_1\tilde{\alpha}_1} g^{\alpha_2\tilde{\alpha}_2} H^u_{\alpha_1\alpha_2} H^u_{\tilde{\alpha}_1\tilde{\alpha}_2}, \\ |H^{t,u}|^2 &= g^{\alpha_1\tilde{\alpha}_2} g^{\alpha_2\tilde{\alpha}_1} H^t_{\alpha_1\alpha_2} H^u_{\tilde{\alpha}_1\tilde{\alpha}_2}. \end{aligned} \tag{4.13}$$

As in Eq. (3.12), the propagators $P_V(x)$ are to be understood as BW propagators for all V in the CW approximation and BW propagators for $V = \omega, \phi$ but dispersively improved variants for $V = \rho$ in the variant VW. For the numerical implementation of the dispersively improved variants in Eq. (4.12), we use the Sokhotski–Plemelj theorem to rewrite Eq. (3.5) according to

$$P_V^{\mathrm{disp}}(s) = \frac{1}{\pi} \int_{s_{\mathrm{thr}}}^{\infty} \mathrm{d}x \, \frac{\mathrm{Im}\left[P_V^{\mathrm{BW}}(x)\right]}{x - s} + \mathrm{i}\,\mathrm{Im}\left[P_V^{\mathrm{BW}}(s)\right], \tag{4.14}$$

and $\theta(s - s_{\mathrm{thr}})$ for the imaginary part is implied by $\mathrm{Im}\left[P_V^{\mathrm{BW}}(s)\right]$. The principal-value integral can then be written in terms of a once-subtracted dispersion relation,

$$P_V^{\mathrm{disp,\,p.v.}}(s) = \frac{1}{\pi} \int_{s_{\mathrm{thr}}}^{\infty} \mathrm{d}x \, \frac{\mathrm{Im}\left[P_V^{\mathrm{BW}}(x)\right]}{x - s} = P_V^{\mathrm{disp,\,p.v.}}(0) + \frac{s}{\pi} \int_{s_{\mathrm{thr}}}^{\infty} \mathrm{d}x \, \frac{\mathrm{Im}\left[P_V^{\mathrm{BW}}(x)\right]}{x(x - s)}, \tag{4.15}$$

where

$$\int_{s_{\mathrm{thr}}}^{\infty} \mathrm{d}x \, \frac{\mathrm{Im}\left[P_V^{\mathrm{BW}}(x)\right]}{x(x - s)} = \int_{s_{\mathrm{thr}}}^{\infty} \mathrm{d}x \, \frac{\mathrm{Im}\left[P_V^{\mathrm{BW}}(x)\right] - \mathrm{Im}\left[P_V^{\mathrm{BW}}(s)\right]}{x(x - s)} + \frac{\mathrm{Im}\left[P_V^{\mathrm{BW}}(s)\right]}{s} \log\left|\frac{s_{\mathrm{thr}}}{s_{\mathrm{thr}} - s}\right|, \tag{4.16}$$

with $\int_{s_{\mathrm{thr}}}^{\infty} 1/[x(x-s)]$ solved analytically.[10] Inserting the kinematics of the process, the expressions given in Eq. (4.13) simplify to

$$\begin{aligned} |H^{t,t}|^2 &= |H^0|^2 + t_\gamma^2 (s^2 + u_\gamma^2), \\ |H^{u,u}|^2 &= |H^0|^2 + u_\gamma^2 (s^2 + t_\gamma^2), \\ |H^{t,u}|^2 &= |H^0|^2 + t_\gamma u_\gamma (s^2 + t_\gamma u_\gamma), \end{aligned} \tag{4.17}$$

where we defined

$$|H^0|^2 = M^4_{\pi^0/\eta}\big(s^2 + t_\gamma^2 + u_\gamma^2 + 2st_\gamma + 2su_\gamma + 4t_\gamma u_\gamma\big) - 2M^2_{\pi^0/\eta}\Sigma_\gamma t_\gamma u_\gamma - 2M^6_{\pi^0/\eta}\Sigma_\gamma + M^8_{\pi^0/\eta}. \tag{4.18}$$

[10] Had we not subtracted the dispersion relation, the analytic integration would not have converged.

Finally, we consider the normalized semileptonic branching ratio

$$\widehat{B}(\eta^{(\prime)} \to [\pi^0/\eta]\ell^+\ell^-) = \frac{B(\eta^{(\prime)} \to [\pi^0/\eta]\ell^+\ell^-)}{B(\eta^{(\prime)} \to [\pi^0/\eta]\gamma\gamma)}, \tag{4.19}$$

which is particularly useful from the theoretical point of view since it reduces the effect of the uncertainties from the coupling constants.

We perform the phase-space integrations of the differential decay widths, Eq. (4.1) and Eq. (4.10), numerically with the *Cuhre* and *Vegas* algorithm from the *Cuba* library [76]. For the numerical evaluation of the PV functions contained in the quantities $\mathcal{M}_V^{u(0)v}$, see Eq. (4.5), we use *Collier* [77–80].[11] The integration is carried out following the decomposition of Eq. (4.6) and Eq. (4.12),

$$\Gamma_{(\gamma)} = C_\rho^2\Gamma^{(\gamma)}_{\rho,\rho} + C_\omega^2\Gamma^{(\gamma)}_{\omega,\omega} + C_\phi^2\Gamma^{(\gamma)}_{\phi,\phi} + C_\rho C_\omega\Gamma^{(\gamma)}_{\rho,\omega} + C_\rho C_\phi\Gamma^{(\gamma)}_{\rho,\phi} + C_\omega C_\phi\Gamma^{(\gamma)}_{\omega,\phi}; \tag{4.20}$$

numerical results for the decay rates $\Gamma^{(\gamma)}_{V_1,V_2}$ are listed in App. B.[12]

[11] A C++ interface to the native Fortran library *Collier* written for this purpose, including an executable demo file, is attached as supplemental material to the published article [75].

[12] In App. B, we also discuss some peculiar problems that we observed when evaluating the PV functions with *LoopTools* [81] instead of *Collier*.

Chapter 5

Scalar rescattering contributions

While there are strong arguments in favor of the VMD model capturing the most significant contribution to the semileptonic $\eta^{(\prime)}$ decays, we will furthermore assess the numerical impact of scalar rescattering contributions based on a paradigmatic calculation for $\eta \to \pi^0\ell^+\ell^-$. For the η' channels, the vector mesons have sufficient energy to go quasi on shell, so that an even stronger leverage of the VMD mechanism is expected.

5.1 Isolating the *S*-wave in the hadronic subamplitude

With the decay $\eta \to \pi^0\ell^+\ell^-$ being driven by the two-photon intermediate state, as discussed in Ch. 1, we first revisit the hadronic subprocess $\eta \to \pi^0\gamma\gamma$. The corresponding subamplitude $H_{\lambda\lambda'}$, see Eq. (2.10), can be written by means of a tensor amplitude $H_{\mu\nu}$ according to

$$e^{\mathrm{i}(\lambda-\lambda')\varphi} H_{\lambda\lambda'} = \epsilon_\lambda^{*\mu}(q_1)\epsilon_{\lambda'}^{*\nu}(q_2) H_{\mu\nu}; \tag{5.1}$$

the explicit polarization vectors are chosen as

$$\epsilon_\pm(q_1) = \frac{1}{\sqrt{2}}(0, \mp 1, -\mathrm{i}, 0)^\intercal, \qquad \epsilon_\pm(q_2) = \frac{1}{\sqrt{2}}(0, \mp 1, \mathrm{i}, 0)^\intercal \tag{5.2}$$

in the following. For on-shell photons, the tensor amplitude $H^{\mu\nu}$ can be expanded in terms of two tensor structures $T_{1/2}^{\mu\nu}$ that manifestly fulfill the Ward identity [28],

$$\begin{aligned} T_1^{\mu\nu} &= \frac{s}{2}\, g^{\mu\nu} - q_2^\mu q_1^\nu, \\ T_2^{\mu\nu} &= 2s\Delta^\mu\Delta^\nu + 4(q_1\cdot\Delta)(q_2\cdot\Delta)g^{\mu\nu} - 4(q_2\cdot\Delta)\Delta^\mu q_1^\nu - 4(q_1\cdot\Delta)q_2^\mu\Delta^\nu, \end{aligned} \tag{5.3}$$

with $\Delta^\mu = (P + p_0)^\mu$, and two scalar amplitudes as per

$$H^{\mu\nu} = A(s, t_\gamma) T_1^{\mu\nu} + B(s, t_\gamma) T_2^{\mu\nu}. \tag{5.4}$$

Contracting Eq. (5.4) with the polarization vectors yields

$$\begin{aligned} H_{++}(s, t_\gamma) &= -\frac{s}{2} A(s, t_\gamma) - s\big[2(M_\eta^2 + M_{\pi^0}^2) - s\big] B(s, t_\gamma), \\ H_{+-}(s, t_\gamma) &= \big[(t_\gamma - u_\gamma)^2 - \lambda_{\pi^0\eta}(s)\big] B(s, t_\gamma), \end{aligned} \tag{5.5}$$

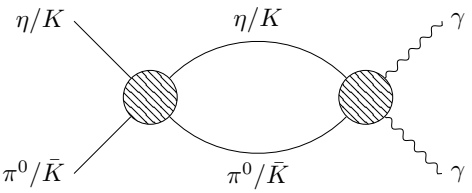

Figure 5.1: The two intermediate states $\pi^0\eta/K\bar{K}$ that contribute to the two-photon amplitudes; the dispersive representation of the amplitudes is constructed in Ref. [28].

where we introduced the abbreviation $\lambda_{\pi^0\eta}(s) \equiv \lambda(s, M_{\pi^0}^2, M_\eta^2)$. In order to isolate the S-wave, we neglect D- and higher partial waves, which requires the elimination of the entire contribution from $H_{+-}(s,t_\gamma)$ since its partial-wave expansion starts with D-waves. Consequently, we have to impose $B(s,t_\gamma) = 0$, and, hence, the S-wave contributes only through the tensor structure $T_1^{\mu\nu}$. Furthermore, setting $B(s,t_\gamma) = 0$ allows us to use the S-wave amplitude $h_{++}^L(s)|_{L=0}$ to fix the scalar amplitude $A(s,t_\gamma)$ via Eq. (5.5),

$$A^0(s) = -\frac{2}{s}\, h_{++}^0(s). \tag{5.6}$$

Note that $h_{++}^0(s)$ features a soft-photon zero at $s = 0$, so that $A^0(s)$ has no singularity at $s = 0$ despite the factor of $1/s$.

5.2 Rescattering effects in the hadronic subprocess

In Ref. [28], the rescattering effects in $\eta \to \pi^0\gamma\gamma$ are described through a coupled-channel analysis, taking into account $\pi^0\eta$ and $K\bar{K}$ intermediate states, *cf.* Fig. 5.1. Using the Omnès matrix $\Omega(s)$ for the $\pi^0\eta/(K\bar{K})_{I=1}$ system constructed therein, one obtains the dispersive representation

$$\begin{pmatrix} h_{++}^0(s) \\ k_{1,++}^0(s) \end{pmatrix} = \Omega(s)\left[\begin{pmatrix} a \\ b \end{pmatrix} s + \frac{s^2}{\pi}\left(\sum_V \int_{-\infty}^{s_V} \mathrm{d}z\, \frac{\Omega^{-1}(z)}{z^2(z-s)} \mathrm{Im}\begin{pmatrix} h_{++}^{0,V}(z) \\ k_{++}^{0,V}(z) \end{pmatrix} - \int_{s_{\pi^0\eta}}^{\infty} \mathrm{d}z\, \frac{\mathrm{Im}\left[\Omega^{-1}(z)\right]}{z^2(z-s)} \begin{pmatrix} 0 \\ k_{1,++}^{0,\mathrm{Born}}(z) \end{pmatrix}\right)\right] \tag{5.7}$$

for the S-wave amplitudes, with $s_{\pi^0\eta} = (M_{\pi^0} + M_\eta)^2$ being the threshold for the $\pi^0\eta$ intermediate state and $s_V = -(M_V^2 - M_{\pi^0}^2)(M_V^2 - M_\eta^2)/M_V^2$ the onset of the left-hand cut. Here, we include the VMD contributions from the ρ, ω, and ϕ mesons for the $\pi^0\eta$ channel ($h_{++}^{0,V}(s)$) and the K^* for the $K\bar{K}$ channel ($k_{++}^{0,V}(s)$) in the zero-width approximation. Using the polarization vectors from Eq. (5.2) and the coupling constants C_V defined in Eq. (4.5), the $\pi^0\eta$-channel VMD amplitude for photons with $(\lambda,\lambda') = (+,+)$ and the corresponding S-wave amplitude are given by

$$H_{++}^V(s,t_\gamma) = \frac{C_V}{4}\frac{st_\gamma}{M_V^2 - t_\gamma - \mathrm{i}\epsilon} + (t_\gamma \leftrightarrow u_\gamma), \tag{5.8}$$

$$h_{++}^{0,V}(s) = \frac{C_V}{2}\left[\frac{sM_V^2}{\lambda_{\pi^0\eta}^{1/2}(s)} \log\frac{X_V(s)+1}{X_V(s)-1} - s\right], \quad X_V(s) = \frac{2M_V^2 - (M_\eta^2 + M_{\pi^0}^2) + s}{\lambda_{\pi^0\eta}^{1/2}(s)},$$

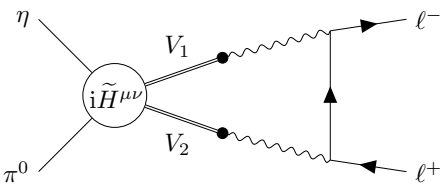

Figure 5.2: The triangle loop contributing to $\pi^0\eta \to \ell^+\ell^-$, which contains the tensor amplitude $\widetilde{H}^{\mu\nu}$ that captures the rescattering effects in $\pi^0\eta \to \gamma^*\gamma^*$, with the photon virtualities modeled via vector-meson propagators. This process is related to the corresponding η decay via crossing symmetry.

where the logarithm induces the left-hand cut starting from s_V. The VMD contribution to the $K\bar{K}$ channel, $K^V_{++}(s,t_\gamma)$, can be treated in complete analogy; for this channel, our representation additionally includes the QED BORN term projected onto isospin $I=1$,

$$\begin{aligned} K^{\text{BORN}}_{1,++}(s,t_\gamma) &= \frac{\sqrt{2}\,sM_K^2}{(t_\gamma - M_K^2)(u_\gamma - M_K^2)}, \\ k^{0,\text{BORN}}_{1,++}(s) &= \frac{2\sqrt{2}M_K^2}{s\sigma_K(s)}\log\frac{1+\sigma_K(s)}{1-\sigma_K(s)}, \qquad \sigma_K(s) = \sqrt{1-\frac{4M_K^2}{s}}. \end{aligned} \tag{5.9}$$

Moreover, the soft-photon zero is already implemented in Eq. (5.7); the remaining subtraction constants a and b are determined in accordance with Ref. [28], where one of them is fixed by incorporating an ADLER zero at $s_A = M_\eta^2$ and the other one is fit to experimental data.

Subtracting the VMD contributions, Eq. (5.8), from the full S-wave amplitude $h^0_{++}(s)$, Eq. (5.7), allows us to isolate the rescattering effects in Eq. (5.6) according to

$$A^0_{\text{resc}}(s) = -\frac{2}{s}\left(h^0_{++}(s) - \sum_{V=\rho,\omega,\phi} h^{0,V}_{++}(s)\right). \tag{5.10}$$

With this, we can construct an S-wave tensor amplitude that only contains the rescattering contributions in the form

$$\widetilde{H}^{\mu\nu} = A^0_{\text{resc}}(s)T_1^{\mu\nu}. \tag{5.11}$$

5.3 Loop calculation

To calculate the contribution of S-wave rescattering effects to the decay $\eta \to \pi^0\ell^+\ell^-$, we use Eq. (5.11) for the $\eta \to \pi^0\gamma^*\gamma^*$ vertex, which reduces the loop from a box to a triangle topology, see Fig. 5.2. The QED subamplitude for $\gamma^*\gamma^* \to \ell^+\ell^-$ is denoted by $L^{\mu\nu}$ in the following; its construction (at tree level) is straightforward and after simplifying with Eq. (2.7), one finds

$$L^{\mu\nu} = -\bar{u}_s\frac{2p_-^\mu - \gamma^\mu \not{q}_1}{(p_- - q_1)^2 - m_\ell^2 + \mathrm{i}\epsilon}\gamma^\nu v_r. \tag{5.12}$$

Note that we do not have to perform the S-wave projection of the QED subamplitude, since this is implicit in the loop integration. Furthermore, to avoid double counting, we

do not include the crossed channel, which is described by the same amplitude due to the symmetry of the triangle loop.

When taking into account the photon virtualities, the gauge-invariant tensor structure $T_1^{\mu\nu}$, in particular, acquires additional terms [82–84],

$$T_1^{\mu\nu}(q_1^2, q_2^2) = \frac{(s - q_1^2 - q_2^2)}{2} g^{\mu\nu} - q_2^\mu q_1^\nu. \tag{5.13}$$

The dependence on the photon virtualities is then further modeled by including factors of $M_V^2 P_V^{\mathrm{BW}}(q^2)$ for both photons, resulting in the hadronic tensor amplitude

$$\widetilde{H}^{\mu\nu}(q_1^2, q_2^2) = M_{V_1}^2 P_{V_1}^{\mathrm{BW}}(q_1^2) M_{V_2}^2 P_{V_2}^{\mathrm{BW}}(q_2^2) A_{\mathrm{resc}}^0(s) T_1^{\mu\nu}(q_1^2, q_2^2). \tag{5.14}$$

This is a naive generalization to virtual photons that corresponds to a scalar-resonance approximation, which we deem a sufficient approximation in the context of the semileptonic decays. It avoids the known complications from, *e.g.*, the modified partial-wave projections of the VMD amplitudes; see Refs. [85, 86] for a more rigorous treatment. The prescription in Eq. (5.14) is consistent with the monopole model for the form factors constructed in Ch. 3. The rescattering contributions to the $\eta \to \pi^0 \ell^+ \ell^-$ amplitude are then given by

$$\mathrm{i}\widetilde{\mathcal{M}}(s) = \frac{\alpha^2}{\pi^2} \int \mathrm{d}^4 q_1 \, \frac{\widetilde{H}^{\mu\nu}(q_1^2, q_2^2) L_{\mu\nu}}{(q_1^2 + \mathrm{i}\epsilon)(q_2^2 + \mathrm{i}\epsilon)}, \tag{5.15}$$

with $q_2 = p_+ + p_- - q_1$.

Understanding the S-wave amplitude as an enhancement due to the $a_0(980)$ resonance with $I^G(J^{PC}) = 1^-(0^{++})$, only the combination of ρ and ω is allowed for the vector mesons V_1 and V_2, so that the S-wave rescattering contributions become

$$\widetilde{\mathcal{M}}(s) = -\frac{\mathrm{i}\alpha^2}{\pi^2} M_\rho^2 M_\omega^2 A_{\mathrm{resc}}^0(s) \int \mathrm{d}^4 q_1 \, P_\rho^{\mathrm{BW}}(q_1^2) P_\omega^{\mathrm{BW}}(q_2^2) \frac{T_1^{\mu\nu}(q_1^2, q_2^2) L_{\mu\nu}}{(q_1^2 + \mathrm{i}\epsilon)(q_2^2 + \mathrm{i}\epsilon)}. \tag{5.16}$$

As a consequence of the reduction from a box to a triangle loop, and with $T_1^{\mu\nu}(q_1^2, q_2^2) \propto \mathcal{O}(q_1^2)$, the integral is convergent only because of the dependence on the photon virtualities introduced in Eq. (5.14). Contracting the tensor structures and performing a PV decomposition allows one to separate a factor of $m_\ell s/(M_\rho^2 M_\omega^2)$, with only the $\bar{u}_s v_r$ spinor structure from Eq. (4.5) contributing, resulting in

$$\widetilde{\mathcal{M}}(s) = 16\pi^2 \mathrm{i}\alpha^2 s A_{\mathrm{resc}}^0(s) \widetilde{\mathcal{M}}_{\mathrm{H}}^{uv}(s) \mathcal{M}_{\mathrm{QED}}^{uv}, \tag{5.17}$$

where $\widetilde{\mathcal{M}}_{\mathrm{H}}^{uv}(s)$ contains the remaining PV master integrals.

Chapter 6

Results and discussion

We present the results for the semileptonic decays in the form of branching ratios as well as singly- and doubly-differential decay widths; of these, the branching ratios are particularly convenient to demonstrate the effects of the different form-factor models. Furthermore, we examine the contribution of scalar rescattering effects to the branching ratios and normalize the latter to the corresponding two-photon analogs. For all of our results, the quoted uncertainties stem from the experimental uncertainties that enter via the coupling constants and amount to $\sim 10\%$. The uncertainties from the numerical integration, on the other hand, are at least one order of magnitude smaller and therefore omitted.

6.1 Differential decay width

The doubly- and singly-differential distributions of the semileptonic decays exhibit distinct characteristics, with the most prominent differences being observable between the decays with electrons and muons in the final state, see Fig. 6.1–Fig. 6.3. While the majority of the doubly-differential distribution for the electron channels is contained in a small fraction close to the threshold in the invariant lepton mass, the decays with muons in the final state display a spread-out distribution that covers large parts of the available phase space. For the electron final state, in particular, it is important to take into account the region close to the threshold in the invariant lepton mass, both when integrating over the phase space and when performing measurements, as significant parts of the decay width are readily missed otherwise. Furthermore, the logarithmic scale shows that the distributions possess a minimum for $\nu = 0$, where $\nu \propto \cos\theta_s$, with θ_s the s-channel scattering angle. With only even partial waves contributing to the decays, this feature can be attributed to the dominance of D-waves over the helicity-suppressed S-waves—which do not show such an angular distribution—whereas for the muon channels, this suppression is less pronounced. Beyond the difference in the final-state leptons, the principal visible differentiations concern the size of the phase space, which is significantly larger for $\eta' \to \pi^0\ell^+\ell^-$ than for $\eta \to \pi^0\ell^+\ell^-$ and $\eta' \to \eta\ell^+\ell^-$.

For all decay channels, the obtained Dalitz plots do not follow a flat distribution, which was assumed for the experimental analysis of $\eta \to \pi^0 e^+e^-$ in Ref. [16]. While this assumption is justified for a potential C-violating contribution [4], it is insufficient for the SM result; we therefore propose a reevaluation of the experimental data and a reassessment of the reported upper limit.

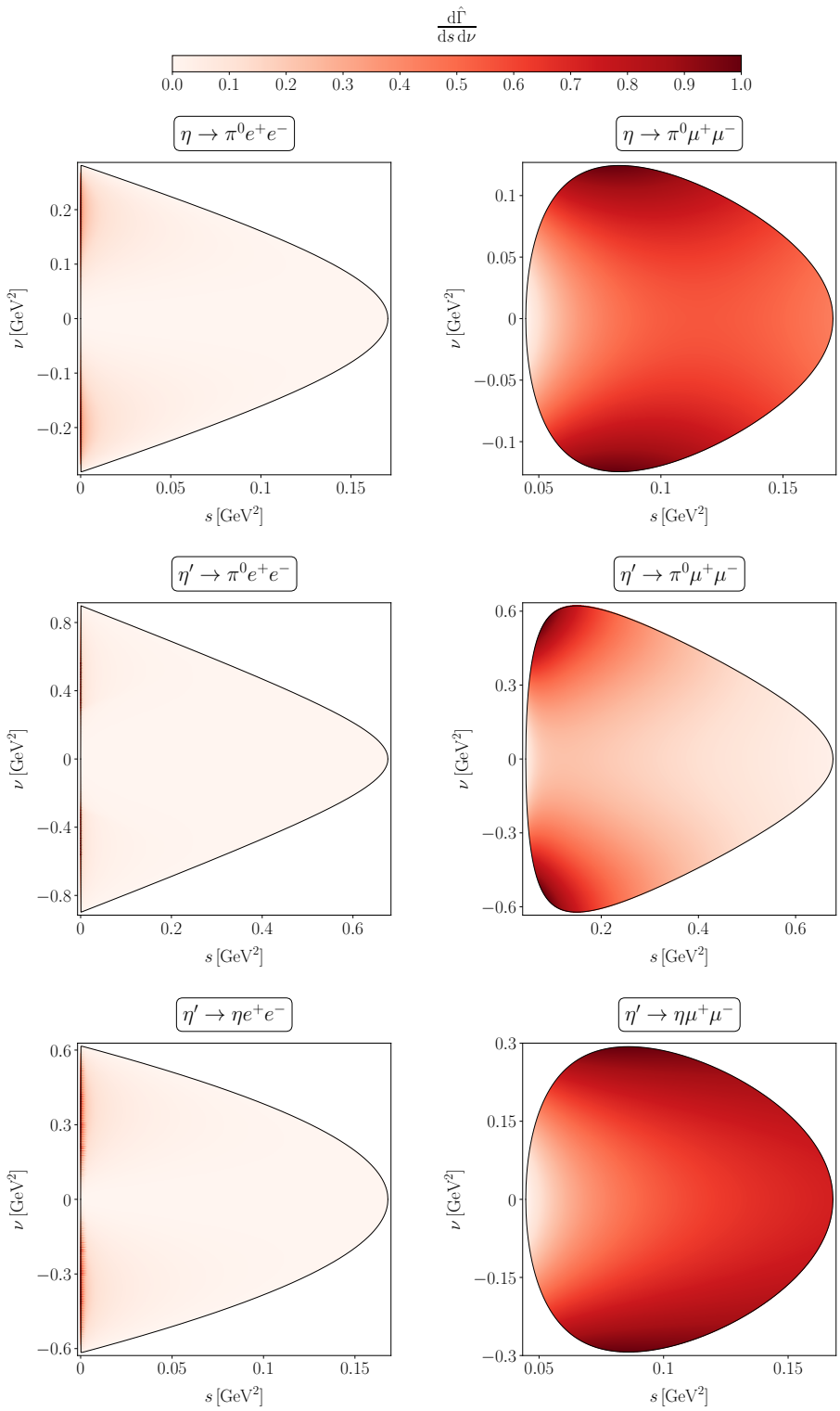

Figure 6.1: Dalitz plots for the MP model in the variant CW, normalized to the maximum value within the available phase space of the respective channel, $\mathrm{d}\hat{\Gamma}/(\mathrm{d}s\,\mathrm{d}\nu) = [\mathrm{d}\Gamma/(\mathrm{d}s\,\mathrm{d}\nu)]/[\max \mathrm{d}\Gamma/(\mathrm{d}s\,\mathrm{d}\nu)]$.

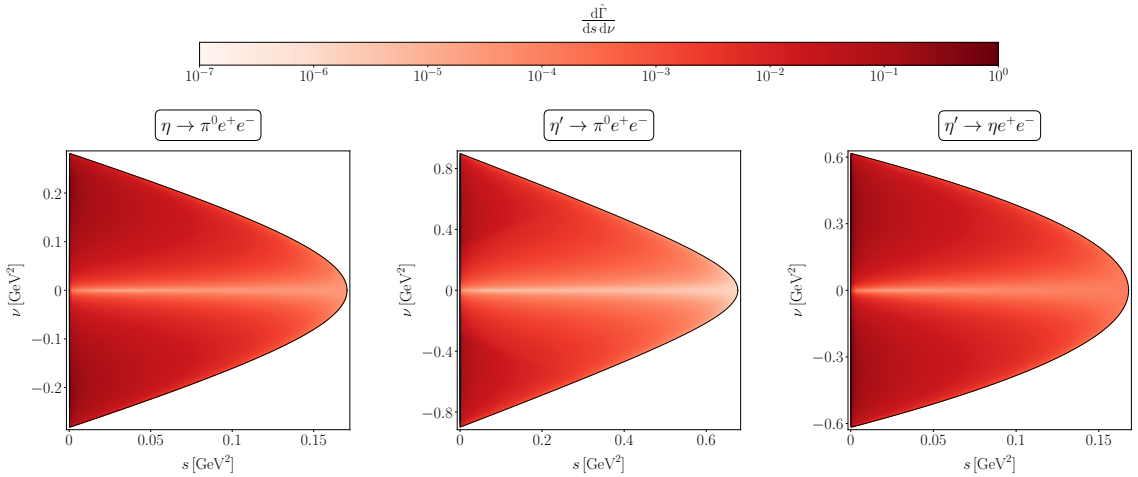

Figure 6.2: Logarithmic DALITZ plots for the electron channels with the MP model in the variant CW, normalized to the respective maximum value within the available phase space; see also Fig. 6.1.

The singly-differential distributions for the electron channels explicitly resolve a strongly peaked structure for invariant lepton masses close to the threshold and a subsequent rapid decrease. For muons in the final state, the singly-differential distribution is much different, with a broad peak that is situated further in the center of the phase space. This behavior is in correspondence with the observation that for $m_\ell \approx 0$, the threshold in s approximately collapses to the threshold of the two-photon intermediate state, $s = 0$, where the two-photon cut induces a behavior $\propto \log(s)$ [12]. Hence, for the electron final state, this logarithmic divergence manifests itself as a peak close to the threshold in s, regularized by a phase-space factor and forced to zero at $s = 4m_\ell^2$, see Eq. (4.2), whereas the muon channels have a much higher threshold, far from the logarithmic divergence.

6.2 Branching ratios in the different models

The sensitivity of the semileptonic decays to the different form-factor parameterizations, *i.e.*, a point-like, monopole, or dipole interaction, each with constant or energy-dependent widths, can be probed by comparing the results for the branching ratios collected in Table 6.1.

Our results for $\eta \to \pi^0 \ell^+ \ell^-$ obtained with constant form factors and widths are compatible with the results of Ref. [30], which similarly assumed a point-like interaction. Instead of determining the coupling constants purely from phenomenology, the authors modeled these using a symmetry-driven quark model, which results in only slightly different numerical values. For the η' decays, on the other hand, we find significant disagreement, which might be due to numerical difficulties when calculating the box diagrams in a non-automated way via FEYNMAN parameters.

Implementing non-trivial form factors leads to a significant decrease of the branching ratio for all decays, with the muon channels being subject to a larger reduction than the electron channels and the η' decays to less reduction than the η decays. More specifically,

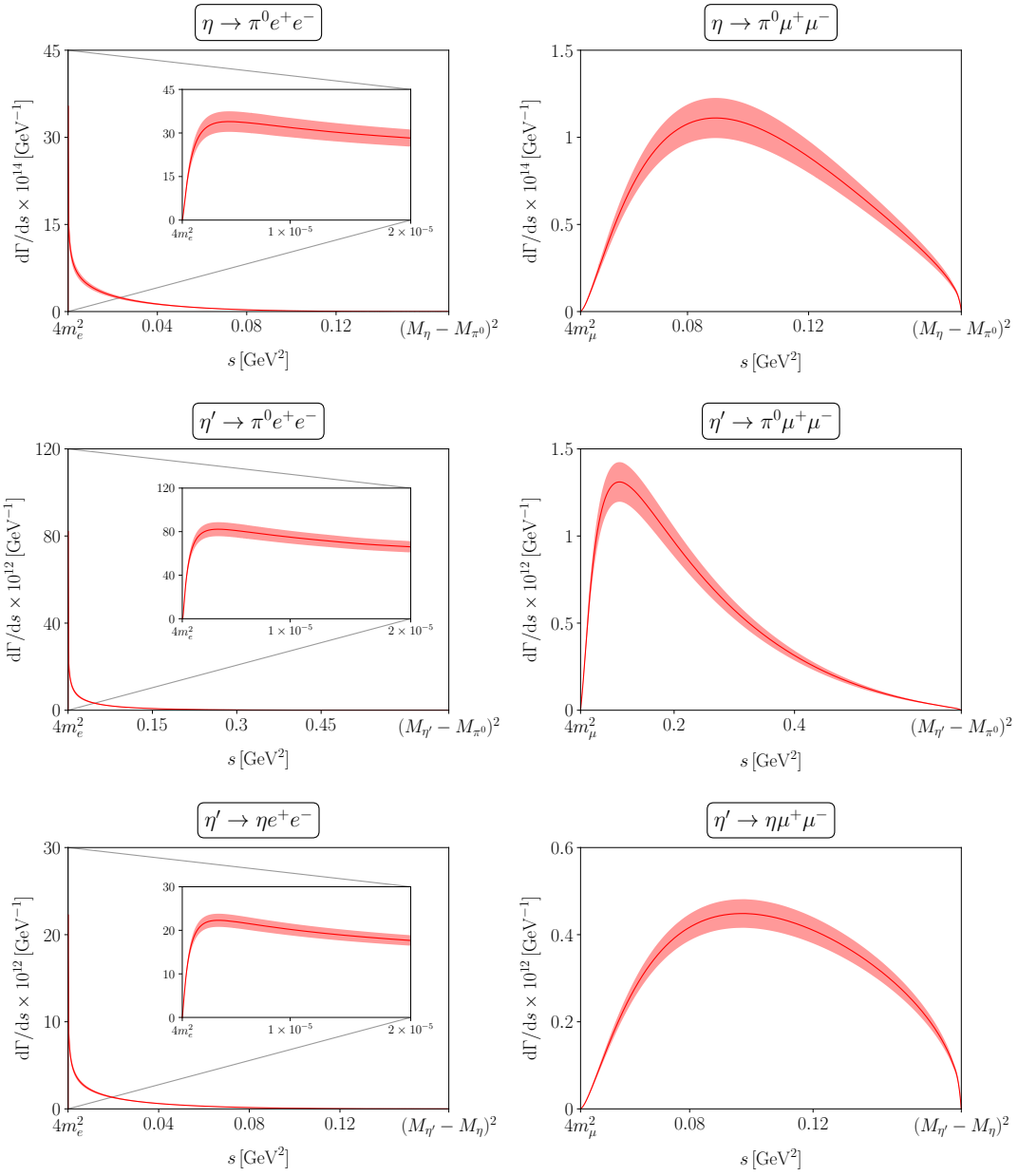

Figure 6.3: Singly-differential decay widths in the MANDELSTAM variable s, obtained with the MP model in the variant CW. Here, the inlays amplify the behavior close to the lower threshold of the phase space, where the distribution shows a strong peak for the channels with electrons in the final state. The uncertainty is entirely due to the dominant phenomenological uncertainty of $|\mathcal{F}_{VP}(0)|$, see Table 2.1.

		Branching ratio/10^{-9}			
		PL	MP	DP	Ref. [30]
$\eta \to \pi^0 e^+ e^-$	CW	2.10(23)	1.35(15)	1.33(15)	2.0(2)
	VW	2.06(22)	1.40(15)	1.36(15)	
$\eta \to \pi^0 \mu^+ \mu^-$	CW	1.37(15)	0.70(8)	0.66(7)	1.1(2)
	VW	1.32(14)	0.71(8)	0.67(7)	
$\eta' \to \pi^0 e^+ e^-$	CW	3.82(33)	3.08(27)	3.14(27)	4.5(6)
	VW	3.81(33)	3.30(28)	3.30(28)	
$\eta' \to \pi^0 \mu^+ \mu^-$	CW	2.57(23)	1.69(15)	1.68(15)	1.7(3)
	VW	2.53(23)	1.81(16)	1.81(16)	
$\eta' \to \eta e^+ e^-$	CW	0.53(4)	0.48(4)	0.49(4)	0.4(2)
	VW	0.51(4)	0.50(4)	0.50(4)	
$\eta' \to \eta \mu^+ \mu^-$	CW	0.287(26)	0.213(18)	0.207(18)	0.15(5)
	VW	0.280(25)	0.225(20)	0.240(21)	

Table 6.1: The branching ratios of the semileptonic decays, Eq. (4.4), resulting for the models PL, MP, and DP in both variants CW and VW. The uncertainty is entirely due to the dominant experimental uncertainty of $|\mathcal{F}_{VP}(0)|$, see Table 2.1. For reference, we also give the corresponding results from Ref. [30], where we added the quoted uncertainties in quadrature.

the decrease amounts to $\sim 35\%$ for $\eta \to \pi^0 e^+ e^-$ and $\sim 50\%$ for $\eta \to \pi^0 \mu^+ \mu^-$. For $\eta' \to \pi^0 \ell^+ \ell^-$, the branching ratio is reduced by $\sim 20\%$ for electrons and $\sim 35\%$ for muons in the final state. Regarding $\eta' \to \eta \ell^+ \ell^-$, the branching ratio decreases by $\sim 10\%$ for electrons and $\sim 25\%$ for muons in the final state. This gives strong indication that the photon virtualities cannot be neglected in the analyzed processes, since constant form factors are likely to overestimate the decay widths.

The dipole form factors, which feature the expected high-energy behavior $\sim 1/q^4$, further assess the sensitivity on the precise parameterization of the form factors. Compared to the variation observed between constant form factors and the monopole parameterization, their effect is, however, negligible, leading to a further decrease for $\eta \to \pi^0 \ell^+ \ell^-$, $\eta' \to \pi^0 \mu^+ \mu^-$, and $\eta' \to \eta \mu^+ \mu^-$ and a slight increase for $\eta' \to \pi^0 e^+ e^-$ and $\eta' \to \eta e^+ e^-$, both not exceeding the level of 5%.

Using spectral representations to implement energy-dependent widths for the broad vector mesons, *i.e.*, $\rho^{(\prime)}$, ω', and ϕ', leads to a decrease in the branching ratio of less than 4% for all decays with constant form factors and an increase of not more than 8% both in the monopole and dipole models, with the exception of $\eta' \to \eta \mu^+ \mu^-$, where the increase even reaches $\sim 15\%$.

	Branching ratio		
	VMD	Rescattering	Mixed
$\eta \to \pi^0 e^+ e^-$	$1.36(15) \times 10^{-9}$	2.5×10^{-13}	4.6×10^{-13}
$\eta \to \pi^0 \mu^+ \mu^-$	$0.67(7) \times 10^{-9}$	2.8×10^{-11}	-2.6×10^{-11}

Table 6.2: The scalar rescattering contributions to the branching ratio of $\eta \to \pi^0 \ell^+ \ell^-$, Eq. (6.1), separated into the pure rescattering and mixed term, as well as the corresponding VMD contributions from Table 6.1 for comparison.

All these variations are more or less small compared to the difference between the results in the PL model and any other model and mostly even small compared to the phenomenological uncertainties. We thus infer the semileptonic decays to be rather insensitive to the precise parameterization of the photon virtualities in the form factors. At the same time, this justifies why we restricted our discussion of the Dalitz and singly-differential plots in Sec. 6.1 to the monopole model, as finer details are hardly discernible; see the dipole analogs provided for completeness in App. C.

6.3 Scalar rescattering contributions

Adding the S-wave rescattering contributions for $\eta \to \pi^0 \ell^+ \ell^-$ to the VMD amplitude leads to two additional terms on the level of the squared amplitude: one pure rescattering term and one interference term,

$$\left|\mathcal{M} + \widetilde{\mathcal{M}}\right|^2 = |\mathcal{M}|^2 + |\widetilde{\mathcal{M}}|^2 + 2\mathrm{Re}\left[\mathcal{M}\widetilde{\mathcal{M}}^*\right]; \tag{6.1}$$

see Table 6.2 for the contributions to the branching ratio.[13] For $\eta \to \pi^0 e^+ e^-$, both the rescattering and the mixed contribution are suppressed by $\mathcal{O}(10^{-4})$ compared to the VMD result. This order of magnitude seems reasonable, given that coupling a scalar resonance to two leptons requires a spin flip, resulting in an amplitude proportional to m_ℓ. For $\eta \to \pi^0 \mu^+ \mu^-$, the rescattering and mixed contributions are at the level of 5% in comparison to the VMD contributions, still notably below the uncertainties of the latter. In addition, the two contributions have opposite signs and thus largely cancel, leading to a suppression of $\mathcal{O}(10^{-3})$.

A similar order of magnitude is expected for the corrections to the decays $\eta' \to [\pi^0/\eta]\ell^+\ell^-$, an explicit demonstration of which is, however, beyond the scope of this thesis.

6.4 Photonic decays and normalized branching ratios

The primary motivation for calculating the branching ratio of the two-photon decays $\eta^{(\prime)} \to [\pi^0/\eta]\gamma\gamma$ within our VMD framework is the normalization of the corresponding

[13] In light of their negligible contribution, we refrain from calculating uncertainties on the rescattering effects. Apart from the impact of the errors on the coupling constants C_V within the dispersive integral in Eq. (5.7), such a calculation would also have to take into account the uncertainties from fixing the subtraction constants as estimated in Ref. [28].

	Branching ratio/10^{-4}	
	CW	VW
$\eta \to \pi^0\gamma\gamma$	1.21(13)	1.18(13)
$\eta' \to \pi^0\gamma\gamma$	27.8(1.7)	28.1(1.8)
$\eta' \to \eta\gamma\gamma$	1.10(8)	1.10(8)

Table 6.3: Branching ratios of the two-photon decays, Eq. (4.9), in both variants CW and VW. The uncertainty is entirely due to the dominant experimental uncertainty of $|\mathcal{F}_{VP}(0)|$, see Table 2.1.

semileptonic decays, Eq. (4.19); numerical results for both observables are collected in Table 6.3 and Table 6.4, respectively. Currently, however, there is also thriving interest in resolving a discrepancy arising from an updated experimental measurement of the $\eta \to \pi^0\gamma\gamma$ decay [87]. The effect of implementing dispersively improved ρ propagators for the two-photon decays amounts to less than 2% and is therefore insignificant as the phenomenological uncertainties range between (6–11)%.

Our branching ratios with constant widths are in agreement with the VMD results of Ref. [29]; supplementing those with a linear-σ-model scalar contribution and chiral loops, the authors quote $B(\eta \to \pi^0\gamma\gamma) = 1.35(8) \times 10^{-4}$, $B(\eta' \to \pi^0\gamma\gamma) = 2.91(21) \times 10^{-3}$, and $B(\eta' \to \eta\gamma\gamma) = 1.17(8) \times 10^{-4}$ based on empirical couplings. These results are slightly larger than the plain VMD numbers but still compatible within uncertainties, indicating that the effects of these model extensions are insignificant at the current level of precision [29].

The dispersive analysis of $\eta \to \pi^0\gamma\gamma$ [28] referenced in Ch. 5 also includes the a_2 tensor resonance as well as isospin-breaking $\pi^+\pi^-$ contributions, with the result $B(\eta \to \pi^0\gamma\gamma) = 1.81^{+0.46}_{-0.33} \times 10^{-4}$ showing a $\sim 50\%$ discrepancy with the VMD model. This deviation can be traced back largely to the a_2 contribution, suggesting that the impact of this resonance might be relevant for $\eta \to \pi^0\gamma\gamma$, specifically at very low diphoton invariant masses.

In light of this finding, it is important to note that we have not included any tensor-meson effects for $\eta \to \pi^0\ell^+\ell^-$ in Ch. 5. For electrons in the final state, the lower threshold in s is close to the two-photon threshold, so that an effect of similar size as in the photonic case is within the bounds of possibility; the higher threshold for muons, on the other hand, is expected to exclude the region where the a_2 resonance is most relevant. For the η' decays, the exchanged vector mesons can go quasi on shell, so that the VMD mechanism is even more likely to dominate the effect of the tensor resonance.

While our results for the two-photon decays of the η' meson are compatible with the experimental results from BESIII, $B(\eta' \to \pi^0\gamma\gamma) = 3.20(24) \times 10^{-3}$ [88] and $B(\eta' \to \eta\gamma\gamma) = 8.3(3.4) \times 10^{-5}$ [89],[14] the experimental situation for $\eta \to \pi^0\gamma\gamma$ is presently inconclusive. For this decay, the PDG average $B(\eta \to \pi^0\gamma\gamma) = 2.55(22) \times 10^{-4}$ [15]—the main input being $B(\eta \to \pi^0\gamma\gamma) = 2.52(23) \times 10^{-4}$ from the A2 experiment at MAMI [24]—is in agreement with the theoretical calculation performed in Ref. [28] but in severe tension

[14]Here and in the following, we combine statistical and systematic uncertainties of experimental branching ratios in quadrature for simplicity.

		Normalized branching ratio/10^{-6}		
		PL	MP	DP
$\eta \to \pi^0 e^+ e^-$	CW	17.422(28)	11.197(11)	11.032(9)
	VW	17.510(20)	11.855(7)	11.531(4)
$\eta \to \pi^0 \mu^+ \mu^-$	CW	11.371(20)	5.781(7)	5.450(6)
	VW	11.197(25)	6.020(10)	5.647(5)
$\eta' \to \pi^0 e^+ e^-$	CW	1.37(7)	1.11(6)	1.13(6)
	VW	1.36(7)	1.17(6)	1.18(6)
$\eta' \to \pi^0 \mu^+ \mu^-$	CW	0.92(5)	0.610(35)	0.603(35)
	VW	0.90(5)	0.64(4)	0.65(4)
$\eta' \to \eta e^+ e^-$	CW	4.77(7)	4.38(6)	4.41(6)
	VW	4.65(7)	4.56(7)	4.56(7)
$\eta' \to \eta \mu^+ \mu^-$	CW	2.60(6)	1.93(4)	1.88(4)
	VW	2.54(5)	2.05(4)	2.18(4)

Table 6.4: The same as Table 6.1 but for the normalized branching ratios of the semileptonic decays, Eq. (4.19). Due to partial cancellations in this ratio, the quoted uncertainties are given with the caveat that they are likely to underestimate the true uncertainty; see main text.

with the preliminary result from the KLOE-2 collaboration, $B(\eta \to \pi^0\gamma\gamma) = 0.99(26) \times 10^{-4}$ [87], which corroborates the older KLOE measurement $B(\eta \to \pi^0\gamma\gamma) = 0.84(30) \times 10^{-4}$ [90] and is consistent with the VMD-only result.

The results for the normalized branching ratio can be found in Table 6.4, and the discussion of the differences between the distinct form-factor parameterizations is analogous to Sec. 6.2. Due to partial cancellations in this ratio, the quoted uncertainties are reduced drastically, however with the caveat that they are likely to underestimate the true uncertainty, given that some neglected systematic effect beyond the error estimates of the couplings potentially becomes dominant here. At the same time, potential corrections to the semileptonic branching ratios that are not included in the plain VMD model, *e.g.*, the a_2 resonance, are assumed to partially cancel as well because they emerge in the hadronic part of the amplitudes that is shared with the photonic decays.

The doubly- and singly-differential decay widths for the two-photon decays are depicted in Fig. 6.4. While the η decay does not show much structure in either plot—being dominated by a D-wave at low and an S-wave at high diphoton invariant masses—the η' decays are dominated by vector-meson resonances that can go quasi on shell. The ω resonance is clearly visible as two narrow bands in the Dalitz plots and as a peak in the singly-differential distributions, whereas the ρ is disguised in comparison due to its

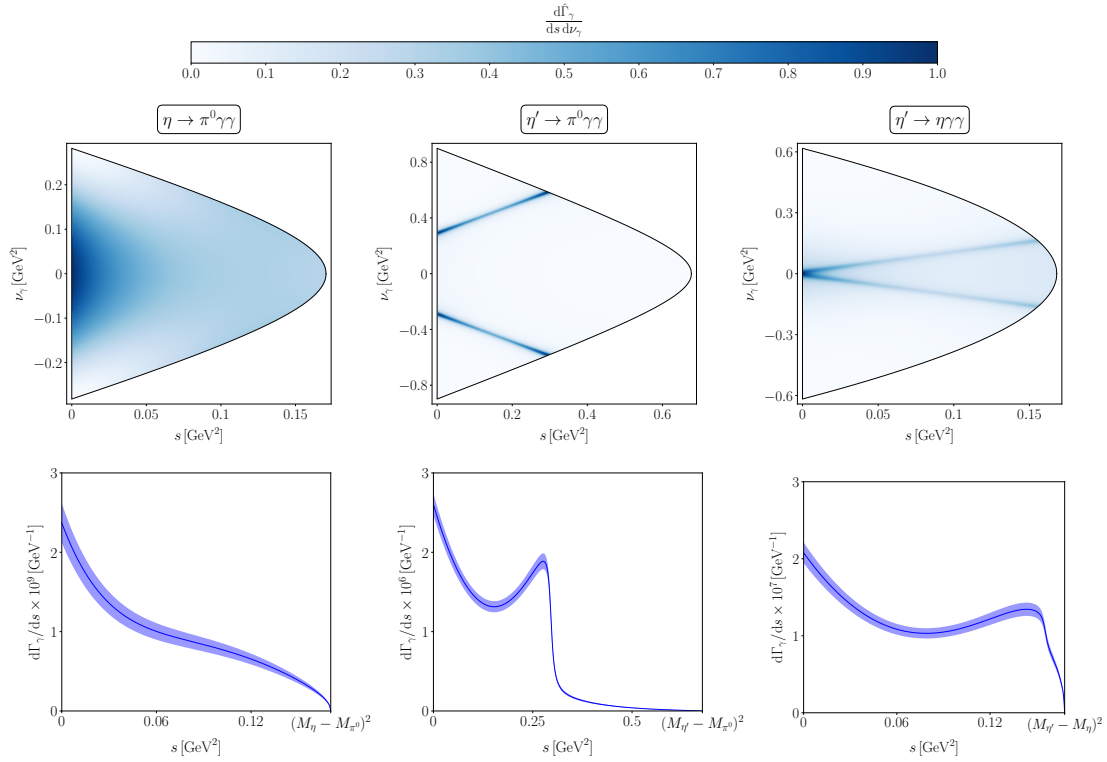

Figure 6.4: Dalitz plots for the two-photon decays in the variant CW (*top*), normalized to the maximum value within the available phase space of the respective channel, $\mathrm{d}\hat{\Gamma}_\gamma/(\mathrm{d}s\,\mathrm{d}\nu_\gamma) = [\mathrm{d}\Gamma_\gamma/(\mathrm{d}s\,\mathrm{d}\nu_\gamma)]/[\max \mathrm{d}\Gamma_\gamma/(\mathrm{d}s\,\mathrm{d}\nu_\gamma)]$, and singly-differential decay widths in the Mandelstam variable s, obtained in the variant CW (*bottom*).

much larger width and the scaling $\propto M_\rho/\Gamma_\rho$. The angular dependence perceivable as a less saturated band in the Dalitz plots and as a dip in the singly-differential distributions can be attributed to the fact that the $\omega \to [\pi^0/\eta]\gamma$ decay must be in a P-wave due to parity.

Chapter 7

Summary

We have reanalyzed the SM contribution to the semileptonic decays $\eta^{(\prime)} \to \pi^0\ell^+\ell^-$ and $\eta' \to \eta\ell^+\ell^-$, where $\ell = e, \mu$. Since C parity is conserved in the strong and EM interactions, these processes are mediated via a two-photon mechanism and therefore loop-induced. This two-photon mechanism is known to be dominated by vector exchanges; as a major improvement compared to the existing literature, we have, for the first time, implemented a realistic dependence of the hadronic subprocess on the photon virtualities via vector-to-pseudoscalar TFFs. To assess the sensitivity to the chosen parameterizations, we compared three different schemes: constant couplings (as a reference point), monopole form factors, and dipole form factors, with the dipole model being motivated by having the correct asymptotic behavior at high virtualities; in addition, we probed the impact of using energy-dependent widths for the vector mesons by constructing dispersively improved variants of the form factors. Non-trivial form factors turn out to be important in order not to overestimate the branching ratios, and we thereby improve previous theoretical results for the semileptonic $\eta^{(\prime)}$ decays. On the other hand, the observables are mostly insensitive to the details of the parameterization at the level of uncertainty induced by the phenomenological coupling constants.

All predicted branching ratios are, as expected, well below the current experimental upper limits. For the latter, we however recommend a reanalysis, given the far-from-flat Dalitz-plot distributions of the SM contributions. With improved experimental sensitivities in the future, our theoretical branching ratios of these rare $\eta^{(\prime)}$ decays can hopefully be compared to experiment and thus help cast a light on possible symmetry violations and BSM physics in the light-meson sector.

Appendix A

U(3) flavor symmetry

For the U(3) parameterizations of the pseudoscalar and vector-meson multiplets, we write

$$\Phi^P = \begin{pmatrix} \pi^0 + \frac{\sqrt{2}\,\eta+\eta'}{\sqrt{3}} & 0 & 0 \\ 0 & \pi^0 + \frac{\sqrt{2}\,\eta+\eta'}{\sqrt{3}} & 0 \\ 0 & 0 & \frac{-\sqrt{2}\,\eta+2\eta'}{\sqrt{3}} \end{pmatrix},$$

$$\Phi_\mu^{V^{(\prime)}} = \begin{pmatrix} \rho_\mu^{0\,(\prime)} + \omega_\mu^{(\prime)} & 0 & 0 \\ 0 & -\rho_\mu^{0\,(\prime)} + \omega_\mu^{(\prime)} & 0 \\ 0 & 0 & -\sqrt{2}\,\phi_\mu^{(\prime)} \end{pmatrix}, \tag{A.1}$$

where we only retain flavor-neutral states. Here, mixing effects between the (physical) mesons are taken into account via the pattern

$$\begin{pmatrix} \eta' \\ \eta \end{pmatrix} = \begin{pmatrix} \cos\theta_P & \sin\theta_P \\ -\sin\theta_P & \cos\theta_P \end{pmatrix} \begin{pmatrix} \eta_1 \\ \eta_8 \end{pmatrix},$$

$$\begin{pmatrix} \omega^{(\prime)} \\ \phi^{(\prime)} \end{pmatrix} = \begin{pmatrix} \cos\theta_{V^{(\prime)}} & \sin\theta_{V^{(\prime)}} \\ -\sin\theta_{V^{(\prime)}} & \cos\theta_{V^{(\prime)}} \end{pmatrix} \begin{pmatrix} \omega_1^{(\prime)} \\ \omega_8^{(\prime)} \end{pmatrix}, \tag{A.2}$$

with η_1, η_8 and $\omega_1^{(\prime)}$, $\omega_8^{(\prime)}$ denoting the isoscalar singlet and octet states of the pseudoscalar and vector-meson multiplets, respectively. In the above, the mixing angles are assumed to be given by $\theta_P = \arcsin(-1/3)$ for the pseudoscalar nonet (canonical mixing) and $\theta_{V^{(\prime)}} = \arcsin(1/\sqrt{3})$ for the vector mesons (ideal mixing). We furthermore introduce the charge matrix according to

$$\mathcal{Q} = \frac{1}{3}\mathrm{diag}(2,-1,-1). \tag{A.3}$$

Using Eq. (A.1), we calculate $\mathrm{Tr}[\Phi^P \Phi_\mu^V \Phi_\nu^{V^{(\prime)}}]$ to find the allowed couplings $\eta^{(\prime)}\rho\rho^{(\prime)}$, $\eta^{(\prime)}\omega\omega^{(\prime)}$, $\eta^{(\prime)}\phi\phi^{(\prime)}$, $\pi^0\rho\omega^{(\prime)}$, and $\pi^0\omega\rho^{(\prime)}$. To derive the relative signs between the corresponding coupling constants $C_{VP\gamma}$ introduced in Sec. 3.1, we calculate $\mathrm{Tr}[\Phi^P \Phi_\mu^V \mathcal{Q}]$ and take the appropriate ratios of coefficients that emerge in Eq. (2.5). For our analysis, we furthermore include the OZI-suppressed coupling $C_{\phi\pi^0\gamma}$, whose sign cannot be determined

from U(3) symmetry. Instead, we resort to analyses of $e^+e^- \to 3\pi$ and $e^+e^- \to \pi\gamma$ [54–56], which suggest that the product of the $\phi\gamma$ and $\phi\pi\gamma$ couplings carries a relative sign as compared to the product of the $\omega\gamma$ and $\omega\pi\gamma$ couplings. Hence, calculating $\mathrm{Tr}[\Phi_\mu^V \mathcal{Q}]$ indicates a relative sign between $C_{\phi\pi^0\gamma}$ and $C_{\omega\pi^0\gamma}$. Fixing the sign of $C_{\rho\eta\gamma}$ to be positive, the sign convention of Table 3.2 follows.

Appendix B

Intermediate results

The numerical values of the decay rates $\Gamma^{(\gamma)}_{V_1,V_2}$ defined in Eq. (4.20), for a point-like interaction ("PL"), monopole form factors ("MP"), and dipole form factors ("DP"), are collected in Table B.1 and Table B.2; for Γ_{V_1,V_2}, we used *Collier* to evaluate the PV functions contained in $\mathcal{M}_V^{u(0)v}$. Using *LoopTools* for the evaluation of the PV functions instead, we observed severe numerical instabilities for some integrations in the variant VW. These issues were most extreme in Γ_{V_1,V_2} with at least one $V_i = \phi$ for the decays $\eta^{(\prime)} \to \pi^0 e^+ e^-$ but also notably problematic in $\Gamma_{\omega,\omega}$ for $\eta' \to \pi^0 e^+ e^-$. They can be traced back to problems with the evaluation in certain regions of the phase space and might be related to vanishing Gram determinants in the PV reduction procedure; their exact origin remains obscure to us, however, in particular because a decomposition into coefficient functions does not improve this behavior and the evaluation with *Collier* using scalar functions does not suffer from such instabilities. In Fig. B.1, we illustrate the described issues by calculating the MP model in the variant CW, with both *Collier* and *LoopTools*, using a mass of the ρ that varies around its physical value and $\Gamma_\rho = 0$ in the BW propagator of the ρ. This breakdown mimics the variant VW to the effect that the shown curves correspond to the integrands that subsequently would have to be integrated over the spectral parameter $y = M_\rho + x\,\Gamma_\rho$.

			$\Gamma_{\rho,\rho}/\,\mathrm{MeV}^5$	$\Gamma_{\omega,\omega}/\,\mathrm{MeV}^5$	$\Gamma_{\phi,\phi}/\,\mathrm{MeV}^5$	$\Gamma_{\rho,\omega}/\,\mathrm{MeV}^5$	$\Gamma_{\rho,\phi}/\,\mathrm{MeV}^5$	$\Gamma_{\omega,\phi}/\,\mathrm{MeV}^5$
$\eta \to \pi^0 e^+ e^-$	PL	CW	0.5302	0.5684	0.1864	1.077	0.6041	0.6485
		VW	0.4992			1.065	0.6060	
	MP	CW	0.3463	0.3627	0.1093	0.6914	0.3707	0.3966
		VW	0.3422	0.3814	0.1151	0.7226	0.3945	0.4174
	DP	CW	0.3419	0.3573	0.1033	0.6814	0.3615	0.3835
		VW	0.3285	0.3630	0.09942	0.7160	0.3869	0.3903
$\eta \to \pi^0 \mu^+ \mu^-$	PL	CW	0.3440	0.3686	0.1383	0.7022	0.4222	0.4498
		VW	0.3123			0.6785	0.4136	
	MP	CW	0.1772	0.1870	0.06392	0.3569	0.2029	0.2173
		VW	0.1697	0.1972	0.06742	0.3657	0.2123	0.2293
	DP	CW	0.1674	0.1764	0.05756	0.3366	0.1888	0.2009
		VW	0.1603	0.1802	0.06073	0.3473	0.1916	0.2102
$\eta' \to \pi^0 e^+ e^-$	PL	CW	154.6	283.5	57.20	405.1	125.7	183.3
		VW	152.8			406.5	138.9	
	MP	CW	125.8	227.7	37.08	323.0	82.41	126.6
		VW	133.7	241.9	39.93	349.2	103.0	135.4
	DP	CW	128.1	232.0	35.95	328.3	84.42	128.8
		VW	131.5	253.1	38.66	340.9	101.0	134.6
$\eta' \to \pi^0 \mu^+ \mu^-$	PL	CW	121.2	169.8	55.13	284.5	131.0	168.1
		VW	116.9			281.7	139.1	
	MP	CW	80.02	111.0	30.42	185.6	70.21	94.91
		VW	83.84	119.3	32.79	199.8	84.77	101.9
	DP	CW	79.10	109.8	28.68	183.4	68.78	92.80
		VW	80.95	121.1	29.78	201.0	82.23	97.28
$\eta' \to \eta e^+ e^-$	PL	CW	19.68	50.07	6.701	60.79	8.303	14.86
		VW	19.47			60.64	10.11	
	MP	CW	16.44	48.33	5.100	48.56	−1.684	10.79
		VW	18.50			57.98	6.724	
	DP	CW	16.54	51.24	4.902	47.02	−2.518	12.45
		VW	18.37	46.79	4.827	57.81	6.109	10.82
$\eta' \to \eta \mu^+ \mu^-$	PL	CW	12.45	20.56	4.847	31.57	10.52	15.70
		VW	12.38			31.86	11.66	
	MP	CW	8.240	16.03	3.170	19.66	2.342	9.959
		VW	9.471			24.59	6.988	
	DP	CW	7.980	16.28	2.944	18.15	1.682	10.13
		VW	10.05	15.35	2.937	23.61	6.266	9.555

Table B.1: Numerical results for the decay rates defined in Eq. (4.20) for the models PL, MP, and DP in both variants CW and VW, rounded to four significant digits.

		$\Gamma^{\gamma}_{\rho,\rho}/\,\mathrm{MeV}^5$	$\Gamma^{\gamma}_{\omega,\omega}/\,\mathrm{MeV}^5$	$\Gamma^{\gamma}_{\phi,\phi}/\,\mathrm{MeV}^5$	$\Gamma^{\gamma}_{\rho,\omega}/\,\mathrm{MeV}^5$	$\Gamma^{\gamma}_{\rho,\phi}/\,\mathrm{MeV}^5$	$\Gamma^{\gamma}_{\omega,\phi}/\,\mathrm{MeV}^5$
$\eta \to \pi^0\gamma\gamma$	CW	3.154×10^4	3.193×10^4	8.719×10^3	6.175×10^4	3.218×10^4	3.335×10^4
	VW	2.921×10^4			6.108×10^4	3.189×10^4	
$\eta' \to \pi^0\gamma\gamma$	CW	3.088×10^7	4.586×10^8	4.286×10^6	1.097×10^8	1.115×10^7	1.884×10^7
	VW	3.341×10^7			1.130×10^8	1.386×10^7	
$\eta' \to \eta\gamma\gamma$	CW	3.203×10^6	6.537×10^7	4.473×10^5	1.425×10^7	2.031×10^5	7.406×10^5
	VW	3.280×10^6			1.411×10^7	5.056×10^5	

Table B.2: Numerical results for the decay rates defined in Eq. (4.20) in both variants CW and VW, rounded to four significant digits.

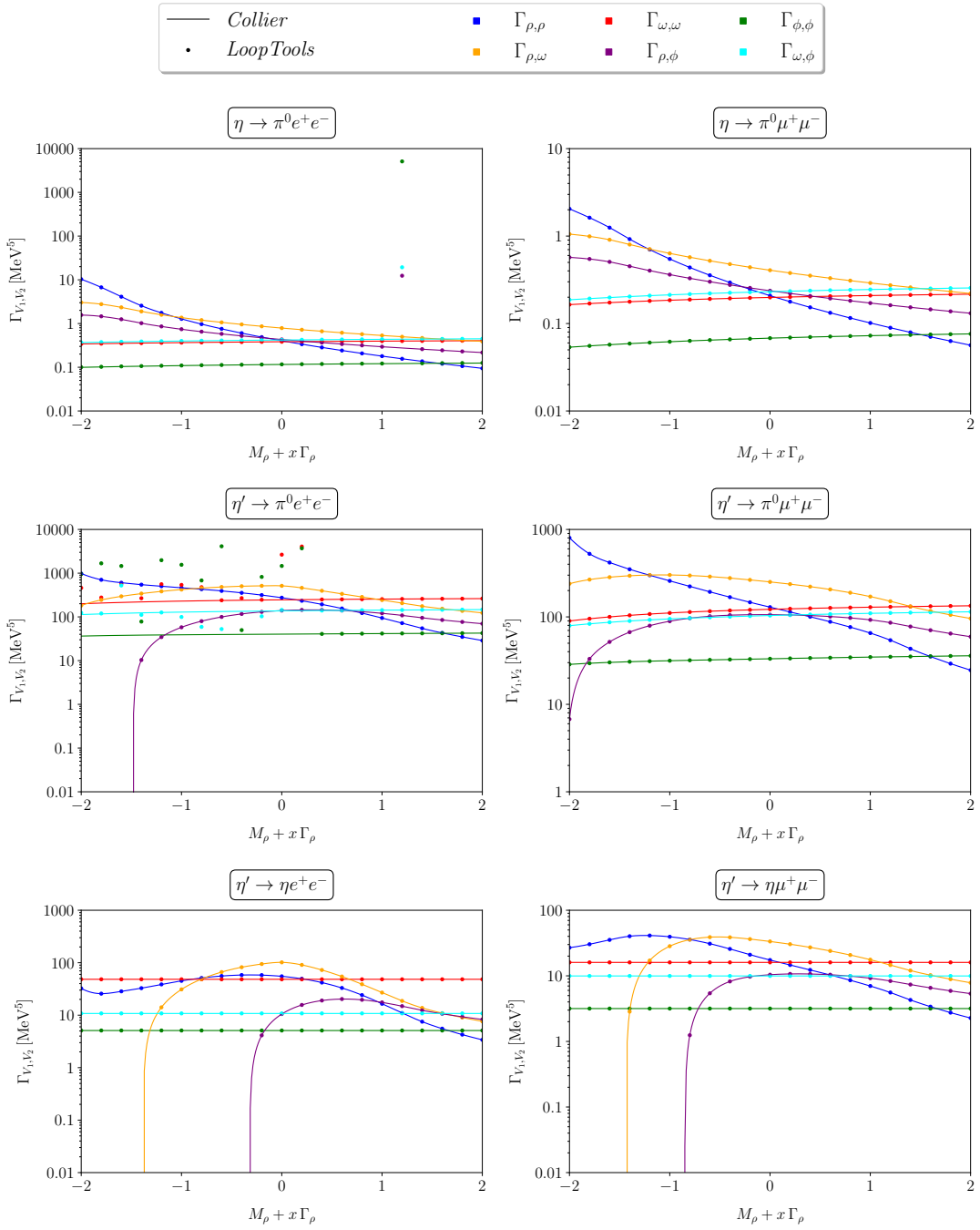

Figure B.1: Benchmark between *Collier* and *LoopTools* for the MP model in the variant CW with a varying ρ mass and $\Gamma_\rho = 0$ in the BW propagator; see also main text. The uncertainties on the problematic values resulting with *LoopTools*—which are not shown here—are rather large, some of them reaching $\sim 100\%$, whereas all other, compliant values have uncertainties below 1%.

Appendix C

Plots for the dipole model

In Fig. C.1–Fig. C.3, we depict the singly- and doubly-differential decay widths for the DP model in the variant CW, which are virtually indistinguishable from the MP analogs, Fig. 6.1–Fig. 6.3.

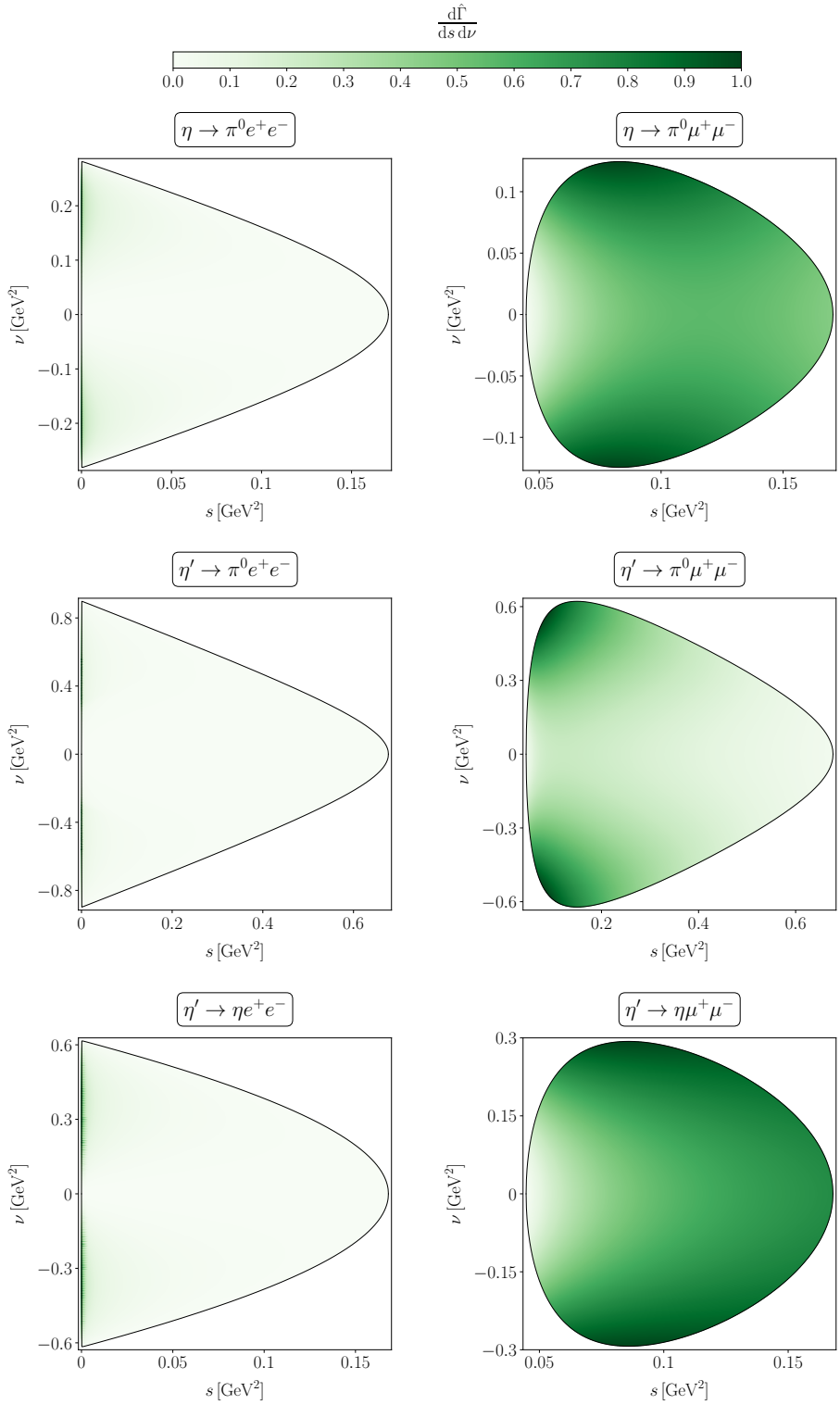

Figure C.1: The same as Fig. 6.1 but for the DP model.

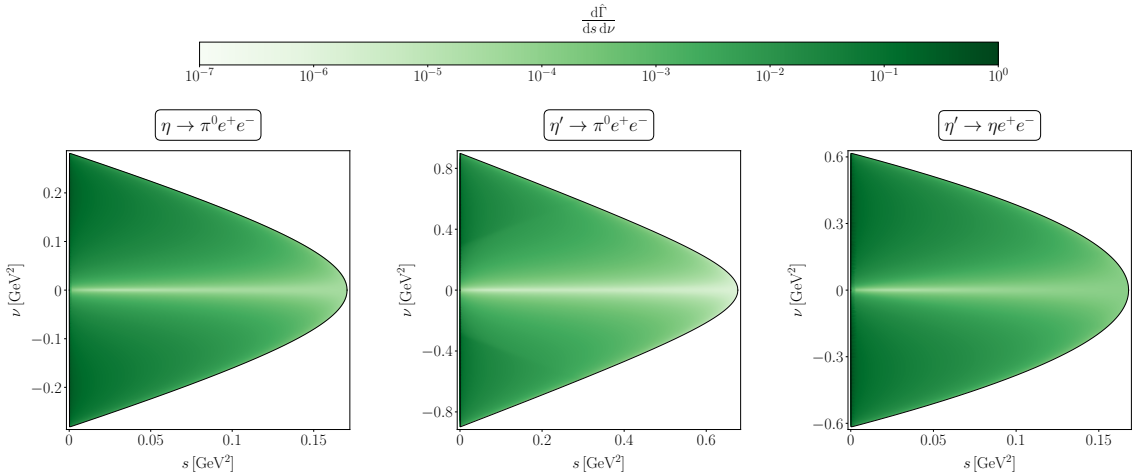

Figure C.2: The same as Fig. 6.2 but for the DP model.

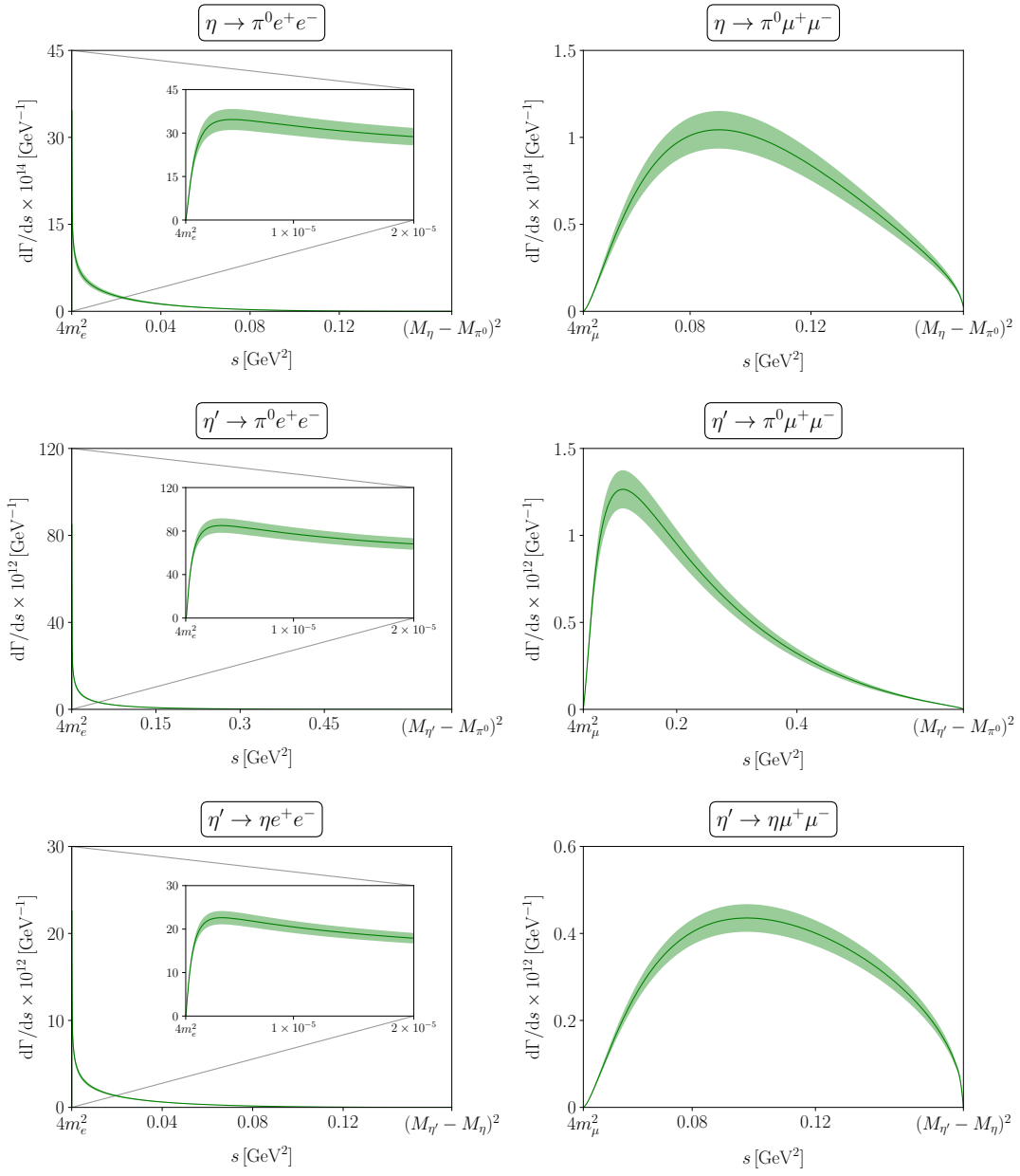

Figure C.3: The same as Fig. 6.3 but for the DP model.

Appendix D

Constants and parameters

We collect the masses and widths used throughout the calculations in this part of the thesis in Table D.1.

Quantity	Variable	Value [15]
Mass π^0	M_{π^0}	134.9768(5) MeV
Mass $\pi^\pm$	$M_{\pi^\pm}$	139.57039(18) MeV
Mass K	M_K	497.611(13) MeV
Mass η	M_η	547.862(17) MeV
Width η	Γ_η	1.31(5) keV
Mass $\eta'(958)$	$M_{\eta'}$	957.78(6) MeV
Width $\eta'(958)$	$\Gamma_{\eta'}$	188(6) keV
Mass $\rho(770)$	M_ρ	775.26(23) MeV
Width $\rho(770)$	Γ_ρ	147.4(8) MeV
Mass $\omega(782)$	M_ω	782.66(13) MeV
Width $\omega(782)$	Γ_ω	8.68(13) MeV
Mass $K^*(892)$	M_{K^*}	895.55(20) MeV
Mass $\phi(1020)$	M_ϕ	1019.461(16) MeV
Width $\phi(1020)$	Γ_ϕ	4.249(13) MeV
Mass $\rho(1450)$	$M_{\rho'}$	1465(25) MeV
Width $\rho(1450)$	$\Gamma_{\rho'}$	400(60) MeV
Mass $\omega(1420)$	$M_{\omega'}$	1410(60) MeV
Width $\omega(1420)$	$\Gamma_{\omega'}$	290(190) MeV
Mass $\phi(1680)$	$M_{\phi'}$	1680(20) MeV
Width $\phi(1680)$	$\Gamma_{\phi'}$	150(50) MeV

Table D.1: The masses and widths needed for the calculations in this part of the thesis, with the values taken from Ref. [15]. For the $\rho^{(\prime)}$ and the $K^{(*)}$, the parameters are identified with those of the neutral mesons.

References

[1] J. Bernstein, G. Feinberg, and T. D. Lee, Phys. Rev. **139**, B1650 (1965).

[2] B. Barrett, M. Jacob, M. Nauenberg, and T. N. Truong, Phys. Rev. **141**, 1342 (1966).

[3] H. Akdag, B. Kubis, and A. Wirzba, JHEP **06**, 154 (2023) [arXiv:2212.07794 [hep-ph]].

[4] H. Akdag, B. Kubis, and A. Wirzba, JHEP **03**, 059 (2024) [arXiv:2307.02533 [hep-ph]].

[5] L. Gan, B. Kubis, E. Passemar, and S. Tulin, Phys. Rept. **945**, 2191 (2022) [arXiv:2007.00664 [hep-ph]].

[6] R. Escribano, E. Royo, and P. Sánchez-Puertas, JHEP **05**, 147 (2022) [arXiv:2202.04886 [hep-ph]].

[7] P. Masjuan and P. Sánchez-Puertas, JHEP **08**, 108 (2016) [arXiv:1512.09292 [hep-ph]].

[8] E. Weil, G. Eichmann, C. S. Fischer, and R. Williams, Phys. Rev. D **96**, 014021 (2017) [arXiv:1704.06046 [hep-ph]].

[9] M. Hoferichter, B.-L. Hoid, B. Kubis, and J. Lüdtke, Phys. Rev. Lett. **128**, 172004 (2022) [arXiv:2105.04563 [hep-ph]].

[10] C. H. Llewellyn Smith, Nuovo Cim. A **48**, 834 (1967), [Erratum: Nuovo Cim. A **50**, 374 (1967)].

[11] J. Smith, Phys. Rev. **166**, 1629 (1968).

[12] T. P. Cheng, Phys. Rev. **162**, 1734 (1967).

[13] J. N. Ng and D. J. Peters, Phys. Rev. D **46**, 5034 (1992).

[14] J. N. Ng and D. J. Peters, Phys. Rev. D **47**, 4939 (1993).

[15] R. L. Workman *et al.* [Particle Data Group], PTEP **2022**, 083C01 (2022).

[16] P. Adlarson *et al.* [WASA-at-COSY], Phys. Lett. B **784**, 378 (2018) [arXiv:1802.08642 [hep-ex]].

[17] R. I. Dzhelyadin *et al.*, Phys. Lett. B **105**, 239 (1981).

[18] R. A. Briere *et al.* [CLEO], Phys. Rev. Lett. **84**, 26 (2000) [arXiv:hep-ex/9907046].

[19] J. Gasser and H. Leutwyler, Nucl. Phys. B **250**, 465 (1985).

[20] L. Ametller, J. Bijnens, A. Bramon, and F. Cornet, Phys. Lett. B **276**, 185 (1992).

[21] M. Jetter, Nucl. Phys. B **459**, 283 (1996) [arXiv:hep-ph/9508407].

[22] S. Prakhov *et al.*, Phys. Rev. C **72**, 025201 (2005).

[23] S. Prakhov *et al.*, Phys. Rev. C **78**, 015206 (2008).

[24] B. M. K. Nefkens *et al.* [A2 at MAMI], Phys. Rev. C **90**, 025206 (2014) [arXiv:1405.4904 [hep-ex]].

[25] I. Danilkin, O. Deineka, and M. Vanderhaeghen, Phys. Rev. D **96**, 114018 (2017) [arXiv:1709.08595 [hep-ph]].

[26] E. Oset, J. R. Peláez, and L. Roca, Phys. Rev. D **67**, 073013 (2003) [arXiv:hep-ph/0210282].

[27] E. Oset, J. R. Peláez, and L. Roca, Phys. Rev. D **77**, 073001 (2008) [arXiv:0801.2633 [hep-ph]].

[28] J. Lu and B. Moussallam, Eur. Phys. J. C **80**, 436 (2020) [arXiv:2002.04441 [hep-ph]].

[29] R. Escribano, S. Gonzàlez-Solís, R. Jora, and E. Royo, Phys. Rev. D **102**, 034026 (2020) [arXiv:1812.08454 [hep-ph]].

[30] R. Escribano and E. Royo, Eur. Phys. J. C **80**, 1190 (2020) [arXiv:2007.12467 [hep-ph]], [Errata: Eur. Phys. J. C **81**, 140 (2021); Eur. Phys. J. C **82**, 743 (2022)].

[31] L. G. Landsberg, Phys. Rept. **128**, 301 (1985).

[32] S.-s. Fang, B. Kubis, and A. Kupść, Prog. Part. Nucl. Phys. **120**, 103884 (2021) [arXiv:2102.05922 [hep-ph]].

[33] C. Terschlüsen and S. Leupold, Phys. Lett. B **691**, 191 (2010) [arXiv:1003.1030 [hep-ph]].

[34] C. Terschlüsen, S. Leupold, and M. F. M. Lutz, Eur. Phys. J. A **48**, 190 (2012) [arXiv:1204.4125 [hep-ph]].

[35] S. P. Schneider, B. Kubis, and F. Niecknig, Phys. Rev. D **86**, 054013 (2012) [arXiv:1206.3098 [hep-ph]].

[36] I. V. Danilkin, C. Fernández-Ramírez, P. Guo, V. Mathieu, D. Schott, M. Shi, and A. P. Szczepaniak, Phys. Rev. D **91**, 094029 (2015) [arXiv:1409.7708 [hep-ph]].

[37] R. A. Briceño, J. J. Dudek, R. G. Edwards, C. J. Shultz, C. E. Thomas, and D. J. Wilson, Phys. Rev. Lett. **115**, 242001 (2015) [arXiv:1507.06622 [hep-ph]].

[38] R. A. Briceño, J. J. Dudek, R. G. Edwards, C. J. Shultz, C. E. Thomas, and D. J. Wilson, Phys. Rev. D **93**, 114508 (2016) [arXiv:1604.03530 [hep-ph]], [Erratum: Phys. Rev. D **105**, 079902 (2022)].

[39] C. Alexandrou *et al.*, Phys. Rev. D **98**, 074502 (2018) [arXiv:1807.08357 [hep-lat]], [Erratum: Phys. Rev. D **105**, 019902 (2022)].

[40] M. Niehus, M. Hoferichter, and B. Kubis, JHEP **12**, 038 (2021) [arXiv:2110.11372 [hep-ph]].

[41] G. R. Farrar and D. R. Jackson, Phys. Rev. Lett. **35**, 1416 (1975).

[42] A. I. Vainshtein and V. I. Zakharov, Phys. Lett. B **72**, 368 (1978).

[43] G. P. Lepage and S. J. Brodsky, Phys. Lett. B **87**, 359 (1979).

[44] G. P. Lepage and S. J. Brodsky, Phys. Rev. D **22**, 2157 (1980).

[45] V. L. Chernyak and A. R. Zhitnitsky, Phys. Rept. **112**, 173 (1984).

[46] A. Rittenberg and G. R. Kalbfleisch, Phys. Rev. Lett. **15**, 556 (1965).

[47] M. J. Bazin, A. T. Goshaw, A. R. Zacher, and C. R. Sun, Phys. Rev. Lett. **20**, 895 (1968).

[48] M. R. Jane *et al.*, Phys. Lett. B **59**, 99 (1975).

[49] C. Gatto [REDTOP] [arXiv:1910.08505 [physics.ins-det]].

[50] J. Elam *et al.* [REDTOP] [arXiv:2203.07651 [hep-ex]].

[51] S. Okubo, Phys. Lett. **5**, 165 (1963).

[52] G. Zweig, *An $SU(3)$ model for strong interaction symmetry and its breaking. Version 2* in *Developments in the quark theory of hadrons. Vol. 1. 1964–1978*, pp. 22–101 (1964).

[53] J. Iizuka, Prog. Theor. Phys. Suppl. **37**, 21 (1966).

[54] M. Hoferichter, B. Kubis, S. Leupold, F. Niecknig, and S. P. Schneider, Eur. Phys. J. C **74**, 3180 (2014) [arXiv:1410.4691 [hep-ph]].

[55] M. Hoferichter, B.-L. Hoid, and B. Kubis, JHEP **08**, 137 (2019) [arXiv:1907.01556 [hep-ph]].

[56] B.-L. Hoid, M. Hoferichter, and B. Kubis, Eur. Phys. J. C **80**, 988 (2020) [arXiv:2007.12696 [hep-ph]].

[57] M. N. Achasov *et al.*, Phys. Rev. D **94**, 112001 (2016) [arXiv:1610.00235 [hep-ex]].

[58] B. Aubert *et al.* [BaBar], Phys. Rev. D **76**, 092005 (2007) [arXiv:0708.2461 [hep-ex]], [Erratum: Phys. Rev. D **77**, 119902 (2008)].

[59] J. P. Lees *et al.* [BaBar], Phys. Rev. D **97**, 052007 (2018) [arXiv:1801.02960 [hep-ex]].

[60] S. Holz, J. Plenter, C.-W. Xiao, T. Dato, C. Hanhart, B. Kubis, U.-G. Meißner, and A. Wirzba, Eur. Phys. J. C **81**, 1002 (2021) [arXiv:1509.02194 [hep-ph]].

[61] M. Hoferichter, B. Kubis, and D. Sakkas, Phys. Rev. D **86**, 116009 (2012) [arXiv:1210.6793 [hep-ph]].

[62] M. Hoferichter, B. Kubis, and M. Zanke, Phys. Rev. D **96**, 114016 (2017) [arXiv:1710.00824 [hep-ph]].

[63] F. Stollenwerk, C. Hanhart, A. Kupść, U.-G. Meißner, and A. Wirzba, Phys. Lett. B **707**, 184 (2012) [arXiv:1108.2419 [nucl-th]].

[64] B. Kubis and J. Plenter, Eur. Phys. J. C **75**, 283 (2015) [arXiv:1504.02588 [hep-ph]].

[65] S. Holz, C. Hanhart, M. Hoferichter, and B. Kubis, Eur. Phys. J. C **82**, 434 (2022) [arXiv:2202.05846 [hep-ph]], [Addendum: Eur. Phys. J. C **82**, 1159 (2022)].

[66] G. Colangelo, M. Hoferichter, B. Kubis, M. Procura, and P. Stoffer, Phys. Lett. B **738**, 6 (2014) [arXiv:1408.2517 [hep-ph]].

[67] M. Hoferichter and P. Stoffer, JHEP **07**, 073 (2019) [arXiv:1905.13198 [hep-ph]].

[68] A. Crivellin and M. Hoferichter, Phys. Rev. D **108**, 013005 (2023) [arXiv:2211.12516 [hep-ph]].

[69] M. Zanke, M. Hoferichter, and B. Kubis, JHEP **07**, 106 (2021) [arXiv:2103.09829 [hep-ph]].

[70] C. Adolph *et al.* [COMPASS], Phys. Rev. D **95**, 032004 (2017) [arXiv:1509.00992 [hep-ex]].

[71] F. von Hippel and C. Quigg, Phys. Rev. D **5**, 624 (1972).

[72] V. Shtabovenko, R. Mertig, and F. Orellana, Comput. Phys. Commun. **207**, 432 (2016) [arXiv:1601.01167 [hep-ph]].

[73] V. Shtabovenko, R. Mertig, and F. Orellana, Comput. Phys. Commun. **256**, 107478 (2020) [arXiv:2001.04407 [hep-ph]].

[74] R. Mertig, M. Bohm, and A. Denner, Comput. Phys. Commun. **64**, 345 (1991).

[75] See supplemental material attached to Phys. Rev. D **108**, 074025 (2023) [arXiv:2307.10357 [hep-ph]] for (i) the text files with the explicit expressions for $\mathcal{M}_V^{u(0)v}$ and (ii) the C++ interface to *Collier* and the accompanying demo file.

[76] T. Hahn, Comput. Phys. Commun. **168**, 78 (2005) [arXiv:hep-ph/0404043].

[77] A. Denner and S. Dittmaier, Nucl. Phys. B **658**, 175 (2003) [arXiv:hep-ph/0212259].

[78] A. Denner and S. Dittmaier, Nucl. Phys. B **734**, 62 (2006) [arXiv:hep-ph/0509141].

[79] A. Denner and S. Dittmaier, Nucl. Phys. B **844**, 199 (2011) [arXiv:1005.2076 [hep-ph]].

[80] A. Denner, S. Dittmaier, and L. Hofer, Comput. Phys. Commun. **212**, 220 (2017) [arXiv:1604.06792 [hep-ph]].

[81] T. Hahn and M. Pérez-Victoria, Comput. Phys. Commun. **118**, 153 (1999) [arXiv:hep-ph/9807565].

[82] W. A. Bardeen and W. K. Tung, Phys. Rev. **173**, 1423 (1968), [Erratum: Phys. Rev. D **4**, 3229 (1971)].

[83] R. Tarrach, Nuovo Cim. A **28**, 409 (1975).

[84] G. Colangelo, M. Hoferichter, M. Procura, and P. Stoffer, JHEP **09**, 074 (2015) [arXiv:1506.01386 [hep-ph]].

[85] B. Moussallam, Eur. Phys. J. C **73**, 2539 (2013) [arXiv:1305.3143 [hep-ph]].

[86] B. Moussallam, Eur. Phys. J. C **81**, 993 (2021) [arXiv:2107.14147 [hep-ph]].

[87] S. Giovannella [KLOE-2], *Light meson decays at KLOE/KLOE-2*, Talk at the ECT^* workshop, Trento (2023).

[88] M. Ablikim *et al.* [BESIII], Phys. Rev. D **96**, 012005 (2017) [arXiv:1612.05721 [hep-ex]].

[89] M. Ablikim *et al.* [BESIII], Phys. Rev. D **100**, 052015 (2019) [arXiv:1906.10346 [hep-ex]].

[90] B. Di Micco *et al.* [KLOE], Acta Phys. Slov. **56**, 403 (2006).

[91] H. Schäfer, Master's thesis, University of Bonn (2021).

[92] Y. Korte, PhD thesis, University of Bonn, to be published (2024).

Part III

Dispersion relations for $B^- \to \ell^- \bar{\nu}_\ell \ell'^- \ell'^+$ form factors

based on a project

in collaboration with
Stephan Kürten, Bastian Kubis, and Danny van Dyk

published in
Phys. Rev. D **107**, 053006 (2023) [arXiv:2210.09832 [hep-ph]]

Prologue

The Cabibbo–Kobayashi–Maskawa matrix determines the strength of charged-current weak transitions by parameterizing the mismatch between mass and weak eigenstates. Two of its elements, $|V_{ub}|$ and $|V_{cb}|$, are, for instance, accessible in weak decays of charged B mesons, that is hadrons containing one b and one u (anti-)quark. More specifically, the former of these matrix elements can be extracted from, *e.g.*, $B^- \to \ell^- \bar{\nu}_\ell$, an important background to which is given by $B^- \to \ell^- \bar{\nu}_\ell \gamma$ [1, 45]. This radiative process is of interest in itself and has been studied extensively in the literature, in particular regarding its factorization properties [46–49], for which so-called B-meson light-cone distribution amplitudes are of special importance [50–52]. These distribution amplitudes involve a set of *a priori* undetermined parameters, among other things the inverse moment λ_B, which, conversely, is relevant also for non-leptonic B-meson decays [51]. Since a reliable calculation of λ_B is difficult with theoretical methods [1], an experimental determination using the branching ratio of $B^- \to \ell^- \bar{\nu}_\ell \gamma$ has been proposed in the literature [1]. While such measurements are possible with the Belle II experiment [53], they are difficult to perform with the LHCb, given that the photon cannot be reconstructed easily with its detector [3]. The four-lepton decay $B^- \to \ell^- \bar{\nu}_\ell \ell^{(\prime)-} \ell^{(\prime)+}$, with the production of a lepton–antilepton pair from a virtual photon, on the other hand, has been identified as a suitable candidate for studies with both the Belle II and the LHCb experiment [28], at the same time retaining some sensitivity to λ_B [3]. Beyond providing valuable information on B-meson light-cone distribution amplitudes, the four-lepton decay can also be used to probe our understanding of the standard model [3], which is the main objective of the analysis in this part.

The analysis of the four-lepton decay $B^- \to \ell^- \bar{\nu}_\ell \ell'^- \ell'^+$, $\ell = e, \mu, \tau$, $\ell' = e, \mu$, presented in this part of the thesis employs dispersive methods to study the underlying $B \to \gamma^*$ form factors. While a dispersive treatment naturally implies that the form factors comply with the fundamental principles of analyticity and unitarity, it also involves some challenges. Most importantly, the decomposition of the amplitude describing the process needs to be chosen such that the basis of form factors is free of kinematic singularities; dynamic singularities, *i.e.*, poles and cuts of genuinely physical nature, on the contrary, are inherent to the amplitude and dictate the complex analytic structure of the form factors. Although a procedure to obtain such a singularity-free basis for photon processes—the crucial property being gauge invariance—has been developed by Bardeen, Tung, and Tarrach [10, 11], it is not straightforward to apply this method to the amplitude in question; this is due to the fact that gauge invariance is only manifest when including the charged lepton's final-state radiation, which, in turn, leads to an ambiguity, as will be explained in detail in this part. The derivation of a basis with form factors free of kinematic singularities was indeed an open problem for this project, which Stephan Kürten had been working

on already before the author of this dissertation started to investigate $B \to \gamma^*$ form factors. Having familiarized himself with the Bardeen–Tung–Tarrach procedure for the analyses presented in Part I and its Addendum, the author eventually joined this project in the year 2021.

After introducing a hadronic and a final-state-radiation tensor by splitting the amplitude for the process $B^- \to \ell^- \bar{\nu}_\ell \gamma^*$ into its (non-)perturbative parts—performed independently by the author and Stephan Kürten—explicit formulae for the final-state-radiation piece, including lepton-mass effects, are derived by the author of this thesis. While Stephan Kürten focused on calculating the final-state-radiation tensor in the limit $m_\ell = 0$ [1, 3], the author extended this result to also account for non-vanishing lepton masses [16, 17]. The formula including lepton masses, in particular, needs to be recast into a form that allows for a unified analysis of the hadronic and the final-state-radiation tensor, which is carefully deduced in this dissertation. Next, the role of gauge invariance for $B^- \to \ell^- \bar{\nu}_\ell \gamma^*$ is discussed, which is shown to be fulfilled only for the sum of both tensors and thus rules out a straightforward application of the Bardeen–Tung–Tarrach procedure. In order to transfer the ideas developed by Bardeen, Tung, and Tarrach to the problem at hand, the hadronic tensor is then decomposed into homogeneous and inhomogeneous parts by the author of this dissertation, with the homogeneous part referring to a contribution that individually complies with gauge invariance. Furthermore, the hadronic tensor is demonstrated to contain a pseudoscalar component, which is described in terms of an associated tensor, similar to the hadronic equivalent. Performing an analogous decomposition of the pseudoscalar tensor into homogeneous and inhomogeneous parts, an essential condition on the established inhomogeneities is derived by the author of this thesis, who benefitted from insightful discussions with Bastian Kubis and Danny van Dyk as well as cross-checks by Stephan Kürten along the way of the derivation. With the defined quantities, amplitudes for the process $B^- \to \ell^- \bar{\nu}_\ell \ell'^- \ell'^+$ are calculated, which, for $\ell \neq \ell'$, was done independently by the author and Stephan Kürten.[*]

Following these general considerations, the homogeneous part of the hadronic tensor is decomposed into a set of Lorentz structures and form factors free of kinematic singularities, which is done using a method based on the procedure by Bardeen, Tung, and Tarrach, as developed by the author of this thesis in collaboration with Stephan Kürten, Bastian Kubis, and Danny van Dyk. For the inhomogeneous parts of the hadronic and the pseudoscalar tensor, generic parameterizations consistent with all the priorly imposed gauge constraints are specified by the author. These parameterizations induce a set of free parameters, which are studied by comparing with previous choices from the literature [1, 4, 5, 14–17, 19]; this comparison was carried out by both the author of this dissertation and Stephan Kürten.[‡] Here, particular emphasis is put on the aspect of the singularity-free property of the form factors, *i.e.*, which choices lead to an extension of the homogeneous part of the hadronic tensor that is eligible for a dispersive treatment. Having analyzed explicit choices for the free parameters, the inhomogeneity is shown to be restricted to a very specific form under three reasonable assumptions, as deduced by the author of this thesis. Together, these considerations lead to definite choices for the

[*] The amplitude for $\ell = \ell'$ given in this part of the thesis was calculated by the author of the dissertation and is not discussed in the published article.

[‡] Studying the parameterization from Ref. [5], the author of this thesis, Stephan Kürten, and Danny van Dyk found an error that led to the publication of an Erratum to that article.

inhomogeneous parts of the hadronic and the pseudoscalar tensor, for which projectors—derived independently by the author and Stephan Kürten—are given that allow one to obtain singularity-free form factors from a hadronic tensor in an arbitrary basis.

By establishing a set of dispersion relations [23, 24], the $B \to \gamma^*$ form factors are then related to the well-known $B \to V$, $V = \omega, \rho$, analogs [9]; the corresponding calculation was first performed by Stephan Kürten and subsequently cross-checked by the author of this dissertation. Here, the structures and form factors needed to describe $B \to V$ [25] are reviewed in great detail, including the parameterization of the form factors by means of a series expansion in a conformal variable [9]. Proposing a similar expansion for the $B \to \gamma^*$ form factors, with the additional momentum dependence of the photon being modeled using a vector-meson-dominance ansatz, explicit parameterizations for the $B \to \gamma^*$ form factors are obtained by inferring the undetermined parameters from the available input on $B \to V$ through the dispersion relations; this result was derived by Stephan Kürten with the assistance of this thesis' author as well as keen insights of Bastian Kubis and Danny van Dyk.

The phenomenological application of the formalism consists of the calculation of integrated branching ratios and forward–backward asymmetries for $B^- \to \ell^- \bar{\nu}_\ell \ell'^- \ell'^+$ as well as differential distributions for $\ell \neq \ell'$.[§] In the case of distinct lepton flavors, $\ell \neq \ell'$, the angular integrations are performed analytically by the author of this thesis. The remaining integrations need to be carried out numerically, where the analysis was split as follows: while the author focused on propagating the uncertainties using an analytic method, Stephan Kürten concentrated on conducting a statistical error analysis; both approaches yielded results that are in good agreement within uncertainties and were eventually also reproduced by the respective other party. Additional cross-checks for $\ell \neq \ell'$ are obtained by also performing the angular integrations numerically, as implemented by the author of this thesis. In fact, for $\ell = \ell'$, all integrations are carried out numerically by necessity, which is clarified in detail in this part.

In the appendices, formulae related to the hadronic and the pseudoscalar tensor are derived [1, 3] by the author, which were also verified by Stephan Kürten. Furthermore, the appendices elaborate on the arguments that lead to the constrained form of the inhomogeneity. Besides giving additional information on the modified Bardeen–Tung–Tarrach procedure, the appendices also contain the explicit formulae for the form-factor projectors. Further details on the kinematics of the processes $B^- \to \ell^- \bar{\nu}_\ell \gamma^*$ and $B^- \to \ell^- \bar{\nu}_\ell \ell'^- \ell'^+$ are included in the appendices as well, which were deduced independently by the author and Stephan Kürten. Moreover, the asymptotic behavior of the transition form factors is discussed in the appendices [15], which was first obtained by Stephan Kürten and subsequently cross-checked by this thesis' author.[¶]

[§]The results for the observables with $\ell = \ell'$ as well as the differential distributions given in this part of the thesis were obtained by the author of the dissertation and are not included in the published article.

[¶]Note also that all plots except for Fig. D.1 in this part of the thesis have been created by the author of the dissertation.

Chapter 1

Introduction

The radiative leptonic decay $B^- \to \ell^- \bar{\nu}_\ell \gamma$ is considered an excellent source of information on the leading-twist B-meson light-cone distribution amplitude (LCDA) by elucidating the inner structure of the B meson [1–3]. However, measurements of this decay are likely only possible with the ongoing Belle II experiment, which precludes leveraging the upcoming large datasets from the LHC—primarily the LHCb—that will become available from run 3 onwards. The four-lepton decay of the B meson, $B^- \to \ell^- \bar{\nu}_\ell \ell'^- \ell'^+$, with $\ell' \neq \ell$, $\ell^{(\prime)} = e, \mu$, has been identified as a suitable candidate for studies with data from both Belle II and the LHC. This decay has been studied to some extent in the literature, with a variety of models for the relevant $B \to \gamma^*$ form factors [4–7]. Nevertheless, its usefulness to extract B-meson LCDA parameters is hampered by the need to describe a virtual photon in the time-like region, which requires a particularly careful treatment.

We propose a dispersive approach for $B \to \gamma^*$, which is based on the fundamental principles of analyticity and unitarity, where we apply methods that were originally developed for dispersive analyses of low-energy processes in the time-like region—see, *e.g.*, Ref. [8] and references therein for an application to the pion vector form factor—to hadronic TFFs of B mesons. By establishing a set of dispersion relations in the photon momentum, we relate the isoscalar and isovector components of the $B \to \gamma^*$ transition inherent to the hadronic part of the amplitude through $B^- \to \ell^- \bar{\nu}_\ell \gamma^* (\to \ell'^- \ell'^+)$ to available input on $B \to \omega$ and $B \to \rho$ [9]. In doing so, we use a VMD ansatz, but our results provide the foundation for more sophisticated future analyses. Here, our approach, in particular, has the potential to enable the transfer of information from the region of time-like photon momenta to the space-like region, where the sensitivity to the LCDA parameters is less affected by soft interactions [3]. Since using dispersion relations requires the form factors to be free of kinematic singularities, we present a modification of the BTT [10, 11] procedure—which has not been designed for hadronic form factors in weak transitions—that allows us to obtain such a set of form factors. At this, we face a problem: the separation of the amplitude into a hadronic term—containing the non-perturbative dynamics of the process—and a final-state-radiation (FSR) term turns out ambiguous; the two terms are not individually gauge invariant but only their sum is. A further issue is the lack of definite angular-momentum and parity quantum numbers of the form factors. Our modification to the BTT procedure addresses this issue, where we take special care not to spoil the singularity-free structure.

To ensure a consistent treatment of lepton-mass effects, we work with non-zero lepton

masses throughout our analysis; taking the limit $m_{\ell^{(\prime)}} \to 0$ in our formulae remains possible at all reasonable stages. While the considerations in this part of the thesis are restricted to the decay of a negatively charged B meson, the decay of a positively charged B meson can be calculated in complete analogy, with minor adjustments to the given formulae and identical numerical results.

The outline of this part of the thesis is as follows: in Ch. 2, we introduce the Lagrangian of the weak effective theory (WET) that describes semileptonic $b \to u\ell\bar{\nu}$ transitions. The amplitude for $B^- \to \ell^-\bar{\nu}_\ell\gamma^*(\to \ell'^-\ell'^+)$ and its decomposition into a hadronic tensor and an FSR piece is discussed in Ch. 3. Using our modified BTT procedure, the hadronic tensor is then parameterized in terms of four form factors that are free of kinematic singularities in Ch. 4, where the ambiguity arising from the separation of the full amplitude is a subject of special attention. In Ch. 5, we establish a set of dispersion relations that relate the $B \to \gamma^*$ transition inherent to the hadronic part of the amplitude to available input on $B \to V$ form factors, $V = \omega, \rho$, and provide predictions for the $B \to \gamma^*$ form factors. Using these, we present numerical results for the branching ratios and integrated forward–backward (FB) asymmetries of the process $B^- \to \ell^-\bar{\nu}_\ell\ell'^-\ell'^+$, with $\ell = e, \mu, \tau$ and $\ell' = e, \mu$, in Ch. 6, where we additionally provide differential distributions of the decay width and FB asymmetry for $\ell' \neq \ell$. We conclude and give a brief outlook in Ch. 7. Some supplementary material is outsourced to the appendices.

Chapter 2

Weak effective theory

At the energy scale of the B meson, the SM's flavor-changing processes are conveniently described within an effective field theory [12, 13]. The leading terms in this theory arise at mass dimension six, with higher-dimensional operators being suppressed by at least $m_B^2/M_W^2 \approx 0.4\%$. Moreover, such an effective field theory allows us to transparently include potential BSM effects as long as new matter fields and mediators live above the scale of electroweak symmetry breaking. For $b \to u\ell\bar{\nu}_\ell$ transitions, in particular, we use the effective Lagrangian

$$\mathcal{L}_{\text{WET}}^{ub\ell\nu} = \frac{4G_{\text{F}}}{\sqrt{2}} V_{ub} \sum_i \mathcal{C}_i^{ub\ell\nu} \mathcal{O}_i^{ub\ell\nu} + \text{h.c.}, \tag{2.1}$$

where G_{F} is the Fermi constant as measured in muon decays, V_{ub} is the Cabibbo–Kobayashi–Maskawa (CKM) matrix element for the $b \to u$ transition, and $\mathcal{C}_i^{ub\ell\nu} \equiv \mathcal{C}_i^{ub\ell\nu}(\mu)$ are the so-called Wilson coefficients at the scale μ that are multiplied with the local field operators $\mathcal{O}_i^{ub\ell\nu} \equiv \mathcal{O}_i^{ub\ell\nu}(x)$. A convenient basis of operators up to dimension six and with only left-handed neutrinos is given by

$$\begin{aligned}
\mathcal{O}_{V,L(R)}^{ub\ell\nu} &= \big[\bar{u}(x)\gamma^\mu P_{L(R)} b(x)\big]\big[\bar{\ell}(x)\gamma_\mu P_L \nu_\ell(x)\big], \\
\mathcal{O}_{S,L(R)}^{ub\ell\nu} &= \big[\bar{u}(x) P_{L(R)} b(x)\big]\big[\bar{\ell}(x) P_L \nu_\ell(x)\big], \\
\mathcal{O}_{T}^{ub\ell\nu} &= \big[\bar{u}(x)\sigma^{\mu\nu} b(x)\big]\big[\bar{\ell}(x)\sigma_{\mu\nu} P_L \nu_\ell(x)\big],
\end{aligned} \tag{2.2}$$

where, in the SM, $\mathcal{C}_{V,L}^{ub\ell\nu}|_{\text{SM}} = 1 + \mathcal{O}(\alpha)$ and $\mathcal{C}_i^{ub\ell\nu}|_{\text{SM}} = 0$ for all other Wilson coefficients. To leading order in the EM interaction, matrix elements of the above operators factorize into matrix elements of a purely hadronic and a purely leptonic current. For our analysis, we limit ourselves to the SM operator $\mathcal{O}_{V,L}^{ub\ell\nu}$ and—implicitly—to the scalar operator $\mathcal{O}_{S,L}^{ub\ell\nu}$.

Chapter 3

Hadronic tensor

We first study the decay $B^-(p) \to \ell^-(p_\ell)\bar{\nu}_\ell(p_\nu)\gamma^*(q)$, $k = p_\ell + p_\nu$, whose amplitude in the SM is given by [1]

$$\mathcal{M}(B^- \to \ell^-\bar{\nu}_\ell\gamma^*) = \frac{4G_\mathrm{F}V_{ub}}{\sqrt{2}}\,\langle \ell^-\bar{\nu}_\ell\gamma^*|\mathcal{O}^{ub\ell\nu}_{V,L}|B^-\rangle \tag{3.1}$$

up to corrections of $\mathcal{O}(\alpha)$. It is convenient to write the WET operator in terms of the leptonic and hadronic weak currents $J^\nu_\mathrm{W}(x) = \bar{\ell}(x)\gamma^\nu(1-\gamma_5)\nu_\ell(x)$ and $J^\nu_\mathrm{H}(x) = \bar{u}(x)\gamma^\nu(1-\gamma_5)b(x)$ according to[1]

$$\mathcal{O}^{ub\ell\nu}_{V,L} = \frac{1}{4}J_{\mathrm{H}\nu}(0)J^\nu_\mathrm{W}(0). \tag{3.2}$$

Within the framework of the WET, there are two possible diagrammatic ways for the emission of the (virtual) photon: either from the constituents of the B meson or from the charged final-state lepton; the respective diagrams are shown in Fig. 3.1.

At leading order in the EM coupling, the hadronic matrix element on the right-hand side of Eq. (3.1) can be written as

$$\begin{aligned}\langle \ell^-\bar{\nu}_\ell\gamma^*|J_{\mathrm{H}\nu}(0)J^\nu_\mathrm{W}(0)|B^-\rangle &= e\epsilon^*_\mu\Big[\,\langle \ell^-\bar{\nu}_\ell|J_{\mathrm{W}\nu}(0)|0\rangle\int \mathrm{d}^4x\,\mathrm{e}^{\mathrm{i}qx}\,\langle 0|\mathrm{T}\{J^\mu_\mathrm{EM}(x)J^\nu_\mathrm{H}(0)\}|B^-\rangle \\ &\qquad + \langle 0|J_{\mathrm{H}\nu}(0)|B^-\rangle\int \mathrm{d}^4x\,\mathrm{e}^{\mathrm{i}qx}\,\langle \ell^-\bar{\nu}_\ell|\mathrm{T}\{J^\mu_\mathrm{EM}(x)J^\nu_\mathrm{W}(0)\}|0\rangle\,\Big] \\ &= e\epsilon^*_\mu\big[Q_BL_\nu T^{\mu\nu}_\mathrm{H}(k,q) + Q_\ell T^\mu_\mathrm{FSR}(p_\ell,p_\nu,q)\big],\end{aligned} \tag{3.3}$$

where e is the elementary charge and $\epsilon^*_\mu \equiv \epsilon^*_\mu(q;\lambda)$ the polarization vector of the outgoing photon with momentum q and polarization λ. Furthermore,

$$J^\mu_\mathrm{EM}(x) = \bar{q}(x)\mathcal{Q}\gamma^\mu q(x) + \sum_\ell Q_\ell\bar{\ell}(x)\gamma^\mu\ell(x) \tag{3.4}$$

is the EM current, with $q(x) = (u(x), d(x), s(x), c(x), b(x))^\intercal$, $\mathcal{Q} = \mathrm{diag}(2,-1,-1,2,-1)/3$ the quark charge matrix, and $Q_B = -1 = Q_\ell$ the charge of the B meson and lepton in units of e. With the aim to render the transfer of our analysis to the positively charged channel more transparent, we will explicitly retain factors of $Q_B = Q_\ell$ in our formulae; it

[1] Translational invariance implies that we can fix $x = 0$ for the WET operator in the matrix elements evaluated below; see also the Foundations part of this thesis.

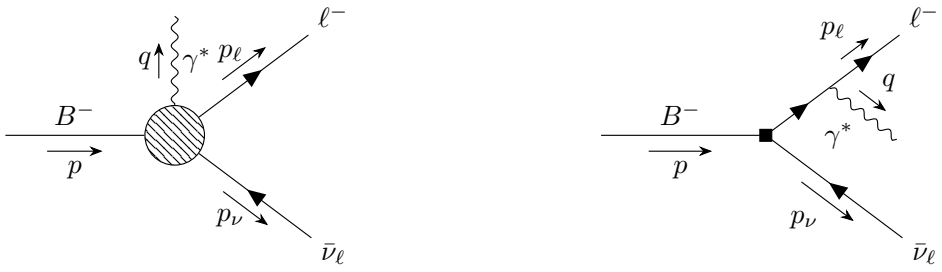

Figure 3.1: The FEYNMAN diagrams contributing to the decay $B^- \to \ell^- \bar{\nu}_\ell \gamma^*$ at dimension six in the WET on the hadronic level: pole and cut contributions of $T_{\mathrm{H}}^{\mu\nu}(k,q)$, *e.g.*, from the intermediate states B in k^2 or $\pi\pi$ in q^2 (*left*) and emission from the charged final-state lepton in $T_{\mathrm{FSR}}^{\mu}(p_\ell, p_\nu, q)$ (*right*). The hadronic tensor $T_{\mathrm{H}}^{\mu\nu}(k,q)$ and the FSR tensor $T_{\mathrm{FSR}}^{\mu}(p_\ell, p_\nu, q)$ are defined in Eq. (3.5) and Eq. (3.6), respectively. Note that an effective four-particle vertex is discarded here since it contributes at dimension eight in the WET.

is, however, to be kept in mind that further modifications of the spinor structure apply beyond this simple alteration. In Eq. (3.3), we moreover introduced the leptonic matrix element $L_\nu = \bar{u}_\ell \gamma_\nu (1-\gamma_5) v_{\bar{\nu}}$, with $\bar{u}_\ell \equiv \bar{u}_\ell(p_\ell)$ and $v_{\bar{\nu}} \equiv v_{\bar{\nu}}(p_\nu)$, the hadronic tensor $T_{\mathrm{H}}^{\mu\nu}(k,q)$,

$$Q_B T_{\mathrm{H}}^{\mu\nu}(k,q) = \int \mathrm{d}^4x\, \mathrm{e}^{\mathrm{i}qx}\, \langle 0|\mathrm{T}\{J_{\mathrm{EM}}^{\mu}(x) J_{\mathrm{H}}^{\nu}(0)\}|B^-\rangle\,, \tag{3.5}$$

and the FSR tensor $T_{\mathrm{FSR}}^{\mu}(p_\ell, p_\nu, q)$,

$$Q_\ell T_{\mathrm{FSR}}^{\mu}(p_\ell, p_\nu, q) = -\mathrm{i} f_B p_\nu \int \mathrm{d}^4x\, \mathrm{e}^{\mathrm{i}qx}\, \langle \ell^- \bar{\nu}_\ell|\mathrm{T}\{J_{\mathrm{EM}}^{\mu}(x) J_{\mathrm{W}}^{\nu}(0)\}|0\rangle\,, \tag{3.6}$$

where f_B is the decay constant of the B meson, $\langle 0|\bar{u}(0)\gamma^\nu\gamma_5 b(0)|B^-\rangle = \mathrm{i} f_B p^\nu$. While the hadronic tensor $T_{\mathrm{H}}^{\mu\nu}(k,q)$ describes the genuinely non-perturbative physics of the process, $T_{\mathrm{FSR}}^{\mu}(p_\ell, p_\nu, q)$ comprises the FSR from the charged lepton and can be reduced to the B-meson decay constant f_B and an entirely perturbative remainder. The hadronic tensor can be decomposed into a set of LORENTZ structures and associated scalar-valued functions, which are customarily referred to as the $B \to \gamma^*$ form factors. It is the purpose of this part of the thesis to study these form factors within a dispersive framework, which requires knowledge of their singularity structure in the two independent kinematic variables and of the form factors' asymptotic behavior, see Ch. 4.

In the case of a massless charged lepton, one finds the remarkably simple result [1, 4, 5, 14, 15]

$$T_{\mathrm{FSR},0}^{\mu}(p_\ell, p_\nu, q) = f_B L^\mu \tag{3.7}$$

for the FSR tensor, whereas the case of non-zero mass leads to the more intricate formula [16, 17]

$$\begin{aligned} T_{\mathrm{FSR},m_\ell}^{\mu}(p_\ell, p_\nu, q) &= f_B (p_\ell + p_\nu + q)_\nu \bar{u}_\ell \gamma^\mu \frac{\not{p}_\ell + \not{q} + m_\ell}{(p_\ell+q)^2 - m_\ell^2} \gamma^\nu (1-\gamma_5) v_{\bar{\nu}} \\ &= f_B \Big[L^\mu + m_\ell \bar{u}_\ell \frac{2p_\ell^\mu + \gamma^\mu \not{q}}{(p_\ell+q)^2 - m_\ell^2} (1-\gamma_5) v_{\bar{\nu}} \Big]. \end{aligned} \tag{3.8}$$

For our purpose, it proves convenient to bring the FSR contribution into such a form that it shares a common factor of L_ν with its hadronic counterpiece, *i.e.*,

$$\langle \ell^- \bar{\nu}_\ell \gamma^* | J_{\mathrm{W}}^\nu(0) J_{\mathrm{H}\nu}(0) | B^- \rangle = eQ_B \epsilon_\mu^* \big[T_{\mathrm{H}}^{\mu\nu}(k,q) + T_{\mathrm{FSR}}^{\mu\nu}(p_\ell, p_\nu, q) \big] L_\nu. \tag{3.9}$$

It is straightforward to achieve such a description for the massless case, $m_\ell = 0$, from Eq. (3.7). For the massive case, $m_\ell \neq 0$, we make use of the DIRAC equation and the CHISHOLM identity[2] in Eq. (3.8) to obtain

$$\begin{aligned} T_{\mathrm{FSR},m_\ell}^{\mu}(p_\ell, p_\nu, q) &= f_B \Big[g^{\mu\nu} L_\nu + \frac{2p_\ell^\mu p_\ell^\nu}{(p_\ell+q)^2 - m_\ell^2} L_\nu + \bar{u}_\ell \frac{(p_\ell)_\nu q_\rho}{(p_\ell+q)^2 - m_\ell^2} \gamma^\nu \gamma^\mu \gamma^\rho (1-\gamma_5) v_{\bar{\nu}} \Big] \\ &= f_B \Big[g^{\mu\nu} L_\nu + \frac{2p_\ell^\mu p_\ell^\nu}{(p_\ell+q)^2 - m_\ell^2} L_\nu + \bar{u}_\ell \frac{p_\ell^\mu q^\rho}{(p_\ell+q)^2 - m_\ell^2} \gamma_\rho (1-\gamma_5) v_{\bar{\nu}} \\ &\quad - \bar{u}_\ell \frac{p_\ell \cdot q}{(p_\ell+q)^2 - m_\ell^2} \gamma^\mu (1-\gamma_5) v_{\bar{\nu}} + \bar{u}_\ell \frac{q^\mu p_\ell^\nu}{(p_\ell+q)^2 - m_\ell^2} \gamma_\nu (1-\gamma_5) v_{\bar{\nu}} \\ &\quad - \mathrm{i}\epsilon^{\nu\mu\rho\sigma} \bar{u}_\ell \frac{(p_\ell)_\nu q_\rho}{(p_\ell+q)^2 - m_\ell^2} \gamma_\sigma (1-\gamma_5) v_{\bar{\nu}} \Big], \end{aligned} \tag{3.10}$$

leading to

$$T_{\mathrm{FSR}}^{\mu\nu}(p_\ell, p_\nu, q) = f_B \left[g^{\mu\nu} + \frac{2p_\ell^\mu p_\ell^\nu + p_\ell^\mu q^\nu + q^\mu p_\ell^\nu - (p_\ell \cdot q) g^{\mu\nu} + \mathrm{i}\epsilon^{\mu\nu\rho\sigma} (p_\ell)_\rho q_\sigma}{(p_\ell+q)^2 - m_\ell^2} \right], \tag{3.11}$$

which is valid only when contracted with the leptonic matrix element L_ν.[3]

Due to gauge invariance, the full amplitude necessarily complies with the WARD identity

$$q_\mu \big[T_{\mathrm{H}}^{\mu\nu}(k,q) + T_{\mathrm{FSR}}^{\mu\nu}(p_\ell, p_\nu, q) \big] L_\nu = 0. \tag{3.12}$$

However, the hadronic and the FSR tensor are not individually gauge invariant but satisfy [1, 4, 5]

$$\begin{aligned} q_\mu T_{\mathrm{H}}^{\mu\nu}(k,q) &= -f_B (k+q)^\nu, \\ q_\mu T_{\mathrm{FSR}}^{\mu\nu}(p_\ell, p_\nu, q) &= f_B (k+q)^\nu, \end{aligned} \tag{3.13}$$

see App. A, so that gauge invariance indeed only holds for the sum of both contributions. Based on Eq. (3.13), we split the hadronic tensor into a homogeneous and an inhomogeneous part by means of $T_{\mathrm{H}}^{\mu\nu}(k,q) = T_{\mathrm{H,hom.}}^{\mu\nu}(k,q) + T_{\mathrm{H,inhom.}}^{\mu\nu}(k,q)$, which obey

$$\begin{aligned} q_\mu T_{\mathrm{H,hom.}}^{\mu\nu}(k,q) &= 0, \\ q_\mu T_{\mathrm{H,inhom.}}^{\mu\nu}(k,q) &= -f_B (k+q)^\nu. \end{aligned} \tag{3.14}$$

Up to this point, we have not made any choice on the LORENTZ decomposition of the hadronic tensor $T_{\mathrm{H}}^{\mu\nu}(k,q)$ or its (in-)homogeneous part. In App. A, we demonstrate that any such choice leads to the relation

$$k_\nu T_{\mathrm{H,hom.}}^{\mu\nu}(k,q) = T_{\mathrm{P}}^{\mu}(k,q) + f_B (k+q)^\mu - k_\nu T_{\mathrm{H,inhom.}}^{\mu\nu}(k,q), \tag{3.15}$$

[2] The CHISHOLM identity is derived in the Foundations part of this thesis.

[3] Note that one can, in principle, further make the replacement $p_\ell^\nu \to k^\nu$ in Eq. (3.11) by virtue of the DIRAC equation for the neutrino.

where the pseudoscalar tensor $T_{\mathrm{P}}^{\mu}(k,q)$ is defined in terms of the pseudoscalar weak current $J_{\mathrm{P}}(x) = \bar{u}(x)\gamma_5 b(x)$ via

$$Q_B T_{\mathrm{P}}^{\mu}(k,q) = (m_b + m_u) \int \mathrm{d}^4x\, \mathrm{e}^{\mathrm{i}qx}\, \langle 0|\mathrm{T}\{J_{\mathrm{EM}}^{\mu}(x) J_{\mathrm{P}}(0)\}|B^-\rangle\,, \tag{3.16}$$

with m_b and m_u being the $\overline{\mathrm{MS}}$ masses of the b- and u-quarks. As also shown in App. A, this tensor is not gauge invariant but, similar to Eq. (3.13), fulfills

$$q_\mu T_{\mathrm{P}}^{\mu}(k,q) = -f_B m_B^2. \tag{3.17}$$

For this reason, we proceed in analogy to Eq. (3.14) and split $T_{\mathrm{P}}^{\mu}(k,q) = T_{\mathrm{P,hom.}}^{\mu}(k,q) + T_{\mathrm{P,inhom.}}^{\mu}(k,q)$, where

$$\begin{aligned} q_\mu T_{\mathrm{P,hom.}}^{\mu}(k,q) &= 0, \\ q_\mu T_{\mathrm{P,inhom.}}^{\mu}(k,q) &= -f_B m_B^2. \end{aligned} \tag{3.18}$$

In the following, we additionally impose that the homogeneous part of the hadronic tensor fulfills

$$k_\nu T_{\mathrm{H,hom.}}^{\mu\nu}(k,q) \stackrel{!}{=} T_{\mathrm{P,hom.}}^{\mu}(k,q), \tag{3.19}$$

which, using Eq. (3.15), leads to the condition

$$T_{\mathrm{P,inhom.}}^{\mu}(k,q) + f_B(k+q)^\mu - k_\nu T_{\mathrm{H,inhom.}}^{\mu\nu}(k,q) = 0. \tag{3.20}$$

The constraint given in Eq. (3.19) corresponds to an intrinsically natural choice because it links one of the hadronic form factors of the axial-vector current to that of the pseudoscalar current, as is the case with hadronic form factors in other weak transitions, too.

The tensors $T_{\mathrm{H}}^{\mu\nu}(k,q)$ and $T_{\mathrm{FSR}}^{\mu\nu}(p_\ell, p_\nu, q)$ emerge in predictions for the decay $B^-(p) \to \ell^-(p_\ell)\bar{\nu}_\ell(p_\nu)\ell'^-(q_1)\ell'^+(q_2)$, with $\ell' \neq \ell$, $q = q_1 + q_2$,

$$\begin{aligned} \mathcal{M}(B^- \to \ell^-\bar{\nu}_\ell\ell'^-\ell'^+) &= \frac{4G_{\mathrm{F}}V_{ub}}{\sqrt{2}} \langle \ell^-\bar{\nu}_\ell\ell'^-\ell'^+|\mathcal{O}_{V,L}^{ub\ell\nu}|B^-\rangle \\ &= \frac{G_{\mathrm{F}}V_{ub}}{\sqrt{2}} \frac{e^2}{q^2} Q_B \big[T_{\mathrm{H}}^{\mu\nu}(k,q) + T_{\mathrm{FSR}}^{\mu\nu}(p_\ell, p_\nu, q)\big] l_\mu L_\nu, \end{aligned} \tag{3.21}$$

where we introduced the leptonic matrix element $l_\mu = \bar{u}_{\ell'}\gamma_\mu v_{\bar{\ell}'}$, with $\bar{u}_{\ell'} \equiv \bar{u}_{\ell'}(q_1)$ and $v_{\bar{\ell}'} \equiv v_{\bar{\ell}'}(q_2)$. It is straightforward to calculate the spin-summed amplitude squared,

$$\begin{aligned} |\overline{\mathcal{M}}(B^- \to \ell^-\bar{\nu}_\ell\ell'^-\ell'^+)|^2 = \frac{e^4 G_{\mathrm{F}}^2 |V_{ub}|^2}{2q^4} &\big[T_{\mathrm{H}}^{\mu\nu}(k,q) + T_{\mathrm{FSR}}^{\mu\nu}(p_\ell, p_\nu, q)\big] \\ &\times \big[T_{\mathrm{H}}^{\alpha\beta}(k,q) + T_{\mathrm{FSR}}^{\alpha\beta}(p_\ell, p_\nu, q)\big]^\dagger \sum_{\text{spins}} l_\mu l_\alpha^\dagger \sum_{\text{spins}} L_\nu L_\beta^\dagger, \end{aligned} \tag{3.22}$$

where taking the trace in Dirac space yields

$$\begin{aligned} \sum_{\text{spins}} l^\mu l^{\dagger\alpha} &= 4\big[q_1^\mu q_2^\alpha + q_2^\mu q_1^\alpha - [(q_1\cdot q_2) + m_{\ell'}^2]g^{\mu\alpha}\big], \\ \sum_{\text{spins}} L^\nu L^{\dagger\beta} &= 8\big[p_\ell^\nu p_\nu^\beta + p_\nu^\nu p_\ell^\beta - (p_\ell\cdot p_\nu)g^{\nu\beta} - \mathrm{i}\epsilon^{\nu\beta\rho\sigma}(p_\ell)_\rho(p_\nu)_\sigma\big]. \end{aligned} \tag{3.23}$$

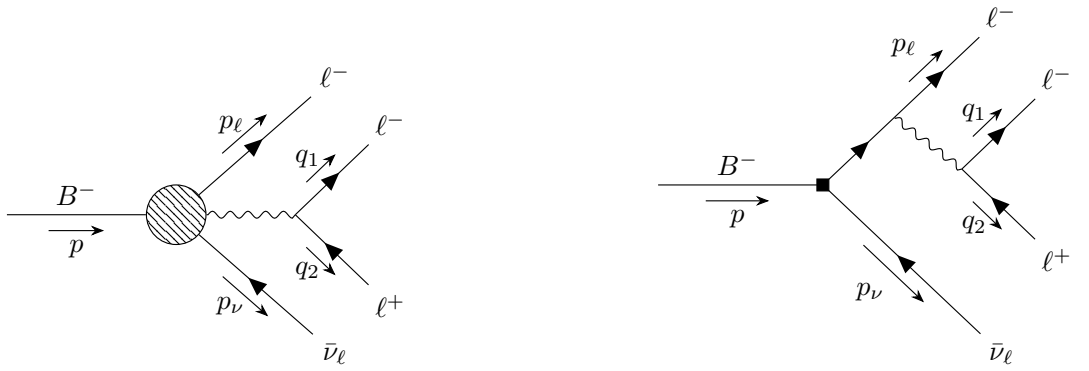

Figure 3.2: Two of the four diagrams contributing to the decay $B^- \to \ell^-\bar\nu_\ell\ell^-\ell^+$ with identical lepton flavors; see also Fig. 3.1. The other two diagrams are obtained by interchanging $p_\ell \leftrightarrow q_1$, which implies $k \to \widetilde{k} = q_1 + p_\nu$ and $q \to \widetilde{q} = p_\ell + q_2$.

The discussion of the decay with identical lepton flavors, $\ell' = \ell$, is more involved [4, 18] since an additional set of diagrams has to be taken into account due to the interchangeability of two final-state fermions, see Fig. 3.2. In this case, the amplitude can be written as

$$\mathcal{M}(B^- \to \ell^-\bar\nu_\ell\ell^-\ell^+) = \mathcal{M}(B^- \to \ell^-\bar\nu_\ell\ell'^-\ell'^+)\big|_{\ell'=\ell} - (p_\ell \leftrightarrow q_1), \tag{3.24}$$

where concurrent adjustments to the DIRAC spinors in the expressions l_μ and L_ν are implied, and we have $k \to \widetilde{k} = q_1 + p_\nu$ and $q \to \widetilde{q} = p_\ell + q_2$ for the term indicated by $(p_\ell \leftrightarrow q_1)$; the relative minus sign between the two contributions arises from a simple counting of permutations in the corresponding WICK contractions. For the spin-summed amplitude squared, we then find

$$\begin{aligned}|\overline{\mathcal{M}}(B^- \to \ell^-\bar\nu_\ell\ell^-\ell^+)|^2 = {} & \big[|\overline{\mathcal{M}}(B^- \to \ell^-\bar\nu_\ell\ell'^-\ell'^+)|^2\big|_{\ell'=\ell} + (p_\ell \leftrightarrow q_1)\big] \\ & - \sum_{\text{spins}} \big[\mathcal{M}(B^- \to \ell^-\bar\nu_\ell\ell'^-\ell'^+)\big|_{\ell'=\ell} \times (p_\ell \leftrightarrow q_1)^\dagger + \text{h.c.}\big].\end{aligned} \tag{3.25}$$

Upon integration over the phase space, the first two terms are related by a LORENTZ transformation, $|\overline{\mathcal{M}}(B^- \to \ell^-\bar\nu_\ell\ell'^-\ell'^+)|^2\big|_{\ell'=\ell} + (p_\ell \leftrightarrow q_1) \mathrel{\widehat{=}} 2\,|\overline{\mathcal{M}}(B^- \to \ell^-\bar\nu_\ell\ell'^-\ell'^+)|^2\big|_{\ell'=\ell}$,[4] so that the complications of the decay $B^- \to \ell^-\bar\nu_\ell\ell^-\ell^+$ with identical leptons in principle reduce to the evaluation of the interference term. An additional peculiarity of the interference term is that the summation over the spins does not factorize into two separate sums as in Eq. (3.22) but needs to be performed with a single trace, leading to a cumbersome expression that we refrain from providing here.

[4]The factor of 2 is eventually countered by an additional factor of 1/2 that has to be taken into account for the decay with identical lepton flavors to avoid double counting in the phase-space integration.

Chapter 4

$B \to \gamma^*$ form factors

For the parameterization of the homogeneous part of the hadronic tensor, we develop a method that closely resembles the BTT procedure [10, 11]; in contrast to the native BTT procedure, our modification ensures that the emerging form factors have definite angular-momentum and parity quantum numbers, see App. B, leading to the result

$$\begin{aligned} T^{\mu\nu}_{\mathrm{H,hom.}}(k,q) = \frac{1}{m_B}[(k\cdot q)g^{\mu\nu} - k^\mu q^\nu]\mathcal{F}_1(k^2,q^2) \\ + \frac{1}{m_B}\Big[\frac{q^2}{k^2}k^\mu k^\nu - \frac{k\cdot q}{k^2}q^\mu k^\nu + q^\mu q^\nu - q^2 g^{\mu\nu}\Big]\mathcal{F}_2(k^2,q^2) \\ + \frac{1}{m_B}\Big[\frac{k\cdot q}{k^2}q^\mu k^\nu - \frac{q^2}{k^2}k^\mu k^\nu\Big]\mathcal{F}_3(k^2,q^2) + \frac{\mathrm{i}}{m_B}\epsilon^{\mu\nu\rho\sigma}k_\rho q_\sigma \mathcal{F}_4(k^2,q^2). \end{aligned} \tag{4.1}$$

Here, the factors of m_B and the imaginary unit render the form factors dimensionless and—with the phase of the B meson chosen appropriately—real-valued below the onset of the first branch cut. The form factors $\mathcal{F}_1(k^2,q^2)$ and $\mathcal{F}_2(k^2,q^2)$ have axial-vector, $\mathcal{F}_3(k^2,q^2)$ has pseudoscalar, and $\mathcal{F}_4(k^2,q^2)$ vector quantum numbers with respect to the weak current;[5] assuming no modification due to the inhomogeneous part $T^{\mu\nu}_{\mathrm{H,inhom.}}(k,q)$, they are free of kinematic singularities in k^2 and q^2 as well as kinematic zeroes in q^2. However, to ensure a finite amplitude at $k^2 = 0$, the relation $\mathcal{F}_2(0,q^2) = \mathcal{F}_3(0,q^2)$ must hold for all q^2.

The relations given in Eq. (3.14) constrain the inhomogeneous part of the hadronic tensor to the generic form

$$T^{\mu\nu}_{\mathrm{H,inhom.}}(k,q) = -f_B\bigg[a g^{\mu\nu} + b\frac{k^\mu k^\nu}{k\cdot q} + c\frac{k^\mu q^\nu}{k\cdot q} + (1-b)\frac{q^\mu k^\nu}{q^2} + (1-a-c)\frac{q^\mu q^\nu}{q^2}\bigg], \tag{4.2}$$

where $a \equiv a(k^2,q^2)$, $b \equiv b(k^2,q^2)$, and $c \equiv c(k^2,q^2)$ are arbitrary real-valued coefficients. Given that the inhomogeneity is entirely due to the axial-vector part of Eq. (3.5), see App. A, the Levi-Civita tensor does not carry the proper quantum numbers to be part of this expression. On account of Eq. (3.18), the inhomogeneous part of the pseudoscalar tensor furthermore takes the generic form

$$T^{\mu}_{\mathrm{P,inhom.}}(k,q) = -f_B m_B^2\bigg[d\frac{k^\mu}{k\cdot q} + (1-d)\frac{q^\mu}{q^2}\bigg], \tag{4.3}$$

[5] Note that for on-shell photons, only the form factors $\mathcal{F}_1(k^2,q^2)$ and $\mathcal{F}_4(k^2,q^2)$ contribute, which correspond to transverse polarizations.

	a	b	c	$T^{\mu\nu}_{\text{H,inhom.}}(k,q)$	d	$T^{\mu}_{\text{P,inhom.}}(k,q)$	References
$\mathcal{A}$	1	$\frac{2(k\cdot q)}{2(k\cdot q)+q^2}$	0	$-f_B\left[g^{\mu\nu}+\frac{(2k^\mu+q^\mu)k^\nu}{2(k\cdot q)+q^2}\right]$	$\frac{2(k\cdot q)}{2(k\cdot q)+q^2}$	$-f_B m_B^2\frac{2k^\mu+q^\mu}{2(k\cdot q)+q^2}$	[15–17, 19]
$\mathcal{B}$	0	$\frac{k\cdot q}{k\cdot q+q^2}$	$\frac{k\cdot q}{k\cdot q+q^2}$	$-f_B\frac{(k+q)^\mu(k+q)^\nu}{k\cdot q+q^2}$	$\frac{k\cdot q}{k\cdot q+q^2}$	$-f_B m_B^2\frac{k^\mu+q^\mu}{k\cdot q+q^2}$	[1, 14]
$\mathcal{C}$	0	1	1	$-f_B\frac{k^\mu(k+q)^\nu}{k\cdot q}$	$\frac{2(k\cdot q)+k^2}{2(k\cdot q)+k^2+q^2}$	$-f_B\left[m_B^2\frac{k^\mu}{k\cdot q}-\frac{q^2k^\mu-(k\cdot q)q^\mu}{k\cdot q}\right]$	[4]
$\mathcal{D}$	0	0	0	$-f_B\frac{q^\mu(k+q)^\nu}{q^2}$	$\frac{k\cdot q}{2(k\cdot q)+k^2+q^2}$	$-f_B\left[m_B^2\frac{q^\mu}{q^2}-\frac{(k\cdot q)q^\mu-q^2k^\mu}{q^2}\right]$	[5]

Table 4.1: The ansätze for the inhomogeneous part of the hadronic tensor used in the literature, expressed as in Eq. (4.2) for specific choices of the coefficients a, b, and c. Also shown are the resulting inhomogeneous parts of the pseudoscalar tensor, Eq. (4.3), and its associated coefficient d, Eq. (4.4). The basis for the homogeneous part of the hadronic tensor differs from our choice, Eq. (4.1), in some of the references. A thorough discussion of the various choices can be found in the main text.

where $d \equiv d(k^2, q^2)$ is an arbitrary real-valued coefficient. Adopting the condition imposed in Eq. (3.20), we find that

$$d = \frac{(1+a+c)(k\cdot q)+bk^2}{m_B^2}, \tag{4.4}$$

which fixes $T^{\mu}_{\text{P,inhom.}}(k,q)$ once $T^{\mu\nu}_{\text{H,inhom.}}(k,q)$ is specified. We collect four different choices for the coefficients, labeled $\mathcal{A}$ through $\mathcal{D}$, in Table 4.1. With regard to the dispersive treatment of the form factors in our analysis, *i.e.*, the requirement of their singularity-free structure, we are faced with the question of what an appropriate choice for these coefficients is.

Among the inhomogeneous parts of the hadronic tensor listed in Table 4.1, $\mathcal{A}$ is the only choice that introduces a term singular in $[2(k\cdot q)+q^2] = (m_B^2 - k^2)$. It is evident that this k^2-pole is associated with an intermediate B meson [19], as sketched in the left diagram of Fig. 3.1; see also Fig. 4.1. The choices $\mathcal{B}$ and $\mathcal{C}$, on the other hand, introduce terms singular in $[(k\cdot q)+q^2]$ and $(k\cdot q)$, respectively, which correspond to q^2-dependent pole positions in the variable k^2; these are not associated with any hadronic intermediate state and are therefore not of dynamic but kinematic origin. Choice $\mathcal{D}$ corresponds to a structure that is orthogonal to all BTT structures and might thus lead to the false conclusion that it leaves the form factors of Eq. (4.1) unaffected and accordingly free of kinematic singularities. However, this choice exhibits a pole in q^2, adversely suggesting the emergence of a dynamic photon pole, which, working at fixed order in QED, cannot arise. In fact, the behavior $\propto 1/q^2$ would lead to a double pole $\propto 1/q^4$ in Eq. (3.21), a feature that is to be avoided in any amplitude. As a consequence of this double pole, choice $\mathcal{D}$ is—in addition to the kinematic nature of the q^2 pole—disqualified by its effect on the longitudinal $B^- \to \ell^-\bar\nu_\ell\gamma^*$ helicity amplitude.

To further illustrate this effect, we investigate the $B^- \to \ell^-\bar\nu_\ell\gamma^*$ amplitude in more detail. From Eq. (3.1) and Eq. (3.9), one finds the squared spin-summed amplitude for photons with polarization λ to be given by

$$|\overline{\mathcal{M}}(B^- \to \ell^-\bar\nu_\ell\gamma^*(\lambda))|^2 = \frac{e^2G_{\text{F}}^2|V_{ub}|^2}{2}\epsilon^*_\mu(q;\lambda)\epsilon_\alpha(q;\lambda)\big[T^{\mu\nu}_{\text{H}}(k,q)+T^{\mu\nu}_{\text{FSR}}(p_\ell,p_\nu,q)\big]$$

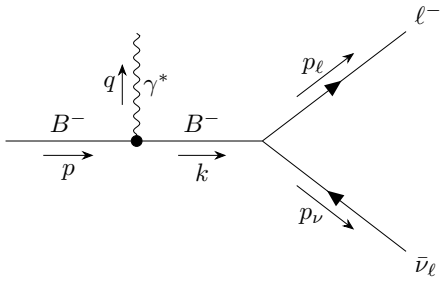

Figure 4.1: FEYNMAN diagram illustrating the B-meson pole in the variable k^2 as part of the hadronic tensor $T_{\mathrm{H}}^{\mu\nu}(k,q)$; see also the left diagram of Fig. 3.1.

$$\times \left[T_{\mathrm{H}}^{\alpha\beta}(k,q) + T_{\mathrm{FSR}}^{\alpha\beta}(p_\ell, p_\nu, q)\right]^\dagger \sum_{\text{spins}} L_\nu L_\beta^\dagger; \tag{4.5}$$

see App. D for details on the kinematics. For a longitudinal photon, $\lambda = 0$, this matrix element ought to vanish in the limit $q^2 \to 0$, *i.e.*, for an on-shell photon. Using choice $\mathcal{D}$, one does, however, find that the matrix element diverges $\propto f_B^2$, independent of any choice of form factors. The discussion of such divergent contributions is not purely academic: in Ref. [5], a supposed collinear enhancement of the $B^- \to \ell^-\bar{\nu}_\ell\ell'^-\ell'^+$ decay rate is discussed, which is caused by such an unphysical behavior as $q^2 \to 0$. Therein, a different choice is made for the decomposition of the homogeneous tensor, in combination with choice $\mathcal{D}$ for the inhomogeneous part and an inconsistent treatment of the charged lepton's finite mass in the FSR term. Using the formulae of Ref. [5] and our result for the FSR tensor, Eq. (3.11), we validated that treating the effects of a finite lepton mass consistently resolves this issue and eliminates the supposed contribution due to a longitudinal on-shell photon.[6] This leads us to infer that the supposed collinear enhancement is not a physical feature of the $B^- \to \ell^-\bar{\nu}_\ell\ell'^-\ell'^+$ decay rate.

Moreover, we can draw conclusions from the results for the hadronic tensor in the decay $K^\pm \to \ell^\pm\nu_\ell\gamma^*(\to \ell'^-\ell'^+)$, where an explicit calculation in chiral perturbation theory at next-to-leading order [16, 17] confirms that choice $\mathcal{A}$ yields form factors that are free of kinematic singularities. Transforming between choice $\mathcal{A}$ and any other choice of Table 4.1 modifies the homogeneous part through the incorporation of kinematic singularities; consequently, the assumption that choice $\mathcal{A}$ leads to form factors free of kinematic singularities unavoidably implies the emergence of such singularities for all the other choices considered here.

Under some rather general, reasonable assumptions, it is possible to deduce that the inhomogeneous part of the hadronic tensor ought to be of the form

$$T_{\mathrm{H,inhom.}}^{\mu\nu}(k,q) = -f_B\left[\hat{a}g^{\mu\nu} + \frac{(2k^\mu + q^\mu)k^\nu + (1-\hat{a})(2k^\mu + q^\mu)q^\nu}{2(k\cdot q) + q^2}\right] \tag{4.6}$$

in combination with the BTT basis of Eq. (4.1) for the homogeneous part, see App. A. Here, $\hat{a}$ is an *a priori* undetermined real-valued coefficient that does not depend on any of the momenta. The assumptions underlying the above form are the following:

[6] This has since been confirmed to us by the authors of Ref. [5] and is revised in an Erratum.

- there exists a unique choice for the coefficients in Eq. (4.2) that leaves the form factors free of kinematic singularities;
- the apparent kinematic poles in $T^{\mu\nu}_{\mathrm{H,inhom.}}(k,q)$ cancel and no new such poles are introduced;
- a dynamic B-meson pole appears at most in the pseudoscalar form factor $\mathcal{F}_3(k^2,q^2)$.

Consequently, the inhomogeneous part of the pseudoscalar tensor, Eq. (4.3), turns out to be given by

$$T^{\mu}_{\mathrm{P,inhom.}}(k,q) = -f_B\left[m_B^2\frac{2k^\mu+q^\mu}{2(k\cdot q)+q^2} - (1-\hat{a})\frac{q^2k^\mu-(k\cdot q)q^\mu}{2(k\cdot q)+q^2}\right]. \tag{4.7}$$

Furthermore, assuming that $\hat{a}=1$ meets the above requirements, which corresponds to choice $\mathcal{A}$ from Table 4.1, it is straightforward to verify that any other choice of $\hat{a}$ would introduce a dynamic pseudoscalar B-meson pole in the axial-vector form factors $\mathcal{F}_1(k^2,q^2)$ and $\mathcal{F}_2(k^2,q^2)$.

For the reasons stated above, we make $\mathcal{A}$ the default choice and parameterize the hadronic tensor as

$$T^{\mu\nu}_{\mathrm{H}}(k,q) = T^{\mu\nu}_{\mathrm{H,hom.}}(k,q) - f_B\left[g^{\mu\nu}+\frac{(2k^\mu+q^\mu)k^\nu}{2(k\cdot q)+q^2}\right] \tag{4.8}$$

in the following. This yields a total of six independent Lorentz structures, which form a basis—see the discussion in the appendix of Ref. [4]—and thus allow us to find projectors $\mathcal{P}_i^{\mu\nu}(k,q)$ that fulfill

$$\mathcal{P}_{i\mu\nu}(k,q)T^{\mu\nu}_{\mathrm{H}}(k,q) = \begin{cases}\mathcal{F}_i(k^2,q^2), & i=1,\dots,4,\\ f_B/m_B, & i=5,6.\end{cases} \tag{4.9}$$

Explicit formulae for these projectors are provided in App. C.

Chapter 5

Dispersion relations and z expansion

For our analysis, we split the form factors with respect to the photon's isospin according to $\mathcal{F}_i(k^2,q^2) = \mathcal{F}_i^{I=0}(k^2,q^2) + \mathcal{F}_i^{I=1}(k^2,q^2)$, $i = 1,\dots,4$. To parameterize the form factors in accordance with analyticity and unitarity, we will establish a set of dispersion relations for each component and assume the underlying discontinuities to be dominated by the one-body intermediate states ω and ρ, respectively, which allows us to relate the $B \to \gamma^*$ form factors to the $B \to V$, $V = \omega, \rho$, analogs. In doing so, we neglect contributions due to $B \to \phi$ in the isoscalar components for two reasons: first, these contributions are expected to be small due to the OZI mechanism [20–22], and secondly, we lack non-perturbative input for the $B \to \phi$ form factors. Beyond that, we also do not model contributions from further excited states, such as ω' and ρ'. As a consequence, we provide our principal phenomenological results for the region $q^2 \lesssim 1\,\mathrm{GeV}^2$.

Based on Eq. (3.5), the discontinuity[7] of the form factors with respect to q^2 and for fixed k^2 is given by [23, 24]

$$\begin{aligned}\mathrm{disc}_{q^2}[Q_B\mathcal{F}_i(k^2,q^2)] &= \mathrm{disc}_{q^2}[\mathcal{P}_{i\mu\nu}(k,q)Q_B T_{\mathrm{H}}^{\mu\nu}(k,q)] \\ &= \mathcal{P}_{i\mu\nu}(k,q)\Big[\mathrm{i}\sum_n \int \mathrm{d}\Phi_n(q;p_1,\dots,p_n)\ \langle 0|J_{\mathrm{EM}}^{\mu}(0)|n\rangle\,\langle n|J_{\mathrm{H}}^{\nu}(0)|B^-\rangle\Big].\end{aligned} \tag{5.1}$$

Here, we use the n-body phase-space volume

$$\begin{aligned}\mathrm{d}\Phi_n(q;p_1,\dots,p_n) &= (2\pi)^4\delta^{(4)}(q-P_n)\prod_j \frac{\mathrm{d}^3p_j}{(2\pi)^3 2p_j^0} \\ &= (2\pi)^4\delta^{(4)}(q-P_n)\prod_j \frac{\mathrm{d}^4p_j}{(2\pi)^4}\,(2\pi)\delta(p_j^2-M_j^2)\theta(p_j^0),\end{aligned} \tag{5.2}$$

where $P_n = \sum_j p_j$ is the total momentum of the intermediate state. Assuming the discontinuities of the isoscalar and isovector components to be dominated by the one-body intermediate states ω and ρ, respectively, we use

$$\int \mathrm{d}\Phi_n(q;p_1,\dots,p_n)\,f(P_n) = 2\pi\delta(q^2-M_n^2)f(q) \tag{5.3}$$

[7] Note that in the discontinuity, the x-dependence of the EM current $J_{\mathrm{EM}}^{\mu}(x)$ turns into the δ distribution for momentum conservation, which, on the other hand, is absorbed into $\mathrm{d}\Phi_n(q;p_1,\dots,p_n)$ here.

for the one-body phase-space volume to obtain

$$\begin{aligned}\mathrm{disc}_{q^2}[Q_B\mathcal{F}_i^I(k^2,q^2)] = \mathcal{P}_{i\mu\nu}(k,q)\Big[2\pi\mathrm{i}\sum_\lambda \delta(q^2-M_V^2)\,\langle 0|J^\mu_{\mathrm{EM}}(0)|V(q,\lambda)\rangle \\ \times\langle V(q,\lambda)|J^\nu_{\mathrm{H}}(0)|B^-\rangle\Big],\end{aligned} \tag{5.4}$$

with $V=\omega$ for $I=0$ and $V=\rho$ for $I=1$. For the above matrix elements, we employ [9]

$$\begin{aligned}\langle 0|J^\mu_{\mathrm{EM}}(0)|V(q,\lambda)\rangle &= \frac{\eta^\mu}{c_V} d_V M_V f_V,\\ \langle V(q,\lambda)|J^\nu_{\mathrm{H}}(0)|B^-\rangle &= \frac{\eta^*_\alpha}{c_V}\big[P_1^{\nu\alpha}(k,q)V^{B\to V}(k^2)+P_2^{\nu\alpha}(k,q)A_1^{B\to V}(k^2)\\ &\quad + P_3^{\nu\alpha}(k,q)A_3^{B\to V}(k^2)+P_P^{\nu\alpha}(k,q)A_0^{B\to V}(k^2)\big],\end{aligned} \tag{5.5}$$

where the structures are given by [9]

$$\begin{aligned}P_P^{\nu\alpha} &= -\frac{2M_V}{k^2}k^\nu k^\alpha, & P_2^{\nu\alpha} &= -\frac{1}{m_B-M_V}\big[(m_B^2-M_V^2)g^{\nu\alpha}-(k^\nu+2q^\nu)k^\alpha\big],\\ P_1^{\nu\alpha} &= \frac{2\mathrm{i}}{m_B+M_V}\epsilon^{\nu\alpha\beta\gamma}q_\beta k_\gamma, & P_3^{\nu\alpha} &= \frac{2M_V}{k^2}\Big[k^\nu-\frac{k^2}{m_B^2-M_V^2}(k^\nu+2q^\nu)\Big]k^\alpha,\end{aligned} \tag{5.6}$$

with the phases adjusted to our convention. Here, $d_\omega = Q_u+Q_d = 1/3$, $d_\rho = Q_u-Q_d = 1$, and the composition of the ω and ρ wave function is accounted for by the factors $c_\omega = \sqrt{2} = c_\rho$. Furthermore, the decay constant of the respective vector meson is denoted by f_V and $\eta^\mu \equiv \eta^\mu(q;\lambda)$ represents the polarization vector of the incoming vector meson with momentum q and polarization λ. The form factors $V^{B\to V}(k^2)$, $A_1^{B\to V}(k^2)$, $A_3^{B\to V}(k^2)$, and $A_0^{B\to V}(k^2)$ in Eq. (5.5) are given in the so-called traditional basis and account for a vector-, two axial-vector-, and a pseudoscalar-like $B\to V$ transition. Using the additional relation [9, 25]

$$A_{12}^{B\to V}(k^2) = \frac{k^2(m_B+M_V)(m_B^2-k^2+3M_V^2)A_1^{B\to V}(k^2)+2M_V\lambda_V(k^2)A_3^{B\to V}(k^2)}{16m_BM_V^2(m_B^2-M_V^2)}, \tag{5.7}$$

where $\lambda_V(k^2)\equiv\lambda(m_B^2,k^2,M_V^2)$, we can express all form factors in terms of $V^{B\to V}(k^2)$, $A_1^{B\to V}(k^2)$, $A_{12}^{B\to V}(k^2)$, and $A_0^{B\to V}(k^2)$, which fulfill the exact relation [9]

$$A_0(0) = \frac{8m_BM_VA_{12}(0)}{m_B^2-M_V^2}. \tag{5.8}$$

The generic parameterization of $F^{B\to V}(k^2)\in\{V(k^2),A_1(k^2),A_{12}(k^2),A_0(k^2)\}$ in terms of a simplified series expansion in the conformal variable

$$z_V(t) = \left.\frac{\sqrt{t_+-t}-\sqrt{t_+-t_0}}{\sqrt{t_+-t}+\sqrt{t_+-t_0}}\right|_{V=\omega,\rho}, \tag{5.9}$$

with $t_0=(1-\sqrt{1-t_-/t_+})t_+$ and $t_\pm=(m_B\pm M_V)^2$, is given by [9]

$$F^{B\to V}(k^2) = R_{J^P}(k^2)\sum_{j\geq 0}\alpha_j^{F,V}[z_V(k^2)-z_V(0)]^j, \tag{5.10}$$

$F^{B\to V}(k^2)$	J^P	m_{J^P}	$\alpha_0^{F,\omega}$	$\alpha_1^{F,\omega}$	$\alpha_2^{F,\omega}$	$\alpha_0^{F,\rho}$	$\alpha_1^{F,\rho}$	$\alpha_2^{F,\rho}$
$V^{B\to V}(k^2)$	1^-	m_{B^*}	0.304(38)	−0.83(29)	1.7(1.2)	0.327(31)	−0.86(18)	1.80(97)
$A_1^{B\to V}(k^2)$	1^+	m_{B_1}	0.243(31)	0.34(24)	0.09(57)	0.262(26)	0.39(14)	0.16(41)
$A_{12}^{B\to V}(k^2)$	1^+	m_{B_1}	0.270(40)	0.66(26)	0.28(98)	0.297(35)	0.76(20)	0.46(76)
$A_0^{B\to V}(k^2)$	0^-	m_B	0.328(48)	−0.83(30)	1.4(1.2)	0.356(42)	−0.83(20)	1.3(1.0)

Table 5.1: The quantum numbers J^P, resonance masses m_{J^P}, and numerical values (rounded to two significant digits) of the series coefficients $\alpha_j^{F,V}$ [9] for the z expansion of the form factors $F^{B\to V}(k^2)$, truncated after three summands, see Eq. (5.10). The corresponding values of the resonance masses can be found in App. G. Due to parity conservation of the strong interactions, no form factor with $J^P = 0^+$ exists. For the exact numerical values of $\alpha_j^{F,V}$ and the covariances as well as correlations between these, see Ref. [9]. Note that $\alpha_0^{A_0,V}$ and $\alpha_0^{A_{12},V}$ are not independent but have to fulfill the exact relation given in Eq. (5.8).

where the series is truncated after three summands; this truncation is imposed by the $B \to V$ parameters provided in Ref. [9]. In this expansion, the dominant subthreshold poles of the $B \to V$ form factors are taken into account through the term $R_{J^P} = (1 - k^2/m_{J^P}^2)^{-1}$, where J^P refers to the angular-momentum and parity quantum number of the respective form factor, see Table 5.1.

The isoscalar and isovector form factors can then be reconstructed from

$$Q_B \mathcal{F}_i^I(k^2, q^2) = \frac{1}{2\pi \mathrm{i}} \int_{s_{\mathrm{thr}}}^{\infty} \mathrm{d}s \, \frac{\mathrm{disc}_s[Q_B \mathcal{F}_i^I(k^2, s)]}{s - q^2}, \tag{5.11}$$

where $s_{\mathrm{thr}} = 9M_\pi^2, 4M_\pi^2$ for $I = 0, 1$, respectively. In the above, no subtractions are needed for convergence since the discontinuities drop off as $1/q^2$ asymptotically, see App. E. Inserting Eq. (5.4) into Eq. (5.11) and using the polarization sum of the ω and ρ mesons,

$$\sum_\lambda \eta_\mu(q;\lambda)\eta_\nu^*(q;\lambda) = -g_{\mu\nu} + \frac{q_\mu q_\nu}{M_V^2}, \tag{5.12}$$

we obtain the VMD result for the $B \to \gamma^*$ form factors,

$$\begin{aligned}
Q_B \mathcal{F}_1^I(k^2, q^2) &= M_V C_V \frac{16 m_B M_V^2 A_{12}^{B\to V}(k^2) - (m_B + M_V)(m_B^2 - k^2 - M_V^2) A_1^{B\to V}(k^2)}{\lambda_V(k^2)(q^2 - M_V^2)}, \\
Q_B \mathcal{F}_2^I(k^2, q^2) &= 2 M_V C_V \frac{4 m_B (m_B^2 - k^2 - M_V^2) A_{12}^{B\to V}(k^2) - (m_B + M_V) k^2 A_1^{B\to V}(k^2)}{\lambda_V(k^2)(q^2 - M_V^2)}, \\
Q_B \mathcal{F}_3^I(k^2, q^2) &= C_V \frac{A_0^{B\to V}(k^2)}{q^2 - M_V^2}, \\
Q_B \mathcal{F}_4^I(k^2, q^2) &= M_V C_V \frac{V^{B\to V}(k^2)}{(m_B + M_V)(q^2 - M_V^2)},
\end{aligned} \tag{5.13}$$

where $C_V = m_B f_V d_V$. Compared to $\mathcal{F}_1(k^2, q^2)$ and $\mathcal{F}_4(k^2, q^2)$, the form factors $\mathcal{F}_2(k^2, q^2)$ and $\mathcal{F}_3(k^2, q^2)$ enter observables with a relative suppression factor of q^2, thereby ensuring that unphysical longitudinal on-shell photons do not contribute.

$\mathcal{F}_i(k^2,q^2)$	J^P	m_{J^P}	$N^\omega_{i,0}$	$N^\omega_{i,1}$	$N^\omega_{i,2}$	$N^\rho_{i,0}$	$N^\rho_{i,1}$	$N^\rho_{i,2}$
$\mathcal{F}_1(k^2,q^2)$	1^+	m_{B_1}	0.0156(30)	−0.033(19)	0.003(85)	0.0557(88)	−0.115(48)	0.01(24)
$\mathcal{F}_2(k^2,q^2)$	1^+	m_{B_1}	−0.186(27)	0.39(14)	−0.17(52)	−0.676(79)	1.34(41)	−0.6(1.5)
$\mathcal{F}_3(k^2,q^2)$	0^-	m_B	−0.186(27)	0.47(17)	−0.80(71)	−0.676(79)	1.58(39)	−2.5(2.0)
$\mathcal{F}_4(k^2,q^2)$	1^-	m_{B^*}	−0.0222(28)	0.061(21)	−0.125(91)	−0.0795(75)	0.209(44)	−0.44(23)

Table 5.2: The quantum numbers J^P, resonance masses m_{J^P}, and numerical values (rounded to two significant digits) of the normalizations $N^V_{i,j}$ for the z expansion of the form factors $\mathcal{F}_i(k^2,q^2)$, truncated after three summands, see Eq. (5.14). The corresponding values of the resonance masses can be found in App. G. Our uncertainties on the normalizations take into account the uncertainties on the series coefficients $\alpha_j^{F,V}$ only, which, by far, give the dominant contribution. For the covariances between the normalizations, see App. F. Note that $N^V_{2,0}$ and $N^V_{3,0}$ are identical due to the exact relation given in Eq. (5.8) (or, equivalently, the condition $\mathcal{F}_2(0,q^2)=\mathcal{F}_3(0,q^2)$ imposed below Eq. (4.1)).

Naturally, we now aim to use an expansion similar to Eq. (5.10) for the $B\to\gamma^*$ form factors,

$$Q_B\mathcal{F}_i^I(k^2,q^2)=R_{J^P}(k^2)\sum_{j\geq 0}\beta^V_{i,j}(q^2)[z_V(k^2)-z_V(0)]^j, \tag{5.14}$$

where the form factors have definite angular-momentum and parity assignments, with the term $R_{J^P}(k^2)$ again accounting for the dominant subthreshold poles in the variable k^2. In contrast to Eq. (5.10), the series coefficients have a dependence on q^2, for which we will assume VMD and use an *ad hoc* BW ansatz,

$$\beta^V_{i,j}(q^2)=N^V_{i,j}P_V^{\mathrm{BW}}(q^2). \tag{5.15}$$

At this, it is justified to use a monopole ansatz since the form factors drop off as $1/q^2$ asymptotically, see App. E. Because of its smallness, we use a constant approximation for the ω decay width above the 3π threshold, whereas we incorporate the broad ρ width energy-dependently,

$$P_\omega^{\mathrm{BW}}(q^2)=\frac{M_\omega^2}{M_\omega^2-q^2-\mathrm{i}M_\omega\,\Gamma_\omega},\qquad P_\rho^{\mathrm{BW}}(q^2)=\frac{M_\rho^2}{M_\rho^2-q^2-\mathrm{i}\sqrt{q^2}\,\Gamma_\rho(q^2)}. \tag{5.16}$$

Here, the proper threshold behavior is implied for the ω, *i.e.*, $\Gamma_\omega=0$ for $q^2<9M_\pi^2$, and the energy-dependent width of the ρ is parameterized according to [26]

$$\Gamma_\rho(q^2)=\theta(q^2-4M_\pi^2)\frac{\gamma_{\rho\to\pi\pi}(q^2)}{\gamma_{\rho\to\pi\pi}(M_\rho^2)}\Gamma_\rho,\qquad \gamma_{\rho\to\pi\pi}(q^2)=\frac{(q^2-4M_\pi^2)^{3/2}}{q^2}. \tag{5.17}$$

The normalizations $N^V_{i,j}$ can be computed by inserting Eq. (5.10) and Eq. (5.14) into

$$\begin{aligned}Q_B\mathcal{F}_i^I(k^2,q^2)=&\frac{K^I_{i,A_{12}}(k^2)}{q^2-M_V^2}A_{12}^{B\to V}(k^2)+\frac{K^I_{i,A_1}(k^2)}{q^2-M_V^2}A_1^{B\to V}(k^2)+\frac{K^I_{i,A_0}(k^2)}{q^2-M_V^2}A_0^{B\to V}(k^2)\\&+\frac{K^I_{i,V}(k^2)}{q^2-M_V^2}V^{B\to V}(k^2),\quad K^I_{i,F}(k^2)=\sum_{j\geq 0}\kappa^{I,j}_{i,F}[z_V(k^2)-z_V(0)]^j,\end{aligned} \tag{5.18}$$

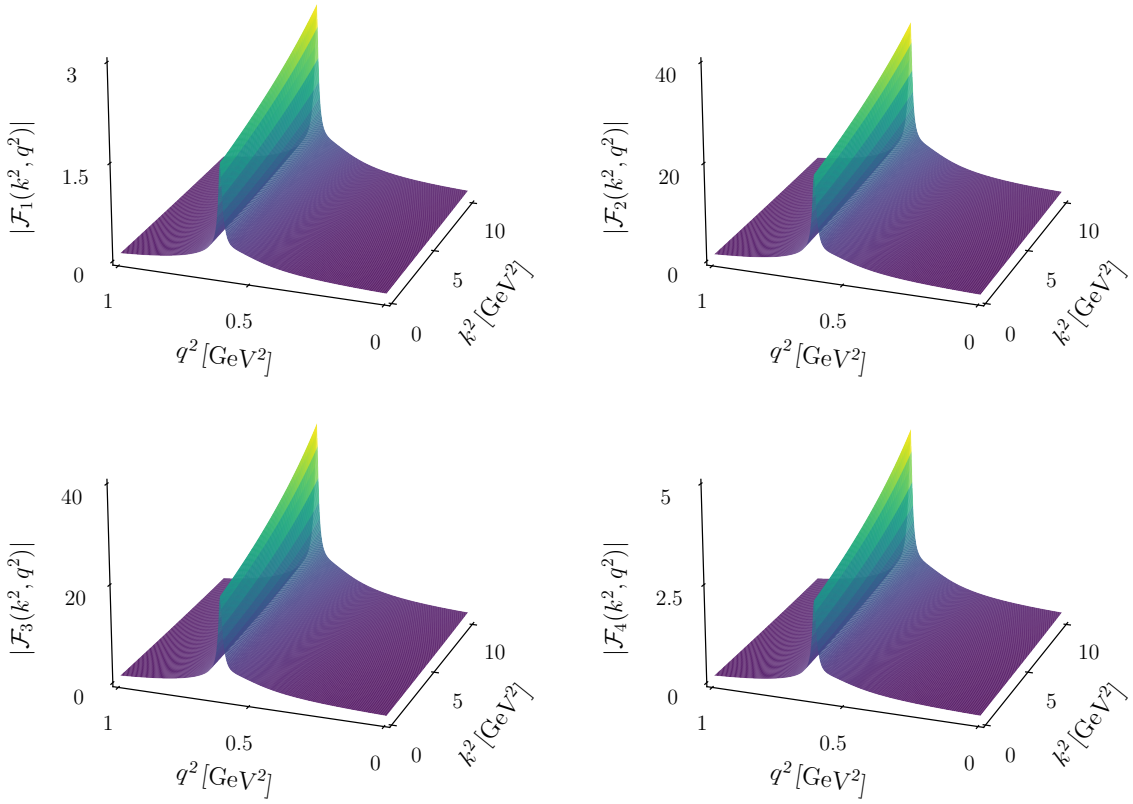

Figure 5.1: Three-dimensional plots showing the absolute values of the full form factors, Eq. (5.19), in the range $k^2 \in [0, 10]\,\mathrm{GeV}^2$ and $q^2 \in [0, 1]\,\mathrm{GeV}^2$. The peak of the ω resonance is clearly visible, while the ρ resonance is lower in magnitude due to the scaling $\propto M_\rho/\Gamma_\rho$ and hardly discernible here.

with coefficients $\kappa_{i,F}^{I,j}$ that can be determined from an expansion of Eq. (5.13) around $z_V(k^2) = z_V(0)$. Using the numerical values from Table 5.1 to match both sides of the above equation at $q^2 = 0$, order by order in the conformal variable, results in the normalizations collected in Table 5.2. Adding both isospin components, the full form factors can further be written as

$$\begin{aligned} Q_B \mathcal{F}_i(k^2,q^2) &= Q_B[\mathcal{F}_i^{I=0}(k^2,q^2) + \mathcal{F}_i^{I=1}(k^2,q^2)] \\ &= R_{J^P}(k^2) \sum_{\substack{V=\omega,\rho \\ j\geq 0}} N_{i,j}^V P_V^{\mathrm{BW}}(q^2)[z_V(k^2) - z_V(0)]^j. \end{aligned} \tag{5.19}$$

We present three-dimensional plots of the absolute values of the full form factors, Eq. (5.19), in Fig. 5.1. In addition, we provide two-dimensional plots, including uncertainties and with $k^2 = 1\,\mathrm{GeV}^2$ and $q^2 = 1\,\mathrm{GeV}^2$ fixed, in Fig. 5.2 and Fig. 5.3, where we also show the absolute values of the isoscalar and isovector components separately.

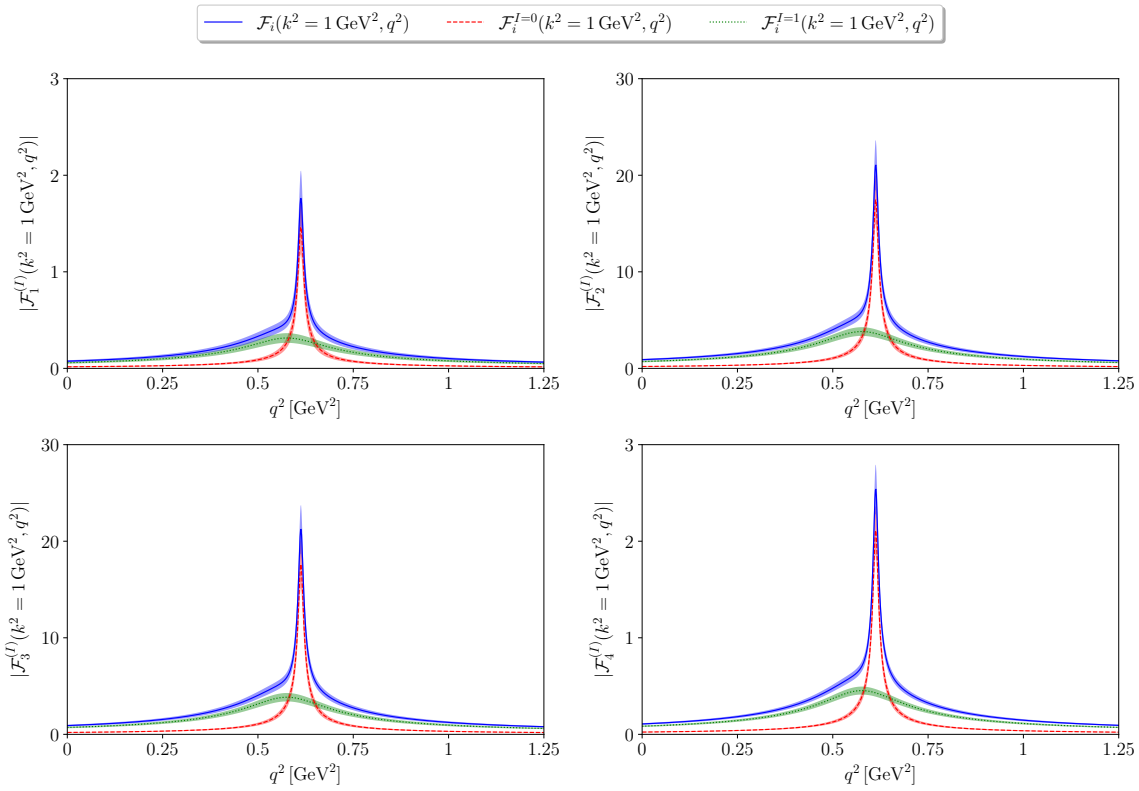

Figure 5.2: Two-dimensional plots of the absolute values of the form factors' isoscalar and isovector components as well as the sum of these for $k^2 = 1\,\mathrm{GeV}^2$ fixed in the range $q^2 \in [0, 1.25]\,\mathrm{GeV}^2$. Additionally shown are the uncertainties of the corresponding contributions.

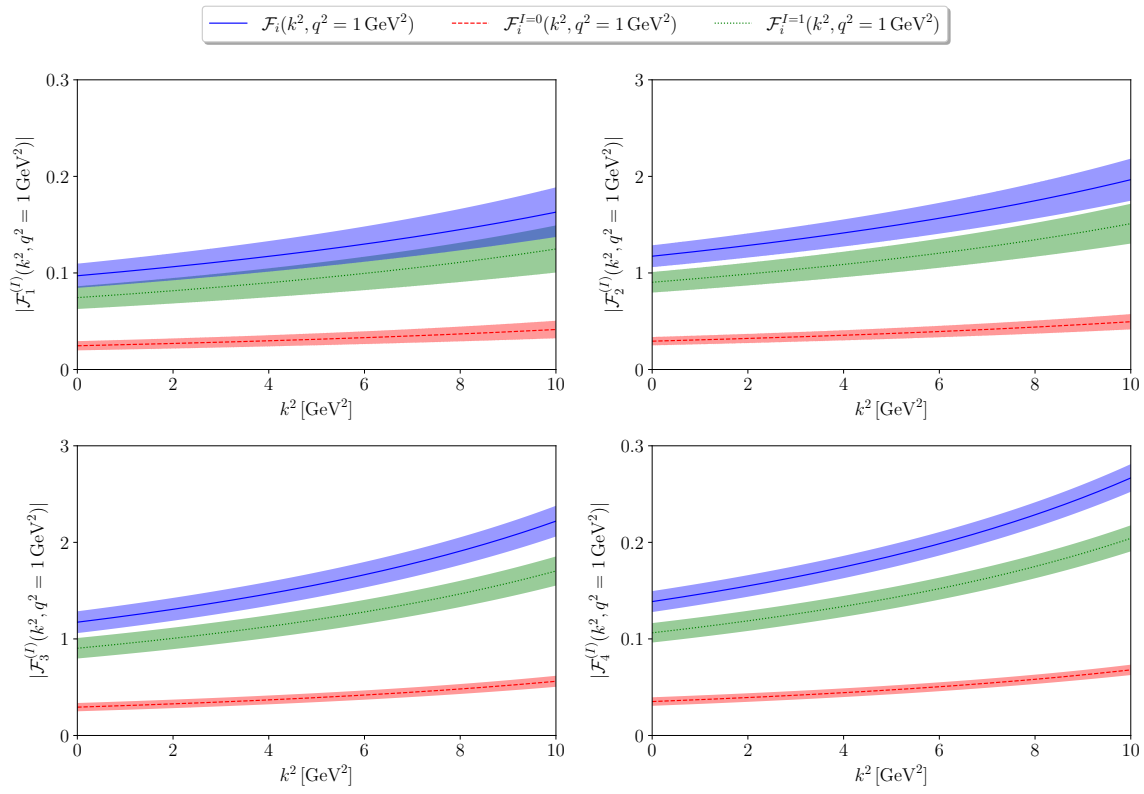

Figure 5.3: The same as Fig. 5.2 but with $q^2 = 1\,\mathrm{GeV}^2$ fixed and in the range $k^2 \in [0, 10]\,\mathrm{GeV}^2$.

Chapter 6

Phenomenology

The decay $B^- \to \ell^- \bar{\nu}_\ell \ell'^- \ell'^+$ provides a rich phenomenology through a large number of angular observables, which arise from the differential decay width $\mathrm{d}\Gamma \equiv \mathrm{d}\Gamma(B^- \to \ell^- \bar{\nu}_\ell \ell'^- \ell'^+)$,

$$\mathrm{d}\Gamma = \frac{1}{2m_B} |\overline{\mathcal{M}}|^2 \mathrm{d}\Phi_4(p; p_\ell, p_\nu, q_1, q_2). \tag{6.1}$$

Here, $|\overline{\mathcal{M}}|^2 \equiv |\overline{\mathcal{M}}(B^- \to \ell^- \bar{\nu}_\ell \ell'^- \ell'^+)|^2$ is given by Eq. (3.22) for $\ell' \neq \ell$ and Eq. (3.25) for $\ell' = \ell$; the LORENTZ-invariant four-body phase space is conveniently split according to [27]

$$\mathrm{d}\Phi_4(p; p_\ell, p_\nu, q_1, q_2) = \mathrm{d}\Phi_2(p; k, q)\, \mathrm{d}\Phi_2(k; p_\ell, p_\nu)\, \mathrm{d}\Phi_2(q; q_1, q_2)\, \frac{\mathrm{d}k^2}{2\pi}\, \frac{\mathrm{d}q^2}{2\pi}, \tag{6.2}$$

where $\mathrm{d}\Phi_2(p; k, q)$, $\mathrm{d}\Phi_2(k; p_\ell, p_\nu)$, and $\mathrm{d}\Phi_2(q; q_1, q_2)$ are the respective LORENTZ-invariant two-body phase spaces of the $\{\ell^- \bar{\nu}_\ell(k), \ell'^- \ell'^+(q)\}$, $\{\ell^-(p_\ell), \bar{\nu}_\ell(p_\nu)\}$, and $\{\ell'^-(q_1), \ell'^+(q_2)\}$ subsystems. The fivefold differential decay rate reads

$$\frac{\mathrm{d}^5\Gamma}{\mathrm{d}k^2\, \mathrm{d}q^2\, \mathrm{d}\cos\vartheta_W\, \mathrm{d}\cos\vartheta_\gamma\, \mathrm{d}\varphi} = \frac{|\boldsymbol{p}_\gamma||\boldsymbol{p}_\ell||\boldsymbol{p}_{\ell'}|}{4096 m_B^2 \pi^6 \sqrt{k^2}\sqrt{q^2}} |\overline{\mathcal{M}}|^2, \tag{6.3}$$

where ϑ_W and ϑ_γ are the polar angles of $\ell^-(p_\ell)$ and $\ell'^-(q_1)$ in the center-of-mass frames of $\{\ell^-(p_\ell), \bar{\nu}_\ell(p_\nu)\}$ and $\{\ell'^-(q_1), \ell'^+(q_2)\}$, respectively, and φ is the relative azimuthal angle between the planes of these two subsystems. Moreover, $|\boldsymbol{p}_\gamma|$, $|\boldsymbol{p}_\ell|$, and $|\boldsymbol{p}_{\ell'}|$ are the magnitudes of the three-momenta of the photon and the negatively charged leptons in the respective center-of-mass frame; further details on the kinematics and the four-body phase space are provided in App. D. For $\ell' \neq \ell$, the angular integrations can be performed analytically, leading to

$$\begin{aligned}\frac{\mathrm{d}^2\Gamma}{\mathrm{d}k^2\, \mathrm{d}q^2} = \mathcal{N}\Bigg[&\sum_{i=1}^{4} \frac{f_{i,i}}{m_B^2} |\mathcal{F}_i(k^2, q^2)|^2 + 2 \sum_{\substack{i=1 \\ j>i}}^{4} \frac{f_{i,j}}{m_B^2} \mathrm{Re}\left[\mathcal{F}_i(k^2, q^2) \mathcal{F}_j^*(k^2, q^2)\right] \\ &+ 2 f_B \sum_{i=1}^{4} \frac{f_{i,5}}{m_B} \mathrm{Re}\left[\mathcal{F}_i(k^2, q^2)\right] + f_{5,5} f_B^2 \Bigg], \quad \mathcal{N} = \frac{G_\mathrm{F}^2 |V_{ub}|^2 e^4 |\boldsymbol{p}_\gamma||\boldsymbol{p}_\ell||\boldsymbol{p}_{\ell'}|}{8192 m_B^2 \pi^6 \sqrt{k^2}\sqrt{q^{10}}},\end{aligned} \tag{6.4}$$

where the dependence of the functions $f_{i,j} \equiv f_{i,j}(k^2, q^2)$ on the lepton masses $m_{\ell^{(\prime)}}$ is suppressed; the resulting expressions for these functions are collected in App. F. The remaining integrations over k^2 and q^2 have to be performed numerically,

$$\Gamma = \int \mathrm{d}q^2 \int \mathrm{d}k^2 \, \frac{\mathrm{d}^2\Gamma}{\mathrm{d}k^2 \, \mathrm{d}q^2}, \tag{6.5}$$

where the available phase space is bounded by the region $k^2 \in [m_\ell^2, (m_B - \sqrt{q^2})^2]$ and $q^2 \in [4m_{\ell'}^2, (m_B - m_\ell)^2]$. Our results will be quoted for the branching ratio, $B = \Gamma \, \tau_B/\hbar$, where τ_B is the lifetime of the charged B meson.

Beyond the integrated decay rate, another observable of interest is the FB asymmetry, $A_{\mathrm{FB}} \equiv A_{\mathrm{FB}}(k^2, q^2)$, which is defined as

$$A_{\mathrm{FB}} = \left(\frac{\mathrm{d}^2\Gamma}{\mathrm{d}k^2 \, \mathrm{d}q^2}\right)^{-1} \int \mathrm{d}\cos\vartheta_W \, \mathrm{d}\cos\vartheta_\gamma \, \mathrm{d}\varphi \, \mathrm{sgn}[\cos\vartheta_W] \frac{\mathrm{d}^5\Gamma}{\mathrm{d}k^2 \, \mathrm{d}q^2 \, \mathrm{d}\cos\vartheta_W \, \mathrm{d}\cos\vartheta_\gamma \, \mathrm{d}\varphi} \tag{6.6}$$

and provides a complementary probe of the form factors. As for the decay width, the integration over the angles can be performed analytically for $\ell' \neq \ell$, resulting in

$$\begin{aligned} A_{\mathrm{FB}} = \left(\frac{\mathrm{d}^2\Gamma}{\mathrm{d}k^2 \, \mathrm{d}q^2}\right)^{-1} \mathcal{N} \Bigg[& \sum_{i=1}^{4} \frac{g_{i,i}}{m_B^2} |\mathcal{F}_i(k^2, q^2)|^2 + 2 \sum_{\substack{i=1 \\ j>i}}^{4} \frac{g_{i,j}}{m_B^2} \mathrm{Re}\left[\mathcal{F}_i(k^2, q^2) \mathcal{F}_j^*(k^2, q^2)\right] \\ & + 2 f_B \sum_{i=1}^{4} \frac{g_{i,5}}{m_B} \mathrm{Re}\left[\mathcal{F}_i(k^2, q^2)\right] + g_{5,5} f_B^2 \Bigg], \end{aligned} \tag{6.7}$$

where the functions $g_{i,j} \equiv g_{i,j}(k^2, q^2)$ also depend on the lepton masses $m_{\ell^{(\prime)}}$ and their explicit expressions are collected in App. F. Experimentally, it is convenient to access the integrated asymmetry

$$\langle A_{\mathrm{FB}} \rangle = \left\langle \frac{\mathrm{d}^2\Gamma}{\mathrm{d}k^2 \, \mathrm{d}q^2} \right\rangle^{-1} \int \mathrm{d}\cos\vartheta_W \, \mathrm{d}\cos\vartheta_\gamma \, \mathrm{d}\varphi \, \mathrm{sgn}[\cos\vartheta_W] \left\langle \frac{\mathrm{d}^5\Gamma}{\mathrm{d}k^2 \, \mathrm{d}q^2 \, \mathrm{d}\cos\vartheta_W \, \mathrm{d}\cos\vartheta_\gamma \, \mathrm{d}\varphi} \right\rangle, \tag{6.8}$$

where $\langle \cdots \rangle$ denotes the integration over a suitable bin in the variables k^2 and q^2.

We provide numerical results for both observables for the process $B^- \to \ell^- \bar{\nu}_\ell \ell'^- \ell'^+$, with $\ell \in \{e, \mu, \tau\}$ and $\ell' \in \{e, \mu\}$; see Table 6.1 for $\ell' \neq \ell$ and Table 6.2 for $\ell' = \ell$. Decays involving a $\tau^-\tau^+$ pair are not considered here, since the corresponding threshold is large compared to our asserted upper cutoff in the variable q^2. While parts of the decay with identical lepton flavors can, in principle, be treated in complete analogy to the case with distinct leptons—see the discussion at the end of Ch. 3—the interference term necessarily requires all integrations to be performed numerically because the variables $\widetilde{k}^2$ and $\widetilde{q}^2$ introduce an angular dependence in the form factors. Furthermore, an additional factor of 1/2 has to be taken into account for the decay with identical lepton flavors in order to avoid double counting in the phase-space integration. Our results are obtained

(i) after integrating over the full phase space in k^2 and q^2;

(ii) after integrating over the phase space with an upper cutoff at $q^2 = 1\,\mathrm{GeV}^2$;

	Upper cutoff	Branching ratio/10^{-8}	A_{FB}
$B^- \to e^-\bar{\nu}_e\mu^-\mu^+$	None	$3.19(43)_N(25)_{V_{ub}}$	$-0.358(31)_N$
	$q^2 = 1\,\mathrm{GeV}^2$	$3.13(42)_N(25)_{V_{ub}}$	$-0.361(32)_N$
$B^- \to \mu^-\bar{\nu}_\mu e^-e^+$	None	$3.78(47)_N(30)_{V_{ub}}$	$-0.398(38)_N$
	$q^2 = 1\,\mathrm{GeV}^2$	$3.72(46)_N(30)_{V_{ub}}$	$-0.401(38)_N$
$B^- \to \tau^-\bar{\nu}_\tau e^-e^+$	None	$2.75(27)_N(22)_{V_{ub}}$	$-0.500(18)_N$
	$q^2 = 1\,\mathrm{GeV}^2$	$2.72(27)_N(22)_{V_{ub}}$	$-0.502(18)_N$
$B^- \to \tau^-\bar{\nu}_\tau\mu^-\mu^+$	None	$1.77(23)_N(14)_{V_{ub}}$	$-0.458(15)_N$
	$q^2 = 1\,\mathrm{GeV}^2$	$1.75(23)_N(14)_{V_{ub}}$	$-0.460(15)_N$

Table 6.1: Numerical results for the branching ratio and FB asymmetry, see Eq. (6.5) and Eq. (6.8), for $B^- \to \ell^-\bar{\nu}_\ell\ell'^-\ell'^+$, $\ell' \neq \ell$, in the SM. The quoted uncertainties originate from the uncertainties on the normalizations $N^V_{i,j}$ and V_{ub}, respectively. Due to the absence of CP violation in the SM, the results for the CP-conjugated decay modes are identical. Within uncertainties, our predictions for the branching ratio of the process $B^- \to e^-\bar{\nu}_e\mu^-\mu^+$ agree well with Ref. [5], $B(B^- \to e^-\bar{\nu}_e\mu^-\mu^+) = (3.01\times10^{-8}, 2.96\times10^{-8})$, without and with an upper cutoff, respectively. For the process $B^- \to \mu^-\bar{\nu}_\mu e^-e^+$, however, our results are in strong tension with Ref. [5], $B(B^- \to \mu^-\bar{\nu}_\mu e^-e^+) = (6.38\times10^{-7}, 6.37\times10^{-7})$, which can be attributed to the unphysical collinear enhancement inferred therein;[a] see the discussion in Ch. 4. The results of Ref. [4], table 2, are—within their uncertainties—compatible with our results; note the numerically insignificant impact of the slight difference in the upper integration boundary used therein.

[a]The tension with our result for the electron channel is reduced but not removed entirely with the results quoted in the Erratum to Ref. [5].

and for $\ell' = \ell$, due to the indistinguishability of the two final-state fermions, additionally

(iii) with a cutoff at $\min\{q^2, \widetilde{q}^2\} = 1\,\mathrm{GeV}^2$, mimicking the LHCb measurement [28].[8]

Beyond the $q^2 = 1\,\mathrm{GeV}^2$ cutoff, the omission of the ϕ meson and further resonances introduces a hardly quantifiable model uncertainty, so that variant (ii) provides our principal results for $\ell \neq \ell'$; modeling the contributions beyond the cutoff seems possible in light of similar efforts in the case of $B \to \pi\pi$ form factors [29, 30] and is left for future work. For $\ell = \ell'$, the situation is more intricate: while a cutoff according to variant (ii) is inappropriate here for physical reasons, it is important to note that the cutoff implied by variant (iii) still entails the critical region through one of the variables. With the caveat that a more realistic comparison to the experiment inevitably requires the inclusion of the ϕ meson and, potentially, yet higher resonances, we thus designate variant (iii) to yield our principal results for $\ell = \ell'$.

[8]For the variant with the LHCb cutoff, the integrations of all terms—as opposed to the interference term only—have to be performed numerically since $\widetilde{q}^2$ and thus the cutoff depends on the angles.

	Upper cutoff	Branching ratio/10^{-8}	A_{FB}
$B^- \to e^-\bar{\nu}_e e^- e^+$	None	$3.43(43)_N(27)_{V_{ub}}$	$-0.410(41)_N$
	$q^2 = 1\,\mathrm{GeV}^2$	$3.31(42)_N(26)_{V_{ub}}$	$-0.416(42)_N$
	LHCb	$3.35(42)_N(27)_{V_{ub}}$	$-0.413(40)_N$
$B^- \to \mu^-\bar{\nu}_\mu \mu^- \mu^+$	None	$3.15(42)_N(25)_{V_{ub}}$	$-0.366(31)_N$
	$q^2 = 1\,\mathrm{GeV}^2$	$3.07(41)_N(24)_{V_{ub}}$	$-0.370(31)_N$
	LHCb	$3.08(42)_N(25)_{V_{ub}}$	$-0.372(32)_N$

Table 6.2: The same as Table 6.1 but for $\ell' = \ell$. Here, the interference term yields a negative correction to both observables at the level of 10% for the electron channel and 1% for the muon channel. This observation is in line with what was found in Ref. [18], with consistent numerical results for the branching ratio of the muon channel within uncertainties, $B(B^- \to \mu^-\bar{\nu}_\mu\mu^-\mu^+) = (2.82 \times 10^{-8}, 2.73 \times 10^{-8})$, without cutoff and with the LHCb cutoff, respectively. Our values are also compatible with Ref. [4]. Although our result for the muon channel is incompatible with the current experimental upper limit $B(B^- \to \mu^-\bar{\nu}_\mu\mu^-\mu^+) < 1.6 \times 10^{-8}$ determined by the LHCb collaboration [28], it is in far better agreement than the prediction cited therein, $B(B^- \to \mu^-\bar{\nu}_\mu\mu^-\mu^+) = 1.3 \times 10^{-7}$ [31].

In order to cross-check the results obtained with the functions $f_{i,j}$ and $g_{i,j}$ after performing the angular integrations analytically for $\ell' \neq \ell$, we further implemented a variant with the phase-space integration performed numerically over all variables also in this case, leading to results that are consistent with Table 6.1. Moreover, we performed a statistical error analysis for these decays, using 50 000 samples drawn from a multivariate normal distribution, to assess the relevance of subtleties such as the distinction between the mean and median or regarding the propagation of uncertainties. Doing so, we found results compatible with the analytic method, with a difference $\sim 1\%$ between mean and median being overshadowed by the uncertainty and a $\sim 1\%$ asymmetry between upper and lower uncertainties corresponding to approximately symmetrical errors. Naturally, both margins are expected to decrease further once increasing the sample size.

Besides the integrated observables, we additionally provide two-dimensional plots of the doubly-differential distributions of the decay width $\mathrm{d}^2\Gamma/(\mathrm{d}k^2\,\mathrm{d}q^2)$ and the angular FB asymmetry $A_{\mathrm{FB}}(k^2, q^2)$ for $\ell' \neq \ell$ in Fig. 6.1 and Fig. 6.2, respectively, with either $k^2 = 1\,\mathrm{GeV}^2$ or $q^2 = 1\,\mathrm{GeV}^2$ fixed.

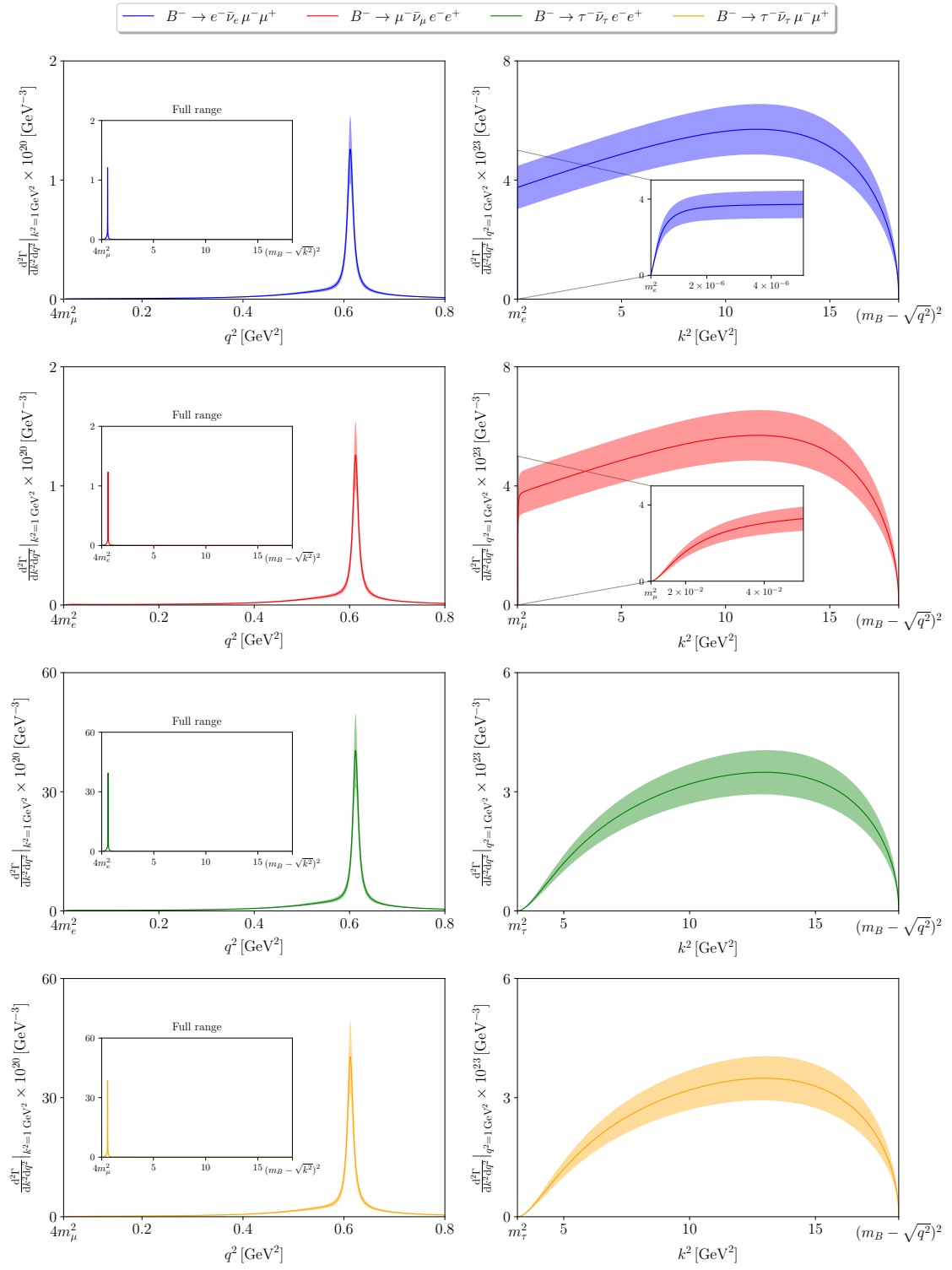

Figure 6.1: Two-dimensional plots of the doubly-differential decay width $\mathrm{d}^2\Gamma/(\mathrm{d}k^2\,\mathrm{d}q^2)$ for $\ell' \neq \ell$, with $k^2 = 1\,\mathrm{GeV}^2$ (*left*) and $q^2 = 1\,\mathrm{GeV}^2$ (*right*) fixed. In order to verify the—in some cases—numerically problematic limits, we performed analytic expansions of our formulae at the phase-space boundaries.

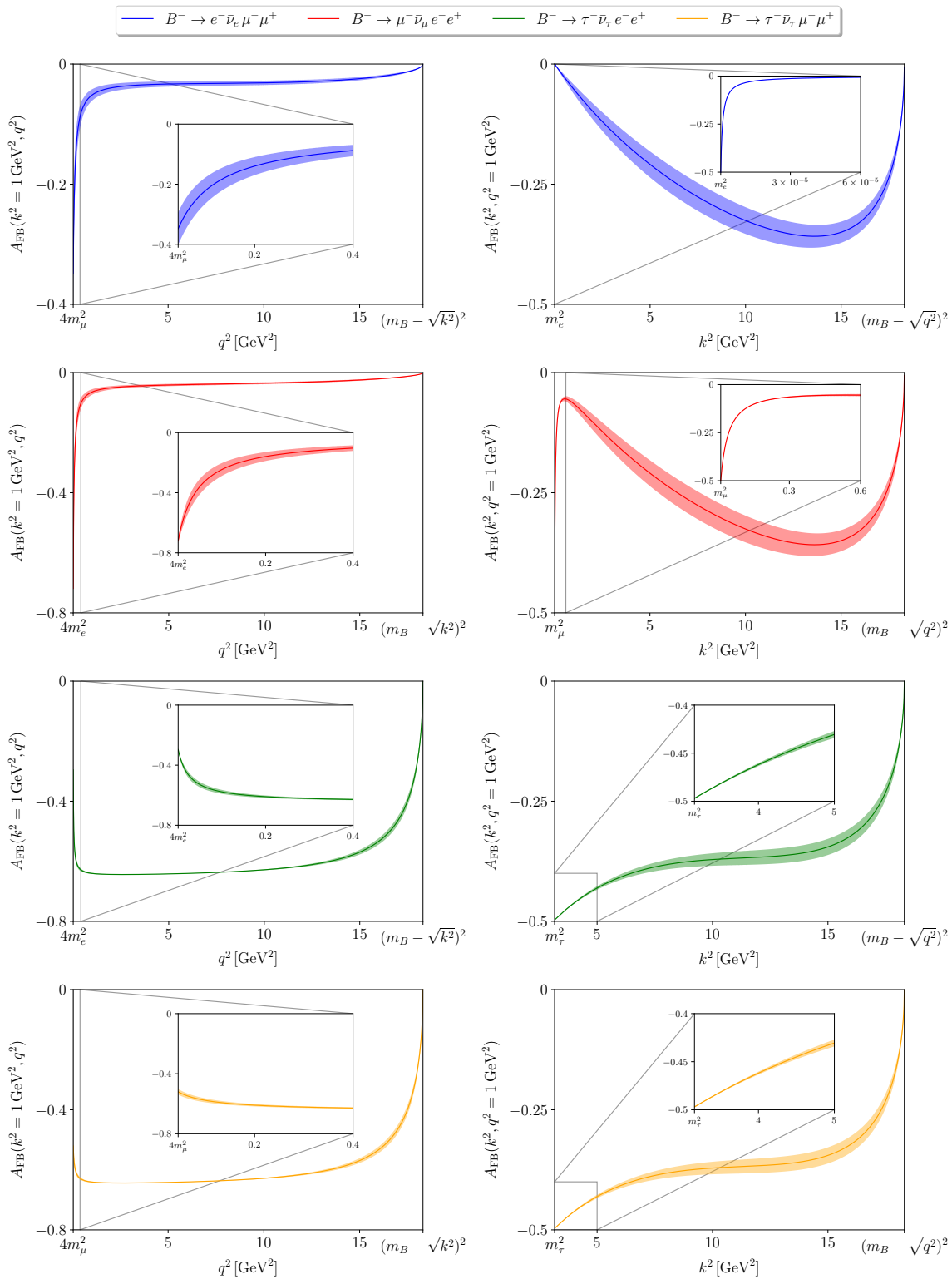

Figure 6.2: The same as Fig. 6.1 but for the doubly-differential FB asymmetry $A_{\rm FB}(k^2, q^2)$.

Chapter 7

Summary and outlook

In this part of the thesis, we used dispersive methods to study the $B \to \gamma^*$ form factors underlying the decay $B^- \to \ell^- \bar{\nu}_\ell \ell'^- \ell'^+$. We separated the full $B^- \to \ell^- \bar{\nu}_\ell \ell'^- \ell'^+$ amplitude into a non-perturbative hadronic tensor and a perturbative FSR piece and, in doing so, thoroughly investigated the properties of these individual objects. From our studies of these, we inferred that the separation leads to an ambiguity concerning the dispersive treatment; more specifically, it complicates the effort to find a decomposition of the hadronic tensor into LORENTZ structures and form factors that are free of kinematic singularities. As a remedy, we discussed in great detail how the hadronic tensor can be split into a homogeneous and an inhomogeneous part, with the homogeneous part being chosen such that it contains form factors with well-defined angular-momentum and parity quantum numbers. From these considerations, we proposed a decomposition of the homogeneous part into a set of LORENTZ structures and four form factors that are free of kinematic singularities in both the weak momentum and the photon momentum, thus rendering a dispersive treatment possible. For the parameterization of the inhomogeneous part, we considered several choices from the literature and investigated their effect on the full amplitude in great detail, in particular with regard to the singularity-free property of the form factors. Under a few reasonable assumptions, we were able to deduce that the inhomogeneous part ought to be of a very specific form, which allowed us to eliminate all choices from the literature but one for our analysis. Another major advancement of our analysis is the consistent treatment of non-zero lepton masses in the FSR piece at all stages.

Having found a decomposition of the hadronic tensor with form factors that are free of kinematic singularities, we split these into their isospin components and established a set of dispersion relations that relate the $B \to \gamma^*$ form factors to the well-known $B \to V$, $V = \omega, \rho$, analogs. The $B \to V$ form factors were expanded in a series in the conformal variable $z(t)$, with the dominant subthreshold poles taken into account via a plain pole factor. Performing a similar series expansion for the $B \to \gamma^*$ form factors and using a VMD ansatz for the virtual photon, we provided a parameterization of these form factors in the region below the onset of the ϕ meson.

Using our framework, we carried out a phenomenological analysis by means of the branching ratio and the integrated FB asymmetry of the decay $B^- \to \ell^- \bar{\nu}_\ell \ell'^- \ell'^+$, with $\ell = e, \mu, \tau$ and $\ell' = e, \mu$, and, for $\ell' \neq \ell$, the doubly-differential distributions of the decay width and FB asymmetry. The numerical results obtained for the branching ratio and

FB asymmetry agree with recent determinations from the literature to a large extent but exceed the current experimental upper limits for $\ell' = \ell$, albeit showing less tension than earlier theoretical estimates.

Possible future improvements of our framework involve the inclusion of the contribution from the ϕ meson and the replacement of the resonant ρ by a description of the two-pion intermediate state, in which the ρ can be included model-independently through pion–pion rescattering [32]. The $B \to \gamma^*$ form factors are then obtained via a dispersion relation in a similar way to the reconstruction of, *e.g.*, the $\eta^{(\prime)}$ TFFs from $\pi\pi$ intermediate states [33, 34].

Appendix A

Tensor identities[9]

In this appendix, we derive the identities for the hadronic tensor $T_{\mathrm{H}}^{\mu\nu}(k,q)$ and the pseudoscalar tensor $T_{\mathrm{P}}^{\mu}(k,q)$ given in Eq. (3.13), Eq. (3.15), and Eq. (3.17), where we further argue that the Levi-Civita tensor cannot be present in the inhomogeneous part of the hadronic tensor, Eq. (4.2). Moreover, we elaborate on the arguments that lead to the constrained form of the inhomogeneity in Eq. (4.6).

A.1 Hadronic tensor

The identity for the hadronic tensor stated in Eq. (3.13) can be derived in two instructive ways. For both variants, we start from Eq. (3.5) and perform an integration by parts, assuming that the surface term can be dropped, leading to

$$\begin{aligned} q_\mu[Q_B T_{\mathrm{H}}^{\mu\nu}(k,q)] &= -\mathrm{i}\int \mathrm{d}^4x\,[\partial_\mu \mathrm{e}^{\mathrm{i}qx}]\,\langle 0|\mathrm{T}\{J_{\mathrm{EM}}^{\mu}(x)J_{\mathrm{H}}^{\nu}(0)\}|B^-\rangle \\ &= \mathrm{i}\int \mathrm{d}^4x\,\mathrm{e}^{\mathrm{i}qx}\partial_\mu\,\langle 0|\mathrm{T}\{J_{\mathrm{EM}}^{\mu}(x)J_{\mathrm{H}}^{\nu}(0)\}|B^-\rangle\,. \end{aligned} \tag{A.1}$$

Inserting the definition of the time-ordered product and using that the EM current is conserved, $\partial_\mu J_{\mathrm{EM}}^{\mu}(x)=0$, we find

$$\begin{aligned} q_\mu[Q_B T_{\mathrm{H}}^{\mu\nu}(k,q)] &= \mathrm{i}\int \mathrm{d}^4x\,\mathrm{e}^{\mathrm{i}qx}\,\langle 0|\delta(x^0)[J_{\mathrm{EM}}^{0}(x),J_{\mathrm{H}}^{\nu}(0)]|B^-\rangle \\ &= \mathrm{i}\int \mathrm{d}^3x\,\mathrm{e}^{-\mathrm{i}\boldsymbol{q}\cdot\boldsymbol{x}}\,\langle 0|[J_{\mathrm{EM}}^{0}(\bar{x}),J_{\mathrm{H}}^{\nu}(0)]|B^-\rangle\,, \end{aligned} \tag{A.2}$$

where $\bar{x}=(x^0=0,\boldsymbol{x})^\intercal$. For the first variant of the derivation, we then apply an appropriate Lorentz transformation and write $q=(\sqrt{q^2},0)$, so that

$$q_\mu[Q_B T_{\mathrm{H}}^{\mu\nu}(k,q)] = \mathrm{i}\,\langle 0|[\hat{Q}_{\mathrm{EM}},J_{\mathrm{H}}^{\nu}(0)]|B^-\rangle\,, \tag{A.3}$$

where the charge $\hat{Q}_{\mathrm{EM}}=\int \mathrm{d}^3x\,J_{\mathrm{EM}}^{0}(\bar{x})$ associated with the conserved EM current acts as the generator of the global $\mathrm{U}(1)_{\mathrm{EM}}$ symmetry. Under this symmetry, $q_f(x)\to \mathrm{e}^{-\mathrm{i}Q_f}q_f(x)$,

[9] Some of the commutation relations and formulae for the time-ordered product of two currents implicitly utilized in this appendix are derived for generic expressions in the Foundations part of the thesis.

where the quark field $q_f(x) \in \{u(x), b(x)\}$ holds the $\mathrm{U}(1)_{\mathrm{EM}}$ charge $Q_u = 2/3$, $Q_b = -1/3$, with the hadronic weak current $J^\nu_{\mathrm{H}}(x) = \bar{u}(x)\gamma^\nu(1-\gamma_5)b(x)$ transforming according to

$$J^\nu_{\mathrm{H}}(0) \to J^\nu_{\mathrm{H}}(0)' = \mathrm{e}^{-\mathrm{i}(Q_b - Q_u)} J^\nu_{\mathrm{H}}(0). \tag{A.4}$$

Infinitesimally, this corresponds to the variation

$$\delta J^\nu_{\mathrm{H}}(0) = -\mathrm{i}(Q_b - Q_u) J^\nu_{\mathrm{H}}(0), \tag{A.5}$$

and thus, by Noether's theorem,

$$q_\mu [Q_B T^{\mu\nu}_{\mathrm{H}}(k,q)] = -\mathrm{i}(Q_b - Q_u) \langle 0 | J^\nu_{\mathrm{H}}(0) | B^- \rangle \,. \tag{A.6}$$

Inserting the definition of the hadronic weak current and using $\langle 0|\bar{u}(0)\gamma^\nu b(0)|B^-\rangle = 0$, which holds due to the pseudoscalar nature of the B meson, as well as the defining relation of the B-meson decay constant, $\langle 0|\bar{u}(0)\gamma^\nu\gamma_5 b(0)|B^-\rangle = \mathrm{i} f_B p^\nu$, we finally arrive at

$$q_\mu [Q_B T^{\mu\nu}_{\mathrm{H}}(k,q)] = -Q_B f_B p^\nu, \tag{A.7}$$

where $Q_B = Q_b - Q_u$. An interesting by-product from the last step is the observation that the inhomogeneity of the hadronic tensor is entirely due to its axial-vector part. In other words, the vector part of the hadronic tensor is completely homogeneous, so that the Levi-Civita tensor indeed cannot be part of the inhomogeneity.

Since the Lorentz transformation performed in the above calculation is somewhat problematic—in particular in view of the photon's massless nature—we additionally give a derivation that starts from Eq. (A.2) and spares such an intermediate step. To this end, we explicitly calculate the commutator

$$\begin{aligned}
[J^0_{\mathrm{EM}}(\bar{x}), J^\nu_{\mathrm{H}}(0)] &= \Big[\sum_f Q_f q_f^\dagger(\bar{x}) q_f(\bar{x}) + \sum_\ell Q_\ell \ell^\dagger(\bar{x}) \ell(\bar{x}), u^\dagger(0)\gamma^0\gamma^\nu(1-\gamma_5)b(0) \Big] \\
&= \delta^{(3)}(\bar{x}) \big(Q_u u^\dagger(\bar{x})\gamma^0\gamma^\nu(1-\gamma_5)b(0) - Q_b u^\dagger(0)\gamma^0\gamma^\nu(1-\gamma_5)b(\bar{x}) \big),
\end{aligned} \tag{A.8}$$

where we inserted the definition of the hadronic weak current and the EM current $J^\mu_{\mathrm{EM}}(x) = \bar{q}(x)\mathcal{Q}\gamma^\mu q(x) + \sum_\ell Q_\ell \bar{\ell}(x)\gamma^\mu \ell(x)$ as well as the canonical equal-time anticommutation relations for fermionic fields. Hence, Eq. (A.2) yields

$$q_\mu [Q_B T^{\mu\nu}_{\mathrm{H}}(k,q)] = -\mathrm{i}(Q_b - Q_u) \langle 0 | J^\nu_{\mathrm{H}}(0) | B^- \rangle \,, \tag{A.9}$$

which is equivalent to Eq. (A.6), so that following the remaining steps of the first derivation again results in Eq. (A.7).

In order to prove Eq. (3.15), we start by using translational invariance of the vacuum to rewrite the hadronic tensor, Eq. (3.5), as

$$\begin{aligned}
Q_B T^{\mu\nu}_{\mathrm{H}}(k,q) &= \int \mathrm{d}^4x \, \mathrm{e}^{-\mathrm{i}x(p-q)} \langle 0 | \mathrm{T}\{ J^\mu_{\mathrm{EM}}(0) J^\nu_{\mathrm{H}}(-x) \} | B^- \rangle \\
&= \int \mathrm{d}^4x \, \mathrm{e}^{\mathrm{i}kx} \langle 0 | \mathrm{T}\{ J^\nu_{\mathrm{H}}(x) J^\mu_{\mathrm{EM}}(0) \} | B^- \rangle \,,
\end{aligned} \tag{A.10}$$

where we transformed $x \to -x$ in the integral and used that $k = p - q$. By means of an integration by parts and a differentiation of the HEAVISIDE step function in the time-ordered product, we then find, similar to Eq. (A.2),

$$k_\nu[Q_B T_{\mathrm{H}}^{\mu\nu}(k,q)] = \mathrm{i}\int \mathrm{d}^4x\, \mathrm{e}^{\mathrm{i}kx}\, \langle 0|\mathrm{T}\{\partial_\nu J_{\mathrm{H}}^{\nu}(x) J_{\mathrm{EM}}^{\mu}(0)\}|B^-\rangle + \mathrm{i}\int \mathrm{d}^3x\, \mathrm{e}^{-\mathrm{i}\boldsymbol{k}\boldsymbol{x}}\, \langle 0|[J_{\mathrm{H}}^{0}(\bar{x}), J_{\mathrm{EM}}^{\mu}(0)]|B^-\rangle\,. \tag{A.11}$$

Here, the DIRAC equation implies

$$\partial_\nu J_{\mathrm{H}}^{\nu}(x) = \mathrm{i}(m_u - m_b) J_{\mathrm{S}}(x) - \mathrm{i}(m_u + m_b) J_{\mathrm{P}}(x), \tag{A.12}$$

with the scalar weak current $J_{\mathrm{S}}(x) = \bar{u}(x)b(x)$ and the pseudoscalar weak current $J_{\mathrm{P}}(x) = \bar{u}(x)\gamma_5 b(x)$, so that

$$k_\nu[Q_B T_{\mathrm{H}}^{\mu\nu}(k,q)] = (m_b + m_u)\int \mathrm{d}^4x\, \mathrm{e}^{\mathrm{i}kx}\, \langle 0|\mathrm{T}\{J_{\mathrm{P}}(x) J_{\mathrm{EM}}^{\mu}(0)\}|B^-\rangle + \mathrm{i}\int \mathrm{d}^3x\, \mathrm{e}^{-\mathrm{i}\boldsymbol{k}\cdot\boldsymbol{x}}\, \langle 0|[J_{\mathrm{H}}^{0}(\bar{x}), J_{\mathrm{EM}}^{\mu}(0)]|B^-\rangle\,, \tag{A.13}$$

where we used that a scalar–vector current–current matrix element for the transition B-meson to vacuum vanishes due to conservation of angular momentum and parity, $\langle 0|\mathrm{T}\{J_{\mathrm{S}}(x) J_{\mathrm{EM}}^{\mu}(0)\}|B^-\rangle = 0$. Using translational invariance of the vacuum once more, we thus obtain

$$k_\nu[Q_B T_{\mathrm{H}}^{\mu\nu}(k,q)] = Q_B T_{\mathrm{P}}^{\mu}(k,q) + \mathrm{i}\int \mathrm{d}^3x\, \mathrm{e}^{-\mathrm{i}\boldsymbol{k}\cdot\boldsymbol{x}}\, \langle 0|[J_{\mathrm{H}}^{0}(\bar{x}), J_{\mathrm{EM}}^{\mu}(0)]|B^-\rangle\,, \tag{A.14}$$

with the pseudoscalar tensor

$$Q_B T_{\mathrm{P}}^{\mu}(k,q) = (m_b + m_u)\int \mathrm{d}^4x\, \mathrm{e}^{\mathrm{i}qx}\, \langle 0|\mathrm{T}\{J_{\mathrm{EM}}^{\mu}(x) J_{\mathrm{P}}(0)\}|B^-\rangle\,. \tag{A.15}$$

From an explicit calculation of the commutator in the second term of Eq. (A.14),

$$\begin{aligned}[J_{\mathrm{H}}^{0}(\bar{x}), J_{\mathrm{EM}}^{\mu}(0)] &= \Big[u^\dagger(\bar{x})(1-\gamma_5)b(\bar{x}), \sum_f Q_f q_f^\dagger(0)\gamma^0\gamma^\mu q_f(0) + \sum_\ell Q_\ell \ell^\dagger(0)\gamma^0\gamma^\mu \ell(0)\Big] \\ &= \delta^{(3)}(\bar{x})\big(Q_b u^\dagger(\bar{x})\gamma^0\gamma^\mu(1-\gamma_5)b(0) - Q_u u^\dagger(0)\gamma^0\gamma^\mu(1-\gamma_5)b(\bar{x})\big),\end{aligned} \tag{A.16}$$

similar to Eq. (A.8), we finally arrive at

$$k_\nu[Q_B T_{\mathrm{H}}^{\mu\nu}(k,q)] = Q_B T_{\mathrm{P}}^{\mu}(k,q) + Q_B f_B (k+q)^\mu, \tag{A.17}$$

which is equivalent to Eq. (3.15) after inserting the decomposition of the hadronic tensor into its homogeneous and inhomogeneous parts, $T_{\mathrm{H}}^{\mu\nu}(k,q) = T_{\mathrm{H,hom.}}^{\mu\nu}(k,q) + T_{\mathrm{H,inhom.}}^{\mu\nu}(k,q)$.

A.2 Pseudoscalar tensor

For the derivation of Eq. (3.17), we proceed in analogy to the previous section and use the definition of the pseudoscalar tensor, Eq. (3.16), to calculate

$$\begin{aligned} q_\mu[Q_B T_{\mathrm{P}}^\mu(k,q)] &= \mathrm{i}(m_b+m_u)\int \mathrm{d}^4x\, \mathrm{e}^{\mathrm{i}qx}\partial_\mu \langle 0|\mathrm{T}\{J^\mu_{\mathrm{EM}}(x)J_{\mathrm{P}}(0)\}|B^-\rangle \\ &= \mathrm{i}(m_b+m_u)\int \mathrm{d}^3x\, \mathrm{e}^{-\mathrm{i}\boldsymbol{q}\cdot\boldsymbol{x}}\, \langle 0|[J^0_{\mathrm{EM}}(\bar{x}), J_{\mathrm{P}}(0)]|B^-\rangle\,. \end{aligned} \tag{A.18}$$

An explicit calculation of the commutator, similar to Eq. (A.8),

$$\begin{aligned} [J^0_{\mathrm{EM}}(\bar{x}), J_{\mathrm{P}}(0)] &= \Big[\sum_f Q_f q_f^\dagger(\bar{x})q_f(\bar{x}) + \sum_\ell Q_\ell \ell^\dagger(\bar{x})\ell(\bar{x}), u^\dagger(0)\gamma^0\gamma_5 b(0)\Big] \\ &= \delta^{(3)}(\bar{x})\big(Q_u u^\dagger(\bar{x})\gamma^0\gamma_5 b(0) - Q_b u^\dagger(0)\gamma^0\gamma_5 b(\bar{x})\big), \end{aligned} \tag{A.19}$$

results in

$$q_\mu[Q_B T_{\mathrm{P}}^\mu(k,q)] = -\mathrm{i}(m_b+m_u)(Q_b-Q_u)\,\langle 0|J_{\mathrm{P}}(0)|B^-\rangle\,. \tag{A.20}$$

In order to calculate $\langle 0|J_{\mathrm{P}}(0)|B^-\rangle = \langle 0|\bar{u}(0)\gamma_5 b(0)|B^-\rangle$, we observe that, due to translation invariance of the vacuum,

$$\mathrm{i}f_B p^\nu = \langle 0|\bar{u}(0)\gamma^\nu\gamma_5 b(0)|B^-\rangle = \langle 0|\bar{u}(x)\gamma^\nu\gamma_5 b(x)|B^-\rangle\,\mathrm{e}^{\mathrm{i}xp}, \tag{A.21}$$

and differentiating both sides of the equation gives

$$\begin{aligned} 0 &= \langle 0|\bar{u}(x)\overleftrightarrow{\not\partial}\gamma_5 b(x)|B^-\rangle\,\mathrm{e}^{\mathrm{i}xp} + \mathrm{i}p_\nu\,\langle 0|\bar{u}(x)\gamma^\nu\gamma_5 b(x)|B^-\rangle\,\mathrm{e}^{\mathrm{i}xp} \\ &= \mathrm{i}(m_b+m_u)\,\langle 0|\bar{u}(x)\gamma_5 b(x)|B^-\rangle\,\mathrm{e}^{\mathrm{i}xp} - f_B m_B^2, \end{aligned} \tag{A.22}$$

where we used the Dirac equation and $p^2 = m_B^2$. Then, again by translational invariance of the vacuum, we obtain

$$\langle 0|\bar{u}(0)\gamma_5 b(0)|B^-\rangle = -\mathrm{i}f_B\frac{m_B^2}{m_b+m_u}, \tag{A.23}$$

so that Eq. (A.20) finally becomes

$$q_\mu[Q_B T_{\mathrm{P}}^\mu(k,q)] = -Q_B f_B m_B^2. \tag{A.24}$$

A.3 Constrained form of the inhomogeneity

The inhomogeneity in the constrained form stated in Eq. (4.6) was based on the three assumptions that

(i) there exists a unique choice for the coefficients in Eq. (4.2) that leaves the form factors free of kinematic singularities;

(ii) the apparent kinematic poles in $T^{\mu\nu}_{\mathrm{H,inhom.}}(k,q)$ cancel and no new such poles are introduced;

(iii) a dynamic B-meson pole appears at most in the pseudoscalar form factor $\mathcal{F}_3(k^2, q^2)$.

In the following, we analyze the consequences of (i)–(iii) in more detail and outline how Eq. (4.6) follows from these assumptions. We start by examining (ii) with the additional constraint that the coefficients of the generic inhomogeneity

$$T^{\mu\nu}_{\text{H,inhom.}}(k,q) = -f_B\left[ag^{\mu\nu} + b\frac{k^\mu k^\nu}{k\cdot q} + c\frac{k^\mu q^\nu}{k\cdot q} + (1-b)\frac{q^\mu k^\nu}{q^2} + (1-a-c)\frac{q^\mu q^\nu}{q^2}\right], \quad \text{(A.25)}$$

see Eq. (4.2), cancel the trivial poles but do not show an explicit dependence on q^2 (and, for a, also on k^2) beyond that, *i.e.*,

$$a = \hat{a}, \qquad b = (k\cdot q)\hat{b}, \qquad c = (k\cdot q)\hat{c}, \quad \text{(A.26)}$$

with some reduced coefficients $\hat{a}$, $\hat{b} \equiv \hat{b}(k^2)$, and $\hat{c} \equiv \hat{c}(k^2)$; that this is indeed a necessary condition to also fulfill (i) and (iii) will be shown subsequently.[10] For the residual poles in $T^{\mu\nu}_{\text{H,inhom.}}(k,q)$ to be cancelled, we thus need

$$\begin{aligned}(1-b) &= 1 - \frac{\hat{b}}{2}(m_B^2 - k^2 - q^2) \overset{!}{\propto} q^2,\\ (1-a-c) &= 1 - \hat{a} - \frac{\hat{c}}{2}(m_B^2 - k^2 - q^2) \overset{!}{\propto} q^2,\end{aligned} \quad \text{(A.27)}$$

which implies[11]

$$\hat{b} = \frac{2}{2(k\cdot q) + q^2}, \qquad \hat{c} = \frac{2(1-\hat{a})}{2(k\cdot q) + q^2}. \quad \text{(A.28)}$$

Inserting this into the generic form of the inhomogeneity leads to Eq. (4.6),

$$T^{\mu\nu}_{\text{H,inhom.}}(k,q) = -f_B\left[\hat{a}g^{\mu\nu} + \frac{(2k^\mu + q^\mu)k^\nu + (1-\hat{a})(2k^\mu + q^\mu)q^\nu}{2(k\cdot q) + q^2}\right]. \quad \text{(A.29)}$$

In order to show that (i) and (iii) require $\hat{a}$ to have no dependence on k^2 or q^2 and $\hat{b}$ as well as $\hat{c}$ to have no dependence on q^2, we consider the family of vectors

$$\begin{aligned}\mathcal{S}[\hat{a}_n, \hat{b}_n, \hat{c}_n] = \Bigg(&\frac{1}{m_B}\left[(k\cdot q)g^{\mu\nu} - k^\mu q^\nu\right], \frac{1}{m_B}\left[\frac{q^2}{k^2}k^\mu k^\nu - \frac{k\cdot q}{k^2}q^\mu k^\nu + q^\mu q^\nu - q^2 g^{\mu\nu}\right],\\ &\frac{1}{m_B}\left[\frac{k\cdot q}{k^2}q^\mu k^\nu - \frac{q^2}{k^2}k^\mu k^\nu\right], \frac{\mathrm{i}}{m_B}\epsilon^{\mu\nu\rho\sigma}k_\rho q_\sigma, m_B\Bigg[\hat{a}_n g^{\mu\nu} + \hat{b}_n k^\mu k^\nu + \hat{c}_n k^\mu q^\nu\\ &+ [1 - (k\cdot q)\hat{b}_n]\frac{q^\mu k^\nu}{q^2} + [1 - \hat{a}_n - (k\cdot q)\hat{c}_n]\frac{q^\mu q^\nu}{q^2}\Bigg]\Bigg)^\intercal, \end{aligned} \quad \text{(A.30)}$$

composed of the homogeneous and inhomogeneous basis structures, Eq. (4.1) and Eq. (4.2), with the trivial $(k\cdot q)$ poles of the latter cancelled according to (ii). The corresponding vector with the form-factor basis is given by

$$\mathcal{G}[\hat{a}_n, \hat{b}_n, \hat{c}_n] = \left(\mathcal{F}_1^n(k^2,q^2), \mathcal{F}_2^n(k^2,q^2), \mathcal{F}_3^n(k^2,q^2), \mathcal{F}_4^n(k^2,q^2), -f_B/m_B\right)^\intercal, \quad \text{(A.31)}$$

[10] The independence of $\hat{a}$ on k^2 is not needed to deduce Eq. (A.28) but still follows from our assumptions.
[11] Note that $[2(k\cdot q) + q^2] = (m_B^2 - k^2)$ is not considered an explicit dependence on q^2.

i.e., $T_{\mathrm{H}}^{\mu\nu}(k,q) = \mathcal{S}[\hat{a}_n,\hat{b}_n,\hat{c}_n]\cdot\mathcal{G}[\hat{a}_n,\hat{b}_n,\hat{c}_n]$. Let $(\hat{a}_f,\hat{b}_f,\hat{c}_f)$ be the unique choice of reduced coefficients that yields form factors free of kinematic singularities and with a dynamic B-meson pole at most in $\mathcal{F}_3^f(k^2,q^2)$, in line with our assumptions (i)–(iii). We then consider the transformation to a basis arising from a different choice $(\hat{a}_s,\hat{b}_s,\hat{c}_s)\neq(\hat{a}_f,\hat{b}_f,\hat{c}_f)$,

$$\mathcal{S}[\hat{a}_s,\hat{b}_s,\hat{c}_s] = M\mathcal{S}[\hat{a}_f,\hat{b}_f,\hat{c}_f], \qquad M = \begin{pmatrix} 1 & 0 & 0 & 0 & 0\\ 0 & 1 & 0 & 0 & 0\\ 0 & 0 & 1 & 0 & 0\\ 0 & 0 & 0 & 1 & 0\\ M_{51} & M_{52} & M_{53} & 0 & 1 \end{pmatrix}, \tag{A.32}$$

where

$$\begin{aligned} M_{51} &= m_B^2(\hat{c}_f-\hat{c}_s), \qquad M_{52} = m_B^2\frac{(\hat{a}_f-\hat{a}_s)+(\hat{c}_f-\hat{c}_s)(k\cdot q)}{q^2},\\ M_{53} &= m_B^2\frac{(\hat{a}_f-\hat{a}_s)+(\hat{b}_f-\hat{b}_s)k^2+(\hat{c}_f-\hat{c}_s)(k\cdot q)}{q^2}, \end{aligned} \tag{A.33}$$

with the form factors accordingly being subject to the transformation

$$\begin{aligned} \mathcal{G}[\hat{a}_s,\hat{b}_s,\hat{c}_s] &= (M^{\intercal})^{-1}\mathcal{G}[\hat{a}_f,\hat{b}_f,\hat{c}_f] \\ &= \Big(\mathcal{F}_1^s(k^2,q^2),\mathcal{F}_2^s(k^2,q^2),\mathcal{F}_3^s(k^2,q^2),\mathcal{F}_4^s(k^2,q^2),-f_B/m_B\Big)^{\intercal}\\ &= \Big(\mathcal{F}_1^f(k^2,q^2)+m_Bf_B(\hat{c}_f-\hat{c}_s),\mathcal{F}_2^f(k^2,q^2)-m_Bf_B\frac{\hat{c}_f-\hat{c}_s}{2}+m_Bf_B\\ &\quad\times\frac{2(\hat{a}_f-\hat{a}_s)+(\hat{c}_f-\hat{c}_s)(m_B^2-k^2)}{2q^2},\mathcal{F}_3^f(k^2,q^2)-m_Bf_B\frac{\hat{c}_f-\hat{c}_s}{2}+m_Bf_B\\ &\quad\times\frac{2(\hat{a}_f-\hat{a}_s)+2(\hat{b}_f-\hat{b}_s)k^2+(\hat{c}_f-\hat{c}_s)(m_B^2-k^2)}{2q^2},\mathcal{F}_4^f(k^2,q^2),-f_B/m_B\Big)^{\intercal}. \end{aligned} \tag{A.34}$$

In contradiction to the assumed uniqueness of $(\hat{a}_f,\hat{b}_f,\hat{c}_f)$, the form factor basis $\mathcal{G}[\hat{a}_s,\hat{b}_s,\hat{c}_s]$ could be rendered free of kinematic singularities and with a dynamic B-meson pole at most in the pseudoscalar form factor if either of the coefficients $\hat{a}$, $\hat{b}$, or $\hat{c}$ were allowed to depend on q^2, *e.g.*, by choosing $\hat{a}_f=\hat{a}_s$, $\hat{b}_f=q^2=2\hat{b}_s$, $\hat{c}_f=q^2=2\hat{c}_s$. We thus infer that all of the reduced coefficients ought to be independent of q^2, for otherwise, an infinite tower of valid bases would emerge. Even then, choosing the reduced coefficients such that $\hat{b}_f=\hat{b}_s$ and

$$\hat{c}_f-\hat{c}_s = \frac{2(\hat{a}_s-\hat{a}_f)}{m_B^2-k^2} \tag{A.35}$$

leads to $\mathcal{F}_2^s(k^2,q^2)$ and $\mathcal{F}_3^s(k^2,q^2)$ being free of kinematic singularities; for a basis consistent with (iii), however, we would need $(\hat{a}_s-\hat{a}_f)\propto(m_B^2-k^2)$ to cancel the dynamic B-meson poles arising in $\mathcal{F}_1^s(k^2,q^2)$ and $\mathcal{F}_2^s(k^2,q^2)$. Consequently, to ensure uniqueness, we require $\hat{a}$ to also be independent of k^2, making it a constant parameter.

Appendix B

Bardeen–Tung–Tarrach decomposition

In this appendix, we outline the modification to the BTT procedure [10, 11] that leads to the decomposition of the homogeneous part of the hadronic tensor into the Lorentz structures and form factors given in Eq. (4.1). To this end, we recall that the homogeneous part fulfills

$$q_\mu T^{\mu\nu}_{\mathrm{H,hom.}}(k,q) = 0 \tag{B.1}$$

and that we additionally impose

$$k_\nu T^{\mu\nu}_{\mathrm{H,hom.}}(k,q) \stackrel{!}{=} T^{\mu}_{\mathrm{P,hom.}}(k,q), \tag{B.2}$$

see Eq. (3.14) and Eq. (3.19), with $q_\mu T^{\mu}_{\mathrm{P,hom.}}(k,q) = 0$. Hence, we can split $T^{\mu\nu}_{\mathrm{H,hom.}}(k,q)$ according to

$$T^{\mu\nu}_{\mathrm{H,hom.}}(k,q) = \widetilde{T}^{\mu\nu}_{\mathrm{H,hom.}}(k,q) + T^{\mu}_{\mathrm{P,hom.}}(k,q)\frac{k^\nu}{k^2}, \tag{B.3}$$

where $q_\mu \widetilde{T}^{\mu\nu}_{\mathrm{H,hom.}}(k,q) = 0 = k_\nu \widetilde{T}^{\mu\nu}_{\mathrm{H,hom.}}(k,q)$. In the above, $T^{\mu}_{\mathrm{P,hom.}}(k,q)$ enters with a factor k^ν/k^2 due to its pseudoscalar nature; *cf.* the fact that the spin-0 component of a spin-1 field is of time-like polarization. Since the explicit k^2-pole attached to $T^{\mu}_{\mathrm{P,hom.}}(k,q)$ is thus an inherent feature of the pseudoscalar contribution, it needs to be regularized either by a zero in the accompanying form factor or by a corresponding pole contribution within $\widetilde{T}^{\mu\nu}_{\mathrm{H,hom.}}(k,q)$. We follow the second approach and perform the BTT procedure for $T^{\mu}_{\mathrm{P,hom.}}(k,q)$ and $\widetilde{T}^{\mu\nu}_{\mathrm{H,hom.}}(k,q)$ separately, where we use the native blueprint for the former and a variant that introduces an explicit k^2-pole to cancel the aforementioned pole of the pseudoscalar contribution for the latter.

We first perform the BTT procedure for $T^{\mu\nu}_{\mathrm{P,hom.}}(k,q)$, where the only available building blocks for the Lorentz structures are

$$\{L^{\mu}_{\mathrm{P,hom.},i}\} = \{k^\mu, q^\mu\}, \tag{B.4}$$

and gauge invariance in the form $q_\mu T^{\mu}_{\mathrm{P,hom.}}(k,q) = 0$ is imposed by means of

$$\big\{\widetilde{L}^{\mu}_{\mathrm{P,hom.},i}\big\} = \mathcal{I}^{\mu}{}_{\alpha}\big\{L^{\alpha}_{\mathrm{P,hom.},i}\big\}, \qquad\qquad \mathcal{I}^{\mu\nu} = g^{\mu\nu} - \frac{k^\mu q^\nu}{k\cdot q}. \tag{B.5}$$

The resulting set

$$\{\widetilde{L}^{\mu}_{\mathrm{P,hom.},i}\} = \Big\{0, q^\mu - \frac{q^2}{k\cdot q}k^\mu\Big\} \tag{B.6}$$

consists of a single non-vanishing structure with a pole in $(k\cdot q)$. Following the original recipe, this irreducible pole is to be eliminated by multiplying with $(k\cdot q)$, leading to the structure

$$\widehat{L}^{\mu}_{\mathrm{P,hom.}} = (k\cdot q)q^\mu - q^2 k^\mu. \tag{B.7}$$

In order to perform the BTT procedure for $\widetilde{T}^{\mu\nu}_{\mathrm{H,hom.}}(k,q)$, we note that the interaction is of the form $V-A$. Hence, the available building blocks for the Lorentz structures are given by

$$\{L^{\mu\nu}_{\mathrm{H,hom.},i}\} = \big\{g^{\mu\nu}, k^\mu k^\nu, k^\mu q^\nu, q^\mu k^\nu, q^\mu q^\nu, \epsilon^{\mu\nu\alpha\beta}k_\rho q_\sigma\big\}, \tag{B.8}$$

and we impose $q_\mu \widetilde{T}^{\mu\nu}_{\mathrm{H,hom.}}(k,q) = 0 = k_\nu \widetilde{T}^{\mu\nu}_{\mathrm{H,hom.}}(k,q)$ by means of

$$\{\widetilde{L}^{\mu\nu}_{\mathrm{H,hom.},i}\} = \mathcal{I}^\mu{}_\alpha \{L^{\alpha\beta}_{\mathrm{H,hom.},i}\}\widetilde{\mathcal{I}}_\beta{}^\nu, \qquad \widetilde{\mathcal{I}}^{\mu\nu} = g^{\mu\nu} - \frac{k^\mu k^\nu}{k^2}. \tag{B.9}$$

The resulting set

$$\{\widetilde{L}^{\mu\nu}_{\mathrm{H,hom.},i}\} = \Big\{g^{\mu\nu} - \frac{k^\mu q^\nu}{k\cdot q}, 0, 0, 0, \frac{q^2}{k^2}k^\mu k^\nu - \frac{q^2}{k\cdot q}k^\mu q^\nu - \frac{k\cdot q}{k^2}q^\mu k^\nu + q^\mu q^\nu, \epsilon^{\mu\nu\rho\sigma}k_\rho q_\sigma\Big\} \tag{B.10}$$

contains structures with poles in $(k\cdot q)$ as well as k^2. While we explicitly keep the k^2 poles, as mentioned above, we remove one of the two poles in $(k\cdot q)$ by following the original procedure, *i.e.*, by taking an appropriate linear combination with non-singular coefficients and multiplying the remaining pole by $(k\cdot q)$. This leads to the minimal [10, 11] set

$$\begin{aligned}\{\widehat{L}^{\mu\nu}_{\mathrm{H,hom.},i}\} &= \{(k\cdot q)\widetilde{L}^{\mu\nu}_{\mathrm{H,hom.},1}, \widetilde{L}^{\mu\nu}_{\mathrm{H,hom.},5} - q^2\widetilde{L}^{\mu\nu}_{\mathrm{H,hom.},1}, \widetilde{L}^{\mu\nu}_{\mathrm{H,hom.},6}\} \\ &= \Big\{(k\cdot q)g^{\mu\nu} - k^\mu q^\nu, \frac{q^2}{k^2}k^\mu k^\nu - \frac{k\cdot q}{k^2}q^\mu k^\nu + q^\mu q^\nu - q^2 g^{\mu\nu}, \epsilon^{\mu\nu\rho\sigma}k_\rho q_\sigma\Big\}.\end{aligned} \tag{B.11}$$

Combining Eq. (B.7) and Eq. (B.11) with Eq. (B.3), the homogeneous part of the hadronic tensor thus takes the form given in Eq. (4.1).

Appendix C

Form-factor projectors

In this appendix, we collect the formulae for the projectors $\mathcal{P}_i^{\mu\nu}(k,q)$ introduced in Ch. 4 that fulfill $\mathcal{P}_{i\mu\nu}(k,q)T_{\mathrm{H}}^{\mu\nu}(k,q) = \mathcal{F}_i(k^2,q^2)$, $i = 1,\ldots,4$, and $\mathcal{P}_{i\mu\nu}(k,q)T_{\mathrm{H}}^{\mu\nu}(k,q) = f_B/m_B$, $i = 5,6$, for an arbitrary choice of basis for $T_{\mathrm{H}}^{\mu\nu}(k,q)$ [35–38]:

$$
\begin{aligned}
\frac{1}{m_B}\mathcal{P}_1^{\mu\nu}(k,q) &= \frac{k\cdot q}{2[(k\cdot q)^2-k^2q^2]}g^{\mu\nu} + \frac{3q^2(k\cdot q)}{2[(k\cdot q)^2-k^2q^2]^2}k^\mu k^\nu - \frac{(k\cdot q)^2+2k^2q^2}{2[(k\cdot q)^2-k^2q^2]^2}k^\mu q^\nu \\
&\quad - \frac{3(k\cdot q)^2}{2[(k\cdot q)^2-k^2q^2]^2}q^\mu k^\nu + \frac{3k^2(k\cdot q)}{2[(k\cdot q)^2-k^2q^2]^2}q^\mu q^\nu, \\
\frac{1}{m_B}\mathcal{P}_2^{\mu\nu}(k,q) &= \frac{k^2}{2[(k\cdot q)^2-k^2q^2]}g^{\mu\nu} + \frac{2(k\cdot q)^2+k^2q^2}{2[(k\cdot q)^2-k^2q^2]^2}k^\mu k^\nu - \frac{3k^2(k\cdot q)}{2[(k\cdot q)^2-k^2q^2]^2}k^\mu q^\nu \\
&\quad - \frac{3k^2(k\cdot q)}{2[(k\cdot q)^2-k^2q^2]^2}q^\mu k^\nu + \frac{3k^4}{2[(k\cdot q)^2-k^2q^2]^2}q^\mu q^\nu, \\
\frac{1}{m_B}\mathcal{P}_3^{\mu\nu}(k,q) &= \frac{1}{(k\cdot q)^2-k^2q^2}k^\mu k^\nu - \frac{2k^2}{[(k\cdot q)^2-k^2q^2][2(k\cdot q)+q^2]}q^\mu k^\nu \\
&\quad - \frac{k^2}{[(k\cdot q)^2-k^2q^2][2(k\cdot q)+q^2]}q^\mu q^\nu, \\
\frac{1}{m_B}\mathcal{P}_4^{\mu\nu}(k,q) &= -\frac{\mathrm{i}}{2[(k\cdot q)^2-k^2q^2]}\epsilon^{\mu\nu\rho\sigma}k_\rho q_\sigma, \\
m_B\mathcal{P}_5^{\mu\nu}(k,q) &= -\frac{k\cdot q}{(k\cdot q)^2-k^2q^2}q^\mu k^\nu + \frac{k^2}{(k\cdot q)^2-k^2q^2}q^\mu q^\nu, \\
m_B\mathcal{P}_6^{\mu\nu}(k,q) &= \frac{q^2}{(k\cdot q)^2-k^2q^2}q^\mu k^\nu - \frac{k\cdot q}{(k\cdot q)^2-k^2q^2}q^\mu q^\nu.
\end{aligned}
\tag{C.1}
$$

At this, an ambiguity is hidden in how to collect the terms of the inhomogeneous part into basis structures in Eq. (4.8) since different such choices will lead to another set of projectors than the one given above. However, any difference $\overline{\mathcal{P}}_i^{\mu\nu}(k,q)$ between two sets of valid projectors is of the form

$$
\overline{\mathcal{P}}_i^{\mu\nu}(k,q) = A_i q^\mu \big[k^\nu[(k\cdot q)+q^2] - q^\nu[(k\cdot q)+k^2]\big] \tag{C.2}
$$

for $i = 3, 5, 6$, with the coefficients $A_i \equiv A_i(k^2, q^2)$ given by

$$\begin{aligned}
A_3 &= \frac{2m_B^2 k^2}{\bar{D}}\big[x_1(z_2 - y_2) + x_2(y_1 - z_1) - y_1 z_2 + y_2 z_1\big],\\
A_5 &= -\frac{2(k\cdot q) + q^2}{\bar{D}}\Big[2\big[x_1(y_2 - 1) - x_2(y_1 - 1) + y_1 - y_2\big](k\cdot q)\\
&\qquad\qquad + \big[x_1(z_2 - 1) - x_2(z_1 - 1) + z_1 - z_2\big]q^2\Big],\\
A_6 &= -\frac{2(k\cdot q) + q^2}{\bar{D}}\big[2(x_1 y_2 - x_2 y_1)(k\cdot q) + (x_1 z_2 - x_2 z_1)q^2\big], \qquad \text{(C.3)}\\
\bar{D} &= m_B\big[(k\cdot q)^2 - k^2 q^2\big]\big[2(x_1 - y_1)(k\cdot q) + (x_1 - z_1)q^2\big]\big[2(x_2 - y_2)(k\cdot q) + (x_2 - z_2)q^2\big].
\end{aligned}$$

Here, x_i, y_i, and z_i account for the splitting of the inhomogeneous contribution in Eq. (4.8) into two basis structures according to

$$\begin{aligned}
T^{\mu\nu}_{\text{H,inhom.}}(k,q) \mathrel{\widehat{=}} -f_B\Big\{&x_i g^{\mu\nu} + y_i\frac{2k^\mu k^\nu}{2(k\cdot q) + q^2} + z_i\frac{q^\mu k^\nu}{2(k\cdot q) + q^2},\\
&(1 - x_i)g^{\mu\nu} + (1 - y_i)\frac{2k^\mu k^\nu}{2(k\cdot q) + q^2} + (1 - z_i)\frac{q^\mu k^\nu}{2(k\cdot q) + q^2}\Big\}, \qquad \text{(C.4)}
\end{aligned}$$

where the projectors of Eq. (C.1) correspond to $x_i = 1$, $y_i = 0 = z_i$. Hence, we find

$$\begin{aligned}
\overline{\mathcal{P}}_{i\mu\nu}(k,q)T^{\mu\nu}_{\text{H,hom.}}(k,q) &= A_i\big[q_\mu T^{\mu\nu}_{\text{H,hom.}}(k,q)\big]\big[k_\nu[(k\cdot q) + q^2] - q_\nu[(k\cdot q) + k^2]\big]\\
&= 0,\\
\overline{\mathcal{P}}_{i\mu\nu}(k,q)T^{\mu\nu}_{\text{H,inhom.}}(k,q) &= A_i\big[q_\mu T^{\mu\nu}_{\text{H,inhom.}}(k,q)\big]\big[k_\nu[(k\cdot q) + q^2] - q_\nu[(k\cdot q) + k^2]\big]\\
&= A_i[-f_B(k+q)^\nu]\big[k_\nu[(k\cdot q) + q^2] - q_\nu[(k\cdot q) + k^2]\big]\\
&= 0. \qquad \text{(C.5)}
\end{aligned}$$

For $i = 1, 2, 4$, on the other hand, the projectors are independent of the particular choice of how the terms of the inhomogeneous part are collected into basis structures, *i.e.*, $A_i = 0$.

Appendix D

Kinematics

In this appendix, we present some details on the kinematics for the processes $B^- \to \ell^- \bar{\nu}_\ell \gamma^*$ and $B^- \to \ell^- \bar{\nu}_\ell \ell'^- \ell'^+$, which are needed to calculate the squared spin-summed amplitudes $|\overline{\mathcal{M}}(B^- \to \ell^- \bar{\nu}_\ell \gamma^*)|^2$ and $|\overline{\mathcal{M}}(B^- \to \ell^- \bar{\nu}_\ell \ell'^- \ell'^+)|^2$.

D.1 $B^- \to \ell^- \bar{\nu}_\ell \gamma^*$

For a consistent treatment of the kinematics in the process $B^- \to \ell^- \bar{\nu}_\ell \gamma^*$, all momenta and polarization vectors have to be evaluated in a single frame of reference. To this end, we calculate the corresponding quantities in the center-of-mass frames of the $\{\ell^- \bar{\nu}_\ell(k), \gamma^*(q)\}$ and $\{\ell^-(p_\ell), \bar{\nu}_\ell(p_\nu)\}$ subsystems and perform a Lorentz transformation of the latter to the former frame.

In the center-of-mass frame of $\{\ell^- \bar{\nu}_\ell(k), \gamma^*(q)\}$, one finds the magnitude of the photon's three-momentum and the energies

$$|\boldsymbol{p}_\gamma| = \frac{\sqrt{\lambda(m_B^2, k^2, q^2)}}{2m_B}, \qquad E_W = \frac{m_B^2 + k^2 - q^2}{2m_B}, \qquad E_\gamma = \frac{m_B^2 - k^2 + q^2}{2m_B}. \tag{D.1}$$

The four-momentum of the leptonic subsystem thus reads

$$k = (E_W, 0, 0, |\boldsymbol{p}_\gamma|)^\intercal, \tag{D.2}$$

and, accordingly, the four-momentum of the photon and its polarization vectors are given by

$$\begin{aligned} q &= (E_\gamma, 0, 0, -|\boldsymbol{p}_\gamma|)^\intercal, & \epsilon(q;\lambda=\pm1) &= \mp\frac{1}{\sqrt{2}}(0, 1, \mp\mathrm{i}, 0)^\intercal, \\ \epsilon(q;\lambda=0) &= \frac{1}{\xi}(-|\boldsymbol{p}_\gamma|, 0, 0, E_\gamma)^\intercal, & \epsilon(q;\lambda=T) &= \frac{1}{\xi}(E_\gamma, 0, 0, -|\boldsymbol{p}_\gamma|)^\intercal, \end{aligned} \tag{D.3}$$

where any physical observable is necessarily independent of $\xi = \sqrt{q^2}$.

In the center-of-mass frame of $\{\ell^-(p_\ell), \bar{\nu}_\ell(p_\nu)\}$, we have

$$|\boldsymbol{p}_\ell| = \frac{k^2 - m_\ell^2}{2\sqrt{k^2}}, \qquad E_\ell = \frac{k^2 + m_\ell^2}{2\sqrt{k^2}}, \qquad E_\nu = \frac{k^2 - m_\ell^2}{2\sqrt{k^2}} \tag{D.4}$$

for the magnitude of the negatively charged lepton's three-momentum and the corresponding energies. Hence, transforming the subsystem $\{\ell^-(p_\ell), \bar{\nu}_\ell(p_\nu)\}$ to the center-of-mass frame of $\{\ell^-\bar{\nu}_\ell(k), \gamma^*(q)\}$, the four-momenta of the leptons are found to be

$$p_\ell = \begin{pmatrix} \gamma_W(E_\ell + \beta_W|\boldsymbol{p}_\ell|\cos\vartheta_W) \\ |\boldsymbol{p}_\ell|\sin\vartheta_W \\ 0 \\ \gamma_W(\beta_W E_\ell + |\boldsymbol{p}_\ell|\cos\vartheta_W) \end{pmatrix}, \qquad p_\nu = \begin{pmatrix} \gamma_W(E_\nu - \beta_W|\boldsymbol{p}_\ell|\cos\vartheta_W) \\ -|\boldsymbol{p}_\ell|\sin\vartheta_W \\ 0 \\ \gamma_W(\beta_W E_\nu - |\boldsymbol{p}_\ell|\cos\vartheta_W) \end{pmatrix}, \tag{D.5}$$

where $\beta_W = |\boldsymbol{p}_\gamma|/E_W$, $\gamma_W = (1-\beta_W^2)^{-1/2}$, and ϑ_W is the polar angle of $\ell^-(p_\ell)$ in the center-of-mass frame of $\{\ell^-(p_\ell), \bar{\nu}_\ell(p_\nu)\}$.

D.2 $B^- \to \ell^-\bar{\nu}_\ell\ell'^-\ell'^+$

In addition to the magnitudes of three-momenta $|\boldsymbol{p}_\gamma|$ and $|\boldsymbol{p}_\ell|$ in the center-of-mass frames of $\{\ell^-\bar{\nu}_\ell(k), \gamma^*(q)\}$ and $\{\ell^-(p_\ell), \bar{\nu}_\ell(p_\nu)\}$, respectively, we need the three-momentum and energy of the leptons in the center-of-mass frame of $\{\ell'^-(q_1), \ell'^+(q_2)\}$ to describe the process $B^- \to \ell^-\bar{\nu}_\ell\ell'^-\ell'^+$,

$$|\boldsymbol{p}_{\ell'}| = \frac{\sqrt{q^2 - 4m_{\ell'}^2}}{2}, \qquad E_{\ell'} = \frac{\sqrt{q^2}}{2}. \tag{D.6}$$

Furthermore, two additional angles besides ϑ_W are necessary here: the polar angle ϑ_γ of $\ell'^-(q_1)$ in the center-of-mass frame of $\{\ell'^-(q_1), \ell'^+(q_2)\}$ and the azimuthal angle φ between the decay planes of the subsystems $\{\ell^-(p_\ell), \bar{\nu}_\ell(p_\nu)\}$ and $\{\ell'^-(q_1), \ell'^+(q_2)\}$, see Fig. D.1. A transformation of the subsystem $\{\ell'^-(q_1), \ell'^+(q_2)\}$ to the center-of-mass frame $\{\ell^-\bar{\nu}_\ell(k), \ell'^-\ell'^+(q)\}$ then yields the four-momenta

$$q_1 = \begin{pmatrix} \gamma_\gamma(E_{\ell'} + \beta_\gamma|\boldsymbol{p}_{\ell'}|\cos\vartheta_\gamma) \\ -|\boldsymbol{p}_{\ell'}|\sin\vartheta_\gamma\cos\varphi \\ -|\boldsymbol{p}_{\ell'}|\sin\vartheta_\gamma\sin\varphi \\ \gamma_\gamma(-\beta_\gamma E_{\ell'} - |\boldsymbol{p}_{\ell'}|\cos\vartheta_\gamma) \end{pmatrix}, \qquad q_2 = \begin{pmatrix} \gamma_\gamma(E_{\ell'} - \beta_\gamma|\boldsymbol{p}_{\ell'}|\cos\vartheta_\gamma) \\ |\boldsymbol{p}_{\ell'}|\sin\vartheta_\gamma\cos\varphi \\ |\boldsymbol{p}_{\ell'}|\sin\vartheta_\gamma\sin\varphi \\ \gamma_\gamma(-\beta_\gamma E_{\ell'} + |\boldsymbol{p}_{\ell'}|\cos\vartheta_\gamma) \end{pmatrix}, \tag{D.7}$$

where $\beta_\gamma = |\boldsymbol{p}_\gamma|/E_\gamma$, $\gamma_\gamma = (1-\beta_\gamma^2)^{-1/2}$.

For the four-body phase space, we used

$$\mathrm{d}\Phi_4(p; p_\ell, p_\nu, q_1, q_2) = \mathrm{d}\Phi_2(p; k, q)\,\mathrm{d}\Phi_2(k; p_\ell, p_\nu)\,\mathrm{d}\Phi_2(q; q_1, q_2)\,\frac{\mathrm{d}k^2}{2\pi}\,\frac{\mathrm{d}q^2}{2\pi} \tag{D.8}$$

in Eq. (6.2), where

$$\begin{aligned} \mathrm{d}\Phi_2(p; k, q) &= \frac{1}{16\pi^2}\frac{|\boldsymbol{p}_\gamma|}{m_B}\mathrm{d}\Omega_B, & \mathrm{d}\Phi_2(k; p_\ell, p_\nu) &= \frac{1}{16\pi^2}\frac{|\boldsymbol{p}_\ell|}{\sqrt{k^2}}\mathrm{d}\Omega_W, \\ \mathrm{d}\Phi_2(q; q_1, q_2) &= \frac{1}{16\pi^2}\frac{|\boldsymbol{p}_{\ell'}|}{\sqrt{q^2}}\mathrm{d}\Omega_\gamma \end{aligned} \tag{D.9}$$

are the two-body phase spaces of the subsystems $\{\ell^-\bar{\nu}_\ell(k), \ell'^-\ell'^+(q)\}$, $\{\ell^-(p_\ell), \bar{\nu}_\ell(p_\nu)\}$, and $\{\ell'^-(q_1), \ell'^+(q_2)\}$, respectively. Here, $\mathrm{d}\Omega_B$, $\mathrm{d}\Omega_W$, and $\mathrm{d}\Omega_\gamma$ denote the differential solid

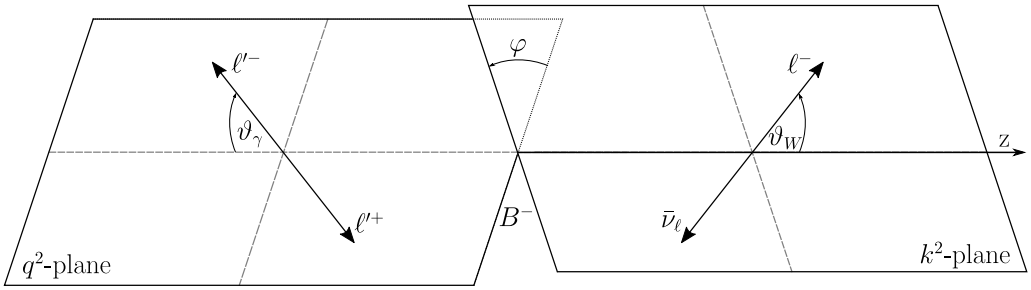

Figure D.1: Illustration of the decay $B^- \to \ell^- \bar{\nu}_\ell \ell'^- \ell'^+$, with the two decay planes of the leptonic subsystems and the three angles necessary to describe the process.

angles in the corresponding center-of-mass frames. Three of the six angular integrations can be rendered trivial by rotating the coordinate system appropriately, leading to the expression

$$\mathrm{d}\Phi_4(p; p_\ell, p_\nu, q_1, q_2) = \frac{1}{2048\pi^6} \frac{|\boldsymbol{p}_\gamma|}{m_B} \frac{|\boldsymbol{p}_\ell|}{\sqrt{k^2}} \frac{|\boldsymbol{p}_{\ell'}|}{\sqrt{q^2}} \mathrm{d}\cos\vartheta_W \, \mathrm{d}\cos\vartheta_\gamma \, \mathrm{d}\varphi \, \mathrm{d}k^2 \, \mathrm{d}q^2 \tag{D.10}$$

for the four-body phase space, with the remaining angles being as illustrated in Fig. D.1.

Appendix E

Asymptotics

In this appendix, we show that the form factors $\mathcal{F}_i^I(k^2, q^2)$ introduced in Ch. 5 as well as their discontinuities drop off as $1/q^2$ asymptotically. This behavior was assumed to avoid subtracting the dispersion relation of Eq. (5.11) and justified the monopole ansatz for the form factors in Eq. (5.15). We determine the form factors' asymptotic behavior for $q^2 \to \infty$ by inspecting the results of a calculation of the $B \to \gamma^*$ form factors within an OPE [15]. For our purposes, it suffices to inspect the leading-power terms within this OPE, which are illustrated diagrammatically in Fig. E.1. The OPE uses an interpolating quark current for the B meson, namely [15] $J_B(x) = \bar{u}(x)\gamma_5 b(x)$, which fulfills $\langle 0|J_B(0)|B^-\rangle = -\mathrm{i}f_B m_B^2/(m_b + m_u)$, see Eq. (A.23). Calculating the sum of the two diagrams depicted in Fig. E.1, we find

$$\begin{aligned} X^I_{\mu\nu}(k,q) = e \int \frac{\mathrm{d}^4 l}{(2\pi)^4} \mathrm{Tr}\Big[&- \gamma_5 \frac{\mathrm{i}(\not{l} - \not{q} + m_u)}{(l-q)^2 - m_u^2} Q_u^I \gamma_\mu \frac{\mathrm{i}(\not{l} + m_u)}{l^2 - m_u^2} \gamma_\nu (1-\gamma_5) \frac{\mathrm{i}(\not{l} + \not{k} + m_b)}{(l+k)^2 - m_b^2} \\ &- \gamma_5 \frac{\mathrm{i}(\not{l} - \not{k} + m_u)}{(l-k)^2 - m_u^2} \gamma_\nu (1-\gamma_5) \frac{\mathrm{i}(\not{l} + m_b)}{l^2 - m_b^2} Q_b^I \gamma_\mu \frac{\mathrm{i}(\not{l} + \not{q} + m_b)}{(l+q)^2 - m_b^2} \Big], \end{aligned} \tag{E.1}$$

where l is the loop momentum, $q^2 < 0$ is large, and the isospin charges are given by $(Q_u^{I=0}, Q_b^{I=0}) = (1/6, -1/3)$ and $(Q_u^{I=1}, Q_b^{I=1}) = (1/2, 0)$.

For the discontinuities, it then follows that

$$\mathrm{disc}_{q^2} \mathcal{F}_i^{I,\mathrm{OPE}}(k^2, q^2) \propto \mathrm{disc}_{q^2} \big[\mathcal{P}_i{}^{\mu\nu}(k,q) X^I_{\mu\nu}(k,q) \big], \tag{E.2}$$

and the asymptotic behavior for large $q^2 < 0$ is found to be given by [38]

$$\mathrm{disc}_{q^2} \mathcal{F}_i^{I,\mathrm{OPE}}(k^2, q^2) \sim 1/q^2, \tag{E.3}$$

rendering the dispersion integrals convergent without any subtractions.

Similarly, we find

$$\mathcal{F}_i^{I,\mathrm{OPE}}(k^2, q^2) \sim 1/q^2 \tag{E.4}$$

for the asymptotic behavior of the form factors, which justifies a monopole ansatz in the framework of VMD.

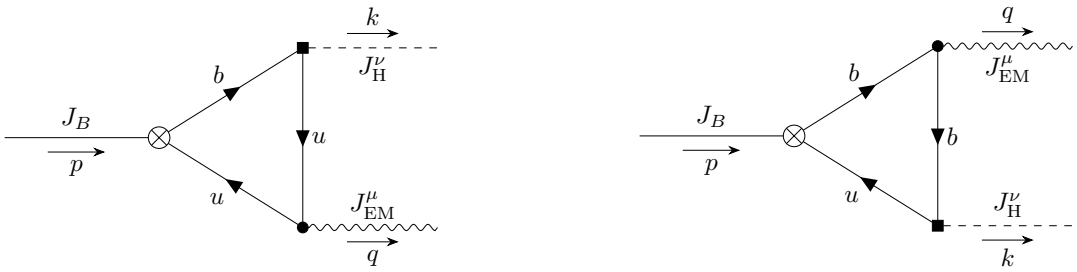

Figure E.1: The leading-order diagrams in the OPE for the form factors $\mathcal{F}_i(k^2, q^2)$. Diagrams contributing at a higher order in the OPE are neglected here.

Appendix F

Intermediate results

In this appendix, we collect the covariance matrices for the normalizations $N^V_{i,j}$ from Table 5.2 and the functions $f_{i,j}$ and $g_{i,j}$ introduced in Eq. (6.4) and Eq. (6.7).

F.1 Covariance matrices

For reasons of consistency with the rounding of the normalization uncertainties, we round the numerical values in the covariance matrices to four significant digits. Since the input used to determine the normalizations does not exhibit a correlation between the parameters of the ω and ρ mesons, the normalizations $N^\omega_{i,j}$ and $N^\rho_{i,j}$ are uncorrelated, *i.e.*, $\mathrm{Cov}(N^\omega_{i,j}, N^\rho_{k,l}) = 0$ for all i, j, k, l, so that our results can be collected in two independent (12×12) matrices.

For the covariances between the normalizations $N^\omega_{i,j}$, we find

$$10^6 \times \mathrm{Cov}(N^\omega_{i,j}, N^\omega_{k,l})_{mn} \tag{F.1}$$

$$= \begin{pmatrix}
9.186 & -11.29 & 66.84 & 16.05 & -65.26 & 739.2 & 16.05 & 57.91 & -371.5 & -7.348 & -37.43 & 135.1 \\
-11.29 & 378.7 & -1444 & -151.5 & 491.6 & -3209 & -151.5 & -186.7 & 1270 & 2.220 & -241.8 & 353.4 \\
66.84 & -1444 & 7180 & 991.8 & -5858 & 24670 & 991.8 & -911.2 & -1778 & -6.404 & 558.3 & -1611 \\
16.05 & -151.5 & 991.8 & 740.4 & -1134 & 7731 & 740.4 & 2429 & -6410 & 13.70 & 3.901 & 134.0 \\
-65.26 & 491.6 & -5858 & -1134 & 20370 & -52440 & -1134 & 14440 & -31960 & -9.187 & 986.6 & -2592 \\
739.2 & -3209 & 24670 & 7731 & -52440 & 266600 & 7731 & -9322 & 46070 & -305.2 & -3351 & 16080 \\
16.05 & -151.5 & 991.8 & 740.4 & -1134 & 7731 & 740.4 & 2429 & -6410 & 13.70 & 3.901 & 134.0 \\
57.91 & -186.7 & -911.2 & 2429 & 14440 & -9322 & 2429 & 28910 & -63340 & 15.82 & 682.5 & 204.0 \\
-371.5 & 1270 & -1778 & -6410 & -31960 & 46070 & -6410 & -63340 & 498000 & 144.6 & -1346 & 13990 \\
-7.348 & 2.220 & -6.404 & 13.70 & -9.187 & -305.2 & 13.70 & 15.82 & 144.6 & 7.794 & 34.85 & -134.1 \\
-37.43 & -241.8 & 558.3 & 3.901 & 986.6 & -3351 & 3.901 & 682.5 & -1346 & 34.85 & 450.4 & -1108 \\
135.1 & 353.4 & -1611 & 134.0 & -2592 & 16080 & 134.0 & 204.0 & 13990 & -134.1 & -1108 & 8249
\end{pmatrix},$$

where $m = (3i + j - 2)$ and $n = (3k + l - 2)$ denote the rows and columns of the matrix, respectively. At this, it is to be noted that $N^\omega_{2,0} = N^\omega_{3,0}$, see the discussion in Ch. 5, so that one row and one column of the matrix is, in fact, redundant, reducing the degrees of freedom to an (11×11) matrix.[12]

[12] Due to this redundancy, the covariance matrix becomes positive definite only after removing the respective row and column.

In the same way and with the analogous caveat $N^{\rho}_{2,0} = N^{\rho}_{3,0}$, we find the covariances between the normalizations $N^{\rho}_{i,j}$ to be given by

$$10^5 \times \mathrm{Cov}(N^{\rho}_{i,j}, N^{\rho}_{k,l})_{mn} \tag{F.2}$$

$$= \begin{pmatrix}
7.758 & -25.35 & 132.8 & 17.88 & -47.77 & 705.8 & 17.88 & 70.38 & -233.2 & -5.403 & -18.46 & 46.61 \\
-25.35 & 231.1 & -988.0 & -151.1 & 393.9 & -3906 & -151.1 & -389.7 & 7.717 & 12.95 & -55.78 & -26.32 \\
132.8 & -988.0 & 5543 & 1059 & -5304 & 26800 & 1059 & 411.8 & -3620 & -55.19 & -90.41 & -25.79 \\
17.88 & -151.1 & 1059 & 631.5 & -1626 & 7978 & 631.5 & 1294 & -2278 & 9.762 & -23.75 & -12.89 \\
-47.77 & 393.9 & -5304 & -1626 & 17200 & -43390 & -1626 & 7476 & -12080 & -44.36 & 814.8 & -1798 \\
705.8 & -3906 & 26800 & 7978 & -43390 & 224000 & 7978 & 2795 & 15740 & -248.9 & -2166 & 8948 \\
17.88 & -151.1 & 1059 & 631.5 & -1626 & 7978 & 631.5 & 1294 & -2278 & 9.762 & -23.75 & -12.89 \\
70.38 & -389.7 & 411.8 & 1294 & 7476 & 2795 & 1294 & 14980 & -16040 & -29.65 & 443.1 & 795.0 \\
-233.2 & 7.717 & -3620 & -2278 & -12080 & 15740 & -2278 & -16040 & 396500 & 42.62 & 123.5 & 27430 \\
-5.403 & 12.95 & -55.19 & 9.762 & -44.36 & -248.9 & 9.762 & -29.65 & 42.62 & 5.693 & 16.05 & -56.63 \\
-18.46 & -55.78 & -90.41 & -23.75 & 814.8 & -2166 & -23.75 & 443.1 & 123.5 & 16.05 & 197.2 & -383.9 \\
46.61 & -26.32 & -25.79 & -12.89 & -1798 & 8948 & -12.89 & 795.0 & 27430 & -56.63 & -383.9 & 5497
\end{pmatrix}.$$

F.2 Functions $f_{i,j}$ and $g_{i,j}$

For the functions $f_{i,j}$ introduced in Eq. (6.4), we obtain

$$\begin{aligned}
f_{1,1} &= \frac{64\pi k_-^2 q_+^2 (k_+^2 + k^2)[\lambda(m_B^2, k^2, q^2) + 6k^2 q^2]}{9k^2}, \qquad f_{3,3} = m_\ell^2 \frac{32\pi k_-^2 q_+^2 q^2 \lambda(m_B^2, k^2, q^2)}{3k^4}, \\
f_{1,2} &= -\frac{64\pi k_-^2 q_+^2 q^2 (k_+^2 + k^2)\Delta(k^2, q^2)}{3k^2}, \qquad f_{4,4} = \frac{64\pi k_-^2 q_+^2 (k_+^2 + k^2)\lambda(m_B^2, k^2, q^2)}{9k^2}, \\
f_{2,2} &= \frac{32\pi k_-^2 q_+^2 q^2 (k_+^2 + k^2)[\lambda(m_B^2, k^2, q^2) + 12k^2 q^2]}{9k^4}
\end{aligned} \tag{F.3}$$

and

$$\begin{aligned}
f_{1,5} &= m_\ell^2 \frac{128\pi q_+^2}{3k_-^2}\Big[k_-^2\big[\Delta(k^2,q^2) - k_+^2\big] - k_B^2 k^2\big[\Delta(k^2,q^2) - 2m_\ell^2\big]L_D(k^2,q^2)\Big], \\
f_{2,5} &= -m_\ell^2 \frac{128\pi q_+^2 q^2}{3k_-^2}\Big[3k_-^2 - \big[3k_B^2 k^2 + (k_-^2)^2\big]L_D(k^2,q^2)\Big], \\
f_{3,5} &= -m_\ell^2 \frac{64\pi q_+^2 q^2}{3k_B^2 k_-^2 k^2}\Big[k_-^2\big[k_-^2\Delta(k^2,q^2) + 2k^2(k_B^2 + 2k_-^2)\big] \\
&\qquad\qquad - 2k_B^2 k^2 (k_B^2 k^2 + k_-^2 k_+^2) L_D(k^2,q^2)\Big], \\
f_{4,5} &= -m_\ell^2 \frac{128\pi q_+^2}{3k_-^2}\Big[k_-^2\Delta(k^2,q^2) - k^2\big[k_B^2\Delta(k^2,q^2) - 2k_-^2 q^2\big]L_D(k^2,q^2)\Big], \\
f_{5,5} &= -m_\ell^2 \frac{128\pi q_+^2}{3(k_B^2)^2 k_-^2 [k_-^2 q^2 (k_B^2 + k_-^2) + m_\ell^2 (k_B^2)^2]} \\
&\quad \times \Big[k_-^2\Big[k_-^2(k_B^2 + k_-^2)\big[k_B^2 - \Delta(k^2,q^2)\big]\big[4(k_-^2)^2 + k_-^2[3k_B^2 + \Delta(k^2,q^2)] + 4(k_B^2)^2\big] \\
&\qquad + m_\ell^2\big[4(k_-^2)^3[k_B^2 - \Delta(k^2,q^2)] + 8k_B^2(k_-^2)^2[2k_B^2 - \Delta(k^2,q^2)]
\end{aligned}$$

$$
\begin{aligned}
&+ (k_B^2)^2 k_-^2 [13k_B^2 - 5\Delta(k^2,q^2)] + 2(k_B^2)^3[2k_B^2 - \Delta(k^2,q^2)]\big] \\
&+ 8m_\ell^4 (k_B^2)^2 (k_B^2 + k_-^2)\Big] \\
&+ 2k_B^2 k^2 \Big[k_B^2\big[\Delta(k^2,q^2) - 2k_B^2\big] - 2k_-^2(k_B^2 + k_-^2) - 4m_\ell^2(k_B^2 + k_-^2)\Big] \\
&\times \big[k_-^2 q^2 (k_B^2 + k_-^2) + m_\ell^2 (k_B^2)^2\big] L_D(k^2,q^2)\Big],
\end{aligned}
\tag{F.4}
$$

where we defined

$$
\begin{aligned}
&k_B^2 = m_B^2 - k^2, \qquad k_\pm^2 = k^2 \pm m_\ell^2, \qquad q_+^2 = q^2 + 2m_{\ell'}^2, \qquad \Delta(k^2,q^2) = k_B^2 - q^2, \\
&L_D = \frac{L_+(k^2,q^2) - L_-(k^2,q^2)}{\sqrt{\lambda(m_B^2,k^2,q^2)}}, \qquad L_\pm(k^2,q^2) = \log\left(1 \pm \frac{k_-^2\sqrt{\lambda(m_B^2,k^2,q^2)}}{k_B^2 k_+^2 + k_-^2 q^2}\right).
\end{aligned}
\tag{F.5}
$$

All other, unlisted functions vanish, *i.e.*, $f_{1,3} = f_{1,4} = f_{2,3} = f_{2,4} = f_{3,4} = 0$. Given the scaling with the lepton mass, one finds that this set further reduces to four functions in the chiral limit $m_\ell = 0$.

For the functions $g_{i,j}$ introduced in Eq. (6.7), we find

$$
\begin{aligned}
g_{1,3} &= m_\ell^2 \frac{32\pi k_-^2 q_+^2 q^2 \sqrt{\lambda(m_B^2,k^2,q^2)}}{3k^2}, \quad g_{1,4} = \frac{32\pi k_-^2 q_+^2 \Delta(k^2,q^2)\sqrt{\lambda(m_B^2,k^2,q^2)}}{3}, \\
g_{2,3} &= -m_\ell^2 \frac{16\pi k_-^2 q_+^2 q^2 \Delta(k^2,q^2)\sqrt{\lambda(m_B^2,k^2,q^2)}}{3k^4}, \quad g_{2,4} = -\frac{64\pi k_-^2 q_+^2 q^2 \sqrt{\lambda(m_B^2,k^2,q^2)}}{3}
\end{aligned}
\tag{F.6}
$$

and

$$
\begin{aligned}
g_{1,5} &= m_\ell^2 \frac{32\pi q_+^2}{3k_B^2 k_-^2}\Big[2(k_-^2)^2\sqrt{\lambda(m_B^2,k^2,q^2)} - 4(k_B^2)^2 k^2\big[\Delta(k^2,q^2) - 2m_\ell^2\big]\widetilde{L}_D(k^2,q^2)\Big], \\
g_{2,5} &= m_\ell^2 \frac{32\pi q_+^2 q^2}{3k_B^2 k_-^2 k^2}\Big[(k_-^2)^2\sqrt{\lambda(m_B^2,k^2,q^2)} + 4k_B^2 k^2\big[3k_B^2 k^2 + (k_-^2)^2\big]\widetilde{L}_D(k^2,q^2)\Big], \\
g_{3,5} &= m_\ell^2 \frac{128\pi q_+^2 q^2}{3k_-^2}(k_B^2 k^2 + k_+^2 k_-^2)\widetilde{L}_D(k^2,q^2), \\
g_{4,5} &= m_\ell^2 \frac{128\pi k^2 q_+^2}{3k_-^2}\Big[2k_-^2\big[\Delta(k^2,q^2) - k_B^2\big] + k_B^2\Delta(k^2,q^2)\Big]\widetilde{L}_D(k^2,q^2), \\
g_{5,5} &= m_\ell^2 \frac{256\pi k^2 q_+^2}{3k_B^2 k_-^2[k_-^2 q^2(k_B^2 + k_-^2) + m_\ell^2(k_B^2)^2][k_+^2\Delta(k^2,q^2) + 2k^2q^2]} \\
&\quad\times\Big[k_B^2(k_-^2)^2(k_B^2 + k_-^2)(q^2 + 2m_\ell^2)\sqrt{\lambda(m_B^2,k^2,q^2)} \\
&\qquad + \big[k_+^2\Delta(k^2,q^2) + 2k^2q^2\big]\big[m_\ell^2(k_B^2)^2 + k_-^2 q^2(k_B^2 + k_-^2)\big] \\
&\qquad\quad\times\Big[4m_\ell^2(k_B^2 + k_-^2) + 2\big[(k_B^2)^2 + (k_-^2)^2 + k_B^2 k_-^2\big] - k_B^2\Delta(k^2,q^2)\Big]\widetilde{L}_D(k^2,q^2)\Big],
\end{aligned}
\tag{F.7}
$$

where we additionally defined

$$
\widetilde{L}_D = \frac{1}{\sqrt{\lambda(m_B^2,k^2,q^2)}}\log\frac{4k_-^2 k^2 q^2(k_B^2 + k_-^2) + 4m_\ell^2(k_B^2)^2 k^2}{[k_+^2\Delta(k^2,q^2) + 2k^2q^2]^2}.
\tag{F.8}
$$

All other, unlisted functions vanish, *i.e.*, $g_{1,1} = g_{2,2} = g_{3,3} = g_{4,4} = g_{1,2} = g_{3,4} = 0$. Again, from the scaling with the lepton mass, one finds that this set further reduces to two functions in the chiral limit $m_\ell = 0$.

Appendix G

Constants and parameters

We collect the constants and parameters used throughout the analysis in this part of the thesis in Table G.1.

Quantity	Variable	Value	Reference
Mass $\pi^{\pm}$	M_π	139.57039(18) MeV	
Mass $B^{\pm}$	m_B	5279.34(12) MeV	
Mass B^*	m_{B^*}	5324.71(21) MeV	
Mass B_1	m_{B_1}	$5725.9^{+2.5}_{-2.7}$ MeV	
Mass $\rho(770)$	M_ρ	775.26(23) MeV	[27]
Mass $\omega(782)$	M_ω	782.66(13) MeV	
Lifetime $B^{\pm}$	τ_B	1638(4) fs	
Width $\rho(770)$	Γ_ρ	147.4(8) MeV	
Width $\omega(782)$	Γ_ω	8.68(13) MeV	
Decay constant $\rho(770)$	f_ρ	216(3) MeV	[9]
Decay constant $\omega(782)$	f_ω	197(8) MeV	
Decay constant $B^{\pm}$	f_B	190.0(1.3) MeV	[39–43]
CKM matrix element $b \to u$	$\lvert V_{ub}\rvert$	$3.77(15) \times 10^{-3}$	[44]

Table G.1: The masses, widths, and other physical parameters needed for the calculations in this part of the thesis. For the ρ meson, the parameters are identified with those of the neutral ρ^0.

References

[1] M. Beneke and J. Rohrwild, Eur. Phys. J. C **71**, 1818 (2011) [arXiv:1110.3228 [hep-ph]].

[2] Y.-M. Wang, JHEP **09**, 159 (2016) [arXiv:1606.03080 [hep-ph]].

[3] M. Beneke, V. M. Braun, Y. Ji, and Y.-B. Wei, JHEP **07**, 154 (2018) [arXiv:1804.04962 [hep-ph]].

[4] M. Beneke, P. Böer, P. Rigatos, and K. K. Vos, Eur. Phys. J. C **81**, 638 (2021) [arXiv:2102.10060 [hep-ph]].

[5] M. A. Ivanov and D. Melikhov, Phys. Rev. D **105**, 014028 (2022) [arXiv:2107.07247 [hep-ph]], [Erratum: Phys. Rev. D **106**, 119901 (2022)].

[6] J. Albrecht, E. Stamou, R. Ziegler, and R. Zwicky, JHEP **09**, 139 (2021) [arXiv:1911.05018 [hep-ph]].

[7] C. Wang, Y.-M. Wang, and Y.-B. Wei, JHEP **02**, 141 (2022) [arXiv:2111.11811 [hep-ph]].

[8] G. Colangelo, M. Hoferichter, and P. Stoffer, JHEP **02**, 006 (2019) [arXiv:1810.00007 [hep-ph]].

[9] A. Bharucha, D. M. Straub, and R. Zwicky, JHEP **08**, 098 (2016) [arXiv:1503.05534 [hep-ph]].

[10] W. A. Bardeen and W. K. Tung, Phys. Rev. **173**, 1423 (1968), [Erratum: Phys. Rev. D **4**, 3229 (1971)].

[11] R. Tarrach, Nuovo Cim. A **28**, 409 (1975).

[12] J. Aebischer, M. Fael, C. Greub, and J. Virto, JHEP **09**, 158 (2017) [arXiv:1704.06639 [hep-ph]].

[13] E. E. Jenkins, A. V. Manohar, and P. Stoffer, JHEP **03**, 016 (2018) [arXiv:1709.04486 [hep-ph]].

[14] A. Khodjamirian and D. Wyler [arXiv:hep-ph/0111249].

[15] T. Janowski, B. Pullin, and R. Zwicky, JHEP **12**, 008 (2021) [arXiv:2106.13616 [hep-ph]].

[16] J. Bijnens, G. Ecker, and J. Gasser, Nucl. Phys. B **396**, 81 (1993) [arXiv:hep-ph/9209261].

[17] J. Bijnens, G. Colangelo, G. Ecker, and J. Gasser, *Semileptonic kaon decays* (1994) [arXiv:hep-ph/9411311].

[18] M. A. Ivanov and D. Melikhov, Phys. Rev. D **105**, 094038 (2022) [arXiv:2204.02792 [hep-ph]].

[19] D. Y. Bardin and E. A. Ivanov, Sov. J. Part. Nucl. **7**, 286 (1976).

[20] S. Okubo, Phys. Lett. **5**, 165 (1963).

[21] G. Zweig, *An $SU(3)$ model for strong interaction symmetry and its breaking. Version 2* in *Developments in the quark theory of hadrons. Vol. 1. 1964–1978*, pp. 22–101 (1964).

[22] J. Iizuka, Prog. Theor. Phys. Suppl. **37**, 21 (1966).

[23] P. Colangelo and A. Khodjamirian, *QCD sum rules, a modern perspective* in *At The Frontier of Particle Physics*, pp. 1495–1576 (2000) [arXiv:hep-ph/0010175].

[24] A. Khodjamirian, *Hadron Form Factors: From Basic Phenomenology to QCD Sum Rules*, CRC Press, Taylor & Francis Group, 2020.

[25] R. R. Horgan, Z. Liu, S. Meinel, and M. Wingate, Phys. Rev. D **89**, 094501 (2014) [arXiv:1310.3722 [hep-lat]].

[26] M. Zanke, M. Hoferichter, and B. Kubis, JHEP **07**, 106 (2021) [arXiv:2103.09829 [hep-ph]].

[27] P. A. Zyla *et al.* [Particle Data Group], PTEP **2020**, 083C01 (2020).

[28] R. Aaij *et al.* [LHCb], Eur. Phys. J. C **79**, 675 (2019) [arXiv:1812.06004 [hep-ex]].

[29] J. T. Daub, C. Hanhart, and B. Kubis, JHEP **02**, 009 (2016) [arXiv:1508.06841 [hep-ph]].

[30] S. Ropertz, C. Hanhart, and B. Kubis, Eur. Phys. J. C **78**, 1000 (2018) [arXiv:1809.06867 [hep-ph]].

[31] A. V. Danilina and N. V. Nikitin, Phys. Atom. Nucl. **81**, 347 (2018).

[32] X.-W. Kang, B. Kubis, C. Hanhart, and U.-G. Meißner, Phys. Rev. D **89**, 053015 (2014) [arXiv:1312.1193 [hep-ph]].

[33] C. Hanhart, A. Kupść, U.-G. Meißner, F. Stollenwerk, and A. Wirzba, Eur. Phys. J. C **73**, 2668 (2013) [arXiv:1307.5654 [hep-ph]], [Erratum: Eur. Phys. J. C **75**, 242 (2015)].

[34] S. Holz, C. Hanhart, M. Hoferichter, and B. Kubis, Eur. Phys. J. C **82**, 434 (2022) [arXiv:2202.05846 [hep-ph]], [Addendum: Eur. Phys. J. C **82**, 1159 (2022)].

[35] R. Mertig, M. Böhm, and A. Denner, Comput. Phys. Commun. **64**, 345 (1991).

[36] V. Shtabovenko, R. Mertig, and F. Orellana, Comput. Phys. Commun. **207**, 432 (2016) [arXiv:1601.01167 [hep-ph]].

[37] V. Shtabovenko, R. Mertig, and F. Orellana, Comput. Phys. Commun. **256**, 107478 (2020) [arXiv:2001.04407 [hep-ph]].

[38] H. H. Patel, Comput. Phys. Commun. **197**, 276 (2015) [arXiv:1503.01469 [hep-ph]].

[39] Y. Aoki *et al.* [Flavour Lattice Averaging Group (FLAG)], Eur. Phys. J. C **82**, 869 (2022) [arXiv:2111.09849 [hep-lat]].

[40] A. Bazavov *et al.* [TUMQCD, Fermilab Lattice, MILC], *B- and D-meson leptonic decay constants and quark masses from four-flavor lattice QCD* in *13th Conference on the Intersections of Particle and Nuclear Physics* (2018) [arXiv:1810.00250 [hep-lat]].

[41] A. Bussone *et al.* [ETM], Phys. Rev. D **93**, 114505 (2016) [arXiv:1603.04306 [hep-lat]].

[42] R. J. Dowdall, C. T. H. Davies, R. R. Horgan, C. J. Monahan, and J. Shigemitsu [HPQCD], Phys. Rev. Lett. **110**, 222003 (2013) [arXiv:1302.2644 [hep-lat]].

[43] C. Hughes, C. T. H. Davies, and C. J. Monahan, Phys. Rev. D **97**, 054509 (2018) [arXiv:1711.09981 [hep-lat]].

[44] D. Leljak, B. Melić, and D. van Dyk, JHEP **07**, 036 (2021) [arXiv:2102.07233 [hep-ph]].

[45] D. Becirevic, B. Haas, and E. Kou, Phys. Lett. B **681**, 257 (2009) [arXiv:0907.1845 [hep-ph]].

[46] G. P. Korchemsky, D. Pirjol, and T.-M. Yan, Phys. Rev. D **61**, 114510 (2000) [arXiv:hep-ph/9911427].

[47] S. Descotes-Genon and C. T. Sachrajda, Nucl. Phys. B **650**, 356 (2003) [arXiv:hep-ph/0209216].

[48] E. Lunghi, D. Pirjol, and D. Wyler, Nucl. Phys. B **649**, 349 (2003) [arXiv:hep-ph/0210091].

[49] S. W. Bosch, R. J. Hill, B. O. Lange, and M. Neubert, Phys. Rev. D **67**, 094014 (2003) [arXiv:hep-ph/0301123].

[50] A. G. Grozin and M. Neubert, Phys. Rev. D **55**, 272 (1997) [arXiv:hep-ph/9607366].

[51] M. Beneke, G. Buchalla, M. Neubert, and C. T. Sachrajda, Nucl. Phys. B **591**, 313 (2000) [arXiv:hep-ph/0006124].

[52] M. Beneke and T. Feldmann, Nucl. Phys. B **592**, 3 (2001) [arXiv:hep-ph/0008255].

[53] M. Gelb *et al.* [Belle], Phys. Rev. D **98**, 112016 (2018) [arXiv:1810.12976 [hep-ex]].

Synthesis

The standard model of particle physics has proven extremely successful in describing a plethora of phenomena at small length scales. However, besides its fundamental incompatibility with gravity, the existence of dark matter and the apparent matter–antimatter asymmetry in the universe are examples that give definite proof of its incompleteness. Naturally, any substantial extension of the standard model either needs to involve heavy or weakly coupled particles as experimental evidence from particle colliders remains scarce. There is further indication of physics beyond the standard model from so-called precision observables, which aim at scrutinizing the imprint of new physics on observables that either are strongly suppressed in the standard model or can be calculated to a very high precision within the theory. In this thesis, we discussed three different standard-model probes at the precision frontier: the anomalous magnetic moment a_μ of the muon, rare semileptonic $\eta^{(\prime)}$ decays, and $B \to \gamma^*$ transition form factors.

The longstanding tension between the experiment and the standard-model prediction for a_μ potentially hints at physics beyond the standard model. With the uncertainty on the standard-model value being dominated by hadronic contributions, efforts on the theoretical side are mostly concentrated on the improvement of the latter. Although the subprocess hadronic light-by-light scattering contributes with a comparably small central value, its uncertainty presently comes close to the one of hadronic vacuum polarization. Here, an important role is played by axial-vector mesons—so far evaluated with a Lagrangian model for the hadronic light-by-light tensor—since they are responsible for a large fraction of the current light-by-light uncertainty. In order to improve this situation, we performed a data-driven analysis of the axial-vector transition form factors—the relevant input quantities for a dispersive evaluation of a_μ—in Part I and its Addendum. Given the available data, the analysis is set up for the transition form factors of the f_1, and information on the entire triplet including the f_1' and a_1 is obtained under the assumption of U(3) symmetry.

In view of the intended dispersive application, we employed a decomposition of the $A \to \gamma^*\gamma^*$ amplitude into Lorentz structures and form factors free of kinematic singularities. Using this basis, we put forward various vector-meson-dominance parameterizations for the transition form factors, which primarily differ in their high-energy behavior, as motivated by the inclusion of distinct short-distance constraints from the light-cone expansion. To obtain a description of the form factors that is valid in the whole energy range, the vector-meson-dominance components were further complemented by asymptotic contributions from this expansion. For each of the proposed parameterizations, we performed a combined phenomenological analysis to extract information on the free parameters of the model. Our final result given in the Addendum to Part I consists of two sets of solutions for the coupling constants that emerge within the vector-meson-dominance framework.

Together, the form-factor parameterizations for the triplet of axial-vector mesons established in this thesis pave the way for a revised evaluation of the axial-vector contributions to a_μ. Here, the two scenarios of coupling constants following from our global fit serve as an estimate for the systematic uncertainty, and work is ongoing to determine their effect on the anomalous magnetic moment of the muon. Crucially, the dominant uncertainties of our result are of experimental origin; the process $f_1 \to e^+e^-$, especially, presently suffers from large error bands and needs experimental clarification, but the majority of the remaining data demands a revision as well. One naive leverage point to refine our analysis thus is the improvement of the existing experimental data or measurements of novel observables that entail additional constraints on the axial-vector transition form factors. While a full dispersive analysis does not seem feasible at the moment as it requires differential data on f_1 decays, it might become viable in the distant future. To go beyond the essential solicitation for improved data, it would furthermore be interesting to study the form factors by means of a completely different approach. Performing a calculation using, *e.g.*, a dynamic model instead of a data-driven analysis might, in particular, give further insight into the hierarchy of the three transition form factors of axial-vector mesons.

The semileptonic decays $\eta^{(\prime)} \to \pi^0\ell^+\ell^-$ and $\eta' \to \eta\ell^+\ell^-$, $\ell = e, \mu$, analyzed in Part II provide another probe of the standard model at the precision frontier. Due to the strong suppression of the corresponding decay rates within the standard model, they are considered rare processes, and any experimental signal conclusively deviating from the standard-model value would hint at new physics. Currently, experimental results are limited to upper bounds on the branching ratios, but the prospect of improved measurements from the REDTOP collaboration calls for updated high-precision calculations—thus far carried out under rather radical assumptions—with reasonable, conservative uncertainty estimates.

For our analysis, we constructed amplitudes for the respective semileptonic $\eta^{(\prime)}$ decays by assuming the underlying processes $\eta^{(\prime)} \to \pi^0\gamma^*\gamma^*$ and $\eta' \to \eta\gamma^*\gamma^*$ to be dominated by the exchange of vector mesons. The relevant $V \to P\gamma^*$ transitions were modeled in terms of a set of form factors, for which we proposed numerous vector-meson-dominance parameterizations. In essence, these variants differ in the assumptions about their high-energy behavior, with the normalizations and relative signs determined from phenomenological input and U(3) symmetry. Using the established framework, we calculated singly- and doubly-differential decay widths as well as integrated branching ratios for both the semileptonic and the two-photon decays. Our results for the former demonstrated that the Dalitz plots exhibit a non-flat behavior and that the additional, non-trivial momentum dependence of the vector-to-pseudoscalar transition leads to a significant decrease in the decay rates; the precise parameterization of this dependence was found to be of secondary importance, however. To go beyond the vector-meson-dominance model, we also analyzed S-wave rescattering effects for $\eta \to \pi^0\ell^+\ell^-$, which were found to be negligible.

The semileptonic $\eta^{(\prime)}$ decays investigated in this thesis are considered promising candidates to search for a host of effects beyond the standard model, including

- a tree-level contribution to the processes from a C- and CP-violating one-photon exchange. Given the loop- and coupling-induced suppression of the symmetry-conserving two-photon mechanism, such a contribution has the potential to produce branching ratios that exceed those from within the standard model. Since our analysis showed that the relative standard-model background is even smaller than priorly estimated, the scenario of observing a discernable excess seems yet more likely than

before; here, our results obtained with the different models allow one to assess the systematic uncertainty. While the C-conserving and C-violating mechanisms do not interfere at the level of decay rates, they can lead to an asymmetry in the DALITZ plots, which, in fact, gains in sensitivity if both contributions are of comparable size. The differential distributions provided in this thesis are to nurture the endeavor of corresponding measurements, illustrating that the flat behavior that was previously assumed for the DALITZ plots yields an insufficient description.

- Another source of new physics that can be probed with the discussed $\eta^{(\prime)}$ decays is the simultaneous violation of P and CP. Similar to the violation of C described above, signals of this type can manifest themselves in interference patterns, where the violation of P requires an analysis of polarization observables instead of differential decay distributions. Not only are these quantities more difficult to measure, but the P-violating mechanism underlies stringent bounds from studies on the neutron's electric dipole moment, which renders these effects less favorable to search for physics beyond the standard model. Still, the formalism established in this thesis provides the means to calculate the standard-model contribution to the implied polarization observables, which would be useful for the interpretation of prospective measurements.

- The decays $\eta^{(\prime)} \to \pi^0\ell^+\ell^-$ and $\eta' \to \eta\ell^+\ell^-$ can further be used to search for new light scalar particles; detecting these weakly coupled particles requires the identification of resonance structures in the corresponding lepton–lepton spectra. Although such degrees of freedom could additionally violate the symmetries of the standard model, they may also emerge as symmetry-conserving features, *e.g.*, a HIGGS-like scalar.

There are further effects beyond the standard model that can be tested with the semileptonic $\eta^{(\prime)}$ decays considered in this thesis, *e.g.*, the simultaneous violation of C and P together with CP. Moreover, the two-photon decays $\eta^{(\prime)} \to \pi^0\gamma^*\gamma^*$ and $\eta' \to \eta\gamma^*\gamma^*$ themselves provide an excellent playground to scrutinize new physics.

In Part III, we investigated $B \to \gamma^*$ form factors in the context of the four-lepton decay $B^- \to \ell^-\bar{\nu}_\ell\ell'^-\ell'^+$, $\ell = e, \mu, \tau$, $\ell' = e, \mu$. Besides entailing valuable information on the leading-twist B-meson light-cone distribution amplitude through the transition form factors, the four-lepton decay also qualifies as a candidate for performing precision tests of the standard model. While we utilized a vector-meson-dominance ansatz for the phenomenological analysis in this thesis, the developed framework is based on dispersive methods and, as such, provides the foundation for more sophisticated future analyses.

To construct an amplitude for the process $B^- \to \ell^-\bar{\nu}_\ell\ell'^-\ell'^+$, we first studied the decay $B^- \to \ell^-\bar{\nu}_\ell\gamma^*$, improving on previous results from the literature by retaining the effects from non-zero lepton masses. The deduced amplitude was decomposed into LORENTZ structures and form factors free of kinematic singularities, with the latter parameterized in terms of a series expansion in a conformal variable and the momentum dependence of the virtual photon being incorporated under the assumption of vector-meson dominance. By establishing a set of dispersion relations for the transition form factors, we determined the free parameters of our model using available input from the literature. As a phenomenological application of our formalism, we calculated integrated branching ratios and forward–backward asymmetries for $B^- \to \ell^-\bar{\nu}_\ell\ell'^-\ell'^+$, for both $\ell \neq \ell'$ and $\ell = \ell'$, as well as the corresponding differential distributions for the case of distinct lepton flavors.

The theoretical predictions for the decay $B^- \to \ell^- \bar{\nu}_\ell \ell'^- \ell'^+$ provided in this thesis can be confronted with experimental measurements from, *e.g.*, the Belle II and the LHCb experiment to probe our understanding of the standard model. Currently, though, there exists only a single measurement for this process, which sets an upper limit for the branching ratio of the identical-lepton channel $B^- \to \mu^- \bar{\nu}_\mu \mu^- \mu^+$. Improving this measurement and determining a central value is a crucial step to stimulate further progress at this frontier, but experimental analyses of the other channels—preferably also for the case of distinct lepton flavors—are needed likewise. As soon as the experimental results attain a sufficiently high precision, our formalism can be refined by, *e.g.*,

- including additional contributions from the ϕ meson and other—excited—states in our vector-meson-dominance framework. Such an extension requires non-perturbative input on, *inter alia*, $B \to \phi$ form factors—as relevant for $B^- \to \ell^- \bar{\nu}_\ell \phi$—which is presently lacking; the determination of these form factors would thus also prove advantageous for a better understanding of the $B \to \gamma^*$ analogs.

- Additionally, the resonant contribution from the ρ meson could be replaced by a dispersive description in terms of the two-body intermediate state $\pi\pi$, for which the formalism developed in this thesis is an essential requirement. However, this refinement necessitates currently unavailable input on $B \to \pi\pi$ form factors—as pertinent to $B^- \to \ell^- \bar{\nu}_\ell \pi^- \pi^+$; here, too, one could thus leverage the knowledge on the $B \to \pi\pi$ transition to improve one's understanding of $B \to \gamma^*$ form factors.

The $B \to \gamma^*$ form factors can further be used to extract information on the leading-twist B-meson light-cone distribution amplitude by comparing with predictions from collinear-factorization approaches. Here, our dispersive framework allows for the transfer of information from the region of time-like photon momenta—as accessible experimentally or by studying quantum chromodynamics on the lattice—to the space-like region; in this way, the sensitivity to the extracted parameters is enhanced because the contamination from soft contributions within the collinear-factorization approaches is reduced.

Acknowledgements

First and foremost, I want to express my deepest gratitude to my supervisor Bastian Kubis for his continuous support throughout my studies. Bastian truly showed outstanding insight in proposing interesting problems to investigate and his explanations were always on point. Not once have I felt forsaken in dealing with the many hurdles that need to be overcome in the process of writing a dissertation, whether they were of scientific or organizational nature. But it does not end there: Bastian was a great mentor in many other areas as well, ranging from his extraordinary grammar knowledge to his expertise on how to convince others of your ideas. I am also very grateful to Christoph Hanhart, the co-examiner of this thesis, who, in large part together with Bastian, lectured many of my undergraduate and graduate courses. The pedagogical structure of their lectures provided me with an excellent foundation for a career in research as well as vital teaching skills, and the intuitive approach of Christoph to solving problems was a major source of inspiration. In addition, I thank Florian Bernlochner and Marc Alexander Schweitzer for agreeing to be the third and fourth members of the doctoral committee, respectively.

Furthermore, I want to thank Martin Hoferichter for teaching me various concepts and methods utilized in this thesis as well as the opportunity to give a talk at the "Sixth Plenary Workshop of the Muon $g-2$ Theory Initiative" in Bern, Switzerland. Working with Martin was very demanding but incredibly effective and instructive; the vast knowledge that Martin has in a broad range of fields is fascinating and the ideas he comes up with enrich the scientific community. Moreover, I am thankful to Danny van Dyk for many useful discussions and the opportunity to give a talk at the "Quirks in Quark Flavor Physics" workshop in Zadar, Croatia. The work with Danny was characterized by a casual and friendly atmosphere, which led to many fun and memorable moments.

Many thanks also to my colleagues at the HISKP, in particular the research group of Bastian, whom I shared many relaxing lunch breaks with. The friendly atmosphere in the institute made work enjoyable to the point that I cannot recall a day of not looking forward to going to the office. Over the years, I benefitted from many enlightening discussions with Hakan Akdag, Yannis Korte, Malwin Niehus, and Dominik Stamen from office 2.018 as well as with my third-floor mates Simon Holz, Jonathan Lozano de la Parra, and Fabian Müller during coffee breaks. Furthermore, I enjoyed great chats with Melisa Akdag, Gio Chanturia, Luca Dammann, Leon Heuser, Bai-Long Hoid, Tobias Isken, Stephan Kürten, Philip Lüghausen, Simon Mutke, Miriam Penners, Stefan Ropertz, Hannah Schäfer, Dominic Schuh, and Maximilian Zillinger. I want to express my particular gratitude to Yannis, Stephan, and Hannah, whom I was lucky enough to collaborate with in two very challenging projects. Moreover, I am very grateful to Bernard Metsch, who lectured many courses throughout my studies and played an important role in sparking my interest in theoretical physics. Together with Andreas Nogga, he further was of great help when it came to IT-related questions. Regarding organizational topics, I want to thank Heike Frömbgen-Penkert, Barbara Kraus, and Lara Lagemann.

Last but certainly not least, I am indebted to my parents, Rüdiger and Gudrun, for everything they have done for me. Thank you for raising me to become the person I am today and for teaching me desirable values to stand up for. Thank you for dedicating great parts of your life to this occasionally tedious task and for believing in me, also in testing times. If it were not for your financial and emotional support, writing a dissertation would have been beyond reach for me.

Financial support by the DFG through the funds provided to the Sino–German Collaborative Research Center TRR110 “Symmetries and the Emergence of Structure in QCD” (DFG Project-ID 196253076 – TRR 110) is gratefully acknowledged. Moreover, the author gratefully acknowledges the granted access to the bonna cluster hosted by the University of Bonn along with the support provided by its High Performance Computing & Analytics Lab.

Glossary

Acronyms

BL	Brodsky–Lepage
BSM	beyond the standard model
BTT	Bardeen–Tung–Tarrach
BW	Breit–Wigner
CKM	Cabibbo–Kobayashi–Maskawa
EM	electromagnetic
FB	forward–backward
FSR	final-state radiation
HLbL	hadronic light-by-light
HVP	hadronic vacuum polarization
LCDA	light-cone distribution amplitude
LCE	light-cone expansion
LCSR	light-cone sum rule
OPE	operator product expansion
OZI	Okubo–Zweig–Iizuka
PDG	Particle Data Group
PV	Passarino–Veltman
QCD	quantum chromodynamics
QED	quantum electrodynamics
SCET	soft-collinear effective theory
SM	standard model
TFF	transition form factor
VMD	vector-meson dominance
WET	weak effective theory

Particles

$\boldsymbol{a_1}$	$a_1(1260)$
$\boldsymbol{a_2}$	$a_2(1320)$
$\boldsymbol{f_1}$	$f_1(1285)$
$\boldsymbol{f_1'}$	$f_1(1420)$
$\boldsymbol{\phi}$	$\phi(1020)$
$\boldsymbol{\phi'}$	$\phi(1680)$
$\boldsymbol{\phi''}$	$\phi(2170)$
$\boldsymbol{\eta'}$	$\eta'(958)$
$\boldsymbol{K^*}$	$K^*(892)$
$\boldsymbol{\rho}$	$\rho(770)$
$\boldsymbol{\rho'}$	$\rho(1450)$
$\boldsymbol{\rho''}$	$\rho(1700)$
$\boldsymbol{\omega}$	$\omega(782)$
$\boldsymbol{\omega'}$	$\omega(1420)$
$\boldsymbol{\omega''}$	$\omega(1650)$

Foundations index

Fin